SCHOLARLY PUBLICATIONS

A CURRENT AWARENESS BULLETIN
OF RESEARCH OUTPUT

@DTU

(51st Edition)

MARCH 2017

BY: CENTRAL LIBRARY

DELHI TECHNOLOGICAL UNIVERSITY
(FORMERLY *DELHI COLLEGE OF ENGINEERING)*
GOVT. OF N.C.T. OF DELHI
SHAHBAD DAULATPUR, MAIN BAWANA ROAD
DELHI 110042

PREFACE

This is the **Fifty first** Issue of Current Awareness Bulletin started by Delhi Technological University, Central Library. The aim of the bulletin is to compile, preserve and disseminate information published by the faculty, students and alumni for mutual benefits. The bulletin also aims to propagate the intellectual contribution of Delhi Technological University (DTU) as a whole to the academia.

The bulletin contains information resources available in the internet in the form of articles, reports, presentations published in international journals, websites, etc. by the faculty and students of DTU. The publications of faculty and student which are not covered in this bulletin may be because of the reason that the full text either was not accessible or could not be searched by the search engine used by the library for this purpose.

The learned faculty and students are requested to provide their uncovered publications to the library either through email or in CD, etc to make the bulletin more comprehensive.

This issue contains the information published during **March 2017**. The arrangement of the contents is alphabetical. The full text of the article which is either subscribed by the university or available in the web is provided in this bulletin.

Central Library

CONTENTS

1. Analyzing alternatives for Green Logistics in an Indian automotive organization: a case study, ***6.Deepti Chhabra***, ***3.S. K. Garg*** and Rajesh Kr Singh, Mechanical, DTU

2. Cardiotocography Analysis Using Conjunction of Machine Learning Algorithms, ***8.Anish Batra***, ***6.Ananya Chandra*** and Vishal Matoria, Mathematics and Computing, DTU

3. Characteristics and Properties of Different Reinforcements in Hybrid Aluminium Composites: A Review,***7.Ravi Butola, 3.Ranganath M.Singari, 8.Ashwani Bandhu*** and ***6.R S Walia***, Production and Industrial, DTU

4. Comparative analysis of metabolic network of pathogens, ***7.Kumar Gaurav*** and ***3.Yasha Hasija***, Biotechnology, DTU

5. Detection and classification of multiple power signal patterns with Volterra series and interval type-2 fuzzy logic system, ***Rahul, 3.Rajiv Kapoor*** and ***3.M. M. Tripathi***, Electronics & communication, DTU

6. Development and Characterization of a Diaphragm-Shaped Force Transducer for Static Force Measurement, R. Kumar, B. D. Pant and ***3.S. Maji***, DTU

7. Different Tool coatings: An Overview, ***3.Navriti Gupta*** and ***3.Ranganath M. Singari***, Mechanical Engineering, DTU

8. Effect of Machining Parameters on Cutting Force , Tool Wear and Surface Roughness of AISI 304 Austenitic Stainless Steel – A Review, ***6.Md Jamil Akhtar, 6.Md. Gulam Mustafa, 3.Ranganath M. Singari, 6.Shadab Ahmad*** and ***6.Parvesh Ali***, DTU

9. Enhancement of Ancient Manuscript Images by Log based Binarization Technique, ***3.Jayanthi Natarajan*** and ***3.Dr.Sreedevi Indu***, Electronics and Communication, DTU

10. Fish Species Classification using Graph Embedding Discriminant Analysis, ***8.Snigdhaa Hasija, 8.Manas Jyoti Buragohain*** and ***3.Dr. S. Indu***, ECE, DTU

11. Grid Interfaced Distributed Generation System with Modified Current Control Loop Using Adaptive Synchronization Technique, A. B. Shitole, H. M. Suryawanshi, ***7.1.G. G. Talapur,*** Shelas Sathyan, M. S. Ballal, V. B. Borghate, M. R. Ramteke and M. A. Chaudhari, Electrical, DTU

12. Implementation of Echo-State Network Based Control for Power Quality Improvement, Manoj Badoni, Bhim Singh and ***3.Alka Singh***, Electrical, DTU

13. Influence of Aliphatic and Aromatic Isocyanates on the Properties of Polyether-Ester Polyol Based PU Adhesive System, ***6.Manjeet Malik*** and ***3.Raminder Kaur***, Applied Chemistry & Polymer Technology, DTU

14. Influences of Process Parameter and Microstructural Studies in Friction Stir Welding of Different Alloys: A Review, ***6.Husain Mehdi*** and ***3.R.S. Mishra,*** Mechanical, DTU

15. INNOVATION PRACTICES IN SME –A REVIEW, Piu Jain and ***3.Prof S.K Garg***, Mechanical, DTU

16. Investigation of parasitic capacitances of In2O5Sn gate electrode recessed channel MOSFET for ULSI switching applications***, 6.Ajay Kumar[1], 3.M. M. Tripathi[1]*** and ***3.Rishu Chauja[2],*** [1]Electrical and [2]Physics, DTU

17. Non-human Looking Robot Arms Induce Illusion of Embodiment, Laura Aymerich-Franch, Damien Petit, ***8.1.Gowrishankar Ganesh*** and Abderrahmane Kheddar, DTU

18. Non-invasive oil based method to increase topical delivery of nucleic acids to skin, Manika Vij, Shamshad Alam, ***6.Nidhi Gupta***, Vishvabandhu Gotherwal, Hemlata Gautam, Kausar M. Ansari, ***3.Deenan Santhiya***, Vivek T. Natarajan and Munia Ganguli, DTU

19. Numerical Simulation of N+ Source Pocket PIN-GAA-Tunnel FET: Impact of Interface Trap Charges and Temperature, ***6.Jaya Madan*** and ***3.Rishu Chaujar***, Applied Physics, DTU

20. On Improving the Performance of Dynamic DCVSL Circuits, ***7.1.Pratibha Bajpai***, ***3.Neeta Pandey***, Kirti Gupta, Shreya Bagga and ***3.Jeebananda Panda***, ECE, DTU

21. Optimisation of Cutting Parameters on Surface Roughness in Turning: A Review, ***7.Yashwant Koli***, ***8.1.Prashant Kumar Singh***, ***3.Vipin*** and ***3.Ranganath M. S***., Mechanical Engineering, DTU

22. Quantum Transport in Two-Dimensional Group-IV monolayers and Topological Insulators, ***8.Gaurav Gupta*** and Liang Gengchiau, Electrical and Computer, DTU

23. REVIEW ON PRODUCTION OF BIODIESEL FROM TRANSESTERIFICATION, Deepak Verma, Janmit Raj, ***3.Amit Pal*** and Manish Jain, Mechanical, DTU

24. Role of cellulose functionality in bio-inspired synthesis of nano bioactive glass, ***6.Nidhi Gupta*** and ***3.Deenan Santhiya***, ACPT, DTU

25. Single NUV Band Pumped PbO-GeO2-TeO2:Tb3+ Yellowish Green Emitting Glass Material for Tricolor White LEDs, ***3.M. Jayasimhadri***, ***6.Kaushal Jha***, B.V. Ratnam, Hyun-Joo Woo, Kiwan Jang, ***3.A.S. Rao***, D. Haranath, Luminescent Materials Research Lab, DTU

26. Software Defined Millimeter Wave 5th Generation Communications System, S. K. Agrawal and ***3.Dr. Kapil Sharma,*** Computer Science, DTU

27. Spectroscopic and Photoluminescence Characteristics of Sm3+ doped Calcium Aluminozincate Phosphor for Applications in w-LEDs ***6.Sumandeep Kaur***, ***3.A.S.Rao*** and ***3.M. Jayasimhadri***, Applied Physics, DTU

28. Spectroscopic studies of Pr3+ doped lithium lead alumino borate glasses for visible reddish orange luminescent device applications, ***6.Nisha Deopa***, ***3.A.S. Rao***, Sk. Mahamuda, Mohini Gupta, ***3.M. Jayasimhadri***, D. Haranath and G. Vijaya Prakash, Applied Physics, DTU

29. Study of Compilation and Heap Tuning Parameters across Virtual Machines for the Application Performance Improvements, ***7.Vijayanand Kumar***, Ankit Babbar, Vikas Kala, Mudit Khare and Amitesh Anand, Computer Science, DTU

30. Synthesis and Wear Behaviour of (Al, Cu)3Ti Powder Blend by Mechanical Alloying, Shailesh Kumar Singh, Satyajeet Kumar, Jay Shankar kumar, Sitikantha Behera and ***3.Shailesh Mani Pandey***, mechanical Engineering, DTU

31. Thermoelectric silicides: A review, Amin Nozariasbmarz, ***8.1.Aditi Agarwal***, Zachary A. Coutant, Michael J. Hall, Jie Liu, Runze Liu, Abhishek Malhotra, Payam Norouzzadeh, Mehmet C. Öztürk, Viswanath P. Ramesh, Yasaman Sargolzaeiaval, Francisco Suarez and Daryoosh Vashaee, Electrical and Computer Engineering, DTU

1. *Chancellor*

2. *Pro Vice Chancellor* ***2.1.*** *Ex Pro Vice Chancellor*

3. *Faculty* ***3.1.*** *Ex Faculty*

4. *Teaching-cum-Research Fellow* ***4.1.****Asst. Librarian*

5. *Alumni*

6. *Research Scholar* ***6.1.*** *Ex Research Scholar*

7. *PG Scholar* ***7.1.*** *Ex PG Scholar*

8. *Undergraduate Student* ***8.1.*** *Ex Undergraduate Student*

Accepted Manuscript

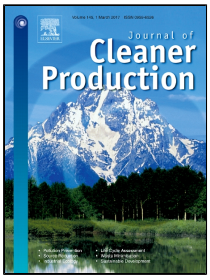

Analyzing alternatives for Green Logistics in an Indian automotive organization: a case study

Deepti Chhabra, S.K. Garg, Rajesh Kr Singh

PII:	S0959-6526(17)30384-0
DOI:	10.1016/j.jclepro.2017.02.158
Reference:	JCLP 9084
To appear in:	*Journal of Cleaner Production*
Received Date:	27 March 2016
Revised Date:	21 February 2017
Accepted Date:	22 February 2017

Please cite this article as: Deepti Chhabra, S.K. Garg, Rajesh Kr Singh, Analyzing alternatives for Green Logistics in an Indian automotive organization: a case study, *Journal of Cleaner Production* (2017), doi: 10.1016/j.jclepro.2017.02.158

This is a PDF file of an unedited manuscript that has been accepted for publication. As a service to our customers we are providing this early version of the manuscript. The manuscript will undergo copyediting, typesetting, and review of the resulting proof before it is published in its final form. Please note that during the production process errors may be discovered which could affect the content, and all legal disclaimers that apply to the journal pertain.

ACCEPTED MANUSCRIPT

Highlights

- Analysis of alternatives using AHP for green practices in Indian context is proposed.
- Green efficiency, factor of safety and ease of operation are the criteria used.
- Paper provides guidelines for sustainable adaptation of green practices.

ACCEPTED MANUSCRIPT

ACCEPTED MANUSCRIPT

Analyzing alternatives for Green Logistics in an Indian automotive organization: a case study

Deepti Chhabra
Research Scholar, Mechanical Engineering Department
Delhi Technological University, Delhi, India
Email: deepti 2226@gmail.com

Prof. S. K. Garg
Professor and Pro -Vice Chancellor
Delhi Technological University, Delhi, India
Email: skgarg63@yahoo.co.in

Dr. Rajesh Kr Singh
Professor, Operations Management Area
Management Development Institute, Gurgaon, India
Email: rksdce@yahoo.com

Abstract

Green logistics is an important aspect of production system in today's world. It combines various efforts to quantify and control the environmental effect of production activities in an enterprise. This research is intended to emphasize upon the ways by which organizations can accomplish positive ecological effects simply by modifying their logistics practices. This paper presents a case study of an Indian automobile company by analyzing alternatives for green practices along with organizational objectives. It is imperative to focus on the green practices in context of Indian automobile sector as the volume of vehicles in India has increased considerably during last few decades. Accordingly, this paper attempts to improve the performance for sustainable adaptation of green practices of an Indian company by selecting the best alternative obtained from the use of Analytical Hierarchy Process to analyze alternatives for green practices in the assembly and packaging processes. Alternatives have been evaluated on the basis of three criteria i.e. green efficiency, factor of safety and ease of operation. The study revealed that clinch joint is the most appropriate alternative for assembly operation while carbon positive packaging material is the best alternative for packaging.

ACCEPTED MANUSCRIPT

ACCEPTED MANUSCRIPT

Keywords: Green production, Green Logistics, Analytical Hierarchy Process, Green Packaging, Green Assembly.

ACCEPTED MANUSCRIPT

ACCEPTED MANUSCRIPT

Analyzing alternatives for Green Logistics in an Indian automotive organization: a case study

Abstract

Green logistics is an important aspect of production system in today's world. It combines various efforts to quantify and control the environmental effect of production activities in an enterprise. This research is intended to emphasize upon the ways by which organizations can accomplish positive ecological effects simply by modifying their logistics practices. This paper presents a case study of an Indian automobile company by analyzing alternatives for green practices along with organizational objectives. **It is imperative to focus on the green practices in context of Indian automobile sector as the volume of vehicles in India has increased considerably during last few decades. Accordingly, this paper attempts to improve the performance for sustainable adaptation of green practices of an Indian company by selecting the best alternative obtained from the use of Analytical Hierarchy Process to analyze alternatives for green practices in the assembly and packaging processes.** Alternatives have been evaluated on the basis of three criteria i.e. green efficiency, factor of safety and ease of operation. The study revealed that clinch joint is the most appropriate alternative for assembly operation while carbon positive packaging material is the best alternative for packaging.

Keywords: Green production, Green Logistics, Analytical Hierarchy Process, Green Packaging, Green Assembly.

1. Introduction

Due to the global economic growth and worldwide network of supply chains, the logistics network has become more complex and distantly located. Larger distances covered in the transportation tend to increase emissions, resulting in larger environmental problems. The term "Green logistics" is related to planning, controlling and implementing the flow of logistics by incorporating modern logistics techniques with an aim to minimize the environmental hazards (Chang and Qin, 2008). This flow of logistics should also achieve the satisfaction of the customers as well as the organization goals along with the aim of reducing the effect of these activities on the environment (Rodrigue et al., 2001). In this view, green logistics is the ability of the organization to deliver products and services in an environmental friendly way along with the economic efficiency. Green logistics also refers to the ability of

ACCEPTED MANUSCRIPT

an organization to preserve resources, decrease waste, increase working efficiency, and fulfil the societal requirement for ecological fortification (Lai and Wong, 2012). The domain of green logistics and production can be illustrated as practices that focus mainly on the reduction of the environment related problems such as greenhouse gas emissions during manufacturing operations, issues pertaining to noise, accidents etc. Sbihi and Eglese (2007) defined green logistics as a sustainable approach to produce and distribute goods by taking environmental and social factors in consideration. The concept of green logistics can also be useful in defining sustainability in environmental, economic and social terms (Lozano, 2012). It is important to have a balance between preservation of the environment, prosperity and the quality of life while implementing triple bottom-line approach. Firms can exploit the advantages of efficiency improvement and several other benefits such as market shares and increased profit by the introduction of green concept in the logistics systems (Rao and Holt, 2005). Green logistics highlights various practices followed to reduce the environmental problems of logistics operations, specially related to greenhouse emissions, transportation, packaging, noise pollutions and to achieve sustainability among economy, environment and society (Lai and Wong, 2012). Green logistics issues are gaining interest due to its relevance in today's highly competitive environment. Due to the evolving environmental awareness and regulations in the early 1990s, many companies decided to supplement the green element to their supply chain management policies (Wu and Dunn, 1995).

The research on green logistics is still in the preliminary stage. Literature clearly indicates that the social and economic relevance of green logistics was first highlighted in 1990 (Srivastava, 2007). Various environmental requirements and practices such as transportation, warehousing, inventories, packaging have been discussed by various authors in the past (Singh et al., 2012; Singh, 2011, Wu and Dunn, 1995; Carter and Dresdner, 2001; Bowen et al., 2001; Zhu and Sarkis, 2004; Sheu et al., 2005; Ebinger et al., 2006). Authors such as Dey et al. (2011), Rao and Holt (2005) and Porter and Vanderlinde (1995) have presented different researches on the sustainability and environmental considerations in the firms to decrease risks and to recover the competitive state of the firm. To justify that ecological performance of venders has an impact on the green performance of a firm, authors such as Ates et al. (2012) and Vachon and Klassen (2006) have studied the ecological investment decisions and the collaboration actions with suppliers in relation with logistics. In an innovative study presented by Palanivelu and Dhawan (2011), a number of green warehouses with minimum emission were discussed. These warehouses can be made by equipping energy

ACCEPTED MANUSCRIPT

saving equipment, using solar installations. In another work by Iakovou et al. (2010), an analytical model was proposed to investigate the economic and environmental effect of locating a part of manufacturing operations near markets. Abduaziz et al. (2015) have discussed that logistics in an automobile industry involves the integration of manufacturing operations, assembly operations, and distribution activities. They also proposed a simulation model for the assessment of green logistics activities in automobile Industry to assist managers and decision makers obtain an in-depth understanding of green logistics and its environmental impacts. Green logistics in automotive industry focus on reducing the harmful greenhouse gases and optimal utilization of energy as discussed by Abduaziz et al.(2015). In a recent study by Lu and Geng (2015), an industrial transformation model and implementation of green manufacturing were suggested to reduce harmful environmental emissions. These emissions can pose serious threats to anthropological health and the environment. Numbers of cases are found in the literature to show the successful implementation of green logistics. One of such studies is presented by Ubeda et al. (2011) who successfully depicted that the green logistics practices can be implemented without compromising with performance of an enterprise. It is also true that the most of the manufacturing enterprises cannot afford the high acceptance costs of considering green concepts in the logistics. Enterprises are also devising modern methods of prioritizing customers' demands based on least negative environmental impact (Niesten and Lozano, 2015). This will also involve various stakeholders along with environment towards the improvement of organization's sustainability (Lozano, 2012a). Under the domain of green logistics, green packaging is another important issue which has been given importance in the literature. Authors, such as Zhang and Zhao (2012), emphasized upon the role of government in development of new and innovative green packaging materials. They also suggested to standardize the packaging materials with the active participation of government and established institutions. Some efforts regarding the minimization of waste weight by reducing packaging volume were also discussed in the literature (Palanivelu and Dhawan, 2011). It was found that the packaging corresponds to 23% of all waste weight. It is also found that the reduced packaging saves the environment as all packages have to be transported among retailers and waste processor.

Indian manufacturing enterprises involve in large scale production, storage and transportation of various products, therefore creating large environmental problems. Today, the top environmental concern is global warming often associated with the large scale emissions of

ACCEPTED MANUSCRIPT

greenhouse gasses from factories especially in manufacturing sector. Various eco-societies, Government bodies, and companies are raising their concerns to deal with this threat. Green manufacturing initiatives are implemented for improving economic and environmental performance (Rehman et al., 2016). Green practices also helps in balancing cost and environmental aspects. It is not very uncommon to observe that the reduced emissions can be possible with only a marginal cost increase (Zhanga and Zhaob, 2012; Pazirandeh and Jafari, 2013; Kim et al., 2009). Keeping in mind the contribution of manufacturing sector in the growth of Indian economy, authors feel the need of research to motivate these enterprises towards adapting the procedures of green logistics in the greater interest of the global ecological framework. It is also evident that the most of manufacturing enterprises are not very rich in resources and majority of these are located in distant places from the target markets. In view of this, Indian manufacturing enterprises need to implement ecologically managed and environmentally sustainable logistics practices for devising strategies for cost-effective management of environmental issues. Therefore, it is important to examine the situations under which green operations are beneficial for Indian manufacturing enterprises, so that it does not result in higher green costs resulting overall loss. It is clear from the literature that most of the research on the green logistics is based on exploring and reducing the ecological impact of various industrial emissions in non-Indian context (Geerlings and Van Duin, 2011; McKinnon, 2007; Aronsson and Huge Brodin, 2006; McKinnon, 2003). Therefore, this research is aimed to cater the Indian manufacturing scenario by evaluating available alternatives to green packaging and green production thus to justify the adaptation using analytical hierarchy process (AHP) through a case study. The AHP approach has been used to select the suitable alternatives in terms of green initiatives for assembly and packaging operations in an automobile company.

The main objectives of this study are:

- Studying assembly and packaging operations in context to automotive organizations.
- Finding ways to make the above processes environment friendly i.e. implementing the green initiatives without sacrificing the efficiency and economy of the organization.
- Evaluating all alternatives on the basis of cost (Benefit-cost analysis).

The remainder of the paper is organized as follows. Section 2 gives the description and profile of the Case Company. Section 3 gives the description of the approach and framework

ACCEPTED MANUSCRIPT

followed in the paper. Section 4 underlines results and appropriate discussion. Finally, conclusion and future scope are presented in Section 5.

2. Profile of Organization

XYZ Pvt. Ltd. is a 100% subsidiary of a Japanese automobile company, which is a leading name in automobile industry across the globe. It is one of the major two wheeler manufacturers in the world. It is manufacturing a wide variety of products in automobile and power sectors. XYZ Ltd. is engaged in manufacturing of two wheelers in India since March 2001. The factory is spread over 210,000 sq. Meters with a covered area of about 102,808 sq. meters (49 %) at Manesar in Gurgaon district of Haryana (Delhi-NCR), India. The current installed capacity is 1,647,000 two wheelers per year, which accounts for 675,000 scooters & 972,000 motorcycles. The total investment outlay is INR 3000 million. In-house facilities consists of gravity die-casting, steel and aluminum machining, heat treatment, press and fabrication shop, paint shop, frame assembly and engine assembly. Schematic presentation of different functions of XYZ Ltd is shown in figure 1.

Manufacturing process at XYZ Company involves three main stages:

1. Frame manufacturing
2. Engine manufacturing
3. Final assembly and Packaging

The first stage is the frame manufacturing. The material for frame is processed in this stage and processing is done on the frame. The material pass through various shops like press shop, die casting and machining shop. After this stage the semi processed frame is sent to the engine assembly where the engine is assembled in the weld and assembly shop. The third stage is the final assembly and packaging, various components manufactured and processed earlier are assembled in this stage. Packaging of the final product is also done at this stage.

The firm realizes that the environment protection is an important concern. XYZ Company through its industrial activities is focusing on the conservation of environment and thus improving the future of our planet.

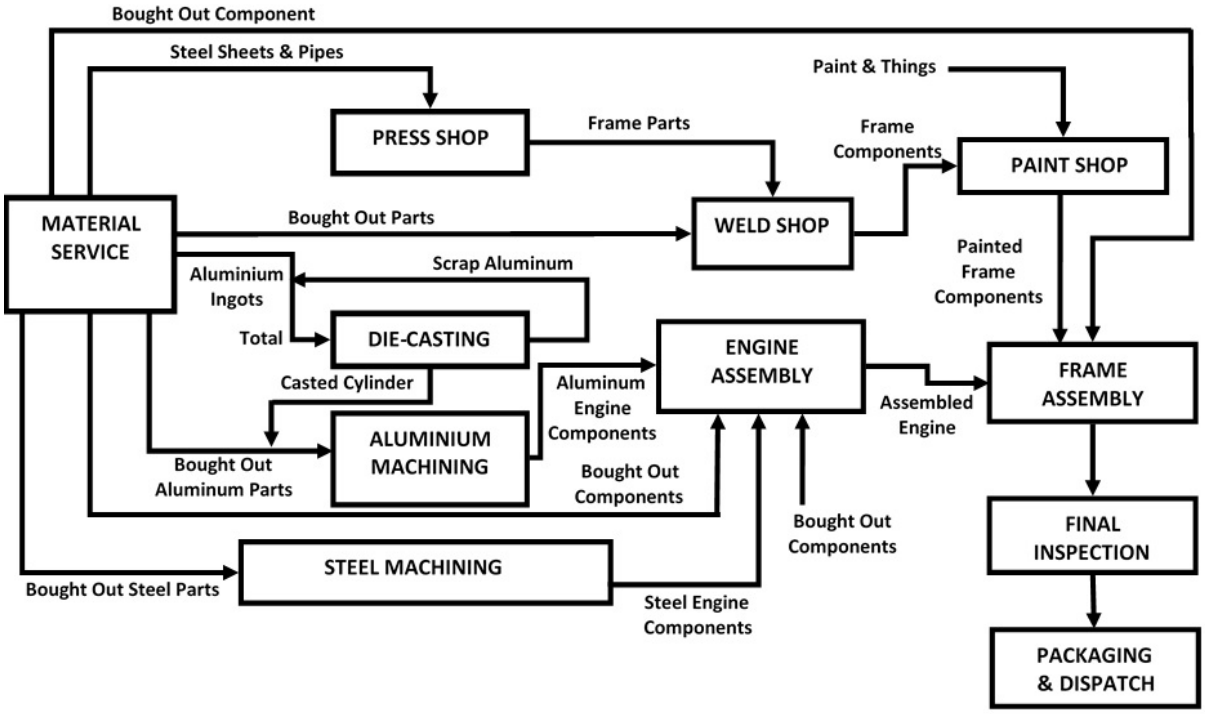

Figure – 1 In-house facilities at XYZ Pvt. Ltd. (Source – Discussion with XYZ Ltd)

The following are the guidelines which company follows in daily operations:

- It shall work towards economizing energy, resources and recycling raw materials at each stage of life cycle of waste, research, development, production, sales and service of goods.
- It shall endeavor to minimize the volume of pollutants and waste material generated at each stage of life cycle of goods and work towards their proper disposal.
- Being as members of industry and society, it recognizes that it is important to work towards the conservation of environment and well-being of humans.
- It shall analyze the influence of industrial activity on the people's health and environment and endeavor to get good image from the society.

XYZ Ltd has led the way in developing environment friendly technologies and developing green factory concept. This case study is focused primarily on the implementation of green strategies in the assembly and packaging processes of the supply chain. Following section will provide the overview of the approach followed for deciding alternatives during this study.

3. Development of framework for selection of alternatives

In this paper, the analytic hierarchy process (AHP) is used to select the suitable green alternatives for assembly and packaging operations in an automobile company. AHP is a

ACCEPTED MANUSCRIPT

method developed by Saaty (1980) to solve complex, multi factor and unstructured real life problems. Managers use AHP in various strategic and tactical decision making situations such as selecting vendors, selecting optimal plant layout and location, choosing suitable technology, designing products etc. (Subramanian and Ramanathan, 2011). This section presents the development of framework for selecting environmental friendly alternatives. The proposed framework is explained in the following subsections.

3.1 Define and structure the problem

The first step in this research defines and structures the overall problem domain along with the identification of major criteria based on which the process alternatives need to be evaluated and compared using AHP. Literature review and domain expert reviews were considered to select best alternatives on basis of three criteria i.e. green efficiency, ease of operation and factor of safety.

3.2 Formulate the AHP model

This involves the formulation of AHP model which consists of goal, criteria and alternatives. In this case, the goal is to evaluate green practices i.e. green assembly and green packaging and is shown on the top level of hierarchy in figure 2 (a & b). The evaluation criteria for the AHP model have been selected on the basis of verbal discussion held with the company officials especially working in logistics department. However, relevant literature has been cited to justify the selection. These criteria are green efficiency (Ubeda et al., 2011), ease of operation (Gunjal et al., 2015) and factor of safety (Srisorn, 2013). These are shown on the mid level of hierarchy in figure 2 (a & b). Details of these criteria are given below:

Green Efficiency: This indicates the environmental friendliness of a process. It can be estimated on the basis of the several parameters such as low emission of exhaust gases (NOx, CO etc.), less usage of metal, ease of recycling, reduced energy consumption, usage of organic components in manufacturing etc. Environmental efficiency of the manufacturing systems is important due to scarcity of resources (Satoglu et al., 2015)

Factor of Safety: This criteria represents the safety concerns of a process. Various material and process parameters in respect of shear, vibrations, impact and fatigue loading, distortion etc. are also included in factor of safety assessment (Srisorn, 2013).

ACCEPTED MANUSCRIPT

Ease of Operation: This describes the ease of performing a process. It is estimated as easiness of performing operations, implementing automation technologies, applying reuse strategies, dismantling and testing etc. (Gunjal et al., 2015).

The last level of hierarchy (AHP) model consists of three alternatives to adhere goals of green assembly and green packaging. Spot welding, clinch joint and self-piercing rivets for assembly process, while cardboard packaging, mushroom packaging and carbon positive plastic for packaging process. Detailed discussion on these alternatives is as follows:

3.2.1 Assembly alternatives

Assembly refers to the joining of metallic and non-metallic components, wires, etc. to obtain a complete structure. Following are the possible alternatives for assembly operation:

Spot Welding-(SW): In an automobile shop, assembly operations are performed by various non-green welding methods such as metal inert gas welding (MIG), tungsten inert gas welding (TIG), spot welding (SW), manual metal arc welding (MMAW), etc. Often, these welding methods are primary source of various harmful pollutants such as metal and ozone fumes, nitrogen oxide (NOx) fumes, carbon monoxide (CO) fumes, lead fumes etc. The exposure to these pollutants can cause serious health problems such as metal fume fever, respiratory tract inflammation, hypoxia, Pulmonary Oedema, and other permanent behavior/ learning disorders (Beamon, 1999). Due to the harmful effect of welding methods some comparatively greener alternatives for the assembly process are required to be thought of. XYZ automobile company always strives for improving their green performance across the plant which motivated us to plan detailed interactions with experts to delineate green alternatives. Domain experts and environmentalists have suggested (during face to face interviews) following alternatives to encounter the adverse effects of non-green welding methods:

Mechanical Fasteners: Mechanical fasteners are alternative to welding and can be effectively used to join metallic sheets. Self-piercing rivets and clinch joints are the type of fasteners which can potentially be used in automobiles. These are cold forming methods with no requirement of pre-drilling. Clinch joints (CJ) are used for joining thin and ductile metallic sheets without the requirement of other additional components. Special tools are used to plastically create an interlock between metal sheets. These joints are useful in various automotive applications (Srivastava, 2007). Self-piercing rivets (SPR) are also used for

ACCEPTED MANUSCRIPT

piercing and forming permanent fastening of metallic sheets. In SPR, the rivet enlarges in the second metal sheet after piercing the first metal sheet to make a mechanical interlock in a single stroke.

3.2.2 Packaging alternatives

Packaging process is another potential domain where the implementation of green concepts can be done. Packaging is not only to protect the product but also conveys the company's image in the public domain. It also has to be compliant with regulations and fulfill environmental impact reduction obligations while being cost effective. During our study, it is found that XYZ is using plastics for packaging which contains polyvinyl chloride. Polyvinyl chloride is a major environmental offender due to greenhouse gases and toxic byproducts released in its manufacturing.

XYZ Ltd automobile organization is committed to improve their green performance even in the process of packaging. This motivated us to plan detailed interactions with packaging venders and experts to encounter non-green alternatives in packaging industry. Domain experts and environmentalists have suggested (during face to face interviews) three alternatives relevant to packaging requirements namely mushroom packaging (MP), carbon positive packaging (CPP) and cardboard packaging (CP). Mushroom packaging (MP) is manufactured using local agricultural waste such as corn stalks and husks by mixing with mycelium. Mushroom packaging biodegrades much quicker than traditional polystyrene, e.g. a piece of their packaging can decompose in just a few months. It also adds helpful nutrients back into the soil. Carbon positive packaging (CPP) is a poly-air material made from sugar cane and uses photosynthesis to absorb CO2 and release oxygen. It is also hundred percent recyclable, very cost effective and reduces carbon footprint. Cardboard packaging (CP) is a popularly used material in the packaging industry. Its chlorine chemical structure makes various byproducts predisposed in environment and build up in the bodies of animals and human. Cardboard packaging (CP) is currently being used in XYZ Company for their major packaging requirements.

Based on the above discussion, a comprehensive AHP model is prepared and shown in figure-2 (a & b).

3.3 Collect and measure AHP data

In the literature, researchers have selected a team of experts with strength up to ten members for AHP data collection and measurement (Bayazit and Karpak, 2013; Koc and Burhan, 2014). Saaty's (1994) nine point scale has been used to assign relative values to pair-wise comparison among criteria and alternatives. For this research, a team of ten experts was chosen from different domains of XYZ Company. This team of experts consists of shop floor managers, supply chain managers and environmentalists. They were assigned to do a pair wise comparison for various criteria and alternatives as mentioned in AHP model.

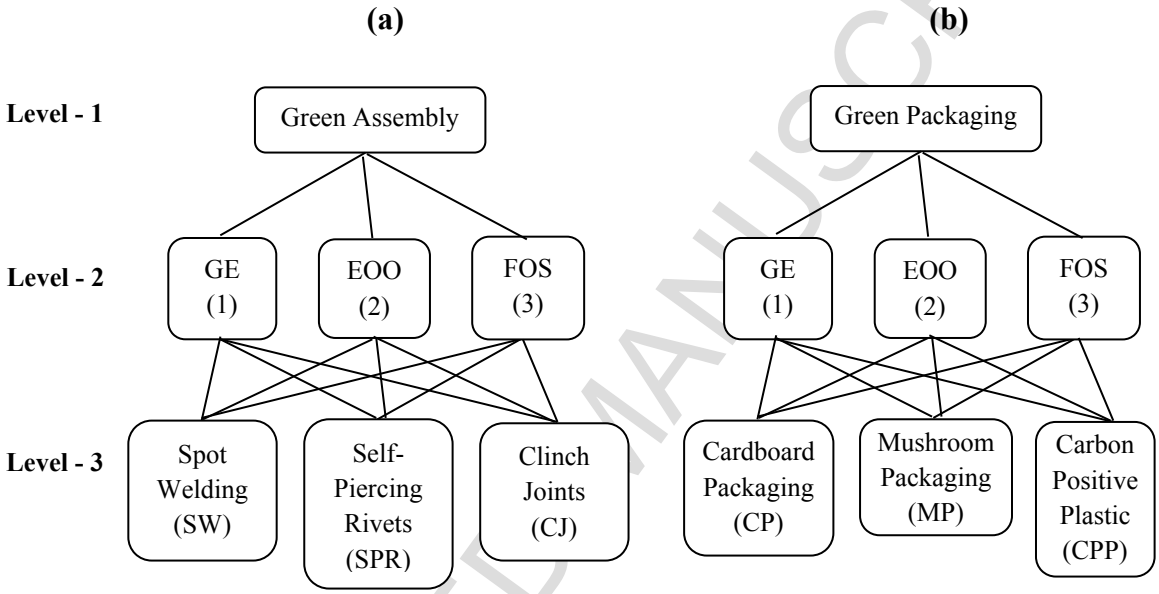

Figure – 2 Schematic diagram of AHP model (a &b)

3.4 Determine the normalized priority weights

On the basis of the opinion of experts, pair wise comparison judgment matrices have been prepared. Pairwise comparison matrices are formulated for each of lower level attributes. Comparison is done between the elements in the lower level to each other. This gives a square matrix of judgments. The pairwise comparison is carried out in terms of domination of an element over other element to express the judgments as integers.

3.5 Find the solution to the problem

Suitable greener alternatives are obtained after normalization of priority weights which were computed previously. For the selected operation (assembly and packaging) a group of global priority weight is obtained by multiplying local weights of lower factors with the weights of higher factors and then summing up all the multiplied products for the alternatives.

ACCEPTED MANUSCRIPT

4. Results and Discussions

The concept of AHP hierarchy model along with the schematic diagram of AHP model are discussed in the previous section, and important criteria for the comparison of various green and non-green alternative processes are also discussed above in detail. This section will present the formulations of comparison matrices for different levels of AHP hierarchy schematic (Figure 2).

4.1 AHP criteria (Level- 2) matrix formulations

The AHP criteria matrix is formed using three major criteria i.e. green efficiency (GE), factor of safety (FOS), and ease of operation (EOO). This matrix will be used as base matrix for finding the best alternative. The following deductions are made from several rounds of interviews with domain experts:

- Green efficiency (GE) is four times as important as ease of operation (EOO).
- Factor of safety (FOS) is three times as important as ease of operation (EOO).
- Green efficiency (GE) is two times as importance as factor of safety (FOS).

The next step is to derive rank and normalized matrix on the basis of criteria comparison and to find out basic Eigen-Values for ranking these criteria in order of their importance (Table-1). Green efficiency is considered the most important criteria as it has the highest eigenvalue i.e. 0.5584.

Table 1. Criteria comparison matrix (Level 2)

	GE	**FOS**	**EOO**	(Fractions)		**GE**	**FOS**	**EOO**	**Eigenvalues**
GE	1/1	2/1	4/1		**GE**	1.00	2.00	4.00	**0.5584**
FOS	1/2	1/1	3/1		**FOS**	0.50	1.00	3.00	**0.3196**
EOO	1/4	1/3	1/1		**EOO**	0.25	0.33	1.00	**0.1219**

4.2 Alternatives comparison matrix formulations for different processes

Level 3 of the AHP schematic diagram (Figure 2) shows various alternatives as defined by the experts. The detailed discussion on these alternatives has been included in the previous section. Now, it is required to formulate the expert opinions in the form of comparison matrix with respect to each criteria defined earlier for different processes.

ACCEPTED MANUSCRIPT

4.2.1 Alternatives comparison matrices for Assembly Process

Various alternatives for assembly process have been defined in section-4. These alternatives are spot welding (SW), clinch joint (CJ) and self-piercing rivets (SPR).Comparison matrix is formed using these alternatives with respect to various criteria. This matrix will be used to rank alternatives for a particular criteria.

Alternatives Matrix with respect to 'Green Efficiency' criteria: The following deductions are made from several rounds of interviews with domain experts, questionnaires and surveys:

- Self-piercing rivet (SPR) is two times better than spot welding (SW).
- Clinch joint (CJ) is three times better than spot welding (SW).
- Clinch joint (CJ) is two times better than Self-piercing rivet (SPR).

The next step is to derive alternatives comparison matrix for assembly on the basis of green efficiency and to find out basic Eigen-Values for ranking these alternatives with respect to green efficiency as criteria (Table-2). Alternative with the highest eigenvalue (CJ) is considered the best with respect to the green efficiency.

Table 2. Alternatives comparison matrix for assembly w.r.t. Green Efficiency

	SPR	**SW**	**CJ**			**SPR**	**SW**	**CJ**	**Eigenvalues**
SPR	1/1	2/1	1/2	(Fractions)	**SPR**	1.00	2.00	0.50	**0.2968**
SW	1/2	1/1	1/3		**SW**	0.50	1.00	0.33	**0.1630**
CJ	2/1	3/1	1/1		**CJ**	2.00	3.00	1.00	**0.5401**

Alternatives Matrix with respect to 'Factor of Safety' criteria: The following deductions are made from several rounds of interviews with domain experts:

- Spot welding (SW) is two times better than Self-piercing rivet (SPR).
- Clinch joint (CJ) is two times better than spot-welding (SW).
- Clinch joint (CJ) is three times better than Self-piercing rivet (SPR).

The next step is to derive alternatives comparison matrix for assembly on the basis of factor of safety and to find out basic Eigen-Values for ranking these alternatives with respect to factor of safety as criteria (Table-3). Alternative with the highest eigenvalue (CJ) is considered the best.

Table 3. Alternatives comparison matrix for assembly w.r.t. Factor of Safety

	SPR	SW	CJ
SPR	1/1	1/2	1/3
SW	2/1	1/1	1/2
CJ	3/1	2/1	1/1

(Fractions) →

	SPR	SW	CJ	Eigenvalues
SPR	1.00	0.50	0.33	**0.1630**
SW	2.00	1.00	0.50	**0.2968**
CJ	3.00	2.00	1.00	**0.5401**

Alternatives Matrix with respect to 'Ease of Operation' criteria: The following deductions are made from several rounds of interviews with domain experts, questionnaires and surveys:

- Self-piercing rivet (SPR) is two times better than spot-welding (SW).
- Clinch joint (CJ) is three times better than spot-welding (SW).
- Clinch joint (CJ) is two times better than Self-piercing rivet (SPR).

The next step is to derive alternatives comparison matrix for assembly on the basis of ease of operation and to find out basic Eigen-Values for ranking these alternatives with respect to ease of operation as criteria (Table-4). Alternative with the highest eigenvalue i.e. Clinch joint (CJ) is considered the best.

Table 4. Alternatives comparison matrix for assembly w.r.t. Ease of Operation

	SPR	SW	CJ
SPR	1/1	2/1	1/2
SW	1/2	1/1	1/3
CJ	2/1	3/1	1/1

(Fractions) →

	SPR	SW	CJ	Eigenvalues
SPR	1.00	2.00	0.50	**0.2968**
SW	0.50	1.00	0.33	**0.1630**
CJ	2.00	3.00	1.00	**0.5401**

Combined criteria-alternative matrix for different criteria i.e. green efficiency (GE), factor of safety (FOS), and ease of operation (EOO) is shown in table 5. This alternatives matrix for green assembly is derived on the basis of combining the criteria as shown in table-5.

Table 5. Combined Criteria - Alternatives matrix for assembly

	GE	FOS	EOO
SPR	0.2968	0.1630	0.2968
SW	0.1630	0.2968	0.1630
CJ	0.5401	0.5401	0.5401

Result for the best green alternative for process -1 (Assembly) can be obtained by multiplying combined criteria-alternative matrix (Table-5) and consolidated basic Eigen value criteria matrix (Table-1). It is concluded that clinch joint is the best alternative among all available

alternatives as it has highest Eigen value followed by self-piercing rivets and spot welding. It is evident that the usage of clinch joints for assembly process instead of non-green spot welding process will eventually improve the green performance of supply chain of XYZ automobile company. This finding is very important and has positive impact towards overall green implementation strategies to be laid down by the management.

$$\begin{matrix} \text{Self-piercing rivet (SPR)} \\ \text{Spot welding (SW)} \\ \text{Clinch joint (CJ)} \end{matrix} \begin{pmatrix} 0.2540 \\ 0.2057 \\ 0.5400 \end{pmatrix} \Leftarrow \text{Best alternative}$$

Cost analysis for the proposed implementation of the best alternative: It is established that the management of any commercial organization would consider the cost implications on the proposed implementation of any new technology or process over the existing one (Chen and Liang, 2012). Though the proposed new alternative offer the greener option among all available processes still the cost analysis is very much necessary to highlight the overall scenario of green implementation in the XYZ facilities. Variable cost of making 100,000 joints during a fixed interval was considered for cost analysis. However, the fixed cost was not taken in to account with an assumption that the company has already in the possession of alternative joining technologies. All other conditions and parameters pertaining to the process are kept constant to simplify the analysis. Following table -6 illustrates the cost-benefit ratio:

Table 6. Cost-Benefit analysis for assembly

Indicative Costs of 100,000 Joints (INR)				
Alternatives	**Total Cost (INR)**	**Normalized Cost**	**Benefit-Cost Ratio**	**Result**
Self-piercing rivet (SPR)	76,529.42	0.3416	0.2540/ 0.3416	0.7435
Spot welding (SW)	91,206.40	0.4071	0.2047/ 0.4071	0.5028
Clinch joint (CJ)	56,270.08	0.2512	0.5400/ 0.2512	2.1496
Total Cost	224,005.90			

It is clearly indicated from the benefit-cost analysis table that 'Clinch Joints' are the best alternative of currently existing non-green assembly process (spot welding). The benefit-cost

ACCEPTED MANUSCRIPT

ratio of clinch joints is very high i.e. 2.1496 over other alternatives and also these joints offer green factors in consideration. In this case, results for AHP approach and cost analysis are same. However, in some cases this could be conflicting also. In such instances, the priority of individual company will play an important role. Some companies are more sensitive towards the issue of environment however some companies are more focused on their economic goals.

4.2.2 Alternatives comparison matrices for Packaging Process

Alternative materials have been identified for packaging process in section 4. These alternatives are mushroom packaging (MP), carbon positive packaging (CPP) and cardboard packaging (CP).Comparison matrix is formed using these alternatives with respect to various criteria. This matrix will be used to rank alternatives for a particular criteria.

Alternatives Matrix with respect to 'Green Efficiency' criteria: The following deductions are made from several rounds of interviews with domain experts.

- Mushroom packaging (MP) is three times better than Cardboard packaging (CP).
- Carbon positive packaging (CPP) is two times better than Mushroom packaging (MP).
- Carbon positive packaging (CPP) is four times better than Cardboard packaging (CP).

Now, we need to derive alternatives comparison matrix for packaging on the basis of green efficiency and to find out basic Eigen-Values for ranking these alternatives with respect to green efficiency as criteria (Table-7). Alternative with the highest Eigen value i.e. Carbon positive packaging (CPP) is considered the best.

Table 7. Alternatives comparison matrix for packaging w.r.t. Green Efficiency

	MP	**CPP**	**CP**			**MP**	**CPP**	**CP**	**Eigenvalues**
MP	1/1	1/2	3/1	**(Fractions)**	**MP**	1.00	0.50	3.00	**0.3190**
CPP	2/1	1/1	4/1		**CPP**	2.00	1.00	4.00	**0.5594**
CP	1/3	1/4	1/1		**CP**	0.33	0.25	1.00	**0.1211**

Alternatives Matrix with respect to 'Factor of Safety' criteria: The following deductions are made from several rounds of interviews with domain experts.

- Mushroom packaging (MP) is three times better than Cardboard packaging (CP).
- Carbon positive packaging (CPP) is two times better than Mushroom packaging (MP).
- Carbon positive packaging (CPP) is four times better than Cardboard packaging (CP).

Next, we need to derive alternatives comparison matrix for packaging on the basis of factor of safety and to find out basic Eigen-Values for ranking these alternatives with respect to factor of safety as criteria (Table-8). Alternative with the highest eigenvalue (CPP) is considered the best.

Table 8. Alternatives comparison matrix for packaging w.r.t. Factor of Safety

	MP	**CPP**	**CP**	(Fractions)		**MP**	**CPP**	**CP**	**Eigenvalues**
MP	1/1	1/2	3/1		MP	1.00	0.50	3.00	0.3190
CPP	2/1	1/1	4/1		CPP	2.00	1.00	4.00	0.5594
CP	1/3	1/4	1/1		CP	0.33	0.25	1.00	0.1211

Alternatives Matrix with respect to 'Ease of Operation' criteria: The following deductions are made from several rounds of interviews with domain experts, questionnaires and surveys:

- Mushroom packaging (MP) is two times better than Carbon positive packaging (CPP).
- Mushroom packaging (MP) is four times better than Cardboard packaging (CP).
- Carbon positive packaging (CPP) is three times better than Cardboard packaging (CP).

Alternatives comparison matrix for packaging on the basis of ease of operation can be derived to find out basic Eigen-Values for ranking these alternatives with respect to ease of operation as criteria (Table-9). Alternative with the highest Eigen value i.e. Mushroom packaging (MP) is considered the best.

Table 9. Alternatives comparison matrix for packaging w.r.t. Ease of Operation

	MP	**CPP**	**CP**	**(Fractions)**		**MP**	**CPP**	**CP**	**Eigenvalues**
MP	1/1	2/1	4/1		**MP**	1.00	2.00	4.00	**0.5777**
CPP	1/2	1/1	3/1		**CPP**	0.50	1.00	3.00	**0.2976**
CP	1/4	1/3	1/1		**CP**	0.25	0.33	1.00	**0.1246**

Combined criteria-alternative matrix for different criteria i.e. green efficiency (GE), factor of safety (FOS), and ease of operation (EOO) is shown in table-10 below:

Table 10. Combined Criteria - Alternatives matrix for packaging

	GE	**FOS**	**EOO**

MP	0.3190	0.3190	0.5777
CPP	0.5594	0.5594	0.2976
CP	0.1211	0.1211	0.1246

Result for the best green alternative for process -2 (Packaging) can be obtained by multiplying combined criteria-alternative matrix (table-10) and consolidated basic Eigen value criteria matrix (table 1). It is observed that carbon positive packaging (CPP) material is the best alternative as it has highest Eigen value followed by mushroom packaging (MP) and cardboard packaging (CP). It is evident from the discussion in section 4 that the usage of carbon positive packaging material for packaging instead of less green cardboard material will improve the green performance of supply chain of XYZ automobile company. This finding is crucial and can impact in the implementation of green strategies to be laid down by the management.

Mushroom packaging (MP)	0.350	
Carbon positive packaging (CPP)	0.527	⇦ Best alternative
Cardboard packaging (CP)	0.121	

Cost analysis for the proposed implementation of the best alternative: Cost implications are the foremost criteria in the proposed implementation of any new technology or process over the existing one (Chen and Liang, 2012). Cost benefit analysis presented in this section compares the benefits selected by AHP with the related cost. Unit cost of packaging material is considered as cost parameter, however the fixed cost has not been considered by assuming that the company has already in possession of these packaging technologies. A general idea about the unit cost was given by the company officials. Other conditions and parameters related to the cost are kept constant to simplify the analysis. Following table - 11 illustrates the cost-benefit ratio:

Table 11. Cost-Benefit analysis for packaging

Indicative Costs of 1 Kg of packaging material (INR)				
Alternatives	**Total Cost (Per Kg.)**	**Normalized Cost**	**Benefit-Cost Ratio**	**Result**
Mushroom Packaging (MP)	63	0.329	0.350/ 0.329	1.063

Carbon Positive Packaging (CPP)	58	0.303	0.527/ 0.303	1.739
Cardboard Packaging (CP)	70	0.366	0.121/ 0.366	0.331
Total Cost	191			

It is clear from the benefit-cost analysis table above that 'Carbon Positive Packaging Material' is the best alternative of currently existing lesser green packaging material (cardboard packaging material). The benefit-cost ratio of Carbon Positive material is very high i.e. 1.739 over other alternatives and also this material offers greener option to XYZ automobile company.

5. Conclusions

In the 21st century, practicing green issues is an important social and business concern. Government regulations, fluctuating customer demand, scarcity of available resources, development of international certificate standards are the few reasons for its importance. Green practices can help to accomplish both economic and environmental goals. In such an era of environmentalism, manufacturing enterprises having green logistics will easily survive in global market. The benefits will ultimately leads to performance improvements, increases market shares and higher profits (Rao and Holt, 2005). Green practices in automotive industry are emerging as an important approach to reduce environmental hazards along with economic performance. Green practices can also improve performance of supply chain. These practices can be applied to any area of supply chain from procurement of raw material to transportation of products. In this study, authors have selected the production areas of supply chain which include assembling and packaging processes. Based on the experts' opinion, different alternatives to these processes (assembling and packaging) are identified and best possible alternative has been obtained by using AHP. Selection of alternatives is based on three criteria i.e. green efficiency, factor of safety and ease of process. Cost analysis is also done to further justify the proposed alternative to these processes. Based on this study, the best alternatives to improve the green performance of supply chain of XYZ automobile company are as follow:

- *For Assembling Process*: Clinch Joints followed by self-piercing rivets

- *For Packaging Material*: Carbon Positive Packaging material followed by Mushroom Packaging

Above proposed alternatives can be implemented in assembly department and packaging department respectively to improve the green performance of XYZ Ltd. The findings of this research are applicable in automotive industry and in any type of manufacturing industry where logistics plays an important role. The conclusion shows that the green alternatives are found most suitable for production as well as for packaging process. This provides guidelines for sustainable adaptation of green practices in existing operations of companies in an Indian context. Thus the recommendation to the companies is to focus and shift towards greener practices in logistics for sustainable performance. As future scope, simulation and fuzzy models can be used to develop the framework and hence to validate the benefits of green logistics in manufacturing enterprises. Fixed cost has been assumed negligible in this study, therefore a detailed cost analysis with all possible costs is required to be done in future studies.

References

Abduaziz, O., Cheng, J.K., Tahar, R.M., Varma, R., 2015. A Hybrid Simulation Model for Green Logistics Assessment in Automotive Industry. In Proceedings of 25th DAAAM International Symposium on Intelligent Manufacturing and Automation, 100, 960-969.

Apaydin O., Gonullu, M.T., 2008. Emission control with route optimization in solid waste collection process: A case study. Sadhana. 33 (2), 71-82.

Apaydın, O., Gonullu, M.T., 2011. Route Time Estimation of Solid Waste Collection Vehicles Based on Population Density. Global NEST Journal. 13 (1), 162-169.

Apaydin, O., Kurt, U., Gonullu, M.T., 2009. An Investigation on the Treatment of Tannery Wastewater by Electrocoagulation. Global Nest Journal. 11 (4), 546-555.

Aronsson, H., Huge, B.M., 2006. The environmental impact of changing logistics structures. International Journal of Logistics Management. 17 (3), 394-415.

Ateş, M.A., Bloemhof, J., Raaij, V.E.M., Wynstra, J.Y.F., 2012. Proactive environmental strategy in a supply chain context: The mediating role of investments. International Journal of Production Research. 50 (4), 1079- 1095.

Bayazit, O., Karpak, B., 2013. Selection of a third party logistics service provider for an aerospace company: an analytical decision aiding approach. International Journal of Logistics Systems and Management. 15 (4), 382-404.

Beamon, B.M., 1999. Designing the green supply chain. Logistics Information Management. 12 (4), 332 – 342.

Bowen, F.E., Cousins, P.D., Lamming, R.C., Faruk, A.C., 2001. The role of supply management capabilities in green supply. Production and Operations Management. 10, 174–189.

Carter, C., Dresner, M., 2001. Purchasing role in environmental management: cross-functional development of grounded theory. Journal of Supply Chain Management. 37 (3), 12–26.

Cattanach, R.E., Holdreith, J.M., Reinke, D.P., Sibik, L.K., 1995. The Handbook of Environmentally Conscious Manufacturing: From Design and Production to Labeling and Recycling. Irwin, Chicago, USA.

Chang, Q., Qin, R., 2008. Analysis on Development Path of Tianjin Green Logistics. International Journal of Business and Management. 3 (9), 96-98.

Chen, D., Liang, S.W., 2012. Evaluation of internal costs and benefits for Taiwanese computer manufacturers adopting green supply chains. The Asian journal of shipping and logistics. 28 (1), 83-104.

Conding, J., Habidin, N.F., Zubir, A.F.M., Hashim, S., Jaya, N., 2013. A review: the impact of green practices adoption on green performance in the Malaysian automotive industry. Journal of Sustainable Development Studies. 2 (1), 109-126.

Dey, A., LaGuardia, P., Srinivasan, M., 2011. Building sustainability in logistics operations: a research agenda. Management Research Review. 34 (11), 1237-1259.

Ebinger, F., Goldbach, M., Schneidewind, U., 2006. Greening supply chains: a competence based perspective. In: Sarkis, J. (Ed.) Greening the Supply Chain, Springer. New York, 251–269.

Elhedhli, S., Merrick, R., 2012. Green supply chain network design to reduce carbon emissions. Transportation Research Part D: Transport and Environment. 17 (5), 370–379.

Fagerholt, K., 1999. Optimal fleet design in a ship routing problem. International Transactions in Operational Research. 6 (5), 453-464.

Guirong, Z., Zongjian, Z., 2012. Green Packaging Management of Logistics Enterprises. Physics Procedia. 24, 900 – 905.

Gunjal, P. U., Nalwade, P.M., Dhondge, D., Ingale. P.R., Patil, A., 2015. Green logistics: improving the sustainability of logistics in Environmental and organizational point of view. International Journal of Science, Technology & Management. 4 (3), 122-127.

Iakovou, E., Vlachos, D., Chatzipanagioti, M., Mallidis, I., 2010. A Comprehensive Optimization Framework for Sustainable Supply Chain Networks. Viewed on 26 July 2014, <http://im.meng.auth.gr/lascm/data%20files/pdf/Chatzipanagioti/ICLST_2010.pdf>.

Kim, N.S., Janic, M., Wee, B., 2009. Trade-off between carbon dioxide emissions and logistics costs based on multi-objective optimization. Transportation Research Record: Journal of the Transportation Research. Board. No. 2139. Washington, D. C., 107-116.

Koc, E., Burhan, H.A., 2014. An Analytic Hierarchy Process (AHP) approach to a Real World Supplier Selection Problem: A Case Study of Carglass Turkey. Global Business and Management Research: An International Journal, 6 (1), 1-14.

Kohn, C., Brodin, M.H., 2008. Centralized distribution systems and the environment: how increased transport work can decrease the environmental impact of logistics. International Journal of Logistics Research and Applications. 11 (3), 229-245.

Lai, K.H., Wong, C.W.Y., 2012. Green logistics management and performance some evidence from Chinese manufacturing exporters. Omega Journal. 40 (3), 276-282.

Lozano, R., 2012. Towards better embedding sustainability into companies' systems: an analysis of voluntary corporate initiatives. Journal of cleaner production. 25 (0), 14-26.

Lozano, R., 2012a. Are companies planning their organizational changes for Corporate Sustainability? An analysis of three case studies on resistance to change and their strategies to overcome it. Journal of Corporate Social Responsibility and Environmental Management. 20 (5), 275-295.

Lu, Y.L., Geng, J., 2015. Industrial transformation and green production to reduce environmental emissions: Taking cement industry as a case. Advances in Climate Change Research. 6 (3-4), 202-209.

McKinnon, A., 2003. Logistics and the environment. In Hensher, D.A. and Button, K.J. (Eds). Handbook of Transport and the Environment. Elsevier, Oxford.

McKinnon, A., 2007. CO2 emissions from freight transport in the UK. Report prepared for the Climate Change Working Group of the Commission for Integrated Transport, London.

Niesten, E., Lozano, R., 2015. Making, buying and collaborating for more sustainable production and consumption. Journal of Cleaner Production. 100, 1-3.

Palanivelu, P., Dhawan, M., 2011. Green Logistics. White Paper Tata Consulting Systems. Viewed on 03 Aug 2014, http://www.tcs.com/resources/white_papers/Pages/Green_Logistics. aspx.

Pazirandeh, A., Jafari, H., 2013. Making sense of green logistics. International Journal of Productivity and Performance Management. 62 (8), 889-904.

Porter, M.E., Vanderlinde, C., 1995. Toward a new conception of the environment competitiveness relationship. Journal of Economic Perspectives. 9 (4), 97-118.

Rao, P., Holt, D., 2005. Do green supply chains lead to competitiveness and economic performance. International Journal of Operations & Production Management. 25 (9), 898-916.

Rehman, M.A., Seth, D., Shrivastava, R.L., 2016. Impact of green manufacturing practices on organizational performance in Indian context: An empirical study. Journal of Cleaner Production. 137, 427-448.

ACCEPTED MANUSCRIPT

Rizet, C., Browne, M., Cornelis, E., Leonardi, J., 2012. Assessing carbon footprint and energy efficiency in competing supply chains: Review – Case studies and benchmarking. Transportation Research Part D: Transport and Environment. 17 (4), 293–300.

Rodrigue, J.P., Slack, B., Comtois, C., 2001. Green Logistics (The Paradoxes of). Published in Brewer, A.M., Button, K.J., Hensher, D.A. (eds). The Handbook of Logistics and Supply-Chain Management, ISBN: 0-08-043593-9.

Saaty, T.L., 1980. The Analytic Hierarchy Process. McGraw-Hill, New York.

Sambracos E, Paravantis, J.A., Tarantilis, C.D., Kiranoudis, C.T., 2004. Dispatching of small containers via coastal freight liners: The case of the Aegean Sea. European Journal of Operational Research. 152, 365-381.

Satoglu, S.I., Emre, C., Serdar, B., 2015. A Literature Survey on Energy Aware Manufacturing and Logistics Operations with a Lean Thinking Perspective. In the Proceedings of 2nd Global Conference on Engineering and Technology Management. Chicago, USA, September 4 – 5.

Sbihi, A., Eglese, R.W., 2010. Combinatorial optimization and Green Logistics. Annals of Operations Research. 175 (1), 159-175.

Sheu, J.B., Chou, Y.H., Hu, C.C., 2005. An integrated logistics operational model for green supply chain management. Transportation Research. Part E. 41, 287–313.

Singh, R.K., 2011. Developing the framework for coordination in supply chain of SMEs. Business Process Management Journal. 17 (4), 619–638.

Singh, R.K., 2012. Justification of coordinated supply chain in small and medium enterprises using analytic hierarchy process. International Journal of Services Sciences. 4 (3-4), 277-293.

Singh, R.K., Kumar, R. Shankar, R., 2012. Supply chain management in SMEs: a case study. International Journal of Manufacturing Research. 7 (2), 165–180.

Srisorn, W., 2013. The benefit of green logistics to organizations. International Journal of Social Behavioral, Educational, Economic Business and Industrial Engineering. 7 (8), 2451 – 2454.

Srivastava, S.K., 2007. Green supply-chain management: a state-of-the-art literature review. International Journal of Management Reviews. 9 (1), 53–80.

Subramanian, N., Ramanathan, R., 2011. A review of applications of Analytical Hierarchy Process in operations Management. International Journal of Production Economics. 138 (2), 215- 241.

Tavares, Z., Zsigraiova, V., Semiao, Carvalho, M.G., 2008. A case study of fuel savings through optimization of MSW transportation routes. Management of Environmental Quality. 19 (4), 444–454.

Tavares, Z., Zsigraiova, V., Semiao, Carvalho, M.G., 2009. Optimization of MSW collection routes for minimum fuel consumption using 3D GIS modelling. Waste Management. 29 (3), 1176–1185.

ACCEPTED MANUSCRIPT

Ubeda, S., Arcelus, F.J., Faulin, J., 2011. Green logistics at Eroski: a case study. International Journal on Production Economics. 131 (1), 1–8.

Vachon, S., Klassen, R.D., 2006. Extending green practices across the supply chain the impact of upstream and downstream integration. International Journal of Operations & Production Management. 26, 795–821.

Wind, Y., Saaty, T.L., 1980. Marketing applications of the analytic hierarchy process. Management Science. 26 (7), 641–658.

Woensel, V., Creten, R., Vandaele, N., 2001. Managing the environmental externalities of traffic logistics: The issue of emissions. Production and Operations Management. 10 (2), 207–223.

Yetilmezsoy, K., Ilhan, F., Sapci-Zengin, Z., Sakar, S., Gonullu, M.T., 2009. Decolorization and COD Reduction of UASB pretreated poultry manure wastewater by electrocoagulation process: A post-treatment study. Journal of Hazardous Materials. 162 (1), 120-132.

Zhang, G., Zhao, Z., 2012. Green Packaging Management of Logistics Enterprises. In Proceedings of International Conference on Applied Physics and Industrial Engineering. 24 (2), 900 -905.

Zhanga, G., Zhaob, Z., 2012. Green Packaging Management of Logistics Enterprises. In the proceeding of International Conference on Applied Physics and Industrial Engineering. Physics Procedia. 24, 900-905.

Zhu, Q., Sarkis, J., 2004. Relationships between operational practices and performance among early adopters of green supply chain management practices in Chinese manufacturing enterprises. Journal of Operations Management. 22, 265-289.

ACCEPTED MANUSCRIPT

2017 International Conference on Machine Vision and Information Technology

Cardiotocography Analysis Using Conjunction of Machine Learning Algorithms

Anish Batra
Mathematics and Computing
Delhi Technological University
New Delhi, India-110042
Email: anishbatra95@gmail.com

Ananya Chandra
Software Engineering
Delhi Technological University
New Delhi, India-110042
Email: ananyachandra14@gmail.com

Vishal Matoria
Electronics Engineering
Jaypee University, Guna
Madhya Pradesh, India-473001
Email: vmatoria2@gmail.com

***Abstract*—Fetal distress is a primary factor for cesarean section in obstetrics and gynecology. If there is a lack of oxygen for the fetus in the uterus, then there is always a risk of deteriorating health which could lead to death as well. Cardiotocography (CTG) the most popular technique to observe fetal health. Fetal heart rate (FHR) is an essential index to identify occurences of fetal distress. This study makes use of the following to evaluate fetal distress:**

1) **Decision tree (DT)**
2) **Support Vector Machines (SVM)**
3) **Random Forest**
4) **Neural Networks**
5) **Gradient Boosting**

We present in this paper a new algorithm which improves the accuracy to 99.25% which is higher than what was obtained in previous research.

I. Introduction

Data mining is an ultimate tool in knowledge discovery. It finds hidden and unknown, reliable and original knowledge from a large dataset, which makes it an important tool in analysis and prediction of some unknown occurrences [1].

With developments in medicine and technology, clinical difficulties occur for doctors in identifying diseases when facing large amounts of inspection reports being produced by the latest medical equipment. Data mining has effectively aided medical diagnosis in the past few years to prevent misdiagnosis.[2][3]

Cesarean section is among the most common surgical procedures in obstetrics and gynecology. Cesarean section must be performed when irregular fetal position, fetal distress, or any other emergency condition occurs. Fetal distress can be used to refer to the possibility of fetal hypoxia and or metabolic acidosis. It is usually a consequence of a complication during labor. Ample fetal oxygenation is necessary for a healthy neonate, and efficient and efficacious diagnosis on fetal distress is a vital issue.[4]

Cardiotocography (CTG) and fetal scalp blood sampling (FBS) are often used when monitoring fetal distress[5] . Fetal development and health information is provided by CTG, particularly the development status of the autonomous nervous system (ANS). A change in fetal heart rate (FHR) denotes a response to external stimuli. Broadly speaking, mean of FHR, change of FHR, acceleration and deceleration of FHR, along with the fetal movement are all crucial parameters for the diagnosis of fetal distress.[6]

In this study, we aim to analyze the occurrence of fetal distress by applying suitable data mining techniques to shape classification models.

Decision tree (DT) is a method to construct a classification model. As the name suggests, a tree-shaped structure is created using inductive reasoning. Decision tree has proven to be a very effective tool for implementing medical prediction models [7].

Severe sequela is caused on the fetus due to fetal distress. The objective of this analysis is to come up with a classification model that has the highest possible accuracy to subsequently help obstetricians in the diagnosis of fetal distress.

The paper has been divided into sections as follows. Section 2 talks about related work, Section 3 is about the dataset and Section 4 contains Data Preprocessing methods used. Section 5 expounds upon various models and their results. In Section 6, the proposed algorithm is provided. The confinement of our study has also been discussed.

II. Related Work

Cardiotocography (CTG), consisting of Fetal Heart Rate (FHR) and Tocographic (TOCO) measurements, has been used to assess fetal well-being during the deliveries. Since 1970, many researchers have employed different techniques to help the doctors to interpret the CTG trace pattern from the field of computer programming and signal processing.

They have helped doctors with explanations in order to reach a satisfactory level of consistency so as to behave as a decision support system in obstetrics.

There is currently no general agreement on the best methodology for baseline evaluation in computer analysis of cardiotocography.

Currently we divide the medical condition into 3 classes. Refer to Figure 1.

More than 30 years after the establishment of antepartum cardiotocography into clinical practice, the predictive ability of the method remains controversial. From the review articles published on this subject, it was found that the experimental

978-1-5090-4993-6/17 $31.00 © 2017 IEEE
DOI 10.1109/CMVIT.2017.27

	Normal CTG	Suspicious CTG	Pathological CTG
Baseline	110-160 bpm	Lacking at least one of normal characteristics, but with no pathological features	<100 bpm
Variability	5-25 bpm		Reduced/increased variability, sinusoidal pattern
Decelerations	No repetitive decelerations		Repetitive late or prolonged decelerations for > 30 min (or > 20 min if reduced variability); one deceleration > 5 min
Interpretation	*No hypoxia/acidosis*	*Low probability of hypoxia/acidosis*	*High probability of hypoxia/acidosis*

Figure 1. Cardiotocography classes

sensitivity differs between 2% and 100% and its specificity between 37% and 100%.

In principle, a neural network can be trained to identify the data directly. However, a simple network can be very complex and difficult to train. Further, the training process will consume a lot of time if the dimensions of the input data is high and the accuracy of classification can also vary with the increase of dimension in the training data.

Traditional statistical methods rely on an assumption of linearity. However, most of the data gathered are the results of human behavior and since humans rarely behave in a linear way, methods that assume linear separability are doomed to fail.

Furthermore, data collection streams are broadening. The number of variables of concern to modelers has increased by at least an order of magnitude.

To solve this problem, the last few years has seen the emergence of neural networks as a method of non-linear modeling. This came about as a result of the efforts of various cognitive scientists to mimic the learning and memorising process of the brain. Because of the pattern recognition nature, this method has proven robust with respect to missing data and other data irregularities.

III. Data Set

We used cardiotocograms data from UCI Machine Learning Repository.[8]

This data set contains 2126 fetal cardiotocograms belonging to different classes. The data contains 21 attributes and two class labels.

The CTGs were classified by three expert obstetricians and a consensus classification label assigned to each of them. Classification was both with respect to a morphologic pattern (A, B, C. ...) and to a fetal state (N, S, P).

This data set is used for these evaluations.

1) LB - FHR baseline (beats per minute)
2) AC - Number of accelerations per second
3) FM - Number of fetal movements per second
4) UC - Number of uterine contractions per second
5) DL - Number of light decelerations per second
6) DS - Number of severe decelerations per second
7) DP - Number of prolongued decelerations per second
8) ASTV - percentage of time with abnormal short term variability
9) MSTV - mean value of short term variability
10) ALTV - percentage of time with abnormal long term variability
11) MLTV - mean value of long term variability
12) Width - width of FHR histogram
13) Min - minimum of FHR histogram
14) Max - Maximum of FHR histogram
15) Nmax - Number of histogram peaks
16) Nzeros - Number of histogram zeros
17) Mode - histogram mode
18) Mean - histogram mean
19) Median - histogram median
20) Variance - histogram variance
21) Tendency - histogram tendency

IV. Data preprocessing

The following steps were undertaken to pre-process the data-set:

1) The missing values in features were found and replaced with their arithmetic mean values over all the observations for that variable.
2) Z-Normalization: The algorithms used for classification expected a normalized dataset. All the parameters that were not discrete in nature were normalized using the Z-score normalization technique. Z-scores are expressed in terms of standard deviations from their means. The distribution of Z-scores obtained has a mean value of 0 and a standard deviation of 1.
3) Principal Component Analysis: Principal Component Analysis is a statistical procedure, which by using an orthogonal transformation converts a set of possibly correlated variables into a set of linearly uncorrelated variables called the principal components. Therefore, the number of principal components is either equal to or less than the number of original variables. After applying the above mentioned steps, PCA was used convert the set of observations with 95% correlation into a set of less than 100 values of linearly uncorrelated variables.

V. Models Used and Results

1) Decision Trees: As the name suggests, a decision tree consists of root node, the subsequent decision nodes, branch nodes, and leaf nodes. It starts from the root node, and each branch that is encountered is a new decision node in itself or a new leaf node of the tree. At each decision node, we make a decision to choose from two or more possible alternatives. Similarly, each leaf node denotes one possible classification.

The variable which yields maximum information is selected to choose the next node considering the information gain at each step. The particular value that the attribute takes is determined to create the next new branch. This step is continued till the entire decision tree is developed and we stop when the pre-determined stopping criteria is fulfilled. The following steps explain how a decision tree is built:

1) Fragment the entire dataset into training and testing sets.
2) Train your tree using training set.

3) Build the tree further by selecting a single best attribute considering the information gain at each node.
4) Shorten the grown tree using the testing set until each node consists of only one node.
5) Go through steps 1 to 4 till the time all nodes are leaf nodes.

The decision tree obtained in our case is displayed in Figure 2. The results obtained from the tree are displayed in the Figure 3.

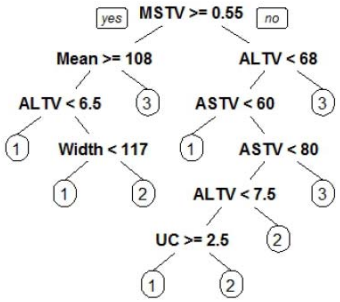

Figure 2. Decision Tree Created

```
Confusion Matrix and Statistics

          Reference
Prediction   1   2   3
         1 402  23   8
         2  14  44   0
         3   5   0  35

Overall Statistics

               Accuracy : 0.9058
                 95% CI : (0.8777, 0.9293)
    No Information Rate : 0.7928
    P-Value [Acc > NIR] : 1.892e-12

                  Kappa : 0.7177
 Mcnemar's Test P-Value : NA

Statistics by Class:

                     Class: 1 Class: 2 Class: 3
Sensitivity            0.9549  0.65672  0.81395
Specificity            0.7182  0.96983  0.98975
Pos Pred Value         0.9284  0.75862  0.87500
Neg Pred Value         0.8061  0.95137  0.98371
Prevalence             0.7928  0.12618  0.08098
Detection Rate         0.7571  0.08286  0.06591
Detection Prevalence   0.8154  0.10923  0.07533
Balanced Accuracy      0.8365  0.81327  0.90185
```

Figure 3. Confusion Matrix for Decision Tree

2) Support Vector Machines: Support Vector Machines are expounded upon the concept of decision planes. These decision planes define certain decision boundaries. A set of objects with different class memberships are separated by decision planes. Let us consider the following example. Let us suppose that each object can be classified to either class A or B. A boundary is defined by the line of separation on one side of which all objects are either A or B, and vice versa on the other side of the line. In case of a new object, it can be classified in either A or B, depending on which side of the plane it lies on.[9]

SVM is primarily a classifier method. This algorithm performs the classification by creating hyperplanes in a multidimensional space, where the different cases are sorted according to their class. There is support both for classification and regression tasks in support vector machines. There is also a facility to handle categorical and continuous variables. In case of categorical variables we make use of dummy variables where case values of 0 or 1 are used.

The results obtained from the SVM are displayed in the Figure 4.

```
          Reference
Prediction   1   2   3
         1 391  13   4
         2  11  66   6
         3   1   0  39

Overall Statistics

               Accuracy : 0.9341
                 95% CI : (0.9095, 0.9537)
    No Information Rate : 0.7589
    P-Value [Acc > NIR] : < 2e-16

                  Kappa : 0.8295
 Mcnemar's Test P-Value : 0.04671

Statistics by Class:

                     Class: 1 Class: 2 Class: 3
Sensitivity            0.9702   0.8354  0.79592
Specificity            0.8672   0.9624  0.99793
Pos Pred Value         0.9583   0.7952  0.97500
Neg Pred Value         0.9024   0.9710  0.97963
Prevalence             0.7589   0.1488  0.09228
Detection Rate         0.7363   0.1243  0.07345
Detection Prevalence   0.7684   0.1563  0.07533
Balanced Accuracy      0.9187   0.8989  0.89692
```

Figure 4. Confusion Matrix for SVM

3) Random Forest: Random forests, or more specifically speaking, random decision forests is a learning method used in classification, regression and some other operations, that work by creating a large number of decision trees at the time of training and then subsequently produce the result as the class that is the mode for all the classes (classification problem) or mean prediction (regression problem) of the individual trees.[10]

Random Forest creates a number of classification trees. Whenever a new object from an input vector has to be classified, the input vector is put down in each of the trees in the forest. Each and every tree gives a specific classification, and then we can say that the tree has "voted" for that particular class. The class which has the most number of votes is then chosen by the forest.

The results obtained from random forest are displayed in Figure 5.

4) Neural Networks: Artificial Neural Networks are processing techniques which are roughly modeled after the neural structure of the mammalian cerebral cortex but on much smaller scales. There might be thousands and millions of processor units in a large neural network, which in comparison to the billions of neurons in a mammalian brain is a negligible quantity. This correspondingly leads to an increase in magnitude of the broad interaction and the resultant behavior.

```
          Reference
Prediction   1   2   3
         1 407  14   5
         2   9  54   3
         3   1   3  35

Overall Statistics

               Accuracy : 0.9341
                 95% CI : (0.9095, 0.9537)
    No Information Rate : 0.7853
    P-Value [Acc > NIR] : <2e-16

                  Kappa : 0.8103
 Mcnemar's Test P-Value : 0.2893

Statistics by Class:

                     Class: 1 Class: 2 Class: 3
Sensitivity            0.9760   0.7606  0.81395
Specificity            0.8333   0.9739  0.99180
Pos Pred Value         0.9554   0.8182  0.89744
Neg Pred Value         0.9048   0.9634  0.98374
Prevalence             0.7853   0.1337  0.08098
Detection Rate         0.7665   0.1017  0.06591
Detection Prevalence   0.8023   0.1243  0.07345
Balanced Accuracy      0.9047   0.8672  0.90288
```

Figure 5. Confusion Matrix for Random Forest

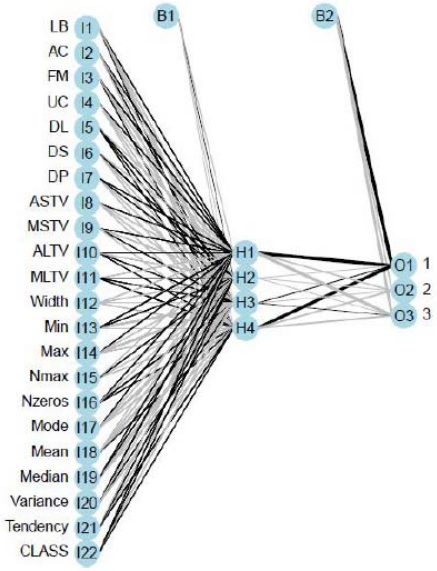

Figure 6. Neural Network Used

```
Confusion Matrix and Statistics

          Reference
Prediction   1   2   3
         1 408   3   1
         2   8  59   5
         3  10   4  33

Overall Statistics

               Accuracy : 0.9416
                 95% CI : (0.9182, 0.96)
    No Information Rate : 0.8023
    P-Value [Acc > NIR] : < 2e-16

                  Kappa : 0.8352
 Mcnemar's Test P-Value : 0.02084

Statistics by Class:

                     Class: 1 Class: 2 Class: 3
Sensitivity            0.9577   0.8939  0.84615
Specificity            0.9619   0.9720  0.97154
Pos Pred Value         0.9903   0.8194  0.70213
Neg Pred Value         0.8487   0.9847  0.98760
Prevalence             0.8023   0.1243  0.07345
Detection Rate         0.7684   0.1111  0.06215
Detection Prevalence   0.7759   0.1356  0.08851
Balanced Accuracy      0.9598   0.9330  0.90885
```

Figure 7. Confusion Matrix Neural Network

Most data scientists aren't concerned with the resemblance of their network with biological systems. Instead they are concerned more about how their model is performing.[11] The mathematics involved with neural networks is indeed complex, however through the plethora of statistical tools that are available in todays world, one can gain a much needed insight into the functional understanding of neural networks and its structure. Layers are an important aspect of neural networks. A number of interconnected nodes constitute what is known as a layer and each node has an activation function. Input data is fed to the input layer which further interacts with one or more hidden layers where the real time processing work takes place through a network of weighted edges (connections). The hidden layer processes the data and then proceeds to its link with the output layer where the result is displayed. The Neural Network used is displayed in Figure 6.

The results obtained from neural networks are displayed in Figure 7.

5) Gradient Boosting: Extreme Gradient Boosting is considered to be more effective and accurate than a simple random forest or neural network.

Extreme Gradient Boosting is somewhat similar to the gradient boosting ideology but certainly a lot more efficient. It consists of both tree learning algorithms and linear problem solvers. Its ability to do parallel computations at once on a single machine is what makes it so fast. This particular niche of this algorithm makes it fast by a factor of at least 10 than the current gradient boosting algorithms. It also has extended support for a number of objective functions like regression and classification. Its slow implementation time yet high predictive power makes it suitable for a number of computations. Additional features such as cross validation are also an important attribute of this algorithm.[12]

The variable importance entropy metric for each cluster obtained from gradient boosting is displayed in Figure 8.

The results obtained from gradient boosting are displayed in the Figure 9.

VI. Conclusion

It was observed that the accuracy of models could be further increased by only selecting important variables and discarding the unimportant variables. We selected the top 16 features using gradient boosting and applied the methods discussed above and obtained the maximum accuracy using neural networks.

The algorithm is showcased in Figure 10.

The final result obtained is showcased in Figure 11.

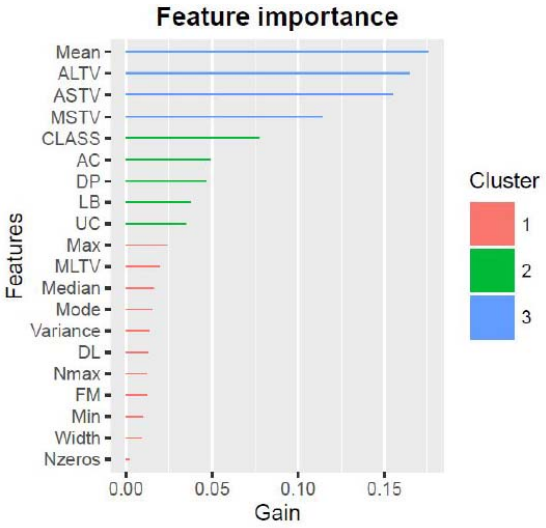

Figure 8. Variable importance for gradient boosting

```
Confusion Matrix and Statistics

          Reference
Prediction   0   1   2
         0 414   2   2
         1  12  68   1
         2   3   2  27

Overall Statistics

               Accuracy : 0.9586
                 95% CI : (0.9379, 0.9739)
    No Information Rate : 0.8079
    P-Value [Acc > NIR] : <2e-16

                  Kappa : 0.8781
 Mcnemar's Test P-Value : 0.0532

Statistics by Class:

                     Class: 0 Class: 1 Class: 2
Sensitivity            0.9650   0.9444  0.90000
Specificity            0.9608   0.9717  0.99002
Pos Pred Value         0.9904   0.8395  0.84375
Neg Pred Value         0.8673   0.9911  0.99399
Prevalence             0.8079   0.1356  0.05650
Detection Rate         0.7797   0.1281  0.05085
Detection Prevalence   0.7872   0.1525  0.06026
Balanced Accuracy      0.9629   0.9581  0.94501
```

Figure 9. Confusion Matrix of Gradient Boosting

ACKNOWLEDGMENT

The authors would like to thank DR S.K Jawa for providing us with her expertise in the field of obstetrics.

REFERENCES

[1] U. M. Fayyad, G. Piatetsky-Shapiro, P. Smyth, and R. Uthurusamy, *"Advances in knowledge discovery and data mining "*, 1996.

[2] Z. Alfirevic, D. Devane, G. Gyte et al., *"Continuous cardiotocography (ctg) as a form of electronic fetal monitoring (efm) for fetal assessment during labour"*, Cochrane Database Syst Rev, vol. 3, no. 3, 2006.

[3] N. Pattison and L. McCowan, *"Cardiotocography for antepartum fetal assessment"*, Cochrane Database of Systematic Reviews, vol. 1, 1999.

[4] L. Zhang, *"Prenatal hypoxia and cardiac programming"*, Journal of the Society for Gynecologic Investigation, vol. 12, no. 1, pp. 213, 2005.

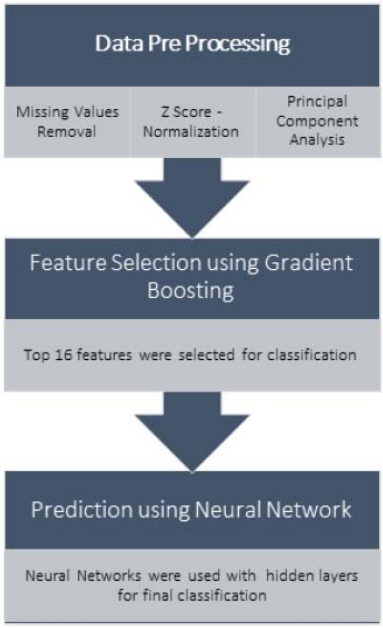

Figure 10. Proposed Algorithm For Maximum Accuracy

```
Confusion Matrix and Statistics

          Reference
Prediction   0   1   2
         0 409   2   0
         1   2  64   0
         2   0   0  54

Overall Statistics

               Accuracy : 0.9925
                 95% CI : (0.9808, 0.9979)
    No Information Rate : 0.774
    P-Value [Acc > NIR] : < 2.2e-16

                  Kappa : 0.9799
 Mcnemar's Test P-Value : NA

Statistics by Class:

                     Class: 0 Class: 1 Class: 2
Sensitivity            0.9951   0.9697   1.0000
Specificity            0.9833   0.9957   1.0000
Pos Pred Value         0.9951   0.9697   1.0000
Neg Pred Value         0.9833   0.9957   1.0000
Prevalence             0.7740   0.1243   0.1017
Detection Rate         0.7702   0.1205   0.1017
Detection Prevalence   0.7740   0.1243   0.1017
Balanced Accuracy      0.9892   0.9827   1.0000
```

Figure 11. Confusion Matrix of Proposed Algorithm

[5] D. Devane, J. G. Lalor, S. Daly, W. McGuire, and V. Smith, *"Cardiotocography versus intermittent auscultation of fetal heart on admission to labour ward for assessment of fetal wellbeing"*, Cochrane Database Syst Rev, vol. 2, 2012.

[6] K. Ojala, M. Vaarasmaki, K. Makikallio, M. Valkama, and A. Tekay, *"A comparison of intrapartum automated fetal electrocardiography and conventional cardiotocographya randomised controlled study"*, BJOG: an international journal of obstetrics and gynaecology, vol. 113, no. 4, pp. 419423, 2006.

[7] S. R. Safavian and D. Landgrebe, *"A survey of decision tree classifier methodology"*, 1990.

[8] M. Lichman, *"UCI machine learning repository"*, 2013. [Online]. Avail-

able: https://archive.ics.uci.edu/ml/datasets/Cardiotocography
[9] I. Steinwart and A. Christmann, *"Support vector machines",* Springer Science and Business Media, 2008.
[10] A. Liaw and M.Wiener, *"Classification and regression by randomforest",* R news, vol. 2, no. 3, pp. 1822, 2002.
[11] K. Hornik, M. Stinchcombe, and H. White, *"Multilayer feedforward networks are universal approximators",* Neural networks, vol. 2, no. 5, pp. 359366, 1989.
[12] K. He, Y. Li, J. Zhu, H. Liu, J. E. Lee, C. I. Amos, T. Hyslop, J. Jin, H. Lin, Q. Wei et al., *"Component-wise gradient boosting and false discovery control in survival analysis with high-dimensional covariates",* Bioinformatics, vol. 32, no. 1, pp. 5057, 2016.

Available online at www.ijapie.org

International Journal of Advanced
Production and Industrial Engineering

IJAPIE-SI-MM 511 (2017) 71–80

Special Issue on

MATERIALS
&
MANUFACTURING

Characteristics and Properties of Different Reinforcements in Hybrid Aluminium Composites: A Review

Ravi Butola*, Ranganath M.Singari, Ashwani Bandhu, R S Walia
(Delhi Technological University, Delhi, India)
**Email: ravimed@dtu.ac.in*

Abstract : Aluminium composites have a wide range of applications and serve as an important tool in various industries. Different reinforcements have different effects on aluminium matrix composite. In this paper these different effects and properties are studied for reinforcing materials such as Silicon Carbide, Graphite, Fly ash, Rice husk ash and boron halide. Properties like hardness, corrosion behaviour, tensile strength, wear resistance etc have been studied rigorously and been summarised. It's been observed that there is an enhancement in the properties of hybrid composites so formed on addition of these reinforcing materials to aluminium composites.

Keywords: Al matrix Composites, Reinforcement, Corrosion behaviour, wear resistance

I. INTRODUCTION

The importance of metal matrix composites has gained a large importance in recent years. MMCS are fast replacing conventional metallic alloys in so many applications as their use have been extended from predominantly aerospace and automobile to defences, marine sports and recreation industries. The different reinforcing materials used in the development can be classified into three broad groups, which are synthetic ceramic particulates, industrial wastes and agro waste derivatives. The final properties of the hybrid reinforcement depend on individual properties of the reinforcement selected and the matrix alloy [1] the aluminium matrix composites (AMCS) represent a class of MMCS possessing properties like low density, high stiffness and strength, superior wear resistance, controlled co-efficient of thermal expansion, higher fatigue resistance and better stability at elevated temperature.[2]Aluminium is most widely used industrial metal and due to its wide applications ,this review emphasizes on studying the effects of different types of reinforcement on aluminium composites .

II. METHODOLOGY

This review revolves around the works of various people in the field of hybrid aluminium composites and studying the effects of different reinforcements used. Various research papers have been studied rigorously for this review considering the reinforcing materials like SiC, rice husk ash, fly ash, graphite and B_4C. All the research works that were used were mainly taken from Sciencedirect.com and have been cited in the work as well. Major properties like Corrosion behaviour, wear behaviour, tensile strength, hardness etc. were studied .Efforts have been made to ensure that similar properties were studied for every reinforcement.

III. DATA AND ANALYSIS

A. ALUMINUM WITH BORON

Tensile strength :

B. Vijaya Ramnath[4] investigated the properties of hybrid composite formed by using alumina and boron carbide as reinforcements to aluminium alloy matrix. Stir casting method was used for production. The tensile test was carried out using a universal testing machine. Three samples were studied are shown in table I

Table I [4]

Sample	Composition of composite specimen	Tensile strength (MPa	Elongation (%)
Sample 1	Aluminium alloy—95% Alumina—3%,Boron carbide—2%	54.60	4.00
Sample 2	Aluminium alloy-95% Alumina-2%,Boron carbide-3%	51.75	3.71
Sample 3	Aluminium alloy	68.24	4.00

It was observed that tensile strength of sample 3 is marginally higher than other two samples because of its aluminum content. But, the sample 1 has higher tensile strength (54.60 MPa) than sample 2 (51.75 MPa)[4]. A. Baradeswaran [5] investigated the Aluminum alloy (AA) 6061 and 7075 that were reinforced with 10 wt.% of boron carbide (B4C) and 5 wt.% of graphite. Liquid casting technique was used.

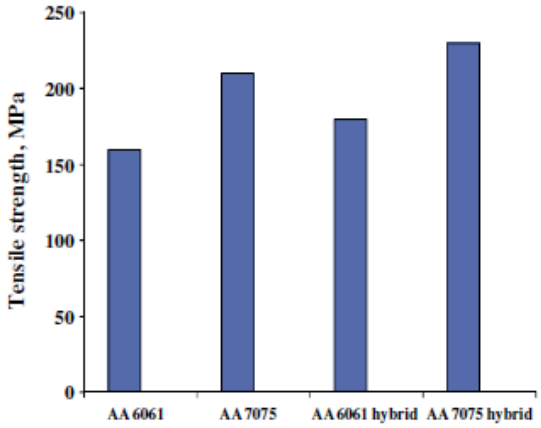

Fig 1.[5]

Thus tensile strength has been observed to increase with increasing B4C particle content and it is significantly higher than the strength of the matrix alloy.

K. Shirvanimoghaddam [6] investigated the effect of ceramic particles on aluminum He observed that the effect of B_4C was temperature dependent for example at 750° Celsius, increase in amount of boron carbide content leads to decrease in tensile strength whereas at 850° Celsius, increasing boron carbide increases the tensile strength.[6]

B. Ravi [10] used Stir casting process for fabrication of aluminum matrix composite and plotted the graph shown in fig 2.

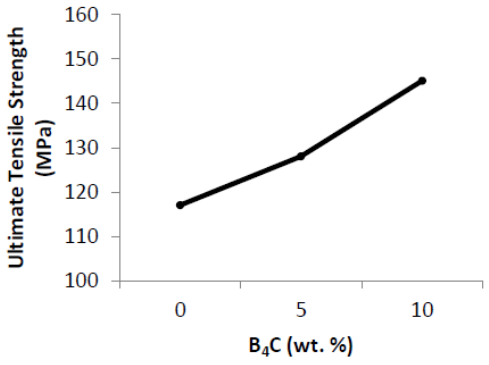

Fig 2[10]

Thus concluded that The B4C reinforcement has enhanced the tensile strength of Aluminum Matrix Composites.

Wear Resistance :

R. Palanivel synthesized and investigated /(TiB2 + BN) hybrid AMCs using Friction Stirring Process and studied the associated microstructure and dry sliding wear behavior. [3]. He observed the values shown in Table.II

Table II [3]

Material	Wear rate (×10 $^{-5}$ mm3/Nm)
AA6082	23.75
AA6082/TiB2 AMC	15.50
AA6082/(TiB2 + BN) hybrid AMC	13.00
AA6082/BN AMC	14.25

Thus concluded that addition of BN particles enhanced the sliding wear resistance of the AMCs. A. Baradeswaran[5] studied the effect of 10 wt.% boron carbide(B_4C) and 5 wt % of graphite as reinforcement and plotted the below shown graphs shown in Fig 4 and Fig 5 . Also it was observed that there is an optimal condition at which the AA 7075/B4C/graphite hybrid composite exhibits higher wear resistance property compared to base alloys and AA 6061 hybrid composite.

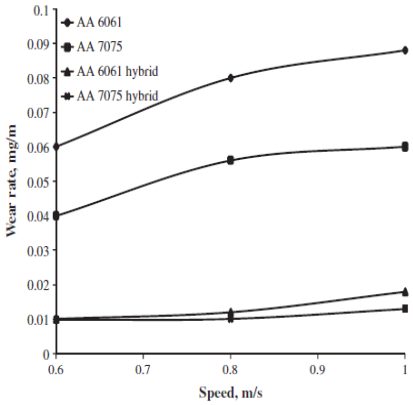

Fig 3 .Effect of sliding speed on wear rate. [5]

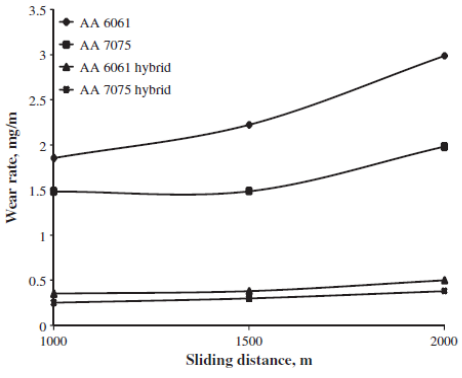

.

Fig 4.Effect of sliding distance on wear rate[5]

Siddhartha Prabhakar[9] also studied the wear behaviour under dry sliding motion of aluminum/B4C composite. Results revealed that wear rate and coefficient of friction

has a direct relation with the load, whereas inverse with the sliding speed and distance.

Hardness :

B. Vijaya Ramnath[4] studied boron carbide metal matrix composite and measured hardness using Brinell's hardness test. The observation of the work is shown in Table III.

Table III [4]

Sample	Composition of composite specimen	Average hardness (BHN)
Sample 1	Aluminum alloy—95%Alumina—3%,Boron carbide—2%	48.53
Sample 2	Aluminum alloy 95% Alumina—2% Boron carbide—3%	52.80
Sample 3	Aluminum alloy	37.83

Thus hardness increases with increase in boron carbide wt %. K. Shirvanimoghaddam[7] investigated manufacturing of aluminum–boron carbide composites using the stir casting method and studied various properties like hardness and density. During his study about hardness of the hybrid composite so formed, the below shown diagrams were plotted.Thus stated that in general increasing the volume fraction of B4C enhances the and hardness of the composite.[7]

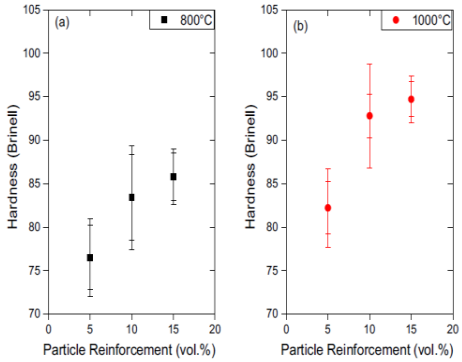

Fig 5[7]

Ehsan Ghasali [11] also studied the properties of B_4C-aluminum metal matrix composite and used the method of microwave sintering for the production. In her work ,she studied the property of microhardness, where it was stated that the average micro hardness of the microwave sintered composites was higher than the corresponding value for the reference 6061 Al alloy and the hardness increased with the increasing amount of B4C.[11]

Impact test :

R. Harichandran [8] used the process of ultrasonic cavitation-assisted solidification for fabrication in his work and studied effect of B_4C as reinforcement on aluminum metal matrix composite.He plotted the graph shown in Fig 6.

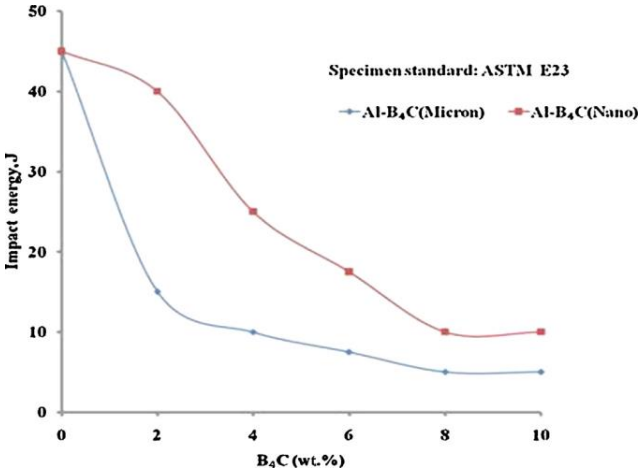

Fig 6.variation of impact energy with B_4C wt%[8]

Thus, the impact energy of the B4C nanoparticle-reinforced aluminum composites was higher than that of the micro B4C particle-reinforced aluminum composites. Similarly B. Vijaya Ramnath[4] used Charpy test to perform the impact test and got the following observations shown in Table IV

Table IV [4]

Sample	Composition of composite specimen	Energy absorbed (J)
Sample 1	Aluminum alloy—95% Alumina—3% Boron carbide—2%	2.18
Sample 2	Aluminum alloy—95% Alumina—2% Boron carbide—3%	2.42
Sample 3	Aluminum alloy	2

It can clearly be seen that the impact value of sample 1 (2.18 J) is lower than the impact value of sample 2 (2.42 J), but higher than that of sample 3 (2 J).[4]Thus addition of Boron Carbide contributes in making the hybrid composite stronger against impacts.

B. ALUMINUM WITH FLY ASH

Hardness :

Liang-Jing Fan[12] prepared Al–3Mg/5 wt.% fly ash composites through stir casting with reactions at 850 °C for various durations (0, 10, 20, 30, and 40 h).He used brinnels hardness tests to study the haedness of the so formed hybrid composite. The hardness fly ash composites increased with increasing reaction time.The plot for the same have plotted below.

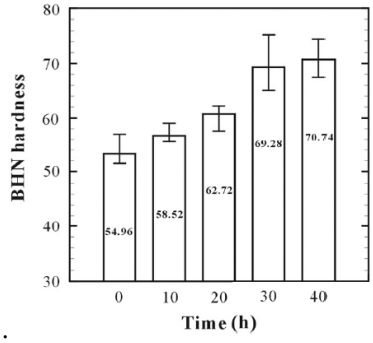

Fig 7 BHN hardness of specimens in different reaction time.[12]

G.Narasaraju [16] made rice husk ash and fly ash reinforced aluminum composite using liquid metal processing technique The hardness was measured using Brinell Hardness Tester at a load of 500 kg for a period of 15 sec in accordance with the ASTM E10.In his work he plotted the below shown diagram.

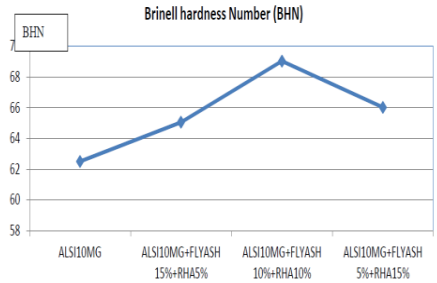

Fig 8[16]

Thus concluded , The hardness of the test specimens increased with increase in Rice Husk Ash and decrease in Fly ash weight proportions.[16]. I. Dinaharan[14] studied wear characteristics and other properties in his work.[14]He studied microhardness of fly ash reinforced aluminum ,plotting the below shown graph. Thus concluding that the use of fly ash as reinforcement greatly enhanced the microhardness of the composite.[14]

Density :

Liang-Jing Fan [12] in is work also studied the reaction of fly ash on density of aluminum hybrid composite so formed. The density was detected using the Archimedes method and plotted the below shown graph on the basis of his experimentation.

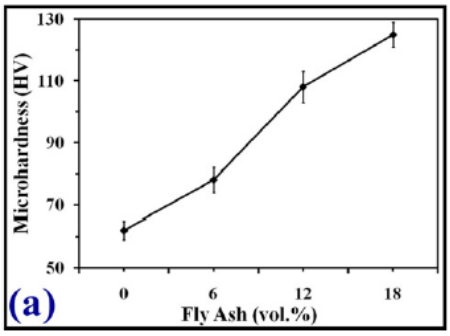

Fig 9 Variation of Micro hardness vs. fly ash wt %[14]

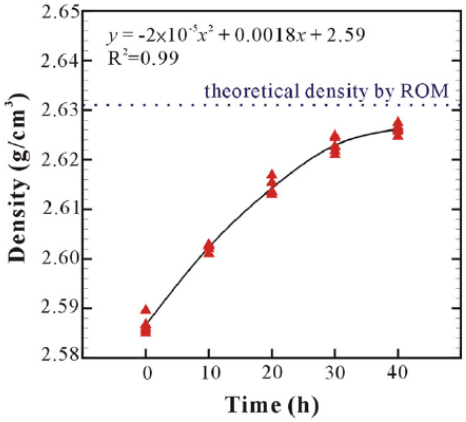

Fig 10 Measured densities of specimens in different reaction time, the dash line indicating the theoretical density.[12]

S.G.Kulkarni [15] during his work on reaction of fly ash hybrid reinforcement on aluminum 356 alloy also studied the density and mechanical properties of the hybrid .He plotted the below shown graph showing theoretical and actual density of various composites.

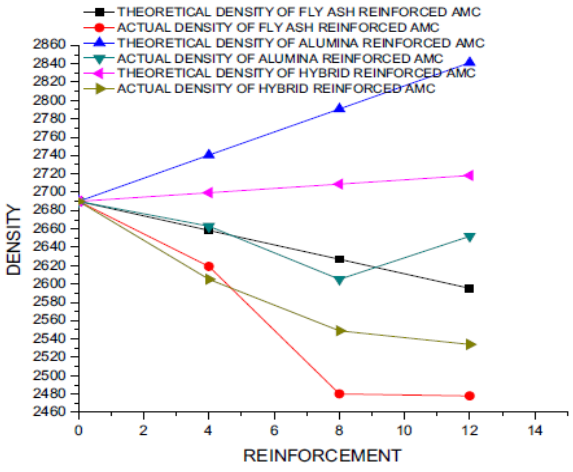

Fig 11 Variation of density with reinforcement %[15]

Thus ,addition of fly ash reinforcement reduces density of composite to much extent.[15]

Wear Resistance :

I. Dinaharan [14] investigated the wear properties of fly ash reinforced aluminum alloy using friction stirring process .He observed that The wear rate reduced as the volume fraction of FA particles was increased. The wear rate was found to be 411 x 10^{-5} mm3/m at 0 vol. % and 203 x 10^{-5} mm3/m at 18 vol. %.

Also FA particles affected the wear mode as well as the morphology of the wear debris. The increased volume fraction of FA particles altered the wear mode from adhesion to abrasive. The wear debris changed from thin plate at 0 vol. % to spherical shape at 18 vol. %. Thus FA particles improved the wear resistance of the composite.

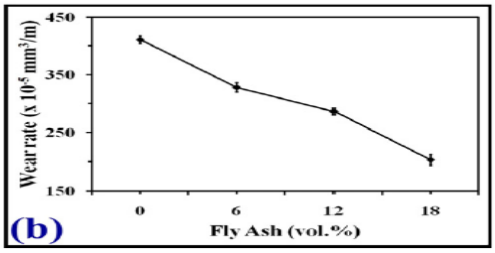

Fig 12 Wear rate vs. Fly ash vol % [14]

Percentage elongation and Tensile strength :

ShueiwanH.Juang [13] observed the the properties like tensile strength and elongation during his work. The tensile strength of the as-cast ALFA composite (ADC6 + 5 wt% fly ash) subjected to Multipath friction stir processing(MS-FSP), as determined from a specimen sampled parallel to the processing paths, increasedto227MPa.This represented significant improvement of the strength compared to the original as-cast ALFA composite. The elongation was 7.18 %, which was far better than that of the original as-cast ALFA composite. The tensile strength of the specimen sample perpendicular to the processing paths also increased to 226 MPa , but its elongation was only 3.12%.[13]. Also G.Narasaraju[16] also studied tensile strength and elongation in his investigation on Rice husk ash and fly ash reinforcement for aluminum alloy .He plotted the below shown diagram for Tensile strength.[16]

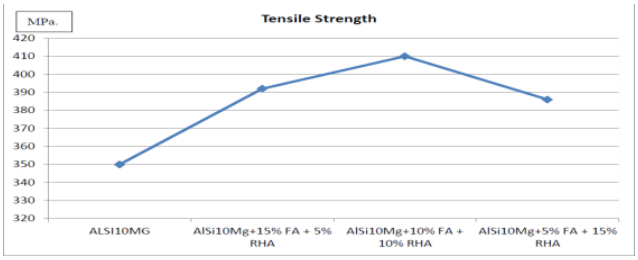

Fig 12 Tensile strength vs. different weight % of reinforcement[16]

Thus concluded That Tensile Strength of MMC increased with increase in Fly ash and percentage elongation is more with decrease in Fly ash by his observations.[16]

C. ALUMINUM WITH GRAPHITE

Hardness :

S. Mosleh-Shirazi [17]studied variation in the hardness of Al/2SiC/Gr hybrid nanocomposites with their Gr . shows that the increased volume fraction of graphite particles resulted in decreased hardness of Al/2SiC/Gr hybrid nano-composites. These results are attributed to the presence of soft graphite particles in the composites that contribute in lowering their hardness values.[17]. Syed Nasimul Alam studied Al-matrix composites reinforced with exfoliated graphite nano- platelets (xGnP) is developed in order to keep the desired properties of Al intact while improving the limiting factors .he gave the following conclusion.[18]

The hardness of the Al- xGnP composites increase up to the ad- dition of 1wt% of xGnP.However,the addition of xGnP beyond 3 wt% leads to a large decrease in the hardness of the Al-xGnP composites. The hardness of the composites possibly reduces due to the agglomeration of xGnP in the Al matrix which also leads to poor densification of the composites. [18]

L.A. Yolshina , R.V. Muradymov used the method for synthesizing aluminum-based metallic composite materials, containing up to 2 wt. % graphene sheets uniformly distributed in a metal matrix,.According to his work synthesis of aluminum-carbon metallic composites with improved structure and unique mechanical properties proceeds at relatively low temperatures without aluminum carbide formation; as a consequence, these composites have sufficiently high corrosion resistance. The hardness, strength, ductility and elasticity of aluminum-graphene composites are higher than the initial aluminum materials, corresponding to the concentration of graphene.[19]. Mohammed Imran [20] in his work made aluminum matrix hybrid composites have been fabricated by stir-casting method using Waste sugarcane bagasse-ash and graphite as reinforcements for aluminum alloy (Al-7075) based matrix. Brinell hardness tests were carried out on samples of both unreinforced alloy and its composites.Thus concluded that increasing the graphite content and keeping the bagasse ash concentration constant contributes in increasing the hardness of composite.[20]

P. Ravindran [21] Studied the tribological behavior of Al 2024–5 wt.% SiC–X wt.% graphite (X = 5 and 10) hybrid nano-composites was produced using powder metallurgy (P/M) technique. The hardness of sintered compacts were performed in Brinell's scale. According to his study hardness of the composites was decreased with the increase in weight percent of Gr reinforcements. [21]

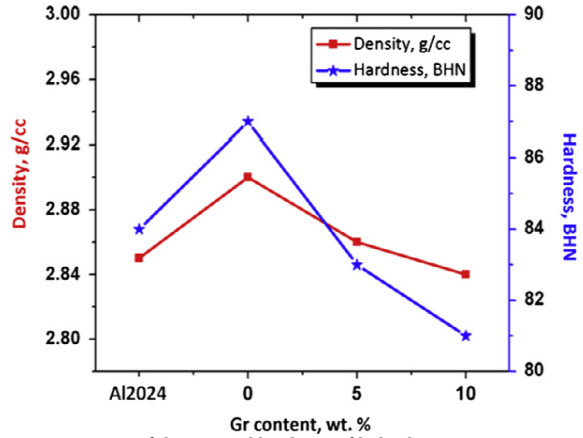

Fig 13 Variation of density and hardness of hybrid nano-composites with different weight percentage of Gr.[21]

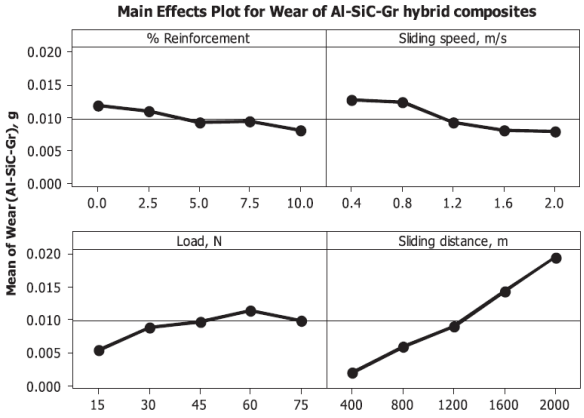

Fig 15 Variation of wear wrt. Various factors [22]

Wear Characteristics :

P. Ravindran [21] investigated properties of aluminum hybrid nano-composites with the additions of solid lubricant. investigation, nano-sized SiC and Gr particles were used as a reinforcement for a nano-aluminum alloy matrix (Al 2024). Dry sliding wear tests were performed in pin-on-disc equipment. The following graphs (fig 14) were obtained showing variation of wear loss with respect to graphite wt % ,.

Thus his investigation gave the following conclusions:
Wear loss of the composite increases as the amount of graphite addition increases up to 5% Gr addition, then drops to a lower value for 10% Gr addition The wear resistance of hybrid nano-composites was higher than the matrix alloy. Amount of the graphite released on the wear surface increases as the percentage of graphite addition increases.[21]. S. Suresha[22] in his work studied wear characteristics using dry sliding wear behavior on aluminum matrix with graphite and SiC as reinforcements. Thus made the below shown graph on the basis of the investigation.

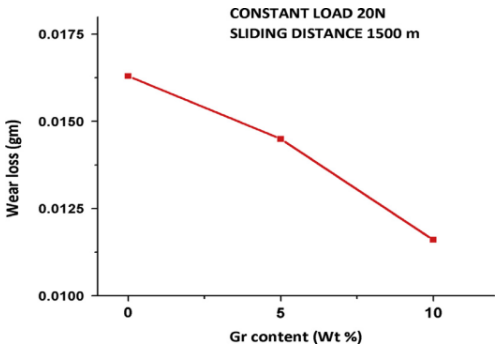

Fig 14 Variation of wear loss vs. Graphite wt %[21]

Kenneth Kanayo Alaneme [23]studied microstructural characteristics, mechanical and wear behaviour of Aluminum matrix hybrid composites reinforced with alumina, rice husk ash (RHA) and graphite. The wear characteristics of the composites were studied using a Taber abrasion wear testing machine He concluded that The composites without graphite exhibited greater wear susceptibility in comparison to the composite grades containing graphite. However the wear resistance decreased with increase in the graphite content from 0.5 to 1.5 wt%.[23]

S. Mosleh-Shirazi studied Effects of graphite (Gr) content on the dry sliding wear, solid-particle erosion and corrosive wear of Al6061based hybrid nano-composites fabricated via powder metallurgy route containing 2 vol% of SiC nano-particles and 0,2, 5 and 7vol%of micron-sized Gr particles and performed Dry sliding wear tests.From these tests concluded that TheAl/2SiC/2Grhybridnano-composite;as compared with Al/2SiC; possessed higher wear resistance and lower friction coefficient. However, when the volume percent of graphite exceeded 2%,both the volume wear loss and friction coefficient of nano-composites increased due to decreased toughness and reduced hardness caused by brittle graphite
Particles.[17]

Corrosion Behaviour :

S. Mosleh-Shirazi corrosion, corrosive wear and abrasive wear, of Al/2SiC/Gr hybrid nano-composites to understand and optimize the materials for improved performance.
The corrosion rates of such nano-composites in that acidic solution as a function of their Gr content were studied. The SiC nano-particles addition increased the corrosion potential of the matrix alloy, due to non-reactivity of a part of the material (nano SiC particles)with the corrosive solution .

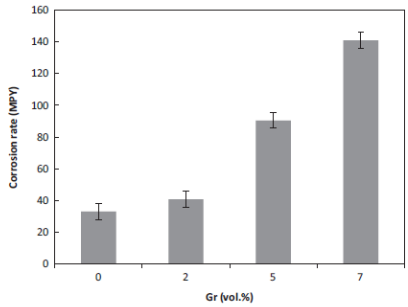

Fig 16 Corrosion rate vs. graphite weight %[17]

Thus concluding That the observed increase in the corrosion rate with Gr particles is attributed to the fact that the added conductive graphite particles may act as micro-cathodes, promoting the galvanic effect and thus increasing the corrosion rate. Both the high-angle solid-particle erosion and the corrosive wear of Al/2SiC/Gr hybrid nano-com- posites increased with their graphite content due to increased amount of the brittle phase (Gr) in the material that contributed in lowering the toughness and hardness of the material.[17]

Elongation and Ductility:
Kenneth Kanayo Alaneme studied effects of varied weight ratios of the three reinforcing materials namely, alumina, rice husk ash, and graphite on the microstructure, mechanical and wear behaviour of Al-Mg-Si alloy matrix.
According to him The % Elongation for all composites produced was within the range of 10 to13% and the values were invariant to the RHA and graphite content.[23]

D. ALUMINUM WITH RICE HUSK ASH

Tensile strength and hardness :
S.D.Saravanan[27] studied Effect of Mechanical Properties on Rice Husk Ash Reinforced Aluminum alloy (AlSi10Mg) Matrix Composites. material. A rice husk ash particle of 3, 6, 9 & 12 % by weight were used to develop metal matrix composites using a liquid metallurgy route. The mechanical properties such as tensile strength, compressive strength, hardness and percentage elongations are studied for reinforced RHA composites.[27]
The tensile tests were conducted using a universal testing machine. The hardness was measured using Brinell's Hardness Test. The following graphs were plotted .

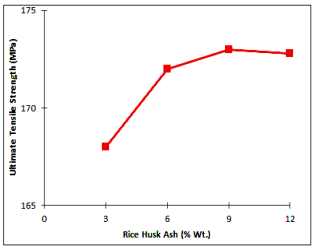

Fig 17 UTS vs. Rice husk ash wt. % [27]

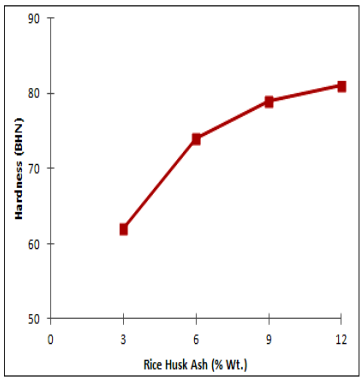

Fig 18 Hardness vs. Rice husk ash wt %[27]

Thus , The Tensile Strength and Hardness increases with the increase in the weight fraction.[27]

Elongation and Ductility :
G.Narasaraju studied Characterization of Hybrid Rice Husk and Fly ash-Reinforced Aluminum alloy (AlSi10Mg) Composites.the investigation on the property of ductility was done. The following results were obtained shown in table V.

Table V [28]

Sl. No	Sample Designation	Percentage elongation
1	AlSi10Mg	2.0
2	AlSi10Mg + 15% Fly Ash +5% Rice Husk Ash	2.9
3	AlSi10Mg + 10% Fly Ash +10% Rice Husk Ash	3.2
4	AlSi10Mg + 5% Fly Ash + 15% Rice Husk Ash	2.7

The percentage elongation is more with decrease in Fly ash and increase in Rice Husk Ash. This is due to decrease in hardness with increase in Rice Husk Ash and decrease in Fly Ash [28]

Damping Behaviour :
Dora Siva Prasad[24] studied the damping behaviour of hybrid composites has been investigated using dynamic mechanical analyzer (DMA). The composites were fabricated with 2, 4, 6, and 8% by weight of rice husk ash (RHA) and SiC in equal proportions using two stage stir casting process. The damping measurements were performed using a GABO Eplexor dynamic mechanical analyser at frequencies ranging from 1 Hz to 15 Hz at room temperature using three point bending mode. All the damping experiments are performed at a static load of 50 N,

a dynamic load of 40 N, and at constant strain amplitude (ε) of 1 × 10−5.

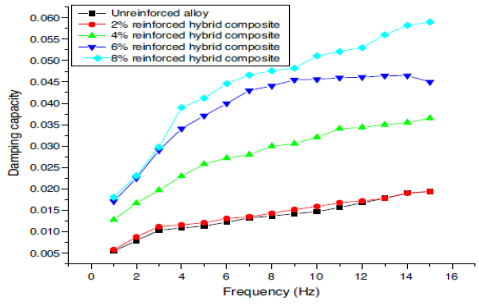

Fig 19 Variation of damping capacity with frequency for unreinforced alloy and hybrid composites.[24]

Wear Resistance :

Kazeem Oladiti Sanusi [26] It is also observed that the effect of RHA on wear susceptibility was not as consistent as the case of graphite but generally for the composites containing RHA there was on the average an increase in wear susceptibility with increase in RHA content. The wear resistance thus decreases with decrease in RHA.[26]

Corrosion:

Kenneth Kanayo Alaneme [25] in his work on corrosion behavior of hybrid composites using rice husk ash and silicon carbide as reinforcements stated that the hybrid composite grades with a higher RHA content generally exhibited a lower tendency to corrode compared to the other composite grades. He used thermally cycled aluminum composites for his study and also concluded that the composites are structurally stable and maintain their corrosion resistance levels even after exposure to thermal cycling.[25]

E. ALUMINUM WITH SiC

Aging behaviour :

Yan Cui [29] studied Aging behaviours of the high-volume-fraction SiCp/Al-Mg-Si composite fabricated by pressure less in filtration and its base alloy at 170° C. The aging behaviours of the base alloy and the composite were studied by Rockwell hardness measurement. Following results were obtained by Yan Cui :

(1) The hardness of the 55% SiCp/Al composite and the matrix alloy could be improved by age-hardening treatment. The maximum hardness increment of the matrix alloy is 242% after aging treatment for 3 h while that of the composite is 22%.(2) The aging kinetic of the 55% SiCp/Al composite is accelerated due to the high density of the dislocation, in comparison to the performance of the Al-Mg-Si alloy.(3) The mechanisms of the age-hardening treatment of the unreinforced Al-Mg-Si alloy and the high volume fraction SiCp/Al composite are quite different. For Al-Mg-Si alloy, double hardness peaks are observed. For 55% SiC/Al composite, only one visible peak is observed.[29]

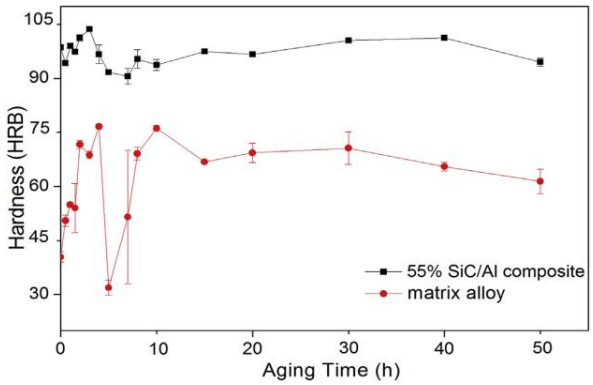

Fig 20 Aging curves at 170° C for solution-treated matrix alloy and solution-treated composite.[29]

Compression Behaviour :

Jufu Jiang studied[30] The compression mechanical behaviour of the fabricated composite in semisolid state .Consequently, they lead to a significant reduction of porosity and an improvement of mechanical properties of the final products.

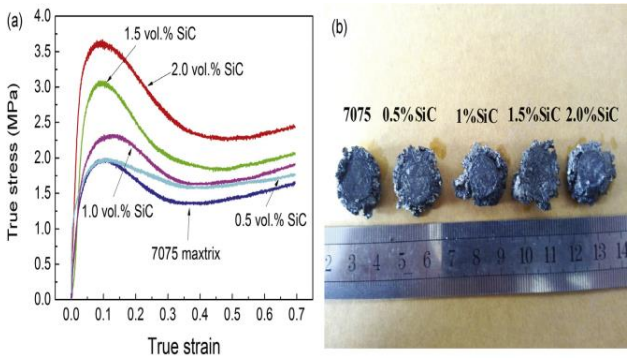

Fig 21 True stress–strain curves (a) and macrograph (b) of the samples with different volume fraction of SiC particles.[30]

Jufu Jiang observed that Peak stress and steady stress increase with increasing volume fraction of SiC particles and there was a significant improvement in properties.

Wear characteristics :

S. Suresha[31] studied the dry sliding wear behaviour of Al matrix composites reinforced with Gr and SiC particulate up to 10%, to study the effect of % reinforcement, load, sliding speed and sliding distance on stir cast Al–SiC–Gr hybrid composites, Al–Gr and Al–SiC composites. Addition of SiC particulates increases both mechanical strength and wear resistance of Al alloy. But the consequent increase in hardness makes the machining difficult . On the other hand, addition of Gr particulates facilitates easy

machining and results in reduced wear of Al–Gr composites compared to Al alloy.[31]
Thus addition of SiC particulates improve the wear characteristics effectively and upto a great extent.

Corrosion Behaviour :
H.M. Zakaria [32]studied the corrosive properties of Al/SiC metal matrix composites (MMCs). Following observations were made by Zakaria in his experiments.
1.) At room temperature, the Al/SiC composites exhibited better corrosion resistance than the pure Al matrix in
3.5 wt.% NaCl aqueous solution.
2.) Increasing the volume fraction of the SiC particulates increased the corrosion resistance of the Al/SiC composites. Moreover, reducing the SiC particles size
enhanced significantly the corrosion resistance of the SiC composites. Increasing the duration exposure reduces the corrosion rate.
3.) At elevated temperature, the Al/SiC composites exhibited lower corrosion resistance than the pure Al matrix in 3.5 wt.% NaCl aqueous solution. However, increasing the volume fraction and/or the SiC particles size reduce(s) the corrosion rates of the Al/SiC composites. The corrosion rates of the pure Al as well as the Al/SiC composites were found to increase linearly with the temperature.[32]

IV. CONCLUSIONS

The conclusion derived by this study about the effects of five different reinforcing materials on aluminium matrix composites is as follows.

- Addition of Boron carbide enhances the tensile strength, wear resistance, hardness. Also impact energy absorbed was higher for hybrid AMC with boron carbide.
- On Addition of Fly ash density and hardness decreases There was an improvement in wear resistance.Tensile Strength of MMC increased with increase in Fly ash and percentage elongation is more with decrease in Fly ash.
- Hardness increased up to a maximum value on addition of graphite and then decreased. Both Corrosion and wear resistance decreases on increasing graphite weight proportion. Elongation is generally invariant on addition of graphite.
- Tensile strength and hardness increases with increase in RHA concentration. Elongation, wear resistance, damping capacity and corrosion resistance showed significant improvement on addition of RHA.
- Aging kinetic of 55% SiCp/Al composite is accelerated due to the high density of the dislocation. Peak stress and steady stress increase with increasing volume fraction of SiC particles and there was a significant improvement in compressive properties. Also wear resistance and corrosion resistance improved on addition of SiC particles.

REFERENCES

[1]. Michael Oluwatosin Bodunrin , Kenneth Kanayo Alaneme, Lesley Heath Chown; Aluminium matrix hybrid composites: a review of reinforcement philosophies; mechanical, corrosion and tribological characteristics. j mater r estec no l . 2015; 4(4):434–445
[2]. Jaswinder Singh, Amit Chauhan; Characterization of hybrid aluminium matrix composites for advanced applications – A review. j mater res tech no l . 2016;5(2):159–169
[3]. R. Palanivel , I. Dinaharan , R.F. Laubscher , J. Paulo Davim, Influence of boron nitride nanoparticles on microstructure and wear behavior of AA6082/TiB2 hybrid aluminium composites synthesized by friction stir processing.. Materials and Design 106 (2016) 195–204
[4]. B. Vijaya Ramnath , C. Elanchezhian , M. Jaivignesh , S. Rajesh , C. Parswajinan , A. Siddique Ahmed Ghias ,Evaluation of mechanical properties of aluminium alloy–alumina–boron carbide metal matrix composites. Materials and Design 58 (2014) 332–338
[5]. A. Baradeswaran , S.C. Vettivel , A. Elaya Perumal , N. Selvakumar , R. Franklin Issac,Experimental investigation on mechanical behaviour, modelling and optimization of wear parameters of B4C and graphite reinforced aluminium hybrid composites. Materials and Design 63 (2014) 620–632
[6]. K. Shirvanimoghaddam, H.Khayyam, H.Abdizadeh, M.KarbalaeiAkbari, A.H.Pakseresht, F. Abdi, A.Abbasi, M.Naebe,Effect of B4C, TiB2 and ZrSiO4 ceramic particles on mechanical properties of aluminium matrix composites Experimental investigation and predictive modelling. Ceramics International 42 (2016) 6206–6220
[7]. K. Shirvanimoghaddam , H.Khayyam, H.Abdizadeh , M.KarbalaeiAkbari , A.H.Pakseresht , E.Ghasali , M.Naebe ,Boron carbide reinforced aluminium matrix composite: Physical, mechanical characterization and mathematical modelling. Materials Science& EngineeringA658(2016)135–149
[8]. R. Harichandran , N. Selvakumar,Effect of nano/micro B4C particles on the mechanical properties of aluminium metal matrix composites fabricated by ultrasonic cavitation-assisted solidification process. archives of civil and m echanical engineering 16 (2016) 147 – 158
[9]. Siddhartha Prabhakar , Radhika , Raghu.R ,Analysis of tribological behavior of aluminium/ B4C composite under dry sliding motion. Procedia Engineering 97 (2014) 994 –1003
[10]. B. Ravi, B. Balu Naik , J. Udaya Prakash ,Characterization of Aluminium Matrix Composites (AA6061/B4C) Fabricated by Stir Casting Technique. Materials Today: Proceedings 2 (2015) 2984 – 2990
[11]. Ehsan Ghasali, Masoud Alizadeh, Touradj Ebadzadeh, Amir hossein Pakseresht, Ali Rahbari,Investigation on Microstructural and mechanical properties of B4C–aluminium matrix composites prepared by microwave sintering. j mater res tech no l . 2015; 4(4):411–415
[12]. Liang-Jing Fan, Shueiwan H. Juang, Reaction effect of fly ash with Al–3Mg melt on the microstructure and hardness of aluminium matrix composites. Materials and Design 89 (2016) 941–949
[13]. Shueiwan H. Juang , Cheng-ShuoXue, Investigation of mechanical properties and microstructures of aluminium-fly ash

composite processed by friction stirring. Materials Science Engineering A640(2015)314–319

[14]. I. Dinaharan , R. Nelson, S.J. Vijay , E.T. Akinlabi ,Microstructure and wear characterization of aluminium matrix composites reinforced with industrial waste fly ash particulates synthesized by friction stir processing. Materials Characterization 118(2016)149–158

[15]. S.G.Kulkarni, J.V.Meghnani, Achchhe Lal ,Effect of fly ash hybrid reinforcement on mechanical property and density of aluminium 356 alloy. Procedia Materials Science 5 (2014)746 – 754

[16]. G.Narasaraju, D. Linga Raju, Characterization of Hybrid Rice Husk and Fly ash-Reinforced Aluminium alloy (AlSi10Mg) CompositesMaterials Today: Proceedings 2 (2015) 3056 – 3064

[17]. S. Mosleh-Shirazi , F.Akhlaghi , D.Y.Li ,Effect of graphite content on the wear behavior of Al/2SiC/Gr hybrid nano-composites respectively in the ambient environment and an acidic solution. Tribology International 103(2016)620–628

[18]. Syed Nasimul Alam , Lailesh Kumar, Mechanical properties of aluminium based metal matrix composites reinforced with graphite nano platelets Materials Science Engineering A667(2016)16–32

[19]. L.A. Yolshina , R.V. Muradymov , I.V. Korsun , G.A. Yakovlev , S.V. Smirnov ,Novel aluminium-graphene and aluminium-graphite metallic composite materials: Synthesis and properties. Journal of Alloys and Compounds 663 (2016) 449e459

[20]. Mohammed Imran, A.R. Anwar Khan, Sadananda Megeri, Shoaib Sadik, Study of hardness and tensile strength of Aluminium-7075 percentage varying reinforced with graphite and bagasse-ash composites.Resource-Efficient Technologies 2(2016) 81–88

[21]. P. Ravindran, K. Manisekar, S. Vinoth Kumar, P. Rathika c, Investigation of microstructure and mechanical properties of aluminium hybrid nano-composites with the additions of solid lubricant. Materials and Design 51 (2013) 448–456

[22]. S. Suresha , B.K. Sridhara,Wear characteristics of hybrid aluminium matrix composites reinforced With graphite and silicon carbide Particulates.Composites Science and Technology 70(2010)1652–1659

[23].Kenneth Kanayo Alaneme, Kazeem Oladiti Sanusi ,Microstructural characteristics, mechanical and wear behaviour of aluminium matrix hybrid composites reinforced with alumina, rice husk ash and graphite. Engineering Science and Technology, an International Journal 18(2015) 416e422

[24]. Dora Siva Prasad , Chintada Shoba ,Experimental evaluation onto the damping behavior of Al/SiC/RHA hybrid composites. j mater res tech no l . 2016; 5(2):123–130

[25]. Kenneth Kanayo Alaneme , Joshua Ogheneakporobo Ekperusi, Samuel Ranti Oke,Corrosion behaviour of thermal cycled aluminium hybrid composites reinforced with rice husk ash and silicon carbide. Journal of King Saud University – Engineering Sciences (2016) xxx, xxx–xxx

[26]. Kenneth Kanayo Alaneme, Kazeem Oladiti Sanusi, Microstructural characteristics, mechanical and wear behaviour of aluminium matrix hybrid composites reinforced with alumina, rice husk ash and graphite. Engineering Science and Technology, an International Journal 18 (2015) 416e422

[27]. S.D.Saravanan, M.Senthil Kumar,Effect of Mechanical Properties on Rice Husk Ash Reinforced Aluminium alloy (AlSi10Mg) Matrix Composites. Procedia Engineering 64 (2013)1505 – 1513

[28]. G.Narasaraju1, D. Linga Raju , Characterization of Hybrid Rice Husk and Fly ash-Reinforced Aluminium alloy (AlSi10Mg) Composites. Materials Today: Proceedings 2 (2015) 3056 – 3064.

[29]. Yan Cui, Tingzhu Jin, Leigang Cao , Fengbin Liu, Aging behavior of high volume fraction SiCp/Al composites fabricated by pressureless infiltration. Journal of Alloys and Compounds 681 (2016) 233e239

[30]. Jufu Jiang ,Gang Chen ,Ying Wang , Compression Mechanical Behaviour of 7075 Aluminium Matrix Composite Reinforced with Nano-sized SiC Particles in Semisolid State. Journal of Materials Science & Technology (2016)

[31]. S. Suresha , B.K. Sridhara, Wear characteristics of hybrid aluminium matrix composites reinforced with graphite and silicon carbide particulates. Composites Science and Technology 70(2010)1652–1659

[32]. H.M. Zakaria, Microstructural and corrosion behavior of Al/SiC metal matrix composites. Ain Shams Engineering Journal (2014) 5, 831–838.

Front. Biol.
DOI 10.1007/s11515-017-1440-8

RESEARCH ARTICLE

Comparative analysis of metabolic network of pathogens

Kumar Gaurav, Yasha Hasija (✉)

Department of Biotechnology, Delhi Technological University, Delhi – 110042, India

© Higher Education Press and Springer-Verlag Berlin Heidelberg 2017

BACKGROUND: Metabolic networks are complex and system of highly connected chemical reactions and hence it needs a system level computational approach to identify the genotype- phenotype relationship. The study of essential genes and reactions and synthetic lethality of genes and reactions plays a crucial role in explaining functional links between genes and gene function predictions.
METHODS: Flux balance analysis (FBA) has been developed as a powerful method for the *in silico* analyses of metabolic networks. In this study, we present the comparative analysis of the genomic scale metabolic networks of the four microorganisms i.e. *Salmonella typhimurium, Mycobacterium tuberculosis, Staphylococcus aureus,* and *Helicobacter pylori*. The fluxes of all reaction were obtained and the growth rate of the organism was calculated by setting the biomass reaction as the objective function.
RESULTS & CONCLUSIONS: The average lethality fraction of all the four organisms studied ranged from 0.2 to 0.6. It was also observed that there are very few metabolites which are highly connected. Those metabolites that are highly connected are supposed to be the 'global players' similar to the hub protein in the protein – protein interaction network.

Keywords essential genes, synthetic lethal genes, metabolite connectivity, robustness analysis

Introduction

As a complex interactive nonlinear system, much attention has been gained by the study related to the metabolic networks in recent years. Efforts have also been made for the analysis of the structure of whole metabolic networks (Feist and Palsson, 2008). The use of flux balance analysis in order to predict the flux distribution in an entire metabolic network under certain physiological conditions is to analyze and compare the metabolic networks related to different organisms. There is already the availability of genome scale reconstructed models of the different organisms like *Helicobacter pylori, Mycobacterium tuberculosis* etc. These metabolic networks are obtained from different metabolic models databases (Hamilton and Reed, 2012). Flux Balance Analysis (FBA) is a widely used constraint based approach for studying biochemical metabolic networks, mainly the genomic scale metabolic network that have been reconstructed in the past decade. It uses the concept of linear programming. Linear programming obtains the maximum potential of the objective function that we are looking at, and therefore, when using flux balance analysis, a single solution is obtained for the optimization problem (Raman and Chandra, 2009). FBA calculates the flow of metabolites taking place in the metabolic network, hence making it possible to predict the growth speed of an organism or the rate of production of a biochemically important metabolite (Edwards and Palsson, 2002). Essential genes comprise of genes whose specific deletion is lethal under a specific environmental condition. Identification of essential genes in the metabolic network of microorganisms helps to identify potential drug targets and in understanding of minimal requirements for a synthetic cell. However, experimental assessment of essentiality of the coding genes of metabolic network is resource intensive and not viable for all bacterial organisms, in particular if they are infective (Plaimas et al., 2010; Chowdhury et al., 2015). A constraint-based analysis of reconstructed metabolic networks has proved to be quite useful in various applications such as metabolic engineering prediction of outcomes of gene deletions, drug-target identification and in the elucidation of cellular regulatory networks (Raman et al., 2005). By analogy, Synthetic Lethals (SLs) refer to the pair of non-essential genes whose simultaneous deletion is proved to be lethal. Synthetic gene lethality can arise for different types of reasons. For example, two protein products can be interchanged with respect to an essential function that act in similar pathway or function in

Received August 30, 2016; accepted December 20, 2016
Correspondence: Yasha Hasija
E-mail: yashahasija@gmail.com

two distinct pathways with redundant or complementary essential functions. The study of synthetic lethality plays an important role in explaining functional links between genes and the prediction of the gene functions (Suthers et al., 2009; Chowdhury et al., 2015; Raman et al., 2015). Occurrence of synthetic lethality can be seen between genes and small molecules, and it can be used to explain the mechanism of action of drugs.

The true potential of synthetic lethality has been widely studied in yeast (Nijman, 2011). Biological systems are prone to mutation, to the variation in environmental conditions and to random variations in the abundance of component molecules of the biological systems. Many physiological and developmental systems are robust to such disturbances and hence immune to any such fluctuations (Masel and Siegal, 2010). Biological systems that have been experimentally proved of being robust to the significant changes in their environmental conditions need mathematical models for robustness analysis of the metabolic network. These mathematical models should themselves be robust. The necessary condition for the model robustness is that the dynamics of the model should be insensitive to small variations in the parameters of the model. The model dynamics may be very much sensitive to simultaneous parameter variations (Kim et al., 2006). Phenotype phase plane analysis can study the optimal utilization of the metabolic network as a function of the constraints. At present metabolic flux maps are typically calculated for the single growth condition, hence gives a limited view of the metabolic phenotype – genotype relation. But phenotypic phase plane analysis maps all the growth conditions characterized by two environmental variables presented in the single plane (Edwards et al., 2001). Fast-SL is an algorithm which computes combinations of reactions, which when deleted, leads to the elimination of the growth of the organism due to the modification in the metabolic pathway. It achieves this by a combination of limiting the search space and exhaustively iterating through the remaining combinations (Pratapa et al., 2015). The functional *in silico* model of *Mycobacterium tuberculosis*, iNJ6611, contains 661 genes, 1025 reactions and 826 metabolites. Genome scale models can be used as hypothesis generating tools and also for analysis and discovery which will expectantly support the rational drug development process (Jamshidi and Palsson, 2007). The functional *in silico* model of bacterium *Staphylococcus aureus*, *iSB619*, consists of 619 genes by which 640 metabolic reactions are catalyzed. The reaction list is the most complete till date for this pathogen (Becker and Palsson, 2005; Heinemann et al., 2005). The reconstructed network, *iIT341* represents a detailed review of the current literature about *Helicobacter pylori* as it integrates biochemical and genomic data in a comprehensive framework. In total, it contains 341 metabolic genes, 476 intracellular reactions, 78 exchange reactions, and 485 metabolites (Schilling et al., 2002; Palsson et al., 2005). Salmonella enterica subspecies I serovar Typhimurium is a human pathogen which causes different diseases and its increasing antibiotic resistance poses many public health problems. Different diseases caused by Salmonella are mainly Typhoid fever, Paratyphoid fever and Food poisoning. The functional *in silico* model of *Salmonella typhimurium*, *STM_v1_0*, consists of 1271 genes, 1802 metabolites and 2545 reactions (McClelland et al., 2001; Thiele et al., 2011). Methods of Constraint Based Reconstruction and Analysis (COBRA) have been successfully applied in the field of microbial metabolic engineering and are being extended to model transcriptional and signaling networks and in the field of public health. The COBRA approach focuses on using physicochemical and biological constraints to analyze the set of feasible phenotypic states of a reconstructed biological network under a given condition (Schellenberger et al., 2011). SBMLToolbox, a toolbox that facilitates importing and exporting models presented in the Systems Biology Markup Language (SBML) format in the MATLAB environment. It also provides functionality that helps an experienced user of either SBML or MATLAB to combine the computing power of MATLAB with the exchangeability and portability of an SBML model. SBMLToolbox supports all levels and versions of SBML (Keating et al., 2006). In this work, we describe the similarities and dissimilarities of metabolic networks of *Salmonella typhimurium* (STM_v1_0), *Helicobacter pylori* (iIT341), *Mycobacterium tuberculosis* (iNJ661) and *Staphylococcus aureus* (iSB619) by pairwise comparison with the help of flux balance analysis and gene deletion method.

Materials and methods

The comparative study of metabolic network for finding the similarity and dissimilarities is conducted for the following four pathogenic bacteria.

1) *Mycobacterium tuberculosis* (iNJ661),
2) *Staphylococcus aureus* (iSB619),
3) *Salmonella typhimurium* (STM_v1_0),
4) *Helicobacter pylori* (iIT341).

The genome scale metabolic networks of the four pathogenic organisms were collected from different sources like BiGG database, BioModel database and TheModelSeed database. The MATLAB compliant files of the four given organisms were downloaded from the BiGG Database.

Flux balance analysis

The constraints in FBA have the form $\alpha \leqslant v_i \leqslant \beta$ where vector v_i represents all the fluxes in the given metabolic network, α and β are the lower and upper limits. Thermodynamic constraints according to the reversibility and irreversibility of a reaction can be applied by setting the lower limit (α) for the equivalent flux to 0 if the reaction is irreversible and -1000 if the reaction is reversible. The upper limit is set to 1000 for reversible and irreversible reactions. The COBRA toolbox was used to run the FBA. For constraint based modeling,

COBRA toolbox is used which has a collection of MATLAB scripts that are run from within the MATLAB environment. The MATLAB compliant metabolic network files of each of the four organisms were loaded in the MATLAB. A specific metabolic flux distribution within the feasible set was found by using linear programming (LP). The Gurobi solver package was used to perform linear programming in COBRA Toolbox. The fluxes of all reaction were obtained and the growth rate of the organism was calculated by setting the biomass reaction as the objective function.

Simulating gene knockouts

Gene-protein-reaction associations are embodied in *rxnGeneMat* matrix in the MATLAB files, which is a matrix with rows equal to number of reactions in the model and columns equal to number of genes in the model. The function – *singleGeneDeletion* and *doubleGeneDeletion* performs the single and double gene deletion respectively.

Performing synthetic lethality analysis

It was performed using the Fast – SL algorithm that is implemented using the MATLAB.

Code to perform the synthetic lethal reaction analysis-fastSL (*model*, *cutoff*, *order*, *eliList*, *atpm*)

Code to perform the synthetic lethal gene analysis-fastSLgenes (model, cutoff, order, flag)

where *model* is metabolic network file to be analyzed, *cutoff* is cutoff percentage value for lethality and have default value of 0.01, *order* is order of synthetic lethals and have default value of 2 and maximum value 3, *eliList* is the list of the reactions to be excluded from the analysis, *flag* is set to 1 for rigorous search and have default value 0, *atpm* is ATP Maintenance Reaction Id in model.rxns if other than ATP Maintenance Reaction.

Robustness analysis

Robustness analysis uses the FBA to analyze the metabolic network properties. In this step, the flux was varied through one reaction and the optimal objective value was calculated as a function of this value. This tells about the sensitivity of the objective value to a particular reaction. We have checked the effect of varying glucose and oxygen uptake on the growth rate. COBRAToolbox has the function *robustnessAnalysis* to perform this method.

Phenotypic phase plane analysis

While performing the Robustness analysis, we varied one parameter and made another parameter to be constant. However, in phenotypic phase plane analysis, we varied two parameters glucose and oxygen uptake rate simultaneously and the results were plotted as phenotypic phase plane. It revealed the interaction between two reactions. COBRA Toolbox has the built in function *phenotypePhasePlane* to perform this step.

Metabolite connectivity

Metabolite connectivity is the number of reactions in which the metabolites occur in. In this step the Stoichiometric matrix S of the metabolic model was converted into the binary matrix S_{bin}. It replaces all nonzero elements in the matrix S with '1' in the binary matrix. Then all '1s' in each row of the S_{bin} was added up to determine metabolite connectivity.

Reaction essentiality and metabolite connectivity

Correlation between essentiality of reaction and metabolite connectivity can be estimated in the metabolic network. In this step, all the reactions which were associated with the metabolites were deleted and checked whether it could still produce the biomass or not. Reactions associated with the metabolites could be found out by scanning through the corresponding rows in the Stoichiometric S matrix. After then all the associated genes were knocked out and FBA was used to predict the possibility of the growth. Lethality fraction was calculated based on the above result. The semi log graph was plotted with this lethality fraction vs. metabolite connectivity.

Results

Calculation of growth rate using FBA

The growth rates of the four organisms were calculated using flux balance analysis. The maximization of biomass was set as the objective function to calculate the growth rate. The growth rate is calculated in the unit mmol/(gDW·h) (millimole/(gramDryWeight·hour)). The growth rates of four organisms are shown in Table 1.

The table showing growth rates, are the growth rates calculated for the wild type strain of each of the model organism. The objective function for each of the organism was

Table 1 Growth rates of all the four organisms using FBA

Organism	Number of reactions	Number of metabolites	Number of genes	Growth rate (mmol/(gDW·h))
Mycobacterium tuberculosis	1025	826	661	0.0522
Staphylococcus aureus	743	655	619	0.0687
Salmonella typhimurium	1076	982	801	0.4779
Helicobacter pylori	554	485	339	0.6928

different. Apart from this, growth rates under the alternative substrates like glucose, succinate, pyruvate etc. were also calculated. The calculation of growth rates was done under both aerobic and anaerobic conditions. The growth rates calculated under the alternative substrates were different compared to the wild type ones. For most of the substrate, growth rate under the anaerobic condition was found to be 0 for each of the organism studied. Alternative substrates under which growth rates were calculated are the important substrates that play an important role in the major metabolic pathways like glycosis, TCA cycle, oxidative phosphorylation, amino acid metabolism etc. The growth rates calculated under alternative substrates are shown in the given below tables for each of the organism separately. The maximum substrate uptake rate was set to -20 mmol/(gDW·h) for every substrate. The calculated growth rates under the alternative substrates in the metabolic networks of each of the four different organisms have been shown in the tables from Tables 2 to 5.

Retrieving essential reactions and essential genes from gene knockouts

If a single gene is associated with multiple reactions, the deletion of that gene results in the removal of all reactions associated to the genes. On the other hand, a reaction that can be catalyzed by multiple gene products which do not interact with one other will not be removed in a single gene deletion. The essential reactions were extracted by reaction knockout method. The essential genes were extracted by gene knockout method. By the aid of the COBRA toolbox, we can retrieve the essential reactions in the metabolic network. After gene knockout, a mutant strain of the organism is generated and it also provides the grRatio (gene-reaction ratio) of the mutant strain and wild type strain of the organisms. The grRatio is the ratio between the grRatio of wild type strain and the grRatio of the mutated strain. Those genes and reactions are the essential genes and essential reactions of the organisms, if the grRatio is less than 0.05. Key metabolites affected by gene deletion were 3PG(3-phosphoglycerate), AcCoA (acetyl CoA), ADP, AKG(α-ketoglutaric acid), ATP, CoA(coenzyme-A), E4P(erythrose-4-phosphate), F6P(fructose-6-phosphate), G3P(glycerol-3-phosphate), G6P(glucose-6-phosphate), Gln-L(L-glutamine), Glu-L(L-glutamic acid), H2O, H(hydrogen), NAD, NADH, NADP, NADPH, OAA (oxaloacetic acid), PEP(phosphoenol pyruvate), Pi(inorganic phosphate), pyr(pyruvate), R5P(ribose-5-phosphate). Number of essential reactions and essential genes present in metabolic network of each organism has been shown in Table 6. The essential reactions thus obtained for each of the organism can be compared pairwise with essential reactions of each of the organism. The pairwise comparison was performed with the help of Compare plugin in the Notepad++. Common essential reactions thus obtained by the pairwise comparison are shown in the below given Table 7.

Table 2 Growth rates of *Mycobacterium tuberculosis* under the alternative substrates

Substrate	Aerobic (mmol/(gDW·h))	Anaerobic (mmol/(gDW·h))
Glucose	0.3060	0
Succinate	0.1393	-2.0512e-26
Aspartate	0.0680	3.9109e-20
Phosphate	0.1440	-1.7094e-27
Glycerol	0.3060	6.9372e-26
Pyruvate	0.3060	-9.6864e-27

Table 3 Growth rates of *Staphylococcus aureus* under the alternative substrates

Substrate	Aerobic (mmol/(gDW·h))	Anaerobic (mmol/(gDW·h))
Glucose	0.0141	2.2559e-26
Succinate	Absent	Absent
Aspartate	0.0123	0
Phosphate	0.0103	0
Glycerol	-9.6865e-18	-4.1655e-18
Pyruvate	Absent	Absent

Table 4 Growth rates of *Helicobacter pylori* under the alternative substrates

Substrate	Aerobic(mmol/(gDW·h))	Anaerobic(mmol/(gDW·h))
Glucose	4.1510	0
Succinate	5.3325	0
Aspartate	5.2489	0
Phosphate	4.1510	0
Glycerol	Absent	Absent
Pyruvate	4.9698	1.5179e-29

Table 5 Growth rates of *Salmonella typhimurium* under the alternative substrates

Substrate	Aerobic (mmol/(gDW·h))	Anaerobic (mmol/(gDW·h))
Glucose	1.9317	0.4500
Succinate	1.5507	0.0525
Aspartate	1.4971	0.2959
Phosphate	0.4779	0.0525
Glycerol	1.1227e-12	-9.3396e-13
Pyruvate	1.1584e-12	-4.6855e-13

Table 6 Essential genes and essential reactions present in metabolic networks of given organisms.

Organism	*S. aureus*	*M. tuberculosis*	*S. typhimurium*	*H. pylori*
Number of essential reactions	244	314	345	256
Number of essential genes	168	188	201	186

In the recent years, genome-scale metabolic networks have been reconstructed for many organisms (Thiele et al., 2005, 2011). These networks have been studied using tools such as Flux Balance Analysis (FBA) (Kauffman et al., 2003), for the

Table 7 Common essential reactions compared among four different organisms.

Pairwise combination of organisms	*M. tuberculosis* *S. typhimurium*	*M. tuberculosis* *S. aureus*	*M. tuberculosis* *H. pylori*	*S. aureus* *S. typhimurim*	*S. aureus* *H. pylori*	*S. typhimurim* *H. pylori*
No. of common essential reactions	48	47	96	60	93	58

identification of targets for metabolic engineering (Alper et al., 2005) and to understand the robustness of organisms through systematic experimental evaluation of gene knock-outs (Deutscher et al., 2006). Another important aspect of analyzing these reconstructed metabolic networks is the identification of combinations of genes, which when simultaneously deleted, abolish growth *in silico* (Deutscher et al., 2006; Suthers et al., 2009).

Essential genes and essential reactions obtained by the gene knockout have been listed in the Table 8 and Table 9 respectively. Since this is a quantitative study, the list contains only selected genes which were found to have scientific evidence in the previous studies. They have been analyzed in the past for prediction of novel genetic interactions and analyzing the extent of robustness of biological networks (Raghunathan et al., 2009).

Table 8 List of essential genes

Organism	*Mycobacterium tuberculosis*	*Staphylococcus aureus*	*Helicobacter pylori*	*Salmonella typhimurium*
Essential genes	*fadD26*	*murA*	*acpS*	*rpiA*
	ppsA	*murB*	*aroQ*	*yedJ*
	ppsE	*fabA*	*dcd*	*talA*
	drrA	*fabB*	*eda*	*talB*
	pks1	*fabG*	*edd*	*talc*
	pks10	*fabD*	*fbp*	*sera*
	pks7	*fabH*	*glcD*	*glyA*
	mmpL1	*fabZ*	*gpt*	*purN*
	mmpL2	*accA*	*mqo*	*purT*
	mmpL3	*accD*	*murB*	*tdk*
	mmpL12	*hisA*	*murF*	*dut*
	mmpL4	*hisB*	*oorA*	*epimerase*
	mmpL11	*hisC*	*oorB*	*argB*
	mmpL6	*hisI*	*oorC*	*rpe*
	fadD26	*hisG*	*oorD*	*argD*
	drrA	*hisD*	*porA*	*aroE*
	drrC	*aroA*	*porB*	*prsA*
	papA5	*aroB*	*porC*	*cytosine deaminase*
	mas	*aroC*	*porD*	*speB*
	fadD28	*aroE*	*pyre*	*speC*
	mmpL7	*aroQ*	*speE*	*speF*
	mmpL5	*trpA*	*tal*	*tktA*
	mmpL8	*trpB*	*trxA*	*tktB*
	mmpL9	*trpF*	*trxB*	*nadA*
	mmpL10	*aroK*		*nadB*
		aroL		*thrC*
		aroP		*gsk*
		aroH		*kbl*
		trpD		
		pheC		
		cysG		
		hemC		
		hemB		
		hemD		
		metK		

Gene knockout performed on each of the organism can be visualized using the MATLAB. Double gene deletion was performed for all the genes present in each of the organism. The lethality of double gene deletion can be visualized where the scale of lethality varies from 0 to 1. Scale of 1 refers to highly lethal deletion for the particular two genes and scale of 0 refers the lethal effect to be normal.

Synthetic lethality analysis

It was performed using the algorithm Fast–SL algorithm. It is MATLAB implemented algorithm using COBRAToolbox. The synthetic gene lethality and the synthetic reaction lethality were performed separately. For synthetic gene lethality, both single and double gene lethality was performed. Similarly for synthetic reaction lethality, both single and double reaction lethality was performed. In single gene lethality there was deletion of single gene and similarly in double gene lethality, pair of genes was deleted. Similar procedure was followed for reaction lethality also. The result for gene lethality has been shown in the Table 10. The result for Reaction Lethality has been shown in the Table 11. The table shows the number of single lethal reactions and double lethal reactions. Single lethal reactions were identified by performing exhaustive single reaction deletions. Double lethal reactions were identified by performing pairwise deletions.

Robustness analysis

Robustness analysis was performed to study the effect of the glucose and oxygen uptake on the growth rates. This analysis was performed for metabolic network of each of the organism. The sensitivity of the growth of the metabolic network was checked against the varying glucose and oxygen uptake rate. To determine the effect of varying glucose uptake on growth, oxygen uptake rate was fixed at 17 mmol/(gDW·h) which is a realistic uptake of oxygen. To determine the effect of varying oxygen uptake on growth, glucose uptake rate was fixed at 10 mmol/(gDW·h) which is a realistic uptake of glucose. Results for the robustness analysis of the metabolic networks of each of the four organisms have been shown in the figures from Fig. 1 to Fig.8. Figures 1 and 2 represent the Robustness study of metabolic network of *Mycobacterium tuberculosis.* In Fig. 1, with oxygen uptake rate kept constant, growth rate remained 0/h until a glucose uptake of around 2.5 mmol/(gDW·h). Growth reached to the maximum level of 0.3/h at the glucose uptake of around 5 mmol/(gDW·h). After the maximum growth rate of 0.3/h growth rate became constant.

Table 9 List of essential reactions

Organism	*Mycobacterium tuberculosis*	*Staphylococcus aureus*	*Helicobacter pylori*	*Salmonella typhimurium*
Essential reactions	'AACPS10'	'ACCOAC'	A5PISO'	'3HAD100'
	'AACPS11'	'ACGK'	'ACCOACr'	'3HAD121'
	'AACPS3'	'ACHBS'	'ADCL'	'3HAD141'
	'ACACT1r'	'ACLS'	'ADK1'	'3HAD161'
	'ACCC'	'ACOTA'	'ADMDCr'	'3HAD181'
	'ACCOACr'	'ADCL'	'ADSL1r'	'3HAD40'
	'ACChex'	'ADCS'	'ADSL2r'	'3HAD60'
	'ACGAMT'	'ADK1'	'ADSS'	'3HAD80'
	'ACGK'	'ADKd'	'AGMHE'	'3OAR100'
	'ACHBS'	'ADMDCr'	'AGMT'	'3OAR121'
	'ACLS'	'ADPT'	'AHCYSNS'	'3OAR140'
	'ACOTA'	'ADSK'	'AICART'	'3OAR141'
	'ADSK'	'ADSL1'	'AIRC2r'	'3OAR161'
	'ADSL1r'	'ADSL2r'	'AIRC3'	'3OAR181'
	'ADSL2r'	'ADSS'	'ALAALAr'	'3OAR40'
	'ADSS'	'AGPR'	'AMAOTr'	'3OAR60'
	'AFE'	'AICART'	'AMMQT6'	'3OAR80'
	'AFTA'	'AIRC2'	'ANPRT'	'3OAS100'
	'AGPAT160'	'AIRC3'	'AOXSr'	'3OAS121'
	'AGPAT160190'	'AKGDa'	'ARGDC'	'3OAS140'
	'AGPAT190'	'AKGDb'	'ARGN'	'3OAS141'
	'AGPR'	'ALAR'	'ARGt2r'	'3OAS161'
	'AHC'	'ALATA_D'	'ASAD'	'3OAS181'
	'ALAALAr'	'ANPRT'	'ASNS2'	'3OAS60'
	'ALAR'	'ANS'	'ASP1DC'	'3OAS80'
	'ANPRT'	'APRAUR'	'ASPCT'	'A5PISO'
	'ANS'	'ASAD'	'ASPK'	'ACCOAC'
	'ARABF'	'ASNS1'	'ASPO2'	'ACGK'
	'ARABI'	'ASPKi'	'ASPTA'	'ACGS'
	'ARACHTA'	'ASPTA'	'BC10_new'	'ACHBS'
	'ASAD'	'ATPPRT'	'BTS2'	'ACLS'
	'ASNS1'	'BPNT'	'BiomassHP_published'	'ACODA'
	'ASPCT'	'CHORM'	'C140SN'	'ACONTa'
	'ASPK'	'CHORS'	'C160SN'	'ACONTb'
	'ASPTA'	'CLPNS_SA'	'C180SN'	'ACOTA'
	'ATPPRT'	'CO2t'	'C181SN'	'ADCL'
	'BDH'	'CPPPGO'	'C190cSN'	'ADCS'
	'BPNT'	'CSNt2'	'CBPS'	'ADMDC'
	'CBPS'	'CYSS'	'CDPMEK'	'ADSK'
	'CDPMEK'	'CYSTL'	'CHCOAL'	'ADSL1r'
	'CDPPT160190'	'CYTBD'	'CHORM'	'ADSL2r'
	'CHORM'	'CYTD'	'CHORS'	'ADSS'
	'CHORS'	'CYTK1'	'CLPNS_HP'	'AGMHE'
	'CHRPL'	'DAPDC'	'CTPS1'	'AGPAT140'
	'CLPNS160190'	'DAPE'	'CYOO_HP'	'AGPAT160'
	'CMCBTFL'	'DASYN_SA'	'CYSS'	'AGPAT161'
	'CYSS'	'DB4PS'	'CYTK1'	'AGPAT180'
	'CYSTL'	'DDPA'	'DAPDC'	'AGPAT181'
	'DAPDC'	'DGK1'	'DAPE'	'AGPR'
	'DAPE'	'DHAD1'	'DASYN_HP'	'AHCYSNS'
	'DASYN160'	'DHAD2'	'DBTSr'	'AICART'
	'DASYN160190'	'DHDPRy'	'DDPA'	'AIRC2'
	'DASYN190190'	'DHDPS'	'DHDPRy'	'AIRC3'
	'DDPA'	'DHFR'		'ALAALAr'

Table 10 Synthetic gene lethality.

Organisms	Number of genes for single lethality	Number of genes for double lethality
Mycobacterium tuberculosis	188	188
Staphylococcus aureus	168	168
Salmonella typhimurium	202	204
Helicobacter pylori	168	168

Table 11 Synthetic reaction lethality

Organism	Number of reactions for single lethality	Number of reactions for double lethality
Mycobacterium tuberculosis	314	314
Staphylococcus aureus	244	244
Salmonella typhimurium	346	346
Helicobacter pylori	135	244

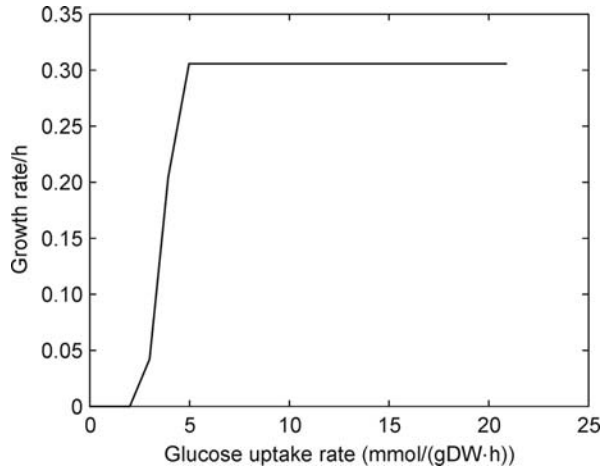

Figure 1 Robustness analysis of metabolic network of *Mycobacterium tuberculosis* with oxygen uptake rate fixed at 17 mmol/(gDW·h).

In Fig. 2, with glucose uptake rate kept constant, growth rate steadily increased with increase in oxygen uptake. Figures 3 and 4 represent the Robustness study of metabolic network of *Staphylococcus aureus*. In Fig.3, with oxygen uptake rate kept constant, growth rate steadily increased with increase in glucose uptake rate. In Fig.4, with glucose uptake rate kept constant, growth rate increased steadily for most of the part with increase in oxygen uptake rate. At oxygen uptake of around 2 mmol/(gDW·h), growth rate remained constant at 0.6/h. Figure5 and Fig.6 represent the Robustness study of metabolic network of *Helicobacter pylori*. In Fig.5, with oxygen uptake rate kept constant, growth rate steadily increased with increase in glucose uptake rate. In Fig.6, with glucose uptake rate kept constant, growth rate increased steadily for most of the part with increase in oxygen uptake rate. Figure7 and Fig.8 represent Robustness study of metabolic network of *Salmonella typhimurium*. In Fig.7, with oxygen uptake rate kept constant, growth rate steadily

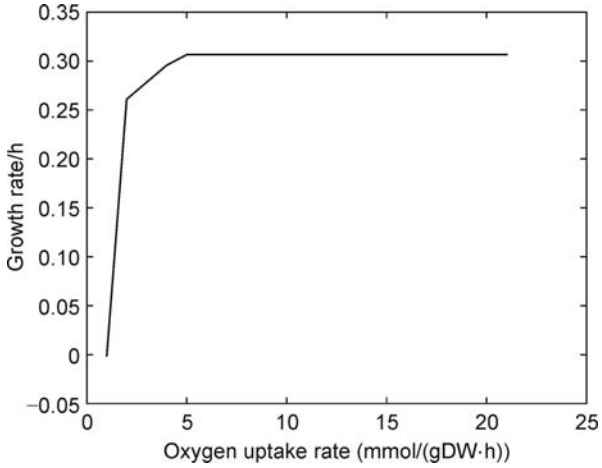

Figure 2 Robustness analysis of metabolic network of *Mycobacterium tuberculosis* with glucose uptake rate fixed at 10 mmol/(gDW·h).

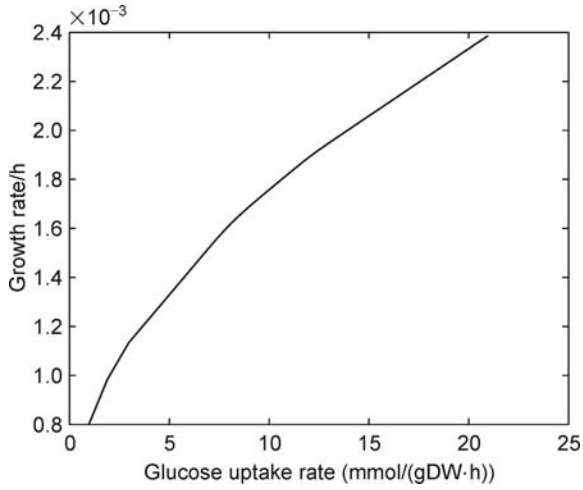

Figure 3 Robustness analysis of metabolic network of *Staphylococcus aureus* with oxygen uptake rate fixed at 17 mmol/(gDW·h).

increased with increase in glucose uptake rate up to the growth rate of around 0.62/h. Then after growth rate becomes constant. In Fig.8, with glucose uptake rate kept constant, growth rate remains 0/h for the oxygen uptake rate of around 12 mmol/(gDW·h). Then after growth rate starts increasing steadily up to the growth rate of 0.62/h and becomes constant.

Phenotypic phase plane analysis

Phenotypic phase plane analysis was performed by varying two substrates simultaneously. In this study phenotypic phase plane analysis is done by varying the glucose and oxygen uptake rate simultaneously. It assesses the effect of the simultaneous variation of the uptake rate of the glucose and oxygen on the growth rate. The effect was plotted on the 2-D graph as well as on the 3-D graph. The plot is divided into

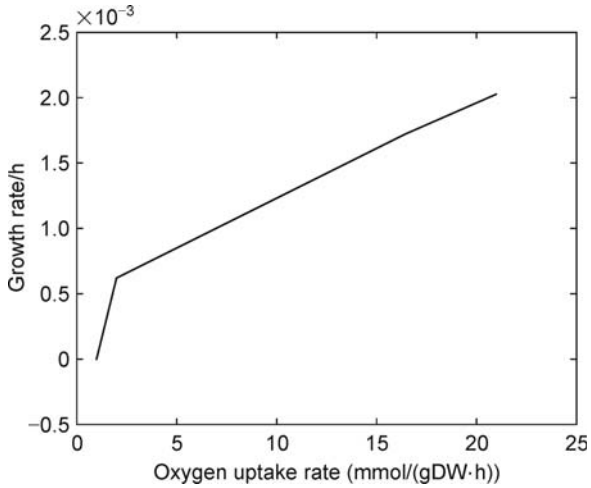

Figure 4 Robustness analysis of metabolic network of *Staphylococcus aureus* with glucose uptake rate fixed at 10 mmol/(gDW·h).

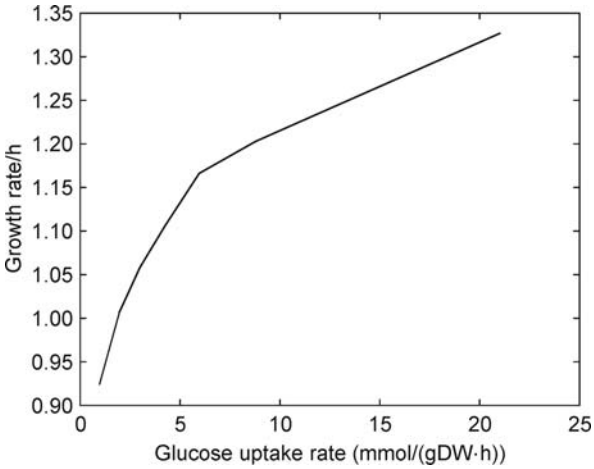

Figure 5 Robustness analysis of metabolic network of *Helicobacter pylori* with oxygen uptake rate fixed at 17 mmol/(gDW·h).

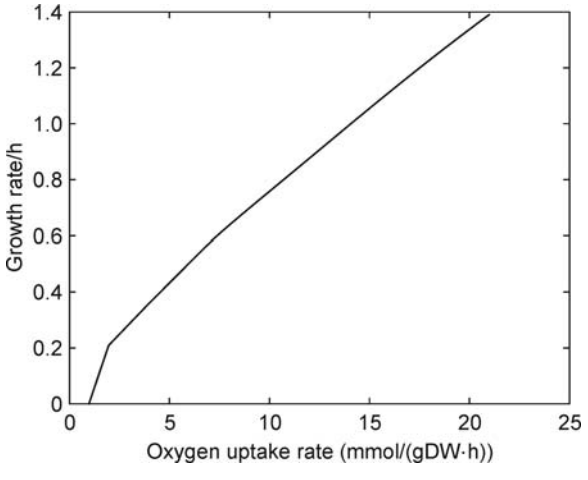

Figure 6 Robustness analysis of metabolic network of *Helicobacter pylori* with glucose uptake rate fixed at 10 mmol/(gDW·h).

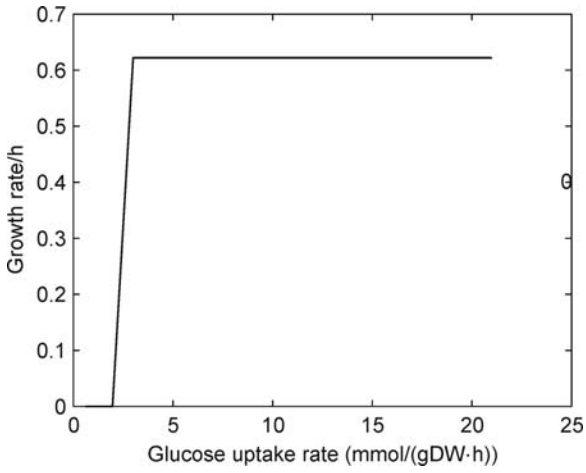

Figure 7 Robustness analysis of metabolic network of *Salmonellatyphimurium* with oxygen uptake rate fixed at 17 mmol/(gDW·h).

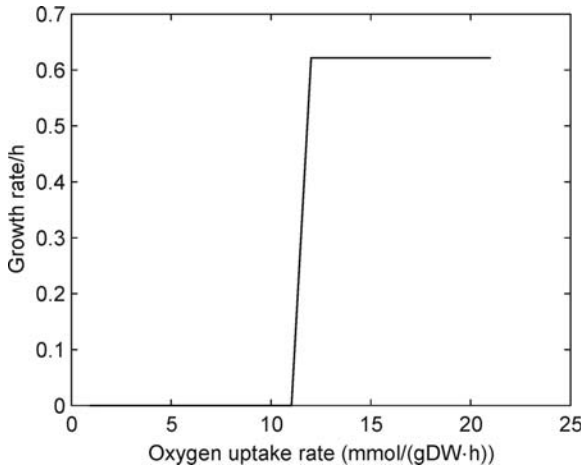

Figure 8 Robustness analysis of metabolic network of *Salmonella typhimurium* with glucose uptake rate fixed at 10 mmol/(gDW·h)

different phases with different color coding. The 3-D graph was plotted using ***surfl*** MATLAB function. The results for the phenotypic phase plane analysis can be visualized in the form of 3-D plot which have been shown in figures from Fig.9 to Fig.12. Figure 9 represents phenotypic phase plane study of metabolic network of *Mycobacterium tuberculosis*. Phase 1, on the far left of the plots, is characterized by 0 growth. In phase 2, growth is limited by oxygen. The line between phase 2 and phase 3 is where glucose and oxygen are perfectly balanced and growth yield is highest. In phases 3, 4, and 5, oxygen and glucose are both limiting growth. Figure10 represents the phenotypic phase plane study of metabolic network of *Staphylococcus aureus.* Phase 1, on the far left of the plots, is characterized by negative growth. In phase 2, growth is limited by oxygen uptake rate. The line between phase 2 and phase 3 is where glucose and oxygen are perfectly balanced and growth yield is highest. In phases 3, 4, and 5, growth rate is limited by glucose uptake rate. Figure 11

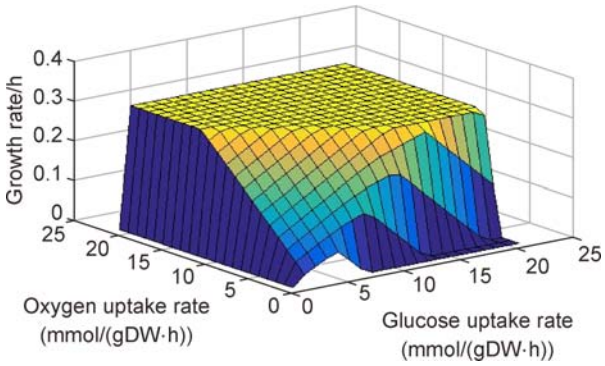

Figure 9 Phenotypic phase plane analysis of metabolic network of *Mycobacterium tubeculosis*.

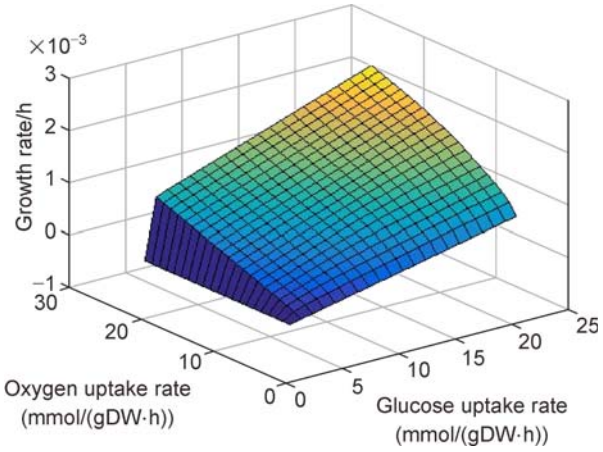

Figure 10 Phenotypic phase plane analysis of metabolic network of *Staphylococcus aureus*.

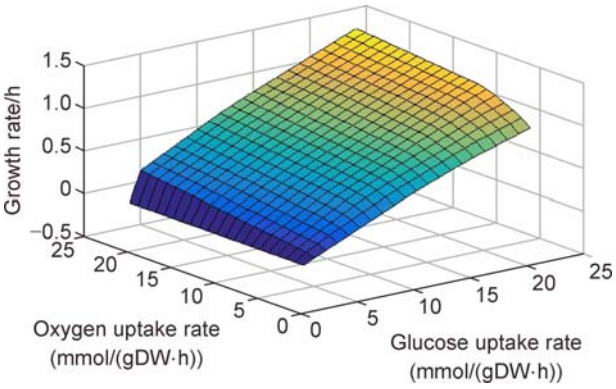

Figure 11 Phenotypic phase plane analysis of metabolic network of *Helicobacter pylori*.

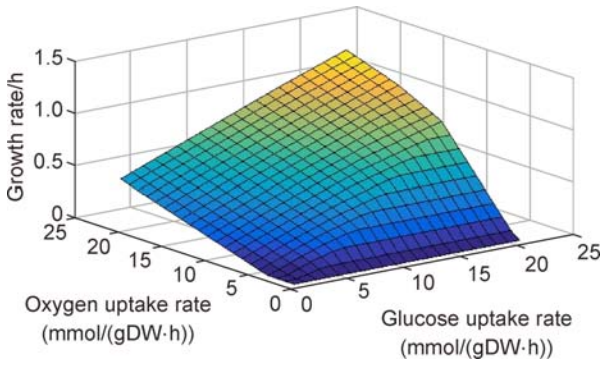

Figure 12 Phenotypic phase plane analysis of metabolic network of *Salmonella typhimurium*.

represents phenotypic phase plane study of metabolic network of *Helicobacter pylori*. Phase 1, on the far left of the plots, is characterized by negative growth. In phase 2, growth is limited by oxygen uptake rate. The line between phase 2 and phase 3 is where glucose and oxygen are perfectly balanced and growth yield is highest. In phases 3, 4, and 5, growth rate is limited by glucose uptake rate. Figure12 represents phenotypic phase plane study of metabolic network of *Salmonella typhimurium*. Phase 1, on the far left of the plots, is characterized by 0 growth. In phase 2, growth is limited by oxygen. The line between phase 2 and phase 3 is where glucose and oxygen are perfectly balanced and growth yield is highest. In phases 3, 4, and 5, oxygen and glucose are both limiting growth.

Metabolite connectivity

For each of the four networks, the number of reactions in which each possible metabolite is occurs was determined. It is the measure of individual connectivity of each of the metabolite in the metabolic network. This metabolite connectivity was plotted on the log-log scale for each of the four metabolic networks. The approximate linear appearance of the curve relates to the power law distribution of the metabolic networks. The plots of four different metabolic networks show that there are very few metabolites, which are highly connected. Most of the metabolites occur only in a few reactions. The highly connected metabolites are the 'global factors' similar to the hub protein in the protein–protein interaction network. The least connected metabolites are the 'local factors' which occur in linear pathway. The power law distribution shows that the networks are scale-free. Metabolite connectivity in the metabolic network of each of the four different organisms has been shown in the figures from Fig.13 to Fig. 16.

Reaction participation, i.e., the number of metabolites per reaction, for each of the reactions in the network was also calculated. The most common type of reaction in the metabolic network of each of the organism was the bi-linear reaction involving two substrates and two products. Average of the reaction participation in each of the network is shown in the Table13.

Reaction essentiality and metabolite connectivity

To correlate the reaction essentiality and the metabolite connectivity in each of the metabolic networks, metabolite

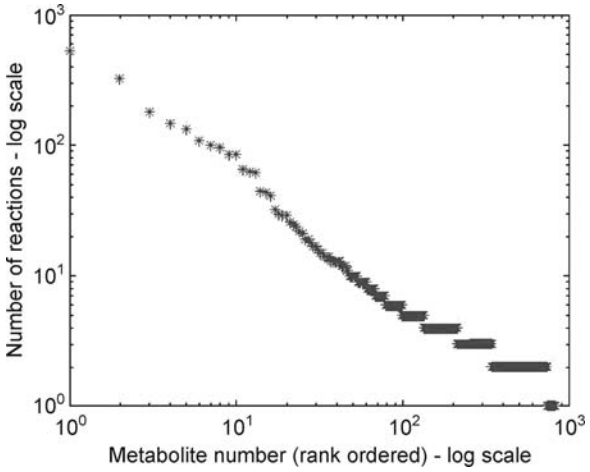

Figure 13 Metabolite connectivity in metabolic network *Mycobacterium tuberculosis.*

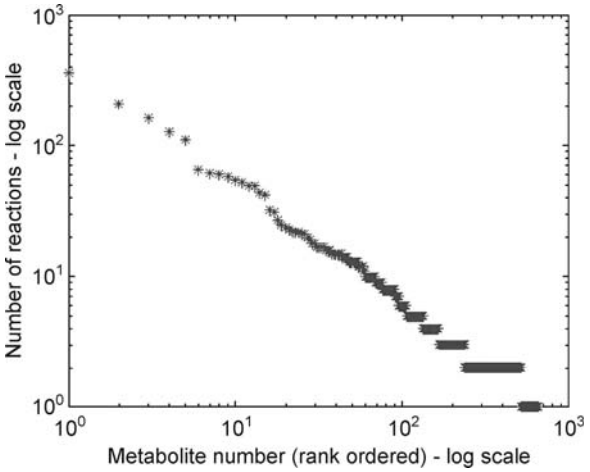

Figure 14 Metabolite connectivity in metabolic network *Staphylococcus aureus.*

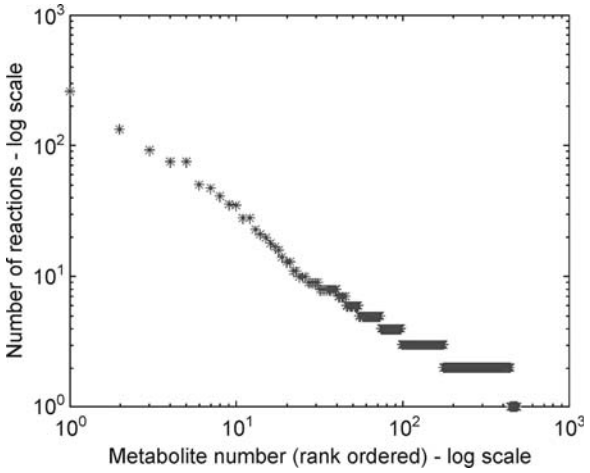

Figure 15 Metabolite connectivity in metabolic network *Helicobacter pylori.*

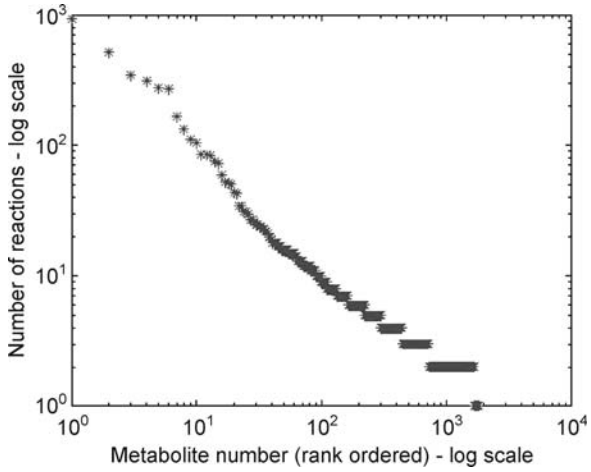

Figure 16 Metabolite connectivity in metabolic network *Salmonella typhimurium.*

associated reactions were found out and finally they are deleted. After then FBA was used to predict the growth if possible. This step was performed for the metabolic networks of each of the four organisms. The results were plotted on the semi-log scale with metabolite connectivity and lethality of the network. The results for the metabolic network of four different organisms show that some less connected metabolites have a higher lethality fraction than highly connected metabolites. For the *H. pylori* core model, the average lethality fraction lies between 0.3 and 0.6 for the majority of the metabolites, regardless of their connectivity as shown in the Fig.19. For the *M. tuberculosis* core model, the average lethality fraction lies between 0.3 and 0.6 for the majority of the metabolites, regardless of their connectivity as shown in the Fig.17. For the *S. aureus* core model, the average lethality fraction lies between 0.2 and 0.6 for the majority of the metabolites, regardless of their connectivity which has been shown in the Fig.18. For the *S. typhimurium* core model, the average lethality fraction lies between 0.2 and 0.5 for the majority of the metabolites, regardless of their connectivity and is shown in the Fig.20.

Discussion

All the four metabolic network files are the reconstructed models of these organisms. Maximization of growth is very important compartmental objective to find out good FBA estimation using the kind of objective function explored. While performing the FBA analysis, growth was possible both aerobically and anaerobically for each of the four organisms. In this study, the variations in flux values were generally associated with important metabolic pathways like glycolysis, oxidative phosphorylation, and amino acid biosynthesis etc. Single gene deletion and single reaction deletion functions estimate the amount of essential genes and reactions by deleting the certain genes and reactions and

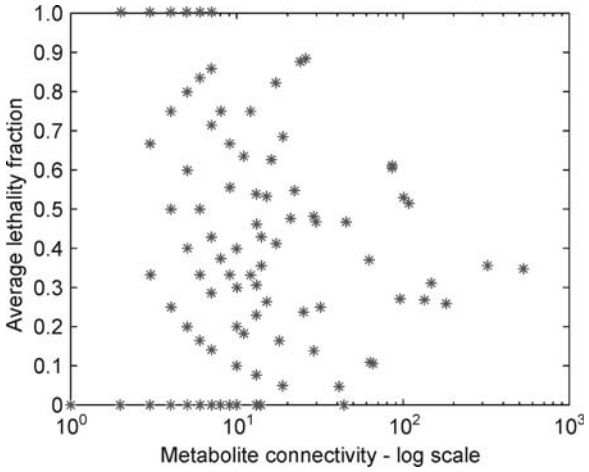

Figure 17 Correlation between metabolite connectivity and average lethality of *Mycobacterium tuberculosis*.

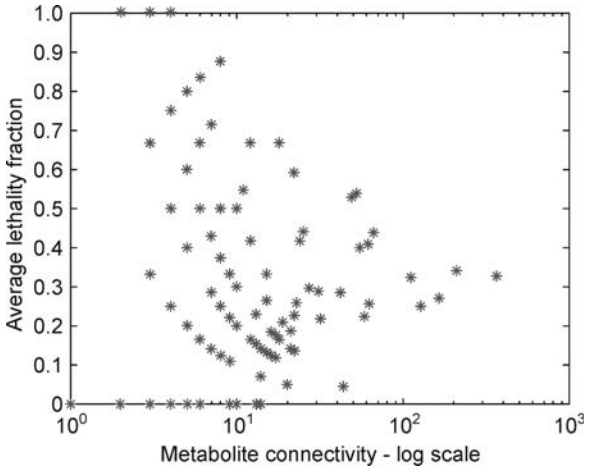

Figure 18 Correlation between metabolite connectivity and average lethality of *Staphylococcus aureus*.

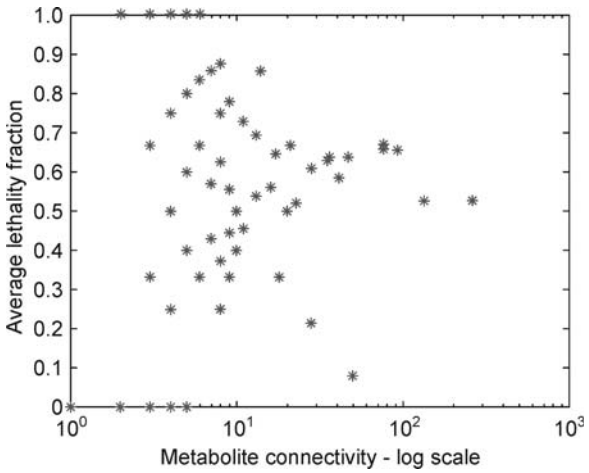

Figure 19 Correlation between metabolite connectivity and average lethality of *Helicobacter pylori*.

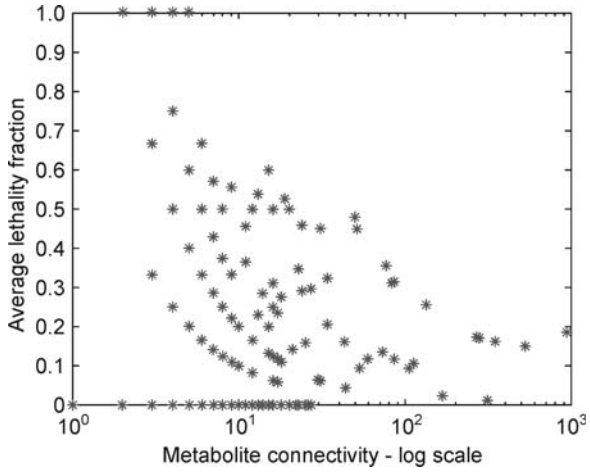

Figure 20 Correlation between metabolite connectivity and average lethality of *Salmonella typhimurium*.

analyzing the impact of the deletion. These essential genes and reactions are the major players in the regulation of important pathways of the organisms. These genes and reactions are also involved in the signal transduction pathways. These genes and reactions serve as the candidate for the potential drug target against diseases caused by these organisms. The identification of synthetic lethals in organisms can be used to understand complex genetic interactions between genes and identify drug targets for combinatorial therapy. In this comparative study, it has been found that *Salmonella typhimurium*'s metabolic network contains more number of essential genes and essential reactions compared to that of other three. Similar comparison applies for the synthetic lethal genes and reactions also. Since metabolic networks of Salmonella typhimurium has more number of essential genes and reactions, visualization of gene deletion confirms the same. Most of the gene deletions were found to be in the lethal range having the value close to '1' on the lethality scale. Gene deletion in *Mycobacterium tuberculosis*'s and *Staphylococcus aureus*'s metabolic networks were found to be almost similar on the lethality scale. This implies that it may present more number of drug targets and hence to target the disease more effectively caused by this organism. Robustness analysis estimates up to what extent a given network is stable under the given physiological conditions. We have performed the robustness analysis by analyzing the effect of variation of the glucose and oxygen uptake rate on the growth rate of the organism. Growth rates of these two organisms were stable for most of the part of varying the glucose and oxygen uptake rate. Metabolic Metabolite connectivity enables us to understand the basic structure of these metabolic networks of four different organisms. Among the metabolic networks of all the four organisms studied, there are very few metabolites that are highly connected. Most of the metabolites are scattered. Metabolites which are highly connected serve as 'global factor' similar to the hub protein in the protein – protein interaction network. The

correlation study between metabolite connectivity and reaction essentiality gives the major insight into the lethality fraction of the metabolic networks. The lethality fraction is computed as the ratio between metabolite connectivity and reaction essentiality. The average lethality fraction of all the four organisms studied, ranged from 0.2 to 0.6.

Compliance with ethics guidelines

Kumar Gaurav and Yasha Hasija declare that they have no conflict of interest. This article does not contain any studies with human or animal subjects performed by any of the authors.

References

Feist and Palsson (2008). The growing scope of applications of genome-scale metabolic reconstructions using *Escherichia coli*. Nature Biotechnol, 226(6): 659–667

Alper H, Jin Y S, Moxley J F, Stephanopoulos G (2005). Identifying gene targets for the metabolic engineering of lycopene biosynthesis in Escherichia coli. Metab Eng, 7(3): 155–164

Plaimas K, Eils R, König R. Identifying essential genes in bacterial metabolic networks with machine learning methods. BMC systems biology. 2010 May 3;4(1):1

Chowdhury R, Chowdhury A, Maranas C D (2015). Using gene essentiality and synthetic lethality information to correct yeast and CHO cell genome-scale models. Metabolites, 5(4): 536–570

Becker S A, Palsson B Ø (2005). Genome-scale reconstruction of the metabolic network in *Staphylococcus aureus* N315: an initial draft to the two-dimensional annotation. BMC Microbiol, 5(1): 8

Schilling C H, Covert M W, Famili I, Church G M, Edwards J S, Palsson B O (2002). Genome-scale metabolic model of *Helicobacter pylori* 26695. J Bacteriol, 184(16): 4582–4593

Deutscher D, Meilijson I, Kupiec M, Ruppin E (2006). Multiple knockout analysis of genetic robustness in the yeast metabolic network. Nat Genet, 38(9): 993–998

Edwards J S, Ramakrishna R, Palsson B O (2001). Characterizing the metabolic phenotype: a phenotype phase plane analysis. Biotechnol Bioeng, 77(1): 27–36

Hamilton J J, Reed J L (2012). Identification of functional differences in metabolic networks using comparative genomics and constraint-based models. PLoS One, 7(4): e34670

Heinemann M, Kummel A, Ruinatscha R, Panke S (2005). In *silico* genome-scale reconstruction and validation of the *Staphylococcus aureus* metabolic network. Biotechnol Bioeng, 92(7): 850–64

Jamshidi N, Palsson B Ø (2007). Investigating the metabolic capabilities of *Mycobacterium tuberculosis* H37Rv using the in silico strain iNJ661 and proposing alternative drug targets. BMC Syst Biol, 1(1): 26

Schellenberger J, Que R, Fleming R M, Thiele I, Orth J D, Feist A M, Zielinski D C, Bordbar A, Lewis N E, Rahmanian S, Kang J, Hyduke D R, Palsson B Ø (2011). Quantitative prediction of cellular metabolism with constraint-based models: the COBRA Toolbox v2.0. Nat Protoc, 6(9): 1290–1307

Keating S M (2006). SBMLToolbox: an SBML toolbox for MATLAB users. Bioinformatics, 22(10): 1275–1277

Masel J, Siegal M L (2010). Robustness: mechanisms and consequences. Trends Genet, 25(9): 395–403

Raman K, Chandra N (2009). Flux balance analysis of biological systems: applications and challenges. Brief Bioinform, 10(4): 435–449

Kauffman K J, Prakash P, Edwards J S(2003). Advances in flux balance analysis. Curr Opin Biotechnol, 14(5): 491–496

McClelland M, Sanderson K E, Spieth J, Clifton S W, Latreille P, Courtney L, Porwollik S, Ali J, Dante M, Du F, Hou S, Layman D, Leonard S, Nguyen C, Scott K, Holmes A, Grewal N, Mulvaney E, Ryan E, Sun H, Florea L, Miller W, Stoneking T, Nhan M, Waterston R, Wilson R K (2001). Complete genome sequence of *Salmonella enterica* serovar Typhimurium LT2. Nature, 413(6858): 852–856

Nijman S M B (2011). Synthetic lethality: general principles, utility and detection using genetic screens in human cells. FEBS Lett, 585(1): 1–6

Pratapa A, Balachandran S, Raman K (2015). Fast-SL: an efficient algorithm to identify synthetic lethal sets in metabolic networks. Bioinformatics, 31(20): 3299–3305

Raghunathan A, Reed J, Shin S, Palsson B, Daefler S (2009). Constraint-based analysis of metabolic capacity of *Salmonella typhimurium* during host-pathogen interaction. BMC Syst Biol, 3(1): 38

Raman K, Rajagopalan P, Chandra N (2005). Flux balance analysis of mycolic acid pathway: targets for anti-tubercular drugs. PLOS Comput Biol, 1(5): e46

Suthers P F, Zomorrodi A, Maranas C D (2009). Genome-scale gene/reaction essentiality and synthetic lethality analysis. Mol Syst Biol, 5: 301

Thiele I, Hyduke D R, Steeb B, Fankam G, Allen D K, Bazzani S, Charusanti P, Chen F C, Fleming R M, Hsiung C A, De Keersmaecker S C, Liao Y C, Marchal K, Mo M L, Özdemir E, Raghunathan A, Reed J L, Shin S I, Sigurbjörnsdóttir S, Steinmann J, Sudarsan S, Swainston N, Thijs I M, Zengler K, Palsson B O, Adkins J N, Bumann D (2011). A community effort towards a knowledge-base and mathematical model of the human pathogen *Salmonella* Typhimurium LT2. BMC Syst Biol, 5: 8

Thiele I, Vo TD, Price ND, Palsson B Ø (2005). Expanded metabolic reconstruction of Helicobacter pylori (iIT341 GSM/GPR): an in silico genome-scale characterization of single- and double-deletion mutants. J Bacteriol, 187(16): 5818–5830

Rahul et al. Protection and Control of Modern Power Systems (2017) 2:9
DOI 10.1186/s41601-017-0039-z

Protection and Control of Modern Power Systems

ORIGINAL RESEARCH Open Access

Detection and classification of multiple power signal patterns with Volterra series and interval type-2 fuzzy logic system

Rahul[1*], Rajiv Kapoor[1] and M. M. Tripathi[2]

Abstract

The paper deals with the application of Volterra bound Interval type −2 fuzzy logic techniques in power quality assessment. This work proposes a new layout for detection, localization and classification of various types of power quality events. The proposed method exploits Volterra series for the extraction of relevant features, which are used to recognize different PQ events by Interval type-2 fuzzy logic based classifier. Numerous single as well as multiple powers signal disturbances have been simulated to testify the efficiency of the proposed technique. This time–frequency analysis results in the clear visual detection, localization, and classification of the different power quality events. The simulation results signify that the proposed scheme has a higher recognition rate while classifying single and multiple power quality events unlike other methods. Finally, the proposed method is compared with SVM, feed forward neural network and type −1 Fuzzy logic system based classifier to show the efficacy of the proposed technique in classifying the Power quality events.

Keywords: Non-stationary power signals, Power quality (PQ), Volterra series, Interval type-2 fuzzy logic system (IT2FLS), Power Spectral Entropy (PSE), Standard Deviation (SD)

1 Introduction

In the new era of power systems, power quality (PQ) issues have attained considerable attention in the last few decades due to increased demand of power electronics and/or microprocessor based non-linear controlled loads. While these devices create power quality problems, at the same time, devices may also malfunction due to the severe power quality problems [1]. Electricity is now treated as commercial product that is evaluated not only by its reliability but also by its quality. The customer will choose the supplier providing electrical energy having better power quality, at lower cost and acceptable reliability that meet his load needs. The utilities or other electric power providers have to ensure a high quality of power delivery to remain competitive and to retain/attract the customers in new electricity market scenario [2].

PQ disturbances/events cover a broad frequency range with significantly different magnitude variations and can be stationary or non-stationary signals [3]. The on-line detection and identification of PQ disturbances are essential so that source and cause of such disturbances is known for taking appropriate mitigation/corrective actions. A feasible approach to achieve this goal is to incorporate detection capabilities into monitoring equipment so that the events of interest can be recognized, captured and classified automatically. This is done in a sequential manner by detecting the disturbance, then localizing it and finally classifying the various PQ events [4]. To carry out this task a tool is required which has both the capability to analyze different PQ events and classify them as well.

This paper proposes a tool which is the combination of Volterra series and Type-2 fuzzy logic. Volterra series does signal decomposition to extract valuable information from the signal in order to detect power quality disturbances. The proposed type-2 fuzzy logic method classifies the power quality disturbances even in the presence of higher level of uncertainty hence it is very useful in real time scenario. The general structure of fuzzy reasoning

* Correspondence: rahulverma@dtu.ac.in
[1]Department of Electronics & communication Engineering, Delhi Technological University, Delhi, India
Full list of author information is available at the end of the article

Springer Open

© The Author(s). 2017 **Open Access** This article is distributed under the terms of the Creative Commons Attribution 4.0 International License (http://creativecommons.org/licenses/by/4.0/), which permits unrestricted use, distribution, and reproduction in any medium, provided you give appropriate credit to the original author(s) and the source, provide a link to the Creative Commons license, and indicate if changes were made.

handles much of the uncertainties and fuzzy systems utilize type-1 fuzzy sets (which express uncertainty by numbers in the range [0, 1]) for classification.

This paper has following 5 sections. First, the Volterra series expansion for nonlinear systems explained in Section II; Application of Volterra series in power quality events' detection presented in Section III; in Section IV power spectral entropy for analysis of power quality events, the utilization of the Interval type-2 fuzzy logic system (IT2FLS) for classification PQ events is presented in Section V, Proposed methodology for classification of PQ events given in Section VI, results and discussion included in section VII and Section VIII concludes the paper.

2 Volterra series expansion for nonlinear systems

Let x[n] and y[n] represent the input and output signals, respectively, of a discrete-time and causal nonlinear system. The Volterra series expansion for y[n] using x[n] is given by:

$$y(n) = h_0 + \sum_{m_1=0}^{\infty} h_1[m_1]x[n-m_1] + \sum_{m_1=0}^{\infty}\sum_{m_2=0}^{\infty} h_2[m_1, m_2]x[n-m_1]x[n-m_2] + .. \quad (1)$$

In (1), $h_p\ [m_1, m_{2,}..., m_p]$ is known as the p-the order Volterra kernel of the system, Without any loss of generality, the kernels can be assumed to be symmetric. In general any kernel $h_p\ [m_1, m_2. ..., m_p]$ can be replaced by symmetric one by simple setting.

$$\left[h_p^{sym}[m_1, m_2, ...m_p] = \frac{1}{n!}\sum\left(m_{i_1}, m_{i_2} .....m_{i_p}\right)\varepsilon_s h_p\left[m_{i_1}, m_{i_2} .....m_{i_p}\right]\right] \quad (2)$$

Where s is set of all permutations of $m_1, m_{2,}.... m_p$. The Volterra series is a power series with memory. This can be checked by changing the input by a gain factor d so that the new input is dx(t). By using (2), the new output is

$$y(n) = h_0 + d^m\left[\sum_{m_1=0}^{\infty} h_1[m_1]x[n-m_1] + \sum_{m_1=0}^{\infty}\sum_{m_2=0}^{\infty} h_2[m_1, m_2]x[n-m_1]x[n-m_2] + ...\right] \quad (3)$$

This is a power series with amplitude factor d. The integrals are convolutions it shows that series having memory. As an effect of its power series features, it has some limitations associated with the application of the Volterra series to nonlinear problems. The convergence of Volterra series is one of the major limitations. One can think of the Volterra series expansion as a Taylor series expansion with memory. The limitations of the Volterra series expansion are similar to those of the Taylor series expansion both expansions do not do well when there are discontinuities in the system description [5].

2.1 Volterra kernels estimation by exponential method

Numerous methods have been explored in the literature for determining the kernels or the associated transfer functions. Among them, the method of exponential inputs specifically chosen for calculating Volterra kernel in this paper. Let us consider the Volterra series expansion of a nonlinear system of the form

$$y(t) = \sum_{p=1}^{\infty}\int_0^{t_1} ....\int_0^{t_p} h_p(m_{1,}m_2, ...m_p)x(t-m_1) ....x(t-m_p)dm_1 .....dm_p \quad (4)$$

Let the input x(t) be a sum of exponentials

$$x(t) = e^{s_1 t} + e^{s_2 t} + ...e^{s_q t}$$

Where $s_1, s_2, ...s_q$ are rationally independent. This means that there are no rational numbers $\beta_1, \beta_2, ...\beta_q$ such that the sum $\beta_1 s_1 + \beta_2 s_2 + ...\beta_q s_q$ is rational. Then (4) becomes

$$y(t) = \sum_{p=1}^{\infty}\left[\sum_{q_1}^{q} ....\sum_{q_p=1}^{q} H_p\left(sq_1 ....sq_m\right)e^{\left(sq_1 + ...sq_m\right)t}\right] \quad (5)$$

if each s_i occurs $(s_{q_1.....}s_{q_m})$, r_i times, then there are

$$\frac{p!}{r_1!r_2!... ..r_q!}$$

Then (4) can be written in the form

$$y(t) = \sum_{p=1}^{\infty}\sum_{r}\frac{p!}{r_1!r_2!....r_q!}H_p(S_{q_1} ....S_{q_m})e^{\left(sq_1 + ...sq_m\right)t}] \quad (6)$$

where r under the summation sign indicates that the sum includes all the distinct vectors $(r_1, r_2, ...r_q)$ such that $\sum_{i=1}^{q} r_i = p$. If $r_1 = r_2 = ... = r_q = 1$ then the amplitude associated with the exponential term $e^{\left(s_{q_1} + ... s_{q_m}\right)t}$ is $q\ !H_q(s_1, ...s_q)$. Now just calculating the transfer function of the system, we can calculate Volterra series kernel.

Volterra series having application in various fields of engineering and physics and can be practically classified into two distinct categories. In the first classification, a model of an observed dynamical phenomenon is build using Volterra series and the estimation of Volterra frequency response function requires experimental and numerically generated data. The second classification comprises the analysis of dynamical systems that are already represented by an analytic model, such as

differential equation in mathematics. The harmonically excited nonlinear systems' behavior can be investigated better using Volterra series representation [6].

Volterra series expansion exists for nonlinearity and non-stationarity. Even though PQ events are non-stationary in nature so this technique is applicable to power quality disturbances, Volterra system models have been successfully employed in PQ events detection and localization applications in this paper and such models can also be implemented in real time PQ events monitoring system which can change the present scenario of PQ events monitoring system.

3 Application of Volterra series

In this section application for Volterra series for analysis & detection of power quality events has been performed. Volterra series method for detection of power quality events involve applying Volterra series on nonstationary PQ events cause variation in output as compare to pure power signal. Sag refers to decrease in rms voltage or current between 0.1 and 0.9 pu at the power frequency for durations of 0.5 cycles to 60 s. Swell causes an increase in rms voltage and current to between 1.1 pu and 1.8 pu at the power frequency durations from half cycle to 60 s. During the starting time electric motors draw high current, starting an electric motor can be a main cause of voltage sag. While the effects of sag are more prominent, the effects of a voltage swell are often more fatal. It may cause destruction of components on the power supplies of the equipment, though the effect may be a progressive, cumulative effect. When there is no disturbance than series output is approximately linearly vary with time in Fig. 1a, but in case of sag it will be different from that of pure signal, it lies below the pure signal output in Fig. 1b. In case of swell PQ event Volterra series output lie above the pure sine wave output in Fig. 1c, after swell the event sag will be appear so it will come below the pure sine wave Volterra series output after swell is over.

In contrast to no disturbance output in Fig. 2a, when transient event occurs due to switching action in power system then Volterra series output shows irregularity in output due to disturbance shown in Fig. 2b. General solution of transient is to use controlled switches in the system. Another PQ event harmonics which cause voltage waveform distortion, can change the amplitude of signal 0-20% from its nominal value, by applying Volterra method, different curves for different harmonics appear on the plot which shows the number of harmonics present in the disturbed signal in Fig. 2c.

Multiple disturbances can also be detected with the given technique and output can be correlate with no disturbance output in Fig. 3a. When sag with harmonics occurs as a disturbance in the system then Volterra series output clearly detect the harmonics with different

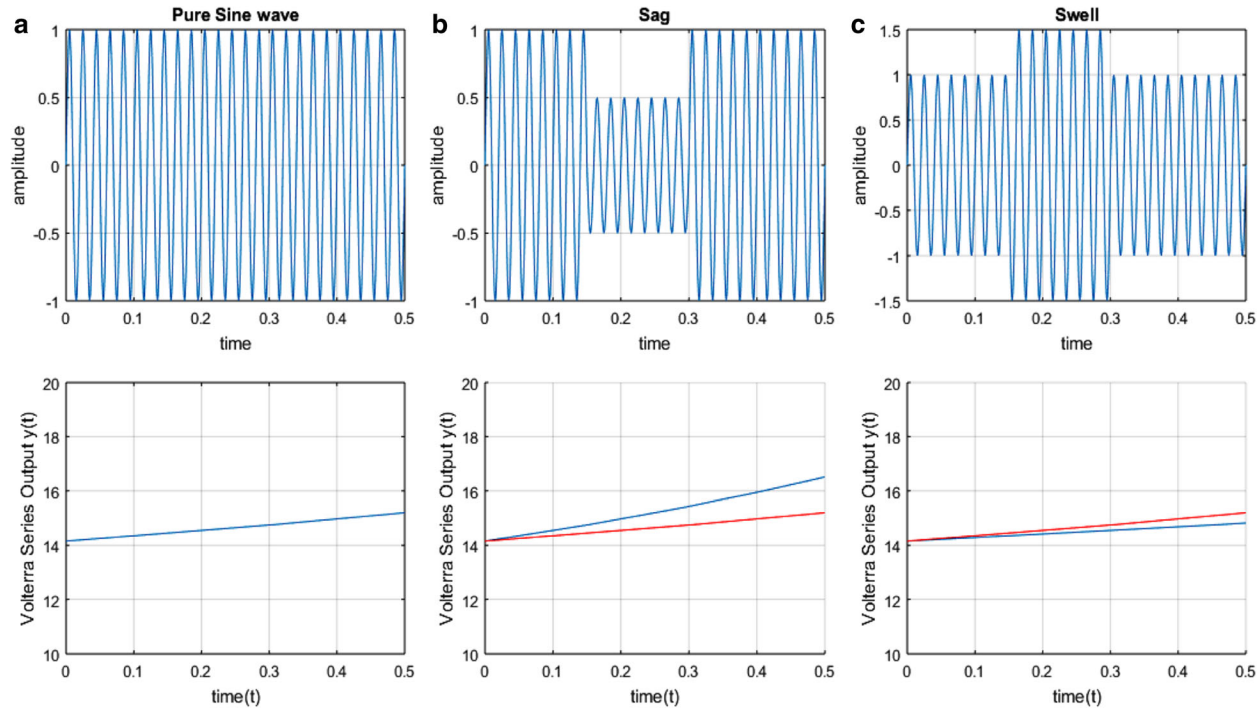

Fig. 1 Volterra series output for **a** Pure sine wave **b** Sag **c** Swell

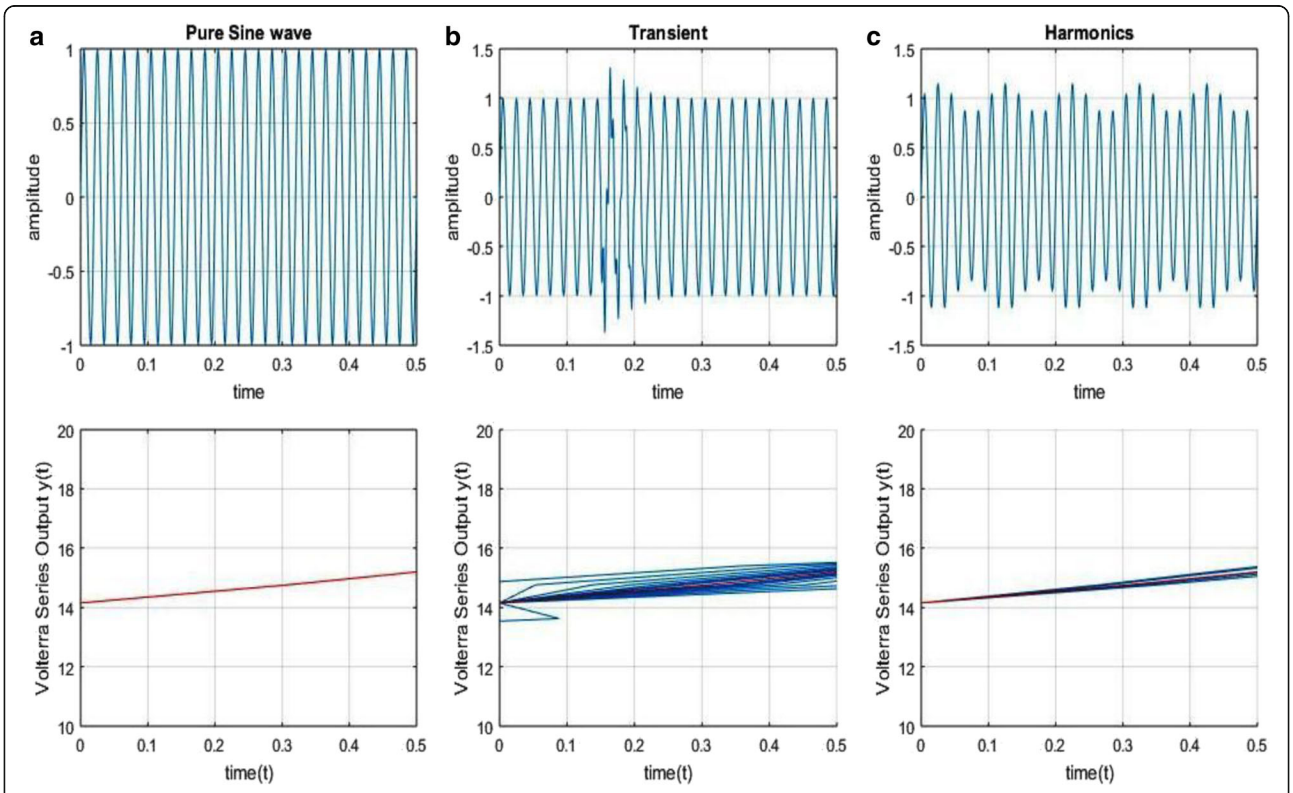

Fig. 2 Volterra series output for **a** Pure sine wave **b** Transient **c** Harmonics

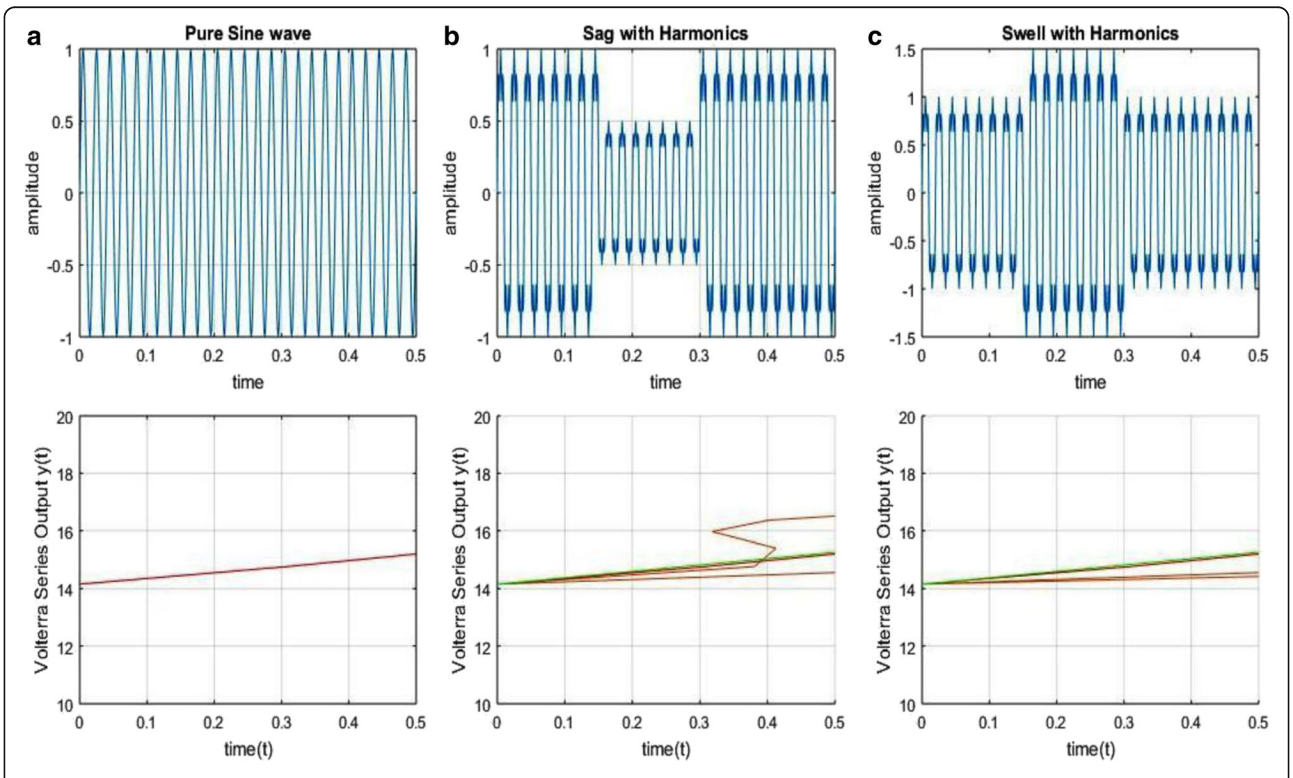

Fig. 3 Volterra series output for **a** Pure sine wave **b** sag with Harmonics **b** Swell with Harmonics

curve for different harmonic in Fig. 3b. In case of swell with harmonics, the event swell and harmonics both detected with different curves in the Volterra series output in Fig. 3c. These results are used for feature extraction which helps in classification of PQ events. In this study features extraction phase is different from that inspected in literature, due to the fact that these two features requires less computational overhead. The power spectral entropy i.e. frequency domain feature and time domain feature, standard deviation selected to classify events, These specifically extracted features are used for classification using Interval type-2 fuzzy logic system.

4 Power spectral entropy

Power spectral entropy describes randomness and complexity in spectrum and also a measure used to characterize signal spectrum flatness. Calculation of PSE requires the spectrum $S(\boldsymbol{w_i})$ of PQ events. Now Calculation of the Power Spectral Density ($\mathbf{P}(\mathbf{w_i})$) by squaring its amplitude and Normalizing the Power Spectral Density between [0, 1], so that it can be treated as a probability density function $\boldsymbol{p_i}$. Now PSE can be calculated using the standard formula for entropy.

$$p(w_i) = \frac{1}{N}|s(w_i)|^2 \tag{7}$$

$$p_i = \frac{p(w_i)}{\sum_i p(w_i)} \tag{8}$$

$$PSE = -\sum_{i=1}^{n} p_i \ln p_i \tag{9}$$

In this paper PSE used for feature extraction of PQ events for classification purpose. PSE calculated for each and every event. This PSE based data is used as input in interval type 2 fuzzy logic system for classification of power quality disturbance. In Fig. 4. Power spectral entropy values for various PQ events plotted, for each event this value is different.

The standard deviation is a measure that is used to evaluate the amount of variation in sample values form its mean value, taking for observation. A low standard deviation reveals that the sample values approaching towards the mean value, high standard deviation indicates that the sample values are spread out over a wider range of values. In this paper Standard deviation accounts for feature extraction of PQ events, Volterra series output calculated for each events and then SD of Volterra series output for every events taken as feature for classfier (IT2FLS). In Fig. 5. SD values plotted for every event considered in this paper. In normal case when no disturbance then value of SD is 4.2. this value is different for every disturbances in case of sag, this is one.

In Fig. 6 when plotting of PSE Vs SD done then its shows the difference clearly between the various PQ events on the bases of extracted features from Volterra series output, it shows that any disturbance in power can easily be detected by Volterra series with easy computations. Volterra series takes very less time to detect disturbances in power quality signal as compare to other method which takes large time, large computing overhead and large memory. Volterra series method can be applied in real time scenario as its computing time is very less and its take less computing overhead to detect disturbances.

5 Interval type-2 fuzzy logic system (IT2FLS)

Fuzzy systems play vital role in different scientific and engineering applications, especially in controlling

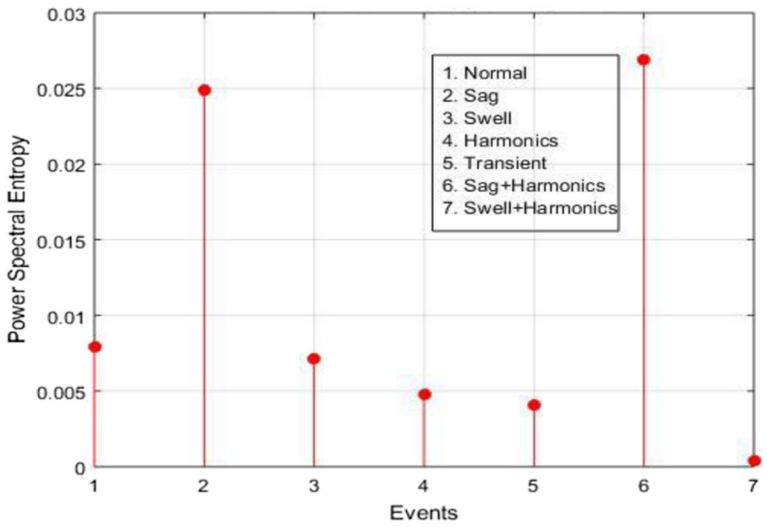

Fig. 4 Power Spectral Entropy of PQ events

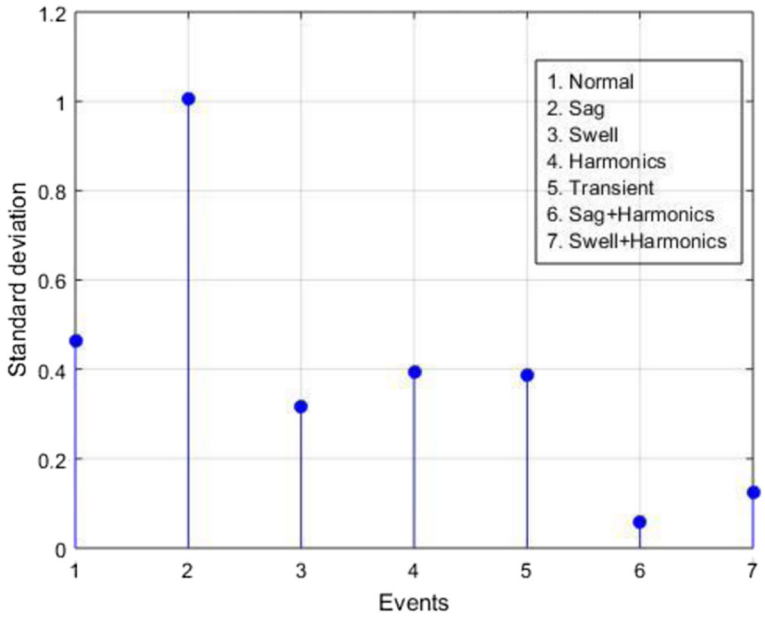

Fig. 5 Standard deviation of PQ events

mechanism. The fuzzy sets firstly used by L.A. Zadeh in 1965 to process data and information affected by un-probabilistic uncertainty. The information that is used to formulate the rules in a fuzzy logic system (FLS) is totally uncertain [7]. Antecedent and Consequent uncertainties converted into uncertain antecedent and consequent membership functions. In Type-2 FLSs antecedent and consequent membership functions are type-2 fuzzy sets, can easily handle rule uncertainties. The concept of type-2 fuzzy sets was introduced as an extension of the concept of an ordinary fuzzy set, i.e., a type-1 fuzzy set. The grades of membership function in type 2 fuzzy are itself fuzzy. A type-2 membership grade can be any subset in (0, 1) and it is called as primary membership [8]. Corresponding to each primary membership, there is a secondary membership (also be in (0, 1)) that defines the possibilities for the primary membership. A type 2 fuzzy is a special case of type 1 fuzzy that totally represented by membership function as shown in Fig. 7, with triangular membership function. A type-2 FLS includes fuzzifier, rule base, fuzzy inference

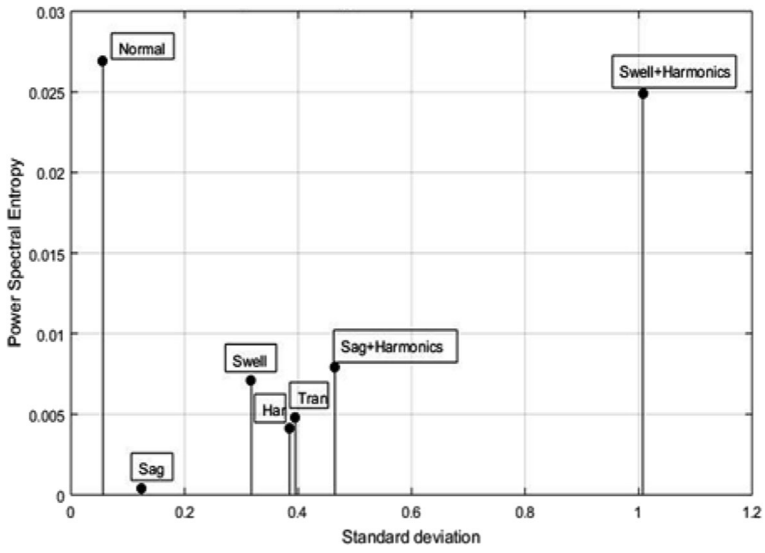

Fig. 6 Power spectral entropy Vs Standard deviation of PQ events

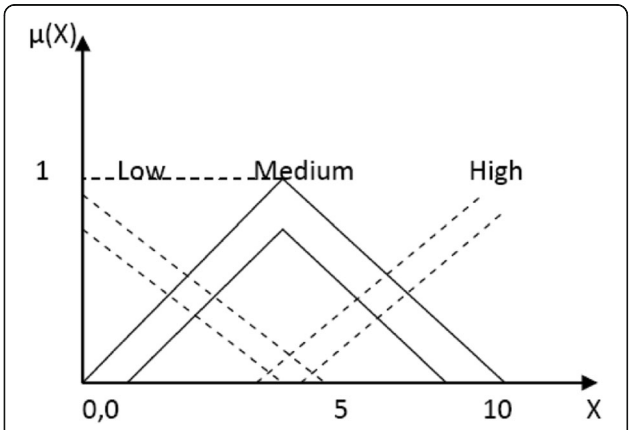

Fig. 7 Type-2 membership function

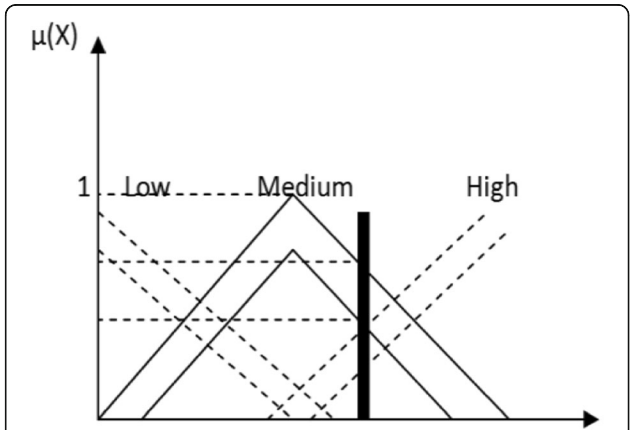

Fig. 8 Membership function showing grading

engine, and output processor as in type 1 fuzzy [9]. The output processor includes defuzzifier and type-reducer, it generates a type-1 fuzzy set output or a crisp number. Mostly If-then rules are used to characterize type 2 fuzzy logic, but its antecedent or consequent sets are now type-2. If membership function in type 2 logic represented in the form of interval, then type 2 fuzzy logic become "interval type 2 fuzzy logic".

Interval type-2 fuzzy set, $\tilde{A}$, can be represented as

$$\tilde{A} = \left\{((x,\mu),\mu_{\tilde{A}}(x,\mu))\middle|\forall_x \in X, \forall_\mu \in J_x \subseteq [0,1]\right\} \quad (10)$$

In (10) $\mu_{\tilde{A}}(x,u)$ is the IT2FLS membership function, which vary as

$$0 \leq \mu_{\tilde{A}}(x,u) \leq 1.$$

$\tilde{A}$, can be calculated as

$$\tilde{A} = \int_{x \in X} \int_{\mu \in JX} \mu_{\tilde{A}}(x,\mu)/(x,\mu) J_X \subseteq [0,1] \quad (11)$$

In (11) $\iint$ represents union over all acceptable x and u. J_x is primary membership of x. According to each primary membership value, there is a secondary membership value that explains the possibility for primary membership value. Although, the secondary membership functions can take values in the interval of [0,1] showing in Fig. 8. The specification of MFs is one of the major tasks in design of type 2 fuzzy logic system. The selection of type of MF (Gaussian, triangular etc.) and the choice of their certain parameters directly affects the performance [10]. A variety of methods to mitigate this issue have been researched for interval type-2 FLSs. These techniques are generally based on the use of expert knowledge, genetic algorithms, neural networks etc. However, there is still scope in this area to standardize and abridge the selection of particular MFs. Interval Type-2 fuzzy logic techniques are applied in various field of engineering and science, due to more feasibility in the computations. If the position of membership functions may not be certain accurately, then in such cases, the membership degree cannot be chosen as a particular number in [0, 1], then the use of type-2 fuzzy sets is the better option. If the edges of the triangular function in Fig. 4 are blurred, Fig. 5 can be produced. In Fig. 8, the membership function does not have a unique value for a specific value of X. The values on the intersection of vertical line and the region of membership function do not need all to be weighted same. The three-dimensional membership function of type-2 fuzzy logic that indicates the features of a type-2 fuzzy set is generated if all $x \in X$ have attributed to its own distribution. The union of all primary memberships is said to be the bounded region that express the uncertainty in the incipient memberships of a type-2 fuzzy set termed as footprint of uncertainty (FOU). Both upper membership function and a lower membership function can be taken as two type-1 membership functions that are the constrained for the footprint of uncertainty of a type-2 fuzzy set. In this research article IT2FLS used for classification of multiple power quality disturbances. It can handle higher degrees of uncertainty as compare to type-1 fuzzy logic. One extra third dimension in type-2 fuzzy logic systems provide more degrees of freedom for better analysis of uncertainty compared to type-1 fuzzy sets. IT2FLS are beneficial in circumstances where it is difficult to determine the exact membership function for a fuzzy set [11].

Interval type-2 FLS provides the capability of handling a higher level of uncertainty and provides a number of missing components that have held back successful deployment of fuzzy systems in human decision making.

6 Proposed methodology for classification

Power quality events generated with MATLAB software and data base is created for detection of power quality

events then Volterra series method is applied for detection and extraction of features of power quality events then rule based fuzzification is done to classify power quality events as shown in Fig. 9.

The Proposed state of art uses limiting method to handle the lengthy calculations of type-2 FLS. Now type-2 fuzzy converted into type −1. The obtained output of IT2FLS provides more feasible result in comparison of other classification techniques.

7 Results and Discussion

On the basis of rules designed based on analysis done by Volterra series, classification can be done easily for example in Table 1. If SD is low and PSE is also low then event classified surely be swell, when SD is high and PSE also having higher value in this case event will be sag. If SD is moderate and PSE is low then harmonics will be the cause of disturbance, transient disturbance occurs when SD is moderate and PSE is also moderate. In Fig. 10 classification results for single events shown as surface of interval type 2 fuzzy logic.

The rules designed for classification of multiple events such as sag plus harmonics and swell plus harmonics show in Table 1, if SD is moderate and PSE is high then multiple events sag plus harmonics occur as disturbance in power quality. In another case when SD is low and PSE is moderate then disturbance classified will be swell + harmonics.

Table 1 Rule Editor for IT2FLS

SD\PSE	Low	Moderate	High
Low	Swell	Swell+Harmonics	None
Moderate	Harmonics	Tansient	Sag+Harmonics
High	None	None	Sag

In Fig. 11 classified multiple events shown as surface of IT2FLS. Type- 2 fuzzy logic can easily classify PQ events on the basis of rule design for the fuzzification, this novel technique can classify multiple events with more than 85% of efficiency. In Table 2. Testing is done for calculation of efficiency based on Volterra series and IT2FLS.

When classification of power quality events done under ideal condition, then no noise in present in the system then IT2FLS system classify sag and swell events with 100% classification efficiency but harmonics and Transient events having classification efficiency 98 and 96% respectively. When multiple events occur such as sag plus harmonics and swell plus harmonics then efficiency comes out to be 94%. Overall efficiency in ideal signal condition is 97% which shows that this technique can classify most of the events with more than 95% efficiency respectively as shown in Table 2.

When classification done under certain noise condition with SNR 30 dB in Table 3, then IT2FLS classify sag, swell harmonics with good efficiency (more than 96%) remaining event's like transient, sag plus harmonics and swell plus harmonics also have efficiency more than 85% as shown in Table 3, overall efficiency in this case is 93% this shows that given classification technique is also applicable for real time scenario. If classification performed under SNR 20 dB in Table 4, then IT2FLS

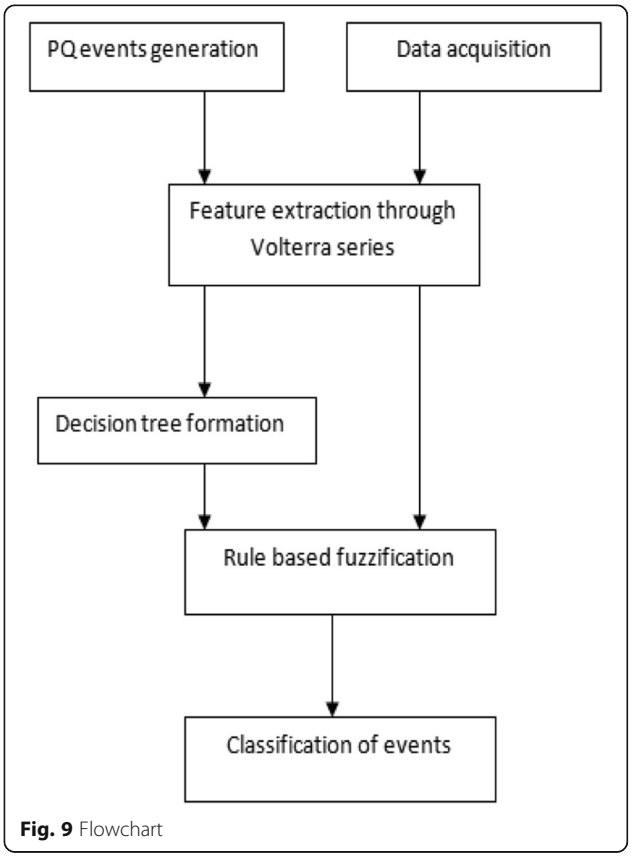

Fig. 9 Flowchart

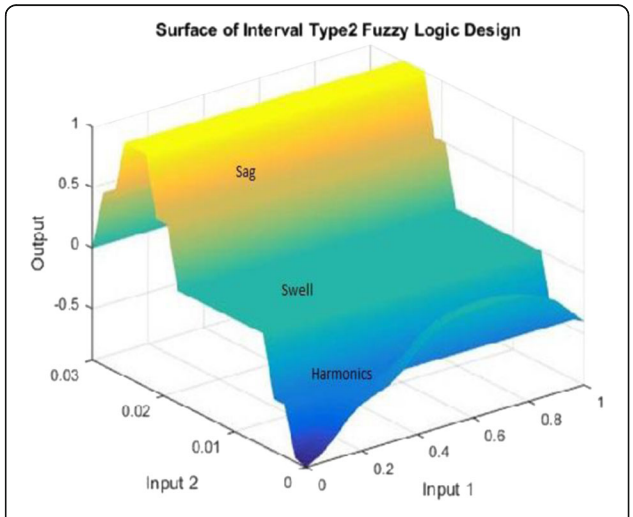

Fig. 10 Classification Results (sag, swell and harmonics)

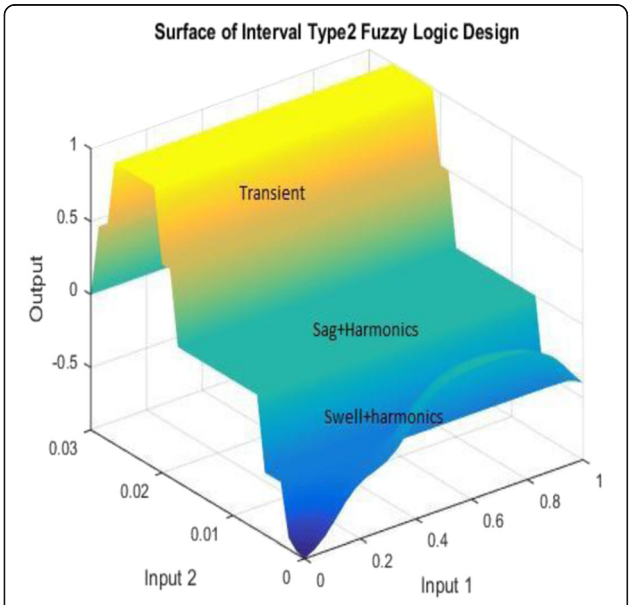

Fig. 11 Multiple events classification

classify sag, swell harmonics with good efficiency (more than 94%) remaining event's harmonics, transient and remaining multiple events also have efficiency more than 84% as shown in Table 4, and Overall efficiency in this case is 89%. All these classifications performed in MATLAB R2015a 64 bit software.

All these classification results show that in ideal and practical situation this technique performed well for with overall efficiency more than 85%. We can apply this technique in real time monitoring, this novel method definitely perform well in detection and classification of power quality events in real time scenario.

8 Conclusions

This paper proposes a PQ event detection and classification scheme utilizing a Volterra series based feature extractor and a classifier based on interval type-2 fuzzy logic system. The proposed method can reduce the quantity of extracted features of distorted signal without losing its characteristics and thus, requires less memory space and computation time. The performance of classifier is test under three conditions i.e. ideal, SNR 30 dB and SNR 20 for effective classification of PQ events. It is observed that IT2FLS correctly classifies the PQ event with high accuracy and IT2FLS gives the best performance as compared to neural network based classifier and SVM [12]. Therefore, the proposed method can be used as the PQ event classifier in real time system. The overall classification efficiency of IT2FLS is 93% if take average of all three condition mention in this paper. The simulations result show that IT2FLS has higher performance than ANN with feed forward multilayer back propagation (FFML), learning vector quantization (LVQ), probabilistic neural network (PNN) [13, 14].

Table 2 Classification results under ideal signal condition

Events	Sag	Swell	Harmonics	Transcient	Sag +Har	Swell +Har
Sag	50					
Swell		50				
Harmonics			49			
Transcient				48		
Sag+Har					47	
Swell+Har						47
Calssification efficiency in %	100	100	98	96	94	94
Classificatione error in %	0	0	2	4	6	6
Overall efficiency	97					

Table 3 Classification results under SNR 30 db

Events	Sag	Swell	Harmonics	Transcient	Sag +Har	Swell +Har
Sag	50					
Swell		48				
Harmonics			48			
Transcient				45		
Sag+Har					43	
Swell+Har						44
Classification efficiency in %	100	96	96	90	86	88
Classification error in %	0	4	4	10	14	12
Overall Efficiency	93					

Table 4 Classification results under SNR 20 db

Events	Sag	Swell	Harmonic	Transcient	Sag +Har	Swell +Har
Sag	48					
Swell		47				
Harmonic			47			
Transcient				42		
Sag+Har					42	
Swell+Har						41
Classification efficiency in %	96	94	94	84	84	82
Classification error in %	6	6	6	16	16	18
Overall efficiency	89					

Acknowledgment
This work was supported by my mentors Prof. Rajiv Kapoor & Dr. M M Tripathi. I am grateful for their guidance, feedback and advice. I would like to express my deepest thanks to my mentors. They are supportive in their feedback and always motivated me to do work hard.

Authors' contributions
R - Analysis for detection of power quality with volterra series and feature based on volterra series extracted by this author. RK - Interval Type-2 fuzzy logic for classification of power quality is applied for power quality signals by this author. MMT analyzed the results of classification technique and calculated efficiency of classification in different noisy condition and concluded this research article. All authors read and approved the final manuscript.

About the authors
Rahul having B.Tech, M.Tech Degree in electronics & communication and pursuing PhD in electronics & communication department of Delhi technological university, Delhi, India his areas of interest in Power quality, Power line communication, Digital communication and Digital signal processing.
Rajiv Kapoor having BE, ME & PhD degree in electronics & communication and working as a Professor in EC department of Delhi technological university, Delhi India, his areas of interest in Power Quality, Image Processing, Computer Vision, Signal Processing, Cognitive Radio.
MM Tripathi having B. Tech and PhD degree in Electrical Engineering and working as Associate Professor in EE Department of Delhi Technological University, Delhi, India and his area of interest are Power quality, Artificial Intelligence (AI) application in power system and Embedded Systems.

Competing interests
The authors declare that they have no competing interests.

Author details
[1]Department of Electronics & communication Engineering, Delhi Technological University, Delhi, India. [2]Department of Electrical Engineering, Delhi Technological University, Delhi, India.

Received: 3 September 2016 Accepted: 28 February 2017
Published online: 29 March 2017

References

1. Kapoor, R., & Saini, M. K. (2012). Classification of power quality events – a review. *International Journal of Electrical Power & Energy Systems, 43*, 11–19.
2. Kapoor, R., & Saini, M. K. (2007). A new signal processing technique for power system disturbances detection and classification. *Int. J. Electrical Engineering, 88*, 9–14.
3. Saini, M. K., Kapoor, R., & Sharma, B. B. (2011). PQ event classification using fuzzy classifier. *Advanced Materials Research, 403–408*, 3854–3858.
4. Kapoor, R., & Gupta, R. (2011). Statistically matched wavelet-based method for detection of power quality events. *International Journal of Electronics, 98*(1), 109–127.
5. Richard, T. (1991). Volterra Series Modeling of Power Conversion Systems. *IEEE Transactions on power electronics*, *6*(4) 712–718.
6. Nam, S-W., Powers E.J., (2003). Volterra Series Representation of Time-Frequency Distributions. *IEEE transactions on signal processing*, *51*(6) 1532–1537.
7. Kapoor, R., & Gupta, R. (2012). Fuzzy lattice based technique for classification of power quality disturbances. *International transaction on electrical energy system, 22*(8), 1053–1064.
8. Liang Q., Mendel J.M., (2000) Interval Type-2 Fuzzy Logic Systems: Theory and Design. *IEEE transactions on fuzzy systems*, *8*(5) 535–550.
9. Mizumoto, M., & Tanaka, K. (1976). Some properties of fuzzy sets of type-2. *Information and Control, 31*, 312–340.
10. Mendel J.M., John, Liu F. (2006). Interval Type-2 Fuzzy Logic Systems Made Simple. *IEEE transactions on fuzzy systems*, *14*(6) 808–821.
11. Wu H., Mendel J.M. (2002). Uncertainty Bounds and Their Use in the Design of Interval Type-2 Fuzzy Logic Systems. *IEEE transactions on fuzzy systems*, *10*(5) 622–639.
12. De Yong D., Bhowmik S., Magnago F. (2015). An effective Power Quality classifier using Wavelet Transform and Support Vector Machines. *Expert Systems with Applications*, *42*(15–16) 6075–6081.
13. Biswal B., Biswal M., Mishra S., Jalaja R. (2014). Automatic Classification of Power QualityEvents Using Balanced Neural Tree. *IEEE transactions on industrial electronics*, *61* (1).
14. Mishra S., Bhende C. N., Panigrahi B. K. (2008). Detection and Classification of Power Quality Disturbances Using S-Transform and Probabilistic Neural Network. *IEEE transactions on power delivery*, *23* (1).

Submit your manuscript to a SpringerOpen journal and benefit from:

► Convenient online submission
► Rigorous peer review
► Immediate publication on acceptance
► Open access: articles freely available online
► High visibility within the field
► Retaining the copyright to your article

Submit your next manuscript at ► springeropen.com

MĀPAN-Journal of Metrology Society of India
DOI 10.1007/s12647-017-0207-7

ORIGINAL PAPER

Development and Characterization of a Diaphragm-Shaped Force Transducer for Static Force Measurement

R. Kumar[1]*, B. D. Pant[2] and S. Maji[3]

[1]CSIR-National Physical Laboratory, New Delhi, India

[2]CSIR- Central Electronics Engineering Research Institute, Pilani, Rajasthan, India

[3]Delhi Technological University, Delhi, India

Received: 22 July 2016 / Accepted: 22 February 2017

© Metrology Society of India 2017

Abstract: There are different types of force transducers, used over the years, comprising of different principles and have different grades of uncertainty. Force transducers may be analog or digital and may be strain gauged, tuning fork type, piezoresistive type, Hall Effect based etc. Though different types of force transducers have been developed in last few decades, still strain gauged force transducers are used over the larger scale due to practical viability and reliability for force measurement. The paper describes low-cost indigenous development of a force transducer, which has been developed for a nominal capacity of 5 kN with ease of design and manufacturing. It has strain gauges applied at suitable locations to form a Wheatstone bridge. The force transducer has been calibrated according to the standard calibration procedures based on *ISO 376* and *IS 4169* standards. Measurement results and an uncertainty analysis have been presented. The uncertainty of measurement of the force transducer is found up to 0.06%. The paper also discusses the implications of applying multiple strain gauges at a single location in series to enhance the sensitivity of the force transducer. Two strain gauges are arranged in series for the given location and the sensitivity of the force transducer is enhanced. It also indicates that the uncertainty of measurement of the force transducer in such case is enhanced up to 0.05% or better to make force transducer suitable for most of metrological and industrial applications.

Keywords: Force transducer; Diaphragm; Uncertainty of measurement; Metrological characteristics

1. Introduction

Force measurement has been very useful for various scientific and industrial applications, from verification of material testing machines to the cutting force in machining processes. Force transducers have been used to measure force for many decades. They also serve as force transfer standards and are used to establish traceability chains from force standard machines to force calibration and material testing machines. There are several types of force transducers, including the dial gauged, strain gauged, and tuning fork types. However, the strain gauged type is the most wide type of force transducers utilized for the precise measurement of force and as a force transfer standard. Force transducers with measurement uncertainties of up to 0.10% are used for various metrological purposes, but our focus is on force transducers with uncertainties smaller than 0.05%.

Force measuring devices like proving ring, elliptical dynamometers have been used for many decades, but they have inherent shortcomings when compared to strain gauged force transducers. The dial gauged force transducers are utilized for specific types of force measurement but their poor resolution and stability leads to large measurement uncertainties. The ring shaped force transducers have been suitably modified into other shapes and results have been reported, but such developments are limited to specific applications [1–3]. Other types of force transducers, such as tuning fork type force transducers, have been reported upon and employed as force transfer standards, but their large scale suitability has yet to be established [4].

Strain gauged transducers, now a day's are developed indigenously for various measurement related applications like pressure, force, torque etc. to promote in-house research and development. Such developments are prompt

*Corresponding author, E-mail: kumarr@nplindia.org

Published online: 17 March 2017

in promoting laboratory developments and evaluation of the practical viability of developed transducers [5]. Strain gauged force transducers offer better resolution and interpolation for measurement of intermediate step forces. In addition, their digital indicators allow remote operation. Some commercial strain gauged force transducers are available that reduce measurement uncertainties to as low as 0.025%, but they have complex shapes and their strain gauging is a difficult task in addition to economical concern. Hence, there has been always thrust over the development of simple shaped force transducers with comparable metrological features to promote in-house design and development for their practical utility for in-house applications as well as metrological applications. Such force transducers may lead to the economic viability of force transducers over a larger scale, if found suitable. Recently, some of the development has been reported in respect of the development of simple shaped force transducers [6]. Square ring shaped force transducer has been developed in-house and the uncertainty of measurement is reported up to 0.1%. For most of the industrial applications, the uncertainty of measurement 0.05% is acceptable, and thrust is to be given for the development of force transducers with an uncertainty of measurement up to 0.05% or better.

We present here the development of a force transducer with a simple design (Fig. 3a, b) that employs strain gauges arranged in the form of a Wheatstone bridge and record their output through digital indicators. We characterize its metrological performance as per the *ISO 376* [7] and *IS 4169* [8] standards. A 50 kN dead weight force machine, described in [9], was used to calibrate this force transducer. The force transducer has been designed and developed for a nominal capacity of 5 kN and has been computationally studied using finite element analysis (FEA). Though the force transducer has been developed for 5 kN only, this same type of design can be used to measure force in the range from kilo newtons to mega newtons. The uncertainty of measurement of the force transducer is found to be 0.05% ($k = 2$) using strain gauge. This includes the uncertainty contributed by repeatability, reproducibility, resolution, zero offsets, and reversibility.

2. Computational Investigations

The force transducer we have developed is designed for the measurement of static force. It has a nominal capacity of 5 kN and is made of EN 24 steel. The sensing element is shown in Fig. 1a, b.

Strain gauges are used (as shown in Fig. 3b) for the extraction of electrical signals, and the gauge factor of the strain gauge is 2.1. Two strain gauges are applied in the radial direction and two in the tangential direction. The chosen EN 24 steel diaphragm (Fig. 1) is 120 mm in diameter and its thickness is 3 mm. The diaphragm has been clamped at its periphery using a ring of 15 mm width and 20 mm thickness, carved out of the same EN 24 steel block.

Force is applied to the diaphragm through a hardened steel ball over a hemispherical slot at the center of the diaphragm. Simulations using COMSOL Multiphysics, have been carried out. Von Mises Stress and displacement of the diaphragm has been simulated for forces from 0 to 5000 N at intervals of 500 N. The strain gauges are applied at the locations to have moderate stress. The stress is maximum at the point, where force is being applied. In order to have an optimum sensitivity, location with moderate stress as shown in Fig. 3a, has been opted for application of strain gauges. (Figure 2). In other words, the strain gauges are applied on locations in between the center and periphery.

Based on the findings of the FEA analysis, the four strain gauges are located at an angle of 90°, 180°, 270° and 360° from vertical axis on the outer surface of the transducer as the surface is made flat (Fig. 3). Strain gauges of precisely known resistance are used. The strain gauges consist of fine metallic wire and their resistance changes when they are elongated or contracted. This property is used for development of strain gauged force transducers. Before the strain gauges are fixed to the defined locations, the machined element is normalized by applying maximum axial force so that the stress is in operational range. For applying the strain gauges, the surface is smoothened and the surface roughness is restricted to few micrometers. Strain gauges are applied using a hot curing adhesive. Suitable curing for pre and post of applying strain gauges has been done and in accordance to Wheatstone bridge, connections are made. Nominal resistance of strain gauges is $350 \pm 0.3\ \Omega$ and when there is no external force, Wheatstone bridge is balanced. Electrical output (mV/V) is the indication of the external force applied, which causes unbalancing of the bridge.

3. Measurement Results

The force transducer was calibrated using the 50 kN dead weight force machine. The 50 kN dead weight force machine employs dead weights ranging from 0.5 to 5 kN to realize precisely known force in the range from 0.5 to 50 kN. The dead weight force machine has a hanger (of nominal force 0.5 kN) with a stack to which all of the weights are attached [9]. The dead weight force machine is able to apply the force in ascending or descending order according to the calibration procedures in the *ISO 376* [7]

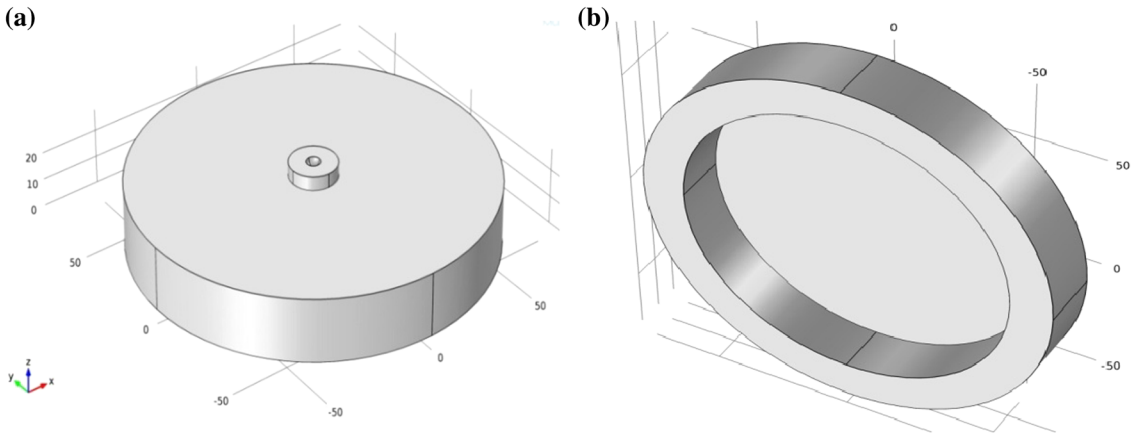

Fig. 1 **a** Top section of force transducer, **b** lower section of force transducer

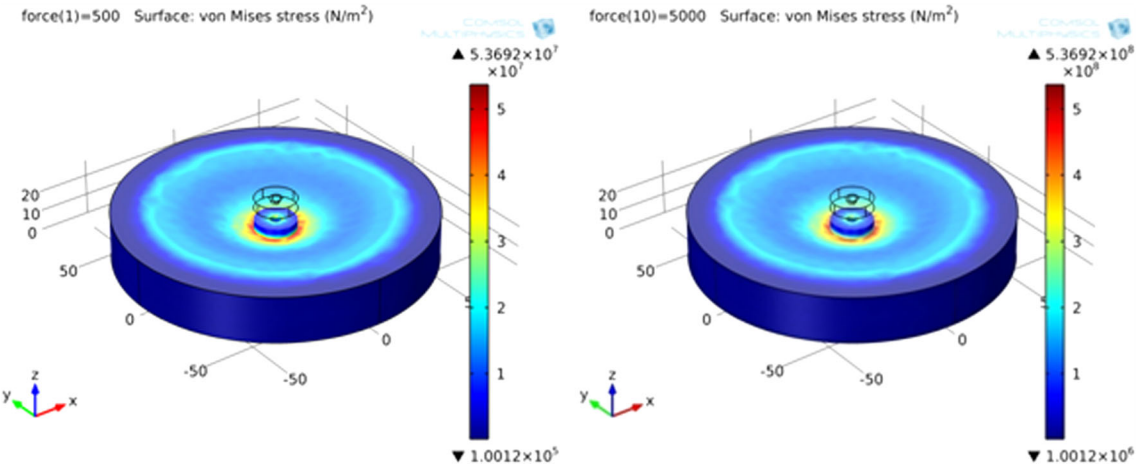

Fig. 2 Stress distribution of the sensing element at 500 and 5000 N force

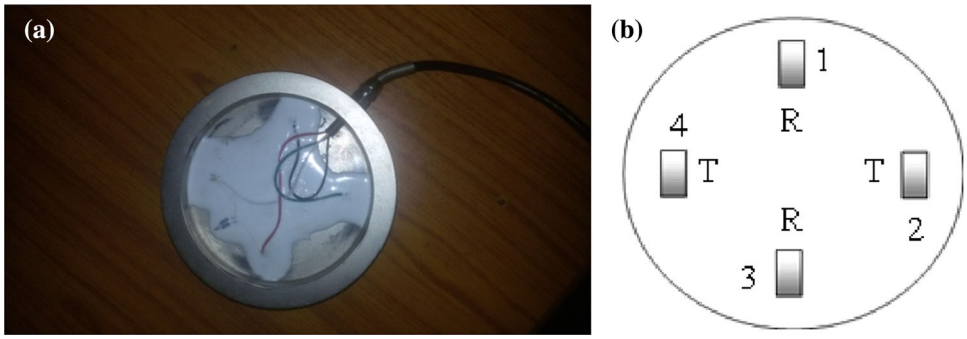

Fig. 3 **a** Force transducer with strain gauges. **b** Typical arrangement of strain gauges (*T* Tangential; *R* Radial; 1, 2, 3 and 4 are the strain gauges)

and *IS 4169* [8] standards. A digital indicator (DK 38 of HBM, Germany) of resolution 0.00001 mV/V is utilized to record the measurements. As the measurement is done at controlled environmental conditions (Temperature 23 ± 1 °C, Relative humidity 50 ± 10%), no uncertainty due to temperature has been computed [10–12].

The relative combined standard uncertainty $w_{c\ (tra)}$ and the relative expanded uncertainty $W_{(tra)}$ ($k = 2$) of the measurements are calculated as

$$w_{c(tra)} = \sqrt{\left(w_{rep}^2 + w_{rpr}^2 + w_{int}^2 + w_{rev}^2 + w_{zer}^2 + w_{res}^2\right)} \quad (1)$$

$$W_{tra} = k \cdot w_{c(tra)}. \quad (2)$$

Other terms represents the relative variances of relative uncertainty, expressed as percentages, due to repeatability (rep), reproducibility (rpr), reversibility (rev), zero offsets(zer), interpolation (int) and resolution (res). The

Table 1 Uncertainty components and their relative contribution according to ISO 376 [7]

Sl. no.	Relative uncertainty component	Probability distribution, type of error	Estimated relative variances of input quantities
1	Repeatability	Rectangular, type B	$w_{rep} = a^2/3$
2	Reproducibility	U shaped, type B	$w_{rpr} = a^2/2$
3	Interpolation	Triangular, type B	$w_{int} = a^2/6$
4	Reversibility	Rectangular, type B	$W_{rev} = a^2/3$
5	Zero offset	Rectangular, type B	$w_{zer} = a^2/3$
6	Resolution	Rectangular, type B	$w_{res} = a^2/3$

Table 2 Uncertainty components and their relative contribution according to IS 4169 [8]

Sl. no.	Relative uncertainty component	Probability distribution, type of error	Estimated relative variances of input quantities
1	Repeatability	U shaped, type B	$w_{rep} = a^2/2$
2	Interpolation	Triangular, type B	$w_{int} = a^2/6$
3	Reversibility	Rectangular, type B	$W_{rev} = a^2/3$
4	Zero offset	Rectangular, type B	$w_{zer} = a^2/3$
5	Resolution	Rectangular, type B	$w_{res} = a^2/3$

relative uncertainty of measurement, W shall be determined by Eq. (3), considering the Uncertainty associated with the reference standard (force machine) W_{REF} [9],

$$W = \sqrt{\left(W_{tra}^2 + W_{REF}^2\right)}. \quad (3)$$

A brief description of the different factors has been mentioned below for better understanding and relevance of each factor to uncertainty of measurement of force transducer.

3.1. Relative Error due to Repeatability (*rep*)

We take the relative error due to repeatability by taking two calibration series at a given position into consideration e.g. Series 1 and 2 at the position, 0°.

3.2. Relative Error due to Reproducibility (*rpr*)

We take the relative error due to reproducibility by taking three calibration series (ascending order) at different positions e.g. Series 1, Series 2, Series 3 at positions 0°, 120° and 240° respectively) into consideration.

3.3. Relative Error due to Zero offsets (*zer*)

We compute the relative error due to zero offsets is from the zero values remaining once there is no force applied after the calibration series is over. It may also be noted that the relative error due to zero offsets is constant for each force step.

3.4. Relative Error due to Resolution (*res*)

We take the relative error due to resolution by dividing the resolution (units) of the indicator to the average of values indicated by the indicator at the given force step during the calibration. It may also be noted that the value of the relative error due to resolution keep on decreasing as we move from lower force step to higher force step during the calibration procedure.

3.5. Relative Error due to Reversibility (*rev*)

We take the difference of two force calibration series in ascending and descending order at a given force value to evaluate the relative error due to reversibility. In case of analogue force measuring devices, there is no reversibility related measurements taken into account.

3.6. Relative Error due to Interpolation (*int*)

We compute the relative error due to interpolation by a in-house developed software, only in case of digital instruments.

Uncertainty of measurement is computed in accordance to the factor taken into account and dividing it by suitable factor according to the type of error and its distribution (Tables 1, 2).

'a' is the obtained by dividing the relative deviation due to respective uncertainty component by 2 for the component considered.

Table 3 Comparison of IS 4169 and ISO 376

Sl. no.	Title	IS 4169*	ISO 376
1	Number of calibration series	Three	Four
		One each at 0°, 120° and 240°	Two at 0° and one each 120° and 240°
2	Calibration Series at 0° position	One	Two

Table 4 Different factors discussing the metrological characterization with uncertainty of measurement of force transducer in accordance to *IS 4169*

Force (kN)	Relative deviation due to (%)					Uncertainty associated with the reference standard (force machine) W_{REF}	Uncertainty of measurement (%) ($k = 2$)
	Zero offset (2a)	Repeatability (2a)	Resolution (2a)	Interpolation (2a)	Reversibility (2a)		
0.5	0.007	0.028	0.014	0.016	0.061	0.003	0.042
1.0	0.007	0.050	0.007	0.006	0.069	0.003	0.053
1.5	0.007	0.052	0.005	0.013	0.060	0.003	0.051
2.0	0.007	0.053	0.004	0.008	0.056	0.003	0.050
2.5	0.007	0.040	0.003	0.001	0.065	0.003	0.047
3.0	0.007	0.031	0.002	0.003	0.071	0.003	0.047
3.5	0.007	0.053	0.002	0.002	0.067	0.003	0.054
4.0	0.007	0.041	0.002	0.004	0.073	0.003	0.052
4.5	0.007	0.018	0.002	0.001	0.073	0.003	0.044
5.0	0.007	0.043	0.001	0.002	0.000	0.003	0.031

'2a' is divided by 2 to obtain 'a'

Table 5 Computation of uncertainty of measurement for 0.5 kN in case of IS 4169

Force (kN)	Relative deviation due to (%)					Uncertainty associated with the reference standard (force machine) W_{REF}	Uncertainty of measurement (%) ($k = 2$)
	Zero offset $(a^2)/3$	Repeatability $(a^2)/2$	Resolution $(a^2)/3$	Interpolation $(a^2)/6$	Reversibility $(a^2)/3$		
0.5	0.0000041	0.0000653	0.0000163	0.0000094	0.0003101	0.003	0.04

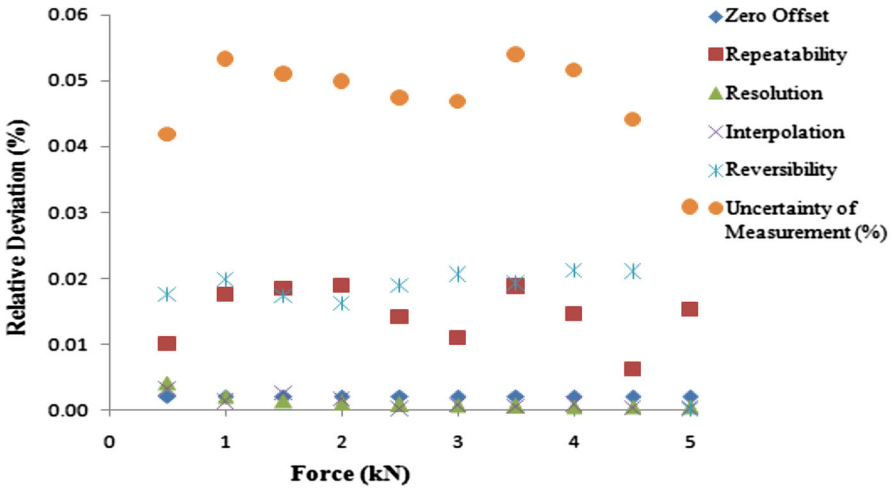

Fig. 4 Metrological characteristics of the force transducer (*IS 4169*)

Table 6 Different factors pertaining to metrological characterization with uncertainty of measurement of force transducer in accordance to *ISO 376*

Force (kN)	Relative deviation due to (%)						Uncertainty associated with the reference standard (force machine) W_{REF}	Uncertainty of measurement (%) ($k = 2$)
	Zero offset (2a)	Repeatability (2a)	Reproducibility (2a)	Resolution (2a)	Interpolation (2a)	Reversibility (2a)		
0.5	0.007	0.028	0.042	0.014	0.012	0.063	0.003	0.051
1.0	0.007	0.014	0.057	0.007	0.012	0.070	0.003	0.058
1.5	0.007	0.014	0.047	0.005	0.001	0.059	0.003	0.049
2.0	0.007	0.011	0.057	0.004	0.001	0.051	0.003	0.050
2.5	0.007	0.009	0.046	0.003	0.008	0.065	0.003	0.050
3.0	0.007	0.007	0.031	0.002	0.003	0.074	0.003	0.048
3.5	0.007	0.014	0.053	0.002	0.012	0.053	0.003	0.050
4.0	0.007	0.021	0.043	0.002	0.000	0.071	0.003	0.053
4.5	0.007	0.021	0.027	0.002	0.008	0.071	0.003	0.047
5.0	0.007	0.017	0.043	0.001	0.003	0.000	0.003	0.032

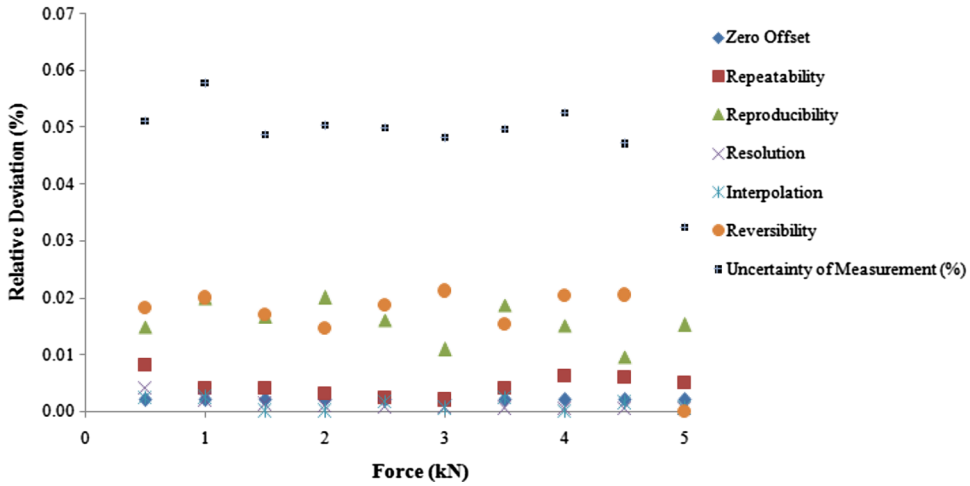

Fig. 5 Metrological characteristics of the force transducer (*ISO 376*)

If a force transducer is calibrated according to the *IS 4169* [8] standard, no relative uncertainty due to reproducibility is taken into account. In fact, the relative repeatability according to the *IS 4169* standard is similar to relative uncertainty due to reproducibility in *ISO 376* [7]. The terms used to evaluate the measurement uncertainty were previously discussed in [9]. The measurement results are summarized in Tables 4, 5 and Fig. 4 for the *IS 4169* [8] calibration, and in Table 6 and Fig. 5 for the *ISO 376* [7] calibration.

A brief comparison of the calibration procedures according to IS 4169 and ISO 376 has been given below (Table 3).

Further investigation has enhanced the sensitivity of the force transducer as shown in Fig. 6. This was done by adding two strain gauges in series as one arm of the Wheatstone bridge. This has enhanced the sensitivity without any much significant impact on the measurement uncertainty of the force transducer. The schematic arrangement has been shown in Fig. 6. Nominal resistance of each strain gauge is 350 Ω. These measurements are summarized in Table 7.

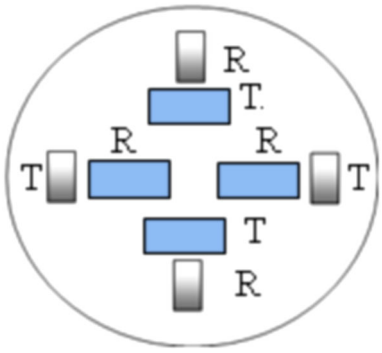

Fig. 6 Schematic diagram of arrangement of strain gauges (*T* Tangential; *R* Radial)

Table 7 Different factors pertaining to metrological characterization with uncertainty of measurement of force transducer with enhanced sensitivity in accordance to *ISO 376*

Force (kN)	Relative deviation due to (%)						Uncertainty associated with the reference standard (force machine) W_{REF}	Uncertainty of measurement (%) ($k = 2$)
	Zero offset (2a)	Repeatability (2a)	Reproducibility (2a)	Resolution (2a)	Interpolation (2a)	Reversibility (2a)		
0.5	0.003	0.014	0.041	0.007	0.023	0.071	0.003	0.052
1.0	0.003	0.010	0.045	0.003	0.007	0.061	0.003	0.048
1.5	0.003	0.007	0.039	0.002	0.015	0.048	0.003	0.040
2.0	0.003	0.007	0.050	0.002	0.001	0.051	0.003	0.046
2.5	0.003	0.005	0.048	0.001	0.001	0.032	0.003	0.039
3.0	0.003	0.006	0.041	0.001	0.012	0.037	0.003	0.036
3.5	0.003	0.006	0.026	0.001	0.001	0.019	0.003	0.022
4.0	0.003	0.004	0.042	0.001	0.003	0.019	0.003	0.032
4.5	0.003	0.005	0.040	0.001	0.006	0.013	0.003	0.030
5.0	0.003	0.005	0.053	0.001	0.004	0.000	0.003	0.038

- When comparing the results summarized in Tables 6 and 7, it is clear that there is hardly any impact over the uncertainty of force transducers, even if the sensitivity has been enhanced. However, there is significant reduction in the relative uncertainty due to resolution in Table 7, when compared with measurements reported in Table 6.
- The uncertainty of measurement of the force transducer is up to 0.06%, which makes it suitable for most of metrological applications as well as industrial applications.

4. Conclusions

Following conclusions are drawn in the regard of the work presented:

- Design, development, and metrological properties of a force transducer have been presented.
- The force transducer has been computationally studied using FEA software for locating the strain gauges, arranged in form of Wheatstone bridge.
- The force transducer has been metrologically characterized in accordance to standard procedure ISO 376 and IS 4169. Suitable factors are taken in consideration to evaluate uncertainty of measurement in accordance to procedure adopted. The uncertainty of force measurement of the force transducer is up to 0.06% ($k = 2$) for the rated capacity of the force transducer.
- To investigate the implications of two strain gauges arranged in series at a location to enhance the sensitivity of the force transducers, two strain gauges are arranged to enhance the sensitivity of the force transducer. After making arrangement suitably, the force transducer has been metrologically characterized according to ISO 376 and uncertainty of measurement of force transducer is found up to 0.05% ($k = 2$).
- The study affirms the metrological features of the force transducers, making them suitable for precision force measurement as well as industrial force measurement related applications.
- The presented force transducers are having simple design—manufacturing and economic considerations. Though authors have presented force transducers for nominal capacity of 5 kN, but these are practically viable in the wider range from kN to MN.

Acknowledgements Authors are thankful to Director, CSIR – NPL for his support.

References

[1] M. Rehman and S. Rehman, A computer program for designing circular proving rings of uniform strength, J. Inst. Eng. (India) Mech. Eng. Div., **88** (2007), 3–7

[2] J. Libii, Design, analysis and testing of a force sensor for use in teaching and research, World Trans. Eng. Technol. Educ., **5**(1), (2006), 175–178

[3] D. Diddens, D. Reynaerts, and H. Van Brussel, Design of a ring shaped three axis micro force/torque sensor, Sens. Actuat. A-Phys., **46**(1–3), (January–February 1995), 225–232

[4] H. Toshiyuki, K. Yoshihisa, U. Kazunaga, H. Tsuyoshi, S. Hoshini, and K. Masaaki, Evaluation of tuning fork type force transducer as a transfer standard, Measurement, **41**(9), (November 2008), 941–949

[5] A. Kumar, S. Yadav, and R. Agarwal (2016), Design and development of a pressure transducer for high hydrostatic pressure measurements up to 200 MPa, J. Inst. Eng. (India): Ser. C, DOI: 10.1007/s40032-016-0257-6

[6] H. Kumar, C. Sharma, and A. Kumar, The development and characterization of a square ring shaped force transducer, Meas. Sci. Technol., **24**(9), (2013), 1–9
[7] ISO, – Metallic materials – Calibration of force proving instruments used for the verification of uniaxial testing machines, ISO 376, 2011
[8] Bureau of Indian Standards, Metallic materials – Calibration of force proving instruments used for verification of uniaxial testing machines, IS 4169, 1988 (reaffirmed 2003)
[9] H. Kumar, A. Kumar, and P. Yadav, Improved performance of 50 kN dead weight force machine using automation as a tool, Meas. Sci. Rev., **11**(2), (2011), 67–70
[10] H. Kumar, Pardeep, M. Kaushik and A. Kumar, Development and characterization of a modified ring shaped force transducer, Mapan J. Metrol. Soc. I., **30**(1), (2015), 37–47
[11] H. Kumar, C. Sharma, A. Kumar and P. K. Arora, Retrospective investigations of force measurement. Mapan J. Metrol. Soc. I., **30**(4), (2015), 291–302
[12] S.S. K. Titus, S.K. Dulkhed, P. Yadav and K.K. Jain, Development and performance evaluation of a dead weight force machine in 2–50 N range, Mapan J. Metrol. Soc. I., **24**(4), (2009), 225–232

Available online at www.ijapie.org

International Journal of Advanced
Production and Industrial Engineering

IJAPIE-SI-MM 513 (2017) 85–87

Special Issue on

MATERIALS
&
MANUFACTURING

Different Tool coatings: An Overview

Navriti Gupta*, Ranganath M. Singari
(Department of Mechanical Engineering, Delhi Technological University, Delhi110042, India)
**Email: navritigupta22@gmail.com*

Abstract : In Surface coated tools plays an important role in metal cutting industry and forming industry. The basic requirement of good finish is achieved due to tool coatings. Tool wear are topic of research interest. Various techniques of tool coatings failure is being studied with advanced experimental and analysis techniques as FEM(Finite Element Modelling) etc. The strength of coating depend on the material used as coating, process employed and thickness of coating. A good quality coating as Ti, W based systems can ensure enhanced tool life. The process of coating deposition can be classified into PVD and CVD based systems. Physical Vapour Deposition involves low temperatures of order of 300°C to 500°C and Chemical Vapour Deposition involves high temperatures in range 800°C-1100°C. PVD is far more superior technology than CVD since the low temperatures encountered. Many polymers can easily deposited by this technique. CVD coatings thicker than PVD coatings, from 10µm to 1mm. In CVD quality of coating is dependant upon materials to be coated, the deposition temperature, the pressure within the vessel, the type and flow rate of the carrier gas.

Keywords: PVD, CVD , coating, Tool failure, Temperature, Techniques

1. INTRODUCTION

The metal cutting and sheet metal forming industry are advancing rapidly due to advance technologies in Machinery(Tool and Dies) and cutting tool. Researchers are experimenting with wide ranges of coating materials as polymers to one point to Metal-Polymer matrix to other point. However the result is wide variety of coatings available to choose from. Industries as Nuclear power plants, Aero-space units, Precision industries as Surgical instruments are possible due to rapid and advancement in tool coating technology.[1-2]

Tool coating enables one or multilayer refractory compounds to be deposited on tool material. Today concept of cutting fluid less machining is finding usage in accordance with pollution norms. This is also term as Green machining and Dry machining. Flexibility and positive ecological effects are other advantages of dry hard machining [3]

Major reason of cutting tool edge failure is thermal, chemical and mechanical loading. Cutting tool wear plays a major role finish turning due to its effects on surface integrity and dimensional accuracy. The types of wear patterns are flank wear and crater wear [4]. Abrasive wear has been cited as a main wear mechanism in turning [5].

Various types of tool coatings has been developed over the years like Ti based coatings as TiN, TiAlN, TiN+TiAlN,TiCN etc. Al_2O_3 as ceramic form has been used in machining; but its brittleness is a limiting factor to its more widespread use as a cutting tool material. The TiC/Al_2O_3 coated carbide insert was first invented in 1975. TiCN and Al_2O_3 sublayers have complementary effects. The intermediate Al_2O_3 layer could improve the heat flow into the chip compared with other types of coating. CVD Al_2O_3 hard coatings have also shown the best results in terms of chemical stability in machining ferrous materials [6-7].

The uses of commercially pure titanium are limited to areas where moderate strength, high corrosion resistance, and good weldability are required [8]. As per statistics available, 40% of all cutting tools used in the industry were reported to be coated tools, which are used for 80% of all machining jobs [9]. Straight grade carbides with 6% cobalt content is optimal for machining Ti6Al4V alloy [10]. TiN-coated cermet, TiC-coated carbide, ceramic aluminum oxide, and CBN tools were not good for machining titanium alloys.

As the first generation of coating ,TiN coatings display many advantages(such as low COF, good friction resistance, and high toughness and hardness) [11] . Natural diamond performed better than PCD .While PCD and showed similar performance [12]. PCD tools have the highest tool life followed by CBN with multi-coated tools showing highest tool wear[13]. multi-coated inserts as TiN/TiCN/TiN had shown better tool life than TiN-coated inserts, at lower feeds [14].

2. TOOL COATING CHARACTERISATION

The most important characteristics which specify the coating:

2.1.Thickness:

In most of coatings the thickness is between 0.2 µm -2 µm. It can be measured with help of CaloTester .

In Calo Tester a hardened steel sphere with a known and fixed diameter rolls on the surface for some seconds depending on coating thickness (for example 20 seconds for thickness in between 0.1 µm and 5 µm). The pressure on the substrate generates artificial superficial craters. Then, through optical microscope it is possible to measure crater depth and diameters.

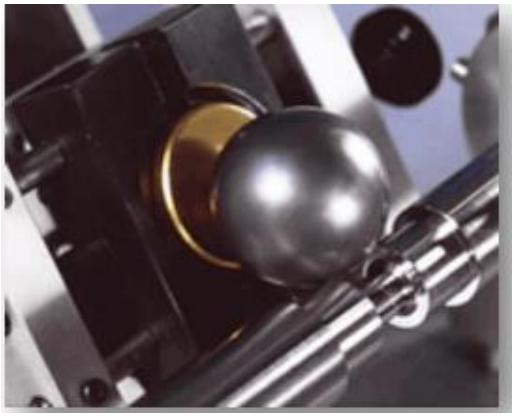

Figure 1: Calo Tester

2.2. Wear Coefficient:

A low wear coefficient is necessary in various applications as molding, forming, tools, automotive etc. Wear coefficient quantifies substrate wear caused by mechanical brushing. "Tribometer" is used to check Wear. Samples roll against a metal tester sphere. It is important to calibrate right forces, rotation speed and sphere diameter. Instrument measure normal and lateral forces in order to calculate wear coefficient.

2.3. Roughness:

It measures surface quality and surface texture.

2.4.Adherence:

It is important to achieve high adhesion to the substrate so as to get thick coating system.

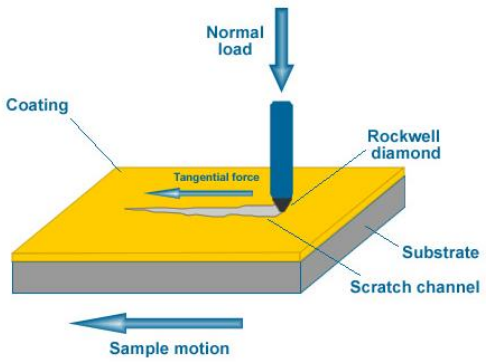

Figure 2: Rockwell Tester

A resistant Rockwell Tester is used.

2.5. Hardness:

It is a parameter to define plastic deformation. Important thin film characteristics are surface hardness and elastic module. A lab tester, called "Nano indentation tester" is used to perform test. During test, a normal force is applied with different intensity. Then the relation between forces and tester depth defines mechanical characteristics, like hardness and elastic module.

2.6. Corrosion Resistance:

Corrosion is the cause of performances reduction during product life. The corrosion behaviour of different coatings are based on climate and ambient conditions of use. Oxidation, reduction, spots, blisters etc fall into this category.

3. RESULTS AND CONCLUSIONS

Various coatings are available in market today. But selection of coating remains a tedious task as cost and other considerations have to be made judiciously.

However on basis of various selection parameters as metal to be machined, cutting conditions, type of finish required, type of machining required, area of application etc will determine type of coating to be selected. For example

1. Titanium-based alloys are classified as difficult to machine materials as they cause high tool wear.

2. Multi-layer thermal barrier coatings with improved surface properties, in terms of reactivity with titanium that could be used effectively in the industry for machining titanium-based alloys[15].

3. The Al_2O_3 + TiO_2, in which theTiO_2 plays a lubricating effect and the Al_2O_3 provides wear resistance and oxidation resistance at high temperatures.[16]

REFERENCES

[1] Wallbank, J.,"Development in tool materials", Proceedings of the Second International Conference on Behaviour of Materials in Machining, York, UK, November 14-15, 1991.
[2] Auezhan .A, Tsukasa W. Ryo T, Shinya. "Fretting wear and fracture behaviors of Cr-doped and non-doped DLC alloy by unbalanced magnetron sputtering". Tribology International; 2013, p. 49–57.
[3] H.K. Tonshoff, C. Arend, R. Ben Amor," Cutting of hardened steel", Ann. ClRP 49 (2):(2000) 547–566.
[4] G. Poulachon, A. Alberta, M. Schluraff, I.S. Jawahir, "An experimental investigation of work material microstructure effects on white layer formation in PCBN hard turning". Int. J. Mach. Tools Manuf. 45 (2005) 211–218.
[5] J.A. Arsecularatne, L.C. Zhang, C. Montross," Wear and tool life of tungsten carbide, PCBN, PCD cutting tools", Int. J. Mach. Tools Manuf. 46 (2006) 482–491.
[6] O. Van Der Biest, J. Vleugels, "Prospective on the development of ceramic composites for cutting tool applications", Key Eng. Mater. 206–213 (2002) 955–960.

[7] M.W. Cook, P.K. Bossom," Trends and recent developments in the material manufacture and cutting tool application of polycrystalline diamond and polycrystalline cubic boron nitride", Int. J. Refract. Met. Hard Mater. 18 (2000) 147–152.
[8] Weiss V (1963) Aerospace structural metals handbook, vol 2. Syracuse Universiyt Press, Syracuse.
[9] Waterman NA, Ashby MF (eds) (1991) Elsevier Material Selector, vol. 2. Elsevier, Barking (Essex, UK).
[10] Dearnley PA, Grearson AN " Evaluation of principal wear mechanisms of cemented carbides and ceramics used for machining titanium alloy IMI318". Mater Sci Technol(1982) 2(1):47–58.
[11] Liang, LiYang, XianChen, YingZhang, YuqingZhao. "Effects of chromium, titanium and aluminium on the friction and wear properties of nitride hard coatings. Vacuum(2012);49(2):47–51.
[12] Narutaki N et al (1983) Study on machining of titanium alloys. CIRP Ann Manuf Technol 32(1):65–69.
[13] Nabhani F (2001) "Wear mechanisms of ultra-hard cutting tools materials". J Mater Process Technol 115(3):402–412
[14] Ezugwu EO, Wang ZM, Machado AR (2000) "Wear of coated carbide tools when machining nickel (inconel 718) and titanium base (Ti-6A1-4V) alloys". Tribol Trans 43(2):263–268
[15] Syed H. Imran Jaffery & Paul T. Mativenga(2012) "Wear mechanisms analysis for turning Ti-6Al-4V—towards the development of suitable tool coatings". Int J Adv Manuf Technol 58:479–493
[16] Kong Dejun , GuoHaoyuan "Friction-wear behaviours of cathodic arc ion plating AlTiN coatings at high temperatures". Tribology International 88(2015)31–39.
.

Available online at www.ijapie.org

International Journal of Advanced
Production and Industrial Engineering

IJAPIE-SI-MM 503 (2017) 18–21

Special Issue on

MATERIALS
&
MANUFACTURING

Effect of Machining Parameters on Cutting Force , Tool Wear and Surface Roughness of AISI 304 Austenitic Stainless Steel – A Review

Md Jamil Akhtar[1] , Md. Gulam Mustafa[2],Ranganath M. Singari[3], Shadab Ahmad [4],Parvesh Ali[5]
[1,2,4,5] *(Research Scholar, Delhi Technological University, Delhi, India)*
[3]*(Associate Professor, Delhi Technological University, Delhi, India)*
*Email: Akhtar.jamil46@gmail.com

Abstract : In this review study, the effect of important parameters of machinability like material removal rate, cutting force and surface roughness were studied. Evaluation of efficiency is based on certain process variable such as flank wear, surface roughness on the work piece, cutting forces developed, temperature developed at the tool chip interface are studied. The optimum cutting speed the impact of cutting speed and cutting fluids on tool wear and surface roughness have been studied during turning an AISI 304 austenitic stainless steel using cemented carbide cutting tools. The studies have been proved that tool wear and surface roughness decreases with the increase in the cutting speed.

Keywords: Speed, Feed,Depth of cut,Cutting Fluid, Surface Roughness, Turning, Optimization, Fuzzy Logic, AISI 304.

INTRODUCTION

Austenitic stainless steels have a high work hardening rate , low thermal conductivity , high corrosion resistance, High strength, high built-up-edge(BUE) tendency, and high deformation hardening. These are the main factors that make their machinability difficult. These factors are responsible for the poor machinability of austenitic stainless steels. Also during cutting they form very strong bond with the cutting tool during cutting . During cutting when chip is broken away, it may bring fragment of tool, particularly when machining with cemented carbide tools. operators encounter problems like poor surface finish and tool failure due to high temperature at tool–work piece interface during machining of AISI 304 . In this study, turning tests were carried to determine the optimum machining parameters i.e best cutting speed and feed rate were according to flank wear,Buil up edge (BUE), chip form, surface roughness of the machined samples and machine tool power consumption.

Tables 1. chemical composition of AISI 304

C	0.05487
Si	0.64
Mn	1.66
Cr	18.2
Ni	9.11
Mo	0.092
Cu	0.14
Ti	0.006
V	0.046
W	0.048
Co	0.040
Nb	0.013
Pb	0.015
Fe	69.7

Table 2. Typical Physical and Thermal Properties of AISI304

PARAMETER	UNIT	VALUE
DENSITY	Kg/m^3	8000
ELASTIC MODULUS	GPa	193
POISSIONS RATIO	-	0.3
Coefficient of thermal expansion	$Mmm^{-1} C^{-1}$	17.8
Thermal Conductivity	W/mK	16.2
Specific heat capacity	J/kgK	500

LITERATURE REVIEW

Many attempts have been made to improve the machinability of austenitic stainless steels (O'Sullivan and Cotterell, 2002) [1]. Problems such as poor surface finish and high tool wear are common in machining of austenitic stainless steel (Kosa, 1989) [2]. Ihsan et al. (2004) carried out turning tests on AISI 304 austenitic stainless steel to determine the optimum machining parameters.

Zafer and Sezgin (2004) [3] determined the best suitable cutting condition for machining considering the acoustic emission during the cutting process of AISI 304 stainless steels. Korkut et al. (2004) [4] investigated the influence of cutting speed on surface roughness, chip characteristics and tool wear during turning of AISI 304 steel. Tekiner and Yeşilyurt (2004) [3] utilized unique process sound technique

to determine optimal condition in order to achieve favourable chip form and minimum flank wear, built-up edge and Ra. Noordin et al. (2001) determined that the surface roughness is dependent on the feed rate therefore by lower feed rate produced better surface finish. It was also determined that the obtained Ra value increased with increase in cutting speed. Xavior and Adithan (2009) [5] studied the influence of different cutting fluids on the tool wear and Ra value during turning. It was observed that coconut oil performed best. Asibu (1985) [6] found that flank wear changes the mechanics of the cutting process, induce chatter and changes in the final dimension of the product. Flank wear is used as the criteria in determining the tool life (Byrd and Ferguson, 1978) [7]. Flank wear may be due to adhesive wear or abrasive wear caused by the hard second phases in the work material (Ramalingam and Wright, 1981) [8]. The presence of the large unstable BUE causes poor surface finish. Wear at the tool cutting edge directly influences the machined surface roughness since the edge is in direct contact with the newly machined surface (Ezugwu and Kim, 1995) [8].

CUTTING FLUID

Lubricants are commonly used in all type of industry for cooling and to lubricates the tool and work-piece interface in order to improve machinability. Cutting fluids have been used in the machining process with the purpose to improve tool life, improved surface finish, improved dimensional accuracy, reduced cutting force and reduced vibrations (De chiffre, 1988) [9] of the work piece–tool–chip system. Coolants for machining was first used by Taylor in 1907, who gained a 40% increase in cutting speed when machining steel with high speed tools using water as coolant (Taylor, 1907) [10]. Cutting fluids provide lubrication between the work piece and tool and also remove heat generated during the cutting process (De Chiffre et al., 1988) [9].

Vegetable-based cutting fluids:

Cutting fluids based on mineral oils are traditionally used in production shops due to their chemical stability and frequent reuse. However, nowadays use of new types of cutting fluids are based on vegetable oils and esters in machining is defined by their higher biodegradability and lower environmental impact. Emulsions of vegetable oils were prepared using ionic and non-ionic surfactants for use as metal working fluids. The use of vegetable oil in metal working applications may reduce problems faced by workers, such as skin cancer and inhalation of toxic mist in the work environments. Jacob et al. (2004) created a vegetable-based emulsion that can be used in the metal working industry to replace partially or completely the commonly used petroleum based emulsions. Vegetable oils have good lubricating ability and have been used for the formulation of metal cutting emulsions (Herdan, 1999) [11]. Recent research was also done on the vegetable oil-based emulsion to produce stable emulsions to be used as metalworking fluid and other application(Alander and Warnheim, 1989) [12]. Rape seed was used by Ioan et al. (2002), in his experiment, and shows that lubricating capacity of rape seed oil compared to that obtained for a usual mineral oil. Cutting fluids based on vegetable oils showed better performance than mineral oils. All type of vegetable-based oils have given the better results than the commercially available mineral oil by improving of tool life and reduction in thrust force.

Coconut oil

Coconut oil belongs lauric oils which is a unique group of vegetable oils. Chemical composition of coconut oil is lauric acid (51%), myristic acid (18.5%), caprilic acid (9.5%), palmitic acid (7.5%), olcic acid (5%), capric acid (4.5%), stearic acid (3%) and linoleic acid (1%). The saturated character of the oil imparts a strong resistance to oxidative stability. It can been said that coconut oil shows better oxidative stability in comparison to other vegetable oils with high percentage of unsaturated fatty acid content. Coconut oil shows comparatively lesser weight gain under oxidative environment among the vegetable oils considered.

METHODOLOGY

During the experiment, a round bar of AISI 304 stainless steel of diameter 60 mm and length 200 mm was machined. AISI 304 was used as the work material and Sandvik's carbide CNMG 12 04 08 insert was used as the cutting tool. The inserts were clamped mechanically on a rigid tool holder. After the machining process, the insert was removed and its flank wear was measured using Mitutoyo's Tool Maker's microscope. To grasp the knowledge of the tool wear, the microscopic picture of inserts were observed using Carl Zeiss optical microscope, with the magnification range of 500×. The average surface roughness on the work piece was measured using Mitutoyo's Surf test surface finish measuring instrument. The experimentation for this work was based on Taguchi's design of experiments (DOE) and orthogonal array. A number of experiments have been carried out with the increase in the number of the process parameters. Taguchi method is used to solve the problem, which utilizes the special design of orthogonal arrays to study the entire parameter space with a small number of experiments. Three cutting parameters namely, cutting speed, depth of cut and feed rate were considered for experimentation, in this work. Apart from this type of cutting fluid is also considered as one of the critical input parameters while designing the experiments. Accordingly there are four input parameters and for each parameters three levels were assumed. The response obtained from the trials conducted as per L27 array experimentation was recorded and further analysed. Cutting fluid is the parameters which does not have any quantitative levels but each oil is being considered as one level for experimentation

Chip formation

120 m/min: Chip curl radii of about 1–1.25 mm (small radius) and a chip thickness of about 0.6 mm, most of chip have this parameter. The rest of the chipss radii have parameter of around 3–3.5 mm and chip thickness were to be 0.4 mm. The chips colour is close to yellow.

150 m/min: With this cutting speed, chip curl shows very less variation in radii, as that was observed at 120 m/min cutting

speed. Chip curl radii were around of 2.5–3 mm and chip thickness to be around 0.4–0.5 mm, in this case. The chips colour were brighter than that produced at 120 m/min cutting speed.

180 m/min: Consider, the chip curl radii to be homogeneous. Chip curl radii and chip thickness were of around 6–7 mm and 0.4 mm, respectively, for this speed. Chip colour matches with the workpiece materials colour.

Tool-chip contact length shows the shiny areas on the tool rake face, which is decreased with increase in the cutting speed. Chip curl radius and chip thickness very much relate the cutting speed at which the machining is performed. Low cutting speed have chip curl of small radius and large chip thickness. With the increase in cutting speed, chip curl radius increase and chip thickness decrease stepwise. The effect of heat on the thicker chips with small curl radii is as explained. Firstly, the thick chips with small curl radii have less surface area than those with small thickness and large curl radius. This shows low efficient of heat dissipation, when the chips are in contact with the tool. Secondly, tool-chip with maximum contact length on the tool rake face was observed at 120 m/min cutting speed. Finally, with cutting speed of 120 m/min thick chips with small curl radii formed , shows that chips remained in contact with the tool for longest duration at the lowest cutting speed than that at higher cutting speeds. Thus, this leads to more friction between the chip and the tool. However, with increasing the cutting speed to 150 m/min, chips curl radii increased and thickness decreased. Thus, the chips becomes more brighter in colour than that obtained at 120 m/min. Further increasing the cutting speed to 180 m/min, the chips became similar in colour to the work piece materials. Thus it can be said that least influence of heat is observed at this cutting speed for the chips having the large curl radii and small chip thickness, compared to the others type of chips.

TOOL WEAR AND SURFACE ROUGHNESS

Influence of heat over the cutting tool is responsible for the low performance of the tool at the lower cutting speed. The reason for this is that generation of large amount of heat during metal cutting and in the machining of AISI 304 stainless steel, it doesn't dissipate heat rapidly due to the low thermal conductivity of this material. The heat generation occurs in three areas: the shear zone, rake face and at the clearance side of the cutting edge. As is explained above, it was deduced from the chips colour, which is the most obvious indication of temperature of steel chips, that the chips formed at lower cutting speed (120 m/min) were affected mostly from the heat. Thus, have the highest temperature in comparison to the others. Also, contact with the tool on the rake face is for the longest time, as the maximim tool-chip contact length was observed at 120 m/min cutting speed on the tool rake face. Impact of low cutting speeds, is contact time increased on the rake face as the chips movement are slower in comparison to the higher cutting speeds. Thus it can be concluded that with longer contact time of rake face and the high chip temperature, rise the thermal softening of the tool by the low conductivity of the heat from the chips to the tool. There by, reduces wear resistance of the tool. Surface roughness values (Ra) were also found to decrease with increasing cutting speed. It is known that the type of chip produced during the machining operation has a significant effect on the surface finish. As chip thickness can be related to shear plane angle, cutting force requirements also changes depending on the chip thickness and also does the vibration. In this study, chip thickness and chip curl radius varied with the cutting speed. Also, relatively inhomogeneous chip thickness and chip curl radius distribution was observed at the lower cutting speeds. The improvement in the surface state with increasing the cutting speed can also be explained by the formation of built-up-edge (BUE) at the lower cutting speeds as the presence of BUE leads to a poorer surface finish. This is the case especially when machining very ductile materials.

CONCLUSIONS

With the machining of AISI 304 austenitic stainless steel, optimum cutting speed leading to the lowest tool flank wear has been sought and the following conclusions can be drawn from this study:

• Flank wear decreases with increase in the cutting speed. The poor performance of the tool is by the thermal softening of the tool.

• Surface roughness values also decrease with the increase in cutting speed. This can be characterize by the presence of BUE at the lower cutting speeds. Non-uniform distribution of chip thickness at the lower cutting speeds, shows the variation in the cutting forces. Poor surface finish is due to the force fluctuations.

Experiments involving cemented carbide tool inserts and AISI 304 stainless steel work material under varying machining parameters and with three different cutting fluids were performed. Cutting fluids were considered as important parameters in the machining process along with cutting speed, feed rate and depth of cut. An analysis of variance (ANOVA) was made and it was found that feed rate has greater influence on surface roughness (61.54% contribution) and cutting speed has greater influence on tool wear (46.49% contribution). Further it was found that cutting fluid has some considerable influence on both surface roughness and tool wear. Effectiveness of the cutting fluids in reducing the tool wear and improving the surface finish was found by comparing the relative performance. In general, coconut oilwas found to be a better cutting fluid than the conventional mineral oils in reducing the toolwear and surface roughness. Surface plots were drawn between the various process parameters so as to understand more about their individual relationship and relative contribution to surface roughness and flank wear.

REFERENCES

[1] O'Sullivan, D., & Cotterell, M. (2002). Machinability of austenitic stainless steel SS303. *Journal of Materials Processing Technology*, *124*(1), 153-159.

[2] Kosa, T., & Ney, R. P. (1989). Machining of stainless steels. *ASM Handbook.*,*16*, 681-707.

[3] Tekıner, Z., & Yeşılyurt, S. (2004). Investigation of the cutting parameters depending on process sound during turning of AISI 304 austenitic stainless steel. *Materials & Design*, *25*(6), 507-513.
[4] Korkut, I., Kasap, M., Ciftci, I., & Seker, U. (2004). Determination of optimum cutting parameters during machining of AISI 304 austenitic stainless steel.*Materials & Design*, *25*(4), 303-305.
[5] Xavior, M. A., & Adithan, M. (2009). Determining the influence of cutting fluids on tool wear and surface roughness during turning of AISI 304 austenitic stainless steel. *Journal of materials processing technology*, *209*(2), 900-909.
[6]Kannatey-Asibu, E. (1985). A transport-diffusion equation in metal cutting and its application to analysis of the rate of flank wear. *Journal of engineering for industry*, *107*(1), 81-89.
[7] Byrd, J. D., & Ferguson, B. L. (1978). Study of the Influence of Hard Inclusions on Carbide Tool Wear Utilizing a Powder Metal Technique. In *1978 SME Manufacturing Engineering Transactions and 6 th North American Metalworking Research Conference Proceedings. SME, Dearborn, Mich. 1978, 310-316*.
[8] Ramalingam, S., & Wright, P. K. (1981). Abrasive wear in machining: experiments with materials of controlled microstructure. *Journal of Engineering Materials and Technology*, *103*(2), 151-156.
[9] De Chiffre, L. (1988). Function of cutting fluids in machining. *Lubr. Eng*.
[10] Taylor, F. W. (1907). On the art of cutting metals.
[11] Herdan, J. M. (1999). Rolling fluids based on vegetable oils. *J Syn Lubr*, *16*, 201-210.
[12] Alander, J., & Warnheim, T. (1989). Model microemulsions containing vegetable oils part 1: nonionic surfactant systems. Journal of the American Oil Chemists Society, 66(11), 1656-1660.

Accepted Manuscript

Regular paper

Enhancement of Ancient Manuscript Images by Log based Binarization Technique

Jayanthi Natarajan, Sreedevi Indu

PII: S1434-8411(17)30509-5
DOI: http://dx.doi.org/10.1016/j.aeue.2017.03.002
Reference: AEUE 51808

To appear in: *International Journal of Electronics and Communications*

Received Date: 8 March 2016
Revised Date: 1 March 2017
Accepted Date: 3 March 2017

Please cite this article as: J. Natarajan, S. Indu, Enhancement of Ancient Manuscript Images by Log based Binarization Technique, *International Journal of Electronics and Communications* (2017), doi: http://dx.doi.org/10.1016/j.aeue.2017.03.002

This is a PDF file of an unedited manuscript that has been accepted for publication. As a service to our customers we are providing this early version of the manuscript. The manuscript will undergo copyediting, typesetting, and review of the resulting proof before it is published in its final form. Please note that during the production process errors may be discovered which could affect the content, and all legal disclaimers that apply to the journal pertain.

ACCEPTED MANUSCRIPT

Enhancement of Ancient Manuscript Images by Log based Binarization Technique

Jayanthi Natarajan[a], Dr. Sreedevi Indu[b]

[A]*M.Tech, B.Tech.Assistant Professor, Electronics and Communication Department, Delhi Technological University (Formerly Delhi College of Engineering) New Delhi-110042, India, njayanthi@dce.ac.in*

[B]*Ph.D, M.tech, B.Tech, Associate Professor, Electronics and Communication Department, Delhi Technological University (Formerly Delhi College of Engineering) New Delhi-110042, India*

Abstract

Enhancement of ancient manuscripts is a predominant field in the world of image processing. Binarization is the essential tool to recognize the text through OCR technologies for the preservation of the ancient manuscripts. This paper addresses the problem of enhancing and binarizing the deteriorated old manuscripts by a simple novel method called Log based binarization. The proposed method modifies the pixel intensity so as to better differentiate the black pixels and thus produce better binarization results, has been explored. Detailed comparison of existing thresholding algorithms with the new algorithm has been given. The inspiration for the new algorithm was drawn from the standard Niblack algorithm and Nick Algorithm.

Keywords: Binarization; Niblack Algorithm; Nick Algorithm; Handwritten documents

1. Introduction

Manuscripts of India contain an astounding wealth of ancient knowledge, pertaining to several spheres of intellectual activity, for instance, philosophy, religion, arts, systems of science and

ACCEPTED MANUSCRIPT

literature. But this wealth today faces a threat of survival. So digitization of such deteriorated manuscripts is essential for preservation. Also a large collection of ancient degraded documents is available in the world and to search for the required information is very time consuming. To aid this information search, digital libraries are created using Optical Character Recognition (OCR). Binarization is an imperative pre-processing step of the digital image processing which leads up to the OCR. The process that segments colored or gray scale images into background and text is known as Image Binarization (or thresholding).

Many different binarization algorithms can be found in existing literature but a method that provides ideal results for the entirety of the document dataset is yet to be found. Several such algorithms have been compared for different documents types in [1, 2, 3]. 11 locally adaptive binarization methods applicable on gray scale images have been evaluated in [19] and Nick's method [6] was found to better on images with low contrast, noise and variable background intensity than all the others. The proposed method further improves the Nick algorithm by shifting down the binarization threshold and hence improving binarization of images that have undergone various degradations (such as ink stains, bleed through, poor contrast and faint text) and connectivity between various alphabets of the text and differentiating between pixel intensities better.

The paper begins with a description of the thresholding methods based on different sliding-windows. Then a thorough explanation of our proposed algorithm is provided. Finally, a comparison of the results obtained by these algorithms using parameters like PSNR (peak signal-to-noise ratio), Precision, Recall and DRD (Distance reciprocal distortion metric).

ACCEPTED MANUSCRIPT

ACCEPTED MANUSCRIPT

2. Related work

Document binarization techniques, which are being proposed regularly over the past years, can be broadly classified as global thresholding techniques and local thresholding techniques [5]. Global thresholding method uses a fixed pixel value to binarize the entire image. Binarization algorithms like Otsu [10], Kitter [11] are based on global thresholding. These algorithms are effective on images when the text is well contrasted in comparison to the background as well as occupies a larger portion of the image. But the global thresholding methods fails to work on images with uneven illumination. The local thresholding methods like Niblack [4], Sauvola [12] uses a varied threshold value that depends on the properties of the neighboring pixels. But this does not provide optimal result especially in case of blurred image and also in cases where the bleed-through regions are much larger than the originating text. The Niblack algorithm fails to adapt to any large variation in illumination. Nick algorithm [6] is an improvement over the existing Niblack algorithm and the calculated threshold value tries to differentiate the lower valued pixels (black) better but introduces unwanted noise in the image.

3. Problem statement

We are addressing the enhancement of faded and damaged manuscript images. The main constraint of binarizing faded degraded documents is separation of text from back ground noise, especially for lower intensity pixels. Generally, the text and back ground is separated by comparing the intensity of each pixel with the mean grey value and fixing a threshold for separating the foreground (text) from the background. If the intensity of text is low (due to fading or bleed through), the threshold technique fails. Nick algorithm [6] calculates threshold using the following equation.

ACCEPTED MANUSCRIPT

ACCEPTED MANUSCRIPT

$$T_{Nick} = \mu + k\sqrt{\left[\frac{1}{N}(\sum {p_i}^2 - \mu^2)\right]} = \mu + k\sqrt{\sigma_Y} \quad (1)$$

where,

μ = mean grey value

k = Niblack Factor =-0.2

p_i = value of pixel intensity in the greyscale image

N = number of pixels

σ_Y = variance = $\frac{\sum(p_i)^2 - \mu^2}{N}$

This equation gives a substantial threshold value for differentiating lower intensity pixels from background noise. But it introduces unwanted noise in the image. Also there is a lack of connectivity in the text. The proposed method filters noise and enhances the text without introducing any unwanted noise.

3.1. Proposed Methodology

The main aim of binarization is to differentiate text of lower intensity from back ground and avoid unwanted noise. We used the same equation of Nick by replacing p_i with $p_i \log p_i$. The use of $p_i \log p_i$ as compared to p_i helps in the filtering of the noise. For lower values of p_i (fig 1), the function $p_i \log p_i$ exhorts a non-linear nature due to which a more appropriate value is assigned to the threshold which indeed helps to differentiate black pixels or text better as compared to p_i.

The proposed method calculates threshold value using following equation

$$T_{Prop} = \mu + k\sqrt{\frac{\sum(p_i \log p_i)^2 - \mu^2}{N}} = \mu + k\sqrt{\sigma} \quad (2)$$

where,

μ = mean grey value

k = Niblack Factor =-0.2

ACCEPTED MANUSCRIPT

p_i = value of pixel intensity in the greyscale image

N = number of pixels

σ = variance = $\frac{\sum(p_i \log p_i)^2 - \mu^2}{N}$

On similar lines,

$$(\sigma) - (\sigma_Y) = \left[\frac{\sum(p_i \log p_i)^2 - \mu^2}{N}\right] - \left[\frac{1}{N}(\sum {p_i}^2 - \mu^2)\right] = \frac{1}{N}\sum {p_i}^2[(\log p_i)^2 - 1] \quad (3)$$

As $(\log p_i)^2 - 1 > 0$ for all values of p_i, therefore $(\sigma) - (\sigma_Y) > 0$

Thus, $(\sigma) > (\sigma_Y)$ and with k being negative, $T_{Prop} < T_{Nick}$.

For lower values of p_i (fig 1), the function $p_i \log p_i$ exhorts a non-linear nature due to which a more appropriate value is assigned to the threshold which indeed helps to differentiate black pixels or text better as compared to p_i and subsequently also helps in removing noise without additional enhancement techniques.

Due to the simplicity of the algorithm, the time required for the computation is next to none as compared other matching learning or co-occurrence matrix based algorithms.

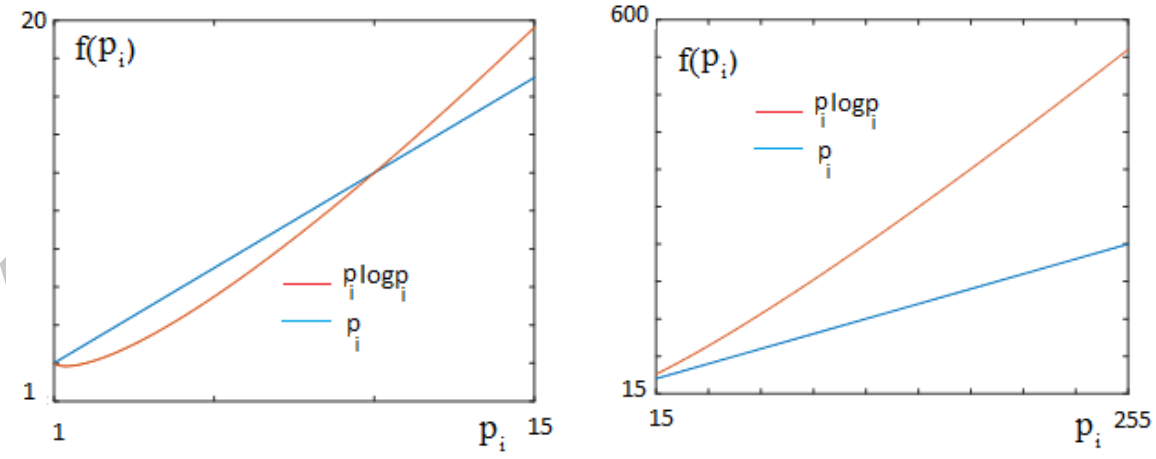

Fig1: (a)Plot of $p_i \log p_i$ and p_i for lower values of p_i;(b) Plot of $p_i \log p_i$ and p_i for higher values of p_i.

ACCEPTED MANUSCRIPT

4. Experimental Results and Discussion

This section illustrates the efficiency of the proposed algorithm.

a. The images of the ancient manuscripts are binarized using existing algorithms and proposed algorithm. The outputs are shown in fig 2 and 3. The binarized output of proposed algorithm is better.

b. The proficiency of the algorithm was tested against Nick and Niblack on images with various degradations and the result is shown in figure 4 through 9. In fig (4), we can see that the proposed method performs better than Nick and Niblack method when there is poor contrast between the foreground and the background due to the age of the paper and the ink. Similarly, other degradations such as blurred or faint text, ink stains , bleed-through have been more successfully removed by proposed method than Nick and Niblack Algorithm, as can be seen in Fig. 5, 6 and 9 respectively.

c. The proposed, Niblack and Nick algorithms were used to binarize the images of DIBCO 2009 dataset [21] and were passed through OCR Software [13] . The results are shown in Table 1 indicates that the proposed algorithm detects a higher percentage of words and characters than Niblack and Nick.

d. Further, table 2 and 3 provides comprehensive evaluation i.e. in quantitative terms, a number of metrics have been provided to contrast the results of the proposed algorithm. Performance parameters such as precision, recall, pseudo F-measure, peak signal to noise ratio and distance reciprocal distortion metric, were calculated using matlab for all the images provided in DIBCO – 2011 dataset using Niblack, Nick and the proposed Algorithm. The results were compared based on performance measures and is shown in table 2. The values of the parameters such as precision, p-Fmeasure , PSNR are higher

ACCEPTED MANUSCRIPT

whereas recall and DRD have lower for the proposed algorithm than Nick and Niblack, which indicates the high accuracy of the proposed algorithm.

e. Apart from Nick and Niblack algorithm the proposed algorithm is compared with recent proposed algorithms by C. Djeddi et al [14] and Sehad, A. et al [15] using same datasets and performance measures used by the authors. The results are tabulated in table 3. Here, again we see a similar trend of superior performance by the proposed algorithm.

f. Additionally, the proposed algorithm also filters out the noise that the Nick Algorithm fails to address. The running time of this algorithm is less due to its simplicity as compared to other algorithms.

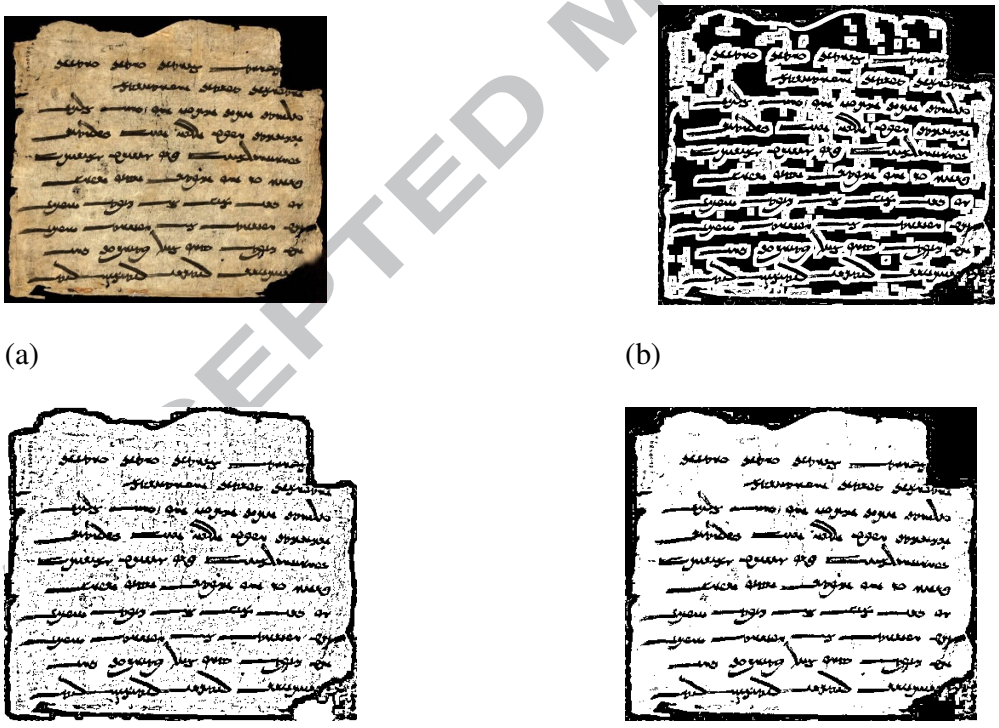

(a) (b)

(c) (d)

Fig.2.(a)Input;(b)Niblack;(c)Nick;(d)Proposed

ACCEPTED MANUSCRIPT

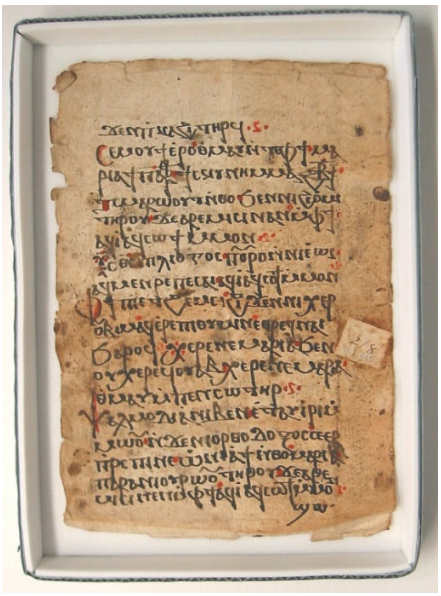

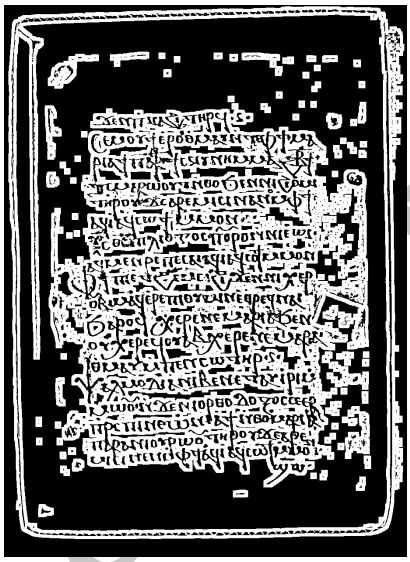

(a) (b)

ACCEPTED MANUSCRIPT

ACCEPTED MANUSCRIPT

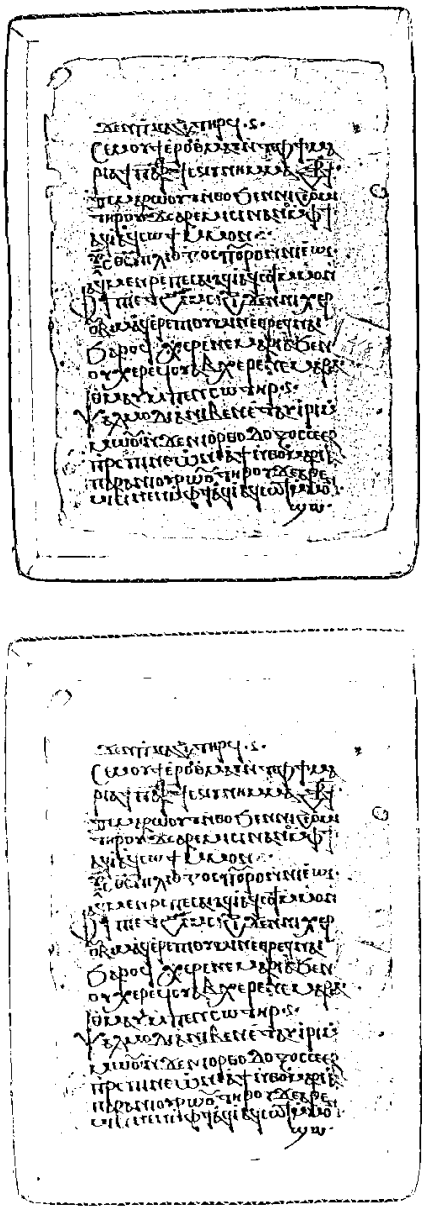

(c) (d)

Fig.3.(a)Input;(b)Niblack;(c)Nick;(d)Proposed

ACCEPTED MANUSCRIPT

ACCEPTED MANUSCRIPT

(a) (b)

(c) (d)

Fig.4.(a)Input;(b)Niblack;(c)Nick;(d)Proposed (Poor Contrast)

(a) (b)

(c) (d)

Fig.5.(a)Input;(b)Niblack;(c)Nick;(d)Proposed (Blurred text)

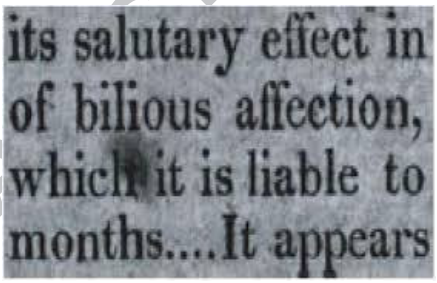

ACCEPTED MANUSCRIPT

(a) 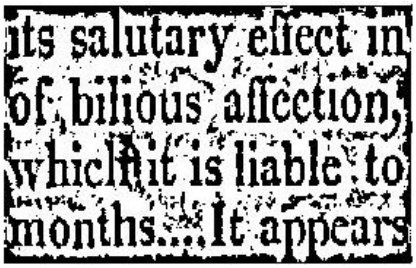

(b) 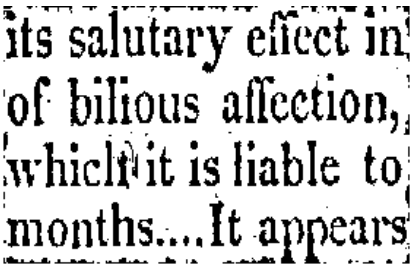

(c) 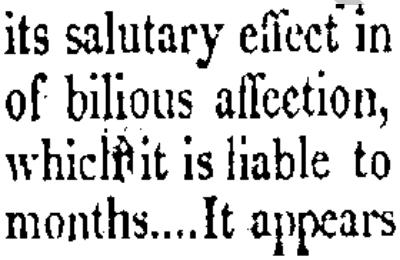

(d)

Fig.6.(a)Input;(b)Niblack;(c)Nick;(d)Proposed algorithm(Poor contrast and ink stain)

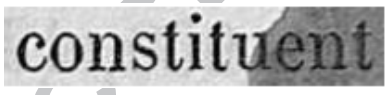

(a)

(b)

ACCEPTED MANUSCRIPT

(c) constituent

(d)

Fig.7.(a)Original image;(b)Niblack;(c)Nick;(d)Proposed algorithm(Variable contrast)

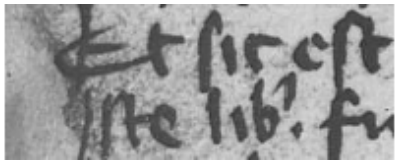

(a)

(b)

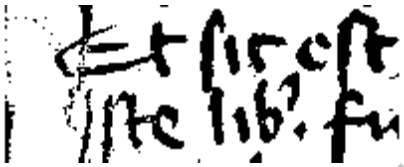

(c)

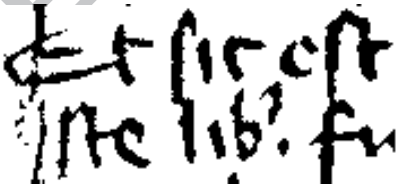

(d)

Fig.8.(a)Input;(b)Niblack;(c)Nick;(d)Proposed algorithm(Poor contrast and blurred text)

Explainations for the parameters that were calculated can be found as follows:

1. Precision: Precision [8] is the proportion of estimated ground truth image EG which is identified in the binarized output image B.

ACCEPTED MANUSCRIPT

$$Precision = \frac{\sum_{x=1,y=1}^{x=Ix,y=Iy} EG(x,y).B(x,y)}{\sum_{x=1,y=1}^{x=Ix,y=Iy} B(x,y)} \times 100\%$$

(4)

Where,

EG(x,y) = ground truth image estimated by the algorithm

B(x,y) = Binarized output image

False alarms are the text (foreground) areas of the binary image which is not identified during the estimation of precision. A higher value of precision indicates higher performance of algorithm under evaluation.

2. Recall: Recall [8] is defined as the proportion of the skeletonized ground truth image SG which is identified in the binarized image B. It is given by:

$$Precision = \frac{\sum_{x=1,y=1}^{x=Ix,y=Iy} SG(x,y).B(x,y)}{\sum_{x=1,y=1}^{x=Ix,y=Iy} B(x,y)} \times 100\% \quad (5)$$

Where SG(x,y) = Skeletonized ground truth image, defined in point 6 (Equation 9)

B(x,y) = Binarized image

A lower value of recall indicates that the algorithm under evaluation has higher merit.

3. Pseudo F-measure (pFmeasure): pfmeasure [18] introduced in [16] is given by -

The skeletonized ground truth image is defined as:

$$SG(x.y) = \begin{cases} 0, background \\ 1, text \end{cases} \quad (9)$$

$$\text{p- Recall} = \frac{\sum_{x=1,y=1}^{x=M,y=N} SG(x,y).B(x,y)}{\sum_{x=1,y=1}^{x=M,y=N} SG(x,y)} \quad (10)$$

$$\text{p-FM} = \frac{2 \text{ x p}-\text{Recall x Precision}}{\text{p}-\text{Recall}+\text{Precision}} \quad (11)$$

Higher the p-FM, better is the quality of binarization.

ACCEPTED MANUSCRIPT

4. Peak Signal to Noise Ratio (PSNR): PSNR [17] is a measure of how close 2 images are. The difference between foreground and background is taken to be equal to C and MSE is the mean square error.

$$PSNR = 10\log\left(\frac{C^2}{MSE}\right) \tag{14}$$

$$MSE = \frac{\sum_{x=1}^{x=M}\sum_{y=1}^{y=N}\left(I(x,y)-I'(x,y)\right)^2}{PQ} \tag{15}$$

Larger value of the PSNR indicates greater is the proximity amongst the images in question.

5. Distance Reciprocal Distortion Metric (DRD): DRD [19] is a measure of the visual distortion in binary images. For S flipped pixels, it is given as-

$$DRD = \frac{\sum_{k=1}^{S} DRD_k}{NUBN} \tag{18}$$

DRD represents the distortion of k^{th} flipped pixel. Lower the value of DRD, better is the performance of the algorithm under evaluation.

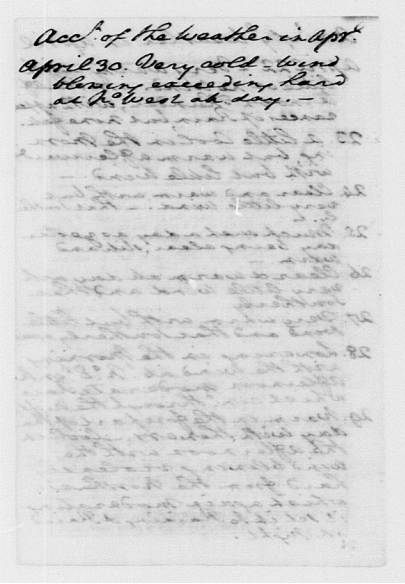

ACCEPTED MANUSCRIPT

(a)

(b)

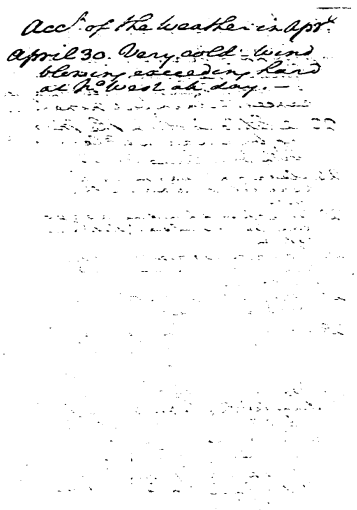

ACCEPTED MANUSCRIPT

ACCEPTED MANUSCRIPT

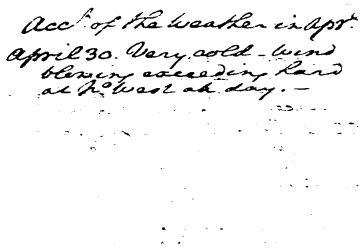

(c)

(d)

Fig.9.(a)Input;(b)Niblack;(c)Nick;(d)Proposed algorithm(Bleed through)

Table 1: OCR Accuracy

	Words Detected (Out of 118)	Characters Detected (Out of 614)	Accuracy (Words) In %	Accuracy (Characters) In %
Proposed Algorithm	97	556	82.20	90.55
Nick Algorithm	83	504	70.33	82.08
Niblack Algorithm	5	198	4.24	32.24

Table 2: Comparative analysis of algorithms using various parameters

		Precision	Recall	pFMeasure	PSNR	DRD
PR1	Niblack	0.38658	0.8149	54.83676	6.04277	55.26305

ACCEPTED MANUSCRIPT

	NICK	0.96736	0.66025	89.49337	12.15255	10.78357
	Proposed	0.98718	0.64002	97.19599	12.078	10.43416
PR2	Niblack	0.30856	0.87507	47.06247	6.12181	51.34555
	NICK	0.82595	0.70828	88.45426	12.87051	8.27035
	Proposed	0.94082	0.60411	91.92682	12.94082	7.27852
PR3	Niblack	0.25158	0.80513	39.83705	5.33059	89.04461
	NICK	0.98808	0.64188	92.53501	13.83052	9.62283
	Proposed	0.99909	0.60404	94.92316	13.48123	10.20915
PR4	Niblack	0.25158	0.80513	39.83705	5.33059	89.04461
	NICK	0.98808	0.64188	92.53501	13.83052	9.62283
	Proposed	0.99909	0.60404	94.92316	13.48123	10.20915
PR5	Niblack	0.37073	0.88641	53.74371	6.51118	36.82657
	NICK	0.98566	0.72811	95.83963	14.09139	4.11009
	Proposed	0.98546	0.68698	95.18965	13.50724	4.61668
PR6	Niblack	0.05277	0.86451	10.0158	4.12471	428.2234
	NICK	0.95356	0.56972	86.81076	19.46232	8.60181
	Proposed	0.99052	0.58742	91.75344	19.85735	7.38787
PR7	Niblack	0.10286	0.91556	18.62488	3.97812	262.3743
	NICK	0.24908	0.88797	39.67281	8.59234	89.41494
	Proposed	0.22392	0.91662	36.4671	7.91444	105.0205

Table 3 Comparative analysis of proposed algorithm with modern algorithms

	Proposed	C. Djeddi et al[14]	Sehad, A. et al [15]
F-measure (%)	72.59402	64.62	78.73
pFMeasure	92.73661	65.35	86.82
PSNR	13.5393	11.1	15.25
DRD	10.94175	46.09	11.3

As humans are progressively moving forward, new documents are being discovered. The space for safe storage of such documents is limited. Their vastness also is a hurdle for epigraphists worldwide. Fortunately, humans are at the same time developing tools, such as the OCR, which

ACCEPTED MANUSCRIPT

are facilitating us to proceed with the task at hand. To make the character recognition easier and more accurate, we subsequently developed a tool used extensively: thresholding.

Global thresholding, which comprises of methods such as Otsu's, is not at all optimal. The most famous global thresholding method, Otsu's, is not successful in segmenting characters after scanning images. For proper results, iterative application of Otsu's is required, which increases the time complexity unnecessarily. These drawbacks led to the shift towards local thresholding methods, wherein the entire image is divided into a large number of small sized windows, on which thresholding is applied individually. To improve the process, various mathematical tools are applied to optimize the threshold calculation, such as those presented in Niblack and Nick algorithm. The proposed algorithm strives to move towards the calculation of a threshold value that is able to enable higher accuracy in character recognition than the existing algorithms.

The above mentioned arguments clearly signify that the use of logarithmic operator produces better binarized output images as compared to the standard contemporary algorithms.

5. Conclusion and Future scope

In this paper, a novel method for binarization of manuscripts has been proposed. The novel logarithm based algorithm derives itself from the Niblack Algorithm tries to overcome the shortcomings of existing algorithms, including both global algorithm (Otsu, Sauvola, etc.) and local thresholding algorithms (Niblack, Nick). After proposing the logic behind the algorithm, it was tested on a varied dataset which included Ancient manuscript images and the DIBCO data set, to check its proficiency. The proposed algorithm also showed promising results when various parameters (included PSNR, Precision, Recall etc.) were calculated for all algorithms under scrutiny. However, the proposed algorithm still needs improvement in case of images that

ACCEPTED MANUSCRIPT

contain very poor contrast between foreground and background. Moreover, the proposed algorithm is not as effective on images consisting of handwritten text with non-uniform strokes and breaks in between. Hence, we are working on preprocessing technique that would close the breaks without introducing additional noise as well as better differentiate the foreground and background pixel values in case of poor contrasted images.

References

[1] Gatos, B., Ntirogianni, K. and Pratikakis, I., "ICDAR 2009 document image binarization contest (DIBCO)", Proc. Int. Conf. Document Anal. Recognit. , pp.1375 -1382 , 2009

[2] Gatos, B., Ntirogianni, K. and Pratikakis, I., "H–DIBCO 2010—Handwritten document image binarization competition", Proc. Int. Conf. Frontiers Handwriting Recognit. , pp.727 - 732 , 2010

[3] Gatos, B., Ntirogianni, K. and Pratikakis, I., "ICDAR 2011 Document Image Binarization Contest (DIBCO 2011)", Proc. 11th Int. Conf. Document Analysis and Recognition,2011.

[4] Niblack, W., An Introduction to Digital Image Processing. Prentice Hall, Englewood Cliffs, (1986).

[5] Ntirogiannis, K. "Document Image Binarization."

[6] Khurshid, K., Siddiqi, I., Faure, C., Vincent, N., "Comparison of Niblack inspired Binarization methods for ancient documents.", Document Recognition and Retrieval XVI, 72470U (January 19, 2009).

[7] DIBCO-2011 Dataset, http://utopia.duth.gr/~ipratika/DIBCO2011/benchmark/dataset/DIBCO11-machine_printed.rar

ACCEPTED MANUSCRIPT

ACCEPTED MANUSCRIPT

[8] Ntirogiannis, K., Gatos, B. and Pratikakis, I., "An Objective Evaluation Methodology for Document Image Binarization Techniques", 2008, International Workshop on Document Analysis Systems (DAS'08), Nara, Japan, Sep. 2008, pp. 217-224.

[9] Matlab script for calculation of parameters http://www.mathworks.com/matlabcentral/fileexchange/27652-objective-evaluation-of-binarization-methods-for-document-image

[10] Otsu, N., "A threshold selection method from gray level histograms," IEEE Trans. Systems, Man and Cybernetics, vol. 9, pp. 62–66, 1979

[11] Kittler, J. and Illingworth, J., "Minimum error thresholding," Pattern Recognition, vol. 19, pp. 41–47, 1986

[12] Sauvola, J. and Pietikinen, M., "Adaptive document image binarization," Pattern Recognition, vol. 33, pp. 225–236, 2000

[13] Onlineocr.net,. "Free Online OCR - Convert Scanned PDF And Images To Word, JPEG To Word". N.p., 2016. Web. 3 Mar. 2016.

[14] Djeddi, C., Siddiqi, I., Souici-Meslati, L. and Ennaji, A., "Codebook for Writer Characterization: A Vocabulary of Patterns or a Mere Representation Space?", in Proceedings of ICDAR 2013.

[15] Sehad, A., Chibani, Y., Cheriet, M. and Yaddaden, Y., "Ancient degraded document image binarization based on texture features", Image and Signal Processing and Analysis (ISPA), 2013 8th International Symposium

[16] Gatos, B., Ntirogianni, K. and Pratikakis, I., "Performance Evaluation Methodology for Historical Document Image Binarization", IEEE Transactions on Image Processing, vol. 22, no.2, pp. 595-609, Feb. 2013

ACCEPTED MANUSCRIPT

ACCEPTED MANUSCRIPT

[17] Gatos, B., Pratikakis, I., Perantonis, S.J., "Adaptive degraded document image binarization", Pattern Recognition 39 : 317 – 327, (2006).

[18] Leedham, G., Yan, C., Takru, K., Tan, J.H.N., Mian, L., "Comparison of Some Thresholding Algorithms for Text/Background Segmentation in Difficult Document Images" *7th International Conference on Document Analysis and Recognition ICDAR*, (2003).

[19] Trier, Ø.D., Taxt, T., "Evaluation of Binarization Methods for Document Images", IEEE *Transactions on Pattern Analysis and Machine Intelligence*, 17: 312 – 315, (1995).

[20] dervish, abu. "Ancient Manuscript Review 120: Antique Hijazi Quran On Vellum / Parchment (8Th Century CE)". *Abudervish.blogspot.in*. N.p., 2016. Web. 14 Dec. 2016.

[21] DIBCO-2009 Dataset, http://www.iit.demokritos.gr/~bgat/DIBCO2009/benchmark/

ACCEPTED MANUSCRIPT

2017 International Conference on Machine Vision and Information Technology

Fish Species Classification using Graph Embedding Discriminant Analysis

Snigdhaa Hasija
Department of Electronics and Communication
Delhi Technological University
Delhi, India
snigdhaa.hasija.in@ieee.org

Manas Jyoti Buragohain
Department of Electronics and Communication
Delhi Technological University
Delhi, India
manasjyoti@dtu.ac.in

Dr. S. Indu
Department of Electronics and Communication
Delhi Technological University
Delhi, India
s.indu@dce.ac.in

***Abstract*— Fish Species classification is of great utility to marine biologists for the understanding of underwater ecology and fish behavior as well as to keep a log of endangered species, which assists in fisheries management. Traditional methods being either tedious or too computationally intensive lead to the requirement of an automated method of analysis and counting. Generally, the classification of underwater images is challenging due to difficulties in camera calibrations, which lead to distortion, background noise, occlusion, and image quality to name a few. This paper proposes a novel method based on an improved image-set matching approach, which makes use of Graph-Embedding Discriminant Analysis. In contrast to the state-of-the-art methods, which operate on single input images, our method makes, use of explicit image set matching which renders it robust computationally. In comparison with the previous classification methods, this method results in considerable discrimination accuracy improvements.**

Keywords- Fish Species Classification, Image Set Matching, Grassmannian Manifolds, Discriminant Analysis, Singular Value Decomposition

I. INTRODUCTION

Counting and classifying fish can be useful for several settings one of which is the monitoring of species and volume of fish going upriver to spawn during spring and summer. This monitoring can provide a useful overview of the population of each species in the area. Apart from this, classifying of fishes is also useful for understanding the behavior and interspecies interaction of fishes in a common ecological environment.

Automating this process, at least partially, will significantly save the time and labor required to analyze the dataset. Although, there have been may advances in classifying fish taken out of water [1-4] or in controlled conditions, such as in tanks with adequate lighting [5], there has been no significant breakthrough in classification of fishes in datasets created from underwater videos. Some of the challenges faced during accurate fish recognition include noise, distortion, overlap, segmentation error and occlusion [6]. Also, the complex environment confounds simpler approaches like luminance, thresholding and background subtraction. Issues include shifting colors, uneven and variable illumination, sediment in the water and undulating underwater plants.

Fish species recognition is a multi-class classification problem and is an interesting research area in the field of computer vision and machine learning. The state-of-the-art includes algorithms implemented on individual input images which perform classification mainly using shape and texture features extraction and matching.[7,8] All the existing work either deals with a small dataset distinguishing between less number of species or has a low accuracy. Our proposed method uses the approach of image-set matching [12] which makes the method more robust even while working with a large dataset. We make use of the fish dataset from the Fish4Knowledge project [24] for testing our algorithm. We perform the classification using an improved version of Grassmannian Discriminant analysis, namely the graph embedding discriminant analysis which results in better accuracy as compared to the existing methods for fish classification as explained in Section 3.

The remaining paper is organized as follows: Section 2 mentions the existing research done in this field; Section 3 delineates the proposed algorithm; Section 4 gives the experimental results; Section 5 mentions the Conclusion and Future Work and Section 6 gives the References.

II. RELATED WORKS

There are numerous approached proposed by researchers for the classification of fish species as delineated below:

Yun-Heh Chen-Burger et al. [7] attempt to classify fishes using texture features extracted from the gray level histogram, Gabor filtering and gray-level co-occurrence matrix and shape features extracted using the Curvature Scale Space Transform and the histogram of Fourier descriptors of boundaries. They tested their algorithm on a dataset of 360 images and achieved an accuracy of 92%.

Yutaka Nagashima et al. [8] used two identification features: speckle patterns and scale forms of fish and used morphological algorithms and filters for discrimination. They just showed the differentiation between three species- Pilchard Sardine (ma-iwashi), Japanese Horse Mackerel (ma-aji), and Common Mackerel (ma-saba) with an accuracy of 90%, 88%, and 90% respectively. Their method is dependent on the size and shape of the morphological filters used.

Bridget Benson et al. [9] used Haar classifiers with the Scythe Butterflyfish as their test species. Their method is

978-1-5090-4993-6/17 $31.00 © 2017 IEEE
DOI 10.1109/CMVIT.2017.23

heavily dependent on the background of the fish image and the angle from which the image is taken.

Andrew Rova et al. [10] attempt to classify fishes using the method of warping the images prior to classification using SVM on a dataset of 320 images achieving an accuracy of 90%.

Chomptip Pornpanomchai et al. [11] proposed and developed a fish recognition system based on shape and texture. They compared Artificial Neural Networks and Euclidean Distance Method (EDM) working on a training set of 600 images and a test set of 300 images. They achieved an accuracy of 99.00% and 81.67% with ANN and EDM respectively.

Rodrigues et al. [13] proposed a method based on SIFT feature extraction and Principal Component Analysis (PCA) but they have worked on a very small dataset of 162 images encompassing six different species achieving an accuracy of 92%.

S. Sclaroff et al. [14] performed object deformable shape detection and object detection was done through model-based region grouping. Computational complexity is the major drawback of this method.

C. Spampinato et al. [15] worked on 20 underwater videos to detect, track and count fishes with an accuracy of 85%. They performed detection using Moving Average Detection Algorithm and Adaptive Gaussian Mixture Model.

Andres Hernandez-Serna et al. [16] used Artificial Neural Networks for the automatic identification of species. They worked on a dataset of 697 images achieving an accuracy of 91.65%.

Arjun Kumar Joginpelly et al. [17] propose an automatic technique using Gabor filters to extract important features from two species, Epinephelus morio and Ocyurus chrysurus. The proposed algorithm is tested on 200 frames, each containing many fish and non-fish regions. The accuracy is 70.6% for Epinephelus morio and 80.3% for Ocyurus chrysurus.

Deokjin Joo et al. [18] extracted color and stripe patterns of wild

cichlids and used Support Vector Machine and Random Forests for classification achieving an accuracy of 72% on a dataset of 594 wild cichlids. They have a low accuracy and they just target Cichlid fishes.

Yi-Haur Shiau et al. [19] proposed a method of maximum probability of partial ranking based on sparse representation based classification (SRC) for the recognition and verification of fishes. They worked on a dataset of 1000 images and achieved the highest accuracy of 81.8% for a particular feature space dimensionality.

S.O. Ogunlana et al. [20] classified using Support Vector Machine technique based on the shape features of the fish. They worked on a training set of 76 fish and testing set of 74 fish achieving an accuracy of 78.59%.

S. Cadieux et al. [21], utilize an infrared silhouette sensor to acquire contours of fish in constrained flow. Results of three classifiers which use Fourier boundary descriptors and invariant moments for fish silhouette recognition were clubbed together and used for classification. However, when the inputs are noisy, these features give a poor performance. The system has reported classification accuracy around 78%.

D. J. Lee et al. [22], removed edge noise and redundant data points through the development of a shape analysis algorithm. Critical landmark points were located using an algorithm of curvature function analysis. These landmark points formed the basis of the classification of fish species by the extraction of the fish contour segments of interest. A large group of nine fish species was used to test this method. However, the dataset with which the authors carried out the experiment was a very small one, consisting only of 22 sample images.

M. Nery et al. [23], proposed a methodology based on feature selection. This method develops a feature vector using a set of available descriptors by analyzing the characteristic contribution of each individual descriptor to the overall performance for classification. Discrimination and independence are the two statistical methods used to help in the process of feature selection. The authors report a classification accuracy of about 85%. The authors focus on the study of robust feature determination methods.

III. PROPOSED METHODOLOGY

Here, we propose a methodology for the discrimination of fish species. The dataset used for our work has been taken from [24]. The process involves the representation of different species of fish as different image sets and utilizes the approach of image-set matching. [25, 26, 27, 28]. Each image set is modeled as a subspace. There are two advantages of using subspaces. Firstly, for large datasets, the comparison between subspaces is less computationally expensive than that between two sets directly and secondly, the subspaces can interpolate the missing data if any. These subspaces are then represented as points on Grassmannian manifolds as shown in Figure. 1 [27, 29, 30, 31]. Just like a euclidean space, a manifold is considered to be a smooth geometric figure. Grassmannian manifolds are a particular type of Riemannian manifolds. [29].

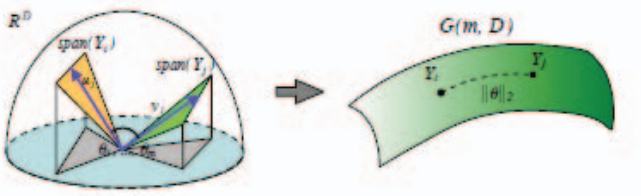

Figure 1. Mapping of subspaces from Euclidean space, RD to the Grassmanian Manifold G (m,D).

Therefore, the image-set matching problem is reduced to a point-to-point classification problem. Figure. 2 illustrates our proposed methodology conceptually.

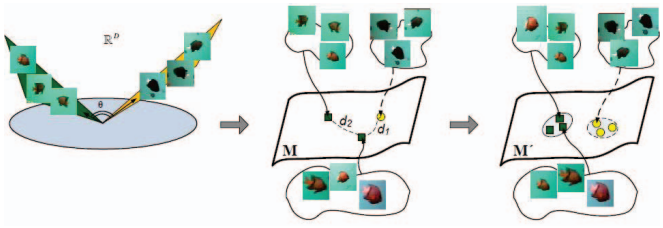

Figure 2. A conceptual explanation of the proposed approach.

We aim to increase the discrimination accuracy with the aid of within-class and between-class separability graphs, which respectively characterize the intra-class compactness and the inter-class separability. These graphs, apart from increasing the accuracy of classification also help to preserve the local information and the geometrical structure of the manifolds. First, we represent the different subspaces as points on the Grassmannian manifold ***M***. Then, these subspace points are mapped to another Grassmannian manifold ***M'***. [32]

To explain this further, a graph (***V, W***), here, denotes a collection of vertices, ***V***, and a collection of edges that connect pairs of vertices. In this context, the similarity between a pair of vertices is described by the symmetric matrix, ***W***. Moreover, the Laplacian matrix ***L*** of a graph is defined as ***L=D-W***, where ***D*** is the diagonal matrix and its diagonal elements are given as:

$$D(i,i)=\Sigma_{j\neq i}W(i,j)$$

When we have the N-labeled points $X=\{(X_i,l_i)\}_{i=1}^{N}$ from the underlying Grassmann manifold M, where $X_i \in R^{D\times m}$ and $l_i \in \{1,2,\ldots,C\}$, C denoting the number of classes, we can model the geometrical structure of M by constructing a within-class similarity graph W_w and a between-class similarity graph W_b. The easiest forms of W_w and W_b are defined below. They are based on the nearest neighbor graphs.

$$W_w(i,j)=\begin{cases}1 & if\ X_i\in N_w(X_j)\ or\ X_j\in N_w(X_i)\\ 0 & otherwise\end{cases} \quad -(1)$$

$$W_b(i,j)=\begin{cases}1 & if\ X_i\in N_b(X_j)\ or\ X_j\in N_w(X_i)\\ 0 & otherwise\end{cases} \quad -(2)$$

Eqn. (1) shows $N_w(X_i)$ as the set of v Neighbors $\{X_i^1, X_i^2, \ldots, X_i^v\}$, which have the same label as l_i. Similarly Eqn. (2) gives $N_b(X_i)$ containing v neighbors which have different labels. We aim to maximize discriminatory power while preserving the geometry simultaneously by mapping the points on ***M*** to a new manifold ***M'***, i.e. The optimization of the following two objective functions describes the mapping:

$$f_1=\min\tfrac{1}{2}\Sigma_{i,j}(Y_i-Y_j)^2W_w(i,j) \quad -(3)$$

$$f_2=\max\tfrac{1}{2}\Sigma_{i,j}(Y_i-Y_j)^2W_w(i,j) \quad -(4)$$

Through these equations, the neighbors of the same class which is mapped far away in ***M'*** are punished by f_1 and the neighbors belonging to different classes which are mapped close together in ***M'*** are punished by f_2.

We work on the assumption of the implicit knowledge of the points on the manifold and the availability of the Grassmann kernel, $k_{ij}=\langle X_i,X_j\rangle$ as the only measure of similarity between these points.

If the solution is confined to be linear, i.e., $a_i=\sum_{j=1}^{N}a_{ij}X_j$, we will have:

$$\mathbf{Y}_i=\left(\langle a_1,X_i\rangle,\langle a_1,X_2\rangle,\ldots\langle a_r,X_i\rangle\right)^T$$

By defining $A_l=(a_{l1},a_{l2},\ldots a_{lN})^T$ and $K_i=(k_{i1},k_{i2},\ldots k_{iN})$ then $\langle a_l,X_i\rangle=A_l^TK_i$. Eqn.(3) can be simplified to:

$$f_1=A^TKD_wK^TA-A^TKW_wA$$

Here $A=[A_1|A_2|..|A_r]$ and. Considering that $L_b=D_b-W_b$, in a similar manner it can be shown that Eqn.(8) can be simplified to:

$$f_2=A^TKL_bK^TA$$

Given the $A^TKD_wK^TA=1$ the overall optimization problem is hence:

$$\max\{A^TK(L_b+\beta W_w)K^TA\}$$

Here β is a Lagrangian multiplier, a regularization parameter. The solution of the equation can be derived through the generalized eigenvalue problem, as follows:

$$K\{L_b+\beta W_w\}K^TA=\lambda KD_wK^TA$$

The r largest eigenvectors of the Raleigh quotient form the desired projection matrix A:

$$\frac{KD_wK^T}{K\{L_b+\beta W_w\}K^T}$$

The proposed algorithm makes implicit use of the points on the Grassmanian manifold (through the measurement of similarities via a kernel) to obtain a mapping, $A=[A_1|A_2|..|A_r]$ this mapping maximizes a quotient like Discriminant analysis. It also retains the overall geometrical structure. After the mapping A is acquired, the matching problem over Grassmannian manifolds is reduced to classification in vector spaces. More precisely, for any query image set X_q, a vector representation using the kernel function and the mapping A is acquired, ie., $V_q=ATK_q$, where,

$$\mathrm{K}_q=\left(\langle X_1,X_q\rangle,\langle X_1,X_q\rangle,\ldots\langle X_N,X_q\rangle\right)^T$$

Similarly, gallery points X_t are represented by r dimensional vectors $V_t=ATK_t$ and classification methods like the Nearest-Neighbor can be used to label X_q. The algorithm as table 1 stated.

Table.1 outlines the proposed graph embedding method on Grassmannian manifolds.

TABLE 1. ALGORITHM FOR THE GRAPH-EMBEDDING DISCRIMINANT ANALYSIS:

Input:

- Training set $\mathbb{X} = \{(\boldsymbol{X}_i, l_i)\}_{i=1}^{N}$ from the underlying Grassmannian manifold, where $\boldsymbol{X}_i \in \mathbb{R}^{D \times m}$ is a subspace (obtained for example via SVD over an image-set) and $l_i \in \{1, 2, \cdots, C\}$, with C denoting the number of classes
- A kernel function k_{ij}, for measuring the similarity between two points on the Grassmannian manifold

Processing:

1. Compute the Gram matrix $[\mathbb{K}]_{ij}$ for all $\boldsymbol{X}_i, \boldsymbol{X}_j$
2. Compute the within-class and between-class graph similarity matrices, $\boldsymbol{W}_w$, $\boldsymbol{W}_b$, respectively, the between Laplacian matrix $\boldsymbol{L}_b$ and the diagonal within matrix $\boldsymbol{D}_w$
3. To obtain $\mathbb{A}$, solve the maximisation problem in Eqn. (11) by eigen decomposition; $\mathbb{A}$ is equal to the r largest eigenvectors of the Rayleigh quotient $\frac{\mathbb{K}\boldsymbol{D}_w\mathbb{K}^T}{\mathbb{K}\{\boldsymbol{L}_b+\beta\boldsymbol{W}_w\}\mathbb{K}^T}$

Output:

- The projection matrix $\mathbb{A} = [\boldsymbol{A}_1|\boldsymbol{A}_2|\cdots|\boldsymbol{A}_r]$, where each $\boldsymbol{A}_i$ is an eigenvector found in step 3 above; the eigenvectors are sorted in a descending manner according to their corresponding eigenvalues

IV. EXPERIMENTAL RESULTS

The proposed algorithm was tested in MATLAB on the dataset [24] of 840 images shown in Figure 3 below.

Figure 3. Dataset used

Table 2 gives the details of the different species covered. Table 3 shows the results obtained using the accuracy as given by Eqn. (5) shown below:

$$Accuracy = \frac{TP}{TP + FP} \times 100\% \quad \text{- (5)}$$

Table 4 compares the results of the proposed method with the other existing classification algorithms for the discrimination between fish species.

TABLE 2. THE SPECIES USED IN THE DATASET

Species	Number of Images
Plectroglyphidodon dickii	100
Chromis chrysura	100
Myripristis kuntee	100
Acanthurus nigrofuscus	100
Amphiprion clarkii	60
Chaetodon trifascialis	50
Hemigymnus fasciatus	100
Neoniphon sammara	100
Scaridae	50
Zebrasoma scopas	70
Total	**840**

TABLE 3. RESULTS

Total No. of Input Images	**840**
Correct Classifications	**770**
Overall Accuracy	**91.66%**

TABLE 4. COMPARISON OF DIFFERENT CLASSIFICATION ALGORITHMS

Algorithm	Dataset	Accuracy
Yun-Heh Chen-Burger et al. [1]	360 images	92%
Yutaka Nagashima et al. [2]	Japanese Horse Mackerel (ma-aji) Pilchard Sardine (ma-iwashi) Common Mackerel (ma-saba)	88% 90% 90%
Andrew Rova et al. [4]	320 images	90%

Chomptip Pornpanomchai et al.[5]	900 images	99%
Rodrigues et al.[7]	162 images	92%
Andres Hernandez-Serna et al. [15]	697 images	91.65%
Arjun Kumar Joginpelly et al. [16]	Epinephelus morio Ocyurus chrysuru	70.6% 80.3%
Deokjin Joo et al. [17]	594 images	72%
Yi-Haur Shiau et al. [19]	1000 images	81.8%
S.O. Ogunlana et al. [20]	150 images	78.59%

V. CONCLUSION AND FUTURE WORK

The proposed method of the classification of fish species gives an accuracy of 91.66% which is very high compared with the other current methods used for this application. Hence the algorithm used can be certainly termed as robust. The method couldn't achieve 100% accuracy as some images couldn't be classified accurately due to the effect of background noise. We plan to improvise the algorithm further as a part of the future work to make it more immune to distortion caused by noisy images.

VI. REFERENCES

[1] White, D. J., Svellingen, C., Strachan, N. J. C., Automated measurement of species and length of fish by computer vision, Elsevier, 2006.

[2] F. Storbeck and B. Daan, Fish species recognition using computer vision and a neural network, Elsevier, 2000.

[3] Nery, M. S., Machado, A. M., Campos, M. F. M., Padua, F. L. C., Carceroni, R., Queiroz-Neto, J. P, Determining the appropriate feature set for fish classification tasks, Proceeding of the XVIII Brazilian Symposium on Computer Graphics and Image Processing, 2005.

[4] M. C.Chuang, J. N.Hwang, C. Rose, Aggregated Segmentation of Fish from Conveyor Belt Videos, IEEE International Conference on Acoustics, Speech and Signal Processing (ICASSP), 1807-1811, 2013.

[5] N. Castignolles, M. Catteon, M. Larinier, Identification and counting of live fish by image analysis, SPIE. Vol 2182, Image and Video Processing II, 1994.

[6] K.A. Mutasem, B.O. Khairuddin, N. Shahrulazman and A. Ibrahim (2010). "Fish Recognition Based on Robust Features Extraction from Size and Shape Measurements Using Neural Network". Journal Computer Science, Volume 6, Issue 10

[7] C. Spampinato, D. Giordano, R. D. Salvo, Y-H C-Burger, R.B. Fisher, G. Nadarajan, Automatic Fish Classification for Underwater Species Behaviour Understanding

[8] Y. Nagashima, Takakazu Ishimatsu, A Morphological Approach to Fish Discrimination, IAPR Workshop on Machine Vision APPLICATIONS, Nov. 17-19,1998

[9] B. Benson, J. Cho, D. Goshorn, R. Kastner, Field Programmable Gate Array (FPGA) Based Fish Detection Using Haar Claasifiers, American Academy of Underwater Sciences, March 1, 2009.

[10] A. Rova, G. Mori, L. M. Dill, One fish, two fish, butterfish, trumpeter: Recognising fish in underwater videos, IAPR Conference on Machine Vision Applications

[11] C. Pornpanomchai, B. Lurstwut, P. Leerasakultham, W. Kitiyanan, Shape and Texture based fish image recognition system, Kasetsart J. (Nat. Sci.) 47 : 624 - 634 (2013)

[12] Mehrtash T.Harandi, Conrad Sanderson, Sareh Shirazi, etc. Graph Embedding Discriminant Analysis on Grassmannian Manifolds for Improved Image Set Matching. CVPR2011.2705-2712,2011

[13] Rodrigues, M.T.A., Freitas, M.H.G., Pádua, F.L.C. et al. Pattern Anal Applic (2015) 18: 783. doi:10.1007/s10044-013-0362-6

[14] S. Sclaroff, L. Liu, Deformable Shape Detection and Description via Model-Based Region Grouping, IEEE TRANSACTIONS ON PATTERN ANALYSIS AND MACHINE INTELLIGENCE, VOL. 23, NO. 5, MAY 2001

[15] Spampinato, C, Chen-Burger, Y-H, Nadarajan, G & Fisher, R 2008, 'Detecting, Tracking and Counting Fish in Low Quality Unconstrained Underwater Videos'. inProc. 3rd Int. Conf. on Computer Vision Theory and Applications (VISAPP). vol. 2, pp. 514-519.

[16] Hernández-Serna, Andrés, and Luz Fernanda Jiménez-Segura. "Automatic Identification of Species with Neural Networks." Ed. Mark Costello. PeerJ 2 (2014): e563. PMC. Web. 30 Sept. 2016.

[17] AK Joginipelly, D Charalampidis, G Ioup, J Ioup, Ch Thompson, Species-Specific Fish Feature Extraction Using Gabor Filters

[18] Joo D1, Kwan YS, Song J, Pinho C, Hey J, Won YJ, Identification of Cichlid Fishes from Lake Malawi using Computer Vision, 2013 Oct 25;8(10):e77686. doi: 10.1371/journal.pone.0077686

[19] Y. H Shiau, F-P. Lin, C-C Chen, Using Sparse Representation for Fish Recognition and Verification in Real World Observation, ICONIP;12 Proceedings of the 19th Internation Conference on Neural Information Processing- Volume Part IV, pages 75-82

[20] S.O. gunlana, O. Olabode, S.A.A. Oluwadare, G.B. Iwasokun, Fish Classification Using Support Vector Machine, African Journal of Computing & ICT, Vol 8. No. 2 June, 2015

[21] S. Cadieux, F. Lalonde, and F. Michaud, "Intelligent System for Automated Fish Sorting and Counting," IEEE IROS, pp. 1279–1284, 2000.

[22] D. J. Lee, S. Redd, R. Schoenberger, X. Xiaoqian, and Z. Pengcheng, "An Automated Fish Species Classification and Migration Monitoring System," in Conf. of the IEEE Industrial Electronics Society, 2003, pp. 1080–1085.

[23] M. Nery, A. Machado, M. Campos, F. Padua, R. Carceroni, and J. Queiroz-Neto, "Determining the Appropriate Feature Set for Effective Fish Classification Tasks," in SIBGRAPI, 2005, pp. 173–180.

[24] B. J. Boom, P. X. Huang, J. He, R. B. Fisher, "Supporting Ground-Truth annotation of image datasets using clustering", 21st Int. Conf. on Pattern Recognition (ICPR), 2012.

[25] H. Cevikalp and B. Triggs. Face recognition based on image sets. In Proc. Computer Vision and Pattern Recognition (CVPR), pages 2567–2573, 2010

[26] T.-K. Kim, J. Kittler, and R. Cipolla. Discriminative learning and recognition of image set classes using canonical correlations. IEEE Trans. Pattern Analysis and Machine Intelligence, 29(6):1005–1018, 2007.

[27] R.Wang, S. Shan, X. Chen, andW. Gao. Manifold-manifold distance with application to face recognition based on image set. In Proc. Computer Vision and Pattern Recognition (CVPR), pages 1–8, 2008.

[28] T. Wang and P. Shi. Kernel grassmannian distances and discriminant analysis for face recognition from image sets. Pattern Recognition Letters, 30(13):1161–1165, 2009

[29] A. Edelman, T. A. Arias, and S. T. Smith. The geometry of algorithms with orthogonality constraints. SIAM J. Matrix Anal. Appl., 20(2):303–353, 1999.

[30] J. Hamm and D. D. Lee. Grassmann discriminant analysis: a unifying view on subspace-based learning. In Proc. Int. Conf. Machine Learning (ICML), pages 376–383, 2008.

[31] Y. M. Lui, J. Beveridge, B. Draper, and M. Kirby. Image-set matching using a geodesic distance and cohort normalization. In Proc. Automatic Face Gesture Recognition (AFGR),pages 1–6, 2008.

[32] S. Yan, D. Xu, B. Zhang, H.-J. Zhang, Q. Yang, and S. Lin. Graph embedding and extensions: A general framework for dimensionality reduction. IEEE Trans. Pattern Anal. Mach. Intell., 29(1):40–51, 2007.

This article has been accepted for publication in a future issue of this journal, but has not been fully edited. Content may change prior to final publication. Citation information: DOI 10.1109/TII.2017.2665477, IEEE Transactions on Industrial Informatics

Grid Interfaced Distributed Generation System with Modified Current Control Loop Using Adaptive Synchronization Technique

A. B. Shitole, H. M. Suryawanshi, *Senior Member, IEEE,* G. G. Talapur, Shelas Sathyan, M. S. Ballal, *Senior Member, IEEE,* V. B. Borghate, *Member, IEEE,* M. R. Ramteke, *Member, IEEE,* and M. A. Chaudhari, *Member, IEEE*

***Abstract*—This paper presents real time implementation of a grid interfaced distributed generation system with modified current control loop using three phase amplitude adaptive notch filter (AANF) based synchronization tool. A grid current feedback based modified dq-current control technique for interfacing inverter is developed in order to achieve constant loading on the grid, transient free operation and power factor improvement close to unity power factor (UPF) of the utility grid during sudden load variations. This technique does not require separate calculation of reference reactive component and harmonics component of currents hence reduces control circuit complexity. In addition, it requires only three voltage and three current sensors. Three phase AANF is developed and is used for online extraction of utility voltage phase angle to generate synchronized reference current signals for interfacing inverter. AANF is used because of its adjustable accuracy and amplitude adaptability even under unbalanced voltage sag and swell, frequency variation and distorted grid conditions. Fast and accurate behavior of three phase AANF improves the dynamic response of entire DG system control performance for sudden load variations. The dynamic behavior of the proposed grid interfaced DG system is experimentally evaluated in maintaining constant loading on grid, transient free operation and power factor improvement close to UPF operation of the utility grid, by compensating total reactive power and harmonic current demanded by variable linear as well as non-linear load.**

***Index Terms*—Amplitude adaptive notch filter (AANF), grid synchronization, grid connected inverters, power quality improvement.**

I. Introduction

RECENTLY, the distributed generation (DG) systems based on renewable energy sources such as solar photovoltaic (PV) systems, wind farms, mini-hydro power generation units, fuel cells, etc. are gaining more attention because of increasing clean energy demand. Power generated by these renewable energy sources can be stored in a battery energy storage system (BESS) and is injected to the utility grid using power electronic converters. The control of power electronic converters plays an important role not only in huge penetration of power generated by these DG systems but also in maintaining quality, reliability and stability of the utility grid [1]–[5]. However, fast and reliable synchronization is the most important aspect of the control performance of the grid interfaced inverters. In order to enhance the control performance and achieve high quality power injection capability, various grid synchronization techniques were proposed in the literature. All these strategies are mainly based on distinct features such as accuracy, fast dynamic response, stability and robustness under normal as well as polluted grid environment [6]–[29]. Grid interfaced DG control circuit mainly consist of: synchronization unit which accurately detects phase angle of the utility grid voltage, adequate control technique for reference compensating current generation and an appropriate switching strategy to drive interfacing inverter [6]–[10].

In the last decade, different phase locked loop (PLL) based synchronization techniques have been proposed of which the synchronous reference frame phase locked loop (SRF-PLL) technique has became very popular [11]. Performance of SRF-PLL is very accurate and fast under normal grid condition. Whereas, under the unbalanced and distorted voltage condition its performance is inaccurate due to presence of negative sequence component and harmonics [12], [13]. These inaccuracies in the phase angle detected by SRF-PLL degrade the control performance and quality of injected power [14]. In order to resolve this important issue, Modified SRF-PLL based numerous advanced strategies have been proposed by the researchers, such as SRF-PLL with a sinusoidal signal integrator [15], double second order generalized integrator SRF-PLL (DSOGI-PLL) [16] and decoupled DSRF-PLL (DDSRF-PLL) [17]. These schemes provides good performance under normal and unbalanced grid condition, however shows inaccurate performance under highly distorted grid condition. In order to detect and eliminate the harmonic components in the distorted grid voltage signal, the cascaded delayed signal cancelation based PLL (CDSC-PLL) was proposed by Y. F. Wang in [18] and moving average filter based PLL (MAF-PLL) [19] was proposed by Golestan S. However, it is observed that these techniques show inefficient performance when the input frequency deviates from its nominal value [20].

To overcome the drawbacks related to unbalanced, frequency variation and distorted grid conditions, various syn-

Manuscript received April 22, 2016; revised August 27, 2016, November 10, 2016 and January 01, 2017; accepted January 29, 2017. This work was supported by the the Department of Science and Technology (DST), Government of India, under the Project Grant No. DST/RCUK/SEGES/2012/04 (dated September 30, 2014).

A. B. Shitole, H. M. Suryawanshi, G. G. Talapur, S. Sathyan, M. S. Ballal, V. B. Borghate, M. R. Ramteke and M. A. Chaudhari are with the Department of Electrical Engineering, Visvesvaraya National Institute of Technology (VNIT), Nagpur 440011, India (e-mail: amardeep.shitole@gmail.com).
Copyright ©2017 IEEE. Personal use of this material is permitted. However, permission to use this material for any other purposes must be obtained from the IEEE by sending a request to pubs-permissions@ieee.org.

1551-3203 (c) 2016 IEEE. Personal use is permitted, but republication/redistribution requires IEEE permission. See http://www.ieee.org/publications_standards/publications/rights/index.html for more information.

This article has been accepted for publication in a future issue of this journal, but has not been fully edited. Content may change prior to final publication. Citation information: DOI 10.1109/TII.2017.2665477, IEEE Transactions on Industrial Informatics

chronization techniques based on filtering concepts were proposed in the recent years such as Discrete Fourier transform (DFT) [21], Kalman filtering [22] and adaptive notch filter (ANF) based techniques [23]–[27]. Adaptive notch filter (ANF) based technique is adaptive for frequency variation as well as distorted grid condition. Amplitude adaptive notch filter (AANF) based technique shows amplitude adaptability under unbalanced voltage sag and swell condition [28], [29]. An appropriate selection of synchronization technique and its real time implementation for grid connected inverter application has became area of research in practice.

In this paper, a grid current feedback based modified dq-current control loop using three phase AANF is proposed. This control technique is designed keeping in mind a specific application of a battery energy storage system (BESS) based grid connected inverter for household application. The specific objective of the proposed algorithm is to achieve constant loading on the grid, transient free operation and power factor improvement close to UPF operation of the utility grid under transient load variation. The main contribution in the proposed DG system control circuit is,

1) In this paper, because of excellent performance of single phase AANF, it is decided to develop its three phase extension. For the first time hardware implementation of extended AANF and its performance evaluation for fundamental frequency and phase angle estimation of utility voltage under unbalanced voltage sag and swell, frequency shift and distorted grid condition is presented.
2) Estimated phase angle is then used to generate synchronized reference current components for grid interfaced inverter.
3) Three phase AANF is used to improve speed of response and performance of overall DG system control circuit.
4) It is very easy to control DC variables than AC variables. Therefore, grid current feedback based modified current control loop in dq-frame is proposed to achieve constant loading on the grid, transient free operation and power factor improvement close to UPF operation of the utility grid during entire dynamic load variations.
5) In the proposed technique, the maximum active power load demand (P_{Load_max}) is predefined and the active power supplied by the grid is taken as reference quantity (P_{Grid_ref}). Therefore, three grid currents are sensed instead of three load currents and three inverter output currents. Hence requires only three current sensors.
6) Additional advantage of this control technique is that it does not require separate calculation of reactive and harmonics component of grid currents hence reduces control circuit complexity.
7) The active power reference value (P_{Grid_ref}) will decide the fixed amount of active power supplied by the utility grid. Hence, it is possible to achieve constant loading on the utility grid during entire load variations.
8) DG is able to supply additional amount of active power demanded by variable load in order to achieve adequate load sharing and transient free operation of the utility grid during dynamic load variations.

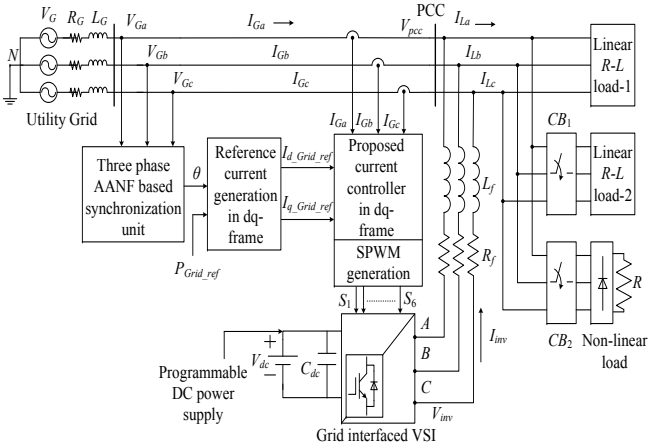

Fig. 1. Proposed DG system.

9) DG provides total reactive power and harmonic current demanded by linear as well as non-linear load under sudden load variations and hence ensures power factor improvement close to UPF operation of the utility grid.

II. DG System Description

The block diagram representation of the proposed DG system is depicted in Fig. 1. R_G and L_G represents the utility source resistance and inductance up to the point of common coupling (PCC) where interfacing inverter is connected. R_f and L_f represents the equivalent resistance and inductance of a passive filter connected at PCC. Two linear loads with different power factors and a non-linear load (diode bridge rectified R-load) are connected at PCC to achieve the variable load conditions.

III. Three phase AANF mathematical structure

In order to improve control performance of the grid interfaced DG system it is very important to accurately detect the phase angle of the utility grid voltage.

A. Single Phase AANF

In any of the grid connected system, voltage signal sensed at PCC and used as input to the synchronization unit is represented as,

$$V(t) = \sum_{i=1}^{n} A_i \sin \phi_i \quad where, \phi_i = \omega_i t + \varphi_i \tag{1}$$

Here, the phase angles φ_i, amplitudes A_i and frequencies ω_i where, $i = 1, 2, 3, ..., n$, are the unknown parameters.

To estimate these parameters, a modified discrete time AANF structure proposed in [28] is dynamically represented by the equations as:

$$\begin{aligned} \ddot{x} + \theta^2 x &= \sqrt{2}\theta e(t) \\ \dot{\theta} &= -\gamma x \theta e(t) \\ e(t) &= V(t) - \dot{x} \\ \gamma &= \frac{\epsilon}{(1+A^2)(1+\mu\theta^2)} \end{aligned} \tag{2}$$

1551-3203 (c) 2016 IEEE. Personal use is permitted, but republication/redistribution requires IEEE permission. See http://www.ieee.org/publications_standards/publications/rights/index.html for more information.

This article has been accepted for publication in a future issue of this journal, but has not been fully edited. Content may change prior to final publication. Citation information: DOI 10.1109/TII.2017.2665477, IEEE Transactions on Industrial Informatics

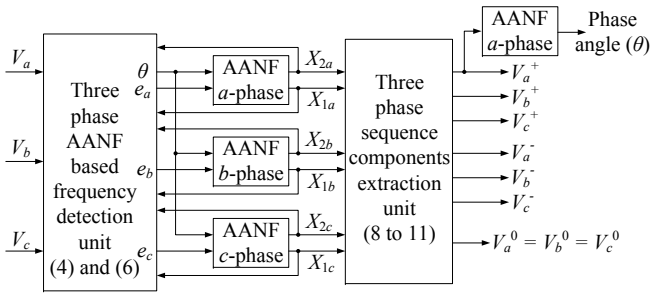

Fig. 2. Structural representation of three phase AANF.

Where, θ represents the frequency and the real positive constants ζ (damping ratio) and γ (adaptation gain) determines the accuracy and the convergence speed of AANF. For a fundamental frequency ω_1, this AANF has a periodic orbit located at,

$$\left(\begin{array}{c} O \end{array} \right) = \left(\begin{array}{c} x \\ \dot{x} \\ \theta \end{array} \right) = \left(\begin{array}{c} \frac{-A_1}{\omega_1}\cos(\omega_1 t + \varphi_1) \\ A_1 \sin(\omega_1 t + \varphi_1) \\ \omega_1 \end{array} \right) \tag{3}$$

Where, A_1 is an amplitude of the fundamental component and the third element of column vector O gives the fundamental frequency ω_1. From (3) it is observed that $\dot{x}$ and θx represents fundamental component and its 90° phase-shift component. Hence, the amplitude of the fundamental component is easily determined as, $A_1 = \sqrt{(\dot{x}_1^2 + \theta^2 x_1^2)}$. Here, in order to achieve non-oscillatory response, ζ value is considered as $1/\sqrt{2}$.

B. Three phase extension of AANF

In this subsection, three phase extension of AANF structure for phase angle estimation based on instantaneous symmetrical component extraction is developed. A basic block diagram of the three phase AANF is depicted in Fig. 2. Three identical single phase AANF sub-filters described in earlier subsection are used to develop three phase AANF structure. The fundamental and its 90° phase-shift component extracted by three single phase AANFs are used to estimate symmetrical components of input grid voltage. Considering three identical AANFs, a three phase AANF structure is mathematically represented as,

$$\begin{aligned} \ddot{x}_n + \theta^2 x_n &= \sqrt{2}\theta e_n(t) \\ \dot{\theta} &= -\theta \sum_{n=a,b,c} \gamma_n x_n e_n(t) \\ e_n(t) &= V_n(t) - \dot{x}_n \\ \gamma_n &= \frac{\epsilon}{(1 + A_n^2)(1 + \mu\theta^2)} \end{aligned} \tag{4}$$

Where, $n = a, b, c$ are three phases of sinusoidal input voltage signals in abc frame represented by the equation,

$$\left(\begin{array}{c} V_a(t) \\ V_b(t) \\ V_c(t) \end{array} \right) = \left(\begin{array}{c} A_a \sin(\omega_0 t + \varphi_a) \\ A_b \sin(\omega_0 t + \varphi_a - \frac{2\pi}{3}) \\ A_c \sin(\omega_0 t + \varphi_a - \frac{4\pi}{3}) \end{array} \right) \tag{5}$$

From (4), $\dot{\theta}$ is calculated as,

$$\dot{\theta} = -\theta[\gamma_a x_a e_a(t) + \gamma_b x_b e_b(t) + \gamma_c x_c e_c(t)] \tag{6}$$

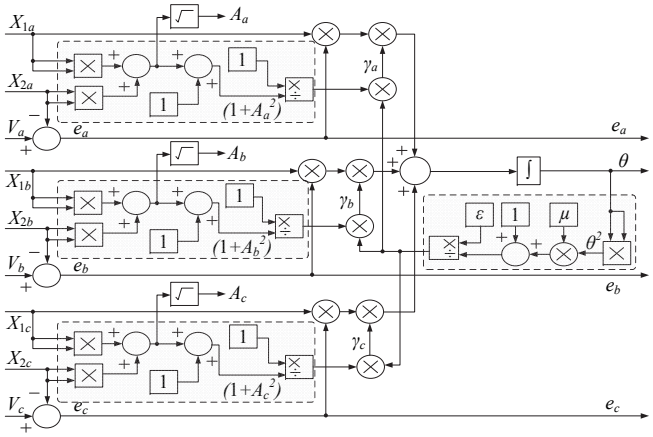

Fig. 3. Three phase AANF based frequency detection unit.

The three phase AANF structure represented by (4) and (6) has an orbit located at,

$$\left(\begin{array}{c} O \end{array} \right) = \left(\begin{array}{c} x_n \\ \dot{x}_n \\ \theta \end{array} \right) = \left(\begin{array}{c} \frac{-A_n}{\omega_0}\cos(\omega_0 t + \varphi_n) \\ A_n \sin(\omega_0 t + \varphi_n) \\ \omega_0 \end{array} \right) \tag{7}$$

Where, third row element $\theta = \omega_0$ is the frequency of a three phase signal. Integration of (6) gives estimated frequency. To estimate the frequency (4) and (6) are mathematically modeled as shown in Fig. 3. $\dot{x}_n = A_n \sin(\omega_0 t + \varphi_n)$ and $-\theta x_n = A_n \cos(\omega_0 t + \varphi_n)$ are the fundamental and 90° phase-shift component of the three phase input voltage respectively. These components are then represented by output column vectors $X_1(t)$ and $X_2(t)$ as,

$$\begin{aligned} X_1(t) &= \left(\begin{array}{ccc} -\theta x_a & -\theta x_b & -\theta x_c \end{array} \right)^t \\ X_2(t) &= \left(\begin{array}{ccc} \dot{x}_a & \dot{x}_b & \dot{x}_c \end{array} \right)^t \end{aligned} \tag{8}$$

The three phase voltage signals in (5) are decomposed into its symmetrical components by using (8) and a linear transformation proposed in [23] as,

$$\begin{aligned} V^+(t) &= T_2 X_2(t) + T_1 X_1(t) \\ V^-(t) &= T_2 X_2(t) - T_1 X_1(t) \\ V^0(t) &= (I - 2T_2) X_2(t) \end{aligned} \tag{9}$$

Where, I is an identity matrix. The transformation matrices T_1 and T_2 are given by,

$$T_1 = \frac{1}{2\sqrt{3}} \left[\begin{array}{ccc} 0 & 1 & -1 \\ -1 & 0 & 1 \\ 1 & -1 & 0 \end{array} \right] \tag{10}$$

$$T_2 = \frac{1}{3} \left[\begin{array}{ccc} 1 & -0.5 & -0.5 \\ -0.5 & 1 & -0.5 \\ -0.5 & -0.5 & 1 \end{array} \right] \tag{11}$$

1551-3203 (c) 2016 IEEE. Personal use is permitted, but republication/redistribution requires IEEE permission. See http://www.ieee.org/publications_standards/publications/rights/index.html for more information.

This article has been accepted for publication in a future issue of this journal, but has not been fully edited. Content may change prior to final publication. Citation information: DOI 10.1109/TII.2017.2665477, IEEE Transactions on Industrial Informatics

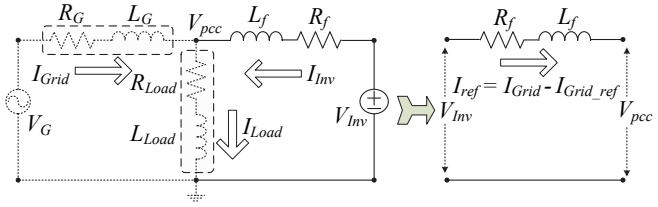

Fig. 4. Equivalent circuit of proposed DG system.

IV. Modified Current Control Technique for Proposed DG System

In this section, a grid current feedback based modified dq-current control technique is developed for generation of synchronized reference compensating current signals. This control technique is designed keeping in mind a specific application of a battery energy storage system (BESS) based grid connected inverter for household application. Because of unavailability of BESS, a programmable DC power supply is used to produce energy from the DG system. The proposed DG system is completely owned by the customers and not by the distribution utility. Here, the minimum (P_{Load_min}) and maximum (P_{Load_max}) value of load power demand is known to the customers for their local loads connected at PCC. From this known values the customer will predefine the average value of the active power load demand (P_{Load_avg}) in order to decide the capacity of the DG system to be installed to satisfy the local load demand. Therefore, the active power capacity of the DG system is selected two times the average active power load demand (P_{Load_avg}). Here, the capacity of the DG system is over designed in order to achieve constant loading, transient free operation and power factor improvement close to UPF operation of the grid at PCC. Even though maximum active power capacity of the DG is fixed, it can supply variable power as per the load demand. The control circuit is designed such that utility grid will supply fixed amount of active power (based on P_{Grid_ref} set value) demanded by variable linear as well as non-linear load. Hence, maintains constant loading, transient free operation and power factor improvement close to UPF operation at PCC. However, additional amount of active power, total reactive power and harmonic current demanded by variable local load is supplied by the DG system. Hence, in the proposed DG system, reactive power compensation and harmonic current compensation operations have given highest priority. However, active power sharing operation is done based on the selected reference value (P_{Grid_ref}) and load demand.

A. Calculation of dq-frame reference current components

The total power demanded by the load (P_{Load}, Q_{Load}) is combination of the power supplied by the utility grid (P_{Grid}, Q_{Grid}) and an interfacing inverter (P_{Inv}, Q_{Inv}) as depicted in Fig. 4. Considering the local load demand, the amount of apparent power demanded by the local load (S_{Load}) is given as,

$$S_{Load} = P_{Load} + j\ Q_{Load} = S_{Grid} + S_{Inv} \quad (12)$$

When the DG is not connected, the total load demand is supplied by the utility grid.

$$S_{Load} = S_{Grid} = P_{Grid} + j\ Q_{Grid} = \sqrt{3}\ V_{pcc}\ I_{Grid} \quad (13)$$

Representing real and reactive components of power supplied by the utility grid in dq-frame,

$$P_{Grid} = \frac{3}{2}[V_{d_pcc}\ I_{d_Grid} + V_{q_pcc}\ I_{q_Grid}]$$
$$Q_{Grid} = \frac{3}{2}[-V_{d_pcc}\ I_{q_Grid} + V_{q_pcc}\ I_{d_Grid}] \quad (14)$$

Here, grid voltage phase angle (θ) estimated by three phase AANF is used for dq-transformation. Assuming the steady state balanced condition, to achieve UPF operation of the utility grid, the active power supplied by the grid is,

$$P_{Grid} = P_{Load} = \frac{3}{2}[V_{d_pcc}\ I_{d_Grid}] \quad (15)$$

In this paper, in order to achieve constant loading and improvement in the power factor close to UPF of the utility grid, active power supplied by the grid is taken as reference quantity and is user defined. The effective reference value (P_{Grid_ref}) is selected equal to the average active power load demand (P_{Load_avg}). This reference quantity can be changed as a percentage of the maximum active power load demand (P_{Load_max}) between 0 to 100% in order to achieve adequate load sharing and stable operation. However, remaining active power, entire reactive power and harmonic current demanded by load is supplied by the DG system. Therefore, the reference active power supplied by the grid is,

$$P_{Grid_ref} = (x\%)\ P_{Load_max} = (x\%)\ \frac{3}{2}[V_{d_pcc}\ I_{d_Grid_ref}] \quad (16)$$

$$I_{d_Grid_ref} = \frac{2}{3}\ [\frac{P_{Grid_ref}}{V_{d_pcc}}] \quad (17)$$

Here, as per the power available with the DG, the value of x is selected between 0 to 100%. To achieve an improvement in the power factor close to UPF of the utility grid, reference reactive power value is assumed zero ($Q_{Grid_ref} = 0$) and hence, $I_{q_Grid_ref} = 0$. These dq-axis reference current components are subtracted from the actual dq-axis grid currents in order to get the reference currents to be supplied by the inverter ($I_{dq_ref} = I_{dq_Grid} - I_{dq_Grid_ref}$) as depicted in Fig. 4. This inverter current contains active power component demanded by load excluding $I_{d_Grid_ref}$. In addition, it also contains entire reactive power component and harmonic component of current demanded by load. Therefore, in this control technique it is not required to calculate the reference reactive component and harmonics component of currents separately, hence reduces control circuit complexity.

B. Mathematical modeling of proposed DG system

Mathematical modeling of the DG system is necessary to calculate control system parameters in order to stabilize its control performance. It is easy to control DC variables than AC variables. Therefore, using park's transformation the feedback

1551-3203 (c) 2016 IEEE. Personal use is permitted, but republication/redistribution requires IEEE permission. See http://www.ieee.org/publications_standards/publications/rights/index.html for more information.

This article has been accepted for publication in a future issue of this journal, but has not been fully edited. Content may change prior to final publication. Citation information: DOI 10.1109/TII.2017.2665477, IEEE Transactions on Industrial Informatics

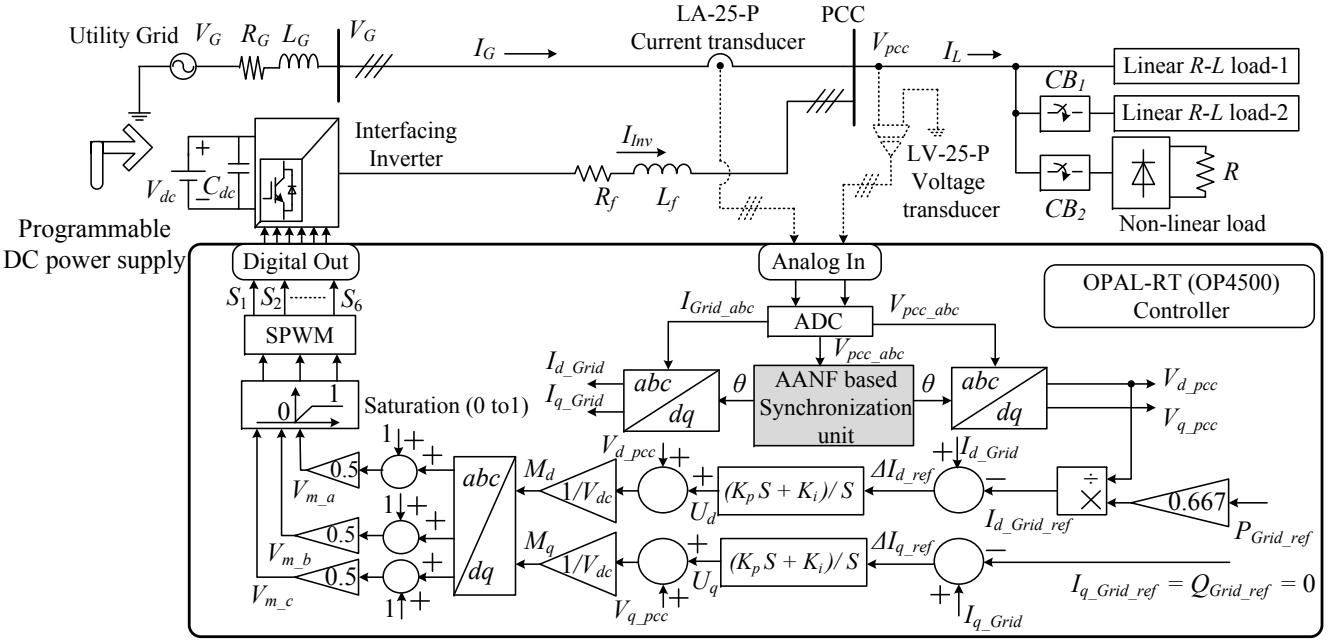

Fig. 5. Schematic diagram of the proposed DG system.

AC variables are transformed into synchronously rotating dq-reference frame [30]. Therefore, the proposed DG system is mathematically modeled in dq-frame as,

$$V_{d_Inv} - L_f \frac{dI_{d_ref}}{dt} - R_f I_{d_ref} - V_{d_pcc} = 0$$
$$V_{q_Inv} - L_f \frac{dI_{q_ref}}{dt} - R_f I_{q_ref} - V_{q_pcc} = 0 \quad (18)$$

The output terminal voltages of the inverter with modulation index M in dq-frame are,

$$V_{d_Inv} = M_d(V_{dc})$$
$$V_{q_Inv} = M_q(V_{dc}) \quad (19)$$

Substituting (19) in (18),

$$M_d(V_{dc}) = L_f \frac{dI_{d_ref}}{dt} + R_f I_{d_ref} + V_{d_pcc}$$
$$M_q(V_{dc}) = L_f \frac{dI_{q_ref}}{dt} + R_f I_{q_ref} + V_{q_pcc} \quad (20)$$

(20) represents, first order linear differential equations of the proposed DG system in dq-frame. PI-controller is used to achieve precise control of dq-axis currents under linear as well as nonlinear load variations. The error signal in the dq-axis currents ($\Delta\, I_{dq_ref} = I_{dq_Grid} - I_{dq_Grid_ref}$) is passed through the PI-controller to get the new control variables U_d and U_q as,

$$U_d = L_f \frac{dI_{d_ref}}{dt} + R_f I_{d_ref}$$
$$U_q = L_f \frac{dI_{q_ref}}{dt} + R_f I_{q_ref} \quad (21)$$

The modulation index in dq-frame to control the currents injected by interfacing inverter at PCC is,

$$M_d = \frac{1}{V_{dc}}[U_d + V_{d_pcc}]$$
$$M_q = \frac{1}{V_{dc}}[U_q + V_{q_pcc}] \quad (22)$$

These modulating signals in dq-frame (M_{dq}) are transformed back to abc-frame (V_{m_abc}) to generate required gate pulses to drive the interfacing inverter. As per the basic requirement of PWM-out block of OPAL-RT (OP-4500) controller, these modulating signals are level shifted by a fixed DC offset of 1 and then multiplied with a gain of 0.5.

V. Laboratory Experimentation Setup

The schematic of the experimental setup is depicted in Fig. 5. This setup is developed in order to evaluate dynamic response of three phase AANF and its effect on the performance of the grid interfaced DG system. The proposed DG control technique is implemented in OPAL-RT (OP-4500) real time digital simulator with an in-built Xilinx Kintex-7 FPGA processor. The experimentation is done in two ways:

A. Real time performance evaluation of AANF

Here, OPAL-RT simulator is used as a plant. A three phase, 415 V, 50 Hz programable voltage source in plant simulator is used to create the disturbances such as, voltage sag and swell of 20% in phase-a, frequency shift of ± 2 Hz and positive sequence 5^{th} and 7^{th} harmonics of 5% in the input voltage signal. To observe the performance of extended AANF, all the analog voltage signals are conditioned within the limit of simulator. The RMS phase voltage of 239.6 V is set to 1.0 p.u. for the performance evaluation.

1551-3203 (c) 2016 IEEE. Personal use is permitted, but republication/redistribution requires IEEE permission. See http://www.ieee.org/publications_standards/publications/rights/index.html for more information.

This article has been accepted for publication in a future issue of this journal, but has not been fully edited. Content may change prior to final publication. Citation information: DOI 10.1109/TII.2017.2665477, IEEE Transactions on Industrial Informatics

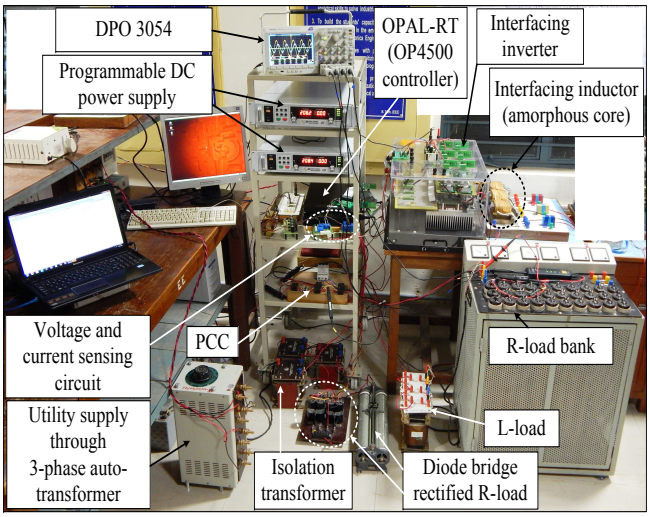

Fig. 6. Laboratory experimental setup.

TABLE I
SYSTEM PARAMETERS

Sr.No.	Parameter	Value
1	Grid voltage (V_G)	415 V (L-L)
2	System frequency (f)	50 Hz
3	Coupling inductance (L_f)	5.9 mH
4	DC link voltage (V_{dc})	750 V
5	Linear load-1 (L_1)	P = 3 kW, P.F. = 0.9 (lag)
6	Linear load-2 (L_2)	P = 1.5 kW, P.F. = 0.8 (lag)
7	Non-linear load (L_3)	R = 600 Ω
8	Switching frequency (f_{sw})	3150 Hz

B. Application of AANF in proposed grid interfaced DG system

Here, For closed loop control circuit operation, OPAL-RT simulator is used as controller unit. Three utility grid voltage signals and three grid current signals are sensed by using LEM LV-25-P voltage and LA-25-P current transducer. The gain of transducers are designed such that, sensed output voltage and currents does not exceed the maximum limit of analog I/O range ($\pm$16V) of the simulator (voltage transducer gain = 88.5 and current transducer gain = 3.03) [31]. The proposed closed loop current control technique generates required PWM pulses for the inverter using three voltage and three current feedback signals. The required dead-band of (0.5 μsec.) between the complementary gate pulses of each leg of the three leg inverter is generated internally to avoid the direct short-circuit of the input DC-link capacitor. These six gate pulses generated at the PWM-output port of OP-4500 are of 0-5V. A separate buffer circuit with SN74LS07N buffer IC, optocoupler IC 6N137 for isolation and then a driver IC MIC4425ZN is used to drive the inverter. A three phase IGBT based inverter is used as an interfacing inverter. MAGNA-XR LXI Programmable DC power supply is used to produce energy from the DG system because of unavailability of BESS. Amorphous core is used to develop filter inductor because of high saturation flux density of 1.6 Tesla. The laboratory setup is as shown in Fig. 6. The DG system parameters considered for real time performance evaluation are tabulated in Table I.

VI. PERFORMANCE EVALUATION WITH REAL TIME SIMULATION AND EXPERIMENTAL RESULTS

At first, an amplitude adaptive nature of three phase AANF for phase angle and frequency detection under unbalanced voltage sag and swell, frequency variation and distorted grid conditions is evaluated. Later, the effect of AANF on the DG system performance is also evaluated for linear as well as non-linear load variations. The AANF parameters are set to $\zeta = \frac{1}{\sqrt{2}}$, $\mu = 0.00001$ and $\epsilon = 100000$. The initial condition for the integrator which outputs the system frequency is considered as $50 \times 2\pi$ rad/s, whereas for all other integrators it is considered as zero.

A. Performance Evaluation for Phase angle Estimation

The performance of three phase AANF for phase angle and frequency estimation is investigated under unbalanced voltage sag and swell, frequency variation and harmonics distorted condition.

1) Unbalanced voltage sag and swell: Initially, RMS value of phase voltage and frequency is set to 239.6V and 50 Hz respectively. Later, a voltage sag and swell of 20% in phase-a is added as shown in Figs. 7(a) and 7(b).

2) Unbalanced voltage sag and swell with harmonics distortions: In order to create unbalanced voltage sag and swell with harmonics distortions, a voltage sag and swell of 20% in phase-a and a positive sequence 5^{th} and 7^{th} harmonics of 5% are added in all phases of input voltage signal as shown in Figs. 7(c) and 7(d).

3) Frequency shift: In this case, a frequency shift of $\pm$2 Hz is added in the input voltage signal as shown in Figs. 7(e) and 7(f).

4) Frequency shift with harmonics distortions : In this case, a frequency shift of $\pm$2 Hz and a positive sequence 5^{th} and 7^{th} harmonics of 5% are added in the input voltage signal as shown in Figs. 7(g) and 7(h).

Real time simulation results shown in Figs. 7(a) to 7(h) demonstrate the dynamic response of three phase AANF for phase angle and frequency detection under unbalanced voltage sag and swell, frequency variation and distorted condition. It is observed that the extracted phase angle (θ) does not contain double frequency oscillations due to negative sequence component under unbalanced voltage sag and swell condition. AANF also effectively filter out the distortions under distorted condition, in addition it also shows frequency adaptability under grid frequency variation. Therefore, three phase AANF accurately estimates phase angle (θ) of the voltage signal. This information is then used for generation of synchronized reference current components for grid interfacing inverter.

B. Grid Interfacing Inverter Control Performance

Here, improved dynamic control performance of proposed DG system due to fast and accurate synchronization is evaluated under steady state as well as transient condition for sudden linear and non-linear load variations. Performance of the proposed control algorithm when the power supplied by the DG is varied over a wide range is verified with three different modes of operation:

1551-3203 (c) 2016 IEEE. Personal use is permitted, but republication/redistribution requires IEEE permission. See http://www.ieee.org/publications_standards/publications/rights/index.html for more information.

This article has been accepted for publication in a future issue of this journal, but has not been fully edited. Content may change prior to final publication. Citation information: DOI 10.1109/TII.2017.2665477, IEEE Transactions on Industrial Informatics

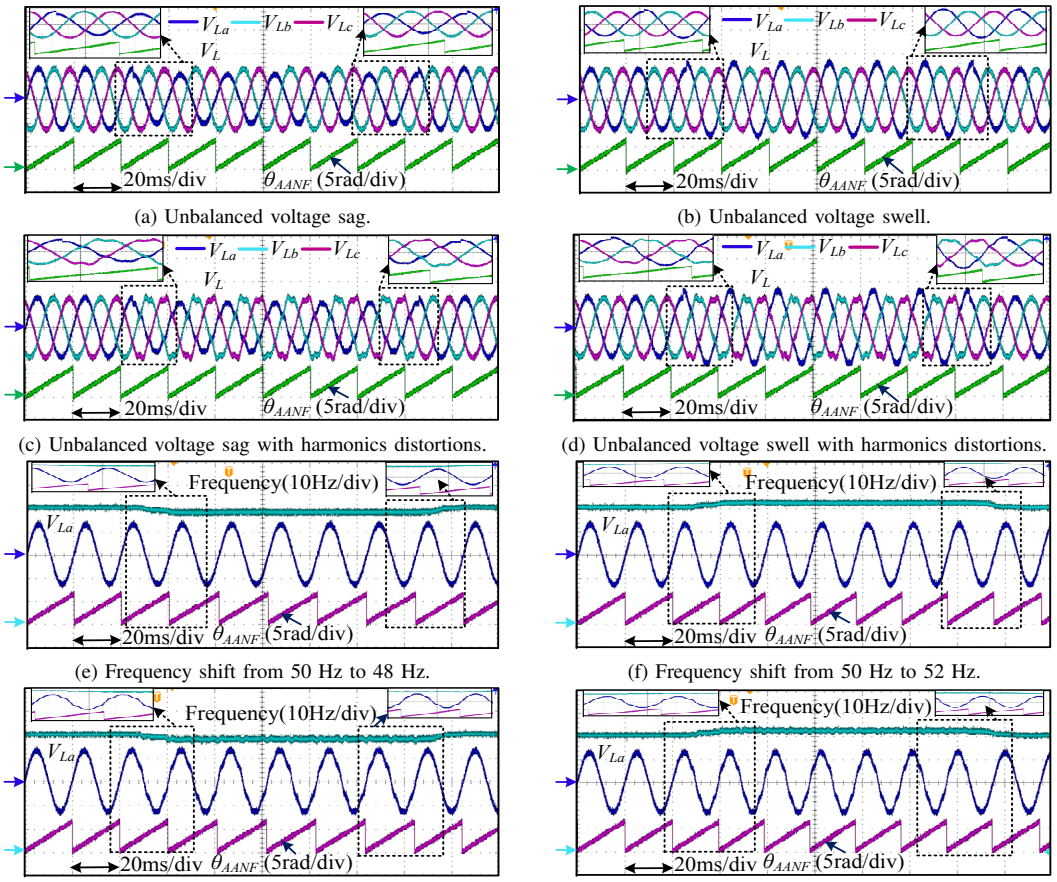

(a) Unbalanced voltage sag.
(b) Unbalanced voltage swell.
(c) Unbalanced voltage sag with harmonics distortions.
(d) Unbalanced voltage swell with harmonics distortions.
(e) Frequency shift from 50 Hz to 48 Hz.
(f) Frequency shift from 50 Hz to 52 Hz.
(g) Frequency shift with harmonics distortions from 50 Hz to 48 Hz.
(h) Frequency shift with harmonics distortions from 50 Hz to 52 Hz.

Fig. 7. Real time simulation results of three phase AANF for phase angle and frequency detection (voltage scale: 1 V/div).

1) Grid sharing mode: At first, DG system performance to supply variable local load demand to achieve constant loading on the grid, transient free operation, and improvement in the power factor close to UPF of the utility grid is evaluated. For simplicity, from the known maximum active power load demand (P_{Load_max}), the average value of the active power load demand (P_{Load_avg}) is predefined. In this paper, the maximum active power demanded by load is P_{Load_max} = 5 kW. In order to achieve adequate load sharing between DG and utility grid, the reference active power value of the grid is initially set to 75% of P_{Load_max} (P_{Grid_ref} = 3.75 kW). The local load is increased in two steps. Initially, a linear load of P_{L1} = 3 kW and Q_{L1} = 1.453 kvar is connected to the grid. As, the inverter is not connected, entire load demand is supplied by the grid. Now, as soon as the inverter is connected, the grid will supply constant active power of (P_{Grid_ref} = 3.75 kW). Here, as the active power load demand (P_{L1} = 3 kW) is less than the reference value (P_{Grid_ref} = 3.75 kW), additional active power is stored in the DC-link of the DG system. However, entire reactive power demanded by load is supplied by the inverter as shown in Fig. 8(a). To increase the load demand, an additional linear load of P_{L2} = 1.5 kW and Q_{L2} = 1.125 kvar is connected to the system as shown in Fig. 8(b). Later, a bridge rectified R-load of R = 600 Ω (non-linear load L_3) is added to the system as shown in Fig. 8(c). Even though the load is suddenly increased, the grid will supply a fixed amount of active power of (P_{Grid_ref} = 3.75 kW) and ensures constant loading and transient free operation.

If the power available with the DG is sufficiently large, loading on the grid is reduced by decreasing P_{Grid_ref}. Here, in order to increase power supplied by the DG system and reduce loading on the utility grid, P_{Grid_ref} is reduced in three steps: 1) P_{Grid_ref} is set to 50% of P_{Load_max} (P_{Grid_ref}=2.5 kW). 2) P_{Grid_ref} is set to 25% of P_{Load_max} (P_{Grid_ref}=1.25 kW). 3) P_{Grid_ref} is set to 12.5% of P_{Load_max} (P_{Grid_ref}=0.625 kW). In each case, the performance of the proposed control algorithm is evaluated for aforementioned loading conditions (L_1, L_2 and L_3) as shown in Figs. 8(d) to 8(l). During this entire process of P_{Grid_ref} variation and sudden load variation (L_1, L_2 and L_3), the proposed DG system shows satisfactory dynamic control performance. The experimental results demonstrate, fast dynamic response of the proposed control algorithm in maintaining constant loading on the grid as per the set reference value (P_{Grid_ref}). However, additional amount of active power, entire reactive power and harmonic current demanded by the load is completely supplied by the DG system.

2) DC-link charging mode: If the local load demand is less than P_{Grid_ref} value then the additional power supplied by the grid is stored in the DC-link of the DG system. Initially,

1551-3203 (c) 2016 IEEE. Personal use is permitted, but republication/redistribution requires IEEE permission. See http://www.ieee.org/publications_standards/publications/rights/index.html for more information.

This article has been accepted for publication in a future issue of this journal, but has not been fully edited. Content may change prior to final publication. Citation information: DOI 10.1109/TII.2017.2665477, IEEE Transactions on Industrial Informatics

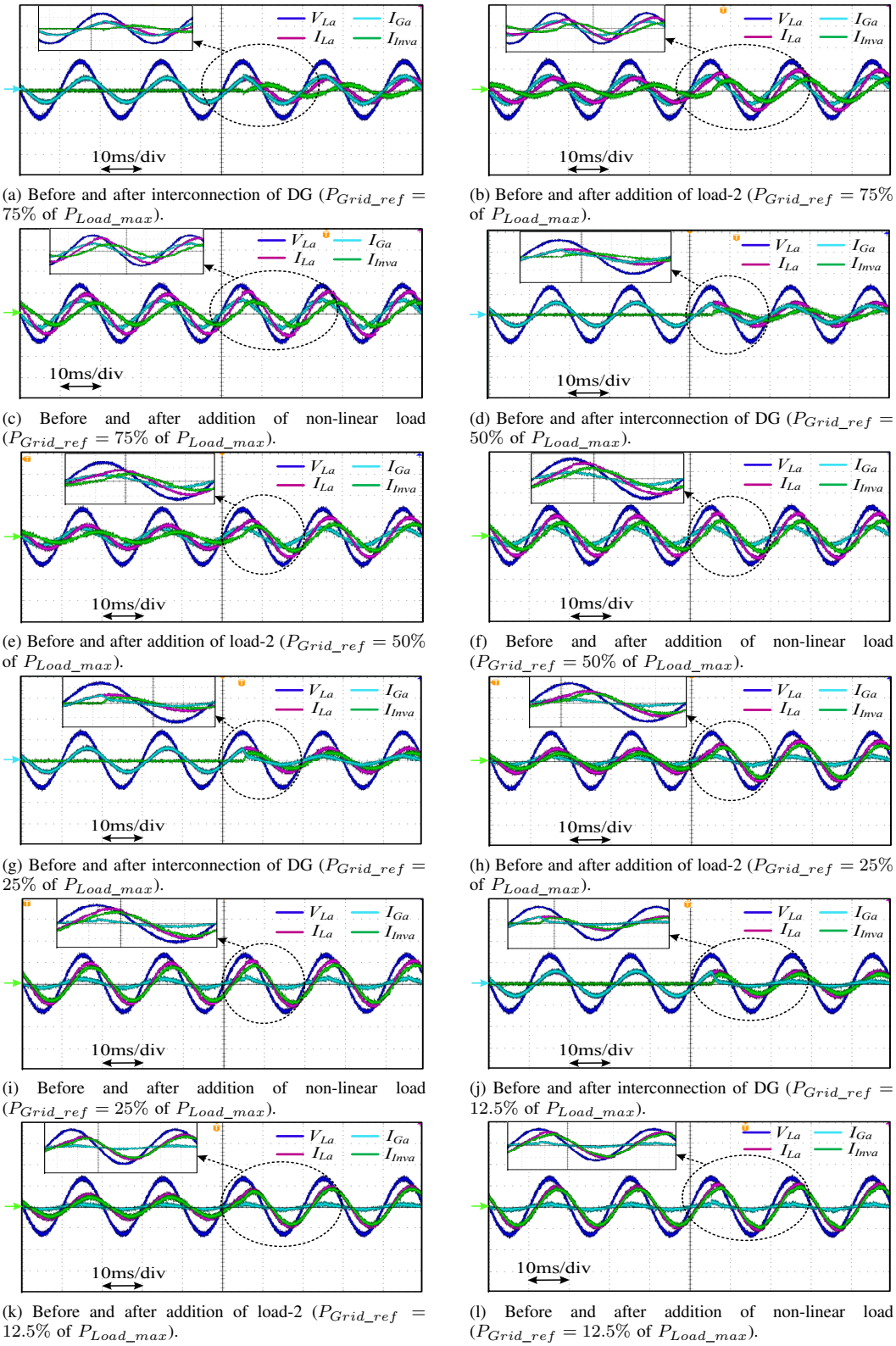

(a) Before and after interconnection of DG (P_{Grid_ref} = 75% of P_{Load_max}).

(b) Before and after addition of load-2 (P_{Grid_ref} = 75% of P_{Load_max}).

(c) Before and after addition of non-linear load (P_{Grid_ref} = 75% of P_{Load_max}).

(d) Before and after interconnection of DG (P_{Grid_ref} = 50% of P_{Load_max}).

(e) Before and after addition of load-2 (P_{Grid_ref} = 50% of P_{Load_max}).

(f) Before and after addition of non-linear load (P_{Grid_ref} = 50% of P_{Load_max}).

(g) Before and after interconnection of DG (P_{Grid_ref} = 25% of P_{Load_max}).

(h) Before and after addition of load-2 (P_{Grid_ref} = 25% of P_{Load_max}).

(i) Before and after addition of non-linear load (P_{Grid_ref} = 25% of P_{Load_max}).

(j) Before and after interconnection of DG (P_{Grid_ref} = 12.5% of P_{Load_max}).

(k) Before and after addition of load-2 (P_{Grid_ref} = 12.5% of P_{Load_max}).

(l) Before and after addition of non-linear load (P_{Grid_ref} = 12.5% of P_{Load_max}).

Fig. 8. Experimental results: DG system load voltage (V), grid current (A), load current (A) and inverter current (A) of phase-a (voltage scale: 250 V/div, current scale: 10 A/div).

P_{Grid_ref} is set to 50% of P_{Load_max} (P_{Grid_ref}=2.5 kW) and a linear load of P_{L1} = 3 kW and Q_{L1} = 1.453 kvar is connected to the grid. The local load demand is higher than reference value therefore, fixed amount of active power is supplied by the grid and the additional amount of active power and entire reactive power demanded by load is supplied

1551-3203 (c) 2016 IEEE. Personal use is permitted, but republication/redistribution requires IEEE permission. See http://www.ieee.org/publications_standards/publications/rights/index.html for more information.

This article has been accepted for publication in a future issue of this journal, but has not been fully edited. Content may change prior to final publication. Citation information: DOI 10.1109/TII.2017.2665477, IEEE Transactions on Industrial Informatics

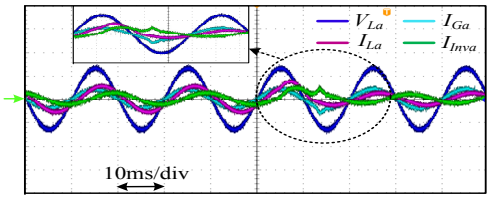

(a) DC link charging mode when load demand is less than P_{Grid_ref}.

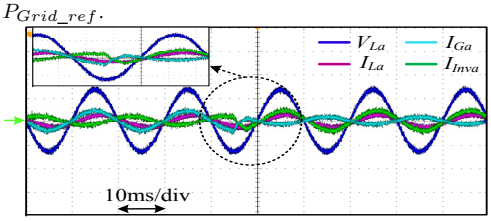

(b) Grid feeding mode when load demand is less than available power with DG.

Fig. 9. Experimental results: DG system load voltage (V), grid current (A), load current (A) and inverter current (A) of phase-a (voltage scale: 250 V/div, current scale: 10 A/div).

by the interfacing inverter of the DG. Now, load demand is suddenly decreased to half of L_1 (P_{L2} = 1.5 kW and Q_{L2} = 0.7265 kvar). As the load demand is less than reference value (P_{Grid_ref}=2.5 kW), additional active power supplied by the grid is stored in the DC-link of the DG system as shown in Fig. 9(a).

3) Grid feeding mode: If power available with DG is sufficiently large and load demand is very less then the additional power is injected into the grid. Initially, P_{Grid_ref} is set to 50% of P_{Load_max} (P_{Grid_ref}=2.5 kW) and half of a linear load (L_1) P_{L1} = 1.5 kW and Q_{L1} = 0.7265 kvar is connected to grid. As P_{Grid_ref} is higher than the load demand, additional active power supplied by the grid is stored in the DC-link of the DG system. Now, P_{Grid_ref} is set to -25% of P_{Load_max} (P_{Grid_ref}=-1.25 kW) and hence additional power available with DG is injected into the grid as shown in Fig. 9(b).

The experimental result shown in Figs. 10(a) and 10(b) demonstrate the power sharing between DG and utility grid. In Fig. 10(a), P_{Grid_ref} is less than the load demand. Here, P_{Grid_ref} is set to 50% of P_{Load_max} (P_{Grid_ref}=2.5 kW). The reference value is less than the load demand of all the aforementioned loading conditions (L_1, L_2 and L_3). Therefore, fixed amount of active power is supplied by the grid and the additional amount of active power demanded by load is supplied by the DG. However, a small amount of active power supplied by the DG is utilized to overcome inverter losses. In addition, entire reactive power and harmonic current demanded by the load is supplied by the DG. In Fig. 10(b), P_{Grid_ref} is higher than the load demand. Here, the local load connected to the grid is increased in two steps. Initially, half of a linear load (L_1) P_{L1} = 1.5 kW is connected and after some time, second load of half of a linear load (L_2) P_{L2} = 0.75 kW is added. As, P_{Grid_ref} is higher than the entire load demand (L_1 and L_2). Therefore, the additional active power supplied by the grid is stored in the DC-link of the DG system. However, a small amount of active power supplied by the grid is utilized to overcome inverter losses. Hence, proposed algorithm ensures constant loading and transient free operation of the utility grid.

During this entire process of dynamic load variation, the proposed DG system shows improved dynamic control performance due to fast and accurate synchronization as shown

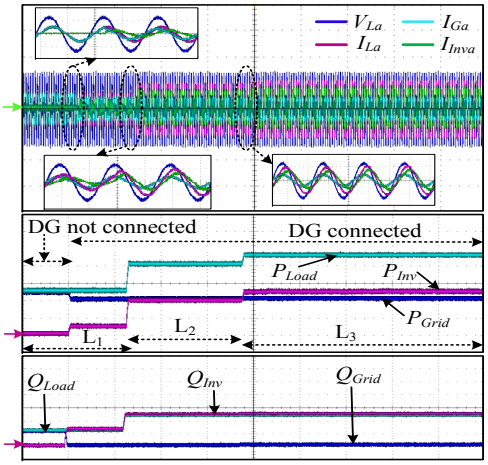

(a) Power flow showing load sharing between grid and DG when P_{Grid_ref} is less than the load demand.

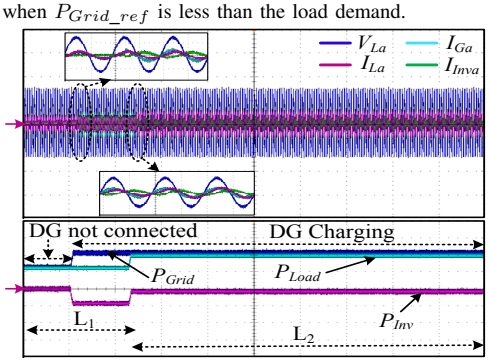

(b) Power flow showing DC-link charging of the DG system when P_{Grid_ref} is higher than the load demand.

Fig. 10. Experimental results: Active and reactive power flow (active power scale: 1.25 kW/div, reactive power scale: 1 kvar/div).

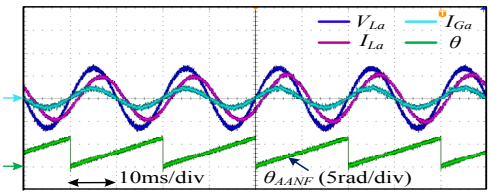

Fig. 11. Experimental results: DG system synchronization before and after addition of non-linear load. (voltage scale: 250 V/div, current scale: 10 A/div).

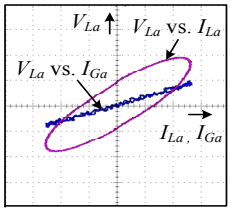

(a) X-Y plot for load-2.

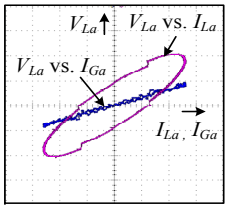

(b) X-Y plot for load-3.

Fig. 12. Experimental results: X-Y plot between load voltage vs. grid current and load current.

During this entire process of dynamic load variation, the proposed DG system shows improved dynamic control performance due to fast and accurate synchronization as shown

1551-3203 (c) 2016 IEEE. Personal use is permitted, but republication/redistribution requires IEEE permission. See http://www.ieee.org/publications_standards/publications/rights/index.html for more information.

This article has been accepted for publication in a future issue of this journal, but has not been fully edited. Content may change prior to final publication. Citation information: DOI 10.1109/TII.2017.2665477, IEEE Transactions on Industrial Informatics

in Fig. 11. The X-Y plot between load voltage at PCC (V_{La}) vs. grid current (I_{Ga}) and load current (I_{La}) is as shown in Figs. 12(a) and 12(b). The graph of V_{La} vs. I_{Ga} is straight line where as V_{La} vs. I_{La} is elliptical in nature. The straight line graph of PCC voltage and grid current indicates zero phase angle between them. In addition, voltage and current waveforms are almost sinusoidal in nature. Hence, according to the proposed algorithm if the inverter is compensating total reactive and harmonic current then the utility grid will only supply sinusoidal active component of current in phase with the PCC voltage. Hence, displacement power factor is unity ($PF_{disp} = 1$). If the PCC voltage is distorted by other non-linear loads then the distortion power factor (PF_{dist}) is not exactly unity. However, the effect of PCC voltage distortions (V_{LTHD}) on the true power factor (PF_{true}) is negligible (if $V_{LTHD} < 10\%$) as compared to current distortions (I_{GTHD}) [32]. In the proposed algorithm, as the output currents supplied by the grid are almost sinusoidal in nature, the distortion power factor (PF_{dist}) is almost unity. Hence, true power factor (PF_{true}) is close to unity. Therefore, the proposed algorithm ensures power factor improvement close to UPF of the utility grid.

VII. Conclusion

The amplitude adaptability and adjustable accuracy of three phase AANF for phase angle extraction of the utility grid voltage signal has been evaluated under unbalanced voltage sag and swell, frequency variation and harmonics distorted condition. The grid current feedback based modified dq-current control technique for interfacing inverter is developed. The effect of estimated phase angle on the dynamic performance of the DG system is investigated. The capability of interfacing inverter to supply additional amount of active power, total reactive power and harmonic current demanded by variable linear as well as non-linear load is verified. The experimental results demonstrate the dynamic performance of proposed control technique in order to achieve constant loading on the grid, transient free operation and power factor improvement close to UPF of the utility grid under dynamic load variations. This control technique does not require separate calculation of reference reactive component and harmonics component of currents hence reduces control circuit complexity, in addition it requires only three voltage and three current sensors.

References

[1] B. Singh, K. Al-Haddad, and A. Chandra, "A review of active filters for power quality improvement," *IEEE Trans. Ind. Electron.*, vol. 46, no. 5, pp. 960–971, Oct. 1999.

[2] J. M. Guerrero, P. C. Loh, T. L. Lee, and M. Chandorkar, "Advanced control architectures for intelligent microgrids part ii: Power quality, energy storage, and ac/dc microgrids," *IEEE Trans. Ind. Electron.*, vol. 60, no. 4, pp. 1263–1270, April 2013.

[3] C. Kumar and M. K. Mishra, "A voltage-controlled dstatcom for power-quality improvement," *IEEE Trans. Power Del.*, vol. 29, no. 3, pp. 1499–1507, June 2014.

[4] M. Manoj Kumar, M. Mishra, and C. Kumar, "A grid-connected dual voltage source inverter with power quality improvement features," *IEEE Trans. Sustain. Energy*, vol. 6, no. 2, pp. 482–490, April 2015.

[5] C. Yoon, H. Bai, R. N. Beres, X. Wang, C. L. Bak, and F. Blaabjerg, "Harmonic stability assessment for multiparalleled, grid-connected inverters," *IEEE Trans. Sustain. Energy*, vol. 7, no. 4, pp. 1388–1397, Oct. 2016.

[6] F. Blaabjerg, R. Teodorescu, M. Liserre, and A. Timbus, "Overview of control and grid synchronization for distributed power generation systems," *IEEE Trans. Ind. Electron.*, vol. 53, no. 5, pp. 1398–1409, Oct. 2006.

[7] Y. Han, M. Luo, X. Zhao, J. M. Guerrero, and L. Xu, "Comparative performance evaluation of orthogonal-signal-generators-based single-phase pll algorithms: A survey," *IEEE Trans. Power Electron.*, vol. 31, no. 5, pp. 3932–3944, May 2016.

[8] Y. Yang, L. Hadjidemetriou, F. Blaabjerg, and E. Kyriakides, "Benchmarking of phase locked loop based synchronization techniques for grid-connected inverter systems," in *2015 9th International Conference on Power Electronics and ECCE Asia (ICPE-ECCE Asia)*, June 2015, pp. 2167–2174.

[9] N. Tummuru, M. Mishra, and S. Srinivas, "An improved current controller for grid connected voltage source converter in microgrid applications," *IEEE Trans. Sustain. Energy*, vol. 6, no. 2, pp. 595–605, April 2015.

[10] M. N. Kabir, Y. Mishra, G. Ledwich, Z. Y. Dong, and K. P. Wong, "Coordinated control of grid-connected photovoltaic reactive power and battery energy storage systems to improve the voltage profile of a residential distribution feeder," *IEEE Trans. Ind. Informat.*, vol. 10, no. 2, pp. 967–977, May 2014.

[11] S.-K. Chung, "A phase tracking system for three phase utility interface inverters," *IEEE Trans. Power Electron.*, vol. 15, no. 3, pp. 431–438, May 2000.

[12] C. da Silva, R. Pereira, L. da Silva, G. Lambert-Torres, B. Bose, and S. U. Ahn, "A digital pll scheme for three-phase system using modified synchronous reference frame," *IEEE Trans. Ind. Electron.*, vol. 57, no. 11, pp. 3814–3821, Nov. 2010.

[13] P. Kanjiya, V. Khadkikar, and M. El Moursi, "A novel type-1 frequency-locked loop for fast detection of frequency and phase with improved stability margins," *IEEE Trans. Power Electron.*, vol. 31, no. 3, pp. 2550–2561, March 2016.

[14] K.-J. Lee, J.-P. Lee, D. Shin, D.-W. Yoo, and H.-J. Kim, "A novel grid synchronization pll method based on adaptive low-pass notch filter for grid-connected pcs," *IEEE Trans. Ind. Electron.*, vol. 61, no. 1, pp. 292–301, Jan. 2014.

[15] R. Bojoi, G. Griva, V. Bostan, M. Guerriero, F. Farina, and F. Profumo, "Current control strategy for power conditioners using sinusoidal signal integrators in synchronous reference frame," *IEEE Trans. Power Electron.*, vol. 20, no. 6, pp. 1402–1412, Nov. 2005.

[16] P. Rodriguez, R. Teodorescu, I. Candela, A. Timbus, M. Liserre, and F. Blaabjerg, "New positive-sequence voltage detector for grid synchronization of power converters under faulty grid conditions," in *Power Electronics Specialists Conference, 2006. PESC '06. 37th IEEE*, June 2006, pp. 1–7.

[17] P. Rodriguez, J. Pou, J. Bergas, J. Candela, R. Burgos, and D. Boroyevich, "Decoupled double synchronous reference frame pll for power converters control," *IEEE Trans. Power Electron.*, vol. 22, no. 2, pp. 584–592, March 2007.

[18] Y. F. Wang and Y. W. Li, "Three-phase cascaded delayed signal cancellation pll for fast selective harmonic detection," *IEEE Trans. Ind. Electron.*, vol. 60, no. 4, pp. 1452–1463, April 2013.

[19] S. Golestan, M. Ramezani, J. Guerrero, F. Freijedo, and M. Monfared, "Moving average filter based phase-locked loops: Performance analysis and design guidelines," *IEEE Trans. Power Electron.*, vol. 29, no. 6, pp. 2750–2763, June 2014.

[20] J. Wang, J. Liang, F. Gao, L. Zhang, and Z. Wang, "A method to improve the dynamic performance of moving average filter-based pll," *IEEE Trans. Power Electron.*, vol. 30, no. 10, pp. 5978–5990, Oct. 2015.

[21] B. McGrath, D. Holmes, and J. Galloway, "Power converter line synchronization using a discrete fourier transform (dft) based on a variable sample rate," *IEEE Trans. Power Electron.*, vol. 20, no. 4, pp. 877–884, July 2005.

[22] V. Moreno, M. Liserre, A. Pigazo, and A. Dell'Aquila, "A comparative analysis of real-time algorithms for power signal decomposition in multiple synchronous reference frames," *IEEE Trans. Power Electron.*, vol. 22, no. 4, pp. 1280–1289, July 2007.

[23] D. Yazdani, M. Mojiri, A. Bakhshai, and G. Joos, "A fast and accurate synchronization technique for extraction of symmetrical components," *IEEE Trans. Power Electron.*, vol. 24, no. 3, pp. 674–684, March 2009.

[24] D. Yazdani, A. Bakhshai, G. Joos, and M. Mojiri, "A real-time extraction of harmonic and reactive current in a nonlinear load for grid-connected converters," *IEEE Trans. Ind. Electron.*, vol. 56, no. 6, pp. 2185–2189, June 2009.

[25] D. Yazdani, A. Bakhshai, and P. K. Jain, "A three-phase adaptive notch filter-based approach to harmonic/reactive current extraction and

1551-3203 (c) 2016 IEEE. Personal use is permitted, but republication/redistribution requires IEEE permission. See http://www.ieee.org/publications_standards/publications/rights/index.html for more information.

This article has been accepted for publication in a future issue of this journal, but has not been fully edited. Content may change prior to final publication. Citation information: DOI 10.1109/TII.2017.2665477, IEEE Transactions on Industrial Informatics

harmonic decomposition," *IEEE Trans. Power Electron.*, vol. 25, no. 4, pp. 914–923, April 2010.

[26] B. Singh, S. Arya, A. Chandra, and K. Al-Haddad, "Implementation of adaptive filter in distribution static compensator," *IEEE Trans. Ind. Appl.*, vol. 50, no. 5, pp. 3026–3036, Sept. 2014.

[27] A. Shitole, H. Suryawanshi, S. Sathyan, and M. Renge, "Adaptive notch filter based synchronization technique for integration of distributed generation systems to utility grid," in *Industrial Electronics Society, IECON 2014 - 40th Annual Conference of the IEEE*, Oct. 2014, pp. 5457–5461.

[28] G. Yin, L. Guo, and X. Li, "An amplitude adaptive notch filter for grid signal processing," *IEEE Trans. Power Electron.*, vol. 28, no. 6, pp. 2638–2641, June 2013.

[29] A. B. Shitole, H. M. Suryawanshi, and S. Sathyan, "Comparative evaluation of synchronization techniques for grid interconnection of renewable energy sources," in *Industrial Electronics Society, IECON 2015 - 41st Annual Conference of the IEEE*, Nov. 2015, pp. 001 436–001 441.

[30] A. Yazdani and R. Iravani, *Grid-Imposed Frequency VSC System: Control in dq-Frame*. Wiley-IEEE Press, 2010, p. 541.

[31] *OP4500 RT-LAB-RCP/HIL SYSTEM USER GUIDE*, OPAL-RT Technologies, Inc. 1751 Richardson, suite 2525 Montral (Qubec) Canada H3K 1G6, 2013.

[32] W. M. Grady and R. J. Gilleskie, "Harmonics and how they relate to power factor," in *Proc. of EPRI PQ Issues and Opportunities Conference (PQA 93), San Diego, CA*, Nov. 1993.

Amardeep B. Shitole received the B.E. degree in electrical engineering from Government College of Engineering Karad, India, in 2008 and M.Tech. degree in power systems (electrical engineering) from College of Engineering Pune, India, in 2012. Currently he is pursing Ph.D. degree in electrical engineering at VNIT, Nagpur, India. His research interests include power electronics, renewable energy integration, AC Micro-grid and power quality.

Hiralal M. Suryawanshi (M'06-SM'12) received the B.E. degree in electrical engineering from Walchand College of Engineering, Sangli, India, in 1988 and M.E. degree in electrical engineering from Indian Institute of Science, Bangalore, India, in 1994. He has been awarded Ph.D. degree by Nagpur University, India, in 1999. Professor Suryawanshi is an Associate Editor of IEEE Transaction on Industrial Electronics. His research interest includes the field of power electronics and drives, resonant converters, renewable energy integration, power factor correction, FACTS devices, multilevel converters, high frequency electronic ballast.

Girish G. Talapur received the B.Tech. degree in electrical and electronics engineering from RGM College of Engineering and Technology, Nandyal, India in 2009; M.Tech. degree in power systems from Delhi Technological University, New Delhi, India in 2012. He is currently working towards Ph.D. degree in electrical engineering at VNIT, Nagpur, India. His research interests include high-power converters, distributed generation, AC Micro-grid, power quality and DC Micro-grid.

Shelas Sathyan received B.Tech. degree in electrical and electronics engineering from Government College of Engineering Kannur, India in 2009 and M.Tech. degree in power electronics and drives from VNIT, Nagpur, India in 2012. Currently he is working towards Ph.D. degree in electrical engineering at VNIT, Nagpur, India. His research interest includes DC-DC converters for renewable energy sources, soft switching and power factor correction.

Makarand S. Ballal (M'15-SM'16) received B.E. degree in electrical engineering from Government College of Engineering, Aurangabad, India in 1993, M.Tech. degree in integrated power system from VNIT, Nagpur, India in 1997 and Ph.D. in electrical engineering from R.T.M. Nagpur University, India in 2007. He is currently an Associate Professor in the department of electrical engineering, VNIT, Nagpur, India. His current research interests include condition monitoring of electrical machines, power quality, power electronics and drives.

Vijay B. Borghate (M'12) received B.E. (electrical engineering), M.Tech. (integrated power system) and Ph.D. (electrical engineering) from VNIT, Nagpur, India, in 1982, 1984 and 2007 respectively. He is currently working as a Professor in the department of electrical engineering, in the same institute. His area of research includes resonant converters, multilevel inverters.

Manoj R. Ramteke (M'15) received M.Tech. and Ph.D. degrees in electrical engineering from Nagpur University, India, in 1994 and 2008 respectively. He is currently working as an Associate Professor in the department of electrical engineering, VNIT, Nagpur. His research interest includes resonant converters and power quality.

Madhuri A. Chaudhari (M'15) received B.E. degree from Amaravati University, India, M.Tech. degree from Visvesvaraya Regional College of Engineering, Nagpur, India, and the Ph.D. degree from VNIT, Nagpur, India, all in electrical engineering. She is currently an Associate Professor with the department of electrical engineering, VNIT, Nagpur. Her research interests are in the areas of power electronics, FACTS, ac-dc drives and power quality.

1551-3203 (c) 2016 IEEE. Personal use is permitted, but republication/redistribution requires IEEE permission. See http://www.ieee.org/publications_standards/publications/rights/index.html for more information.

This article has been accepted for publication in a future issue of this journal, but has not been fully edited. Content may change prior to final publication. Citation information: DOI 10.1109/TIE.2017.2677359, IEEE Transactions on Industrial Electronics

Implementation of Echo-State Network Based Control for Power Quality Improvement

Manoj Badoni, Bhim Singh, *Fellow, IEEE* and Alka Singh, *Senior Member, IEEE*

***Abstract*— This paper proposes a new control algorithm for mitigation of power quality problems at the distribution level. The control algorithm is designed on the basis of echo-state network, which is a type of recurrent neural network. This technique is used to extract fundamental weight components from non-sinusoidal load currents. These weight components are used to evaluate reference grid currents and consequently generate switching logic for the voltage source converter used in the active filter. The shunt connected active filter with the proposed control algorithm is used to overcome several current related power quality problems and provides the load compensation. Problems such as the presence of lower order harmonics, insufficient reactive power and load unbalancing are corrected using a shunt filter in both the power factor correction (PFC) and voltage regulation (VR) modes. The proposed control algorithm is validated on a real time system which is a prototype of a shunt filter. The algorithm is tested in MATLAB using Sim Power Systems and SIMULINK and implemented on a digital signal processor.**

***Index Terms*— Power quality, harmonics, shunt active filter, echo state network, recurrent neural network**

I. Introduction

Electric power system is getting polluted due to an increase in power electronics based converters in household appliances and industrial equipment. Substantial increase in nonlinear loads, such as converters, switch mode power supplies (SMPS), arc furnaces, electric/ electronic discharge lighting, variable speed drives, computers, fax machines and house hold electronic equipment installed at the distribution level play a major role in distorting the sinusoidal waveform of supply voltages and currents. The main concern of electricity consumers is to obtain uninterruptable power supply with improved power quality. For the electrical utility, there are several sensitive loads viz. hospitals and processing plants that require unpolluted and uninterruptable electric power supply [1]. Thus, to ensure quality power to all consumers even when some of the loads are themselves polluting in nature, becomes a major challenge. The power quality problems related to currents are mainly harmonics, insufficient reactive power and unbalanced loads and these affect the performance of other equipment, which are coupled at point of common connection (PCC). International standards have been recommended to specify the permissible limit of power quality problems and to provide guidelines for the end user, manufacturer and utility to improve the quality of power [2]-[3]. The mitigation of harmonics and other power quality issues are important tasks of utility companies. Today shunt active power filters (SAPFs) are the popular choice in achieving good power quality levels. The SAPFs are utilized for harmonics suppression, reactive power generation/ absorption and providing compensating currents to balance the load. An implementation of a shunt active filter in a cost effective way, becomes possible because of remarkable development in area of semiconductor devices related to power and signal processing [4]. Research in this area has led to innovations in the area of different configurations and control algorithms for the control of the shunt active filter. Akagi et al. [5] have discussed a three phase compensator controlled by instantaneous reactive power technique. Singh et al. [6] have developed power balance theory for active power filter for directing AC mains real power, reactive power flow and harmonics from the active filter to the load. Rao et al. [7] have discussed instantaneous symmetrical component theory (ISCT) for compensation under three phase balanced/ unbalanced supply voltages and the advantages and drawbacks of these control algorithms are presented based on various current and voltage related power quality problems. Silva et al. [8] have presented control based on modified synchronous reference frame (MSRF) for SAPF.

An adaptive control theory is based on the automatic adjustment of controller in an organized and calculated manner during the control operation by changing process parameters [9]-[11]. A number of publications are available on control algorithms for SAPF based on adaptive control such as adaptive notch filter [12], Wiener and least mean square (LMS) filters [13], recursive least square [14], improved linear sinusoidal tracer [15], frequency-adaptive fractional-order repetitive control [16], immune feedback controller [17], and recursive least square (RLS) control in which the convergence rate and tracking capabilities are controlled by variable forgetting factor [18]. The field of artificial intelligence has

Manuscript received May 04, 2016; revised July 01, 2016 and December 3, 2016; accepted January 14, 2017.

Manoj Badoni is with the Department of Electrical and Electronics Engineering, KIET Group of Institutions, Ghaziabad, India (e-mail: manojbadoni23@gmail.com).

Bhim Singh is with the Department of Electrical Engineering, Indian Institute of Technology, Delhi, India (e-mail: bhimsinghiitd60@gmail.com).

Alka Singh is with the Department of Electrical Engineering, Delhi Technological University, Delhi, India (e-mail: alkasingh.dr@gmail.com).

0278-0046 (c) 2016 IEEE. Personal use is permitted, but republication/redistribution requires IEEE permission. See http://www.ieee.org/publications_standards/publications/rights/index.html for more information.

This article has been accepted for publication in a future issue of this journal, but has not been fully edited. Content may change prior to final publication. Citation information: DOI 10.1109/TIE.2017.2677359, IEEE Transactions on Industrial Electronics

been recognized as a powerful tool for the design of suitable controllers and tracking. These control algorithms have the capability of learning, self-organizing or self-adapting. Artificial neural network (ANN) and fuzzy inference system based controllers along with their varied combinations are presented in the literature [19]-[21]. The echo state network technique also known as type of recurrent neural network (RNN) has been found suitable for fundamental weight extraction from distorted load currents. The proposed network shows considerable training promptness and tracking properties than other types of recurrent neural network. Fast training speed of echo state network has made this method suitable as a system identifier and closed loop controller in power system [22]-[23]. Some other advantages include good dynamic response making it suitable for real time applications. Due to these characteristics, this technique has been used for varied applications such as satellite channel equalization [24], multimachine power system [25], identification of load harmonics [26] etc.

In this paper, the echo-state network is applied for the computation of fundamental components of load currents from non-sinusoidal load currents. These components of load currents so obtained are then processed for calculation of reference grid currents. This kind of network is simple and easy to implement. All SAPF features such as harmonics rejection, compensation of load reactive power and load unbalancing are implemented in both the control modes using simulation and experimental studies on the system. Results with an echo-state network control algorithm are compared with the SRFT and LMS control algorithms on several parameters.

II. System Configuration

A three-phase, AC mains with grid impedance, shown using series resistive inductive (R_s-L_s) branch, feeds a three phase nonlinear load as shown in Fig. 1. The SAPF is designed using three-leg voltage source converter (VSC) which uses two insulated gate bipolar transistors (IGBTs) with anti-parallel diodes in each of the three legs and DC link capacitor (C_{dc}) at DC side. Three inductors (L_f) are used to couple the VSC to the grid. Passive filters comprise series connected resistive (R_f) and capacitive (C_f) elements coupled to the PCC, and these are suitably chosen to suppress switching noise of VSC. A diode bridge rectifier having R-L series elements represents nonlinear load and is indicative of the actual load that injects harmonics in the AC system. The scaled model of SAPF is implemented in the laboratory (with VSC) and echo state network control is implemented by means of DSP (dSPACE 1104 R&D controller) embedded in the computer.

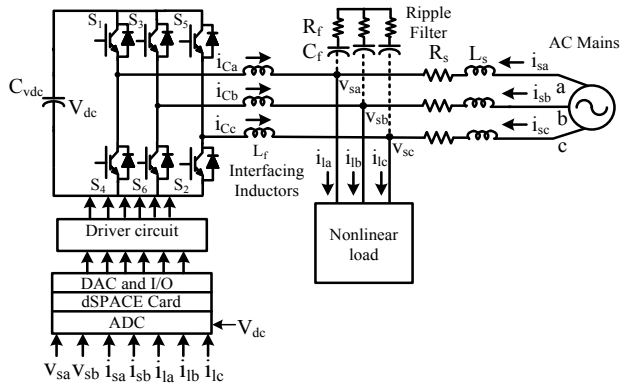

Fig. 1 Configuration of three-phase SAPF

III. Controller Design

The echo-state network control algorithm is developed for the computation of fundamental current components. The extraction of weight components along with formation of reference currents and gating pulses is described here.

A. Computation of Fundamental Active Current Components of Reference Grid Currents

The complete block diagram of control algorithm incorporating echo- state network technique is shown in Fig. 2. Three phase voltages (v_{sa}, v_{sb} and v_{sc}) at the PCC are sensed and their peak value is determined as follows,

$$V_t = \sqrt{2(v_{sa}^2 + v_{sb}^2 + v_{sc}^2)/3} \quad (1)$$

Using PCC voltage magnitude, the unit inphase components are calculated as,

$$u_{pa} = v_{sa}/V_t;\ u_{pb} = v_{sb}/V_t;\ \text{and}\ u_{pc} = v_{sc}/V_t \quad (2)$$

The low pass filter of 12 Hz bandwidth is used to suppress AC ripples in the sensed DC bus voltage. A proportional-integral (PI) controller over DC link voltage regulates it to reference (V_{dc}^*). The output of this controller at n^{th} sampling moment is computed as follows,

$$w_{pdc}(n) = w_{pdc}(n-1) + k_{pd}\{v_{de}(n) - v_{de}(n-1)\} + k_{id}\{v_{de}(n)\} \quad (3)$$

where the gains of PI controller are as k_{pd} and k_{id}.

The fundamental equation describing a computation of active power weights of load currents as described in [23] is as,

$$w_p(n+1) = w_p(n) + \eta x(n+1)^T e(n+1) + \gamma x(n)^T e(n) \quad (4)$$

where 'e' is error computed between sensed load current (i_l) and estimated load current (i_{est}), $x(n)$ is input vector, η and γ are defined as learning and momentum gains. Both the learning and momentum gains vary in a range of 0 to 1 and the selected values for η and γ are 0.5 and 0.35, respectively.

The updation of weights is made in such a manner that the mean square error (MSE) is reduced. At n^{th} sampling instant, this is defined as,

$$\text{MSE} = \frac{1}{r}\sum_{n=1}^{r}\big(i_l(n) - i_{est}(n)\big) = \frac{1}{r}\sum_{n=1}^{r}\big(i_l(n) - x(n)w_p\big) \quad (5)$$

where r is the length of input and output sequence. The length of the input and output sequences for the algorithm is [2×1].

The fundamental active power weights (w_{pa}, w_{pb} and w_{pc}) corresponding to three phase load currents are formulated by (4) as,

$$w_{pa}(n+1) = w_{pa}(n) + \eta u_{pa}\, e_a(n+1) + \gamma u_{pa}\, e_a(n) \quad (6)$$

$$w_{pb}(n+1) = w_{pb}(n) + \eta u_{pb}\, e_b(n+1) + \gamma u_{pb}\, e_b(n) \quad (7)$$

$$w_{pc}(n+1) = w_{pc}(n) + \eta u_{pc}\, e_c(n+1) + \gamma u_{pc}\, e_c(n) \quad (8)$$

0278-0046 (c) 2016 IEEE. Personal use is permitted, but republication/redistribution requires IEEE permission. See http://www.ieee.org/publications_standards/publications/rights/index.html for more information.

This article has been accepted for publication in a future issue of this journal, but has not been fully edited. Content may change prior to final publication. Citation information: DOI 10.1109/TIE.2017.2677359, IEEE Transactions on Industrial Electronics

The average magnitude of weights (w_{pavg}) corresponding to active power components (w_{pa}, w_{pb} and w_{pc}) is given as,

$$w_{pavg} = (w_{pa} + w_{pb} + w_{pc})/3 \quad (9)$$

The total reference weight (w_p) corresponding to active power component is obtained by adding the average weight (w_{pavg}) and the DC bus PI controller weight (w_{pdc}) as,

$$w_p = w_{pavg} + w_{pdc} \quad (10)$$

The reference currents (i_{pa}^*, i_{pb}^* and i_{pc}^*) corresponding to fundamental active component are computed by using (2) and (10) as,

$$i_{pa}^* = w_p u_{pa},\ i_{pb}^* = w_p u_{pb} \text{ and } i_{pc}^* = w_p u_{pc} \quad (11)$$

These active reference grid currents are used to compute total reference grid currents.

B. Computation of Fundamental Reactive Components of Reference Grid Currents Using Echo-State Network

The unit quadrature vectors of PCC voltages are calculated from unit in-phase templates (u_{pa}, u_{pb} and u_{pc}) as,

$$u_{qa} = -u_{pb}/\sqrt{3} + u_{pc}/\sqrt{3} \quad (12)$$

$$u_{qb} = \sqrt{3}\,u_{pa}/2 + (u_{pb} - u_{pc})/2\sqrt{3} \quad (13)$$

$$u_{qc} = -\sqrt{3}\,u_{pa}/2 + (u_{pb} - u_{pc})/2\sqrt{3} \quad (14)$$

The voltage regulation using SAPF is performed by means of an additional PI controller realized over the peak of PCC voltage (V_t). The error between the actual and the desired peak voltage is passed through a PI controller and output (w_t) is computed at n^{th} sampling instant as,

$$w_t(n) = w_t(n-1) + k_{pq}\{v_{te}(n) - v_{te}(n-1)\} + k_{iq}\{v_{te}(n)\} \quad (15)$$

where k_{pq} and k_{iq} represent gains of this PI controller.

The reactive weights (w_{qa}, w_{qb} and w_{qc}) from non-sinusoidal load currents are computed by using (4) as,

$$w_{qa}(n+1) = w_{qa}(n) + \eta u_{qa}\, e_a(n+1) + \gamma u_{qa}\, e_a(n) \quad (16)$$

$$w_{qb}(n+1) = w_{qb}(n) + \eta u_{qb}\, e_b(n+1) + \gamma u_{qb}\, e_b(n) \quad (17)$$

$$w_{qc}(n+1) = w_{qc}(n) + \eta u_{qc}\, e_c(n+1) + \gamma u_{qc}\, e_c(n) \quad (18)$$

The average weight (w_{qavg}) of reactive constituent is calculated from the amplitude of load reactive weight components (w_{qa}, w_{qb} and w_{qc}) as,

$$w_{qavg} = (w_{qa} + w_{qb} + w_{qc})/3 \quad (19)$$

The reference reactive constituent (w_q) is computed by subtracting average weight (w_{qavg}) from output of AC bus PI controller (w_t). Here, w_t is used to compensate for the voltage drop due to grid impedance and loading on the system as,

$$w_q = w_t - w_{qavg} \quad (20)$$

Reference currents of fundamental reactive power component are calculated using unit quadrature templates given in (12) to (14) and reference reactive weight given by (20) as,

$$i_{qa}^* = w_q u_{qa},\ i_{qb}^* = w_q u_{qb} \text{ and } i_{qc}^* = w_q u_{qc} \quad (21)$$

These fundamental reactive components are utilized with fundamental active components given by (11) to generate references given as follows.

C. Computation of References and Gating Pulses

The addition of active (i_{pa}^*, i_{pb}^* and i_{pc}^*) and reactive (i_{qa}^*, i_{qb}^* and i_{qc}^*) components of reference grid currents using (11) and (21) gives total reference grid currents (i_{sa}^*, i_{sb}^* and i_{sc}^*) as,

$$i_{sa}^* = i_{pa}^* + i_{qa}^*,\ i_{sb}^* = i_{pb}^* + i_{qb}^* \text{ and } i_{sc}^* = i_{pc}^* + i_{qc}^* \quad (22)$$

The grid currents are sensed and compared with these reference grid currents, and the current errors (i_{sae}, i_{sbe} and i_{sce}) are generated which are passed over PWM current controller. Thus, appropriate gating pulses are generated for the SAPF.

IV. Simulation Results

The models of SAPF and its control algorithm, which utilize principle of echo-state network, are developed in MATLAB/SIMULINK. The proposed system is tested at 3-phase 415V, 50Hz grid according to Indian power system standard. This system is tested for numerous power quality problems, which include harmonics reduction, compensating reactive power along with load unbalancing in both operating modes using echo state network based control algorithm. Selected system parameters are given in Appendix-A.

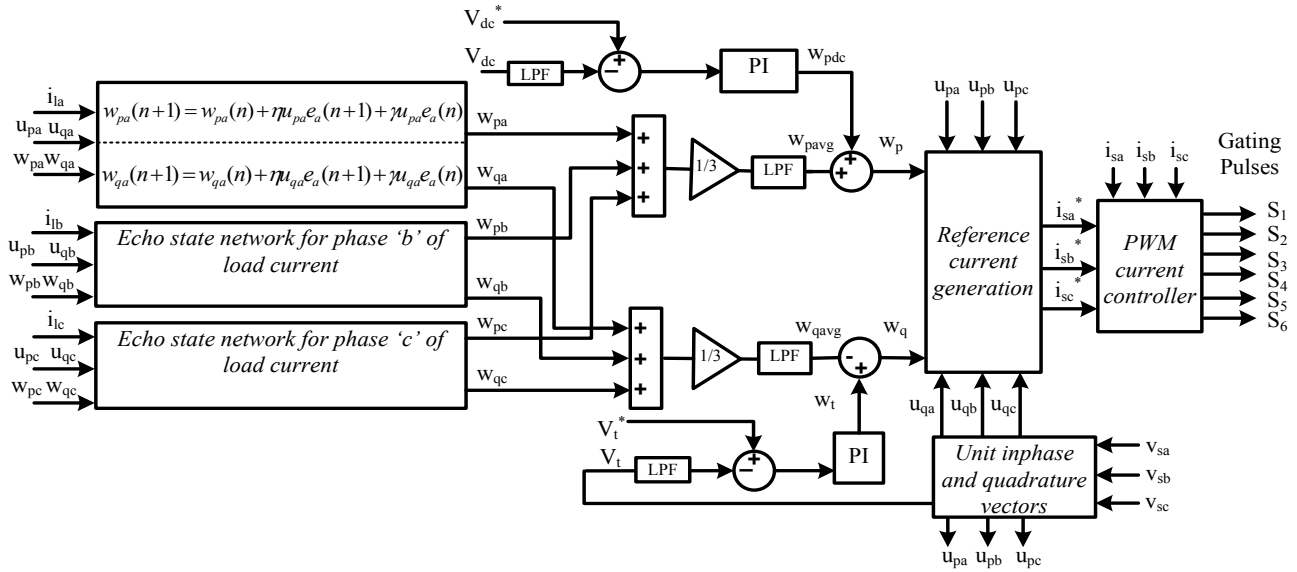

Fig. 2 Controller based on echo-state network for shunt active filter

0278-0046 (c) 2016 IEEE. Personal use is permitted, but republication/redistribution requires IEEE permission. See http://www.ieee.org/publications_standards/publications/rights/index.html for more information.

This article has been accepted for publication in a future issue of this journal, but has not been fully edited. Content may change prior to final publication. Citation information: DOI 10.1109/TIE.2017.2677359, IEEE Transactions on Industrial Electronics

A. Behavior of Echo-State Network Controller in VR Mode

Fig. 3 presents the waveforms and intermediate signals with echo state network based controller for SAPF in VR mode. Fig. 3(a) shows the waveforms of unit in-phase template (u_{pa}), error (e_a) between desired value and estimated value of phase 'a' of load current, its fundamental active weight (w_{pa}), average and filtered weighted value (w_{pavg}) of load currents and reference active power weighed value (w_p) along with PCC voltages (v_s) and load currents (i_l). Fig. 3(a) shows the results for steady state condition (before t=0.3s) under normal load condition and the dynamic load changes are made at t=0.3s and recovered at t=0.4s. The perturbations are introduced in a form of creating a disturbance in loading and sudden switching off the load in phase 'c'. Satisfactory performance of the control algorithm is observed in unbalanced load condition as the grid currents are sinusoidal and balanced under all loading conditions.

Fig. 3(b) presents the unit quadrature template wave shape for phase 'a' (u_{qa}), fundamental reactive power weight (w_{qa}) corresponding to same phase of load current, average and filtered reactive power weight (w_{qavg}), reference reactive power weight (w_q), grid currents (i_s) and reference grid currents (i_s^*). It is clear from Figs. 3(a)-(b) that these obtained weights are settled down within couple of cycles. It is also inferred from these results that grid currents correctly follow reference grid currents in steady state condition even under unbalanced load.

B. Behavior of SAPF in PF Correction Mode

Fig. 4 shows the performance of SAPF in achieving unity PF mode under nonlinear loads. These results depict variation of several system parameters such as voltage (v_s), grid, load and SAF currents along with DC bus voltage (V_{dc}). The steady state condition occurs in the system before t=0.3s and unbalanced load condition is simulated from t=0.3s to t=0.4s. These results confirm that grid currents are perfectly balanced, compensated and in-phase with the supply voltages at PCC. These results show that PF correction is achieved under all considered load conditions and the controller tracks the reference DC bus voltage of 700V.

Harmonic spectra of PCC voltage (v_{sa}), grid current (i_{sa}) and load current (i_{la}) are presented in Fig. 5. The total harmonic distortion (THD) of grid current is achieved to be 1.95% after compensation. The THD in PCC voltage is observed to be 1.55%, which shows there are small distortions in the PCC voltage due to SAPF operation. The harmonic distortions in the grid currents and PCC voltages are observed to be lying within the permitted values as stated in IEEE-519 standard.

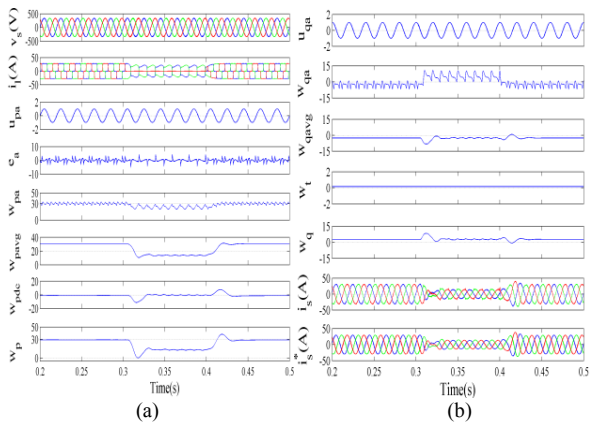

Fig. 3 Behavior of intermediate signals for echo-state network controller

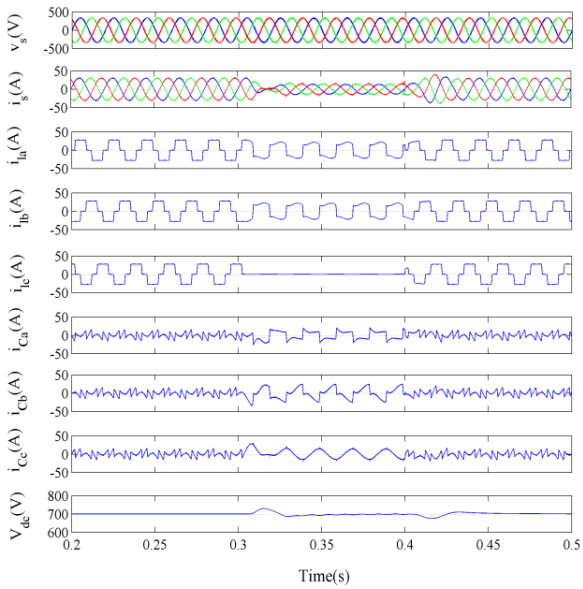

Fig. 4 Behavior of shunt filter in PFC mode

C. Behavior of SAPF in VR Mode Under Unbalanced Load Condition

The behavior of shunt filter is presented in Fig. 6 under different load conditions. The waveforms of grid currents (i_s), SAPF currents along with amplitude of voltage at DC bus (V_{dc}) and AC bus (V_t) are presented in this figure. Besides these, other waveforms shown in Fig. 6 are PCC voltages (v_s) and load currents (i_{la}, i_{lb} and i_{lc}) which are given as inputs to the control algorithm. Reducing distortions in grid currents during steady state condition (before t=0.3s) and under unbalanced load condition (t=0.3s and t=0.4s) are observed. Grid currents obtained after filter action are balanced and sinusoidal under different load conditions due to SAPF control action. The voltages at the DC link and at the PCC terminals are controlled at their reference values of 700V and 338.8V, respectively.

Fig. 7 depicts the harmonics of PCC voltage (v_{sa}), grid current (i_{sa}) and load current (i_{la}) in VR mode. These results show that a low THD of 2.03% in grid current is achieved, though there is THD of 27.18% in load current. This figure shows 1.88% THD in PCC voltage, which indicates less distortion in PCC voltage due to SAPF operation in VR mode. An IEEE-519 standard is thereby adhered for harmonics for the system chosen.

D. Comparative Performance of Echo-State Network Control Algorithm

0278-0046 (c) 2016 IEEE. Personal use is permitted, but republication/redistribution requires IEEE permission. See http://www.ieee.org/publications_standards/publications/rights/index.html for more information.

This article has been accepted for publication in a future issue of this journal, but has not been fully edited. Content may change prior to final publication. Citation information: DOI 10.1109/TIE.2017.2677359, IEEE Transactions on Industrial Electronics

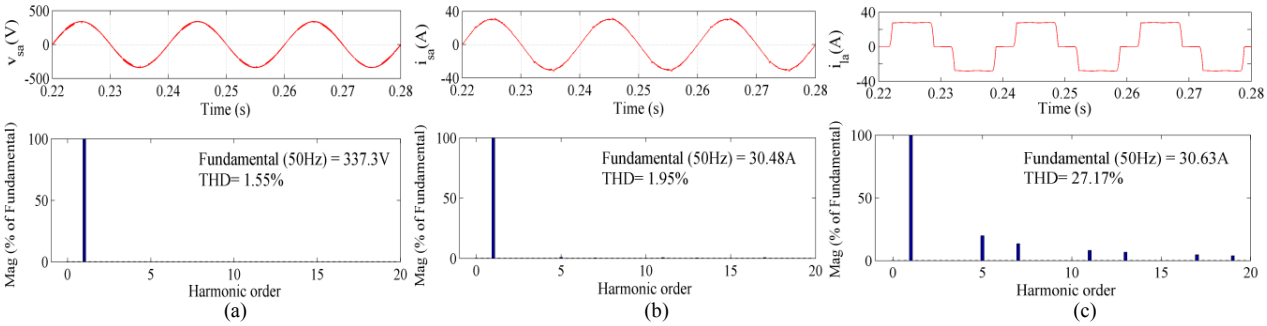

Fig. 5 Harmonic spectra of phase 'a' of (a) PCC voltage, v_{sa} (b) supply current, i_{sa} (c) load current, i_{la} in PFC mode

The proposed echo state network based control algorithm for SAPF is compared with SRFT control algorithm and LMS control algorithm [8], [13]. Figs. 8 (a) and (b) show the harmonic content in grid current (i_{sa}) obtained with SRFT control algorithm and LMS control algorithm, respectively. Harmonic spectra of grid current (i_{sa}) and load current (i_{la}) for echo-state network based control algorithm in PFC mode is shown in Fig. 5. It is observed from a comparison of all these results that THDs of grid current of the order of 2.75% and 3.41% are obtained using SRFT control algorithm and LMS control algorithm, whereas THD of grid current of the order of 1.95% is obtained with echo-state network based control algorithm. Fig. 9 compares a convergence of fundamental active power weight (w_{pa}) in the two weight based algorithms viz. echo-state network and LMS control algorithm. Faster weight convergence with echo-state network controller is a definite advantage. Moreover, there are oscillations in the weight extracted with LMS control algorithm. The echo-state network control algorithm achieves improved performance in load compensation. The comparative performances of echo-state network, SRF and LMS control algorithms are summarized in Table-I demonstrating a superior performance of echo-state network control algorithm.

V. Experimental Results

Performance of the echo-state network control algorithm for active filter is endorsed on an implemented prototype. The rating of shunt filter is scaled down (3-ph, 110V and 50Hz) due to available laboratory equipment constraints. The shunt filter is developed using a three phase VSC, which contains six IGBT switches. The gating pulses for control of VSC are generated by DSP (dSPACE 1104 R&D controller). Voltage and current sensors with suitable buffer circuits are utilized for sensing PCC voltages, voltage at DC bus and grid/load currents. Parameters for experimental prototype are given in Appendix-B.

A. *Behavior of Echo-State Network Controller for Shunt Active Filter*

Intermediate signals obtained with echo-state network control algorithm for the control of SAPF are presented in Fig.10. It represents waveforms of PCC voltage (v_{sa}), filtered PCC voltage (v_{saf}) obtained by second order band pass filter, phase 'a' of load current (i_{la}) and input vector to the control algorithm, which is unit in-phase template (u_{pa}) in Fig 10(a). Fig. 10(b) depicts waveforms of voltage at DC bus (V_{dc}), the output of DC bus PI controller (w_{pdc}), averaged fundamental active power weight component of load currents (w_{pavg}) and reference active power weight (w_p). Fig. 10(c) depicts waveforms of PCC voltage magnitude (V_t), output of PI controller at AC bus (w_t), averaged fundamental reactive weight value of load currents (w_{qavg}) and reference reactive weight (w_q), which is computed by adding w_{qavg} and w_q. These results are obtained for steady state and unbalanced load conditions at nonlinear loads. Active and reactive power weights are observed to converge to their steady state values under dynamic load changes. Fig. 10(d) presents estimated reference currents (i_{sa}^*, i_{sb}^* and i_{sc}^*) along with phase 'a' of grid current (i_{sa}). These results presented in Fig. 10 show adequate behavior of the echo-state network control algorithm for control of SAPF. It is observed that the grid currents follow the reference grid currents generated using echo state network algorithm in different load conditions.

B. *Steady State Behavior of SAPF*

Fig. 11 depicts the behavior of SAF in steady state condition. Waveforms of grid current for phase 'a' (i_{sa}), load current (i_{la}) and SAPF current (i_{ca}) along with phase 'a' of PCC voltage are depicted in Figs. 11(a), (c) and (e). The grid

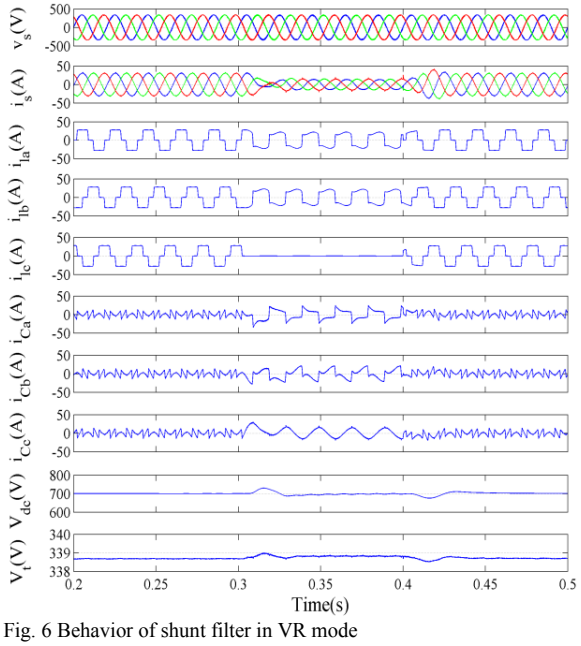

Fig. 6 Behavior of shunt filter in VR mode

0278-0046 (c) 2016 IEEE. Personal use is permitted, but republication/redistribution requires IEEE permission. See http://www.ieee.org/publications_standards/publications/rights/index.html for more information.

This article has been accepted for publication in a future issue of this journal, but has not been fully edited. Content may change prior to final publication. Citation information: DOI 10.1109/TIE.2017.2677359, IEEE Transactions on Industrial Electronics

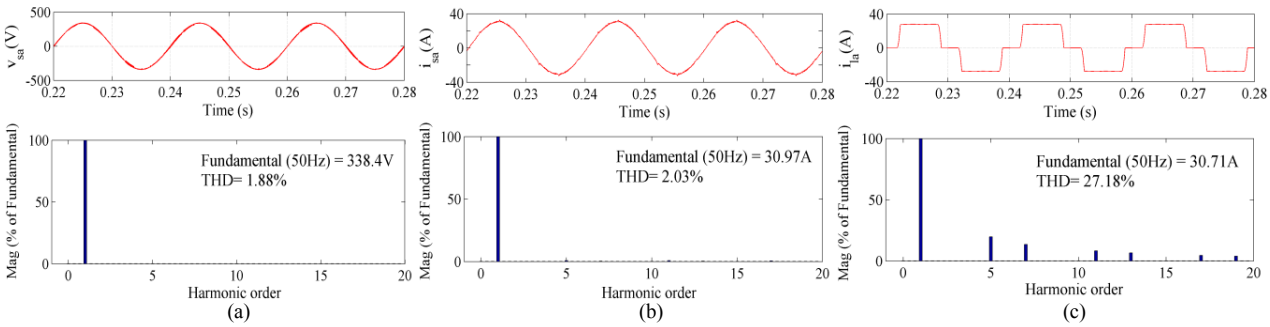

Fig. 7 Harmonic spectra of phase 'a' of (a) PCC voltage, v_{sa} (b) supply current, i_{sa} (c) load current, i_{la} in VR mode

current is compensated by proposed algorithm and is also distortion free, after compensation thus achieving power factor correction. The fundamental constituent of load current is provided by the grid only while SAF provides reactive power and harmonics. Harmonic spectra of grid (i_{sa}) and load current (i_{la}) accompanied by PCC voltage (v_{sa}) are presented in Figs. 11(b), (d) and (f). The obtained THDs in the grid and load current are 3.8%, 21.4% when the PCC voltage has a THD of 2.3% respectively. Grid current distortion after compensation is obtained as 3.8%, which is <5% (limit stated in an IEEE-519 Standard). The voltage at PCC is not affected much by switching of VSC and its THD lies within a limit of 5%.

C. *Dynamic Behavior of SAF Under Nonlinear Load*

Fig. 12 depicts test results under varying load conditions. Fig. 12(a) shows waveforms of grid currents (i_{sa}, i_{sb} and i_{sc}) along with phase 'a' of PCC voltage (v_{sa}) when unbalancing in load is introduced by opening circuit breaker in phase 'c'. These results show the decreased magnitude of grid currents during load unbalancing, but remain balanced and sinusoidal by SAPF action. Fig. 12(b) shows waveforms of load currents (i_{la}, i_{lb} and i_{lc}) drawn by nonlinear load along with v_{sa}. Fig. 12(c) shows SAPF currents (i_{ca}, i_{cb} and i_{cc}) along with v_{sa}, under same load dynamics. Except the fundamental component of load power, all other harmonics, reactive and unbalanced components are delivered by SAPF. Fig. 12(d) depicts the waveforms of all three currents viz. grid (i_{sc}), load (i_{lc}) and filter current (i_{cc}) for phase-'c' along with voltage at DC bus (V_{dc}) for load compensation. This figure shows that the voltage at DC link of SAPF is regulated to V_{dc}^* (200V) within couple of cycles during load unbalancing and this has been achieved using a PI controller and proposed echo control algorithm. These results present the behavior of SAPF using under closed loop echo state network control algorithm for mitigating power quality problems to satisfactory level.

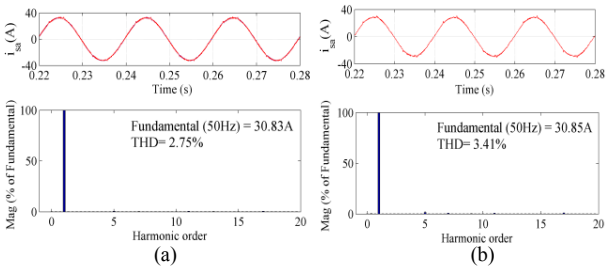

Fig. 8 Harmonic spectra of grid current (a) SRF and (b) LMS techniques

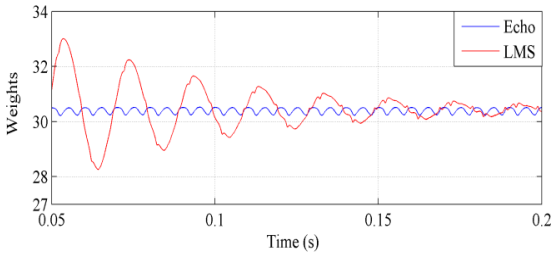

Fig. 9 Weight convergence with echo state network and LMS based controller

TABLE I
COMPARATIVE PERFORMANCE OF ECHO-STATE NETWORK BASED CONTROL

Features		**Echo-state network**	**SRF theory**	**LMS Technique**
Modeling		Easy based on a few mathematical operations	Complex require more mathematical operations	Step-size selection is difficult
PLL required		No	Yes	No
Harmonic compensation	Supply current THD	30.48A, 1.95%	30.83A, 2.75%	30.85A, 3.41%
	Load current THD	30.63A, 27.17%	30.63A, 27.17%	30.63A, 27.17%
Weight convergence		Fast	Not weight based	Large oscillations
Sampling time (T_s)		45µs	60µs	60µs

VI. CONCLUSION

The echo-state network algorithm has been applied for the control of SAPF. This filter has been used for load compensation and improving power factor, reducing lower order harmonics and balancing of three-phase load. These aforesaid power quality problems have been alleviated with SAPF operation in two different modes viz. PFC and VR. The proposed control technique has been found suitable for extracting fundamental active and reactive weights components from the distorted load currents. The advantages of this control algorithm have been observed in terms of simplicity to implement on DSP, improved harmonic

0278-0046 (c) 2016 IEEE. Personal use is permitted, but republication/redistribution requires IEEE permission. See http://www.ieee.org/publications_standards/publications/rights/index.html for more information.

This article has been accepted for publication in a future issue of this journal, but has not been fully edited. Content may change prior to final publication. Citation information: DOI 10.1109/TIE.2017.2677359, IEEE Transactions on Industrial Electronics

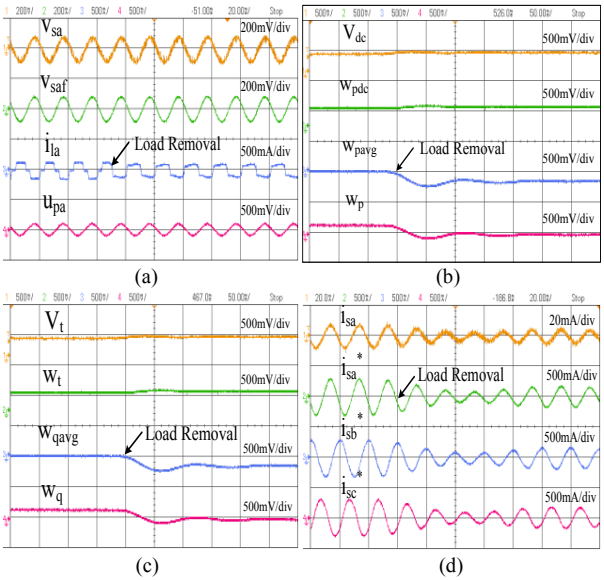

Fig. 10 Intermediate signals of echo-state network controller from experimental setup

compensation, fast weight convergence and less computational burden, when compared to SRFT and LMS based control algorithms. It has offered less computational burden (45µs) in real time implementation on the processor. Extensive results have been presented in detail along with the intermediate signals. These results highlight the satisfactory performance of SAPF using echo state network based control algorithm under a variety of load conditions including load unbalancing of the severest form when one phase of the load is switched off. Experimental validation of the algorithm has been achieved and the results show a 3.8% THD in grid current after compensation, which is a substantial improvement from 21.4% THD in load current, thereby meeting limits specified in an IEEE 519 standard.

APPENDIX-A

AC mains: 415V (L-L), 50Hz; R_s=0.05Ω, L_s=1mH; VSC rating 25kVA; ripple filters R_f=5Ω, C_f=5μF; interfacing inductor L_f=3mH; DC bus capacitor C_{dc}=1650μF; DC bus

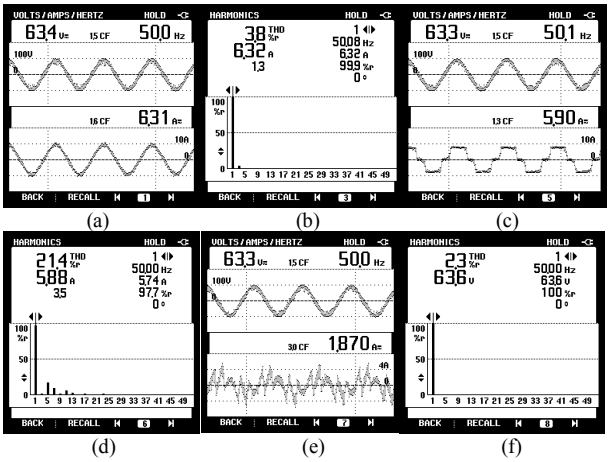

Fig. 11 Steady state behavior of shunt filter under balanced load condition (a), (c) and (d) i_{sa}, i_{la} and i_{ca} along with v_{sa} (b), (d) and (f) Harmonic spectra of grid current, load current and PCC voltage

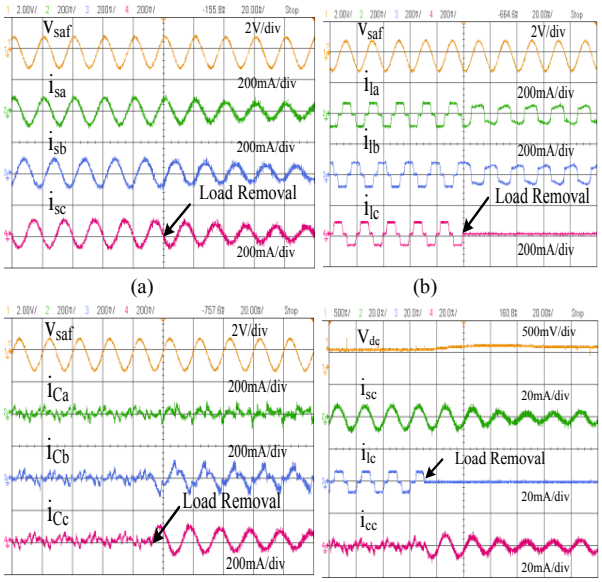

Fig. 12 Dynamic behavior of SAPF under unbalanced nonlinear load (a) grid currents (b) load currents (c) filter currents along with v_{sa} (d) i_{sc}, i_{lc} and i_{cc} along with V_{dc}

voltage V_{dc}=700V; DC bus PI gains k_{pd}=0.25, k_{id}=0.53; AC bus PI gains k_{pq}=0.010, k_{iq}=0.011; diode rectifier (three phase) with R=12Ω and L=200mH.

APPENDIX-B

AC mains 110V (L-L), 50 Hz; L_f=2.5mH; DC bus capacitor C_{dc}=1650μF; DC bus voltage V_{dc}=200V; 3-phase uncontrolled rectifier with R varies from 18 to 60 Ω and L=100mH; f_{sw} of PWM current controller=10kHz, cutoff frequency of LPF=12Hz.

ACKNOWLEDGEMENT

The authors would like to thank the Department of Science and Technology, Government of India for the Sponsored Research project.

REFERENCES

[1] B. Singh, A. Chandra, and K. Al-Haddad, *Power quality: problems and mitigation techniques*, John Wiley & Sons Ltd., U.K, 2015.

[2] A. Ghosh and G. Ledwich, *Power quality enhancement using custom power devices*, Springer International Edition, Delhi, 2009.

[3] B. Singh, K. Al-Haddad and A. Chandra, "A review of active filters for power quality improvement," *IEEE Trans. Ind. Electron.*, vol. 46, no. 5, pp. 960-971, Oct 1999.

[4] C. Lascu, L. Asiminoaei, I. Boldea and F. Blaabjerg, "High Performance Current Controller for Selective Harmonic Compensation in Active Power Filters," *IEEE Trans. Power Electron.*, vol. 22, no. 5, pp. 1826-1835, Sept. 2007.

[5] H. Akagi, Y. Kanazawa and A. Nabae, "Instantaneous reactive power compensators comprising switching devices without energy storage components" *IEEE Trans. Ind. Applications,* vol. 20, no. 3, pp. 625-630, May/June 1984.

[6] B.N. Singh, B. Singh, A. Chandra and K. Al-Haddad, "Design and digital implementation of active filter with power balance theory," *IEE Proc.-Electr. Power Appl.*, vol. 152, no. 5, Sep. 2005, pp. 1149-1160.

[7] U.K. Rao, M.K. Mishra and A. Ghosh, "Control strategies for load compensation using instantaneous symmetrical component theory

0278-0046 (c) 2016 IEEE. Personal use is permitted, but republication/redistribution requires IEEE permission. See http://www.ieee.org/publications_standards/publications/rights/index.html for more information.

This article has been accepted for publication in a future issue of this journal, but has not been fully edited. Content may change prior to final publication. Citation information: DOI 10.1109/TIE.2017.2677359, IEEE Transactions on Industrial Electronics

under different supply voltages," *IEEE Trans. Power Del.*, vol. 23, pp. 2310-2317, 2008.
[8] C. H. da Silva, R. R. Pereira, L. E. B. da Silva, G. Lambert-Torres and B. K. Bose, "Improving the dynamic response of shunt active power filter using modified Synchronous Reference Frame PLL," in *Proc. 34th Annual Conference of IEEE Industrial Electronics*, 2008, pp. 790-795.
[9] Simon S. Haykin, *Adaptive Filter Theory*, Person Education India, 2008.
[10] B. Singh, S. R. Arya, A. Chandra and K. Al-Haddad, "Implementation of adaptive filter in distribution static compensator," *IEEE Trans. Ind. Applications,* vol. 50, no. 5, pp. 3026-3036, Sept.-Oct. 2014.
[11] Q. Wang, N. Wu and Z. Wang, "A neuron adaptive detecting approach of harmonic current for APF and its realization of analog circuit," *IEEE Trans. Instru. and Measu.*, vol.50, no.1, pp.77-84, Feb 2001.
[12] D. Yazdani, A. Bakhshai, G. Joos and M. Mojiri, "An adaptive notch filtering approach for harmonic and reactive current extraction in active power filters," in *Proc. 34th Annual Conference of IEEE Industrial Electronics, IECON*, 10-13 Nov. 2008, pp. 535-538.
[13] M. Badoni, A. Singh and B. Singh, "Comparative performance of Wiener filter and adaptive least mean square-based control for power quality improvement," *IEEE Trans. Ind. Electron.*, vol. 63, no. 5, pp. 3028-3037, May 2016.
[14] R.R. Pereira, C.H. da Silva, L.E.B. da Silva, G. Lambert-Torres and J.O.P. Pinto, "New strategies for application of adaptive filters in active power filters," *IEEE Trans. Ind. Applications*, vol.47, no.3, pp.1136-1141, May-June 2011.
[15] B. Singh and S. R. Arya, "Adaptive Theory-Based Improved Linear Sinusoidal Tracer Control Algorithm for DSTATCOM," *IEEE Trans. Power Electron.*, vol.28, no.8, pp.3768-3778, Aug. 2013.
[16] Z. X. Zou, K. Zhou, Z. Wang and M. Cheng, "Frequency-Adaptive Fractional-Order Repetitive Control of Shunt Active Power Filters," *IEEE Trans. Ind. Electron.*, vol.62, no.3, pp.1659-1668, March 2015.
[17] M. Badoni, A. Singh and B. Singh, "DSP based implementation of an immune feedback algorithm for control of shunt compensator," *IEEE International Conf. on Power Systems (ICPS)*, New Delhi, 2016, pp. 1-6.
[18] M. Badoni, A. Singh and B. Singh, "Variable Forgetting Factor Recursive Least Square Control Algorithm for DSTATCOM," *IEEE Trans. Power Delivery*, vol. 30, no. 5, pp. 2353-2361, Oct. 2015.
[19] B. Singh, V. Verma and J. Solanki, "Neural network-based selective compensation of current quality problems in distribution system," *IEEE Trans. Ind. Electron.*, vol.54, no.1, pp.53-60, Feb. 2007.
[20] M. Singh and A. Chandra, "Real-time implementation of ANFIS control for renewable interfacing inverter in 3P4W distribution network," *IEEE Trans. Ind. Elect.*, vol.60, no.1, pp.121–128, Jan. 2013.
[21] N. Altin and I. Sefa, "dSPACE based adaptive neuro-fuzzy controller of grid interactive inverter," *Energ. Convers. Manage.*, vol. 56, pp.130-139, May. 2012.
[22] J. Dai, P. Zhang, J. Mazumdar, R. G. Harley and G.K. Venayagamoorthy, "A comparison of MLP, RNN and ESN in determining harmonic contributions from nonlinear loads," In *Proc. IEEE Conf. on Industrial Electronics, Orlando*, 2008, pp.3025-3032.
[23] J. Dai, G.K. Venayagamoorthy and R.G. Harley, "Harmonic identification using an Echo State Network for adaptive control of an active filter in an electric ship," In *Proc. International Joint Conference on Neural Networks (IJCNN'09)*, 14-19 June 2009, pp.634-640.
[24] M. Bauduin, S. Massar and F. Horlin, "Non-linear satellite channel equalization based on a low complexity Echo State Network," in *Proc. Annual Conf. on Information Science and Sys.(CISS)*, 2016, pp. 99-104.
[25] G.K. Venayagamoorthy, "Online design of an echo state network based wide area monitor for a multimachine power system," *Neural Networks*, vol.20, no. 3, pp. 404-413, April 2007.
[26] J. Mazumdar and R. G. Harley, "Utilization of echo state networks for differentiating source and nonlinear load harmonics in the utility network," *IEEE Trans. Power Electron.*, vol. 23, no. 6, pp. 2738-2745, Nov. 2008.

Manoj Badoni received the B. Tech. in Instrumentation Engineering form University Science and Instrumentation Centre, Srinagar Garhwal, Uttrakhand in 2006, M.E. degree in Electronics Engineering from Punjab Engineering College, Chandigarh, India in 2008 and Ph.D degree in Electrical Engineering from Delhi Technological University, Delhi, India in 2016.
In 2016, he has joined Department of Electrical and Electronics Engineering, KIET Group of Institutions, Ghaziabad as Assistant Professor. His areas of research interest include power electronics, power quality, and distributed generation.

Bhim Singh (SM'99–F'10) received the B.E. (Electrical) degree from the University of Roorkee, Roorkee, India, in 1977 and the M.Tech. (Power Apparatus & Systems) and Ph.D. degrees from the Indian Institute of Technology (IIT) Delhi, New Delhi, India, in 1979 and 1983, respectively. In 1983, he joined the Department of Electrical Engineering, University of Roorkee, as a Lecturer. He became a Reader there in 1988. In December 1990, he joined the Department of Electrical Engineering, IIT Delhi, as an Assistant Professor, where he became an Associate Professor in 1994 and a Professor in 1997. He has guided 65 Ph.D. dissertations and 162 M.E./M.Tech. theses. He has been granted one U.S. patent and filed 22 Indian patents. He has executed more than seventy five sponsored and consultancy projects. He has co-authored a text book on power quality: *Power Quality Problems and Mitigation Techniques* published by John Wiley & Sons Ltd. 2015. Prof. Singh is a Fellow of the Indian National Academy of Engineering (FNAE), The Indian National Science Academy (FNA), The National Academy of Science, India (FNASc), The Indian Academy of Sciences, India (FASc), The World Academy of Sciences (FTWAS), Institute of Electrical and Electronics Engineers (FIEEE), the Institute of Engineering and Technology (FIET), Institution of Engineers (India) (FIE), and Institution of Electronics and Telecommunication Engineers (FIETE) and a Life Member of the Indian Society for Technical Education (ISTE), System Society of India (SSI), and National Institution of Quality and Reliability (NIQR).

Alka Singh (SM'15) received the B.E. degree in Electrical Engineering from Delhi College of Engineering, Delhi, India, in 1996, the M.Tech. Degree in Power Systems from the Indian Institute of Technology, New Delhi, India, in 2001, and the Ph.D. degree from Netaji Subash Institute of Technology (Delhi University), Delhi, India, in 2006. Currently, she is working as an Associate Professor in the Department of Electrical Engineering, Delhi Technological University, Delhi. Her research interests include power systems, and power quality. She has more than 15 years of teaching and industrial experience. She is a Life Member of the Indian Society for Technical Education.

0278-0046 (c) 2016 IEEE. Personal use is permitted, but republication/redistribution requires IEEE permission. See http://www.ieee.org/publications_standards/publications/rights/index.html for more information.

Influence of Aliphatic and Aromatic Isocyanates on the Properties of Polyether-Ester Polyol Based PU Adhesive System

Manjeet Malik,[1] **Raminder Kaur**[2]
[1] *Research Scholar, Department of Applied Chemistry & Polymer Technology, Delhi Technological University, New Delhi, 110042, India*
[2] *Assistant professor, Department of Polymer Science and Chemical Technology, Delhi Technological University, New Delhi, 110042, India*

This study has been conducted with an emphasis to develop a biobased polyol from canola oil by transesterification reaction followed by epoxidation and ring opening reaction with an intention to insert hydroxyl group at unsaturation sites. The products obtained were characterized by nuclear magnetic resonance and FTIR spectroscopy for structural analysis and to determine the extent of reaction. Furthur, the studies have been conducted on different Polyurethane (PU) adhesives obtained by reacting this resulted canola oil based polyether-ester polyol and various kinds of aliphatic or aromatic diisocyanates commercially available, i.e., Methylenediphenyldiisocyanate (MDI), Toulenediisocyanate (TDI), Isophoronediisocyanate (IPDI), Hexamethylenediisocyanate (HMDI) with a purpose to examine their influence on adhesive properties such as green strength, curing time, gel time, lap shear strength. The properties of resulted polyurethanes had shown considerable (or prominent) variation in their behavior particularly in terms of thermal stability, adhesion strength, corrosion resistance, etc. The synthesized adhesive showed much better performance as compared to commercially available adhesive formulation under different conditions of testing. The thermal stability of PU adhesive formulation were analyzed and compared by thermogravimetric analysis. POLYM. ENG. SCI., 00:000–000, 2017. © 2017 Society of Plastics Engineers

INTRODUCTION

Like many other polymers, the present research on polyurethane synthesis is more focused on the biobased resources due to many major concerns like depletion of crude oil stock in world, its inflated price and most importantly the environmental concerns [1–3]. Till last few decades petroleum resources were the major suppliers of the raw material for manufacturing polyurethanes. But in the recent years, different research groups had done fruitful efforts towards the synthesis of biopolyol based polyurethanes, for example, Kiatsimkul et al. showed synthesized polyols with high hydroxyl equivalent weight from epoxidized soyabean oil [4]. Further, Zhang et al. developed polyols by reacting castor oil with epoxidized soyabean oil via ring opening mechanism [5]. The importance of chemical modification of natural oils and its application in Polyurethane (PU) synthesis has been extensively discussed [6]. The rationality in choosing triglyceride based oil is their easy availability, low cost and high scope of modifications to get desirable results in biopolymer synthesis. Different methods for introduction of OH groups in vegetable oil have been tried in different researches so far, like by hydroformylation [7, 8], hydrolysis [9], ozonolysis [10, 11], epoxidation [12, 13], microbial conversion [14], transesterification [15] etc. The studies revealed that that the properties of polyurethanes largely depends on the nature of raw material used in its preparation, i.e., the type of polyol and diisocyanates used (their functionalities and chemical structure). Lu et al. examined the variations in physical and mechanical properties with hydroxyl functionalities in soy based polyols in PU films [16]. Ugarte, et al. [17] studied the effect of nature of diisocyanate on morphology of thermoplastic PU. Peruzzo et al. in their research showed the variation in different properties of waterborne polyurethane acrylates with different diisocyanates [18]. After the discovery of polyurethanes by Bayer in 1937, the production of diisocyanates has been tremendously increased as properties of the product can be easily altered by simply varying the isocyanate precursors, e.g., Toulenediisocyanate (TDI) introduce flexibility in the product whereas product made from Methylenediphenyldiisocyanate (MDI) are found to be relatively rigid. Basically, the nature of polyol used and the kind of diisocyanate moiety have maximum contribution in determining the properties of PU formulation. So, products with wide range of mechanical strength (or properties) according to the need of end product can be achieved in PU's mainly by varying the polyols and isocyanate moiety. The high reactivity of diisocyanates even at low temperature conditions and for highly viscous solution makes them a much better in tailoring the end product properties by just varying the nature of diisocyanate moiety. So, it is important to study the properties of polyurethanes obtained from different type of isocyanate precursors. In this research, emphasis has been given on the development of canola oil based polyol by transesterification reaction followed by epoxidation and ring opening by alcoholysis with the intention of inserting hydroxyl group at unsaturation (carbon-carbon double bond) present in oil. Furthur, the properties of different PU adhesives obtained by reacting this resulted canola oil based polyether-ester polyol and different kind of aliphatic or aromatic diisocyanates, i.e., MDI, TDI, Isophoronediisocyanate (IPDI), and Hexamethylenediisocyanate (HMDI) has been extensively studied under different conditions. The structural determination and thermal behavior of the products obtained was established by using different characterization techniques namely NMR (nuclear magnetic resonance), IR, Thermogravimetric analysis (TGA), etc.

Correspondence to: R. Kaur; e-mail: rkwalia14@gmail.com
DOI 10.1002/pen.24537
Published online in Wiley Online Library (wileyonlinelibrary.com).
© 2017 Society of Plastics Engineers

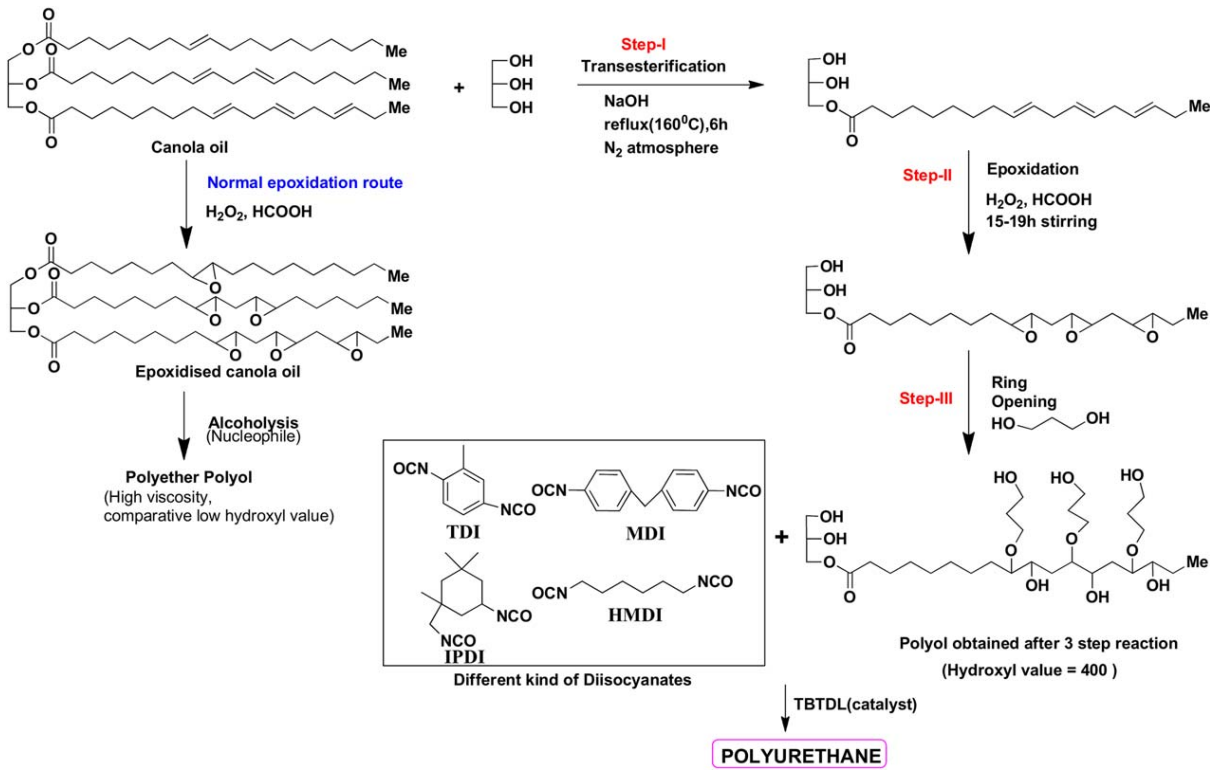

FIG. 1. Synthetic route for the formation of Canola Oil based Polyol and PU adhesive system. [Color figure can be viewed at wileyonlinelibrary.com].

EXPERIMENTAL

Material and Methods

Materials. Canola oil was purchased from Krishna enterprises, Tilak Nagar, Delhi, India. Magnesium sulphate and sodium chloride were obtained from Fisher scientific. Hydrogen peroxide, ethyl acetate and n-hexane of Sigma-Aldrich were used. MDI, TDI, IPDI and HMDI were obtained from Linopack Pvt Ltd., Parwanoo, Himachal Pradesh, India. All the chemical were of analytical grade and were used without any further purification. The canola oil was heated at 100°C for 1 day in vacuum oven, prior to use, to eliminate the moisture of oil, if any.

Methodology

Preparation of Polyols. Polyol was synthesized in a three step reaction as shown in Fig. 1.The steps involved in the polyol synthesis are discussed in the subsequent section.

Transesterification of Canola Oil (Step I in Fig. 1). Canola oil and glycerol in molar ratio 1:3 along with NaOH (0.5% w/w of canola oil) were added in a 500 ml four necked round bottomed flask, equipped with N_2 gas inlet, thermometer, and a reflux condenser. The reaction contents in the flask were continuously stirred for the next 6 h at 160°C in inert atmosphere with the help of a magnetic stirrer. After the completion of the reaction (after 6 h), the reaction mixture was shaken vigorously with 250 ml of n-hexane in a separating funnel to separate the unreacted glycerol. The unreacted glycerol that formed the bottom layer in the funnel, was separated out and collected separately. Further, the n-hexane present in the reaction mixture was removed from transesterified canola oil on rotary evaporator under vacuum to get the concentrated product.

Epoxidation of Transesterified Canola Oil (Step II in Fig. 1). Trans-. Transesterified canola oil obtained from aforementioned procedure is mixed with formic acid (1:3 molar ratio) in a round bottom flask and cooled at zero degree centigrade in an ice bath. A pre-calculated amount of hydrogen peroxide was then added dropwise to the contents of the round bottom flask with continuous stirring. After complete addition of H_2O_2, the reaction was continued at room temperature under vigorous stirring, until iodine value indicate complete consumption of olefinic group. The reaction mixture was then transferred in separating funnel followed by addition of ethyl acetate and removal of lower aqueous layer contents. The remaining organic content was further washed with water, sodium bicarbonate and brine. Lastly the contents were dried with sodium sulphate and concentrated under vacuum in rotary evaporator to get the clear solution of epoxidized oil.

Preparation of Polyol (Ring Opening with 1,3-Propandiol) (Step III in Fig. 1). The dried product obtained after step II, i.e., epoxide oil was stirred with 1,3-propanediol in 1:10 molar ratio along with 10.0 mol% sulphuric acid at 60°C for 48 h under low vacuum (10mm Hg) as previously reported [19]. After the completion of reaction, ethyl acetate was added in equal volume followed by washing of organic layer with sodium bicarbonate and brine. The remaining aqueous content in the product was then removed with anhydrous sodium sulphate, filtered and separated on a rotary evaporator under vacuum to get the final polyol.

 DOI 10.1002/pen

Preparation of PU Adhesive

Different adhesive formulations of PU were prepared by following the method already described by the author in some other studies [20]. Briefly, the above prepared polyol of hydroxyl value approximately 400, were mixed with 0.05% TBTDL for 30 minutes on a magnetic stirrer under nitrogen atmosphere. This solution was then made to react with MDI (taking NCO/OH ratio 1.1:1), by mixing them for 1 minute before applying to the wood substrate (preconditioned at $50 \pm 5\%$ relative humidity at 25°C for 7 days). In the similar manner, more PU adhesives were prepared by varying the isocyanate substrate, i.e., TDI, HMDI, and IPDI by the mentioned procedure.

Substrate Bonding with Prepared Adhesive

Heat treatment, good design, surface treatment are the important factors during joint preparation for better adhesion [21]. In the present work, we have selected good quality teak wood strips of dimensions 300mm × 25mm × 3mm for the adhesive application. After cleaning the surface with sandpaper grit no.60 to make them free from loose particles, the wood substrate were further conditioned at $50 \pm 5\%$ relative humidity at 25°C for 7 days. Each adhesive sample was used to adhere an area of 25 × 30 mm^2 between two wood pieces and further the adhered wood pieces were left undisturbed for one day under 2.5 kg load before testing them for the lap shear strength.

Characterization

FT-IR spectrophotometer (Nicolet 380) was used to obtain IR spectra of prepared samples. The spectra of epoxidized vegetable oil and polyol was taken on liquid assembly by applying a thin layer of it on crystal surface. The NMR of samples were obtained on 400 MHz FT NMR spectrometer by dissolving samples in deuterated chloroform. Thermal behavior of the prepared PU samples were examined on EXSTAR 6300 thermogravimetric analyser instrument from 30 to 600°C by rising temperature at rate of 10°C per minute under nitrogen atmosphere. The adhesion strength of prepared adhesive samples were tested using Instron 3369 UTM according to ASTM 906-82 (1987). Substrates bonded with adhesive for chemical resistance/corrosion resistance were prepared by the method as stated in the previous section. An average of five samples were taken into account for every formulation tested at 5mm/min crosshead speed for lap shear strength. The type of failure of adhesive joint, i.e., adhesive or cohesive type was visually observed.

RESULTS AND DISCUSSION

FTIR Analysis

As evident from Fig. 2, FTIR spectroscopy confirms the conversion of double bonds present in vegetable oil into epoxides by the appearance of band at wavenumber 823 cm^{-1} which was not present in spectra of oil initially and complete disappearance of sp^2 hybridized carbon-hydrogen (=C-H) stretching band at 3,010 cm^{-1} which shows that olefinic group has been consumed during the reaction. Further in spectra of polyols, (which are formed by ring opening reaction) the above stated bands of epoxide functional group disappeared and new strong bands at 3,440 cm^{-1} due to hydroxyl group (symmetrical stretching), 1,180 cm^{-1} due to ether linkage (asymmetric stretching) and

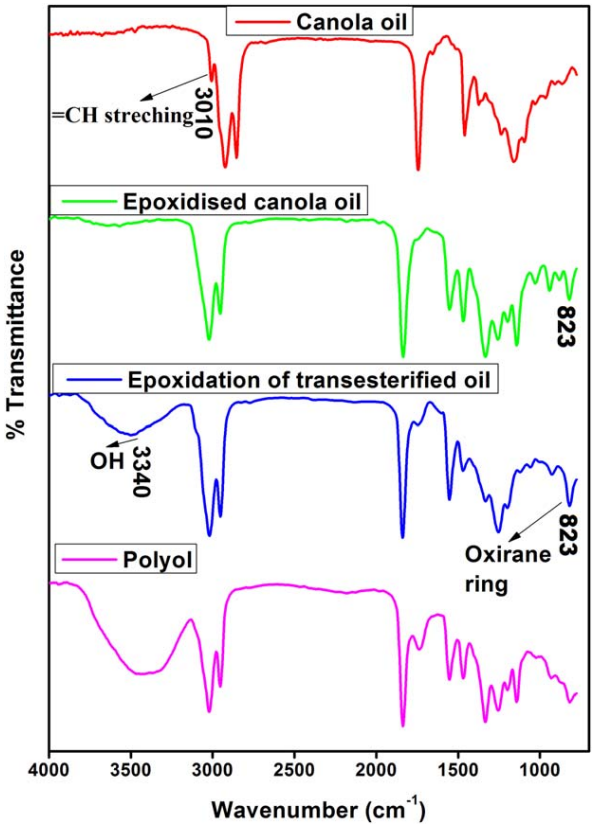

FIG. 2. FTIR spectra of pure Canola oil, fully epoxidised oil, epoxidized - transesterified oil and polyol. [Color figure can be viewed at wileyonlinelibrary.com].

1,740 cm^{-1} stretching band of carbonyl group appeared. The strong signals at wavenumber ranging from 2,800 cm^{-1} to 3,000 cm^{-1} that appeared in all the samples are because of the characteristic stretching vibrations of sp^3 hybridized C-H bond.

NMR Spectra

The ^1H NMR spectras of canola oil and epoxidized oil after transesterification confirms the successful conversion of double bond to epoxy group as seen from Fig. 3. The epoxidised oil sample clearly shows appearance of new peaks at 2.8 to 3.2 ppm (Quatret) due to epoxy protons which were not observed in spectra of canola oil. Also, the spectra of canola oil shows a disappearance of peaks present at 5.2 to 5.4 ppm due to olefinic protons. The common peak shown by both the samples at 0.7–1.0 ppm (Triplet) is due to terminating methyl group. The glycerol moiety shows peak at 4.1–4.2 ppm due to $–CH_2$-OH protons. The CH_2- protons in alkyl chain which are common in both canola oil and the epoxidised product shows peak at 1.2–1.4 ppm. The peaks observed at 2.5–3.0 ppm (Triplet) are due to CH_2 protons adjacent to double bond in case of canola oil sample and are due to CH_2 protons adjacent to epoxy group in epoxidized sample.

Thermal Characterization

In general, polyurethane do not show good thermal stability above 200°C due to the degradation of urethane linkage [22]. The thermal behavior of polyurethane and its complex

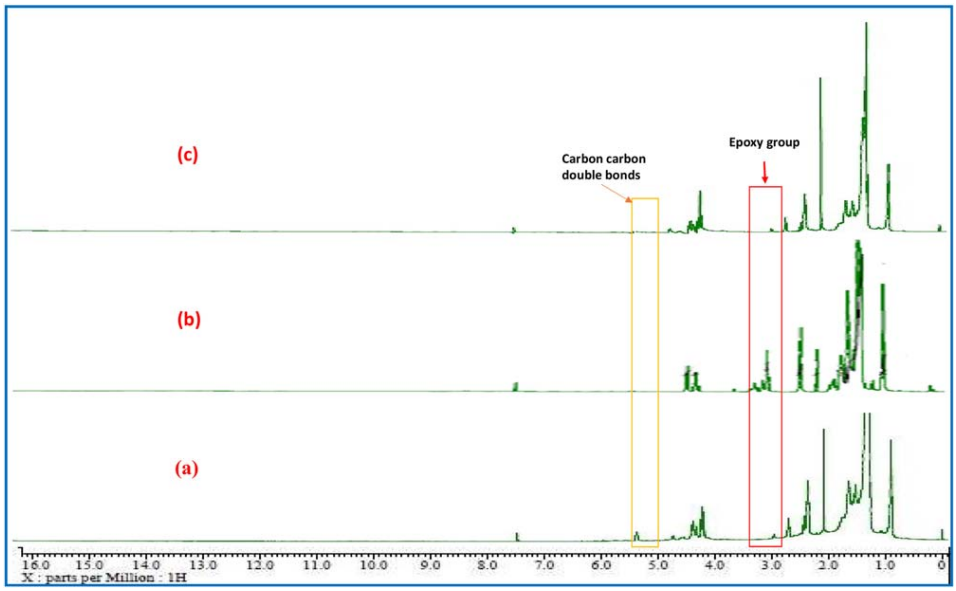

FIG. 3. Proton NMR Spectra of (a) Canola oil (b) Epoxidized oil (c) Polyol. [Color figure can be viewed at wileyonlinelibrary.com].

mechanism of thermal degradation prepared from multifunctional components, for determining its suitability as polymer cores in sandwich plate systems is extensively discussed in the prior studies [23]. Thermal analysis of canola oil based adhesive made up of different isocyanates is shown in Fig. 4 and Fig. 5. As shown in TGA curve, all of the prepared PU adhesive samples have shown a stability upto 250°C and no major degradation has been observed below this temperature. The vegetable oil based PU normally shows degradation in two steps, i.e., first degradation is due to decomposition of the urethane bonding into amines or alcohols or isocyanates and the second is due to breaking of olifienic, carbonyl, ether or carbon-hydrogen linkages, similar to that of previous studies [24]. A comparison of degradation temperatures of PU adhesives made of different kinds of diisocyanates is shown in Table 1. It was suggested

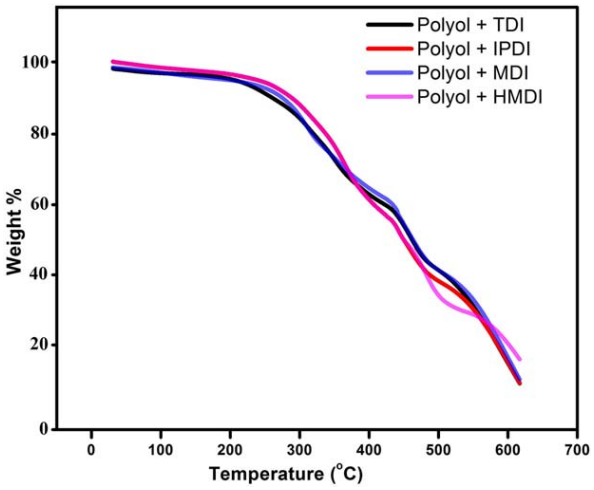

FIG. 4. Comparative TGA of different PU adhesive systems. [Color figure can be viewed at wileyonlinelibrary.com].

that the ease of urethane bond formation is inversely proportional to their stability [25]. Accordingly the following is the thermal stability order of structurely different diisocyanates: aryl-NCO/aryl-OH<alkyl-NCO/aryl-OH<aryl-NCO/alkyl-OH<alky-NCO/alkyl-OH. The polyurethane obtained from aliphatic isocyanates shows somewhat better (at initial stage) thermal stability as compared to the aromatic ones (shows better mid-range stability towards degradation), but the thermal profiles of all the vegetable oil based samples were found to be similar.

Gel Time

The gel time specifies the time period upto which the adhesive formulation remains in the flowing state, thus, indicates its suitability of application between the substrate. The gel time of different PU adhesive formulations are reported in Table 2. From the results obtained, it has been observed that the adhesive formulations with aromatic isocyanate adduct shows lesser gel time as compared to formulations with aliphatic or cycloaliphatic isocyanate moiety.

Green Strength

It is quite clear from the results shown in Table 3 that polyurethane adhesives with aromatic isocyanate moiety shows a little faster curing rate with respect to the adhesives samples possessing aliphatic isocyanates moiety. Although a good curing speed had been shown by all the adhesive samples as they achieved around 70% of their adhesion strength in 24 h and approximately 90% of the fully cured adhesive strength in 48 h. As shown by the experimental results, all the samples show no change in the adhesion strength after 4 days, therefore assumed to be fully cured.

DOI 10.1002/pen

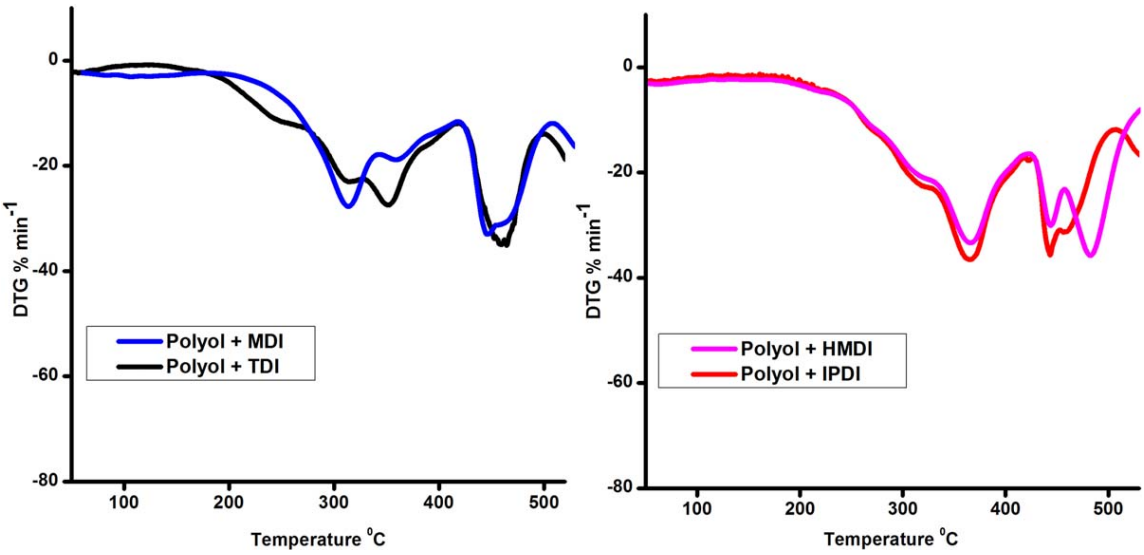

FIG. 5. Comparative DTG of different PU adhesive systems. [Color figure can be viewed at wileyonlinelibrary.com].

TABLE 1. Thermal stability of PU adhesive formulations obtained from different isocyanates.

Components of adhesive sample.	T_{10} (°C)	T_{50} (°C)	T_{90} (°C)	T_{max} (°C)
Polyol+MDI	295	470	616	315, 445
Polyol+TDI	290	465	616	349, 465
Polyol+HMDI	309	452	618	366, 481
Polyol+IPDI	311	455	620	364, 444

TABLE 2. Gel time or pot life of different PU adhesive formulations.

Type of adhesive formulation	Gel time(minutes)
Polyol+MDI	40
Polyol+TDI	35
Polyol+HMDI	50
Polyol+IPDI	55

Chemical/Corrosion Resistance of Prepared PU Samples

The adhesion strength of all the samples remain unaffected from water (both cold and hot water) where as 5% NaCl and 0.1M HCl has shown very little effect. N/10 NaOH has shown the highest deteriorating effect on adhesion strength of prepared PU adhesives. It has been observed that adhesive samples prepared from aliphatic isocyanate and cycloaliphatic moiety show more resistance as compared to isocyanates with aromatic moiety as reported in Table 4.

CONCLUSIONS

Polyether ester polyol from epoxidation of transesterified canola oil were successfully synthesized and the products obtained were characterized by NMR and FTIR spectroscopy for structural analysis. The thermal stability of the resulted PU

TABLE 3. Green strength of different PU adhesive formulations.

Time after adhesive application	Average Lap shear strength in MPa (±5)			
	PU1 adhesive (Polyol+MDI)	PU2 adhesive (Polyol+TDI)	PU3 adhesive (Polyol+HMDI)	PU4 adhesive (Polyol+IPDI)
5h	17	19	14	16
10h	32	33	28	27
24h	39	39	36	34
48h	48	47	44	45
4 day	56	54	53	56

TABLE 4. Chemical resistance of different PU adhesive formulations.

Type of adhesive system	Avg. Lap shear strength (before exposure) MPa ±5	Average Lap shear strength (after exposure) ±5 MPa				
		Cold water	Hot water	5% NaCl	Acid	Base
Polyol+MDI	56	53	52	53	48	44
Polyol+TDI	54	51	51	51	47	42
Polyol+HMDI	53	50	50	50	49	47
Polyol+IPDI	56	53	52	52	50	48
Commercial wood adhesive	36	29	25	26	24	20

adhesive formulations were analyzed by therogravimetric analysis. It was found that formulations possessing aliphatic moiety shows more stability initially whereas the aromatic ones shows better mid-range thermal degradation resistance. Further, PU adhesive having aliphatic isocyanates takes more time for curing and shows lesser green strength but it offers a better environmental resistance in comparison to the the formulations with aromatic isocyanates. Lastly, the synthesized adhesive shows much better performance in different conditions as compared to commercially available adhesive formulation.

NOMENCLATURE

HMDI	Hexamethylenediisocyanate
IPDI	Isophoronediisocyanate
MDI	Methylenediphenyldiisocyanates
NMR	nuclear magnetic resonance
PU	Polyurethane
TDI	Toulenediisocyanates
TGA	Thermogravimetric analysis

REFERENCES

1. B. Nohra, L. Candy, J.F. Blanco, C. Guerin, Y. Raoul, and Z. Mouloungui, *Macromolecules*, **46**, 3771 (2013).
2. D.P. Pfister, Y. Xia, and R.C. Larock, *ChemSusChem*, **4**, 703 (2011).
3. L. Jong and Z. Liu, *Polym. Eng Sci*., **00**, 1 (2016). doi:10.1002/pen.24410.
4. P.P. Kiatsimkul, G.J. Suppes, F.H. Hsieh, Z. Lozada, and Y.C. Tu, *Ind. Crop Prod*., **27**, 257 (2008).
5. C.Q. Zhang, Y. Xia, R.Q. Chen, S. Huh, P.A. Johnston, and M.R. Kessler, *Green Chem*., **15**, 1477 (2013).
6. J. Datta and E. Glowinska, *J. Elastom. Plast*., **46**, 33 (2014).
7. A. Guo, D. Demydov, W. Zhang, and Z.S. Petrovic, *J. Polym. Environ*., **10**, 49 (2002).
8. Z.S. Petrovic, A. Guo, I. Javni, I. Cvetkovic, and D.P. Hong, *Polym. Int*., **57**, 275 (2008).
9. Y. Guo, J.H. Hardesty, V.M. Mannari, and J.L. John Massingill, *J. Am. Oil Chem. Soc*., **84**, 929 (2007).
10. S.N. Narine, J. Yue, and X. Kong, *J. Am. Oil Chem. Soc*., **84**, 173 (2007).
11. P. Tran, D. Graiver, and R. Narayan, *J. Am. Oil Chem. Soc*., **82**, 653 (2005).
12. A. Guo, Y. Cho, and Z.S. Petrovic, *J. Polym. Sci. Part A Polym. Chem*., **38**, 3900 (2000).
13. B. Lin, L. Yang, H. Dai, and A. Yi, *J. Am. Oil Chem. Soc*., **85**, 113 (2008).
14. C.T. Hou and J.T. Lin, *Biocatal Agric Biotechnol*, **2**, 1 (2013).
15. R. Kaur and M. Kumar, *J. Polym. Eng*., **33**, 875 (2013).
16. Y.S. Lu and R.C. Larock, *Biomacromolecules*, **9**, 3332 (2008).
17. L. Ugarte, B. Fernández-d'Arlas, A. Valea, M.L. González, M.A. Corcuera, and A. Eceiza, *Polym. Eng. Sci*., **54**, 2282 (2014).
18. P.J. Peruzzo, P.S. Anbinder, O.R. Pardini, J.R. Vega, and J.I. Amalvy, *Polym. J*., **44**, 232 −(2012).
19. J. Curtis, G. Liu, T. Omonov and E. Kharraz, U.S. Patent, 0274, 494 A1 (2013).
20. M. Malik and R. Kaur, *Adv. Polym. Technol*., **00**, 21637 (2015). doi:10.1002/adv.21637.
21. J. Datta and M. Lewicki, *J. Elastom. Plast*., **47**, 320 (2015).
22. I. Javni, Z.S. Petrovic, A. Guo, and R. Fuller, *J. Appl. Polym. Sci*., **77**, 1723 (2000).
23. J. Datta, M. Laski, and J. Kucinska-Lipka, *Przemysl Chemiczny*, **86**, 63 (2007).
24. K.P. Somani, S.S. Kansara, N.K. Patel, and A.K. Rakshit, *Int. J. Adhes. Adhes*., **23**, 269 (2003).
25. J. Simon, F. Barla, A. Kelemen-Haller, F. Farkas, and M. Kraxner, *Chromatographia*, **25**, 99 (1988).

Available online at www.ijapie.org

International Journal of Advanced
Production and Industrial Engineering

IJAPIE-SI-MM 509 (2017) 55–62

Special Issue on

MATERIALS
&
MANUFACTURING

Influences of Process Parameter and Microstructural Studies in Friction Stir Welding of Different Alloys: A Review

Husain Mehdi*, R.S. Mishra
(Delhi Technological University, Delhi-110042, India)
**Email: husainmehdi4u@gmail.com*

Abstract : Friction stir welding (FSW) is a relatively new solid state joining process that uses a non-consumable tool to join two different material without melting the workpiece material. Heat is generated by friction between the rotating tool and the workpiece material. This joining process is energy efficient, environment friendly and versatile. Friction stir welding (FSW) was developed for microstructural modification of metallic material. This review article provides an overview of effect of FSW/FSP mechanism responsible for the formation of weld, microstructure refinement, wear of FSW tool and mechanical properties. This review conclude with recommendations for future research direction.

Keywords: Process Parameter, Microstructural Studies, Friction Stir Welding, Different Alloys

INTRODUCTION

Friction stir processing (FSP)/FSW is a method of changing the properties of a metal through intense localized plastic deformation. This deformation is produced by forcibly inserting a non-consumable tool into the workpiece and revolving the tool in a stirring motion as it is pushed laterally through the workpiece. The antecedent of this technique, friction stir welding is used to join multiple piece of metal without creating the heat affected zone typical of fusion welding. In friction stir welding the tool usually has a large diameter shoulder and a small threaded pin. The plate to be welded are aligned together and clamped using fixture. A Cylindrical hole is drilled at one end of the workpiece on the centerline and the pin is inserted into the hole, with the shoulder in contact with the top surface of the workpiece. The tool is rotating at high speed as it is moved along the weld centerline. Heat is generated by friction between the tool and the workpiece and by the plastic deformation of the workpiece material. A schematic diagram of the friction stir welding system is shown in figure 1.

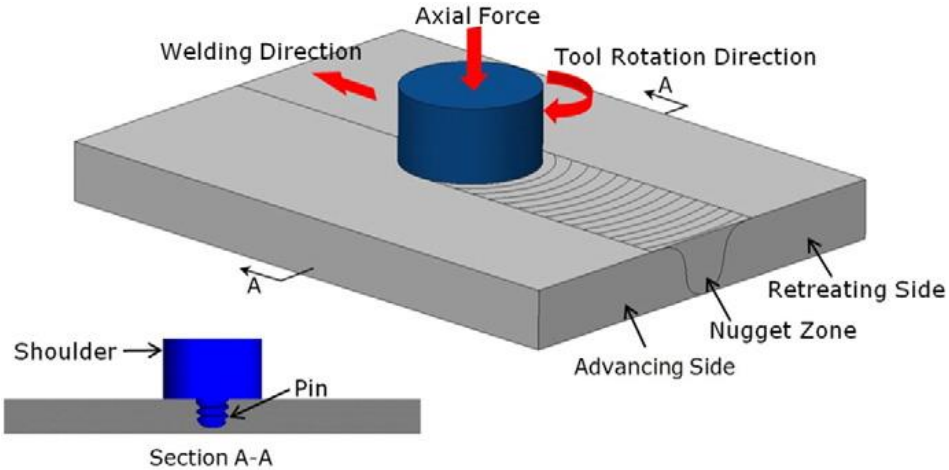

Figure 1:- Friction Stir Welding

LITERATURE REVIEW

The review is presented in a tabular form. 40 research paper related to friction stir welding and friction stir processing of aluminum alloy and other alloys have been considered. The review table given below explain the detail of materials and processing parameters considered by earlier authors.

S.No	Author& year	Material Used	Processing Parameter	Conclusion
1	Y.Wang et al [2007]	Al–4.0Y–4.0Ni–0.9Co Alloy	<table><tr><th>Weld</th><th>Tool Rotation (r.p.m)</th><th>Speed (mm/s)</th><th>Tilt angle</th></tr><tr><td>Weld-1</td><td>1000</td><td>51</td><td>0^0</td></tr><tr><td>Weld-2</td><td>1200</td><td>51</td><td>0^0</td></tr></table>	Significant improvement in ductility was observed after FSW of UFG Al–4.0Y–4.0Ni–0.9Co alloy with a slight decrease in strength. FSW leads to homogenization of the microstructure and change in the shape of intermetallic particles.
2	Indrajit Charit et al [2002]	7475 Al alloy sheets	Two sheets, 2.5 mm thick, were lap joined using two welding conditions, i.e., (a) single-pass and (b) sixpass joints. The FSW parameters were kept the same for both weld procedures. Overlap between passes was one-half of the pin tool diameter. A series of short (5 and 30 min) annealing experiments were performed to evaluate the effect of thermal exposure on the weld joint microstructure.	The microstructure in the weld HAZ is stable and retains superplastic properties. The high strength weld nugget, because of the higher flow stress at 783 K compared to the parent metal (16–18 MPa versus 2–9 MPa), is un-likely to deform during super plastic forming (SPF).
3	V. Jeganathan Arulmoni et al [2015]	99.99% Cu with carbon nano tube	The tool Material used is H13 steel with shoulder diameter 15mm, threaded pin diameter 8 mm, pin length 2.5 mm with tool rotational speed 960 rpm, tool angle 2 and table traverse speed 25 m / min.	It investigate the parameters affecting the friction stir welding of copper with carbon nano tube and enhancement of the microstructure, hardness and tensile properties of the composite material with single pass, double passes and triple passes.
4	Jiye Wang et al [2014]	Titanium alloy Ti–6Al–4V	Processing parameters of 1000 rpm and 25 mm per minute were applied during FSW.	Fracture failure was observed in the CY16 tool. Micro cracking was observed in the WC411 tool with improved fracture toughness, and the crack propagation in the tool was inhibited. Tool degradation due to plastic deformation was observed in the W–La tool, and can be reduced by increasing the pin diameter
5	J-Q-Su et al [2002]	Aluminum alloy 7050-T65	The pin rotation speed was 350 rpm and the pin travel speed was 15 mm/min	Compared to parent material microstructure, the strengthening precipitates have coarsened severely and the precipitate free zone along the grain boundaries has increased by factor of five during friction stir welding, The original base metal grains structure is completely eliminated and replaced by a very fine equiaxed grain structure in the dynamic re-crystallized zone (DXZ).
6	V. Jeganathan et al [2014]	Aluminum Alloy	The rotational speeds (800, 1250, 1600 and 2000rpm) and two traverse speeds 31.5 and 63 mm/min were tried.	It was observed that when the target depth is too large, the shoulder of tool pushes way all the preplaced SiC particles, and basically no surface composite is formed. Too small depth was also ineffective to mix SiC particles into aluminum alloy.
7	S.Jana, et al [2009]	Al–7Si–0.6 Mg alloy	The FSP tool had a pin height of 1.9 mm, a diameter of 4 mm at mid-pin height and a tool	FSP improved the fatigue life of a cast Al–7Si–0.6 Mg alloy by a

			shoulder diameter of 12 mm. Therefore, the FSPed region had a thickness of 2.0 mm. A process parameter combination of 2236 rpm and 2.33 mm/s was used for the FSP runs	factor of 15 when specimens were tested at the same stress level and at a stress ratio of R = 0.
8	Z.Y.Ma et al [2006]	cast A356 aluminum	Tool rotation rate of 300,500,700 and 900 rpm and a traverse speed of 51, 102 and 203 mm/min is used.	Higher tool rotation rate creates a more homogeneous microstructure. The varied distribution pattern, size, and volume fraction of Si particles at different locations within the FSP zone indicates inhomogeneous material flow
9	Patrick B. Berbon [2001]	Aluminum alloys (Al-10%Ti-2%Cu and Al-10%Ti-2%Ni)	Friction stir processing was performed at the Rockwell Science Center using conventional friction stir weld tools and weld parameters.	The homogeneity increased dramatically via friction stir processing. There are no traces of the pure aluminum area left and the largest intermetallic particles have a small size. The strength is very high at the lower temperature. The ductility however is very poor.
10	Z.Y.Ma et al [2002]	7075Aluminum alloy	Two different processing parameters, i.e., 4 ipm/400 rpm and 6 ipm/350 rpm were used to generate the microstructures with different grain sizes.	Grain size will decrease in the temperature range of 420-530 and strain rate range of 1x10-3 to 10-1. For the 3.8µm 7075Al alloy, super plastic elongation of 1250% were obtained at 480 in the strain rate range of 3x10-3 to 3x10-2 s-1, whereas the 7.5 µm 7075Al alloy exhibited a maximum ductility of 1042% at 5000 and 3x10-3 s-1
11	Z.Y.Ma et al [2003]	Al-4Mg-1Zr Alloy	A ram speed of 3 mm/s and temperatures of 400 - 550 C was used.	Fine microstructure with a grain size of 1.5 mm and uniform distribution of fine Al3Zr dispersoids was obtained in Al-4Mg-1Zr alloy via FSP.
12	R.S Mishra et al [2003]	Al-SiC Composite	Tool tranfer rate of 25.4 mm/min and 101.6 mm/min is used for different target depth i.e. 1.78mm, 2.03mm, 2.28mm	When the target depth is too large (2.28mm), the shoulder of tool pushed away all the preplaced SiC particles and basically no surface composite formed. Too small target depth (1.78mm) was also ineffective to mix Sic particles into Al-alloy. A target depth of 2.03 mm resulted in incorporation of SiC particles in Aluminum matrix.
13	S. Jana et al [2007]	Cast Al-Alloy of F357	The tool rotation rate was 2236 rpm, and tool traverse speeds were 0.42, 0.98, 2.33 and 3.67 mm/s.	The multiple pass does not resulted in Si particles refined beyond a certain limit. The multi pass run of second configuration indicate that the extent of AGG can be reduced if the material is FSPed multiple times
14	S. Jana et al [2010]	Al–7Si–0.6Mg alloy	Tool rotation rate of 2236 rpm and travel speed of 2.33 mm/s	FSP led to a five times improvement in fatigue life for a hypoeutectic Al–Si–Mg cast alloy. The cast fatigue specimen showed a life of 45500 cycles. As expected crack were noted to have originated at porosity when the test was stopped after the first 5000 cycles which implies a 10% or lower crack initiation periods.
15	Z.Y.Ma et al [2005]	Al-4Mg-1Zr	The traverse speed of the tool 4ipm and the rotation rate of the tool 350 rpm was used	A maximum super plastic ductility of 1280 pct was observed at 525C and initial strain rate of 1x10-1 s-1. The strain rate sensitivity of

				both as- extruded and FSP Al-4Mg-1Zr increased continuously with increasing strain rate from 1x10-3 s-1 to 1 s-1.
17	S.R Sharma [2004]	A356 Alloy	One plate was processed using a standard FSW pin at 900 rpm and a traverse speed of 203.2 mm per minute and the other plate was processed using a tri-flute pin at 700 rpm and 203.2 mm per minute.	Fatigue life improvement was attributed to significant refinement, homogenization of the microstructure and the elimination of porosity. FSP resulted in a significant breakup and uniform distribution of Si particles in the aluminum matrix as well as elimination of porosity.
18	Jian-Qing Su et al [2011]	Copper	The tool was tilted ~2.5◦opposite the traveling direction during a single processing pass on the Cu sheet at 800 rpm and a travel speed of 120 mm/min.	The material flow in a very thin layer around pin tool resulted in severe strain heterogeneity giving rise to highly concentrated micro plastic deformation at location with in this layer. Under such circumference a very high density of micro band structure were formed.
19	Nilseh Kumar et al [2012]	Al-Mg-Sc alloy	The alloy was processed in as-received and aged (563 K, 22 hours) conditions and at three different tool rotation rates: 800, 400, and 325 rpm.	The grain size varied from 0.89 to 0.39 μm depending on the processing and initial thermos-mechanical condition of the alloy. The grain size reduction was observed with increase in Zener-Holloman parameter.
20	Z.Y.Ma et al [2006]	Al-Si alloy A356	Five-pass FSP with a tool rotation rate of 700 rpm and a traverse speed of 203 mm/min was performed using a tri-flute pin.	Overlapping FSP did not affect the size, aspect ratio and distribution of the Si particles. The Si particles broken by FSP were uniform distributed in the entire processed zones created by multi pass FSP.
21	Z.Y.Ma et al [2004]	Al-Si alloy A356	Single pass FSP with a tool rotation rate of 700 rpm and transverse speed of 203 mm/min was performed on 6.35 mm	The flow stress of FSP A356 was significantly lower than that of cast A356 FSP. Maximum super plasticity of 650% was obtained at 530C and an initial strain rate of 1x10-3 s-1 in FSP A356.
22	Z.Y.Ma et al [2009]	7075 Al Alloy	A Tool rotation rate of 600 rpm and a traverse speed of 102 mm/min was used.	A shift to higher optimum temperature was observed in the two pass FSP 7075Al. Maximum superplastic elongation of 1220% was achieved at 480C and an initial strain rate of 10-2 s-1 in the center region of second pass in the two pass FSP 7075Al
23	Z.Y.Ma et al [2003]	Al-Si alloy A356	Tool rotation rate of 300,700, 900 and 1100 rpm and a traverse speed 2 and 8 ipm	The strength of FSP A356 increased with increasing tool rotation rates. For the standard pin, a maximum strength was observed at a tool rotation rates of 900 rpm
24	Jianqing Su et al [2013]	Ti–6Al–4V alloy	Tool rotational speed (800–1000 rpm) and tool traverse speed (1–4 IPM) was used in this work.	The higher yield and ultimate tensile strength of 1067 MPa and 1156MPa without any losses of ductility were achieved in 900 rpm/4IPM sample having the smallest prior β grains size of ~12μm
25	Z.Y. Ma et al [2010]	Al-4Mg-1Zr alloy with grain size of 0.7 μm	Tool rotation rate was 600 rpm and tool transverse speed 25.4 mm/min used.	High strain rate and low temperature super plasticity of greater than 1200% work observed at 10-2 to -1x10-1 s-1 and 300-

				350C even at 425C a super plasticity of 1400% was achieved at an exception alloy high strain rate of 1s-1.
26	Omar.S.Salih et al [2015]	Aluminium matrix composites (AMCs)	Tool rotation speed was 600, 800 and 1000 rpm and tool transverse speed was 40, 80 mm/min used	Welding parameters such as tool rotation, speed, transverse speed and axial force have a significant effect on the amount of heat generation and strength of FSW joints. Microstructural evaluation showed the formation of tunnel defect due to inappropriate flow of plasticized metal
27	S.R Ren et al [2007]	6061Al–T651	Tool rotaion speed was 400,600, 800, 1200 and 1600 rpm whereas tool transverse speed was 100 and 400 mm/min were used.	Under the welding parameters investigated in this study, the traverse speed appears to be a dominant factor in determining the tensile properties and fracture mode of the welds .FSW 6061Al–T651 joints welded at 400 mm/min exhibited higher strength with a 45 shear fracture, whereas a lower tensile strength with nearly vertical fractures were observed for the samples welded at 100 mm/min.
28	N.Kamp et al [2006]	AA7449 aluminium alloy.	The interfacial energy of the different phases and the diffusion rates was taken	A numerical analytical model based on the Kampmann and Wagner numerical (KWN) model has been developed to predict the precipitate dis-tribution evolution in 7xxx alloys during complex processing.
29	R.Nandan et al [2007]	Mild Steel	Pin radius, pin length, weld speed, and rotational speed are 3.95 mm, 6.22 mm, 0.42 mm/sec and 450 rpm respectively.	Three-dimensional temperature and plastic flow fields during FSW of mild steel have been calculated by solving the equations of conservation of mass, momentum and energy. The spatially variable non-Newtonian viscosity was determined from the computed values of strain rate,
30	M. Maalekian et al [2008]	Steel Bar having Composition 0.75C,1.02Mn, 0.28Si, 0.11Cr, 0.05Ni, 0.015S, 0.009P, 0.08Cu	function of process parameters $q = 2\pi.n.e.\mu.P$ Where q= heat flux, μ=Coulomb coefficient of friction, n= rotational speed, e = Amplitude, P= pressure	The heat-generation rate in orbital friction welding of steel bars is analyzed using four different methods; constant Coulomb friction, sliding–sticking friction, the experimentally measured power data and an inverse heat conduction approach.
31	L.Commin et al [2009]	AZ31 Magnesium Alloy	Four welding condition (1000 rpm/200 mm min, 1300 rpm/300 mm min 1400 rpm/700 mm min, and 600 rpm/2000 mm min was used.	Stress levels observed are higher on the retreating side. Grain growth is observed with an increase in the processing parameters that promote heat generation. FSW induced lower tensile mechanical properties for this hot-rolled base metal alloy.
32	S.Mironov et al [2009]	Pure Titanium	low tool rotational speed of 200 rpm	The microstructure evolution during friction stir welding of commercial purity titanium was studied. Material flow was found to be close to the simple-shear deformation and arose mainly from the prism slip. The grain structure evolution was shown to be a complex process including several stages.

33	L. Fratini et al [2010]	AA7075-T6	The tool rotation rate were 715 and 1500 rpm, and tool traverse speeds were 105 and 214 mm/min	The effects of in process cooling on the material characteristics and joint performance have been presented on AA7075-T6
34	S. Mironov et al [2011]	S31254 superaustenitic stainless steel	A tool rotational speed of 400 r.p.m. and a tool travel speed of 30 mm/min	The structural response of a typical low stacking fault energies (SFE) material S31254 to FSW has been studied. Formation of the final stir zone (SZ) microstructure was deduced to be primarily governed by discontinuous recrystallization occurring during the FSW cooling cycle.
35	Y.S. Sato et al [2004]	Al Alloy 1100	Rotation speed of the welding tool was 500 rpm, and the traveling speed was 12 mm/sec	Friction stir welding (FSW) was applied to an accumulative roll-bonded (ARBed) Al alloy 1100. FSW resulted in reproduction of fine grains in the stir zone and small growth of the ultrafine grains of the ARBed material just outside the stir zone.
36	G.R. Argade at al [2012]	Magnesium Alloy Mg-Y-Re	Tool rotation rate of 800 rpm and tool traverse speed of 25.4 mm/min.	Effect of grain refinement and heat treatment on corrosion behavior of a friction stir processed Mg-Y-RE alloy was studied. Different trends between microstructural conditions and corrosion behavior were observed with electrochemical testing and constant immersion testing.
37	G. Buffa et al [2011]	A 3D FE model, with general validity for different joint configurations, was used to simulate	Tool rotating speed and tilt angle were kept constant and equal to 500 rpm and 21, respectively. Three levels of advancing velocity, i.e. 100, 225 and 325 mm/min were selected.	A new numerical procedure for the prediction of the residual stress distributions in Friction Stir Welding processes is Studied.
38	Seung Hwan C. Park [2003]	304 stainless steel	Tool rotation rate 1400 rpm, tool traverse rate was at 1.3 mm/s and tool was tilted at 3.5 from vertical.	The microstructural observation revealed that sigma phase including the numerous stacking faults was formed at the advancing side of the stir zone.
39	C. Hamilton et al [2008]	AA6061-T6 Aluminum alloy	Range of tool rotation rate 50 to 550 rpm was used.	A thermal model of friction stir welding was developed that utilizes a new slip factor based on the energy per unit length of weld. The thermal model successfully predicts the maximum welding temperature over a wide range of energy levels
40	C. Hamilton et al [2009]	Al–Zn–Mg–Cu alloy	Tool rotation rate 225, 250, 300 and 400 rpm and constant weld velocity of 2.1 mm/sec was used.	In this work, the model successfully predicts the maximum welding temperatures and temperature distributions over the energy range investigated.

CONCLUSIONS

The mechanical properties of welded joint by friction stir welding are largely dependent on the combined effect of both the composition of alloying element and processing parameter, there for, the mechanical performance of friction stir welding joint should be evaluated accordingly. Past researcher showed that FSW is a potential welding process to achieve defect free joint. Welding parameter such as tool rotation, transverse speed and axial force have a significant effect on the amount of heat generated and strength of FSW joints. Microstructure evaluation of FSW joints clearly shows the formation of new fine grains and refinement of reinforcement particles in the weld zone with different amount of heat input by controlling the welding parameter.

REFERENCES

[1] Y.Wang, X.L Shi, R.S mishra, T.J Watson, "Friction stir welding of devitrified AL-4.0Y-4.0Ni-0.9Co alloy produced by amorphose powder", Scripta Materialia 56 (2007) 971-974.
[2] Indrajeet Charit, Rajiv S. Mishra, Murray W. Mahoney, "Multi sheet structure in 7475 aluminum by FSW in concert with post weld superplastic forming", Scripta Materialia 47 (2002) 631-636.
[3] V.Jeganthan Arulmoni, Ranganath M.S, R.S Mishra, "Effect of single and multi passes FSP on microstructure, hardness and tensile properties of a 99.99% Cu with carbon nano tube", International Journal of advance research and innovation, 3(1), 2015, 189-196.
[4] Jiye wang, Jianqing Su, R.S Mishra, Ray Xu, John A. Baumann, "Tool wear mechanism in friction stir welding of Ti-6Al-4V", wear 321 (2014), 25-32.
[5] J.Q. Su, T.W Nelson, R.S Mishra, M.Mahoney, "Microstructure investigation of friction stir welding 7050-T651 aluminum, acta materialia, 2002.
[6] V.Jeganatham Arumoni, R.S Mishra, "Friction stir processing of Al-alloy for defence application, International journal of advance research and innovation, 2(2), 2014, 337-341.
[7] S.Jana, R.S.Mishra, J.B Baumann, G. Grant, "Effect of stress ratio the fatigue behaviour of a friction stir processed cast Al-Si-Mg alloy, Scripta Materialia 61 (2009), 992-995.
[8] Z.Y.Ma, S.R Mishra, R.S Mishra, "Effect of Friction Stir Processing on the microstructure of CastA356 Al", Material Science and Engineering A 433 (2006), 269-278.
[9] Patric B. Berdon, Willam H. Bingel, R.S Mishra, "Friction Stir Processing: A Tool to homogenize nano composite Al Alloy, Scripta mater, 44 (2001), 61-66.
[10] Z.Y.Ma, R.S Mishra, M.W. Mahoney," Super plastic deformation behavior of friction stir processed 7075Al alloy", Acta Materialia 50 (2002), 4419-4430.
[11] Z.y. Ma, R.S.Mishra, M.W.Mahoney, R.Grimes," High strain rate super plasticity in friction stir processed Al-4Mg-1Zr alloy", Material Science and Engineering A 351 (2003) 148-153.
[12] R.S Mishra, Z.Y.Ma, I. Charit, "Friction stir processing: A Novel technique for fabrication of surface composite", Matrial Science and Engineering A 341 (2003) 307-310.
[13] S. Jana, R.S. Mishra, J.A Baumann, G. Grant, " Effect of process parameters on abnormal grain growth during FSP of a cast Al-Alloy", Material Science and Engineering A, 528 (2010) 189-199.
[14] S.Jana, R.S Mishra, J.B Baumann, " Effect of friction stir processing on fatigue behavior of an investigation cast Al-7Si-0.6Mg alloy, Acta Materialia, 58 (2010) 989-1003.
[15] Z.Y Ma, R.S.Mishra, M.W Mahoney, R. Grimes, "Effect of Friction Stir Processing on the the kinectic of superplastic deformation in an Al-Mg-Zr Alloy", Metallurgical and Material Transaction, 36A (2005), 1447-1458.
[16] Z.Y Ma, R.S Mishra, "Cavitation in super plastic 7075 Al alloy prepared via friction stir processing, Acta Materialia 51 (2003) 3551-3569.
[17] S.R Sharma, R.S Mishra, Z.Y Ma, "Effect of friction stir processing on fatigue behaviour of A356 Alloy", Scripta Materialia 51 (2004) 237-241.
[18] Jian Qing Su, T.W Nelson, T.R. McNelley, "Development of Nano crystalline structure in Cu during Friction Stir Processing", Material Science and Engineering A, 525 (2011) 5458-5464.
[19] Nilesh Kumar, R.S Mishra, " Ultrafined Grained Al-Mg-Sc Alloy via friction Stir Processing", Metallurgical and Materials Transaction, 44A (2013) 934-945.
[20] Z.Y Ma, S.R Sharma, R.S Mishra, " Effect of Multipass Friction Stir Processing on Microstructure and tensile propeties of a Cast Al-Si Alloy", Scripta Materialia, 54 (2006) 1623-1626.
[21] Z.Y. Ma, R.S Mishra, M.W Mahoney, " Superplasticity in Cast A356 induced via friction Stir Processing", Scripta Materialia 50 (2004) 931-935.
[22] Z.y.Ma, R.S Mishra, F.C Liu, "Super plastic behaviour of Micro-region in two pass friction stir processing 7075Al alloy", Materialia Science and Engineering A 505 (2009) 70-78.
[23] Z.Y.Ma, S.R Sharma, R.S Mishra, M.W Mahoney, " Micro structural modification of cast aluminum alloy via friction stir processing", Material Science Forum, vol 426-432 (2003) 2891-2896.
[24] Jianqing Su, Jiye Wang, R.S Mishra, Ray Xu, " Microstructure and Mechanical Properties of Friction Stir Processing Ti-6Al-4V Alloy", Material Science and Engineering A 573 (2013) 67-74
[25] Z.Y.Ma, F.C.Liu, R.S Mishra, " Superplastic deformation mechanism of ultrafined grained aluminum alloy produced friction stir welding", Acta Materialia, 58 (2010) 4693-4704.
[26] Omar S. Salih, Hangan Ou, W.Sun, D.G McCartney, "A review of friction stir welding of aluminum matrix composite", Material and Design 86 (2015) 61-71.
[27] S.R. Ren, Z.Y. Ma, L.Q. Chen, Effect of welding parameters on tensile properties and fracture behavior of friction stir welded Al–Mg–Si alloy, Scripta Materialia, 56(2007), 69-72.
[28] N. Kamp, A. Sullivan, R. Tomasi, J.D. Robson, Modelling of heterogeneous precipitate distribution evolution during friction stir welding process, Acta Materialia 54 (2006) 2003–2014.
[29] R. Nandan, G.G. Roy, T.J. Lienert, T. Debroy, Three-dimensional heat and material flow during friction stir welding of mild steel, Acta Materialia 55 (2007) 883–895.
[30] M. Maalekian, E. Kozeschnik, H.P. Brantner, H. Cerjak, Comparative analysis of heat generation in friction welding of steel bars, Acta Materialia 56 (2008) 2843–2855.
[31] L. Commin, M. Dumont, J.-E. Masse, L. Barrallier, Friction stir welding of AZ31 magnesium alloy rolled sheets:Influence of processing parameters, Acta Materialia 57 (2009) 326–334.
[32] S. Mironov, Y.S. Sato, H. Kokawa, Development of grain structure during friction stir welding of pure titanium, Acta Materialia 57 (2009) 4519–4528.
[33] L. Fratini, G. Buffa, R. Shivpuri, Mechanical and metallurgical effects of in process cooling during friction stir welding of AA7075-T6 butt joints, Acta Materialia 58 (2010) 2056–2067.
[34] S. Mironov, Y.S. Sato, H. Kokawa, H. Inoue, S. Tsuge, Structural response of superaustenitic stainless steel to friction stir welding, Acta Materialia 59 (2011) 5472–5481.
[35] Y.S. Sato, Y. Kurihara, S.H.C. Park, H. Kokawa, N. Tsuji, Friction stir welding of ultrafine grained Al alloy 1100 produced by accumulative roll-bonding, Scripta Materialia 50 (2004) 57–60.
[36] G.R. Argade, K. Kandasamy, S.K. Panigrahi, R.S. Mishra, Corrosion behavior of a friction stir processed rare-earth added magnesium alloy, Corrosion Science 58 (2012) 321–326.

[37] G. Buffa, A. Ducato, L. Fratini, Numerical procedure for residual stresses prediction in friction stir welding, Finite Elements in Analysis and Design 47 (2011) 470–476.
[38] Seung Hwan C. Park, Yutaka S. Sato, Hiroyuki Kokawa, Kazutaka Okamoto, Satoshi Hirano, Masahisa Inagaki, Rapid formation of the sigma phase in 304 stainless steel during friction stir welding, Scripta Materialia 49 (2003) 1175–1180.
[39] C. Hamilton, S. Dymek, A. Sommers, A thermal model of friction stir welding in aluminum alloys, International Journal of Machine Tools & Manufacture 48 (2008) 1120–1130.
[40] C. Hamilton, A. Sommers, S. Dymek, A thermal model of friction stir welding applied to Sc-modified Al–Zn–Mg–Cu alloy extrusions, International Journal of Machine Tools & Manufacture 49 (2009) 230–238.

International Conference on Recent Development in Engineering Science, Humanities and Management
National Institute of Technical Teachers Training & Research, Chandigarh, India (ESHM-17)
29th January 2017, www.conferenceworld.in ISBN: 978-93-86171-25-2

INNOVATION PRACTICES IN SME –A REVIEW

Piu Jain[1], Prof S.K Garg[2]

[1]*Mechanical Engineering Department, Maharaja Agrasen Institute of Technology, (India)*

[2]*Mechanical Engineering Department ,Delhi College of Engineering (India)*

ABSTRACT

Globalization has created a world market driven by fierce competition among organizations. Globalization have forced SMEs to develop a variety of global-level capabilities, and contributed a lot to enhancing innovativeness. This paper attempts to focus the importance of innovation to achieve sustainable development of an organization. The key to achieve sustainable development lies in the customer satisfaction through improved quality, reduced cost, reduced delivery lead times and proper communication. A number of studies suggest that a variety of methodology are used on SME's innovativeness and further investigate how those affect SME's business and innovation performance. This paper reviews the different issues related to innovation practices in SMEs.

Keywords: Globalization, Innovation, Industry, SME.

I. INTRODUCTION

The desirable goal for all industries and organizations is that they want to grow quantitatively .But in the current manufacturing scenario; industries are facing tremendous pressure of diversified nature due to extensive sophisticated market, changing customer choice and global competition. Recently, small and medium enterprises (SMEs) have been regarded as the engine of economic growth and employment. As the growth of industry giants have been slowing, the role of SMEs becomes more important [1]. Due to importance of supply chain management issues in the global market environment, big organizations are heavily dependent on SMEs for the provision of high quality product and services with the lowest possible cost. Overcoming challenges, finding adequate financing, are not the only setback for SMEs to be successful [2]. Market pressure now necessitates a strategic and tactical framework that allows companies to behave in an adaptive manner that permits continuous evolution in the market. To boost national innovation and economic growth, it is crucial to drive SMEs' innovation [1].The changing circumstances and growing demands of customers for excellence in quality requires major innovative drives by SMEs in all fields.

Flourishing amidst a challenging environment, the small and medium enterprises are the socio economic developers of the country with a major advantage of generating employment at low cost. Despite various suggestions, there is a consensus that inno vation should depend on a firm's innovativeness, in other words, the capability to introduce new processes, products, ideas, etc. [4,5]. Technology covers all techniques, processes, systems and skills, which are used to convert the sources into products. In any case, development in technology (quitting old and traditional methods of doing tasks) is called “Innovation” [6, 7].

A number of studies have suggested a variety of key determinants on SME's innovativeness, and further investigate how those affect SME's business and innovation performance [8, 9,10].

ISBN: 978-93-86171-25-2

II. ISSUES RELATED TO INNOVATION

This study is motivated by innovation activity in India's fast-changing business scenario influencing SMEs sector which is backbone of economy. Tohidi [7] said Innovation is introduced as any change in technology, and is studied in three parts: product, process, and organization. Rahmana et al [2] said the practice of technological innovation is significantly associated with business performance but its effect towards SME survival is underexplored. Lee,et al[1] felt that requirement of the hour is identifying principal types of business models, and of finding evolving paths of SME's business models with the changing pattern of innovativeness. Klewitz and Hansen [11] found that SME strategic sustainability behavior ranges from resistant, reactive, anticipatory, and innovation-based to sustainability-rooted. Most published work provides significant proofs of implementation of Innovation in SMEs, though cases of Innovation in Indian industries are very few. Various issues related to innovation in SMEs have been studied from various literatures and given in Table 1.

Table 1: Overview of Issues of Innovation in Sme

SN	Issue	References	Key Observation
1	Importance of innovations	Seo and Chae(2016)	• Market dynamics and firm diversity influences the amount of performance manifested by SMEs' innovative activities. • When market dynamics is high, innovative activities play a more crucial role in contributing to the revelation of performance after a certain period of time has passed, whereas exploitative activities are comparatively important in the early time periods. • SME use technological innovation to improve performance.
		N.A Rahmana,et al (2015)	• Globalization has forced small and medium enterprises to change business models with new innovative capabilities.
		Lee, et al.(2012)	• Before engaging in any innovation activity, managers should analyze their current resources and capabilities associated to the adoption of specific innovation modes. • Organizational innovation requires a higher endeavor in managerial and teamwork practices.
		Apanasovich, et al.(2016)	• Innovation involves new ways of introducing and organizing management systems for production, such as supply chain management systems, business re-engineering, lean production, and quality- management systems.
		Klewitz and Hansen (2013)	• Knowledge on the specificities of sustainability-oriented innovations (SOIs)in SMEs are increasingly recognized as central contributors to sustainable development.

ISBN: 978-93-86171-25-2

		Verdú et al.(2016)	• Combination of high levels of collaboration among small- and medium-sized enterprises, and public investment in research and development facilitates significant rates of organizational innovation. • Collaboration among firms promotes organizational innovation.
2	Areas of innovations	Seo and Chae(2016) N.A Rahmana, et al (2015) Lee, et al.(2012) Apanasovi, et al(2016) Klewitz and Hansen (2013) Verdú et al.(2016)	• Firm performance. • Diversity of product/service range, technological innovations • Business Model Globalization • This study analyzes the most effective innovation modes('science and technology-based innovation', STI, and 'doing, using and interacting-based innovation', DUI)for business innovation performance. • Eco-innovation (e.g. eco-design, cleaner production) and sustainability-oriented innovations (SOIs), that is, the integration of ecological and social aspects into products, processes, and organizational structures. • Key element of regional growth is its ability to transform knowledge into innovation.
3	Processes of innovations	Seo and Chae(2016) N.A Rahmana et. (2015) Lee at al.(2012)	• Considering an SME as an agent, this study analyzed the effects that market dynamics and firm diversity have on innovative activity and firm performance by using an ABS approach. Specifically, NetLogo was utilized to conduct the ABS. • Social networking, computerized record, online marketing • Business Model (BM) of any company goes through transformation, augmentation, extension or evolution to sustain competitiveness, hence the need of Global BM .

ISBN: 978-93-86171-25-2

		Apanasovich, et al.(2016) Klewitz and Hansen(2013) Verdú et al.(2016)	• Firms that combine the STI and DUI modes of innovation are more likely to generate technological innovation than those firms that focus on STI or DUI modes alone • Interaction with external factors (e.g. customers, authorities, research institutes) can ultimately increase the innovative capacity of SMEs for sustainability-oriented innovations (SOI) • Innovations are no longer developed only within organizational boundaries; Innovation frequently is the result of collaboration involving an extensive network of external agents (suppliers, partners, customers)
4	Tools used	Seo and Chae(2016) Lee at al.(2012) Apanasovic,et al.(2016) Verdú, et al.(2016)	• Agent-Based Simulation (ABS) ,ABIS(Agent-Based Innovation Simulator) using NetLogo . • Reviewing 125 previous Business model (BM) studies, principal types of Korean BMs are identified by using K-means vector clustering. • Formulation of hypotheses. • Qualitative comparative analysis (QCA).
5	Difficulties	Seo and Chae(2016) Y.-P. Ho et al(2016) Lee at al.(2012) Apanasovih, et al.(2016) Klewitz and	• Rapid technological changes, intense fluctuations in customer demand, and the instability of market structure. • One key challenge faced by Newly Industrialized Economies (NIEs) is the evolution of an appropriate strategy to sustain long-term economic growth. • SMEs with global infant Business Models(BM) cannot decide which innovation to push because they have little knowledge about global markets and competitors. • The lack of financial capital, innovation management experience and state-of-the-art technology are the peculiarities of developing countries.

ISBN: 978-93-86171-25-2

		Hansen (2013)	• While prior research has often dealt with sustainability-oriented innovations (SOI)s in large firms, the last decade has begun to generate broad knowledge on the specificities of SOIs in small and medium sized enterprises (SMEs) as they are increasingly recognized as central contributors to sustainable development. However, this knowledge is scattered across different disciplines, research communities, and journals.
6	Empirical Studies .	Seo and Chae(2016) N.A Rahmana et al (2015) Lee at al.(2012) Apanasovic, et al.(2016) Klewitz and Hansen(2013)	• Developed a program to simulate real situations using NetLogo, a well-known multi-agent system. • Library search and evaluate previous literature review on the subject of SME Survival and Technological Innovation. • Survey result of 400 Korean SMEs • For empirical analysis, Belarus was selected It is a small open catching-up country with a poor R&D expenditure and a highly educated population. • Systematic review of 84 key journal articles in a time frame between 1987 and 2010

III. LITERATURE REVIEW

Recent large-scale surveys on corporate and public sector leaders show that SME innovation gained lots of importance in practice [12]. Scholars are turning their interest to study SME performance and success factor which significantly heading towards proposing frameworks and models to improve the SME industry from 2009 up till the year 2016 [13,14,15,16]. Findings from these studies, proposed that technology is the determinants of SME success.

3.1 Importance of Innovation

It is an indisputable fact that a nation's economic wealth and growth are dependent on the prosperity of its industrial sector. However, as a consequence of globalization, the manufacturing industry is constantly under tough pressure to increase its competitiveness. Globalization has forced small and medium enterprises to change business models with new innovative capabilities [1]. N.A Rahmana et al.[2] said SME use technological innovation to improve performance. Apanasovich, et al.[18] explains that before engaging in any innovation activity ,managers should analyze their current resources and capabilities associated to the adoption of specific

ISBN: 978-93-86171-25-2

innovation modes. According to him organizational innovation requires a higher endeavor in managerial and teamwork practices. Klewitz and Hansen [11] feels knowledge on the specificities of sustainability-oriented innovations (SOIs) in SMEs are increasingly recognized as central contributors to sustainable development. Combination of high levels of collaboration among small- and medium-sized enterprises, and public investment in research and development facilitates significant rates of organizational innovation [18].According to him collaboration among firms promotes organizational innovation. Innovation involves new ways of introducing and organizing management systems for production, such as supply chain management systems, business re-engineering, lean production, and quality- management systems [17]. Market dynamics and firm diversity influences the amount of performance manifested by SMEs' innovative activities. Seo and Chae [19] says when market dynamics is high, innovative activities play a more crucial role in contributing to the revelation of performance after a certain period of time has passed, whereas exploitative activities are comparatively important in the early time periods.

3.2 Areas of Innovations

Lots of Research work has been done on various area of innovation. Seo and Chae [19] dealt in innovation for firm performance . N.A Rahmana et al. [2] conducted their research work in diversity of product/service range and technological innovations. Lee et al. [1] spoke of Business Model Globalization. Apanasovich, et al. [17] analyzed the most effective innovation modes ('science and technology-based innovation', STI, and 'doing, using and interacting-based innovation', DUI) for business innovation performance. Klewitz and Hansen [11] dealt in eco -innovation (e.g. eco-design, cleaner production) and sustainability-oriented innovations (SOIs), that is, the integration of ecological and social aspects into products, processes, and organizational structures. Verdú et al. [18] said that key element of regional growth is its ability to transform knowledge into innovation.

3.3 Processes of Innovations

Business cannot be successful without the process of innovation. The effective deployment of different processes in innovation in SME has been widely recognized in recent years as a mean of building sustainable competitive advantage and thereby enhancing organizational performance. Considering SME as an agent, Seo and Chae19], in their research analyzed the effects that market dynamics and firm diversity have on innovative activity and firm performance by using an ABS approach. Specifically, Net Logo was utilized to conduct the ABS. N.A Rahmana et. al [2] said social networking, computerized record, online marketing are the framework of innovation process. Lee at al.[1] elaborates that Business Model (BM) of any company goes through transformation, augmentation, extension or evolution to sustain competitiveness, hence the need of Global BM. Apanasovich, et al[17] said that firms that combine the sustainability-oriented innovations (STI) and doing, using and interacting-based innovation (DUI) modes of innovation are that more likely to generate technological innovation than those firms that focus on STI or DUI modes alone. Klewitz and Hansen [11] elaborates that interaction with external factors (e.g. customers, authorities, research institutes) can ultimately increase the innovative capacity of SMEs for sustainability-oriented innovations (SOI). Verdú et al.[18] said innovations are no longer developed only within organizational boundaries; Innovation frequently is the result of collaboration involving an extensive network of external agents (suppliers, partners, customers).

ISBN: 978-93-86171-25-2

3.4 Tools Used

Various authors have researched in various areas of innovation in SME using various tools to find out methods to improve the manufacturing parameters. Seo and Chae [19] used Agent-Based Simulation (ABS) ,ABIS(Agent-Based Innovation Simulator) using NetLogo. Lee at al. [1] reviewed 125 previous Business model (BM) studies; principal types of Korean BMs were identified by using K-means vector clustering. Apanasovich, et al. [17] used formulation of hypotheses method. Verdú et al [18] used Qualitative comparative analysis (QCA).

3.5 Difficulties

A lot of difficulties may arise during implementation of innovation in SMEs. The growing number of business failure and higher failure rate for infant business demands SME survival to be the center of attention with technological innovation acting as the medium leading to higher survival rate. Seo and Chae[19] felt difficulties in innovation arise due to rapid technological changes, intense fluctuations in customer demand, and the instability of market structure. Y.-P. Ho et al [20] said difficulty in innovation may arise due to challenges faced by Newly Industrialized Economies (NIEs) is the evolution of an appropriate strategy to sustain long-term economic growth. Lee at al[1] elaborates that major difficulty in implementation of innovation is due to the fact SMEs with global infant Business Models (BM) cannot decide which innovation to push because they have little knowledge about global markets and competitors. Apanasovich, et al.[17] said that implementation of innovation may difficult due to the lack of financial capital, innovation management experience and state-of-the-art technology of developing countries. Klewitz and Hansen [11] said while prior research has often dealt with sustainability-oriented innovations (SOI) s in large firms, the last decade has begun to generate broad knowledge on the specificities of SOIs in small and medium sized enterprises (SMEs) as they are increasingly recognized as central contributors to sustainable development. However, this knowledge is scattered across different disciplines, research communities, and journals and may be the cause of difficulty to implement innovation strategies in SMEs.

3.6 Empirical Studies

Several empirical studies have been made for innovation and development of SME. Seo and Chae [19] developed a program to simulate real situations using Net Logo, a well-known multi-agent system. After 300 simulated instances using Net Logo, the firm diversity values were distributed from 0.14 to 0.92. Market dynamics was manipulated by the length of the bit string in the solution of the task with 3 (low) and 30 (high). N.A Rahmana et al [2] conducted Library search and evaluate previous literature review on the subject of SME Survival and Technological Innovation and found out that theoretically, social networking, computerized record and online marketing are the main variables that found to be signify cant to SME survival but empirical data is required to prove these connections. Lee at al.[1] analyzed survey result of 400 Korean SMEs identifying principal types of those business models, and of finding evolving paths of SME's business models with the changing pattern of innovativeness. Apanasovich, et al.[17]for their empirical analysis, selected Belarus. It is a small open catching-up country with a poor R&D expenditure and a highly educated population. For the sake of completeness, in this paper, the impact of STI and DUI mode is studied .Klewitz and Hansen [11] made

ISBN: 978-93-86171-25-2

systematic review of 84 key journal articles in a time frame between 1987 and 2010 and found that SME strategic sustainability behavior ranges from resistant, reactive, anticipatory, and innovation-based to sustainability-rooted. They proposed that interaction with external actors (e.g. customers, authorities, research institutes) can ultimately increase the innovative capacity of SMEs.

IV. CONCLUSION

It is an indisputable fact that a nation's economic wealth and growth are dependent on the prosperity of its industrial sector. SME's innovation is essential for economic growth of any country. Although it is quite evident that innovation of any sector should depend on innovativeness, the problem arises that there are too many determinants and influencing factors on innovativeness. In order to overcome this, SME's innovativeness has been investigated based on some key issues.

A number of studies have tackled these issues, and identified several internal and external factors. Importance of innovation have been studied in details, Areas of innovation looked into and effective deployment of various process of innovation reviewed. The different tools used for implementation of innovation and improve manufacturing are studied, the difficulties that are faces are discussed and details of empirical studies related to innovation examined. Innovation will be definitely helpful for Indian industries to improve quality and reduce cost at faster delivery.

This paper tries to highlight the different aspects and benefits of innovation and its implementation in SMEs. Organization in global competitive market as well as those wish to achieve sustainable development should strive for innovation through the application of tools and techniques suitable to their situation. As industry giants face the growth limitation, many countries regard SMEs as new growth engines, and set various policies in motion to increase the number of global leading SMEs. Without any systematic guide of SME's evolution through globalization, doubts cannot help being cast continuously both on effectiveness and efficiency of SME policies. In that regard, this study can serve to improve relevant SME policies and procedure.

REFERENCES

[1] Yongho Lee, Juneseuk Shin, Yongtae Park, The changing pattern of SME's innovativeness through business model globalization, Technological Forecasting & Social Change 79, 2012, 832–842.

[2] Nurul hasanah Abdul Rahmana, Zulnaidi Yaacobb, Rafisah Mat Radzic, An overview of Technological Innovation on SME Survival; A conceptual paper, Procedia - Social and Behavioral Sciences, 224, 2016, 508 – 515.

[3] F. Daman pour., Organizational innovation: a meta-analysis of effects of determinants and moderators, Acad. Manag. J. 34 (3), 1991, 555–590.

[4] G.T.M. Hult, R.F. Hurley, G.A. Knight, Innovativeness: its antecedents and impact on business per formance, Ind. Mark. Manag. 33 (5), 2004, 429–438.

[5] Calan tone, R.J., Cavus gil, T., Zhao, Y., Learning orientation, firm innovation capability, and firm performance, Industrial Marketing Management 31, 2002, 515–524.

[6] H. Tohidi, Modelling of Business Services in Service Oriented Enterprises, Procedia-Computer Science Journal, Elsevier, 2011, USA.

ISBN: 978-93-86171-25-2

[7] G.T.M. Hult, R.F. Hurley, G.A. Knight, Innovativeness: its antecedents and impact on business performance, Ind. Mark. Manag. 33 (5) ,2004, 429–438.

[8] S. Radas, L. Bozic, The antecedents of SME innovativeness in an emerging transition economy, Technovation 29, 2009, 438–450.

[9] L. Voudouris, S. Makridakis, Y. Spanos, "Greek hidden champions: lessons from small, little known firms in Greece", Eur. Manag. J. 18 (6) ,2000, 663–674.

[10] Klewitz, J., Hansen, E.G., Sustainability-oriented innovation of SMEs: a systematic review, Journal of Cleaner Production, 2013, 1-19.

[11] G. Pohle, M. Chapman, IBM's global CEO report, Business model innovation matters, Strat. Leadersh. 34 (1) 2006, 34–40.

[12] Inyang, B. J. & Enuoh, R. O., Entrepreneurial Competencies: The Missing Links to Successful Entrepreneurship in Nigeria, International Business Research, 2 (2), 2009, 62-71

[13] Chittithaworn, C., Islam, M. A., Keawchana, T. & Yusuf, D. H. M., Factors Affecting Business Success of Small & Medium Enterprises (SMEs) in Thailand, Asian Social Science, 7 (5), 2011, 180-190.

[14] Makhbul, Z. M. & Hasun, F. M. ,Entrepreneurial Success:An Exploratory Study among Entrepreneurs, International Journal of Business and Management, 6 (1), 2011, 116-125.

[15] Oyeku, O. M., Oduyoye, O., Asikhia, O., Kabuoh, M. & Elemo, G. N., On Entrepreneurial Success of Small and Medium Enterprises (SMEs): A Conceptual and Theoretical Framework,Journal of Economics and Sustainable Development, 5 (16), 2014, 14-23.

[16] Natalja Apanasovich, Henar Alcalde Heras , Mario Davide Parrilli , The impact of business innovation modes on SME innovation performance in post-Soviet transition economies: The case of Belarus,Technovation,57-58 ,2016, 30–40.

[17] Francisco Mas-Verdú , Dionisio Ortiz-Miranda, José María García-Álvarez-Coque.,Examining organizational innovations in different regional settings, Journal of Business Research,04,2016,132

[18] Young Wook Seo and Seong Wook Chae., Market dynamics and innovation management on Performance in SMEs: Multi-agent simulation approach, Procedia Computer Science, 91, 2016, 707 – 714.

[19] Yuen-Ping Ho , Yi Ruan ,n, Chang-Chieh Hang , Poh-Kam Wong, Technology upgrading of Small-and-Medium-sized Enterpri ses (SMEs)through a manpower second men tstrategy – A mixed-methods study of Singapore's T-Up program, Technovation,2016,07.

Microsyst Technol
DOI 10.1007/s00542-017-3348-2

TECHNICAL PAPER

Investigation of parasitic capacitances of In_2O_5Sn gate electrode recessed channel MOSFET for ULSI switching applications

Ajay Kumar[1] · M. M. Tripathi[1] · Rishu Chaujar[2]

Received: 28 February 2017 / Accepted: 28 February 2017
© Springer-Verlag Berlin Heidelberg 2017

Abstract This work discusses the capacitance–voltage (C–V) analysis and frequency dependent capacitance of In_2O_5Sn (Tin Oxide) gate electrode Recessed Channel (TGRC) MOSFET with an aim to examine the effectiveness of In_2O_5Sn (Transparent) as a gate material on parasitic capacitance which prominently influences the current driving capability and thus, the switching performance. Moreover, capacitance dependent parameters such as Transconductance Frequency Product (TFP), Energy Delay Product (EDP) and Gain Bandwidth Product (GBP) are also assessed and found that, TFP increases to 6.33 times in comparison to metal gate RC MOSFET owing to a noticeable reduction in parasitic capacitance ($C_{gg} = C_{gs} + C_{gd}$), due to which EDP and GBP also improve considerably and thus reflects its effectiveness in RF amplifiers and receivers. In addition, the effect of parameter variation such as gate length (L_g) and negative junction depth (NJD) of TGRC is also observed, and results reveal that with $L_g = 20$ nm and NJD = 5 nm, TGRC unveils outstanding switching performance which is desirable for low power ULSI applications.

✉ Rishu Chaujar
rishu.phy@dce.edu

Ajay Kumar
ajaykumar@dtu.ac.in

M. M. Tripathi
mmtripathi@dce.ac.in

[1] Electrical Engineering Department, Delhi Technological University, Delhi, India

[2] Engineering Physics Department, Delhi Technological University, Delhi, India

1 Introduction

From past few periods, shrinking of device dimensions is the main driving force towards circuit miniaturization, low cost, and portability (Moore 1975). As the dimensions of CMOS device reduces, scaling of silicon-based MOSFET devices for barrier potential, critical electric field, oxide thickness, the threshold voltage becomes tougher (Iwai 2009). To overcome these limitations, numerous techniques are being proposed by researchers. Some of them include modification on the existing structure and technology; and on the other hand, incorporation of some new material instead of prevailing material (Woerlee et al. 2001). These includes multi-gate MOSFET proposed by (Barsan 1981), SOI MOSFET by (An et al. 2003), GAA MOSFET by (Auth and Plummer 1997), and Silicon Nanowire MOSFET by (Hu et al. 2003, 2004; Gupta et al. 2016) etc., to overcome the scaling problems at nano-regime. However, Recessed Channel (RC) MOSFET (Chaujar et al. 2008) comes into the existence and appreciably eliminated SCEs and HCEs due to the existence of trench channel which separates the source and drain regions. Although RC MOSFET has its own limitations that it hinders the current driving capability, to overcome this limitation, there is need of integrating some engineering scheme onto RC MOSFET. Therefore, In_2O_5Sn (Indium tin oxide) as a gate metal is amalgamated onto RC MOSFET and then TGRC MOSFET (Kumar et al. 2016a, b, c) comes into existence.

As device dimensions go into sub-30 nm range, the parasitic capacitances become more protruding, which thus affects the device performance and makes the device unsuitable for switching and low power applications. As the channel length scales down, the gate control over the channel gets reduced due to the increased source/drain

Published online: 07 March 2017

capacitances (Murali and Meindl 2007). Therefore, there is a need to perform and study the capacitance–voltage (C–V) analysis which is more advantageous over current–voltage analysis (Steinke et al. 2012) to scrutinize the effects of parasitic capacitances on device performance. In this work, for the first time, a highly conducive and transparent material (ITO) is used as a gate electrode in RC MOSFET to analyses the effect of parasitic capacitances (both bias dependent and frequency dependent). ITO (In_2O_5Sn) is made of indium oxide (In_2O_3) and tin oxide (SnO_2), and it needs lowest deposition temperature (Murali and Meindl 2007; Singh et al. 2006). ITO has a high concentration in the order of 10^{21} cm^{-3} and a very low resistivity (10^{-5} Ω-cm) with higher Hall mobility (53.5 cm^2 V^{-1} s^{-1}) (Minami 2005). Due to these properties, ITO is frequently used in semiconductor devices, and today silicon-based MOSFET devices having technology less than 30 nm are common. In this work, the bias-dependent parasitic capacitances of TGRC MOSFET are extracted and found that parasitic capacitances are reduced appreciably due to the amalgamation of ITO as a gate electrode (in trenched gate) as compared to the aluminum electrode (CRC MOSFET) at THz frequencies.

Furthermore, the impact of gate length variation and NJD variation has also been observed. The paper is organized as follows: Sect. 2 describes the 3D device structure; and briefs about the simulation models. In Sect. 3, simulation methodology is discussed along with calibration of simulated models. Further, Sect. 4 focused on device comparison in terms of parasitic capacitances and FOMs such as TFP, EDP, and GBP. Also, the effect of gate length and NJD variation on parasitic capacitances of TGRC-MOSFET is examined. Finally, Sect. 5 presents conclusion and its application.

2 Device design and its description

A schematic simulated device i.e. TGRC MOSFET is shown in Fig. 1a. Figure 1b shows the cross-sectional view of TGRC MOSFET with parasitic capacitances. The channel is doped uniformly to 1×10^{17} cm^{-3} (p-type) in both (TGRC and CRC) the devices. The doping in the source and drain region is kept at 5×10^{19} cm^{-3}. The gate length is 30 nm, although total channel length is 54 nm ($L_G + 2t_{ox} + 2NJD$) and thickness of oxide is 2.0 nm as the default device structure parameters of TGRC and CRC MOSFET is shown in Table 1. Figure 1b reflects the parasitic capacitances (C_{gs}, C_{gd}, and C_{gg}) at the gate-source interface, gate-drain interface, and gate–gate interface in the cross-sectional view of TGRC MOSFET.

3 Simulation methodology and calibration

All the results and figure of merits (FOMs) are extracted using ATLAS, a device simulation tool from (Silvaco 2011). The electron and hole currents are calculated by Poisson's equation and the continuity equations. For the simulations, inversion layer Lombardi CVT mobility model has been used due to consideration of temperature variation with accurate results and to allow one to take into account the carrier–carrier scattering, carrier velocity saturation, the influence of the vertical electric field and carrier diffusion at the interface. For minority carrier, Auger recombination model and Shockley–Read–Hall (SRH) recombination are used. In addition, the hydrodynamic energy transport model comprising of the continuity equations and energy balance transport (EBT) model are used to account for non-local transport effects such as

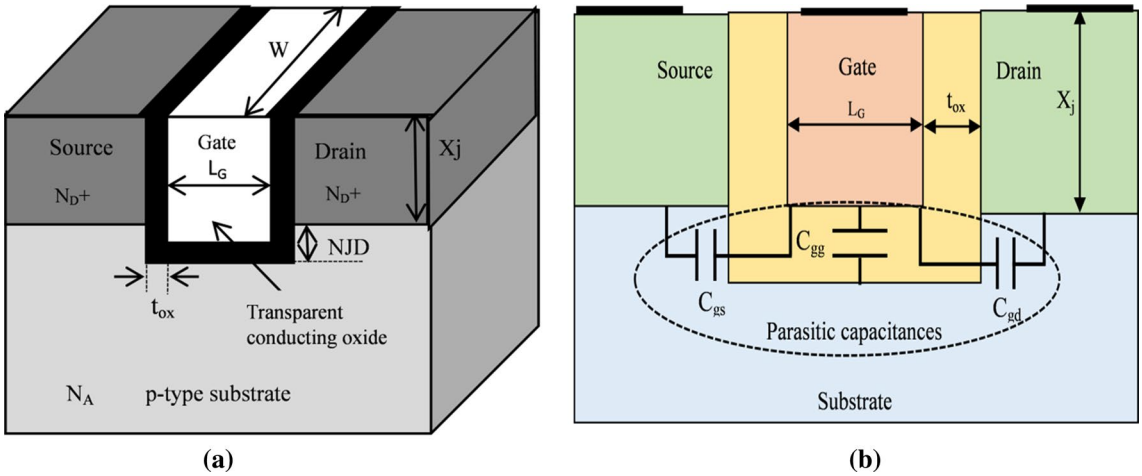

Fig. 1 **a** The schematic simulated structure of TGRC MOSFET. **b** Cross view of THRC MOSFET with parasitic capacitances

Table 1 Default simulated structure parameters of TGRC and CRC MOSFE

Device	TGRC	CRC
Parameters		
Gate length (L_G)	30 nm	
Length of the source and the drain region	30 nm	
Device width (W)	200 nm	
Groove depth	38 nm	
Negative junction depth (NJD)	10 nm	
Substrate doping (N_A)	1×10^{17} cm^{-3}	
Source/drain doping (N_D^+)	5×10^{19} cm^{-3}	
Physical oxide thickness (t_{ox})	2 nm	
Work function	4.7 eV (ITO)	4.2 eV (Al)

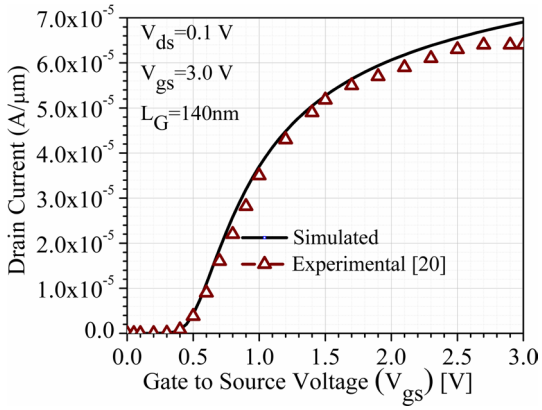

Fig. 2 Experimental and simulation of I_d–V_{gs} characteristics of 140 nm gate length recessed channel MOSFET

diffusion associated with the carrier temperature, velocity overshoot, and the dependence of impact ionization rates on carrier energy distributions (Silvaco 2011). Equations and models used are shown in Table 2.

Where ε = local permittivity; Φ = electrostatic potential; $\rho_{\rightarrow}$ = local space charge density. p = hole concentration; J_p and J_n hole and electron current density respectively. G_p and G_n, are the generation rate for holes and electrons respectively. R_n and R_p are the recombination rate for electrons and holes respectively. q, is the magnitude of the charge on an electron. n/p is the electron/hole concentration. E_{TRAP} is the difference between the trap energy level and the intrinsic Fermi level. τ_n and τ_p, and are the electron and hole lifetimes, respectively. AUGN = 8.3×10^{-32} cm^6/s AUGP = 1.8×10^{-31} cm^6/s. μ_0 is the low-field mobility; υ_{sat}, is the saturation velocity.

In order to authenticate the simulations, the data has been extended (Xiao-Hua et al. 2006) and then plotted as shown in Fig. 2. Model parameters which are used in the simulation have been calibrated according to the experimental results by (Xiao-Hua et al. 2006).

4 Results and discussion

4.1 Impact of In_2O_5Sn on parasitic capacitances

Figure 3a reflects the parasitic capacitances (Kumar et al. 2016c) in terms of gate-source capacitance and gate-drain capacitance. When V_{gs} increases, the accumulation of charge carriers near the gate increases. As a result, the gate-source capacitance and gate-drain capacitance increases. As V_{ds} increases, the pinch-off point moves towards source side, and it leads to accumulation of charges towards source side resulting in an increment of C_{gs}. To maintain the charge neutrality, the charges near the drain decreases and hence C_{gd} decreases as clearly evident from Fig. 3b. It is observed that the value of parasitic capacitances in TGRC device is very less as compared to CRC device as shown in Fig. 3a due to the high conductivity of ITO which shows that applied voltage is a force to charge carriers in current conduction instead of accumulation near the gate (see Fig. 3a, b) and the same trend follows in ref. (Kundu et al. 2014). So higher switching speed is obtained which

Table 2 Used model parameters and equations in simulation (Silvaco 2011; Rahimian and Orouji 2013)

Model	Equation
Poisson's equation	$div(\varepsilon \nabla \phi) = -\rho$
Hole current continuity equation	$\frac{\partial p}{\partial t} = \frac{1}{q} div \vec{J}_p + G_p - R_p$
Electron current continuity equation	$\frac{\partial n}{\partial t} = \frac{1}{q} div \vec{J}_n + G_n - R_n$
SRH recombination	$R_{SRH} = \frac{pn - n_{ie}^2}{\tau_p[n + n_{ie} e^{(-(E_{TRAP}/kT_L))}] + \tau_n[p + n_{ie} e^{(-(E_{TRAP}/kT_L))}]}$
Auger recombination	$R_{Auger} = AUGN(pn^2 - nn_{ie}^2) + AUGP(np^2 - pn_{ie}^2)$
Parallel electric-field-dependent mobility	$\mu(E) = \mu_0 \left[\frac{1}{1 + (\mu_0 E/\upsilon_{sat})^{\beta}}\right]^{1/\beta}$

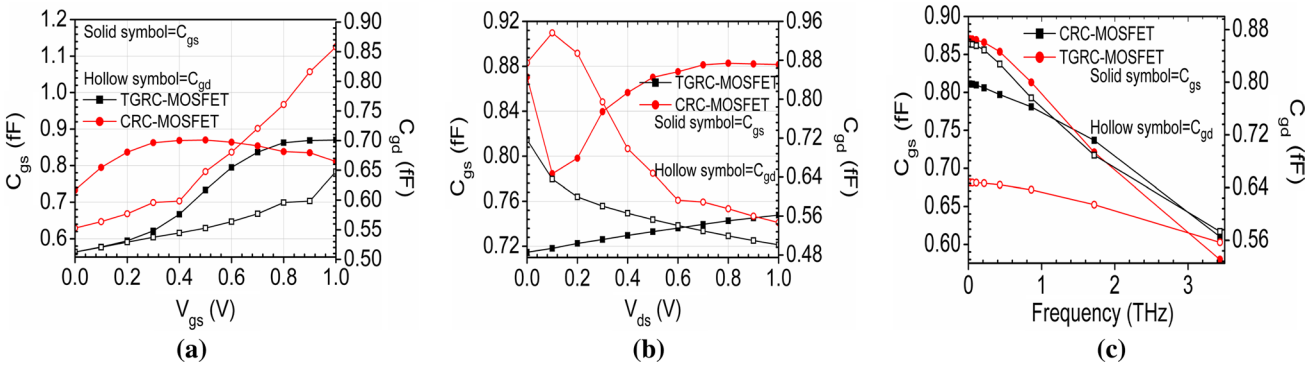

Fig. 3 C_{gs} and C_{gd} as a function of **a** $V_{gs} = 1.0$ V at $V_{ds} = 0.5$ V **b** $V_{ds} = 1.0$ V at $V_{gs} = 0.5$ V **c** frequency at $V_{gs} = 1.0$ V, $V_{ds} = 0.5$ V; of CRC and TGRC MOSFET

also reduces the delay time, making it suitable for the digital applications hence, making TGRC device a promising candidate for switching applications.

Further, the variation of C_{gs} and C_{gd} has also been observed with frequency, and it is clearly reflected from Fig. 3c that when frequency increases to the THz range, then both C_{gs} and C_{gd} reduces. The resultant value of C_{gs} and C_{gd} is very less in TGRC as compared to CRC MOSFET due to the incorporation of ITO as a conducting oxide which indicates the efficacy of transparent material in semiconductor devices for switching applications.

Figure 4a shows the variation of gate capacitance as a function of V_{gs} and V_{ds}. When V_{gs} increases, the accumulation of charges at the gate increases and thus increases the gate capacitance. Moreover, when V_{ds} is increased, the charge carriers near the gate moves towards source side and contributes in drain current thereby lowering the gate capacitance (Marjani and Hosseini 2014) as can be clearly observed in Fig. 4a. It is also noted that, for very high frequency, the gate capacitance is also reduced (3.41%) in TGRC as shown in Fig. 4b. Thus, TGRC device is a suitable device for low power switching applications.

A notable capacitance dependent FOM, transconductance frequency product (TFP) for high-frequency performance is given in Eq. (1). TFP is principally the product of device efficiency and f_T (Kumar et al. 2016b). It signifies a trade-off between bandwidth and power and is used for high-speed designs. Figure 5a shows that TFP is increasing as V_{gs} increases in sub-threshold region (below 0.4 V) and in inversion region, TFP attains a peak value of 650 GHz and with further increase in gate bias, i.e., as biasing go in deep inversion region, TFP falls significantly due to increment in C_{gg} (see Fig. 4a). It is observed that the peak value of TFP is higher in TGRC MOSFET due to the high value of transconductance as reported earlier (Kumar et al. 2016c) and reduction in total gate capacitance (which is the sum of C_{gs} and C_{gd}) in the linear region (see Fig. 3a).

$$TFP = \left(\frac{g_m}{I_d}\right) \times \left(\frac{g_m}{2\pi C_{gg}}\right). \tag{1}$$

Further, energy-delay product (EDP) [given in Eq. (2)] is a valued parameter as far as circuit applications are concerned. It is a measure of energy and is defined by the product of the average energy (E_{ave}) and the gate delay

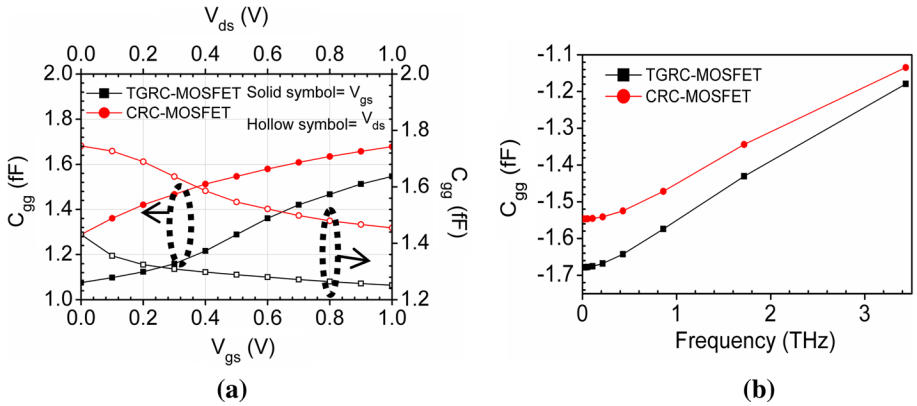

Fig. 4 Gate Capacitance as a function of **a** $V_{gs} = 1.0$ V ($V_{ds} = 0.5$ V) and $V_{ds} = 1.0$ V ($V_{gs} = 0.5$ V) **b** frequency at $V_{gs} = 1.0$ V, $V_{ds} = 0.5$ V; of CRC and TGRC MOSFET

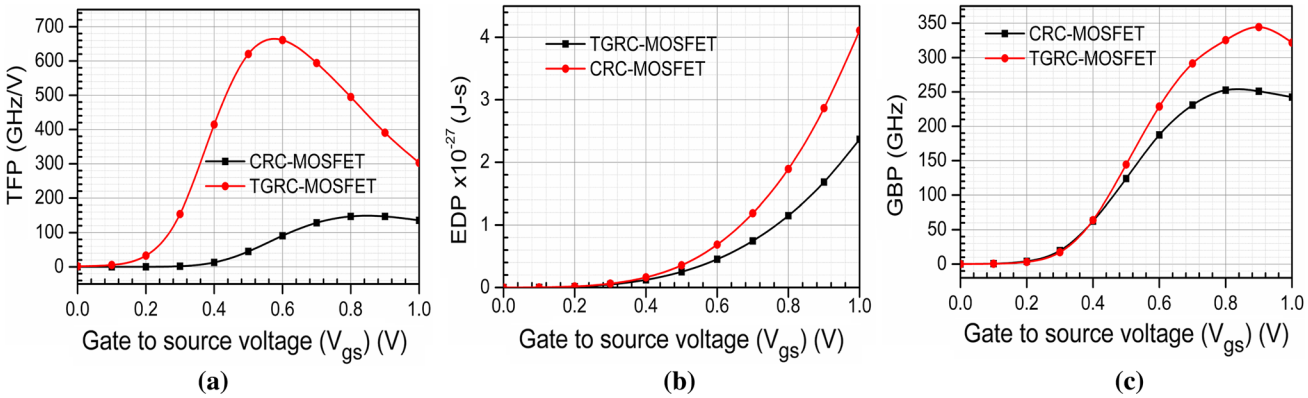

Fig. 5 **a** TFP, **b** EDP, **c** GBP; at $V_{gs} = 1.0$ V, $V_{ds} = 0.5$ V as a function of gate to source voltage for CRC and TGRC MOSFET

(τ). It calculates the energy consumed per switching event (such as in logic families). In TGRC, EDP improves at lower drain bias in comparison to CRC MOSFET as evident from Fig. 5b, due to a reduction in gate capacitance (C_{gg}) and improvement in on-current (Kumar et al. 2016a). In addition, Fig. 5c shows the Gain Bandwidth Product (GBP) [calculated by Eq. (3)] at different drain bias voltage and is a qualitative measure of both gain and bandwidth of a voltage amplifier. It is perceived that GBP improves at higher drain voltage in TGRC device due to a reduction in C_{gd} (see Fig. 3a). GBP peak value indicates the frequency at which the device attains maximum gain.

$$EDP = \left(C_{gg}V_d^2\right) \times \left(\frac{C_{gg}V_d}{I_{on}}\right) \tag{2}$$

$$GBP = \frac{g_m}{2\pi \times 10 \times C_{gd}}. \tag{3}$$

4.2 Impact of gate length (L_G) miniaturization

Furthermore, the impact of parameter variation on the proposed device is studied in terms of the gate length. As evident from Fig. 6a that, when gate length decreases, C_{gs} and C_{gd} decreases as a function of V_{gs}. The similar trend follows in ref. (Cho et al. 2011; Ghosh et al. 2015). When the gate length decreases from 40 to 30 nm, C_{gs} decreases by 8.42% and C_{gd} decreases by 3.03%.

Furthermore, when we reduce the gate length from 30 to 20 nm, then C_{gs} decreases by 9.31%, and C_{gd} decreases by 3.4%. Thus, shrinking the gate length reduces the parasitic capacitances in TGRC MOSFET, which leads to increased circuit density in IC fabrication. As we know that, when V_{ds} increases, the pinch-off point moves towards source side and the number of charge carriers accumulates towards source side. Hence C_{gs} increases and C_{gd} decreases as shown in Fig. 6b. Thereafter, the gate length variation is observed, and it is clearly evident from the figure that as the gate length reduces then, C_{gs} and C_{gd} are also reduced. If we reduce the gate length from 40 to 30 nm, then 4 and 0.98% decrement is observed in C_{gs} and C_{gd}, respectively.

When gate length further reduces from 30 to 20 nm, then 4.28 and 1.59% reduction is observed in C_{gs} and C_{gd}, respectively. Further, the impact of gate length variation on parasitic capacitances is observed for very high frequencies

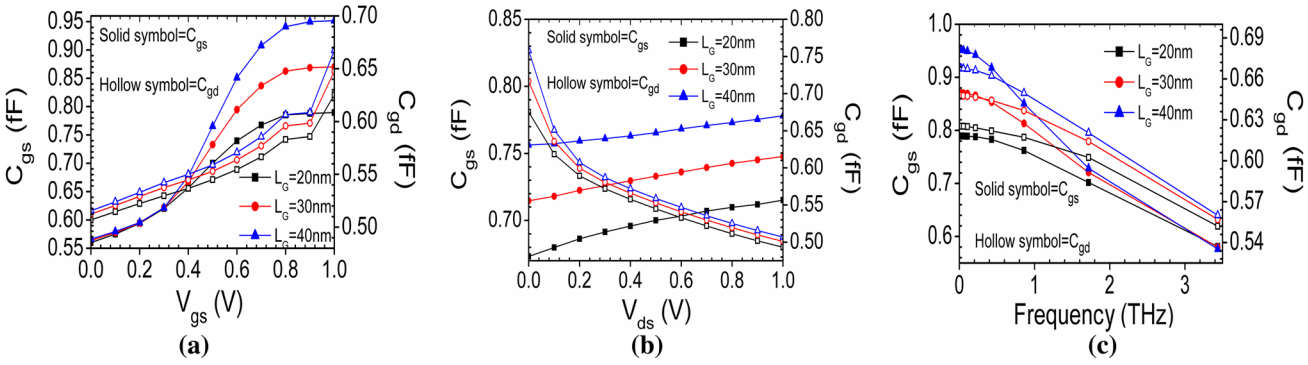

Fig. 6 C_{gs} and C_{gd} as a function of **a** $V_{gs} = 1.0$ V at $V_{ds} = 0.5$ V **b** $V_{ds} = 1.0$ V at $V_{gs} = 0.5$ V **c** frequency at $V_{gs} = 1.0$ V, $V_{ds} = 0.5$ V; of TGRC MOSFET for various gate lengths

(at THz) as shown in Fig. 6c. When the frequency is increased in THz range, and gate length reduces from 40 to 30 nm, then C_{gs} and C_{gd} are reduced by 7.08 and 2.8%, respectively and further 8.2 and 3.5% when gate length varies from 30 to 20 nm. So it is that reduction in parasitic capacitances leads to a device for better switching performances of TGRC MOSFET, as we scale-down the channel length.

Figure 7a reflects the parameter variation of TGRC MOSFET in terms of the gate length. It is evident from figure that gate capacitance increases when V_{gs} is increased (Marjani and Hosseini 2014), and V_{ds} is decreased. As the gate length reduces, and then the gate capacitance is also decreased. If we scale-down the gate length of TGRC MOSFET from 40 to 30 nm, then 7.22 and 2.34% decrement is observed in C_{gg} as a function of V_{gs} and V_{ds}, respectively. If we further scale-down the gate length from 30 to 20 nm, then 7.79 and 4% decrement is reflected in C_{gg} as a function of V_{gs} and V_{ds} respectively. It is also evident from Fig. 7b that, the gate capacitance is also reduced (lower the magnitude) by 6.61 and 7.79% when the gate length scales down from 40 to 30 nm and 30 to 20 nm, respectively at very high frequencies. Therefore, 20 nm gate length device shows that, as we scale-down the device, the parasitic capacitances are reduced, thus making TGRC device a promising device for high-frequency switching applications. Hence, proposed device also leads to increased circuit density in IC fabrication.

Likewise, by scaling down the gate length to 20 nm, TFP and GBP are enhanced while EDP reduces appreciably as is clear from Fig. 8 (Park et al. 1998). This enhancement is due to a reduction in gate capacitance and improvement in I_{on} (see Fig. 3a). EDP is further minimized if TGRC is biased in the linear region in comparison to saturation region owing to reduced supply voltage and capacitance coupling. Whereas in cut-off region, EDP reduces appreciably, as shown in Fig. 8b. This is useful in the field of low power switching applications.

4.3 Impact of variation of negative junction depth (NJD)

Effects of NJD variation on parasitic capacitances have been observed in this section of the proposed device. When NJD is reduced, the number of charge carriers move quickly from source to drain because channel length gets reduced

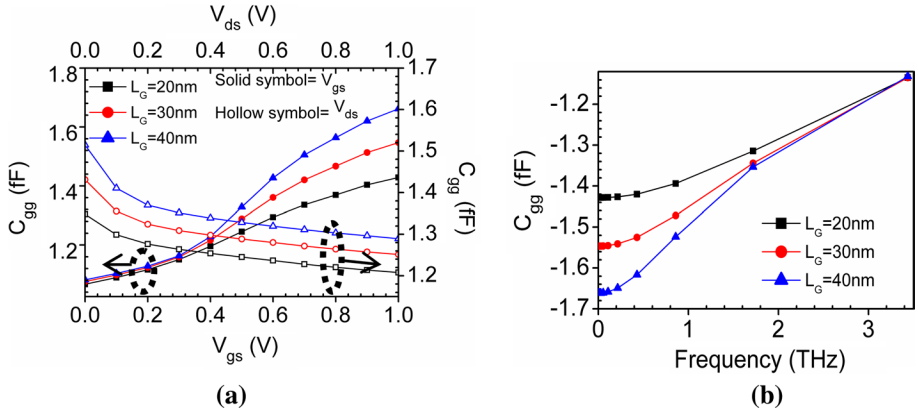

Fig. 7 Gate Capacitance as a function of **a** $V_{gs} = 1.0$ V ($V_{ds} = 0.5$ V) and $V_{ds} = 1.0$ V ($V_{gs} = 0.5$ V) **b** frequency at $V_{gs} = 1.0$ V, $V_{ds} = 0.5$ V; of TGRC MOSFET for various gate lengths

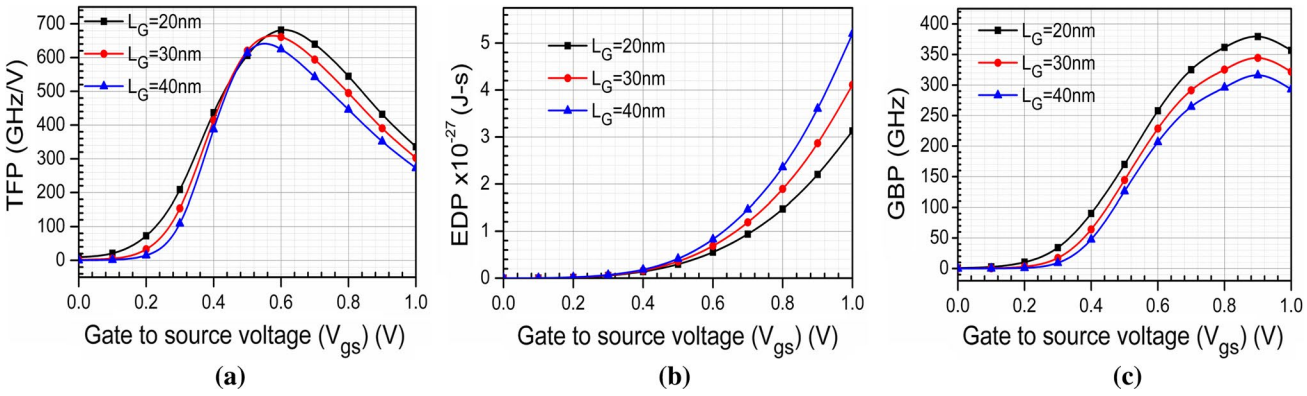

Fig. 8 **a** TFP, **b** EDP, **c** GBP; as a function of $V_{gs} = 1.0$ V ($V_{ds} = 0.5$ V) of TGRC MOSFET for various gate lengths

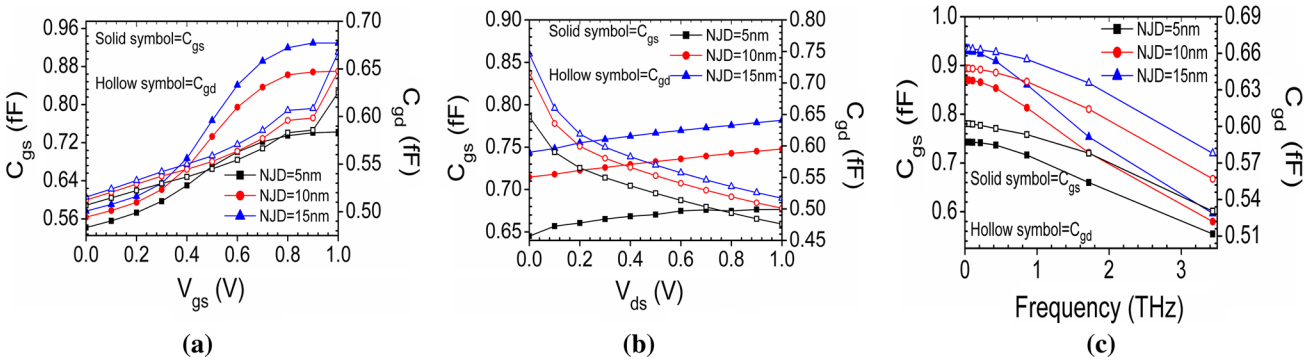

Fig. 9 C_{gs} and C_{gd} as a function of **a** $V_{gs} = 1.0$ V at $V_{ds} = 0.5$ V **b** $V_{ds} = 1.0$ V at $V_{gs} = 0.5$ V **c** frequency at $V_{gs} = 1.0$ V, $V_{ds} = 0.5$ V; of TGRC MOSFET at various NJDs

with the reduction of NJD and the switching time is also reduced making the device operation faster. Figure 9a shows that the decrease in C_{gs} and C_{gd} is reflected when NJD is reduced from 15 to 5 nm, and it is also observed that when V_{gs} increases, the reduction in C_{gs} is enhanced. If NJD is reduced from 15 nm to 10 nm, C_{gs} and C_{gd} is reduced by 7.27 and 1.6%, respectively. Further, reduction in NJD from 10 to 5 nm reduces C_{gs} and C_{gd} by 17.21 and 2.22%, respectively. Similar kind of reduction in parasitic capacitances is observed when V_{ds} is applied, as evident from Fig. 9b. When NJD is reduced from 15 to 10 nm then, C_{gs} and C_{gd} are reduced by 4.4 and 3.1%, respectively. At higher frequencies, C_{gs} and C_{gd} are reduced (by 12.3 and 8.97%) if NJD reduces (from 15 to 10 nm) as reflected from Fig. 9c.

Moreover, the gate capacitance is investigated at different NJDs, and it is observed when V_{gs} and V_{ds} are applied as shown in Fig. 10a. When NJD is reduced from 15 to 10 nm then, C_{gg} is reduced by 4.63 and 4.0% w.r.t V_{gs} and V_{ds}, respectively. Further, NJD reduction from 10 to 5 nm reduces C_{gg} by 13.53 and 8% w.r.t. V_{gs} and V_{ds}, respectively as shown in Fig. 10a. Figure 10b shows a very high reduction in gate capacitance when NJD scales down at THz frequency range. In addition, a decrease in NJD to 5 nm results in an enhancement in TFP and GBP while degrading EDP as shown in Fig. 11 (Park et al. 1998). From Fig. 11b, it is observed that effect of transparent gate scheme strongly affects the EDP. GBP also improves by modulating NJD as reflected in Fig. 11b. It is also found that GBP achieve higher value in saturation mode since C_{gd} is lower in saturation mode [see Fig. 6 (Park et al. 1998)].

5 Conclusion

This work analyzes the capacitance–voltage characteristics of In_2O_5Sn gate electrode recessed channel MOSFET with 30 nm gate length to examine the parasitic capacitances. The simulated results are then used to isolate the parasitic capacitances. The effect of In_2O_5Sn gate electrode (as a transparent gate electrode) in recessed channel MOSFET has been studied in terms of bias and frequency-dependent parasitic capacitances and capacitance dependent FOMs such as TFP, EDP, and GBP for high switching performance. It is observed that with the amalgamation of In_2O_5Sn with RC MOSFET, parasitic capacitances decrease in comparison to aluminum gate metal (CRC MOSFET). When the gate length reduces to 20 nm, then the parasitic capacitances gets reduced, and the overall parasitic capacitances reduce in TGRC architecture by ~25%. Hence, the device is more suitable at sub-20 nm regime. It is also

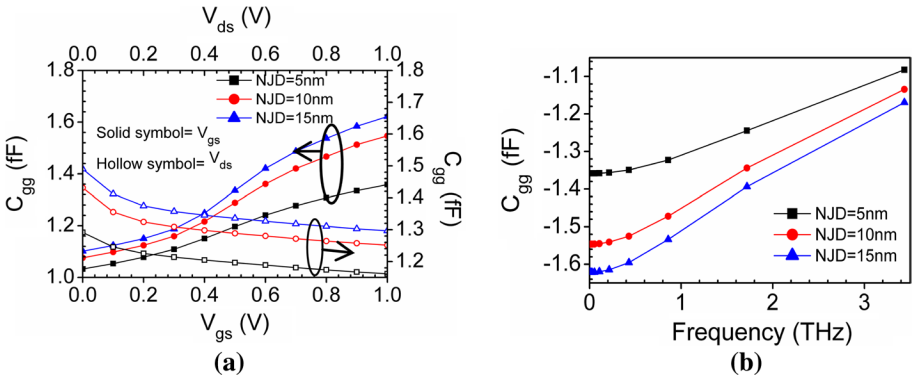

Fig. 10 Gate Capacitance as a function of **a** $V_{gs} = 1.0$ V ($V_{ds} = 0.5$ V) and $V_{ds} = 1.0$ V ($V_{gs} = 0.5$ V) **b** frequency at $V_{gs} = 1.0$ V, $V_{ds} = 0.5$ V; of TGRC MOSFET for various NJDs

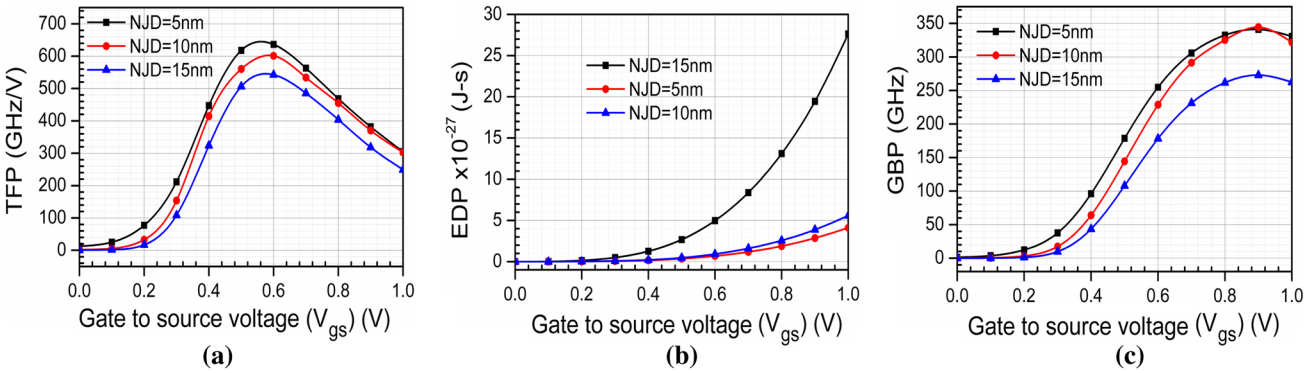

Fig. 11 **a** Transconductance Frequency Product (TFP), **b** Energy Delay Product (EDP), **c** Gain Bandwidth Product (GBP); as a function of $V_{gs} = 1.0$ V ($V_{ds} = 0.5$ V) of TGRC MOSFET for various NJDs

found that with the variation in frequency, parasitic capacitance reduces due to the high current driving capability of TGRC MOSFET; thus, TGRC architecture proves a promising contender for high frequency/switching applications in 22 nm node technology.

Acknowledgements The authors would like to express thankfulness to Microelectronics Research Lab, Department of Engineering Physics and Electrical Engineering Department Delhi Technological University to carry out this work.

References

An X, Huang R, Zhao B, Zhang X, Wang Y (2003) Design guideline of an ultra-thin body SOI MOSFET for low-power and high-performance applications. Semicond Sci Technol 19:347

Auth CP, Plummer JD (1997) Scaling theory for cylindrical, fully-depleted, surrounding-gate MOSFET's. Electron Device Lett IEEE 18:74–76

Barsan RM (1981) Analysis and modeling of dual-gate MOSFET's. Electron Devices IEEE Trans 28:523–534

Chaujar R, Kaur R, Saxena M, Gupta M, Gupta R (2008) TCAD assessment of gate electrode workfunction engineered recessed channel (GEWE-RC) MOSFET and its multilayered gate architecture—part I: hot-carrier-reliability evaluation. Electron Devices IEEE Trans 55:2602–2613

Cho S, Lee JS, Kim KR, Park B-G, Harris JS Jr, Kang IM (2011) Analyses on small-signal parameters and radio-frequency modeling of gate-all-around tunneling field-effect transistors. Electron Devices IEEE Trans 58:4164–4171

Ghosh S, Koley K, Sarkar CK (2015) Impact of the lateral straggle on the Analog and RF performance of TFET. Microelectron Reliab 55:326–331

Gupta N, Kumar A, Chaujar R (2016) Oxide bound impact on hot-carrier degradation for gate electrode workfunction engineered (GEWE) silicon nanowire MOSFET. Microsyst Technol 22(11):2665–2671

Hu S, Wu Y, Sung C, Chang C, Huang T (2003) Single-electron transistor using self-aligned sidewall spacer gates on silicon-on-insulator nanowire. In: Nanotechnology, 2003. IEEE-NANO 2003. 2003 Third IEEE Conference on. (IEEE, 2003), pp 573–576

Hu S-F, Wu Y-C, Sung C-L, Chang C-Y, Huang T-Y (2004) A dual-gate-controlled single-electron transistor using self-aligned polysilicon sidewall spacer gates on silicon-on-insulator nanowire. IEEE Trans Nanotechnol 3:93–97

Iwai H (2009) Roadmap for 22 nm and beyond. Microelectron Eng 86:1520–1528

Kumar A, Gupta N, Chaujar R (2016a) Analysis of novel transparent gate recessed channel (TGRC) MOSFET for improved analog behaviour. Microsyst Technol 22(11):2665–2671

Kumar A, Gupta N, Chaujar R (2016b) Power gain assessment of ITO based transparent gate recessed channel (TGRC) MOSFET for RF/wireless applications. Superlattices Microstruct 91:290–301

Kumar A, Gupta N, Chaujar R (2016c) TCAD RF performance investigation of transparent gate recessed channel MOSFET. Microelectron J 49:36–42

Kundu A, Koley K, Dutta A, Sarkar CK (2014) Impact of gate metal work-function engineering for enhancement of subthreshold analog/RF performance of underlap dual material gate DG-FET. Microelectron Reliab 54:2717–2722

Marjani S, Hosseini SE (2014) Radio-frequency modeling of square-shaped extended source tunneling field-effect transistors. Superlattices Microstruct 76:297–314

Minami T (2005) Transparent conducting oxide semiconductors for transparent electrodes. Semicond Sci Technol 20:S35–S44

Moore GE (1975) Progress in digital integrated electronics. In: Electron Devices Meeting, pp 11–13

Murali R, Meindl JD (2007) Modeling the effect of source/drain junction depth on bulk-MOSFET scaling. Solid State Electron 51:823–827

Park D, King Y-C, Lu Q, King T-J, Hu C, Kalnitsky A, Tay S-P, Cheng C-C (1998) Transistor characteristics with Ta/sub 2/O/sub 5/gate dielectric. IEEE Electron Device Lett 19:441–443

Rahimian M, Orouji AA (2013) Investigation of the electrical and thermal performance of SOI MOSFETs with modified channel engineering. Mater Sci Semicond Process 16:1248–1256

Silvaco Int. (2016) ATLAS user's manual, ver 5. Santa Clara, CA

Singh V, Suman C, Kumar S (2006) Indium Tin Oxide (ITO) films on flexible substrates for organic light emitting diodes. In: Proc. of ASID, p 388

Steinke DR, Piccirillo J, Gausepohl SC, Vivekand S, Rodgers MP, Lee JU (2012) Parasitic capacitance removal of sub-100 nm p-MOSFETs using capacitance–voltage measurements. Solid State Electron 68:51–55

Woerlee PH, Knitel MJ, Van Langevelde R, Klaassen D, Tiemeijer LF, Scholten AJ, Zegers-van Duijnhoven AT (2001) RF-CMOS performance trends. Electron Devices IEEE Trans 48:1776–1782

Xiao-Hua M, Yue H, Bao-Gang S, Hai-Xia G, Hong-Xia R, Jin-Cheng Z, Jin-Feng Z, Xiao-Ju Z, Wei-Dong Z (2006) Fabrication and characterization of groove-gate MOSFETs based on a self-aligned CMOS process. Chin Phys 15:195

Int J of Soc Robotics
DOI 10.1007/s12369-017-0397-8

Non-human Looking Robot Arms Induce Illusion of Embodiment

Laura Aymerich-Franch[1,3] · **Damien Petit**[1,2] · **Gowrishankar Ganesh**[1,2] · **Abderrahmane Kheddar**[1,2]

Accepted: 5 February 2017
© Springer Science+Business Media Dordrecht 2017

Abstract We examine whether non-human looking humanoid robot arms can be perceived as part of one's own body. In two subsequent experiments, participants experienced high levels of embodiment of a robotic arm that had a blue end effector with no fingers (Experiment 1) and of a robotic arm that ended with a gripper (Experiment 2) when it was stroked synchronously with the real arm. Levels of embodiment were significantly higher than the corresponding asynchronous condition and similar to those reported for a human-looking arm. Additionally, we found that visuo-movement synchronization also induced embodiment of the robot arm and that embodiment was even partially maintained when the robot hand was covered with a blue plastic cover. We conclude that humans are able to experience a strong sense of embodiment towards non-human looking robot arms. The results have important implications for the domains related to robotic embodiment.

Keywords Humanoid robot embodiment · Non-human looking robot · Body ownership illusion · Rubber-hand illusion

1 Introduction

Where does the limit lie regarding the brain's capacity to integrate a non-human looking arm as part of one's own body? In the rubber hand illusion (RHI), participants have the sensation that a human-looking rubber hand becomes part of their body when it is stroked synchronously with their real hand, which stays out of sight [1]. On the other hand, the illusion of embodiment is not perceived when the physical characteristics of the fake hand are very different to those of the real hand, such as when a wooden stick is used instead of a rubber hand [2]. Regardless of that, participants can still experience the illusion of touch on a non-hand object like a box [3] or a table [4] when there is prior onset of the basic RHI [3,4].

The acceptance of a fake limb as part of the body by the brain depends on several physical and spatial factors. Regarding physical features, it is known that resemblance of the limb or body to a human body contributes to increase the sense of embodiment [2,5]. However, factors such as color [6] or skin luminance [7] do not affect the illusion of embodiment of fake hands. Interestingly, regarding size, previous work shows that while human participants experience the embodiment illusion of a rubber hand larger than the real one, they do not experience the illusion when a rubber hand smaller than the real one is used [8]. Regarding spatial features, previous research has found that the illusion of embodiment of a rubber hand does not occur when the posture of the rubber hand is spatially incongruent with respect to the real hand [2,9,10] or when the rubber hand is located outside the participant's peri-personal space [11].

Electronic supplementary material The online version of this article (doi:10.1007/s12369-017-0397-8) contains supplementary material, which is available to authorized users.

✉ Laura Aymerich-Franch
laura.aymerich@gmail.com

1 CNRS-AIST Joint Robotics Laboratory (JRL), UMI3218/RL, National Institute of Advanced Industrial Science and Technology (AIST), Central 1, 1-1-1 Umezono, Tsukuba, Ibaraki 305-8560, Japan

2 CNRS-UM LIRMM, Interactive Digital Human Group, UMR5506, Montpellier, France

3 National Institute of Advanced Industrial Science and Technology (AIST), Central 1, 1-1-1 Umezono, Tsukuba, Ibaraki 305-8560, Japan

Published online: 02 March 2017

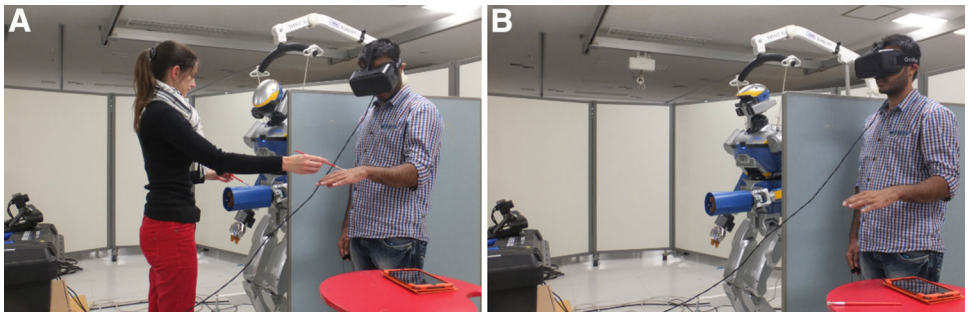

Fig. 1 Humanoid robot embodiment set-up used in both experiments. The participant wears an HMD that provides vision from the robot's perspective and is able to control the robot's head movement. The illusion is either induced by visuo-tactile synchronization (**a**) or visuo-movement synchronization (**b**)

In the particular domain of robots, previous works have reported body ownership transfer towards teleoperated android arms or robot arms either using visuo-movement synchrony [12,13] or brain-computer interface [14], but have only utilized arms with high resemblance to humans in terms of shape (i.e. a hand with five fingers) [12] and texture [3,13]. On the other hand, studies in virtual reality suggest that users are able to identify with avatars even when they present different visual characteristics than their real selves provided that there exists visuo-movement correlation between the human body movement and the avatar movement [15–17]. Thus, it is not clear where the limit lies regarding humans' capacity to integrate non-human looking robot arms as part of their body.

In order to explore this question further, we conducted two experiments utilizing our humanoid robot embodiment set-up (Fig. 1a, b) in which we induced the illusion of embodiment in two different types of humanoid arms by visuo-tactile synchronization (Fig. 1a), following the classic rubber hand illusion experiment [1]. Specifically, the first experiment examined embodiment of a non-human looking robot arm made of metal and plastic which ended with a blue hand (end effector) with no fingers (Fig. 2a) and the second experiment examined embodiment of a robot arm which ended with a metal gripper (Fig. 2b). In addition, previous research suggests that movement synchronization between the real and the fake body or body part are also able to induce the illusion of embodiment in fake or robotic limbs and bodies when they resemble human shape [12,13]. Thus, our experiments also examined whether sense of embodiment of the robot arm is also achieved when visuo-movement synchronization (i.e. arm movement synchronization between the human arm and the humanoid arm) is used to induce the illusion (Fig. 1b). Finally, since previous research suggests that embodiment illusion does not occur when an object such a box is used for the illusion [3], the second experiment additionally explored whether embodiment takes place when the robot hand is covered by a plastic cover (Fig. 2c).

A novelty in our study, compared to previous rubber-hand illusion related experiments, is that we utilize a whole body embodiment set-up [18,19]. In our setup participants embody the humanoid robot using a head-mounted display (HMD) that provides vision of the arm from the robot's perspective (Video S1) and also control the robot's head movement (Fig. 1a, b). This enabled us to present an artificial limb (arm) to the participants at the same location as their real limb, a feature we believe is key to the various results we observed in this study. The robot avatar setup uses similar principles to the ones used in virtual reality to achieve sense of embodiment of the avatar body (i.e. first person perspective from the avatar body and visuo-movement synchronization of the user and the avatar head).

2 Method

2.1 Participants

In total, 31 participants took part in the study. Twelve participants of different nationalities (six males and six females), aged 21–43 ($M = 26.67$, $SD = 8.04$), participated in the first experiment and nineteen participants also of different nationalities (thirteen females and six males), aged 23–44 ($M = 31.77$, $SD = 6.02$), participated in the second experiment. One of the participants was left-handed in each study and the rest were right-handed. Participants were naïve to the purpose of the experiment and received 1500JPY (Japanese yen) to participate. They were recruited through a call for volunteers in a webpage created ad hoc for the experiment, which was allocated on a social network. Working in the Robotics or Neuroscience fields was used as exclusion criteria. A pretest was conducted for each study with five (Experiment 1) and three (Experiment 2) intern master students of the research laboratory in which the study was conducted. The study was carried out with ethical approval of the National Institute of Advanced Industrial Science and Technology (AIST) in Tsukuba, Japan.

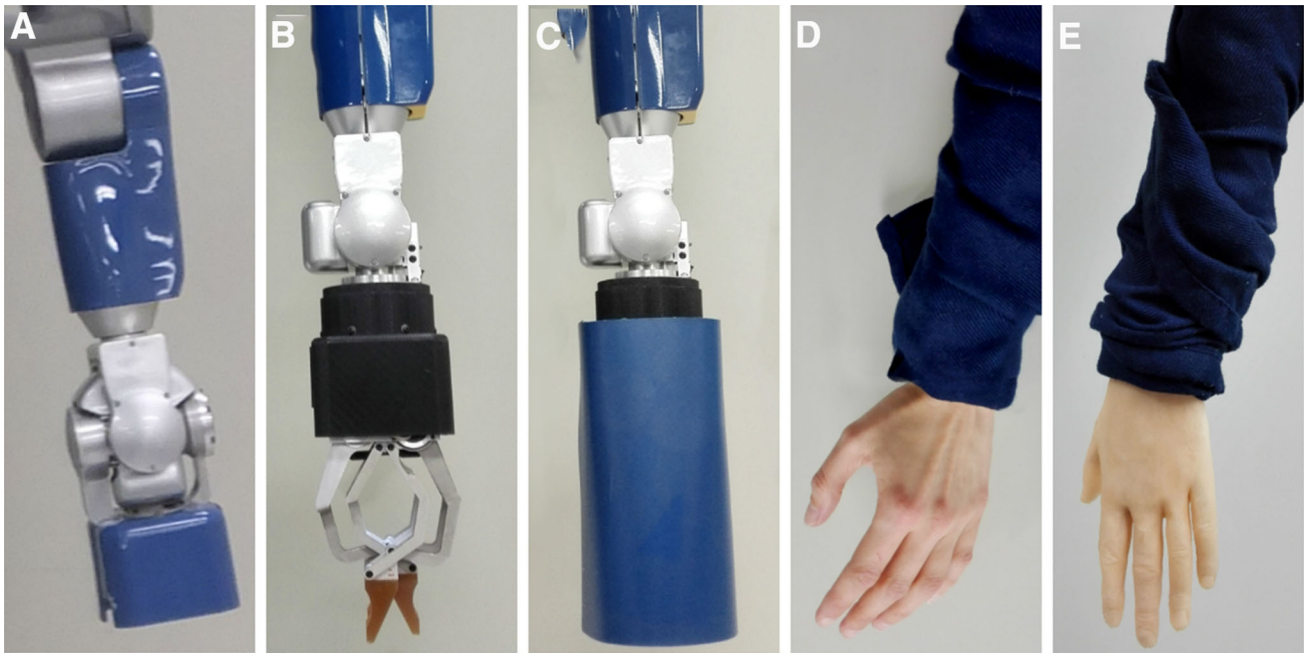

Fig. 2 Blue hand with no fingers (**A**), gripper (**B**), hand covered with a blue plastic cover (**C**), human hand (**D**), human-looking rubber hand (**E**) used in the experiments A and D were used in Experiment 1 while B, C, and D were used in Experiment 2

2.2 Apparatus and Material

A human size humanoid robot HRP-2 [20] was used to create embodiment in the robot arm conditions. The material of the robot arm was composed of plastic and metal of blue and silver colors. Each arm had seven degrees of freedom. A RGB-D camera (Asus XtionPRO live) was mounted on the robot's head which sent visual feedback to an Oculus Rift HMD worn by the user (Fig. 1a, b). Sensors integrated in the HMD allowed the tracking of the user's head motion in order to control the robot's head. A second RGB-D camera (similar to the previous one) was used externally to track the hand motion of the user in the robotic arm visuo-movement conditions (Fig. 1b). OpenNI, a framework to track body and hand motion, was used to track the user's hand position. In our experiment, only the user's hand position was tracked. The hand tracker was initialized after detecting a waving motion of the user's hand. Once the hand was tracked, participants were asked to place their hand in a position which corresponded to the robot's hand position (See Procedure). Next, the user hand motion was mapped on the robot hand (teleoperation mode). In order to control the robot arm and head, the Stack-of-Task (SoT) controller was used [21], which took as input the hand position provided by OpenNI as well as the user's head orientation provided by the HMD. In the SoT, the tasks are defined as state error vectors in the sensory space, and projected in the robot joint space with the robot (pseudo-)inverse kinematic Jacobian. The Robot Operating System (ROS) was used to integrate the HMD, the robot's camera, the SoT, and the human hand tracking. In Experiment 1, the robot had a blue square ending at the place of the hand, which had no fingers (Fig. 2a, Video S1). In Experiment 2, the robot had a metal gripper with three fingers (Fig. 2b, Video S1). For the cover condition in Experiment 2, a blue cylinder composed of hard plastic was used to cover the robot arm (Fig. 2c, Video S1).

For the human arm conditions, we used a medium big sized bare arm corresponding to a female researcher (Fig. 2d, Video S1) in Experiment 1 and a rubber hand (Fig. 2e, Video S1) in Experiment 2. In those conditions, the robot arm was lowered and left aligned to its body and substituted by the human arm, so that the participants were able to see a human arm when they looked down through the HMD (Fig. 1a, b, Video S1). In order to keep the human arm in Experiment 1 neutral (Fig. 2d), it did not have any visible clothes or jewelry. The nails were cut short and did not have any nail polish.

2.3 Procedure

After reading and signing the consent form, participants were placed next to a panel. The humanoid robot was at the other side of the panel and was not visible to them (Fig. 1a, b). Participants then wore an Oculus Rift visor which was used to display real-time video feedback from the camera located at the forefront of the robot's head, right above its eyes. Once the participants wore the visor they were able to control the robot's head movement and visualize what the robot was seeing in real-time (Video S1). The participants were then

told to place their arm (left, or right arm, depending on the condition and experiment) creating a 90° angle between the arm and the forearm, with the elbow next to the hip, and to leave their hand opened. This specific arm position was similar to the robot's arm posture so that users observed the robot arm coinciding with their own arm position. Also, they were told to look at the robot's arm through the visor. This position was valid for all experimental conditions. After this, the first trial started. For the human arm synchronous and asynchronous condition, the robot's arm was removed from the vision of the participant and either one of the researchers put her real arm on the place of the robot's arm while the other researcher stroked the researcher's arm (Experiment 1) or a rubber arm was positioned at the place of the robot arm (Experiment 2). For the visuo-tactile synchronous and asynchronous conditions, a researcher stroked the robot's or the human-looking arm and the participant's arm either synchronously or asynchronously, with two small paintbrushes. For the robot visuo-movement synchronization condition, participants were told to look front and wave. A camera was placed in front of the participant to track the arm movement. Participants could not see the camera because they wore the visor. Then, they were asked to place their real arm creating a 90° angle and looking at the robotic arm through the visor. After that, participants were able to move their arm and the robot's arm responded with the same movement. For the asynchronous robot arm control conditions, the camera that tracked the participant's movement was flipped and faced one of the researchers, who performed the control instead. In Experiment 1, after 90 s of either stroking or arm movement, the participants were verbally asked the three questions corresponding to the embodiment questionnaire (see Measures) by another researcher while they kept observing the arm, and responded the answers out loud. In Experiment 2, before asking the questions, one of the experimenters passed his hands around the fake limb for 15 s in order to examine potential changes on skin conductance. GSR data was recorded during this period of time. After that, the embodiment questionnaire was asked while the participant kept looking at the arm. Then, they relaxed and moved their arm for few seconds and continued to the next condition. The participants looked front every time the setup was modified so that they were not able to see the modifications taking place among the different conditions. Participants were also requested to look front for few seconds between the synchronous and the corresponding asynchronous condition even if the setup was not modified. In Experiment 1, after completing all conditions, participants started over with the opposite arm. In Experiment 2, participants only completed each condition once, with the left arm. At the end of Experiment 1 participants answered an open-ended question while in Experiment 2 a short-interview was conducted by one of the experimenters (see Measures). Finally, they were thanked and paid for their participation.

2.4 Measures

2.4.1 Embodiment Questionnaire

As a working definition, we understand embodiment as the illusion of adopting an artificial body or body part as part of the own body. Although there is no broad consensus, embodiment can be considered to consist of three subcomponents: the sense of body ownership, the sense of self-location, and the sense of agency [22,23]. Body-ownership is the sense of owning a body or body part. Self-location is a determinate volume in space in which one feels to be located, normally localized within the bodily boundaries [24]. Finally, agency is "global motor control, including the subjective experience of action, control, intention, motor selection and the conscious experience of will" [24]. For Experiment 1, a short-form embodiment questionnaire was designed to measure arm embodiment of the embodied arm based on other studies [22,23]. Also following previous studies [17], the questionnaire was specifically designed to be responded in situ in order to minimize the effect of recall bias [25]. Brief versions of self-rated questionnaires such as the Mini-Social Phobia Inventory [26], consisting of only three items, demonstrate that shortened versions of assessment instruments are as efficient [26], and demonstrate reliability and validity [27] similar to the corresponding longer versions. The questionnaire has also been implemented elsewhere [18,28]. It consisted of three questions ("Appendix 1" section), one for each of the sub-dimensions of embodiment: body ownership, self-location, and agency [22]. The questionnaire was designed so that the same questions were suitable to measure human arm embodiment and robot arm embodiment. The scale obtained an average reliability of $\alpha = .94$, KMO $= .605$, and Bartlett's test of Sphericity $= .002$. For Experiment 2, we adapted the embodiment questionnaire from [23] to measure the sense of embodiment to the robot's arm. The questionnaire consisted of nine items ("Appendix 1" section) which were rated on a 7-point scale that ranged from (1) *not at all* to (7) *very strongly*. The scale consisted of the same sub-dimensions described for the previous questionnaire: sense of body ownership (five items), sense of self-location (two items), and sense of agency (two items). Average reliability of the scale was $\alpha = .93$.

2.4.2 Demographic Measures

At the end of the experiment participants completed their age, gender, and whether they were right or left-handed in a PC-based questionnaire.

2.4.3 Galvanic Skin Response (GSR)

In Experiment 2 we measured skin conductance which was recorded using a *Mindfield Biosystems eSense Skin Response* device and processed using MatLab. Skin conductance was measured with two electrodes attached to the middle and index finger of the right hand. Sampling frequency of the device was 10 Hz (10 values per second) with a resolution of 18 bit, with five values per second saved for exported data to a CVS file. The participants wore the electrodes throughout the experiment and skin conductance was recorded from the beginning to the end of each experimental condition. We examined a period of 15 s occurring right after the 90 s of visuo-tactile or visuo-motor stimulation during which one of the researchers passed his hands around the embodied arm while the participants looked at it.

2.4.4 Open-Ended Question/Interview After the Experiment

In Experiment 1, an open-ended question after completing the demographic measures asked participants to share their thoughts about the experience by explaining in which condition the feeling that the arm was their own arm was stronger. In Experiment 2, a brief interview was conducted with each participant at the end of the experiment to collect qualitative data about the sensations experienced in each experimental condition in more detail ("Appendix 1" section).

2.4.5 Manipulation Check

At the end of each condition participants were asked whether the touch and vision were happening at the same time or at different times or whether the robot arm responded to their movements. One participant in Experiment 2 was discarded because she repeatedly gave higher scores for all the asynchronous conditions compared to the corresponding synchronous conditions.

3 Experiment 1

In the first experiment, we examined the sense of embodiment of a robotic arm that had a blue hand with no fingers (Fig. 2a, Video S1). The sense of embodiment was induced by visuo-tactile synchronization, following the rubber-hand illusion paradigm [1]. Additionally, a condition was added in which the embodiment illusion of the robot arm was induced by visuo-movement synchronization. Specifically, we expected that embodiment would be significantly higher in the robotic arm visuo-tactile synchronous condition (H_{1a}) as well as in the visuo-movement synchronous condition (H_{1b}), compared to the visuo-tactile asynchronous condition. Based on a recent proposal that the functional characteristics of a limb are more important than the physical features for embodiment [30], we expected that embodiment in the robotic arm visuo-tactile synchronous conditions would be similar to that obtained in the synchronous human arm condition (H_{2a}). Similarly, we expected that embodiment in the robotic arm visuo-movement synchronous conditions would be similar to that obtained in the synchronous human arm condition (H_{2b}). Based on previous findings which suggest that embodiment of a fake limb can also be induced using visuo-movement correlation [29], we expected that levels of embodiment in the robotic arm visuo-tactile synchronous condition and embodiment in the robotic arm visuo-movement synchronous condition would be similar (H_{2c}).

In order to examine these hypotheses, a within-subject experiment was conducted in which participants experienced a total of five conditions ("Appendix 2" section):

$$[(\text{robot, human}) \times (\text{sync., async. visuo-tactile})] + (\text{robot visuo-movement sync.})$$

Participants repeated each condition twice: once for the left arm and once for the right arm. Half of the participants started with the left arm and half of them started with the right arm and went through the five trials before switching to the opposite arm. We grouped the synchronous with its corresponding asynchronous condition and randomized the order between them and among the groups of conditions such that each participant experienced the conditions in a different order but synchronous and asynchronous conditions of different types of arms were not mixed among them.

3.1 Results

Descriptive statistics for overall embodiment as well as for each subcomponent are reported by experimental condition in Table 1. For each condition, we averaged the results of the left and the right arm, which were not significantly different ($p > .05$ in all group comparisons). Given the relatively small size of the sample, nonparametric tests were conducted. Friedman test yielded a statistically significant difference among groups $\chi^2(4) = 26.000, p < .001$. Wilcoxon signed-rank tests were conducted with Bonferroni correction (significance level applied at $p = .008$) to further examine the differences between conditions and respond to the hypotheses. The sense of embodiment of a human arm induced by visuo-tactile synchronization was significantly higher in the synchronous condition, compared to the asynchronous condition ($Z = -2.984$, $p = .001$, one-tailed), which validated the experimental design. Regarding the first hypothesis, the sense of embodiment of a robot arm induced by visuo-tactile synchronization was significantly higher in the synchronous condition, compared to the asynchronous condition ($Z = -2.944$, $p = .003$, two-tailed),

Table 1 Mean (SD) for overall embodiment and its subcomponents

	Overall embodiment	Ownership	Self-location	Agency
Human sync.	5.11 (1.06)	5.5 (.96)	5.75 (.69)	5.43 (1.13)
Human async.	3.76 (1.37)	3.78 (1.38)	4 (1.15)	3.57 (1.61)
Robot sync.	5.33 (1.04)	5.78 (.91)	5.64 (1.11)	6.14 (.89)
Robot async.	3.87 (1.44)	4.14 (2.25)	4.5 (1.44)	4.5 (1.25)
Robot visuo-mov	5.29 (1.02)	5.36 (1.18)	5.07 (1.36)	6.14 (.94)

which supports H_{1a}. Also, the sense of embodiment of a robot arm induced by visuo-movement synchronization was significantly different than the asynchronous robot arm condition ($Z = -3.062$, $p = .002$, two-tailed), which supports H_{1b}. Regarding the second hypothesis, the sense of embodiment of a robot arm induced by visuo-tactile synchronization and the sense of embodiment of a human arm induced by visuo-tactile synchronization were not significantly different ($Z = -1.070$, $p = .285$, two-tailed), which supports H_{2a}. Levels of embodiment were equally high for the human and for the robot arm (See Table 1). Also, the sense of embodiment of a robot arm induced by visuo-movement synchronization was not significantly different to the sense of embodiment obtained in the human arm synchronous condition ($Z = -.409$, $p = .683$, two-tailed), which supports H_{2b}, or to the sense of embodiment of a robot arm induced by visuo-tactile synchronization ($Z = -.544$, $p = .579$, two-tailed), which supports H_{2c}. Levels of embodiment obtained in the visuo-movement synchronization condition were very similar to those obtained in the synchronous visuo-tactile human and robot conditions.

Finally, the qualitative data resulting from the open questions supported the results obtained in the questionnaire. In particular, participants reported a strong feeling that the robot arm was part of their body: "The feeling that the robot arm was part of my own body was strong… the feeling when I saw the real arm and the feeling when I saw the robot arm was pretty much the same because I felt the robot arm as my own" or "the robot arm was very similar to my arm… the feeling was very much the same feeling to when I saw the real arm". In addition, the qualitative data revealed that while some participants felt stronger embodiment when they controlled the movement of the robot: "it was stronger when I controlled the movement than when I got the paintbrush stroke", some others felt stronger sense of embodiment when they received visuo-tactile synchronization: "the feeling that it was my own arm was the strongest when I saw the robot's arm and got the paintbrush stroke which was synchronized".

4 Experiment 2

In Experiment 2, we examined embodiment of a robotic arm with a gripper (Fig. 2b, Video S1). To additionally explore where the limit lies regarding the brain capacity to embody external entities, this experiment also examined whether the sense of embodiment was maintained when the robot arm was not visible and was covered by a blue plastic cover. Experiment 2 also improved some aspects of the methodology used in Experiment 1. Specifically, skin conductance was included as a measure to provide objective physiological evidence for the illusion. The human arm was substituted for a rubber hand following the method used in most RHI experiments [1]. Also, we adopted a more validated questionnaire of embodiment [23] and added a brief interview with the participant at the end of the experience instead of the open question to collect the qualitative aspects of the experience in a more interactive and detailed manner ("Appendix 1" section). Finally, we included an asynchronous visuo-movement condition in the design to compare it with the corresponding synchronous condition.

Specifically, for this experiment, participants experienced the embodiment illusion of a gripper (Fig. 2b, Video S1) and a human-looking arm (Fig. 2e, Video S1). We expected that embodiment would be significantly higher in the gripper visuo-tactile synchronous condition compared to the corresponding asynchronous condition (H_1). Also, we expected that embodiment of the gripper would be similar to that obtained in the synchronous human-like rubber hand condition (H_2).

Additionally, we examined whether embodiment was present when the arm was not visible (i.e. covered by a blue cover) and it was stimulated either by visuo-tactile (RQ_{1a}) or visuo-movement synchronization (RQ_{1b}). We chose an object which possessed drastically different visual properties from a human arm, specifically, in terms of shape, material, and color (Fig. 2c, Video S1). In the cover conditions, the illusion was induced by synchronous or asynchronous visuo-tactile or visuo-movement synchronization.

In order to test the hypotheses and research questions, a within-subject design was conducted in which participants experienced a total of eight conditions ("Appendix 2" section):

[(robot, human) × (sync., async. visuo-tactile)]
+ [(visuo-tactile, visuo-movement cover) × (sync., async.)]

Table 2 Mean (SD) for overall embodiment and its subcomponents

	Overall embodiment	Ownership	Self-location	Agency	GSR
Human sync.	5.13 (1.35)	5.27 (1.39)	5.17 (1.55)	4.97 (1.45)	3.23 (1.48)
Human async.	4.33 (1.05)	4.14 (1.38)	4.61 (1.09)	4.25 (1.34)	2.98 (1.3)
Gripper sync.	4.56 (1.41)	4.31 (1.45)	4.82 (1.51)	4.56 (1.63)	3.34 (1.41)
Gripper async.	3.35 (1.6)	2.69 (1.66)	3.79 (1.72)	3.56 (1.99)	3.13 (1.28)
Cover visuo-tact. sync.	4.97 (1.33)	4.6 (1.48)	5.22 (1.32)	5.08 (1.62)	2.90 (1.4)
Cover visuo-tact. async.	3.59 (1.56)	3.12 (1.5)	4.03 (1.87)	3.61 (2.09)	2.93 (1.37)
Cover visuo-mov. sync.	5.01 (1.12)	4.51 (1.39)	4.88 (1.24)	5.65 (1.32)	3.19 (1.3)
Cover visuo-mov. async.	2.76 (1.78)	2.42 (1.65)	2.88 (1.85)	2.97 (2.33)	3.18 (1.39)

Since no significant differences were found between the two arms in Experiment 1 (see Results), in Experiment 2 participants tried each condition only once with the left arm (for being the one used in the classical RHI experiment [1]). We followed the same procedure for randomizing the conditions than in the previous experiment (See Experiment 1).

4.1 Results

Descriptive statistics for overall embodiment (resulting from the average of the three subcomponents: ownership, self-location, and agency) as well as for each subcomponent by experimental condition are reported in Table 2. Some groups of data (i.e. the data in the cover visuo-movement asynchronous condition and in the rubber arm synchronous conditions) did not reach normal distribution according to the Shapiro–Wilk test. Thus, non-parametric tests were used for the statistical analysis. Friedman test yielded a statistically significant difference among groups $\chi^2(7) = 54.715$, $p < .001$. Wilcoxon signed-rank tests with Bonferroni correction (significance level applied at $p = .005$) were conducted in order to further compare the different conditions between them and answer the hypotheses and research questions. It was found that the sense of embodiment was significantly higher in the human-looking rubber arm ($Z = -2.557$, $p = .005$, one-tailed) compared to the corresponding asynchronous version, which validated the experimental design. Also, embodiment of the gripper arm ($Z = -3.364$, $p = .001$, two-tailed) was significantly higher in the synchronous than in the corresponding asynchronous version, which supports H_1. Additionally, in response to RQ_1 and RQ_2, embodiment in the cover arm induced by visuo-tactile synchronization ($Z = -3.724$, $p < .001$, two-tailed), and the cover arm induced by visuo-movement synchronization ($Z = -3.527$, $p < .001$, two-tailed) were also significantly higher compared to their corresponding asynchronous versions. Also, levels of embodiment obtained in all the visuo-tactile and visuo-movement synchronous conditions were very similar among them (see Table 2). In support to H_2, the sense of embodiment was not significantly different in the rubber-hand compared to the gripper ($Z = -.1.065$, $p = .287$, two-tailed). Again regarding RQ_1 and RQ_2, embodiment was also not significantly different in the rubber-hand compared the cover arm induced by visuo tactile synchronization ($Z = -.024$, $p = .981$, two-tailed), or the cover arm induced by visuo-movement synchronization ($Z = -.355$, $p = .723$, two-tailed). Also, levels of embodiment in the gripper were not significantly different than in the cover arm induced by visuo tactile synchronization ($Z = -.848$, $p = .397$, two-tailed) or in the cover arm induced by visuo-movement synchronization ($Z = -1.221$, $p = .222$, two-tailed). Levels of embodiment between the cover arm induced by visuo-movement or visuo-tactile synchronization were also not significantly different between them ($Z = -.398$, $p = .691$, two-tailed).

In line with the results obtained in the questionnaire, participants displayed significantly greater GSR responses in the synchronous visuo-tactile human-like rubber arm condition compared to the corresponding asynchronous condition ($t(14) = 1.929$, $p = .044$, one-way). Also, GSR approached significance in the synchronous gripper arm condition compared to the corresponding asynchronous condition ($t(14) = 1.684$, $p = .057$, one-way). Additionally, GSR levels in the synchronous visuo-tactile human-like arm and synchronous visuo-tactile gripper arm conditions were not significantly different between them ($t(14) = -.731$, $p = .477$, two-way). The arm covered conditions did not reach significance. Cover visuo-movement synchronous and asynchronous conditions were not significantly different between them ($t(14) = .087$, $p = .465$, one-way) due to that in both conditions GSR levels were high (see Table 2). In fact, synchronous visuo-tactile human-like and synchronous visuo-movement cover condition were not significantly different between them ($t(14) = .155$, $p = .879$, two-way). Also, cover visuo-tactile synchronous and asynchronous conditions were not significantly different between them ($t(14) = -.381$, $p = .646$, one-way). In this case, synchronous visuo-tactile human-like was significantly higher

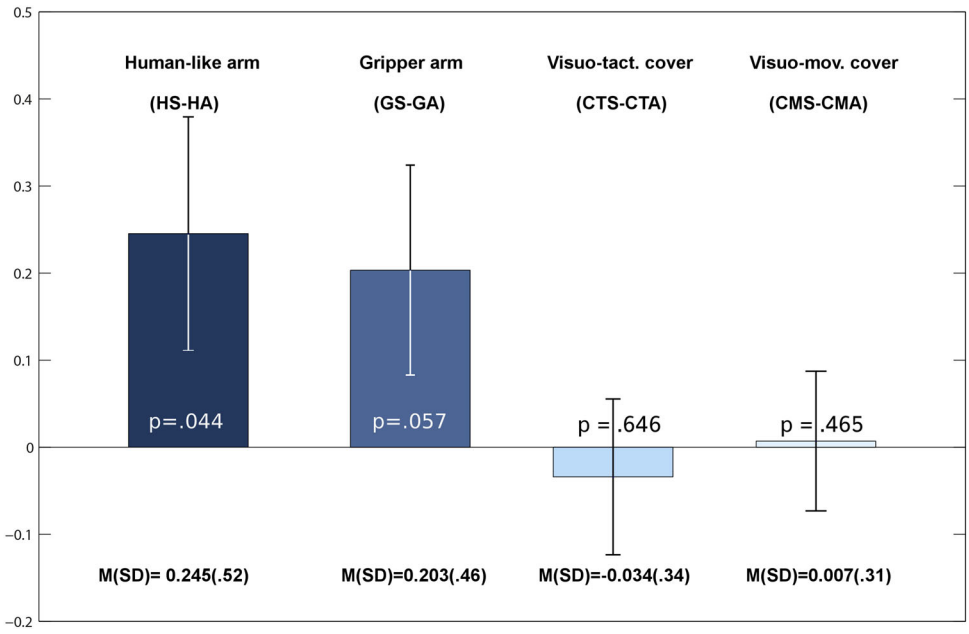

Fig. 3 Skin conductance responses for Experiment 2: M(SD) values resulting from subtracting the responses obtained in the asynchronous condition to the corresponding synchronous condition

than synchronous visuo-tactile cover arm condition ($t(14) = 3.281$, $p = .005$, two-way). Table 2 shows GSR mean and SD by condition (Fig. 3).

Finally, the qualitative data resulting from the interviews after the experiment pointed in the same direction than the reported quantitative measures. In particular, the comments from participants support that the synchronous conditions generated stronger embodiment than the asynchronous conditions both in the human-like and in the robot arms and that embodiment in the robot arms was very similar to that experienced with the human-like arm: "when the hand touched the arm I felt a very strong sensation (that it was touching me) in all the synchronous conditions". However, there was no unified response regarding which of the synchronous conditions (including human and robot conditions) induced the strongest illusion. Also, some participants experienced real sensations in their hands such as heat or tickling when the researcher passed his hand around the robot or the human-looking hand: "I felt tickling during the hand passing with the metal hand" or "I felt warm in the left hand and arm when you touched the arm". The fact that the sense of embodiment was really perceived is also evident in sentences such as "It was a little bit scary and strange when the hands touched me" (i.e. the hands never touched "me", that is, the real person, but only the embodied limb) or "I felt the robot's arms as if they were a prosthesis". For the arm covered condition, some participants felt stronger embodiment when they controlled the movement of the robot: "I feel more embodied when I moved the arm. I felt like it was my real arm. The feeling was increasing from nothing at all to believe that I was the real owner", while some others felt stronger sense of embodiment when they received visuo-tactile synchronization.

5 Discussion

Our study manipulated the specific variables of physical appearance and technique to induce embodiment using a wide range of combinations in order to explore the sense of embodiment of a non-human looking robot arm. Regarding technique, the experiments included the two main paradigms generally employed to generate sense of embodiment in fake bodies and body-parts: visuo-tactile synchronization, which is the technique used in the studies related to the classic rubber-hand illusion paradigm [1], and visuo-movement synchronization, which is the technique generally used in virtual reality to induce sense of avatar embodiment [22]. Regarding physical appearance, two different types of non-human looking humanoid robot arms were tested: a blue hand with no fingers, and a gripper. The blue arm was selected because it presents a series of characteristics that are drastically different from the human arm in terms of material, color, texture, and shape. The gripper was selected because it represents a type of end effector generally employed in non-human looking humanoid robots. Furthermore, we considered these two types of arms because they differed in having fingers or not, which we believe is a key functional feature defining one's hand and arm [30]. In addition to these two types of arms, the cover condition was included to assess whether a robot arm and a non-arm object in the place of the arm produced differences in the sense of embodiment.

The response to the rubber hand illusion is known to greatly vary across individuals, and only about 70% of individuals are known to experience it [9,11,31]. We therefore chose to use a within-subjects design over a between-subjects design for its strength in accounting for individual differences

in subject responses [32,33]. Furthermore, it is generally assumed that within-subjects designs are more powerful (more likely to detect differences between conditions if they exist) than between-subjects designs [32,34]. However, within subject designs can be affected by learning or interference effects. We used a random condition presentation order across participants to attenuate any learning effects [32,33]. To attenuate any interference effects, we asked participants to relax and move their arm between conditions. The significant differences between the synchronous and asynchronous conditions validate our experimental design.

The results of this study demonstrate that people are able to experience a similar sense of embodiment of a non-human looking humanoid robot arm than that experienced for a human-looking arm in a classic rubber-hand illusion experiment [1]. In particular, we show that participants are able to experience a sense of embodiment towards a non-human looking metal and plastic robot arm with a blue hand with no fingers and towards a non-human looking metal and plastic robot arm with a metal gripper. Additionally, we demonstrate that embodiment towards the non-human looking robot arm is also perceived when visuo-movement synchronization is used instead of visuo-tactile stimulation. Finally, we show that embodiment is at least partially maintained when the robot arm is covered, specifically, by a blue plastic cover ("Appendix 3" section).

Our embodiment set-up [18,19,28], which used an HMD that provided first person perspective from the robot's body and robot's head movement control by the participant, enabled us to provide participants with a visual illusion where the robot arm was in the same location as the participant's real arm (Video S1), in turn enabling spatial coincidence between the visually perceived touch and the felt touch. We believe that this aspect of the experimental design, which differs from the traditional RHI experiment in which the real arm is in a different location than the rubber hand, contributed to enhance the sense of embodiment towards the robot's arm. We also speculate that the enhanced embodiment setup might explain why participants felt embodiment even when the arm was covered with a blue plastic cover, which contradicts previous experiments using the traditional rubber-hand illusion setup [2]. On the other hand, the embodiment of the gripper was expected by us as we believe that the functional features like fingers are more important for embodiment than the actual physical appearance of the fingers [30].

Indeed, some participants experienced high sense of embodiment even in the asynchronous conditions. A participant explained that "When you performed the asynchronous move, I felt like it was my brain problem, something like I was drunk so my brain was working slowly… not the robot problem." Previous experiments that have used a similar method to induce embodiment in a humanoid robot have also obtained high ratings of embodiment, which remain even when the robot is not controlled by the human operator [18]. Thus, it would be interesting to examine if the illusion of embodiment remains when a non-human looking robot arm is detached from the robot. We believe that the fact that the arm is attached to the robot and visualized in first person perspective from the viewpoint of the humanoid robot contributes to conceptualize it as an "arm" and thus develop the functions associated to this limb, which in turn contributes to integrate it as part of the body [30]. On the other hand, if the same arm was seen on a table detached from the robot, it might be perceived as an "object", with no connection with the body.

We note here that regarding the cover conditions, whereas the results of the questionnaire indicate that embodiment was significantly higher in the synchronous than asynchronous conditions and similar to the human-like arm synchronous condition, the results of the GSR data did not reach significance. A potential explanation for this might be that while participants experienced the arm being there (and thus they reported that in the questionnaire), they were not as affected as in the uncovered conditions when the hand passed around because the arm was perceived to be under the cover. In the visuo-movement condition, GSR was high in both synchronous and asynchronous conditions. GSR may have been high in the asynchronous condition due to increased anxiety related to the inability to control the robot hand.

In addition, in all robot synchronous conditions of both experiments (visuo-tactile and visuo-movement) embodiment was very high (in a 7-point scale, average mean was rated above 4.5 in all conditions), also compared to previous studies which tested the RHI with other types of objects [2]. However, in Experiment 2, some participants complained that the gripper hand in the second experiment was reflecting the light and that it was not very clearly visible through the HMD: "With the gripper I did not feel that I can move or touch because the vision of the hand was not clear". This might explain why the gripper conditions obtained slightly lower means in the questionnaire than the other synchronous conditions.

As mentioned, the qualitative data resulting from the open-ended question in the first study and the interviews in the second study suggests that some participants experienced a stronger sense of embodiment when the illusion of embodiment was induced by visuo-movement synchronization while others experienced a stronger illusion when it was induced by visuo-tactile synchronization. Further experiments are needed to better understand these individual differences.

Finally, our findings are important in the arena of mediated embodiment, the technologically induced illusion of adopt-

ing an artificial body in which one perceives to be located [35] in the sense that they contribute to explain how the illusion of embodiment in new technologies is created. In this regard, our results are in line with other findings made in virtual reality which suggest that avatar appearance does not necessarily need to be similar to the real appearance of the embodied subject [15,16] to create sense of identification to its owner.

In addition, our results have important implications in the domain of robotics and extend the previous findings, which demonstrate that humans are able to embody highly-human resembling robotic and android limbs [12,14]. Our study demonstrates that humans can embody robotic limbs which are drastically different from a human limb in terms of shape, color, material, and texture. Humanoid robots that present human appearance but fail to attain it may generate eeriness, as shown in the Uncanny Valley hypothesis [36]. The *Threat to distinctiveness hypothesis* suggests that too much perceived similarity between robots and humans may trigger concerns about the negative impact of this technology because similarity blurs category boundaries, undermining human uniqueness [37]. Thus, studies on acceptance of non-human looking humanoids and its potential applications are important because these robots might be more appropriate for certain functions than highly human-resembling robots [38]. Finally, our results might also be relevant for the domain of prosthetics as they open new possibilities for limb prosthesis acceptance, in the sense that visuo-movement synchronization seem to be a more important factor contributing to integrate an external body limb as part of the own body than the visual resemblance to a human arm.

Acknowledgements This project has received funding from the European Union with the Marie Curie IOF Fellowship project HumRob-Cooperation under Grant agreement No. PIOF-CT-622764. It is also partially supported from the FP7 IP VERE No. 257695 and the Kakenhi 'houga' Grant 15616710 from the Japan Society for the Promotion of Science (JSPS). We specially thank Prof. E. Yoshida for his support in the ethical procedures and the interns at our laboratory in Japan who collaborated for the pretest or to appear in the pictures.

Appendix 1

Embodiment questionnaire for Study 1

From 1 (*not at all*) to 7 (*very strongly*), how strongly do you feel as if…

The arm you see was part of your body
The arm you see was in the location of your real arm
You could push an object with the arm you see

Embodiment questionnaire for Study 2

From 1 (*not at all*) to 7 (*very strongly*), it seems like…

You are looking directly at your own arm, rather than at a rubber/robot arm
The rubber/robot arm is part of your body
The rubber/robot arm is your arm
The rubber/robot arm belongs to you
The rubber/robot arm begins to resemble your real arm
The rubber/robot arm is in the location where your arm is
Your arm is in the location where the rubber/robot arm is
You could push an object with the arm you see
You could move the arm you see

Questions for the brief interview in Study 2

1. Describe a little bit the experience you just had.
2. From all the conditions you experienced, in which one the illusion that the arm you saw through the visor was strongest?
3. In general, was the sensation stronger in the synchronous or in the asynchronous conditions?
4. Was the sensation of seeing a human or a robot arm different, which one created a stronger illusion that the arm became your arm?
5. From all the (synch) robot arm conditions you experienced, in which one the illusion was stronger: the gripper or the arm with a blue cover? For the cover arm: the one in which we brushed your hand or the one in which you moved your hand and the robot hand moved?
6. Is there any sensation or anything else that you experienced which we did not ask you during the experiment that you would like to share with us? (e.g. anything that prevented you from having a stronger experience, etc.)

Appendix 2

Experimental conditions in Experiment 1 and 2 (Table 3).

Table 3 Experimental conditions by experiment

	Experiment I		Experiment II		
	Human (real hand)	Robot (blue hand no fingers)	Human (rubber hand)	Robot (gripper)	Covered arm
Visuo-tactile					
Sync.	✓	✓	✓	✓	✓
Async.	✓	✓	✓	✓	✓
Visuo-movement					
Sync.		✓			✓
Async.					✓

Appendix 3

Overall results for embodiment by condition in Experiment 1 and 2 (Table 4).

Table 4 Embodiment scores by experimental condition for the two experiments

	Experiment I		Experiment II		
	Human (real hand) M (SD)	Robot (blue hand no fingers) M (SD)	Human (rubber hand) M (SD)	Robot (gripper) M (SD)	Covered arm M (SD)
Visuo-tactile					
Sync.	5.11 (1.06)	5.33 (1.04)	5.13 (1.35)	4.56 (1.41)	4.97 (1.33)
Async.	3.76 (1.37)	3.87 (1.44)	4.33 (1.05)	3.35 (1.6)	3.59 (1.56)
Visuo-movement					
Sync.		5.29 (1.02)			5.01 (1.12)
Async.					2.76 (1.78)

References

1. Botvinick M, Cohen J (1998) Rubber hands "feel" touch that eyes see. Nature 391:756. doi:10.1038/35784
2. Tsakiris M, Haggard P (2005) The rubber hand illusion revisited: visuotactile integration and self-attribution. J Exp Psychol Hum Percept Perform 31:80–91. doi:10.1037/0096-1523.31.1.80
3. Hohwy J, Paton B (2010) Explaining away the body: experiences of supernaturally caused touch and touch on non-hand objects within the rubber hand illusion. PLoS ONE 5:e9416. doi:10.1371/journal.pone.0009416
4. Armel KC, Ramachandran VS (2003) Projecting sensations to external objects: evidence from skin conductance response. Proc Biol Sci 270:1499–506. doi:10.1098/rspb.2003.2364
5. Maselli A, Slater M (2013) The building blocks of the full body ownership illusion. Front Hum Neurosci 7:83. doi:10.3389/fnhum.2013.00083
6. Holmes NP, Snijders HJ, Spence C (2006) Reaching with alien limbs: visual exposure to prosthetic hands in a mirror biases proprioception without accompanying illusions of ownership. Percept Psychophys 68:685–701. doi:10.3758/BF03208768
7. Longo MR, Schüür F, Kammers MPM et al (2009) Self awareness and the body image. Acta Psychol (Amst) 132:166–172. doi:10.1016/j.actpsy.2009.02.003
8. Pavani F, Zampini M (2007) The role of hand size in the fake-hand illusion paradigm. Perception 36:1547–1554. doi:10.1068/p5853
9. Ehrsson HH, Spence C, Passingham RE (2004) That's my hand! Activity in premotor cortex reflects feeling of ownership of a limb. Science 305:875–877. doi:10.1126/science.1097011
10. Costantini M, Haggard P (2007) The rubber hand illusion: sensitivity and reference frame for body ownership. Conscious Cogn 16:229–240. doi:10.1016/j.concog.2007.01.001
11. Lloyd DM (2007) Spatial limits on referred touch to an alien limb may reflect boundaries of visuo-tactile peripersonal space surrounding the hand. Brain Cogn 64:104–109. doi:10.1016/j.bandc.2006.09.013
12. Romano D, Caffa E, Hernandez-Arieta A et al (2015) The robot hand illusion: Inducing proprioceptive drift through visuomotor congruency. Neuropsychologia 70:414–420. doi:10.1016/j.neuropsychologia.2014.10.033
13. Hellman RB, Chang E, Tanner J et al (2015) A robot hand testbed designed for enhancing embodiment and functional neurorehabilitation of body schema in subjects with upper limb impairment or loss. Front Hum Neurosci 9:1–10. doi:10.3389/fnhum.2015.00026
14. Alimardani M, Nishio S, Ishiguro H (2013) Humanlike robot hands controlled by brain activity arouse illusion of ownership in operators. Sci Rep 3:2396. doi:10.1038/srep02396
15. Aymerich-Franch L (2012) Can we identify with a block ? Identification with non-anthropomorphic avatars in virtual reality games. In: Proc. Int. Soc. Presence Res. Annu. Conf
16. Aymerich-Franch L (2010) Presence and emotions in playing a group game in a virtual environment: the influence of body participation. Cyberpsychol Behav Soc Netw 13:649–654. doi:10.1089/cyber.2009.0412
17. Aymerich-Franch L, Kizilcec RF, Bailenson JN (2014) The relationship between virtual self similarity and social anxiety. Front Hum Neurosci 8:1–10. doi:10.3389/fnhum.2014.00944
18. Aymerich-Franch L, Petit D, Ganesh G, Kheddar A (2015) Embodiment of a humanoid robot is preserved during partial and delayed control. In: 2015 IEEE Int. Work. Adv. Robot. its Soc. Impacts
19. Petit D, Gergondet P, Cherubini A, Kheddar A (2015) An integrated framework for humanoid embodiment with a BCI. In: IEEE Int. Conf. Robot. Autom
20. Kaneko K et al (2004) Humanoid robot HRP-2. In: IEEE Int. Conf. Robot. Autom
21. Mansard N, Stasse O, Evrard P, Kheddar A, (2009) A versatile generalized inverted kinematics implementation for collaborative working humanoid robots: the stack of tasks. In: 2009 Int. Conf. Adv. Robot
22. Kilteni K, Groten R, Slater M (2012) The sense of embodiment in virtual reality. Presence Teleoper Virtual Environ 21:373–387. doi:10.1162/PRES_a_00124
23. Longo MR, Schüür F, Kammers MPM et al (2008) What is embodiment? a psychometric approach. Cognition 107:978–998. doi:10.1016/j.cognition.2007.12.004
24. Blanke O, Metzinger T (2009) Full-body illusions and minimal phenomenal selfhood. Trends Cogn Sci 13:7–13. doi:10.1016/j.tics.2008.10.003
25. Sackett DL (1979) Bias in analytic research. J Chronic Dis 32:51–63. doi:10.1016/0021-9681(79)90012-2
26. Connor KM, Kobak KA, Churchill LE et al (2001) Mini-SPIN: a brief screening assessment for generalized social anxiety disorder. Depress Anxiety 14:137–140
27. Seeley-Wait E, Abbott MJ, Rapee RM (2009) Psychometric properties of the mini-social phobia inventory. Prim Care Companion J Clin Psychiatry 11:231–236. doi:10.4088/PCC.07m00576
28. Aymerich-Franch L, Petit D, Ganesh G, Kheddar A (2016) The second me: seeing the real body during humanoid robot embodiment produces an illusion of bi-location. Conscious Cogn 46:99–109. doi:10.1016/j.concog.2016.09.017
29. Sanchez-Vives MV, Spanlang B, Frisoli A et al (2010) Virtual hand illusion induced by visuomotor correlations. PLoS ONE 5:e10381. doi:10.1371/journal.pone.0010381
30. Aymerich-Franch L, Ganesh G (2015) The role of functionality in the body model for self-attribution. Neurosci Res. doi:10.1016/j.neures.2015.11.001

31. Ehrsson H (2012) The concept of body ownership and its relation to multisensory integration. In: Stein BE (ed) The new handb. multisensory process. Cambridge, MA: Mit Press, pp 775–792
32. MacKenzie IS (2013) Human–computer interaction: an empirical research perspective. Morgan Kaufmann, Waltham
33. Kantowitz BH, Roediger HL III, Elmes DG (2015) Experimental psychology. Cengage Learning, Stamford, CT, USA
34. Greenwald AG (1976) Within-subjects designs: to use or not to use? Psychol Bull 83:314–320. doi:10.1037/0033-2909.83.2.314
35. Aymerich-Franch L Mediated embodiment in new communication technologies. In: Khosrow-Pour M (ed) Encyclopedia of information science and technology, 4th edn. Hershey, IGI Global (**in press**)
36. Mori M (1970) The uncanny valley. Energy 7:33–35. doi:10.1162/pres.16.4.337
37. Ferrari F, Paladino MP, Jetten J (2016) Blurring human–machine distinctions: anthropomorphic appearance in social robots as a threat to human distinctiveness. Int J Soc Robot 1–16. doi:10.1007/s12369-016-0338-y
38. Złotowski J, Proudfoot D, Yogeeswaran K, Bartneck C (2014) Anthropomorphism: opportunities and challenges in human–robot interaction. Int J Soc Robot 7:347–360. doi:10.1007/s12369-014-0267-6

Laura Aymerich-Franch received a Ph.D. cum laude on Audiovisual Communication by Universitat Autònoma de Barcelona. She is currently a Marie Curie IOF fellow at *The Experimental Virtual Environments (EVENT) Lab for Neuroscience and Technology* at the University of Barcelona (return phase). She completed the outgoing phase of the Marie Curie fellowship at the CNRS-AIST Joint Robotics Laboratory (JRL) in AIST, Japan (2014–2016). Previously, she was a Fulbright postdoctoral researcher at Virtual Human Interaction Lab, Stanford University (2012–2014). Her area of expertise is Media Psychology applied to advanced communication technologies. Currently, she studies the psychological aspects of mediated embodiment in humanoid robots and virtual reality.

Damien Petit received his M.Eng. degree and the M.Sc. degree in robotics and computer vision from the Télécom Physique Strasbourg, France, in 2010. He received his Ph.D. in Robotics from the University of Montpellier, France, in December 2015; his research was conducted in large part at the CNRS-AIST Joint Robotics Laboratory in Tsukuba, Japan, and at the Interactive Digital Human group of LIRMM, at Montpellier, in the frame of the European Union FP7 Virtual Embodiment and Robotic re-Embodiment (VERE) project. His research interests include humanoid robotics, robotic embodiment, robot–human interactions and thought-based control of humanoid.

Gowrishankar Ganesh received his Bachelor of Engineering (first-class, Hons.) degree from the Delhi College of Engineering, India, in 2002 and his Master of Engineering from the National University of Singapore, in 2005, both in Mechanical Engineering. He received his Ph.D. in Bioengineering from Imperial College London, UK, in 2010. He worked as a Researcher in Human Motor Control in the Advanced Telecommunication Research (ATR), Kyoto, Japan, from 2004 and through his Ph.D. Following his Ph.D., he worked at the National Institute of Information and Communications Technology (NICT) as a Specialist Researcher in Motor Neuroscience and Robotics till December 2013. Since January 2014, he has joined as a CR1 Researcher at the Centre National de la Recherche Scientifique (CNRS), and is currently located at the CNRS-AIST Joint Robotics Laboratory (JRL) in Tsukuba, Japan. He is a visiting researcher at the Centre for Information and Neural Networks (CINET) in Osaka, ATR in Kyoto and the Laboratoire d'Informatique, de Robotique et de Microlectronique de Montpellier (LIRMM) in Montpellier. His research interests include human sensorimotor control and learning, robot control, social neuroscience and robot–human interactions.

Abderrahmane Kheddar received the BS in Computer Science degree from the Institut National d'Informatique (ESI), Algiers, the M.Sc. and Ph.D. degree in robotics, both from the University of Pierre et Marie Curie, Paris. He is presently Directeur de Recherche at CNRS and the Director of the CNRS-AIST Joint Robotic Laboratory (JRL), UMI3218/RL, Tsukuba, Japan. He is also leading the Interactive Digital Humans (IDH) team at CNRS-University of Montpellier LIRMM, France. His research interests include haptics, humanoids and thought-based control using brain machine interfaces. He is a founding member of the IEEE/RAS chapter on haptics (acting also as a senior advisor), the co-chair and co-founding member of the IEEE/RAS Technical committee on model-based optimization. He is presently Editor of the IEEE Transactions on Robotics, the Journal of Intelligent and Robotic Systems, and Frontiers in Bionics; among the founders of the IEEE Transactions on Haptics he served in its editorial board from 2007 to 2010 and served as an associate editor in the MIT Press Presence journal. He is an IEEE Senior Member, Member of the steering committee of the IEEE Brain Initiative, Titular member of the National Academy of Technology of France, and Knight of the National Order of the Merit.

Accepted Manuscript

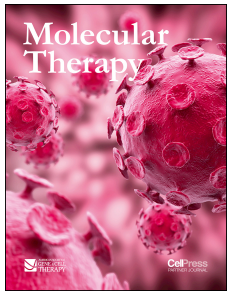

Non-invasive oil based method to increase topical delivery of nucleic acids to skin

Manika Vij, Shamshad Alam, Nidhi Gupta, Vishvabandhu Gotherwal, Hemlata Gautam, Kausar M. Ansari, Deenan Santhiya, Vivek T. Natarajan, Munia Ganguli

PII: S1525-0016(17)30107-7

DOI: 10.1016/j.ymthe.2017.03.009

Reference: YMTHE 4301

To appear in: *Molecular Therapy*

Received Date: 7 June 2016

Revised Date: 2 March 2017

Accepted Date: 8 March 2017

Please cite this article as: Vij M, Alam S, Gupta N, Gotherwal V, Gautam H, Ansari KM, Santhiya D, Natarajan VT, Ganguli M, Non-invasive oil based method to increase topical delivery of nucleic acids to skin, *Molecular Therapy* (2017), doi: 10.1016/j.ymthe.2017.03.009.

This is a PDF file of an unedited manuscript that has been accepted for publication. As a service to our customers we are providing this early version of the manuscript. The manuscript will undergo copyediting, typesetting, and review of the resulting proof before it is published in its final form. Please note that during the production process errors may be discovered which could affect the content, and all legal disclaimers that apply to the journal pertain.

ACCEPTED MANUSCRIPT

Non-invasive oil based method to increase topical delivery of nucleic acids to skin

Manika Vij[1,4], Shamshad Alam[2], Nidhi Gupta[3], Vishvabandhu Gotherwal[1,4], Hemlata Gautam[1], Kausar M. Ansari[2], Deenan Santhiya[3], Vivek T. Natarajan[1,4], Munia Ganguli[1,4*]

[1]CSIR- Institute of Genomics and Integrative Biology, South Campus, Mathura Road, New Delhi - 110020, India.

[2]CSIR- Indian Institute of Toxicology Research, Post Box No.80, Mahatma Gandhi Marg, Lucknow (Uttar Pradesh) - 226001, India.

[3]Delhi Technological University, Shahbad Daulatpur, Main Bawana Road, New Delhi - 110042, India.

[4]Academy of Scientific and Innovative Research (AcSIR), Anusandhan Bhawan, 2 Rafi Marg, New Delhi - 110001, India.

Correspondence should be addressed to:

***Dr. Munia Ganguli (mganguli@igib.res.in, mganguli@igib.in)**

New Delhi, India.

Present Address: Room No. 225/ Lab No. 219, Department of Structural Biology, CSIR-Institute of Genomics and Integrative Biology, South Campus, Mathura Road, New Delhi, 110 020, India.

Tel: 91-11-29879225/+91-9871607437; Fax: 001-27667471;

Email: mganguli@igib.res.in, mganguli@igib.in

Short title

"Enhancement of nucleic acid delivery in skin."

Abstract

Topical delivery of nucleic acids to skin has huge prospects in developing therapeutic interventions for cutaneous disorders. In spite of initial success, clinical translation is vastly impeded by the constraints of bioavailability as well as stability in metabolically active environment of skin. Various physical and chemical methods used to overcome these limitations involve invasive procedures or compounds that compromise skin integrity. Hence there is an increasing demand for developing safe skin penetration enhancers for efficient nucleic acid delivery to skin. Here we demonstrate that pre-treatment of skin with silicone oil can increase the transfection efficiency of non-covalently associated peptide-plasmid DNA nanocomplexes in skin *ex vivo* and *in vivo*. The method does not compromise on the skin integrity as indicated through microscopic evaluation of cellular differentiation, tissue architecture, enzyme activity assessment, dye penetration tests using Franz assay, cytotoxicity and immunogenicity analysis. Stability of nanocomplexes is not hampered on pre-treatment; thereby avoiding nuclease-mediated degradation. The mechanistic insights through FTIR spectroscopy reveal some alterations in the skin hydration status owing to possible occlusion effect of the enhancer. Overall we describe a topical, non-invasive, efficient and safe method to increase the penetration and delivery of plasmid DNA to skin for possible therapeutic applications.

ACCEPTED MANUSCRIPT

Introduction

Recent developments in topical and transdermal delivery across skin highlight its immense potential for administration of therapeutics as well as cosmeceutics.[1-3] In addition to the advantages of large surface area and easy access, therapeutic delivery through skin can also bypass the hepatic metabolism of oral delivery.[4,5] Although a wide repertoire of cargos have been delivered in skin**,** the clinical benefits achieved are still limited. [6,7] This limitation is largely attributed to the poor percutaneous permeability of administered cargo molecules owing to the significant barrier properties of skin. The major barrier is imposed by its superficial layer i.e. stratum corneum, whose unique lipid-rich composition along with richness of desmosomes effectively impedes the entry of hydrophilic macromolecules.[5,8] Moreover the delivered molecules should also enter skin in therapeutically sufficient amounts in order to efficaciously alleviate the condition without disturbing the skin integrity. In order to achieve this, researchers have focused on different strategies based on physical interventions or chemical and carrier based methods.[9-15] However many of these methods suffer from invasive nature, cumbersome application and toxic effects which render them non-compliant for practical use**.**[11,16]

Synthetic and essential oils constitute a category of enhancers being explored for improved delivery to skin in a non-toxic manner. Polysiloxane or silicone oil (polymerized siloxane with organic side chains) is used as a component in many of these enhancers. Silicone oil has many applications determined by its structure, viscosity, volatile nature and thermal stability. In skin care, silicones (oil or variants) have been used to prepare sunscreen formulations, non-sticky moisturizers and body perspirants. It also has therapeutic applications like facilitating collagen production in hypertropic scar and providing sealant properties in wound healing applications to avoid subsequent invasion by pathogens.[17-20] In spite of large scale applications in skin with

limited or no safety concerns, it has still not been explored much as a skin penetration enhancer for increased delivery of macromolecules.

Recently skin penetrating peptides (SPP) have also emerged as relatively safe and non-invasive agents that assist efficient entry of both small and macromolecules across skin either through co-administration or through non-covalent association.[21-29] Therefore it is interesting to explore whether they can serve as potential alternatives to the existing chemical penetration enhancers. Insights will help us not only in better designing of penetration enhancers with minimal side effects but also to realize its therapeutic benefit in clinical settings. Most of these methods mentioned above are able to mediate increased entry of molecules in skin by means of interaction with skin lipids or proteins leading to reversible alterations in skin permeability.[11,16]

In the present work we have chosen silicone oil, a chemical enhancer and a peptide enhancer and analyzed if they are able to improve plasmid DNA delivery efficiency to skin *ex vivo* and *in vivo* in a synergistic manner. We have applied these chemicals as pre-treatments before delivering plasmid DNA as a nanocomplex with a skin penetrating peptide Mgpe9 which has been developed earlier in our laboratory.[30] We have evaluated the safety potential of these enhancers at both tissue and cellular levels using fluorescence microscopy, skin integrity assessment and cytotoxicity as well as immunogenicity analysis. Eventually we propose silicone oil as an efficient penetration enhancer for improved plasmid DNA delivery to skin with minimal side effects. For better understanding of its interaction in skin, we have also tried to elucidate the mechanism by which silicone oil is able to achieve its desired action on skin. Overall we report an effective and safe strategy for enhancing bioavailability of peptide-plasmid DNA nanocomplexes in skin using silicone oil.

Results

We planned our study using two chemical enhancers (SLA-PP, Silicone oil) and a skin penetrating peptide enhancer (TD-1) that have been previously used for enhancing delivery of small molecules but not nanocomplexes.[9,23,31] Initially we studied the effects of their pre-application on transfection efficiency and skin integrity followed by its possible mechanism of action.

Silicone oil enhanced EGFP expression in skin *ex vivo, in vivo* and *in vitro* without altering nanocomplex stability.

We first explored the effect of different enhancers on stability of the nanocomplexes. The complexes were prepared at charge ratio 10 to ensure small particle size, positive surface charge and little or no aggregation through charge-charge repulsion, thereby maintaining its colloidal stability. This has already been standardized and reported by us in a previous study.[30] To check the stability of these nanocomplexes we first estimated their size in presence of enhancers using Dynamic Light Scattering and then performed a DNA condensation assay where integrity of the nanocomplex could be determined. Although we observed overall increase in the size of the nanocomplexes in presence of all the enhancers **(Figure 1A)** the complex integrity remained unaffected in presence of silicone oil and TD-1 as seen by absence of free plasmid DNA in the gel image **(Figure 1B)** unlike in case of SLA-PP where plasmid DNA release along with some degradation was evident.

We then tested the ability of these enhancers to improve the entry of Mgpe9-pDNA nanocomplexes in skin. To study this, human skin tissue was topically pre-treated with each of these enhancers *ex-vivo,* followed by administration of nanocomplex using an application regime

standardized and described in our previous study (see Materials and Methods for further details).[30] The enhancement effect was monitored by checking for increase in transfection efficiency of Mgpe9 nanocomplexes. Both qualitative **(Figure 1C)** as well as quantitative **(Figure 1D, Figure S1)** estimation of EGFP-C1 fluorescence in skin showed that silicone oil achieved maximum increase in EGFP expression. While the basal level of about 30% fluorescence positive cells was obtained using only the Mgpe9-pDNA nanocomplexes, >45% fluorescence positive cells and high mean intensity was observed in presence of silicone oil. Transfection efficiency on application of SLA-PP was slightly less (i.e. ~40% fluorescence positive cells with low mean intensity) as compared to that observed in case of silicone oil. Moreover microscopic investigation shown in Figure 1C indicated some loss of skin architecture upon treatment with SLA-PP which we have explored and discussed later in the text. TD-1 did not seem to show any obvious changes in skin architecture but gave negligible fluorescence upon qualitative estimation and less fluorescence positive cells with very low mean intensity.

Owing to its maximum enhancement efficiency *ex vivo*, we went on to explore the utility of silicone oil as an enhancer under *in vivo* conditions using hairless mouse SKH-1 as model organism. It was observed that pre-treatment with silicone oil increased the percentage of EGFP positive cells obtained by about 10% in comparison to the condition when only Mgpe9 nanocomplexes were applied **(Figure 1E, Figure S2a)**. Moreover luciferase transfection efficiency in SKH-1 mouse also exhibited one order increase in expression upon silicone oil pre-treatment **(Figure S2b)**. Thus, irrespective of the different nature of two skin types (*ex vivo* and *in vivo*), silicone oil exhibited increase in efficiency of delivery in both. Moreover similar trend of expression was observed in human primary keratinocytes *in vitro* **(Figure S3).** However SLA-PP was unable to give similar expression owing to its toxic effect on the cells **(Figure S3)**. Since

these chemical enhancers as well as skin penetrating peptides also have the propensity to enter skin by themselves, we next analyzed whether their application caused any adverse effects on skin.

Silicone oil did not show any toxic effects on *ex-vivo, in vivo* and *in vitro* administration in human skin or SKH-1.

One of the major concerns about use of enhancer molecules in skin is their safety potential. So we next carried out a detailed toxicity assessment of silicone oil and SLA-PP, at both tissue and cellular levels. Since TD-1 was not efficient in enhancing the EGFP signal, it was excluded from further experiments. Any possible change in tissue architecture on enhancer treatment was studied using confocal microscopy. In particular, cellular differentiation and disruption of the barrier layer of stratum corneum was monitored by checking the presence or absence of keratin 10, loricrin and keratin 14 markers in the different layers of skin. It was observed visually that stratum corneum did not get dissociated upon silicone oil pre-treatment followed by topical administration of Mgpe9 nanocomplexes unlike in case of SLA-PP where it was completely dismantled **(Figure 2A)**. Moreover the presence of keratin 10, loricrin and keratin 14 marker proteins in the different layers of skin was clearly evident in case of bare silicone oil treatment contrary to bare SLA-PP where the keratin 14 signal was completely lost from the skin tissue and loricrin or keratin 10 layers were completely distorted **(Figure 2B, Figure S4)**.

Further we also performed a skin integrity assessment through dye penetration test (using low molecular weight FITC and high molecular weight Dextran) across skin in order to assess the adverse effect if any at the tissue level **(Figure 2C, Figure S5a)**. Any recordable presence of these dyes in the receptor solution of Franz apparatus on co-administration with enhancer and

Mgpe9 nanocomplexes would indicate compromise in skin tissue integrity. We observed that silicone oil did not allow dye penetration indicating uncompromised skin integrity and absence of tissue damage unlike what was observed with SLA-PP. However we also did not see presence of any FITC fluorescence in the skin tissue upon microscopic examination indicating no permeation of dye **(Figure S5b)**; the possible reason for this has been elaborated in discussion section.

We next monitored the change in protease activity in skin to see if there was any effect on the active metabolic environment as a result of these treatments. We observed that silicone oil along with treatment with Mgpe9 nanocomplexes did not show any major change in protease activity unlike in case of SLA-PP where significant loss of protease activity (>60% loss) was recorded **(Figure 2D)**. Further we wanted to explore whether silicone oil had any adverse effects on the viable cells in epidermis under similar conditions for which we used Propidium Iodide staining method and checked for cell death in the skin tissue **(Figure 2E)**. Silicone oil did not exhibit any toxic effects as evident from absence of red fluorescence in the skin tissue whereas SLA-PP seemed to be highly toxic. To confirm our observation we also did a cytotoxicity assessment on HaCaT (human adult keratinocyte) cells as well as human primary keratinocytes under *in vitro* conditions (to mimic transfection application) and observed similar trend **(Figure 2F, Figure S6)**. More than 80% cell viability was maintained in presence of silicone oil as compared to SLA-PP where merely 10% cells survived upon exposure to the enhancer at 24h in both the cell lines. We further checked the serum for presence of inflammatory cytokines such as IL-2, IL-6, IL-12 and TNF-α on application of enhancers as well as nanocomplexes on SKH-1 mice *in vivo*. However we did not observe any significant up-regulation of any of these inflammatory cytokines in presence of silicone oil unlike SLA-PP **(Figure S7)**. All these observations

cumulatively indicated that silicone oil was the best enhancer for plasmid DNA delivery amongst the ones we have studied. So we next attempted to understand its mechanism of action on skin.

Silicone oil enhanced entry of nanocomplexes possibly through occlusive effects.

Silicone oil is well-known for its occlusive effects as well as capturing of nanoparticles on skin. Hence we wanted to explore if in this case it allowed longer retention of the nanocomplexes in skin, directed the higher entry in skin through increasing the skin hydration pressure or induced major structural alterations of the skin. FTIR spectroscopy was carried out on the stratum corneum of human skin[10,16,32-35] treated with silicone oil and Mgpe9 nanocomplexes for 24h (to mimic actual one-time application) **(Figure 3A)**. Untreated skin was considered as experimental control. In case of the untreated stratum corneum, we observed peak at 3442cm^{-1} which could be attributed to the C-H asymmetric and symmetric stretching of the skin lipids whose peaks are usually attributed from 2800-2950cm^{-1} but are often merged with the broad peaks coming from the -OH stretching of water. Additionally presence of 1642cm^{-1} peak in untreated tissue in our experiment indicated presence of amide I region of the skin proteins.[10,34]

In case of the treated stratum corneum, we observed the strongest peak at 3438cm^{-1} which is much broader than that in the untreated sample indicating either some mild structural alterations due to lipid extraction or fluidization or alteration in hydration status of skin (as inferred from the assignments described above). Moreover, the fluidity of the lipid and the changes in the nature of lipid packing can also be assessed by the bands in the region 1000-1400cm^{-1} where we observed slight merging of the 1094cm^{-1} and 1000cm^{-1} peaks in 24h treated sample. Another overlapping peak at 1396cm^{-1} seemed to be more evident in the treated sample which could again be due to OH bending indicating probable presence of water molecules.

We also observed broadening of peak at 1631cm^{-1} in the treated sample indicating alteration in protein structure. However observation of tissue sample treated with only silicone oil **(Figure S8a)** does not show such a change indicating that silicone oil is not responsible for this alteration of protein structure. The additional presence of nanocomplexes in the treated sample **(Figure 3A)** might be showing interaction with skin proteins (as shown by us in our earlier report)[30] leading to alteration in this spectral region. Overall no major alterations of skin structure seemed to be evident; however mild lipid reorganization and changes in hydration status of skin seemed to be the primary observed changes and could be contributing to the enhancement of nanocomplex delivery instead of increased retention for mediating entry of nanocomplexes in skin.

In order to confirm this we next checked the tissue uptake of FITC labeled nanocomplexes in skin. We could observe increase in FITC fluorescence across the skin in presence of silicone oil both qualitatively **(Figure 3B)** and quantitatively **(Figure 3C)** with about >10% increase in percentage positive cells in presence of the enhancer. This also helped us to rule out the possibility of longer retention of nanocomplexes on skin by silicone oil where we would have expected less entry of complexes into the viable epidermis with higher localization on stratum corneum unlike the observation in Figure 3B.

We next explored if silicone oil by itself entered skin for which we tried to retrieve it from viable epidermis of treated skin tissue (complete application as described in Materials and Methods). Stratum corneum was removed by tape-stripping and silicone oil was eluted using chloroform:acetone (1:1v/v) mixture from viable epidermis. We compared the FTIR spectra of bare silicone oil and eluted fractions. Silicone oil is known to exhibit signature peaks at 1260cm^{-1} and 1080cm^{-1} denoting Si-CH_3 vibration and peak at ~1000cm^{-1} or ~700cm^{-1} denoting Si-O

vibration respectively. We could observe presence of these peaks in the control sample i.e. bare silicone oil **(Figure S8b)** where peaks at 1260cm^{-1} and 753cm^{-1} were present but peaks at 1080cm^{-1} and 1000cm^{-1} seemed to be merged to show a broad peak at 1028cm^{-1}.[32,33] However the FTIR spectra of eluted fractions **(Figure 3D)** exhibited no traces of silicone oil peaks either in bare treatment or with nanocomplexes indicating its absence from viable epidermis. Overall it indicated that silicone oil did not possibly penetrate into deeper layers of skin and its action is surface-mediated. This would also rule out the risk of immunogenic effects upon its permeation beyond epidermis during *in vivo* delivery as was also observed in previous section **(Figure S7)**. However this could also be attributed to solubility constraints of this enhancer and needs further validation.

Discussion

Stratum corneum forms an effective barrier against movement of large hydrophilic molecules across skin thereby allowing only small (<500Da) lipophilic molecules to go through. Recent technological developments report many carriers that have the ability to penetrate stratum corneum but are unable to reach their designated sites in therapeutically sufficient amounts. Hence their functional utility for both therapeutics and cosmeceutics is vastly impeded by the unique architecture of the tissue. Many strategies have been devised to overcome this limitation and enhance the overall penetration of hydrophilic molecules particularly macromolecules like plasmid DNA across skin either by removing stratum corneum through tape stripping or use of physical methods. However owing to their invasive and cumbersome nature, expensive set ups as well as patient non-compliance, attention has now shifted to use of non-invasive class of molecules i.e. chemical or peptide based penetration enhancers. Additionally careful designing of nanocarriers have also been crucial in achieving this task.

We rationalized that for efficient penetration of small or macromolecules across skin using enhancers, the enhancers should possess certain essential properties eg. safe to administer, non-toxic, highly efficient, should not compromise the stratum corneum in irreversible manner, should be compatible with the other ingredients of formulation. Additionally for enhancing the delivery of plasmid DNA as nanocomplexes, where a cationic agent and plasmid DNA are electrostatically bound together, it is important that the enhancer used should not hamper their complexation and stability.

We have previously reported a secondary amphipathic peptide Mgpe9 as a skin tissue and cell penetrating peptide that can efficiently deliver plasmid DNA to skin in the form of nanocomplexes following non-invasive topical administration.[30] However further enhancement of the bioavailability of these nanocomplexes in skin is desirable to eventually attain improved therapeutic effects. In this study, we have focused on using enhancers for improving nanocomplex mediated delivery of plasmid DNA.

Recent reports emphasizing the feasibility of using penetration enhancers for improved cargo delivery to skin predict sodium laureth sulfate (SLA) and phenyl piperazine (PP) mixture as a safe and potent chemical enhancer to be applied on skin.[9] Moreover skin penetrating peptides such as SPACE, TD-1, AT1002, polyarginines to name few are now being largely explored for the enhancement effects owing to their safe and non-immunological nature. Another chemical penetration enhancer silicone oil, although less explored in this regard, finds wide utility as a constituent of cosmeceutical formulations. However, all these enhancers have only been used to impart increase delivery of small molecules in skin.

Hence we wanted to check if these enhancers can also maintain this efficient activity in synergy with naturally penetrating nanocomplexes and further improve plasmid DNA delivery in skin. From our results we could infer that overall chemical enhancers were more efficient in attaining this effect as compared to the SPP class of enhancers. One probable explanation for this could be that chemical enhancers primarily interact with the more abundant lipid component of the skin and thereby allow entry of large number of nanocomplexes through this route only whereas SPPs are known to primarily interact with the keratin protein of corneocytes and might lead to continuous phase alteration of nanocomplexes for entry into skin.[16] This in turn can reduce their rate of migration and hence desired effects are not attained in same time period leading to low transfection efficiency. Another possibility could be that the various physico-chemical properties of these SPP like charge and hydrophobicity might interfere with the stability of the nanocomplexes causing disruption of electrostatic interactions between peptide and plasmid DNA and reduction in expression. Moreover we observed strong expression in primary keratinocytes as shown in figure S3, both in presence and absence of silicone oil using higher doses of plasmid DNA.

These enhancers are capable of interacting with either lipid or protein component of skin to mediate their activity, hence it is possible that they enter skin and affect its metabolic milieu. So we analyzed their effect on the activity of most abundant protease enzymes in skin. It was seen that SPPs and silicone oil did not hamper the enzymatic activity in skin unlike SLA-PP which is a surfactant and has protein denaturing tendency owing to which it exhibited decreased protease activity in skin. Since silicone oil was found to be both efficient and safe to use, we further analyzed possible toxicity to skin cells and tissue on application of silicone oil.

It was observed that use of this enhancer did not alter the cellular differentiation or skin tissue architecture or hamper the cell viability *in vitro* or *ex vivo*. No necrosis of cells was observed in the human skin tissue treated with this enhancer and >80% cell viability was maintained in HaCaT cells and primary human keratinocytes unlike SLA-PP where significant cell death was recorded. Negligible permeation of skin impermeable dyes on co-administration with silicone oil indicated that whatever changes in skin permeability take place are mild and transient. This is an advantage as it reduces the risk of skin getting exposed to harmful allergens as well as pathogens subsequently. However when we tried to locate FITC presence in skin tissue itself, we observed that in case of silicone oil no fluorescence was present even in the skin section. This was an interesting observation as being an enhancer it is expected that silicone oil should improve entry of FITC molecule. One possible reason could be that being hydrophobic in nature the FITC molecule gets trapped in the silicone oil and is unable to go through or it may also be undergoing rapid exocytosis across the skin thus leading to absence of any detectable signal. Therefore the compatibility of the physico-chemical properties of enhancer and molecules delivered plays a crucial role in determining the enhancement efficiency. This also raises a question whether silicone oil is itself moving into the deeper layers of the skin. This issue has been discussed later.

After evaluating the safety potential of silicone oil we then tried to understand the underlying mechanism by which it mediated its action in skin. Skin has three major pathways for entry of molecules 1. Intercellular pathway through the lipids; 2. Trans-cellular pathway through the cells and 3. Follicular or shunt pathways which are minor contributors. We used the hairless mouse model for our *in vivo* studies. It is a well established mouse model which lacks follicular opening and is thereby a better mimic of human skin than other known mouse models.[36,37] The entry of nanocomplexes is primarily through non-follicular pathways in this model that are otherwise

difficult to breach. Since we observed similar enhancement effect of silicone oil in *ex vivo* study with human skin and *in vivo* study with SKH-1 mouse, it indicates that the presence or absence of follicles and other shunt pathways in skin do not influence the efficiency of this enhancer. Moreover synergistic application of enhancer and nanocomplexes did not cause any immunogenic reaction.

Further, we have used FTIR spectroscopy to understand the mechanism of action of silicone oil. We tried to address two questions: 1. Whether treatment with silicone oil and nanocomplexes causes any major changes in the skin structure on topical application and 2. Whether silicone oil is also entering directly into the skin. Our data indicates possible alteration of skin hydration status which could be a contributing factor for the enhancement observed. Such changes in skin hydration can possibly disrupt the microstructure of skin leading to swelling of corneocytes and creating intercorneocyte gaps and opening of porous aqueous pathways of skin by breaking desmosome junctions. We also observe mild fluidization of skin lipids from the FTIR spectrum which indicates transient disturbance in the lipid assembly.[38-40] Hence overall permeability across skin is enhanced. Still overall spectra of treated skin resembled that of the control skin with no major distortions or shifting of peaks indicating silicone oil as a safe to use enhancer. Moreover the absence of silicone oil peaks in eluted fraction of solvent from viable epidermis seems to indicate the impermeability of enhancer itself to enter skin in spite of its ability to mildly disturb skin lipids making it a safe topical agent that remained on skin surface while the cargo can get into the epidermis efficiently. While the absence of penetration of silicone oil itself indicates its possible occlusive effects, this needs to be further supplemented with validations from other techniques.

In conclusion our study reports silicone oil as a safe and efficient enhancer for effective increase of the bioavailability of nanocomplexes in skin. Mechanistic insights reveal occlusion effect of silicone oil on skin which in turn alters the hydration status leading to possible opening of many porous channels that can mediate efficient movement of hydrophilic molecules into skin. Additionally high positive charge of the nanocomplexes further aids in their efficient entry across the skin. Thus it can assist these nanocomplexes in overcoming the stratum corneum barrier of skin without compromising the tissue architecture and integrity aspects. The strategy paves an efficient way to realize the clinical translational potential of nucleic acid delivery in skin with improved bio-availability characteristics.

Materials and Methods

Chemicals and cell lines

The peptides used in this study i.e. Mgpe9 and TD-1 were custom synthesized (>98% purity) by Beijing SBS Genetech Co., Ltd.(Beijing, China). Silicone oil LR used was purchased from SD-Fine Chemicals Limited, with the specifications weight per ml at 20°C of ~0.970 gram, kinetic viscosity ~300cS and recommended temperature stability 250°C. Chemical enhancer mixture i.e. Sodium laureth sulfate (SLA) and phenyl piperazine (PP) were obtained from Sigma Aldrich. Nanocomplexes were prepared using plasmid pEGFP-C1, 4.7kb or pMIR, 6.4kb (Clontech) that was amplified in Escherichia coli DH5α strain and isolated using GenElute HP Endotoxin-Free Plasmid MaxiPrep kit (Sigma). All the chemicals and culture media used were also obtained from Sigma unless mentioned otherwise. CellTitre Glo viability assay kit were purchased from Promega. HaCaT, which is an adult keratinocyte cell line, was obtained as a

gift from Dr. Sudhir Krishna, NCBS, Bangalore, India. Primary human keratinocytes were obtained from Lonza.

Preparation of nanocomplexes

Nanocomplexes were prepared at N/P ratios (Z (+/-)) of 10 where N/P is defined as the ratio between total number of amines of a peptide and total number of phosphates of a plasmid DNA. The preparation was carried out by gradual addition of 10µl of plasmid DNA (20ng/µl) for gel based and cytotoxicity studies; 500µl of plasmid DNA (40ng/µl) for dynamic light scattering study and 40µl plasmid DNA (100ng/µl) for *ex vivo* and *in vivo* studies to 10µl, 500µl or 40µl of Mgpe9 peptide solution of appropriate concentration respectively in a drop-wise manner accompanied by constant vortexing. These nanocomplexes were then allowed to stabilize for 1h at room temperature before performing any experiment.

Dynamic Light Scattering

Briefly, 1ml of Mgpe9 nanocomplexes were prepared at Z=10. The nanocomplexes were pre-treated with enhancers i.e. Silicone oil; TD-1; SLA-PP for 30minutes in independent set ups, followed by estimation of mean hydrodynamic diameter using Zetasizer Nano ZS90 (Malvern Instruments, U.K.) at 25°C. A minimum of three readings with replicates were recorded per sample. The untreated nanocomplexes were taken as experimental control.

DNA condensation assay

The electrophoretic mobility of the Mgpe9 nanocomplexes prepared at Z=10 and pre-treated with respective enhancers for 30minutes as mentioned before, was studied using agarose gel electrophoresis. 20µl of the nanocomplexes having 200ng total DNA was loaded in each case onto 1% agarose gel containing ethidium bromide. Electrophoresis was carried out at 150V in

1X TAE buffer (pH 7.4) for 45minutes. The presence of free plasmid DNA was detected using ethidium bromide fluorescence as seen through transilluminator (BioRad ChemiDoc^{TM} XRS+). Bare plasmid DNA was taken as experimental control.

Human skin tissue pre-processing for *ex-vivo* studies

Human foreskin tissue (discarded sample, collected and studies approved by institutional human ethics committee [Approval Number: IGIB/HEC/09/13]) obtained in transportation media (Hank's Balanced Salt Solution or HBSS from Invitrogen) was washed three times alternatively with 1X phosphate buffered saline (PBS) and 70% alcohol solution to clear the contamination if any. It was then processed into 0.5cm x 0.5cm sized pieces using sterile scalpel and plated in small inserts (to cover the base area completely and avoid contamination from the edges owing to movement during treatment) in a 24 trans-well plate with 300µl of Keratinocyte-Serum Free medium (K-SFM from Invitrogen) in the outer well such that only the dermis remained submerged in media whereas epidermis was exposed for the topical treatment. The plated tissue pieces were incubated at 37°C and monitored over a period of 24h to check for tissue quality and contaminations before proceeding with the experiments.

Plasmid DNA delivery in human foreskin tissue in presence of enhancers

80µl of Mgpe9 nanocomplexes was prepared at Z=10 using EGFP-C1 plasmid (100ng/µl) as described above. After 24h of skin tissue pre-processing, the tissue was pre-treated for 30minutes with skin penetrating peptide TD-1 or chemical based enhancers SLA-PP or Silicone oil followed by topical administration of nanocomplexes in each well in independent experiments. The treatment with nanocomplexes in absence of any enhancer was considered as experimental control. This treatment was repeated for 3days consecutively with a single such application per

day (4µg plasmid DNA per application) along with intermittent washing of the tissue using 1X phosphate buffered saline (PBS) before each of the fresh applications. 24h after the final application the tissue was again washed in similar manner, fixed using 4% paraformaldehyde for 30minutes at room temperature and transferred to 20% sucrose solution having 0.01% sodium azide to be stored at 4°C until further processing was done. For cryosectioning (24h post-fixation), the tissue was embedded in an OCT compound and sections of 6µm thickness were obtained which was visualized for presence of EGFP protein using immunostaining as explained later. Untreated skin tissue was taken as technical control to avoid spurious results due to auto-fluorescence artifact.

Immunostaining study to locate presence of EGFP protein

Full thickness human foreskin tissue was processed, plated and treated topically as described above. Post treatment tissue cryosections were obtained in a similar manner as mentioned before and rehydrated using wash buffer (1X phosphate buffered saline with 0.1% Triton X-100) for 15minutes followed by 1h of blocking in 5% BSA (bovine serum albumin) at room temperature. Primary antibody, anti-EGFP, was applied to the tissues at dilution of 1:200 and incubated overnight at 2-8°C . The tissues were then given 3 washes of 15minutes each in wash buffer before addition of TRITC labeled secondary antibody, anti-rabbit IgG against EGFP at dilution of 1:250 for 1h, at room temperature. The washing was repeated along with the final rinsing using 1X phosphate buffered saline (PBS). The mounting of tissues was done with DAPI-antefade reagent (Invitrogen) and results were recorded using confocal microscopy (TCS SP8 confocal microscope Leica) .

Flow cytometry to quantify EGFP protein in skin

For quantification of EGFP fluorescence in the epidermis, the epidermis was removed from the full thickness skin tissue using overnight Dispase (0.25%) treatment at 4°C followed by incubation of the epidermis with 200µl of trypsin (0.25%) solution for 20minutes at 37°C to allow cell separation to occur. The dissociated cells obtained were suspended in ice-cold 1X phosphate buffered saline (PBS) and centrifuged at a speed of 2000rpm for 5 minutes at 4°C. After centrifugation, the pellet obtained was again washed using 500µl ice-cold 1X phosphate buffered saline (PBS) in similar manner followed by its resuspension in 200µl of 1X phosphate buffered saline (PBS) for further analysis. The flow cytometry measurements were then performed using FACS Caliber (Becton Dickinson) to quantify the cellular fluorescence and mean fluorescence intensity. Statistical significance for quantitative data obtained was calculated using two-tailed student's t-test (unpaired) in GraphPad Prism.

Plasmid DNA delivery in human primary keratinocytes and cytotoxicity analysis

Human primary keratinocytes were seeded at density of 50,000 cells/well in a 6 well plate format using specific culture medium prescribed by Lonza. After 24h of plate preparation, 200µl of nanocomplexes, formed using Mgpe9 and 10µg of plasmid DNA encoding for EGFP, was added to each well (in presence and absence of enhancers) following which plate was incubated at 37°C. EGFP expression was then visualized 48h post-transfection, after removal of medium and washing the cells twice with 1x HBSS, using inverted DMI6000B fluorescence microscope (Biomedical Research Leica). DAPI was used for nuclear staining of viable cells. Cell viability was also performed under similar conditions using CellTitre GLO method according to manufacturer's protocol.

Assessment of Skin tissue architecture

Full thickness human foreskin tissue was processed, plated and pre treated with silicone oil; SLA-PP for 30minutes in independent experiments followed by topical treatment with nanocomplexes as mentioned before. Tissue treated with nanocomplexes in absence of chemical enhancer and untreated skin tissue were taken as experimental controls. The cryosections obtained after treatment were then examined in the microscope at 40x to identify possible detachment of stratum corneum from viable epidermis or complete loss of stratum corneum. Moreover cellular differentiation and identification of the skin layers was carried out in the cryosections by observing the presence of Keratin10 (ALEXA FLUOR 488 tagged anti-rabbit secondary antibody), Loricrin (ALEXA FLUOR 647 tagged anti-rabbit secondary antibody) and Keratin 14 (ALEXA FLUOR 488 tagged anti-mouse secondary antibody) protein (a biochemical marker for this layer) using immunostaining method as described in previous sections. Untreated skin tissue was taken as control for the latter study.

Skin integrity test

For checking the effect of chemical enhancer and nanocomplexes on skin integrity, skin permeability test was performed using equilibrated full thickness human foreskin tissue pre-soaked for 24h in 1X phosphate buffered saline solution before conducting the study. 80µl of Mgpe9 nanocomplexes following pre-treatment of skin with silicone oil or SLA-PP as described before was added to the donor compartment along with 100µl of 2µg/µl FITC (389Da) solution and 100µl of 1mM Dextran (3000Da) in independent experiments in all the set ups. The system was kept under constant agitation at 250rpm at room temperature and 1ml of sample volume was collected at different time intervals (i.e. 0h or time of application, 1h, 2h, 3h, 4h, 5h, 18h and

24h). The volume of receptor compartment was maintained constant by re-addition of 1ml 1X phosphate buffered saline (PBS) as a replacement. Untreated skin tissue was considered as experimental control. FITC fluorescence was recorded in the collected samples at emission wavelength of 525nm using microplate reader (Infinite 200 Pro Tecan). Dextran was assessed by anthrone test for carbohydrates.

Protease activity assay

Briefly skin tissue was treated with chemical penetration enhancers silicone oil and SLA-PP before application of Mgpe9 nanocomplexes, following which it was homogenized in liquid nitrogen using mortar-pestle and powder tissue obtained was lysed using 500µl RIPA buffer. Enzyme activity was assessed in the obtained tissue lysate using casein as substrate according to the standard bicinchoninic acid assay (BCA) protocol (Pierce). Tyrosine (1mg/ml) was used to plot the standard curve. Protease activity obtained from untreated skin tissue was plotted as 100% and relative activity was assessed.

Tissue toxicity assessment for necrosis

Skin tissue was plated, treated and processed in similar manner as mentioned before. Cryosections were washed three times using 500µl of PBS (1X) and 0.1% Triton X -100. Following this, it was stained using 10µl of propidium iodide solution (0.1µg/µl) in 100µl of 1X PBS for 10minutes at room temperature. After which the three washings were repeated using 500µl of PBS (1X) and red fluorescence was visualized using TCS SP8 confocal microscope (Leica). Untreated tissue and treatment without enhancers were taken as experimental controls.

Cell viability assay

HaCaT cells were seeded in a 96 well plate at density of 5000 cells per well. After 24h when 70% confluency was attained, complete media was replaced with 80µl of Opti-MEM (Invitrogen) in each well. Following this 20µl of nanocomplexes (with final DNA concentration of 200ng/well) in presence and absence of chemical enhancers silicone oil and SLA-PP were added to the cells. Cells were pre-exposed to enhancers for 30minutes before addition of Opti-MEM to each well followed by nanocomplex treatments. Cell viability was analyzed after 4h and 24h of incubation at 37°C (in the latter case media was replaced with complete media after 4h) according to manufacturer's protocol. Measurements were recorded in triplicates with three measurements in each case using microplate reader (Infinite 200 Pro Tecan) and plotted as percentage cell viability.

Mechanism of penetration enhancement in skin using FTIR

(i) **In skin :** Stratum corneum (SC) was obtained by standard heat separation method. SC membrane samples were cut into 0.5cm x 0.5cm pieces and Fourier transform infrared (FTIR) spectra was recorded on the skin tissue sample after pre-treatment with silicone oil with Mgpe9 nanocomplexes for 24h . Untreated skin tissue was taken as experimental control. Spectra was obtained using the Thermo scientific model NICOLET 380 FTIR operating in the range of 400–4000cm^{-1} with the resolution of 4cm^{-1} and averaged over 400 scans.

(ii) **In elute solution :** Skin tissue was treated with only silicone oil and silicone oil with Mgpe9 nanocomplexes to mimic 3 consecutive applications in independent experiment. Following this, SC was tape stripped twenty times and silicone oil eluted from the viable epidermis tissue using chloroform : acetone (1:1 v/v) mixture. The mixture obtained was scanned for FTIR spectra

using the Thermo scientific model NICOLET 380 FTIR operating in the range of 400–4000cm^{-1} with the resolution of 4cm^{-1}. Spectra for bare silicone oil (taken as control for the study) was also recorded to identify the signature peaks.

FITC labeling of plasmid DNA

pDNA (pEGFP-C1) was labeled with FITC using Label IT® Tracker Fluorescein kit (Mirus Bio Corp.) at a ratio of 0.75:1 (v:w) i.e. 0.75µl of labeling reagent/µg of pDNA according to manufacturer's protocol.

Tissue Uptake of FITC labeled complexes

Nanocomplexes were formed using FITC-labeled plasmid DNA and skin tissue was topically treated with Mgpe9 nanocomplexes in presence and absence of silicone oil as described in previous sections. Treatments were performed in similar manner as explained before followed by washing, fixation and cryosectioning of treated tissues. Presence of FITC labeled nanocomplexes in skin was detected using confocal microscopy (TCS SP8 Leica) and quantification of complexes in epidermis was done using flow cytometry analysis (BD FACS).

***In vivo* transfection study**

Entire animal studies were performed using 2-4 weeks old hairless mice SKH-1 (irrespective of gender) and animal usage was in line with the approval by Institutional animal ethics committee [Approval Number:IITR/IAEC/47/13]. Each study was done in two groups where each group comprised of 3 mice (n=6). In one of the groups mice were pre-treated topically with the chemical enhancer, silicone oil whereas in other group mice were kept untreated to serve as experimental controls. This was followed by topical administration of 80µl of Mgpe9

nanocomplexes prepared at charge ratio 10 in both the groups. Treatment was continued for three consecutive days with single application per day involving 4µg plasmid DNA being administered per application on the dorsal surface of mice. This was added into a circular plastic well (diameter = 1cm) pre-adhered to mice skin and covering area of 3.14cm^2 and intermittent washing of skin surface was performed before each fresh application using 1X phosphate buffered saline (PBS). The mice were sacrificed 24h after final application and skin tissue was obtained. Following this, the tissue was washed, fixed, cryosectioned and processed for immunostaining in a similar manner as explained for *ex-vivo* study previously.

Flow cytometry to quantify EGFP protein in SKH-1

SKH-1 was treated with 80µl of nanocomplexes as explained above following which mice was sacrificed and skin tissue from treated area was excised. For quantification of EGFP fluorescence in the skin, single cell suspension in 1X phosphate buffered saline (PBS) was obtained using GentleMacs dissociator. The dissociated cells obtained were suspended in ice-cold 1X phosphate buffered saline (PBS) and centrifuged at a speed of 2000rpm for 5minutes at 4°C. After centrifugation, the pellet obtained was again washed using 500µl ice-cold 1X phosphate buffered saline (PBS) in similar manner followed by its resuspension in 200µl of 1X phosphate buffered saline (PBS) for further analysis. The flow cytometry measurements were then performed using FACS Caliber (Becton Dickinson) to quantify the cellular fluorescence and mean fluorescence intensity.

Luciferase activity estimation in SKH-1

SKH-1 was topically treated with 80µl of nanocomplexes formed using Mgpe9 peptide and pMIR Luciferase plasmid as explained before at different sites within the same animal. 24h after

third application mice was sacrificed and skin tissue from treated areas was excised. The skin tissue obtained was snap freezed using liquid nitrogen in a mortar and lysed by addition of CCLR using pestle. The lysate obtained was then assessed for luciferase activity using standard protocol from Promega and normalized with total protein concentration estimated using BCA method. Values were obtained and plotted as RLU ± SD.

***In vivo* estimation of Inflammatory cytokines**

SKH-1 was topically treated with nanocomplexes and enhancers in similar manner as explained before following which mice was sacrificed and 1.5ml blood was collected in vacutainers. The samples were then allowed to stand at room temperature for 1h for serum separation. After 1h samples were centrifuged at 1500rpm for 15minutes for better separation. Serum samples collected were then analyzed for presence of inflammatory cytokines, IL-2, IL-6, IL-12 and TNF-α using standard ELISA kits (ebiosciences). SLA-PP was taken as positive control for the study. The concentrations were obtained and plotted as Mean ± SD.

Author contributions

M.G. and V.T.N. conceived and designed the experiments; M.G. wrote the manuscript; M.V. planned and performed experiments, assisted in writing of the manuscript; S.A. and K.M.A. contributed to the animal studies; N.G. and D.S. helped with FTIR experiments; V.G. and H.G. assisted with primary keratinocytes and skin tissue studies.

Acknowledgments

We acknowledge Council of Scientific and Industrial Research (CSIR), New Delhi, India (Network Project TOUCH: BSC0302) for providing financial support to conduct this work. We

also thank Rajesh S. Gokhale (CSIR-IGIB) for the valuable suggestions. We further acknowledge Aanchal Gupta (CSIR-IGIB), Balaram Ghosh (CSIR-IGIB) and Bijay Ranjan Pattnaik (CSIR-IGIB) for the experimental support. We also thank Manish Kumar (CSIR-IGIB) and funding from BSC0403 for the confocal studies.

Disclosure/Conflict of interest

The authors declare no conflict of interest.

ACCEPTED MANUSCRIPT

References

1. Prausnitz, MR. and Langer, R. (2008) Transdermal drug delivery. Nat. Biotechnol., 26, 1261-1268.
2. Prausnitz, MR., Mitragotri, S. and Langer, R. (2004) Current status and future potential of transdermal drug delivery. Nat. Rev. Drug Discov., 3, 115-124.
3. Paudel, KS., Milewski, M., Swadley, CL., Brogden, NK., Ghosh, P. and Stinchcomb, AL. (2010) Challenges and opportunities in dermal/transdermal delivery. Ther. Deliv, 1, 109-131.
4. Naik, A., Kalia, YN., Guy, RH. (2000) Transdermal drug delivery: overcoming the skin's barrier function. Pharmaceutical Science and Technology today, 3, 318-326.
5. Barua, S. and Mitragotri, S. (2014) Challenges associated with penetration of nanoparticles across cell and tissue barriers: A review of current status and future prospects. Nano Today, 9, 223-243.
6. Mitragotri, S. (2005) Immunization without needles. Nat Rev Immunol, 5, 905-916.
7. Desai, P., Patlolla, RR., Singh, M. (2010) Interaction of nanoparticles and cell penetrating peptides with skin for transdermal drug delivery. Mol Membr Biol., 27, 247-259.
8. Bos, JD., Meinardi, MM. (2000) The 500 Dalton rule for the skin penetration of chemical compounds and drugs. Exp Dermatol., 9, 165-169.
9. Karande, P., Jain, A., Mitragotri, S. (2004) Discovery of transdermal penetration enhancers by high-throughput screening. Nat. Biotechnol., 22, 192-197.
10. Karande, P., Jain, A., Ergun, K., Kispersky, V., Mitragotri, S. (2005) Design principles of chemical penetration enhancers for transdermal drug delivery. Proc Natl Acad Sci U S A, 102, 4688-4693.

11. Williams, AC., Barry, BW. (2004) Penetration enhancers. Advance Drug Delivery Reviews, 56, 603-618.
12. Guy, RH., Kalia, YN., Delgado-Charro, MB., Merino, V., López, A., Marro, D. (2000) Iontophoresis: electrorepulsion and electroosmosis. J. Control. Release, 64, 129-132.
13. Mitragotri, S., Blankschtein, D. and Langer, R. (1995) Ultrasound-mediated transdermal protein delivery. Science, 269, 850-853.
14. Finnin, BC. and Morgan, TM. (1999) Transdermal penetration enhancers: applications, limitations and potential. J. Pharm. Sci., 88, 955-958.
15. Elsayed, MM., Abdallah, OY., Naggar, VF., Khalafallah, NM. (2007) Lipid vesicles for skin delivery of drugs: reviewing three decades of research. Int J Pharm., 332, 1-16.
16. Kumar, S., Zakrewsky, M., Chen, M., Menegatti, S., Muraski, JA., Mitragotri, S. (2015) Peptides as skin penetration enhancers : Mechanism of action. J Control. Release, 199, 168-178.
17. Aliyar, H., Schalau, G2nd. (2015) Recent developments in silicones for topical and transdermal drug delivery. Ther Deliv., 6, 827-839.
18. Montenegro, L., Paolino, D., Puglisi, G. (2004) Effects of silicone emulsifiers on *in vitro* skin permeation of sunscreens from cosmetic emulsions. J Cosmet Sci., 55, 509-18.
19. Puri, N. and Talwar, A. (2009) The Efficacy of Silicone Gel for the Treatment of Hypertrophic Scars and Keloids. J Cutan Aesthet Surg., 2, 104-106.
20. Bleasdale, B., Finnegan, S., Murray, K., Kelly, S., Percival, SL. (2015) The Use of Silicone Adhesives for Scar Reduction. Adv Wound Care , 4, 422-430.
21. Hsu, T., Mitragotri, S. (2011) Delivery of siRNA and other macromolecules into skin and cells using a peptide enhancer. Proc. Natl. Acad. Sci. U S A, 108, 15816-15821.

22. Rothbard, JB., Garlington, S., Lin, Q., Kirschberg, T., Kreider, E., McGrane, PL. *et al*. (2000) Conjugation of arginine oligomers to cyclosporine A facilitates topical delivery and inhibition of inflammation. Nat. Med., 6, 1253-1257.
23. Chen, Y., Shen, Y., Guo, X., Zhang, C., Yang, W., Ma, M. *et al.* (2006) Transdermal protein delivery by a co-administered peptide identified via phage display. Nat. Biotechnol., 24, 455-460.
24. Uchida, T., Kanazawa, T., Takashima, Y., Okada, H. (2011) Development of an efficient transdermal delivery system of small interfering RNA using functional peptides, Tat and AT-1002. Chem Pharm Bull (Tokyo)., 59, 196-201.
25. Hou, YW., Chan, MH., Hsu, HR., Liu, BR., Chen, CP., Chen, HH. *et al.* (2007) Transdermal delivery of proteins mediated by non-covalently associated arginines rich intracellular delivery peptides. Exp.Dermatol., 16, 999-1006.
26. Kim, YC., Ludovice, PJ., Prausnitz, MR. (2007) Transdermal delivery enhanced by magainin pore forming peptide. J Control Release, 122, 375-383.
27. Chen, M., Gupta, V., Anselmo, AC., Muraski, JA., Mitragotri, S. (2014) Topical delivery of hyaluronic acid into skin using SPACE-peptide carriers. J. Control Release, 173, 67-74.
28. Lee, J., Jung, E., Park, J., Park, D. (2005) Transdermal delivery of interferon-gamma (IFN-gamma) mediated by penetratin, a cell-permeable peptide. Biotechnol Appl Biochem., 42, 169-173.
29. Chen, M., Kumar, S., Anselmo, AC., Gupta, V., Slee, DH., Muraski, JA. *et al.* (2015) Topical delivery of Cyclosporine A into the skin using SPACE-peptide. J Control Release, 199, 190-197.

30. Vij, M., Natarajan, P., Pattnaik, BR., Alam, S., Gupta, N., Santhiya, D. *et al.* (2016) Non-invasive topical delivery of plasmid DNA to the skin using a peptide carrier. J. Control Release, 222, 159-168.

31. Panchaxari, DM., Pampana, S., Pal, T., Devabhaktuni, B., Aravapalli, AK. (2013) Design and characterization of diclofenac diethylamine transdermal patch using silicone and acrylic adhesives combination. J of Pharm. Sci, 21, 1-14.

32. Smith, AL., Winefordner, JD., Kolthoff, IM. (1991) The Analytical Chemistry of Silicones, John Wiley & Sons, Inc.: New York, 210-211.

33. Reusch, W. (2013) Introduction to spectroscopy. [https://www2.chemistry.msu.edu/faculty/reusch/virttxtjml/Spectrpy/spectro.htm#contnt]

34. Barry, BW., Edwards, HGM., Williams, AC. (1992) Fourier Transform Raman and Infrared Vibrational Study of Human Skin: Assignment of Spectral Bands. J. Raman Spectroscopy, 23, 641-645.

35. Clancy, MJ., Corish, J., Corrigan, OI. (1994) Comparison of the effects of electrical current and penetration enhancers on the properties of human skin using spectroscopic (FTIR) and calorimetric (DSC) methods. International Journal of Pharmaceutics, 105, 47-56.

36. Benavides, F., Oberyszyn, TM., VanBuskirk, AM., Reeve, VE. and Kusewitt, DF. (2009) The hairless mouse in skin research. J Dermatol Sci., 53, 10-18.

37. Honzak, L., Sentjurc, M., Swartz, HM. (2000) *In vivo* EPR of topical delivery of a hydrophilic substance encapsulated in multilamellar liposomes applied to the skin of hairless and normal mice. J Control Release, 66, 221-228.

38. Tan, G., Xu, P., Lawson, LB., He, J., Freytag, LC., Clements, JD. *et al.* (2010) Hydration effects on skin microstructure as probed by high-resolution cryo-scanning electron microscopy and mechanistic implications to enhanced transcutaneous delivery of biomacromolecules. J Pharm Sci., 99, 730-740.

39. Prausnitz, MR., Elias, PM., Franz, TJ., Schmuth, M., Tsai, JC., Menon, GK. *et al.* (2012) Skin Barrier and Transdermal Drug Delivery. Medical Therapy, Section 19.

40. Warner, RR., Stone, KJ., Boissy, YL. (2003) Hydration disrupts human stratum corneum ultrastructure. J Invest Dermatol., 120, 275-84.

ACCEPTED MANUSCRIPT

Figure Legends

Figure 1: Effect of skin penetration enhancers on biophysical characteristics and *ex vivo*; *in vivo* transfection efficiency of Mgpe9 nanocomplexes (See also Figure S1, S2, S3).

(A) Size estimation of Mgpe9 nanocomplexes, native or in presence of enhancers i.e. Silicone oil, SLA-PP and TD-1, where hydrodynamic diameter was measured using Dynamic Light Scattering. Data is represented as size ± SD. PDI refers to poly-dispersity index value.

(B) DNA condensation assay was performed to check the stability of Mgpe9 nanocomplexes, either native or in presence of different enhancers as mentioned in Figure 1(A). Stability was assessed visually on 1% agarose gel as the amount of plasmid DNA released upon electrophoresis in comparison to the control plasmid DNA loaded in lane 1. Ethidium bromide was used to impart fluorescence and detect presence of free plasmid DNA in gel.

(C) Visualization of increase in EGFP expression in human skin tissue (*ex vivo*) using confocal microscopy upon enhancer pre-treatment. Skin tissue was topically pre-treated with enhancers, followed by subsequent administration of Mgpe9 nanocomplexes (1 application per day with 4µg of plasmid DNA per application) for 3 consecutive days (as detailed in Materials and Methods section). Immunostaining was carried out using protocol detailed in Materials and Methods (to avoid autofluorescence artifact) and confocal imaging was performed at 40x magnification. TRITC (red) indicates the EGFP expression and DAPI (blue) has been used as nuclear stain to show epidermal cell viability. Scale bar: 20µm.

(D) Quantitative analysis of EGFP expression in human skin tissue (*ex vivo*) was carried out using flow cytometry. The percentage EGFP positive cells (Bar graph) and the mean fluorescence intensity (Line graph) were recorded. The data are shown as Mean ± SD. $p<0.001$

was observed for silicone oil where n=6 (Triplicates). Red bar indicates Mgpe9 nanocomplex, Blue bar indicates Enhancers + Mgpe9 nanocomplex, Grey bar indicates Control with no treatment.

(E) *In vivo* enhancement of transfection efficiency for Mgpe9 nanocomplexes in SKH-1 mice was assessed using confocal microscopy as detailed in Materials and Methods . EGFP expression was checked through immunostaining and imaging was done at 20x magnification. TRITC (red) indicates the EGFP expression and DAPI (blue) has been used as nuclear stain to show epidermal cell viability. Scale bar: 10µm.

Figure 2: Safety evaluation of silicone oil as an enhancer in skin in presence of Mgpe9 nanocomplexes (See also Figure S4, S5, S6, S7).

(A) Synergistic effect of Silicone oil enhancer and Mgpe9 nanocomplexes on stratum corneum barrier of skin was observed using confocal microscopy. Imaging of human skin cryosections (6µm) was performed at 40x magnification to visually locate detachment or complete abolishment of stratum corneum upon topical treatments administration. SLA-PP was taken for comparison . Scale bar: 20µm.

(B) Effect of bare silicone oil and SLA-PP applications on skin tissue architecture was studied through immunostaining to highlight the presence of Keratin 14 protein which is a known biochemical marker for basal layer of skin. Green signal of ALEXA FLUOR 488 indicates basal layer of skin; DAPI dye (blue) was used to stain the nuclei of viable epidermal cells. Untreated skin tissue was taken as experimental control. Complete absence of green fluorescence indicates damage to the basal layer of skin. Scale bar: 20µm.

(C) Skin integrity on application of silicone oil/SLA-PP and Mgpe9 nanocomplexes was assessed by dye penetration test using Franz diffusion assay. SLA-PP was used as a positive control for study. Penetration of low molecular weight dye FITC was studied. The data are shown as Mean ± SD.

(D) Non-specific protease activity in human skin tissue (pre-treated with enhancers and nanocomplexes) was estimated by standard bicinchoninic acid assay (BCA) using casein as the substrate. Tyrosine (1mg/ml) was used to plot the standard curve. Enzymatic activity obtained from untreated skin tissue was taken as 100% and relative % enzyme activity was plotted for treatments. Red bar indicates Mgpe9 nanocomplex, Blue bar indicates Enhancers + Mgpe9 nanocomplex, Grey bar indicates Control with no treatment.

(E) Fluorescence microscopy analysis was performed on treated human skin on application of silicone oil/SLA-PP and Mgpe9 nanocomplexes to check for necrotic cell death in viable epidermis using Propidium Iodide dye staining method. Dead cells were identified by presence of red fluorescence. Images were obtained at 20x magnification. Scale bar: 20µm.

(F) Cell viability in presence of enhancers and Mgpe9 nanocomplexes was assessed using CellTitre Glo Luminescent Cell Viability assay for 4h and 24h in HaCaT cells. Bare nanocomplexes treatment was taken for comparative analysis. Untreated cells were considered as 100% viable. Values were plotted as relative % cell viability for all the treatments. The data are shown as Mean ± SD. Red bar indicates Mgpe9 nanocomplex, Blue bar indicates Enhancers + Mgpe9 nanocomplex, Grey bar indicates Control with no treatment.

Figure 3: Mechanistic insights into enhancement effects of silicone oil upon topical treatment in skin (See also Figure S8).

(A) FTIR spectroscopy was carried out on stratum corneum of human skin treated with silicone oil and Mgpe9 nanocomplexes (as single topical application) for 24h (ii) to predict interaction with skin components. Untreated stratum corneum (i) was taken as experimental control. Critical peaks are indicated in red circles, SL refers to skin lipids, SP refers to skin proteins, SH refers to skin hydration, LF/LE refers to Lipid Fluidization/Lipid extraction, PI refers to protein interaction.

(B) Tissue uptake of labeled Mgpe9 nanocomplexes (formed using FITC labeled plasmid DNA and unlabeled peptide) in presence and absence of silicone oil enhancer was studied using confocal microscopy. Cells were imaged at 40x magnification to demonstrate the entry of nanocomplexes across stratum corneum and into the viable epidermal cells of skin. Scale bar: 20µm.

(C) Quantitative estimation of tissue uptake of labeled Mgpe9 nanocomplexes in presence and absence of silicone oil enhancer was carried out using flow cytometry. The percentage FITC positive cells (Bar graph) and the mean fluorescence intensity (Line graph) was recorded. The data are shown as Mean ± SD. Red bar indicates Mgpe9 nanocomplex, Blue bar indicates Enhancers + Mgpe9 nanocomplex.

(D) To check silicone oil entry in skin FTIR spectroscopy was performed on chloroform : acetone elute solution obtained from viable epidermis of tape stripped human skin tissue pre-treated with (i) bare silicone oil or (ii) silicone oil and Mgpe9 nanocomplexes as three consecutive topical administrations. All peaks are indicated in red.

A

Samples	Size (nm) ± SD	PDI values
Mgpe9	77.1 ± 0.3	0.26
Silicone oil	110.0 ± 3.5	0.27
SLA-PP	130.7 ± 6.9	0.26
TD-1	116.7 ± 1.5	0.10

B

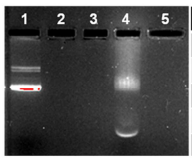

Lanes	Samples
1	Bare plasmid DNA
2	Mgpe9
3	Silicone oil
4	SLA-PP
5	TD-1

C

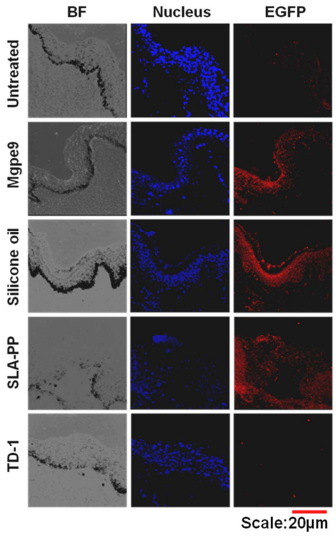

D

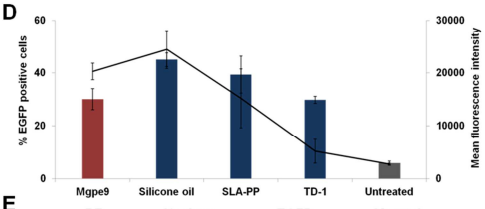

E

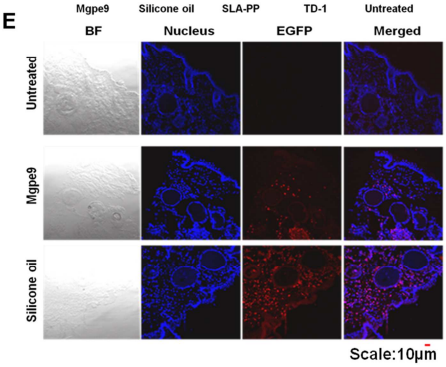

FIG.1

ACCEPTED MANUSCRIPT

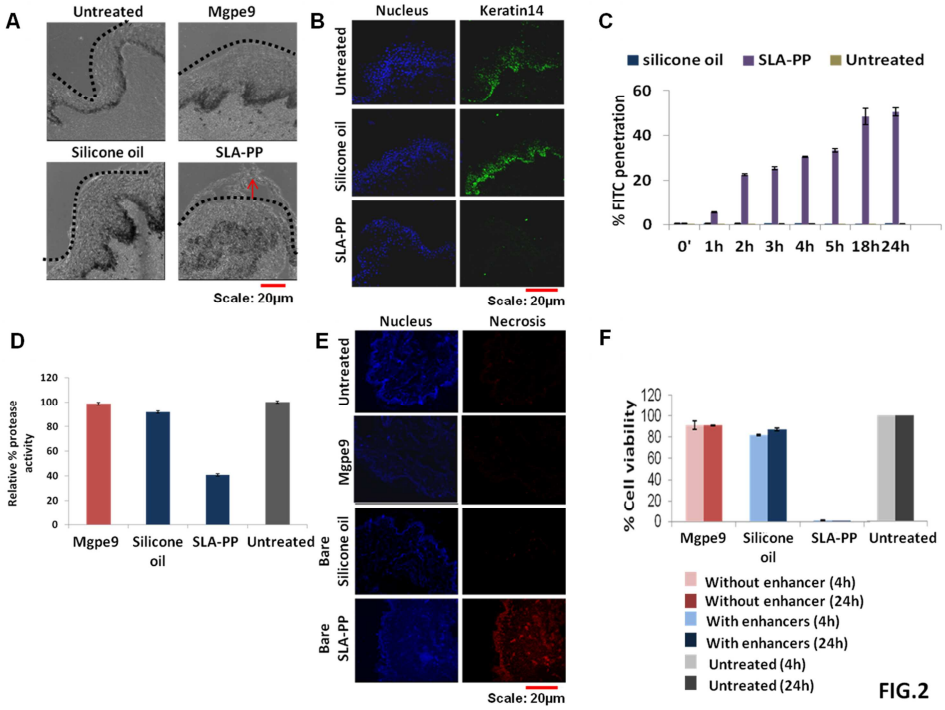

FIG.2

ACCEPTED MANUSCRIPT

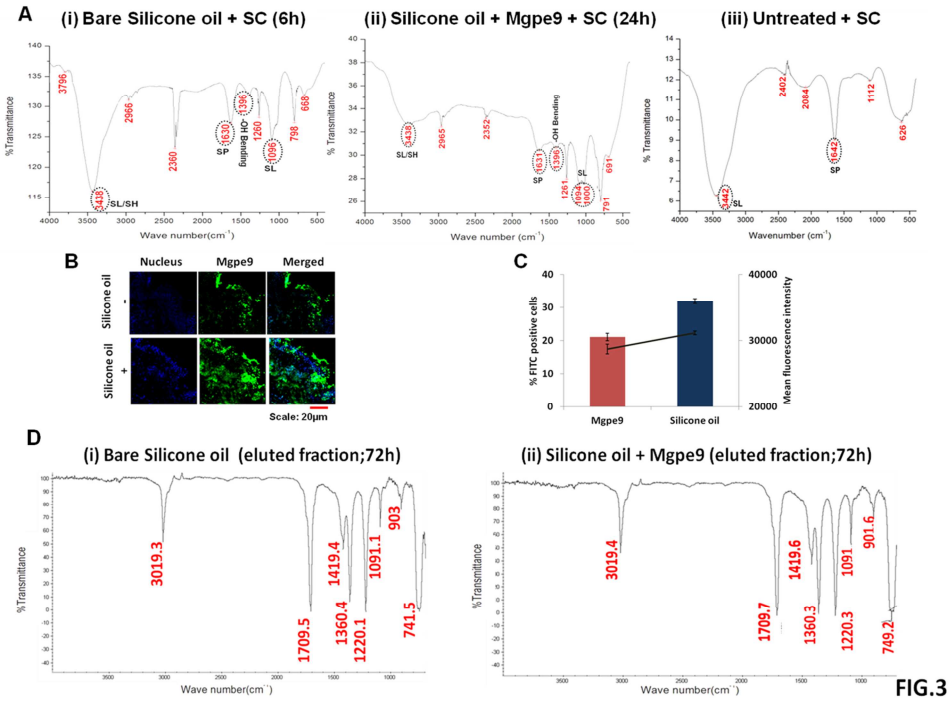

FIG.3

ACCEPTED MANUSCRIPT

Numerical Simulation of N^+ Source Pocket PIN-GAA-Tunnel FET: Impact of Interface Trap Charges and Temperature

Jaya Madan, *Student Member, IEEE*, and Rishu Chaujar, *Senior Member, IEEE*

***Abstract*— This paper investigates the reliability of PIN-gate-all-around (GAA)-tunnel field-effect transistor (TFET) with N^+ source pocket. The reliability of the PNIN-GAA-TFET is examined by analyzing: 1) the impact of interface trap charge (ITC) density and polarity and 2) the temperature affectability on analog/RF performance of the device. It is realized that the interface traps existing at the Si/SiO_2 interface modifies the flatband voltage and, thereby, alters the analog and RF characteristics of the device. The analysis is done at various trap charge densities and polarities. The results, thus, obtained reveal that, at higher trap charge density, the device performance alters significantly. It is obtained that, for a donor trap charge density of 3×10^{12} cm^{-2}, the off-state current of the device degrades tremendously (increases from an order of 10^{-17}–10^{-9}A). The temperature affectability over the device reveals that, at lower gate bias, the Shockley–Read–Hall phenomenon dominates and degrades the subthreshold current of the device at elevated temperatures. However, for the superthreshold regime, the band-to-band tunneling (BTBT) mechanism dominates. Furthermore, the results show enormous degradation in the off-state current at elevated temperatures, such that, with an increase in the ambient temperature from 200 K to 400 K, the I_{OFF} degrades by an order of 10^5, i.e., increases from 10^{-18} A to 10^{-13} A. The results specify that the PNIN-GAA-TFET is insusceptible to the acceptor traps existing at the Si/SiO_2 interface in comparison with the donor traps.**

***Index Terms*— Interface trap charges (ITCs), N^+ source pocket, temperature sensitivity, tunnel FET (TFET).**

I. Introduction

PERPETUAL miniaturization of complementary metal–oxide–semiconductor (CMOS) devices has incredibly revolutionized many areas, such as security, military, mobile communications, and medicine. However, downscaling the CMOS technology results in severe problems, such as high leakage current, high subthreshold swing (SS), and other short channel effects [1]. These challenges enforce for exploring the novel devices that work on new operation mechanisms other than thermionic emission over the thermal barrier as in the case of MOSFET. In this regard, tunnel field-effect transistors (TFETs) that use interband tunneling in the source and channel junction with a control of gate bias has attracted much attention [2]–[6]. The major challenges faced by MOSFET, such as the limitations on the SS that has a fundamental limit of 60 mV/decade and high OFF-state leakage current, have been overcome by TFET up to a great extent. In TFET, the large tunneling barrier width present at the source–channel junction at lower gate bias blocks the tunneling of electrons and, thereby, benefits a very low leakage current. However, the band-to-band tunneling (BTBT) of carriers from the source potentially allows a steep SS values [7]. Apart from these merits, TFET suffers from low ON-current, high threshold voltage (V_{th}), high gate–drain parasitic capacitance, and ambipolar current [8], [9]. For superior analog/RF performance, many device engineering architectures and III–V materials have also been proposed by various researchers [2], [8], [10]–[15]. Among all device engineering architectures, the N^+ source pocket p-i-n TFET or PNIN-TFET proposed by [14] is a strong candidate as it offers higher ON-current with lower SS and lower V_{th}. III–V TFET, however, mitigates the problem of lower I_{ON} offered by their lower bandgap, lower effective mass, and wide range of band alignments; thus, III-V material-based TFETs have the potential of high switching speed, but at the same time suffering from large SS [16]. However, the basic device characteristics, such as improved analog, RF, and linearity of TFET, have been the major encompassing area of the investigation up to now. Recently, Moselund *et al.* [9] fabricated lateral p-type InAs/Si TFET with I_{ON} of a few $\mu A/\mu m$ for $|V_{ds}| = |V_{gs}| = 0.5$ V. A SiGe/Si heterostructure TFET has been fabricated by Blaeser *et al.* [17] that shows I_{ON} of 6.7 $\mu A/\mu m$ at $V_{dd} = 0.5$ V and SS of ~80 mV/decade. Nonetheless, for sub-100-nm devices, the reliability of TFET is also a critical concern, owing to the strong electric field at the source–channel junction. This strong electric field roots to the generation of defects at the $Si–SiO_2$ interface [18]. Along with the high electric field, the fabrication processes for sub-100-nm devices, such as the plasma etching, may damage the gate oxide and the Si-oxide interface. These defects are the origin of fixed interface and oxide

Manuscript received January 16, 2017; revised February 1, 2017; accepted February 14, 2017. Date of publication March 7, 2017; date of current version March 22, 2017. The work of J. Madan was supported by the University Grants Commission. The review of this paper was arranged by Editor Frank Schwierz.

The authors are with the Microelectronics Research Laboratory, Engineering Physics Department, Delhi Technological University, New Delhi 110042, India (e-mail: jayamadan.2012@gmail.com; rishu.phy@dce.edu).

Color versions of one or more of the figures in this paper are available online at http://ieeexplore.ieee.org.

Digital Object Identifier 10.1109/TED.2017.2670603

0018-9383 © 2017 IEEE. Personal use is permitted, but republication/redistribution requires IEEE permission.
See http://www.ieee.org/publications_standards/publications/rights/index.html for more information.

charges. These fixed charges can adversely affect the yield and reliability, and also alters the ideal predicted device characteristics [19], [20]. The impact of interface trap charges (ITCs) has also been investigated on lateral p-type InAs/Si (a III–V TFET) by Sant *et al*. [21], which reported that the high concentration of trap centers formed at the heterojunction of III–V material (source side) and the silicon (channel region) attributes to the carrier generation by the trap-assisted tunneling (TAT) at the heterojunction, which degrades the SS of TFET. The large trap centers at the interface of III–V TFET evaluate the charge density at the interface and, thereby, alter the device electrostatics. In addition to the traps present at the heterojunction, for a III–V TFET, the traps at the interface of channel and oxide add to further degradation of the subthreshold characteristics of TFET. However, till date, not much has been reported regarding the study of the impact of ITCs on the reliability of TFET [18]–[20], [22]–[24]. Moreover, to meet the everlasting demand of transistors with high- and low-temperature tolerance (other than the room temperature) needed in aircraft, space, and automotive technology, the temperature affectability over the device performance must be analyzed [25], [26]. In addition, with an increase in number of on-chip transistors, the heat dissipation increases drastically. Therefore, the operating temperature of transistor also increases. Thus, for better reliability, it is obligatory to analyze the performance of the device at various ambient temperatures. Dey *et al.* [16] and Mookerjea *et al.* [27] reported that the temperature dependence of III–V TFET is a strong function of gate bias, due to the onset of various conduction mechanisms at different gate-bias regions. At lower gate-bias region, the consequence of exponential temperature dependence of Shockley–Read–Hall (SRH) generation recombination results in the exponential rise of I_{OFF}. Further increase in the gate bias thermally excites the carriers from the trap centers into the conduction band. However, at higher gate-bias region, the BTBT contributes to the drain current with negligible contribution from the trap centers. Moreover, it is reported in [27] that the peak interface state density is in the middle of the energy bandgap. Therefore, the major contribution of the midgap traps at the oxide–semiconductor interface in the tunneling process causes a degradation in SS at elevated temperatures. The surface passivation is recommended for reducing the TAT and the degradation caused at the elevated temperatures and the ITCs to the SS and I_{OFF}. In this work, the gate-all-around (GAA) architecture with N^+ source pocket PIN-TFET is considered, and an elaborate study of its analog characteristics and RF figure of merits is reported, including the impact of ITC density and polarity at various ambient temperatures.

II. Device Analysis and Simulation

Fig. 1(a) shows the 3-D view of simulated device structure, i.e., N^+ source pocket PIN-GAA-TFET (PNIN-GAA-TFET). For PNIN-GAA-TFET, the source pocket length (L_p) and the source pocket (N^+) doping (N_p) are assessed for the optimized analog characteristics, and the optimum values of L_p and N_p are obtained as 4 nm and 4×10^{19} cm^{-3}, respectively, as shown in our previous work [4].

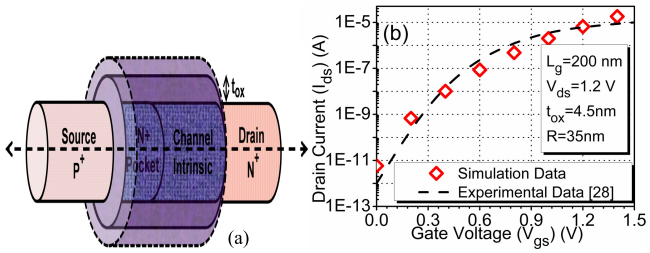

Fig. 1. (a) Simulation structure of PNIN-GAA-TFET. (b) Comparison of experimental [28] and simulated I_{ds}–V_{gs} of GAA-TFET.

The device parameters such as the channel length (L_g), gate oxide thickness (t_{OX}), and radius (R) of the device under consideration are 50, 3, and 10 nm, respectively. The source, channel, and drain are of silicon. The source (P^+), channel, and drain (N^+) regions are uniformly doped. The source is p^+-type doped (1×10^{20} cm^{-3}), and the drain is n^+-doped (5×10^{18} cm^{-3}). The drain doping is 5×10^{18} cm^{-3} (i.e., less than source doping), to minimize the drain–channel tunneling and, thus, the ambipolar conduction [29]. Furthermore, an optimum value of gate metal work function, i.e., 4.3 eV has been chosen for optimum better subthreshold characteristics.

A. Simulation Methodology

The PNIN-GAA-TFET is simulated using the ATLAS device simulator [30]. For TFETs, the BTBT model is significantly important. Local BTBT model estimates a triangular barrier approximation in the energy bands and, thus, considers a constant electric field at the entire tunneling region. However, the non-local BTBT incorporates the dynamic changes in the electric field at the entire tunneling path. Thus, the non-local BTBT that calculates the generation rate at each mesh point in the tunneling region is incorporated in this work [31]. In addition to the non-local BTBT model, concentration- and field-dependent mobility model, SRH model for carrier recombination, bandgap narrowing, and Fermi–Dirac statistics are also invoked during simulation. Besides, Gummel (decoupled) and Newton's (fully coupled) methods have been used to numerically solve the carrier transport equation. Owing to the strong electric field at the source–channel (tunneling) junction, the ITCs are considered only at 10-nm length from the interface of the source and the N^+ pocket and along the Si–SiO_2 interface [19]. In addition, the reliability of device in terms of ITCs is analyzed by transmuting the equivalent positive (negative) localized charges at the Si–SiO_2 interface. The uniform distribution of ITC density is considered in the TCAD simulations. The parameters such as the trap charge density, polarity, and their position along the channel are defined in INTERFACE statement. In this work, the density of the interface charge density (N_f) is chosen in support with various formerly published experimental and simulation data that includes the process damage, radiation damage, and hot carrier damage, and results in ITC density of 10^{11}–10^{13} cm^{-2} eV^{-1} [18], [20], [21]. The reliability of PNIN-GAA-TFET is analyzed in terms of various electrical, analog, and RF figures of merit. Moreover, while analyzing the influence of ITCs on device characteristics, the temperature is kept

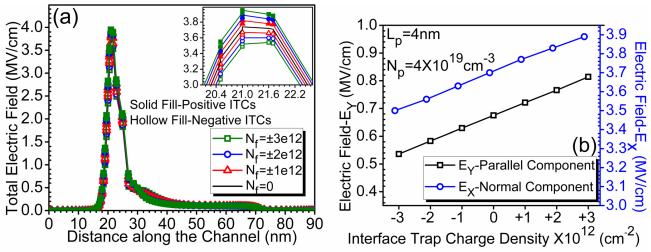

Fig. 2. (a) Electric field profile along the channel of PNIN-GAA-TFET at $N_f = \pm 1, 2, 3$ ($\times 12$) cm^{-2}. (b) Peak intensity of parallel and normal components of electric field near tunneling junction of PNIN-GAA-TFET as a function of ITC density.

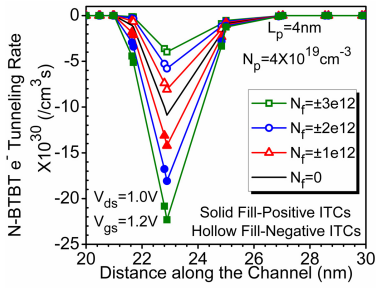

Fig. 3. Nonlocal BTBT of electrons of PNIN-GAA-TFET as a function of channel length at $N_f = \pm 1, 2, 3$ ($\times 12$) cm^{-2}.

constant at 300 K, and during investigation of temperature affectability, the trap charge density is kept constant at $N_f = \pm 1 \times 10^{12}$ cm^{-2}.

B. Model Validation

Simulation setup has been validated by the experimental data, before simulating the device structure [28]. The non-local BTBT model has been calibrated by tuning the tunneling masses from their default values to fit it with [28]. The adjusted value of me.tunnel $= 0.22\ m_o$ and mh.tunnel $= 0.52\ m_o$ [4], [19], where m_o is the rest mass of electron. The validation of simulation setup with the experimental data for the transfer characteristics is shown in Fig. 1(b). The close proximity of simulation model with the experimental data, thereby, authorizes the model considerations of simulation setup.

III. Results and Discussion

A. Impact of Interface Trap Charges—Density and Polarity

In this section, the influence of ITC density and polarity of PNIN-GAA-TFET is examined at a constant temperature of 300 K. Fig. 2(a) shows the impact of ITC density on the total electric field of PNIN-GAA-TFET. It is clearly evident from the inset (that shows the magnified view of the peak of the electric field at the tunneling junction) that, with an increase of donor (acceptor) trap charge density, the peak of electric field increases (decreases) with respect to the case of undamaged device. This increase (decrease) in an electric field is attributed to the decrease (increase) in the flatband voltage caused by the presence of positive (negative) trap charges, defined as

$$\Delta V_{fb} = \frac{qN_f}{C_{\text{ox}}}$$

where q is the electronic charge, N_f is the ITC density, and C_{ox} is the gate oxide capacitance. The presence of positive (negative) ITCs decreases (increases) the flatband voltage and, thereby, increases (decreases) the effective gate bias ($V_{\text{eff}} = V_{\text{gs}} - V_{\text{fb}}$) at the tunneling junction. The enhanced (reduced) V_{eff} caused by the occurrence of donor (acceptor) trap charges, thereby, enhances (reduces) the electric field at the tunneling junction as evident from Fig. 2(a). Moreover, the considerably high electric field peak at the tunneling junction (caused by the steeper band bending) is a merit for enhancing the tunneling rate of electrons, but it also attributes to the generation of trap centers near the source–channel junction. As reported in [32], the parallel component of the electric field, i.e., E_y contributes to the tunneling rate of electrons and, thereby, affects the drain current of TFET. Higher value E_y is required for enhanced BTBT rate of electrons and, thus, for the higher value of I_{ds}. However, the normal component of the electric field, i.e., E_x is responsible for the reliability concerns, such as the interface trap generation along with the gate leakage current. The lower value of E_x is required for improved device reliability. Thus, the peak of parallel (E_y) and normal (E_x) components of electric field at the tunneling junction as a function of ITC density is analyzed and is shown in Fig. 2(b). At higher donor (acceptor) trap charge density, the peaks of both E_x and E_y are large (small). The higher value of E_y enhances the tunneling rate of electrons; however, the larger value of E_x degrades the device reliability. Fig. 3 shows the impact of ITC density on nonlocal BTBT rate of electrons along the channel length. It is examined that, with an increase in the density of donor (acceptor) ITCs, the BTBT rate of electrons increases (decreases) extensively. This increase (decrease) in the BTBT rate of electrons is attributed to the enhanced (reduced) electric field at the tunneling junction, as shown in Fig. 2(a). Fig. 4(a) shows the impact of ITC density on the transfer characteristics of PNIN-GAA-TFET at $T = 300$ K. The result reveals that the positive (negative) traps enhances (reduces) the drain current. This increase (decrease) in the drain current is the consequence of the enhanced (reduced) effective gate bias caused by the reduced (increased) V_{fb} by the presence of positive (negative) trap charges. The degradation posed by the donor traps is more hazardous for the device operated in subthreshold regime in comparison with the superthreshold regime. Furthermore, it is analyzed that, with an increase in positive trap charge density, I_{OFF} degrades significantly from an order of 10^{-17} A to 10^{-9} A. Therefore, as the fixed charges generated by the various process-, radiation-, and stress-induced damages are always present in a practically fabricated device, it may severely degrade the device characteristics. Fig. 4(b) shows the impact of trap charge density on I_{OFF} and the current switching ratio ($I_{\text{ON}}/I_{\text{OFF}}$ ratio). As clearly shown in Fig. 4(b), the damaged region with donor trap charges of 3×10^{12} cm^{-2} degrades I_{OFF} tremendously from an order of 10^{-17} A to 10^{-9} A. However, as shown in Fig. 4(a),

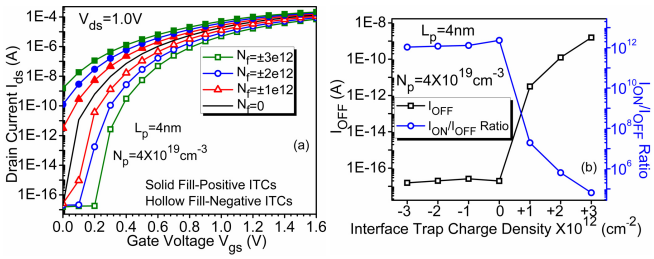

Fig. 4. Impact of ITC density on (a) transfer characteristics (b) I_{off} and switching ratio of PNIN-GAA-TFET at $N_f = \pm 1, 2, 3$ ($\times 12$) cm^{-2}.

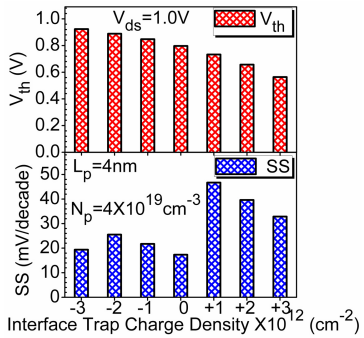

Fig. 5. Impact of ITC density on V_{th} and SS of PNIN-GAA-TFET at $N_f = \pm 1, 2, 3$ ($\times 12$) cm^{-2}.

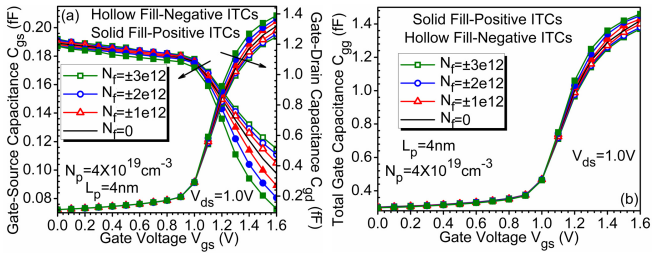

Fig. 6. Influence of ITC density on (a) C_{gs}, C_{gd}, and (b) C_{gg} as a function of gate voltage of PNIN-GAA-TFET.

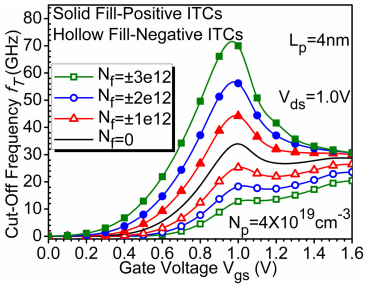

Fig. 7. Effect of ITC density on f_T as a function of V_{gs} of PNIN-GAA-TFET.

the presence of ITC alters the superthreshold current marginally and, thus, the switching ratio is mainly affected by I_{OFF}. It is obtained that the switching ratio degrades from an order of 10^{12} (for the undamaged device) to 10^5 (for a damaged device with donor trap charge density of 3×10^{12} cm^{-2}). However, the consequence of immunity against the presence of acceptor trap charges is also observed in unaltered I_{ON}/I_{OFF} for the negative ITC density.

The impact of ITC density on V_{th} and the SS of PNIN-GAA-TFET are presented in Fig. 5. It is obtained that the presence of donor (acceptor) trap charges decreases (increases) V_{th}. The reduced V_{th} for donor trap charges is attributed to the additional band bending caused by the presence of positive trap charges. V_{th} reduces (enhances) by 29.26% (15.90%) at $N_f = \pm 3 \times 10^{12}$ cm^{-2}. The degradation in the SS due to the presence of ITC is elucidated clearly in Fig. 5. This degradation in the SS is due to the tremendously enhanced I_{OFF} for positive ITC. However, the consequence of little variation in I_{OFF} and I_{ON} for acceptor ITCs is shown by the slight change in the SS at negative ITCs.

Moreover, the reliance of operating speed of TFET on parasitic capacitance and the different switching operation of TFET necessitates the investigation of bias-dependent parasitic capacitances. In this work, the intrinsic capacitances are evaluated through the small-signal ac analysis, at a constant dc solution. In this regard, the intrinsic capacitances among each pair of electrodes (i.e., source, gate, and drain) are calculated at a single constant frequency at 1 GHz with a dc voltage ramp of 0–1.6 V. Moreover, for better convergence, DIRECT parameter is incorporated while simulating the device. As reported in [33], in TFETs, the inversion layer distribution is distinct from MOSFET. This results in fundamentally different partitions of total gate capacitance C_{gg} in TFET from that of a MOSFET. As shown in [34], for TFET, the drain is connected to the inversion layer and, therefore, C_{gd} contributes majorly to C_{gg}, in contrary to MOSFET, where $C_{gg}/2 \sim C_{gd} \sim C_{gs}$. Fig. 6(a) and (b) shows the impact of ITC density on C_{gs}, C_{gd}, and C_{gg} as a function of V_{gs} at the constant $V_{ds} = 1$ V. At lower value of V_{gs}, the inversion layer is first formed at the drain side, and with an increase in V_{gs}, it extends toward the source side as evident from Fig. 6(a). The reduced coupling between gate and source with an increase in V_{gs} monotonically decreases C_{gs} with increasing V_{gs}. Before the inversion layer formation, C_{gs} comprises the parasitic capacitance; after the inversion layer formation, C_{gd} dominates. In addition, the similar values of C_{gg} and C_{gd} are attributed to the small value of C_{gs} that results in almost the same values of C_{gg} and C_{gd}. It is evaluated that the presence of positive (negative) ITCs increases (decreases) the C_{gd} by 0.1% (0.1%) at $V_{gs} = 0$ V and 8.5% (4.9%) at $V_{gs} = 1.2$ V. The influence of ITC density on C_{gg} as a function of V_{gs} of PNIN-GAA-TFET is shown in Fig. 6(b). The consequence of immunity of C_{gd} against ITC density due to low electric field at the drain channel junction is evident from the unaltered C_{gg} with ITC density. An important RF figure of merit is the cutoff frequency (f_T) defined as the frequency at which the current gain falls to 0 dB. The impact of ITC density on f_T as a function of gate voltage is shown in Fig. 7. It is analyzed that the existence of positive (negative) ITCs increases (decreases) f_T. This increase (decrease) is due to the enhanced (reduced) drain current and, thus, the transconductance that has a direct dependence on f_T. Moreover, it is obtained that the peak of f_T, increases (decreases) more prominently at higher ITC density. It is evaluated that, at $V_{gs} = 1$ V, the presence of donor (acceptor) ITCs of $N_f = \pm 3 \times 12$ cm^{-2} increases

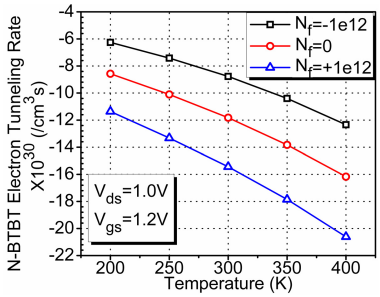

Fig. 8. Variation of nonlocal BTBT rate of electrons at the tunneling junction as a function of temperature of PNIN-GAA-TFET at $N_f = \pm 1 \times 12\ \text{cm}^{-2}$.

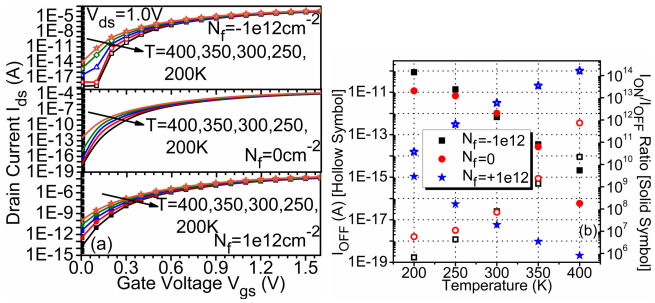

Fig. 9. (a) Drain current (b) I_{off} and current switching ratio as a function of temperature (200–400 K) of PNIN-GAA-TFET at $N_f = \pm 1 \times 12\ \text{cm}^{-2}$.

(decreases) f_T by 2.06 (2.65) times, respectively. As f_T of TFET has a direct variation with g_m and inverse variation with the total gate capacitance C_{gg} ($=C_{\text{gs}} + C_{\text{gd}}$), thus, the demerit of higher C_{gd} in TFET attributes to the lower f_T in comparison with the experimental conventional Si MOSFETs with comparable gate length, as also reported in various published articles [33].

B. Temperature Affectability

In this section, PNIN-GAA-TFET is analyzed at various ambient temperatures at constant ITC density. Fig. 8 presents the variations in the nonlocal BTBT rate at various temperatures, including the effect of ITCs. In the case of TFET, the BTBT rate is reliant on temperature. In addition, the property of semiconductor, such as the energy bandgap, is also dependent on temperature. The reliance of energy bandgap on temperature has been experimentally measured [35], and is defined as

$$E_g(T) = E_g(0) - \frac{\alpha_E T^2}{T + \beta_E}$$

where $E_g(0)$ is the energy bandgap at $T = 0$ K for Si, $E_g(0) = 1.170$ eV, α_E and β_E are the material specific fitting constants for Si, $\alpha_E = 4.37 \times 10^{-4}$ eV/K, $\beta_E = 636$ K, and T is the absolute temperature. With an increase in the temperature, the bandgap of a semiconductor decreases. Thus, the narrower bandgap at elevated temperature lowers the tunneling barrier width and, thereby, enhances the BTBT rate of electrons. It is evaluated that, with an increase in the temperature from 200 K to 400 K, the nonlocal BTBT rate of electrons increases by 97.17% and 81.46% for $N_f = 1 \times 12\ \text{cm}^{-2}$ and $-1 \times 12\ \text{cm}^{-2}$, respectively. The influence of temperature (200–400 K) on the drain current as a function of temperature at $N_f = \pm 1 \times 12\ \text{cm}^{-2}$ and for the undamaged device, i.e., with $N_f = 0$, is shown in Fig. 9(a). It is clearly evident from the results that the temperature affectability on the transfer characteristics is bias-dependent, due to the distinct transport mechanism in OFF and ON states. In the subthreshold region, the drain current increases exponentially with the rise in the temperature. This increase in the drain current is attributed to the dominance of SRH recombination at lower gate bias that has an exponential temperature dependence. However, with an increase in V_{gs}, the BTBT current dominates. The consequence of small temperature

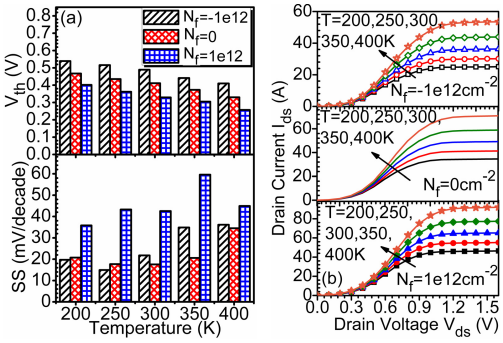

Fig. 10. (a) V_{th} and SS as a function of temperature (b) output characteristics at $V_{gs} = 1.2$ V, for the temperature range of 200–400 K of PNIN-GAA-TFET.

dependence of BTBT (that is caused by the bandgap narrowing with temperature) is dictated by the slight enhancement in the drain current at elevated temperature in the superthreshold region, as clearly shown in Fig. 9(a). The impact of temperature on transfer characteristics remains unaltered for donor/acceptor ITCs. The influence of temperature on I_{OFF} and the $I_{\text{ON}}/I_{\text{OFF}}$ ratio at $N_f = \pm 1 \times 12\ \text{cm}^{-2}$ and for the undamaged device, i.e., with $N_f = 0$, is shown in Fig. 9(b). The results reveal that, with an increase in the temperature from 200 K to 400 K, I_{OFF} increases from 10^{-19} A to 10^{-15} A (for $N_f = -1 \times 12\ \text{cm}^{-2}$) and from 10^{-14} A to 10^{-10} A (for $N_f = +1 \times 12\ \text{cm}^{-2}$). However, the current switching ratio degrades from an order of 10^{14}–10^{9} A (for $N_f = -1 \times 12\ \text{cm}^{-2}$) and from 10^{9} A to 10^{5} A (for $N_f = +1 \times 12\ \text{cm}^{-2}$). This degradation in the $I_{\text{ON}}/I_{\text{OFF}}$ ratio is attributed to the enhanced I_{OFF} at elevated temperatures. The influence of temperature and ITC polarity on V_{th} and the SS of PNIN-GAA-TFET is depicted in Fig. 10(a). The significantly high degradation in I_{OFF} at elevated temperatures (instigated by SRH) and an inconsiderable increase in I_{ON} (instigated by BTBT) degrade the SS at elevated temperatures. It has been analyzed that, for an increase in the temperature from 200 K to 400 K, the SS increases by 83.23% and 25.43% for $N_f = -1 \times 12\ \text{cm}^{-2}$ and $N_f = 1 \times 12\ \text{cm}^{-2}$, respectively. The temperature dependence of V_{th} is also shown in Fig.10(a). As discussed before, the drain current increases with an increase in the temperature, i.e., PNIN-GAA-TFET has positive temperature coefficient in both subthreshold and superthreshold regions. This higher drain current at elevated temperature results in reduced V_{th}.

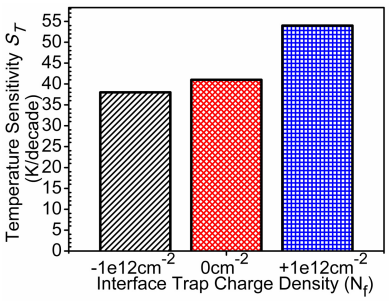

Fig. 11. Influence of ITCs on the temperature sensitivity of the I_{off} variability of PNIN-GAA-TFET at $N_f = \pm 1 \times 12$ cm^{-2} and $N_f = 0$.

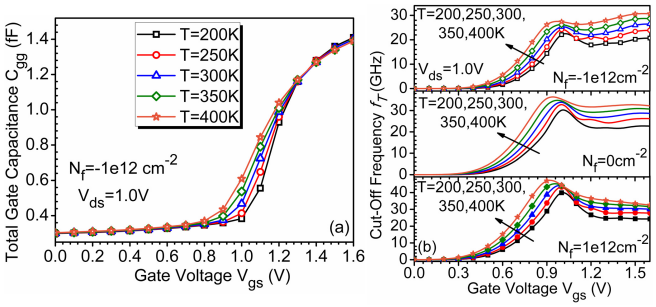

Fig. 12. (a) Variations of C_{gg} as a function of V_{gs} at the temperature range of 200–400 K and (b) f_T as a function of V_{gs} at the temperature range of 200–400 K of PNIN-GAA-TFET at $N_f = \pm 1 \times 12$ cm^{-2}.

In addition, the consequence of bandgap reduction of Si at elevated temperature is the lowered tunneling barrier width at the source–channel junction that, thereby, allows more number of carriers to tunnel through the valence band of the source to the conduction band of the channel. Thus, the band bending at lower gate bias at the tunneling junction for high ambient temperature enhances the tunneling rate at lower gate bias and subsequently decreases V_{th} of the device with an increase in the temperature. The results show that, for an increase in the temperature from 200 K to 400 K, V_{th} decreases by 23.92% and 36.05% for $N_f = -1 \times 12$ cm^{-2} and $N_f = 1 \times 12$ cm^{-2}, respectively. Fig. 10(b) illustrates the output characteristics of PNIN-GAA-TFET for a temperature range of 200–400 K at $N_f = \pm 1 \times 12$ cm^{-2} and for the case when localized charges are absent. In consistent with the above results, the drain current increases with an increase in the temperature. It is analyzed that, at $V_{gs} = 1.2$ V, with a rise in the temperature from 200 K to 400 K, the drain current increases by 2.11 times, 2.03 times, and 1.97 times for $N_f = -1 \times 12$ cm^{-2}, $N_f = 0$, and $N_f = +1 \times 12$ cm^{-2}, respectively.

As the temperature affectability is maximum in the subthreshold region, therefore, a quantitative analysis of the influence of ITCs on the temperature sensitivity (S_T) of the I_{OFF} variability has been done. S_T of PNIN-GAA-TFET as a function of ITCs is shown in Fig. 11, and is evaluated as

$$S_T = \left(\frac{\partial \log\ (I_{OFF})}{\partial T} \right)^{-1} \text{ K/decade.}$$

As shown in Fig. 11, the presence of ITCs modifies S_T of the device. It is assessed that the donor (acceptor) ITCs increase (decrease) S_T of PNIN-GAA-TFET by 31.7% (7.89%) with respect to the ideal device. Moreover, it is analyzed that, for the ideal device, a change in the ambient temperature by 41 K alters I_{OFF} by an order of a decade. However, for the presence of donor (acceptor) ITCs, a change in the temperature by 54 K (38 K) alters I_{OFF} by an order of a decade. Consequently, the presence of donor (acceptor) trap charges enhances (reduces) the temperature sensitivity that must be detrimental for the devices used for sensors applications, in temperature sensitive environment. For the analog and digital applications, the examination of parasitic capacitances is essential. In order to analyze the reliance of temperature on bias-dependent parasitic capacitance, the total gate capacitance as a function of gate bias is examined at various temperatures, and is shown in Fig. 12(a). It is examined that C_{gg} increases with an increase in the gate bias. This increase in C_{gg} with the gate bias is owing to the fact that, at fixed drain bias and at low gate bias, the inversion layer is formed near the drain side. After the inversion layer formation, further increase in the gate bias extends the inversion layer toward the source side. Moreover, it is obtained that, with an increase in the temperature, C_{gg} increases. It is examined that, at $V_{gs} = 1.1$ V, an increase in the temperature from 200 K to 400 K increases C_{gg} by 51.87%. Fig. 12(b) shows the influence of temperature variation on f_T as a function of gate bias. Owing to the consequence of positive temperature coefficient of the drain current, g_m also increases with the temperature and, thus, enhances f_T with the temperature. It is evaluated that, at $V_{gs} = 1$ V for $N_f = -1 \times 12$ cm^{-2} and 1×12 cm^{-2}, an increase in the temperature from 200 K to 400 K increases f_T by 23.97% and 11.76%, respectively.

IV. Conclusion

This work encompasses the reliability of N$^+$ source pocket PIN-GAA-TFET in terms of: 1) impact of ITC density and polarity and 2) temperature affectability over the device characteristics by numerical simulations. It is analyzed that the presence of donor (acceptor) trap charges enhances (reduces) the parallel E_y and normal E_x component of the electric field. The enhanced E_y increases the BTBT rate of electrons. However, the increased E_x contributes to the generation of interface defects and also to the gate leakage current and, thereby, degrades the reliability of the device. Moreover, it is obtained that the presence of donor trap charges tremendously degrades I_{OFF}. In addition, I_{OFF} is immune to the presence of acceptor traps. Furthermore, it is explored that the presence of ITCs alters superthreshold characteristics marginally. The temperature affectability over the device characteristics reveals a more prominent degradation in subthreshold characteristics in comparison with the superthreshold region. In addition, PNIN-GAA-TFET shows a positive temperature coefficient for the complete gate-bias range. Importantly, the temperature sensitivity of the device is also altered by the ITCs that is harmful to the device operating in the temperature sensitive ambience. The results obtained in this analysis could be beneficial while designing TFETs for a temperature sensitive environment.

ACKNOWLEDGMENT

The authors would like to thank the Microelectronics Research Laboratory, Department of Engineering Physics, Delhi Technological University, Delhi, India, to carry out this work.

REFERENCES

[1] A. M. Ionescu and H. Riel, "Tunnel field-effect transistors as energy-efficient electronic switches," *Nature*, vol. 479, no. 7373, pp. 329–337, 2011.
[2] K. Boucart and A. M. Ionescu, "Double-gate tunnel FET with high-K gate dielectric," *IEEE Trans. Electron Devices*, vol. 54, pp. 1725–1733, 2007.
[3] Y. Khatami and K. Banerjee, "Steep subthreshold slope n- and p-type tunnel-FET devices for low-power and energy-efficient digital circuits," *IEEE Trans. Electron Devices*, vol. 56, no. 11, pp. 2752–2761, Nov. 2009.
[4] J. Madan and R. Chaujar, "Gate drain underlapped-PNIN-GAA-TFET for comprehensively upgraded analog/RF performance," *Superlattices Microstruct.*, vol. 102, pp. 17–26, Feb. 2017.
[5] J. Madan, R. S. Gupta, and R. Chaujar, "Analytical drain current formulation for gate dielectric engineered dual material gate-gate all around-tunneling field effect transistor," *Jpn. J. Appl. Phys.*, vol. 54, no. 9, p. 094202, 2015.
[6] Y. Taur, J. Wu, and J. Min, "Dimensionality dependence of TFET performance down to 0.1 V supply voltage," *IEEE Trans. Electron Devices*, vol. 63, no. 2, pp. 877–880, Feb. 2016.
[7] W. Y. Choi, B.-G. Park, J. D. Lee, and T.-J. K. Liu, "Tunneling field-effect transistors (TFETs) with subthreshold swing (SS) less than 60 mV/dec," *IEEE Electron Device Lett.*, vol. 28, no. 8, pp. 743–745, Aug. 2007.
[8] J. Madan and R. Chaujar, "Gate drain-overlapped-asymmetric gate dielectric-GAA-TFET: A solution for suppressed ambipolarity and enhanced ON state behavior," *Appl. Phys. A, Solids Surf.*, vol. 122, p. 973, Nov. 2016.
[9] K. E. Moselund *et al.*, "Lateral InAs/Si p-type tunnel FETs integrated on Si—Part 1: Experimental devices," *IEEE Trans. Electron Devices*, vol. 63, no. 11, pp. 4233–4239, Nov. 2016.
[10] G. B. Beneventi, E. Gnani, A. Gnudi, S. Reggiani, and G. Baccarani, "Optimization of a pocketed dual-metal-gate TFET by means of TCAD simulations accounting for quantization-induced bandgap widening," *IEEE Trans. Electron Devices*, vol. 62, no. 1, pp. 44–51, Jan. 2015.
[11] W. Y. Choi and W. Lee, "Hetero-gate-dielectric tunneling field-effect transistors," *IEEE Trans. Electron Devices*, vol. 57, no. 9, pp. 2317–2319, Sep. 2010.
[12] N. Cui, R. Liang, and J. Xu, "Heteromaterial gate tunnel field effect transistor with lateral energy band profile modulation," *Appl. Phys. Lett.*, vol. 98, no. 14, p. 142105, 2011.
[13] M. J. Lee and W. Y. Choi, "Effects of device geometry on hetero-gate-dielectric tunneling field-effect transistors," *IEEE Electron Device Lett.*, vol. 33, no. 10, pp. 1459–1461, Oct. 2012.
[14] V. Nagavarapu, R. Jhaveri, and J. C. S. Woo, "The tunnel source (PNPN) n-MOSFET: A novel high performance transistor," *IEEE Trans. Electron Devices*, vol. 55, no. 4, pp. 1013–1019, Apr. 2008.
[15] H. Wang *et al.*, "A novel barrier controlled tunnel FET," *IEEE Electron Device Lett.*, vol. 35, no. 7, pp. 798–800, Jul. 2014.
[16] A. W. Dey *et al.*, "High-current GaSb/InAs(Sb) nanowire tunnel field-effect transistors," *IEEE Electron Device Lett.*, vol. 34, no. 2, pp. 211–213, Feb. 2013.
[17] S. Blaeser *et al.*, "Line tunneling dominating charge transport in SiGe/Si heterostructure TFETs," *IEEE Trans. Electron Devices*, vol. 63, no. 1, pp. 4173–4178, Nov. 2016.
[18] Y. Qiu, R. Wang, Q. Huang, and R. Huang, "A comparative study on the impacts of interface traps on tunneling FET and MOSFET," *IEEE Trans. Electron Devices*, vol. 61, no. 5, pp. 1284–1291, May 2014.
[19] J. Madan and R. Chaujar, "Interfacial charge analysis of heterogeneous gate dielectric-gate all around-tunnel FET for improved device reliability," *IEEE Trans. Device Mater. Rel.*, vol. 16, no. 2, pp. 227–234, Jun. 2016.
[20] M. G. Pala, D. Esseni, and F. Conzatti, "Impact of interface traps on the IV curves of InAs tunnel-FETs and MOSFETs: A full quantum study," in *IEDM Tech. Dig.*, Dec. 2012, pp. 6.6.1–6.6.4.
[21] S. Sant *et al.*, "Lateral InAs/Si p-type tunnel FETs integrated on Si—Part 2: Simulation study of the impact of interface traps," *IEEE Trans. Electron Devices*, vol. 63, no. 11, pp. 4240–4247, Nov. 2016.
[22] G. F. Jiao *et al.*, "New degradation mechanisms and reliability performance in tunneling field effect transistors," in *IEDM Tech. Dig.*, Dec. 2009, pp. 1–4.
[23] J. Madan and R. Chaujar, "Temperature associated reliability issues of heterogeneous gate dielectric-gate all around-tunnel FET," *IEEE Trans. Nanotechnol.*, 2017, doi: 10.1109/TNANO.2017.2650209.
[24] R. Wang *et al.*, "Investigations on line-edge roughness (LER) and line-width roughness (LWR) in nanoscale CMOS technology: Part II—Experimental results and impacts on device variability," *IEEE Trans. Electron Devices*, vol. 60, no. 11, pp. 3676–3682, Nov. 2013.
[25] P. G. D. Agopian *et al.*, "Temperature impact on the tunnel FET off-state current components," *Solid-State Electron.*, vol. 78, pp. 141–146, Dec. 2012.
[26] P.-F. Guo *et al.*, "Tunneling field-effect transistor: Effect of strain and temperature on tunneling current," *IEEE Electron Device Lett.*, vol. 30, no. 9, pp. 981–983, Sep. 2009.
[27] S. Mookerjea, D. Mohata, T. Mayer, V. Narayanan, and S. Datta, "Temperature-dependent I-V characteristics of a vertical $In_{0.53}Ga_{0.47}As$ tunnel FET," *IEEE Electron Device Lett.*, vol. 31, no. 6, pp. 564–566, Jun. 2010.
[28] Z. X. Chen *et al.*, "Demonstration of tunneling FETs based on highly scalable vertical silicon nanowires," *IEEE Electron Device Lett.*, vol. 30, no. 7, pp. 754–756, Jul. 2009.
[29] P.-F. Wang *et al.*, "Complementary tunneling transistor for low power application," *Solid-State Electron.*, vol. 48, no. 12, pp. 2281–2286, Dec. 2004.
[30] *Atlas User's Manual*, Silvaco, Santa Clara, CA, USA, 2010.
[31] A. Biswas, S. S. Dan, C. Le Royer, W. Grabinski, and A. M. Ionescu, "TCAD simulation of SOI TFETs and calibration of non-local band-to-band tunneling model," *Microelectron. Eng.*, vol. 98, pp. 334–337, Oct. 2012.
[32] W. Cao, C. J. Yao, G. F. Jiao, D. Huang, H. Yu, and M.-F. Li, "Improvement in reliability of tunneling field-effect transistor with p-n-i-n structure," *IEEE Trans. Electron Devices*, vol. 58, no. 7, pp. 2122–2126, Jul. 2011.
[33] Y. Yang, X. Tong, L.-T. Yang, P.-F. Guo, L. Fan, and Y.-C. Yeo, "Tunneling field-effect transistor: Capacitance components and modeling," *IEEE Electron Device Lett.*, vol. 31, no. 7, pp. 752–754, Jul. 2010.
[34] S. Mookerjea, R. Krishnan, S. Datta, and V. Narayanan, "On enhanced Miller capacitance effect in interband tunnel transistors," *IEEE Electron Device Lett.*, vol. 30, no. 10, pp. 1102–1104, Oct. 2009.
[35] Y. P. Varshni, "Temperature dependence of the energy gap in semiconductors," *Physica*, vol. 34, no. 1, pp. 149–154, 1967.

Jaya Madan (S'14) was born in New Delhi, India, in 1989. She received the B.Sc. degree (Hons.) and M.Sc. degree in electronics from the University of Delhi, New Delhi, India, in 2011 and 2013 respectively. She is currently pursuing the Ph.D. degree in electronics with the Microelectronics Research Laboratory, Department of Engineering Physics, Delhi Technological University, New Delhi.

Rishu Chaujar (SM'16) received the M.Sc. and Ph.D in Electronics from Delhi University in 2005 and 2009 respectively. Since 2010, she has been an Assistant Professor with the Department of Engineering Physics, Delhi Technological University, New Delhi. She has authored or co-authored more than 175 papers in various international and national journals and conferences. She has supervised around 10-11 M.Tech students and 6 Ph.D students are presently working under her guidance.

On Improving the Performance of Dynamic DCVSL Circuits

Pratibha Bajpai[1$], Neeta Pandey [1#], Kirti Gupta [2^], Shreya Bagga[2]*, Jeebananda Panda[1~]

[1]Dept. of Electronics and Communication Engineering, Delhi Technological University, Delhi, India
[2] Dept. of Electronics and Communication Engineering, Bharati Vidyapeeth's College of Engineering, Delhi,India

[$]bajpai18@gmail.com, [#]n66pandey@rediffmail.com, [^]kirtigupta22@gmail.com, [*]shreybagga1994@gmail.com, [~]jpanda@dce.ac.in

Abstract:

This contribution aims at improving performance of Dynamic Differential Cascode Voltage Switch Logic (Dy-DCVSL) and Enhanced Dynamic Differential Cascode Voltage Switch Logic (EDCVSL) and suggests three architectures for the same. The first architecture uses transmission gates (TG) to reduce the logic tree depth and width, which results in speed improvement. As leakage is a dominant issue in lower technology nodes, the second architecture is proposed by adapting leakage control technique (LECTOR) in Dy-DCVSL and EDCVSL. The third proposed architecture combines feature of both first and second architectures. The operation of the proposed architectures has been verified through extensive simulations with different CMOS submicron technology nodes (90 nm, 65 nm and 45 nm). The delay of the gates based on first architecture remains almost same for different functionalities. It is also observed that Dy-DCVSL gates are 1.6 to 1.4 times faster than their conventional counterpart. The gates based on second architecture show a maximum of 74.3 % leakage power reduction. Also, it is observed that the percentage of reduction in leakage power increases with the technology scaling. Lastly, the gates based on third architecture achieves the similar leakage power reduction values as the second one but are not able to exhibit the same speed advantage as achieved with first architecture.

Keywords:

Dynamic Differential Cascode Voltage Switch Logic, Enhanced Dynamic Differential Cascode Voltage Switch Logic, transmission gate, LECTOR

1. Introduction:

Digital design space is filled with variety of logic styles suitable for different applications [1-6]. Conventionally static CMOS has predominance over remaining styles due to low static power consumption. Differential Cascode Voltage Switch Logic (DCVSL) [6] is a static style which is beneficial from circuit delay, layout density, logic flexibility and power consumption. The DCVSL has been employed to develop various circuits for fault-tolerance [7], ternary logic [8], micro pipelining [9], delay cell [10], ring oscillator [11] capacitor neutralization [12] etc. It is well known that static logic styles suffer from high power consumption when output switches its logic state, a situation which worsens with increasing clock frequencies. The performance can be improved by using dynamic version DCVSL which are based on precharge-evaluate logic. Many clocked version of DCVSL style named as Dynamic DCVSL (Dy-DCVSL) and enhanced DCVSL (EDCVSL) [13] are presented in literature. As speed of dynamic circuit depends on logic tree depth and width [13], this paper proposes an architecture to reduce logic tree depth by

employing transmission gates in logic function realization. Apart from speed issue, leakage currents are yet another concern that shows predominance in submicron technologies. Leakage loss occurs when the output is stable i.e. output low or output high. A new architecture incorporating the leakage control technique [14] in dynamic DCVSL circuits is put forward that reduces leakage current. The features of former architectures are combined to present third architecture.

The paper is arranged in five sections including the present one. Section 2 briefly presents existing dynamic DCVSL and EDCVSL circuits. Section 3 describes the proposed dynamic DCVSL circuits. The functional verification and performance of the proposal is placed in Section 4 and conclusions are drawn in Section 5.

2. Dynamic Differential Cascode Voltage Switch Logic family

Differential Cascode Voltage Switch Logic (DCVSL) is a differential style derived from conventional CMOS logic and ratioed pseudo NMOS logic. It combines their advantages and provides a high speed, area efficient and rail-to-rail logic design alternative. Both static and the dynamic version of the DCVSL style are available in open literature. This section briefly describes existing dynamic DCVSL styles (Dy-DCVSL).

2.1 Conventional Dy-DCVSL architecture

The generic architecture of a Dy-DCVSL gate is shown in Fig. 1a. It consists of a pull-down network (PDN) that implements the logic function (OUT) as well as its complement (OUTB) using NMOS transistors only. The operation of the circuit depends in on clock signal (CLK). It works in precharge phase for low CLK signal and in evaluation phase otherwise. In the precharge phase, the transistors (M1, M2) are ON and transistors (M3, M4) remain OFF so both output nodes are precharged to high (= V_{DD}) logic level. Any change in the inputs during this phase will not affect the output nodes potential as a current path from the output nodes to the ground could not be established. A high on CLK signal makes transistors (M1, M2) OFF. One of the output nodes attains a low logic level depending on the value of inputs.

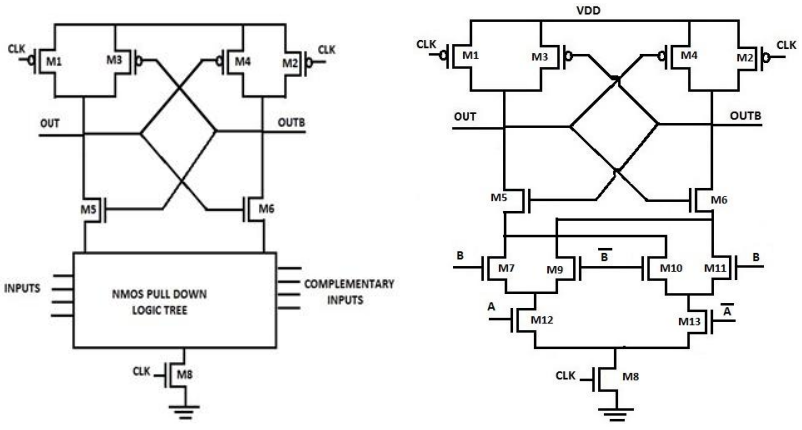

(a) (b)

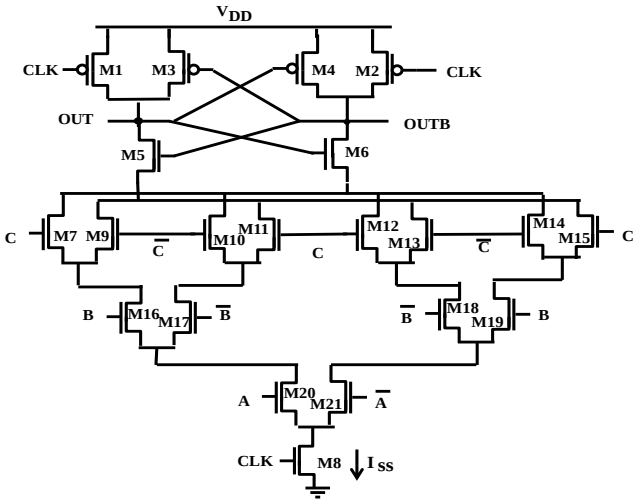

(c)

Fig.1 a) Generic architecture of Dy-DCVSL circuit b) two and c) three input Dy-DCVSL XOR-XNOR gate.

Cross-coupled transistors (M3, M4) helps output to switch and transistors (M5, M6) accelerates this process [13]. The circuit of a two and three input Dy-DCVSL XOR-XNOR gate are shown in Figs. 1b and 1c as illustrations.

2.2 Conventional EDCVSL architecture

The generic architecture of the EDCVSL circuits is drawn in Fig. 2a and two/ three input EDCVSL XOR-XNOR gate is shown as an example in Fig. 2b/ 2c. It is similar to Dy-DCVSL except PDN where only one logic tree branch (OUT) is retained and other is replaced by two stacked transistors M7 and M9. The gate of transistor M7 is connected to CLK signal so it is activated in the evaluation phases only. The transistor M9 is connected to the output of the logic tree branch to achieve complementary operation. To elaborate the behaviour, consider schematic of Fig. 2b. In the precharge phase, both the outputs are precharged and the NMOS cross-coupled transistors M5 and M6 are ON but has no effect on output as M8 is OFF. In the evaluation phase, for low (high) values at both inputs, the transistors M12 and M13 (M10 and M11) are ON therefore transistor M9 is OFF. So OUTB remains high and M5 retains its ON state and finally OUT becomes low. For the case when one input is high and other is low, no path exists between OUT and ground so it remains high and OUTB goes low**.** The operation of three input EDCVSL XOR-XNOR gate is similar to two input EDCVSL XOR-XNOR gate and omitted for the sake of brevity.

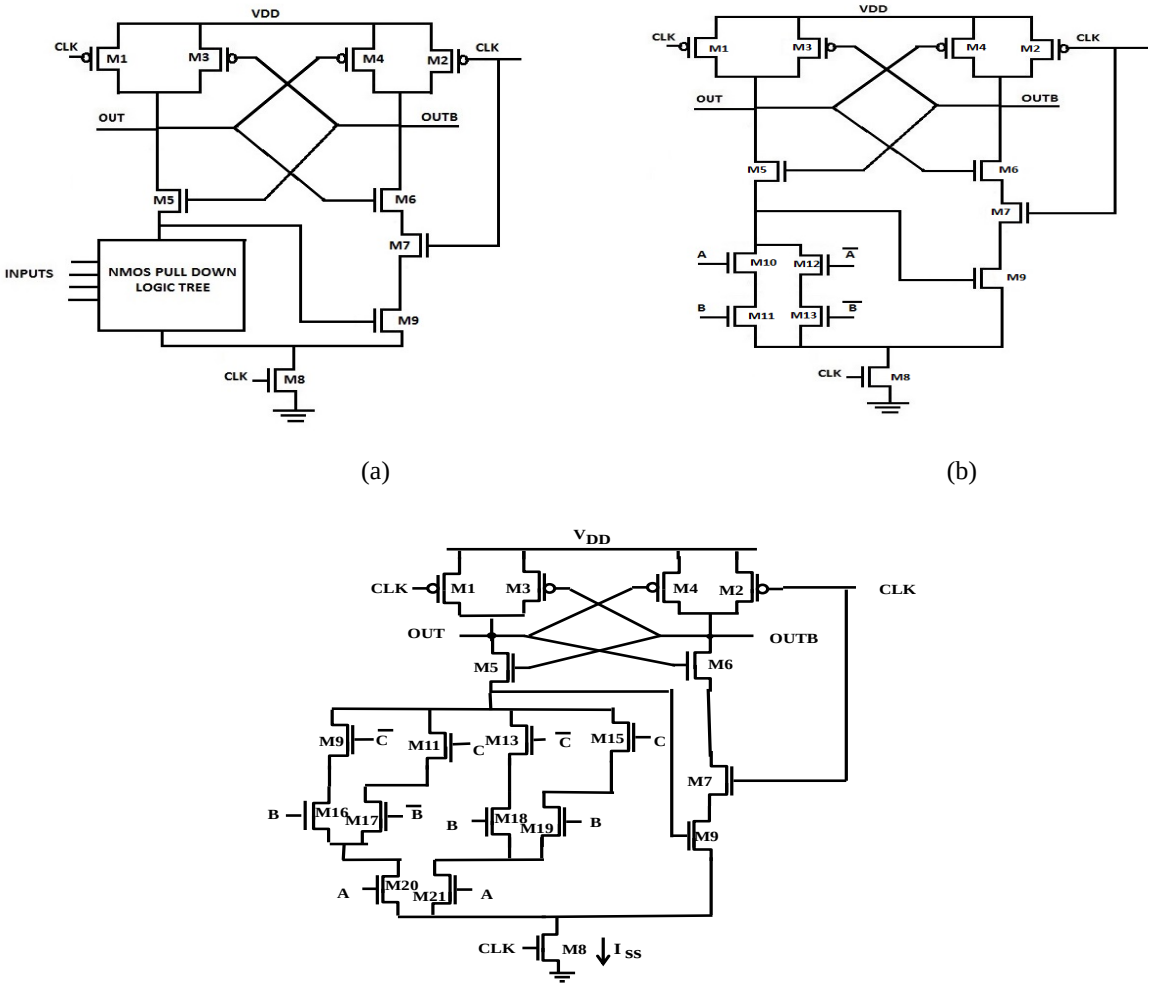

Fig.2 a) Generic architecture of EDCVSL circuit b) two input and c) three input EDCVSL XOR-XNOR gate.

3. Proposed Dynamic DCVSL circuits

This section presents three new architectures to improve performance of existing Dy-DCVSL and EDCVSL. First architecture aims at speed improvement, the second works on leakage reduction and the third combines features of the first two architectures to see their combined effect on performance.

3.1 Proposed Architecture-1 (PA-1)

The proposed architecture-1 is based on shifting the function realized by PDN logic tree to a separate block and using transmission gates (TG) logic for its implementation. The new Dy-DCVSL and EDCVSL circuits based on architecture-1 are named as Dynamic TG based DCVSL (Dy-TG-DCVSL) and Dynamic TG based EDCVSL (TG-EDCVSL) circuits respectively. A generic architecture of Dy-TG-DCVSL circuit along with two and three input XOR-XNOR realization is depicted in Fig. 3. The PDN logic tree consists of two NMOS transistors which are controlled by the outputs of two separate blocks. The two blocks generate the complementary outputs such that either M9 or M10 is ON during evaluation.

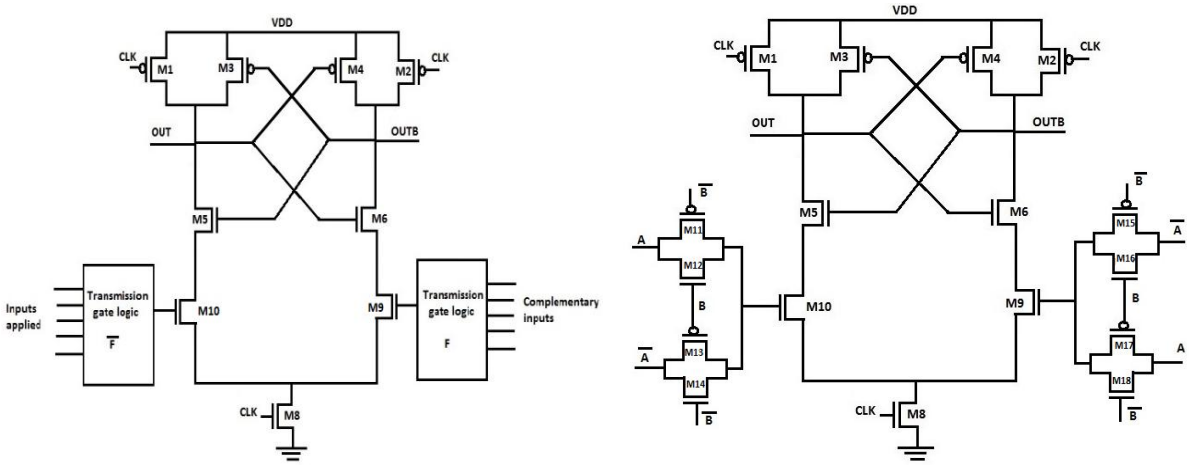

(a) (b)

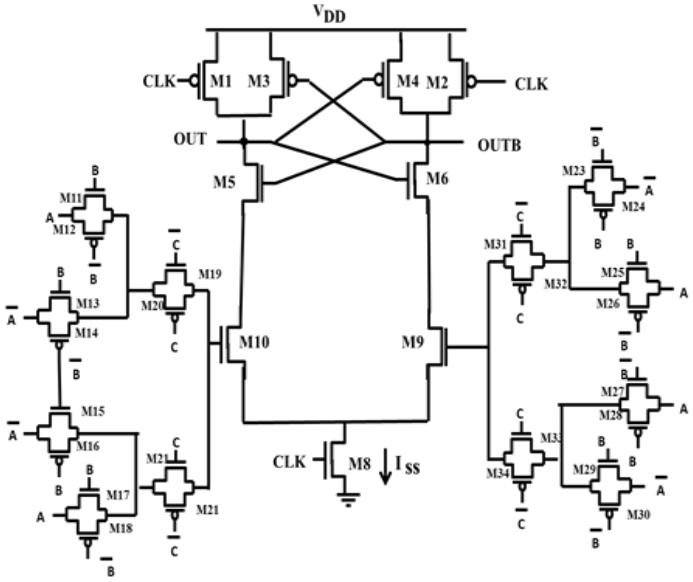

Fig. 3 a) Proposed Architecture-1 for Dy-TG-DCVSL circuits b) Two input and c) Three input Dy-TG-DCVSL XOR-XNOR gate

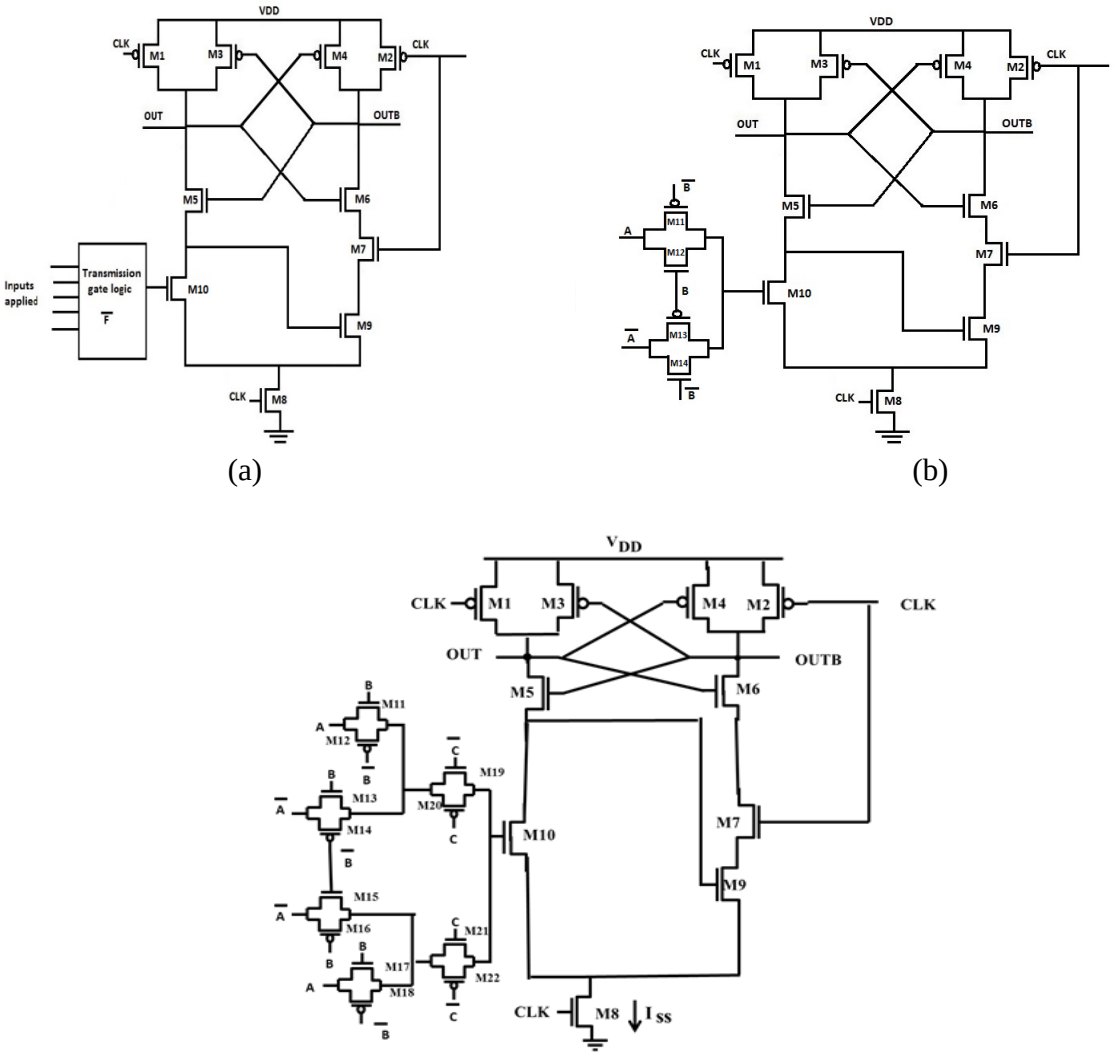

Fig. 4 a) Proposed Architecture-1 for TG-EDCVSL circuits b) Two input and c) Three input TG-EDCVSL XOR-XNOR gates

The working of the proposed Dy-TG-DCVSL XOR2 gate can be explained for the two phases. The operation in precharge phase is same as conventional Dy-DCVSL. Any changes in the inputs A and B may update the gate potential of M9 and M10 but does not affect the output, since M8 is OFF. Consequently, when CLK becomes high, output gets evaluated according to the gate potential of M9 and M10. In comparison to the conventional Dy-DCVSL XOR-XNOR gate (Fig. 1b), there is a speed advantage in terms of evaluation time due to the fact that the intermediate computation of the function is completed in the separate blocks just prior to the start of the evaluation phase. Also, a closer examination of the proposed architecture reveals a unique advantage of maintaining a constant evaluation time irrespective of the realized functionality. Similarly, placing logic functionality of EDCVSL in separate block logic leads to proposed TG-EDCVSL architecture. Generic gate structure, two and three input XOR-XNOR gates are depicted in Fig. 4.

3.2 Proposed Architecture-2 (PA-2)

The differential nature of the DCVSL logic style has several advantages but in submicron regions it needs attention. For all input combinations, one of the two logic tree branch in the PDN will conduct while the other would remain non-conducting. The non-conducting branch in submicron regions would have some amount of current due to OFF transistors in the path both pre-charge and evaluation phases. This current can be classified as leakage current. To improve the performance in sub-micron region these current need to be minimized. Various leakage reduction techniques based on the use of sleep transistor [15], high threshold voltage transistors [16] are available for static DCVSL circuits. These techniques require either routing of sleep signal [15] or complex algorithm for selection of high threshold voltage transistors. A self-controlled technique named as LECTOR [14], is presented for CMOS circuits that reduces both type of currents, is adapted for dynamic DCVSL circuits and resulting topology is referred as proposed architecture 2 (PA-2). LECTOR technique introduces two leakage control transistors (a PMOS and a NMOS) in between the PUN and PDN of the logic gate with the gate terminal of each of the leakage control transistor (LCT) controlled by the source of the other. This arrangement ensures that one of the LCTs is always in "near cut-off region" for any possible input combination. This results in an increase in the resistance of the path from power supply to the ground, leading to substantial drop in leakage currents through the path [14]. A further modification in achieving much more leakage control is to use high Vth LCTs. The architectures incorporating LECTOR technique in Dy-DCVSL and EDCVSL circuits are shown in Fig. 5. The proposed architectures add four high Vth LCTs (LCT1-4) in the basic architectures of the Dy-DCVSL (Fig. 1a) and EDCVSL (Fig. 2a) circuits and are called Dy-DCVSL-LCT and EDCVSL-LCT respectively.

To understand leakage control mechanism in Dy-DCVSL-LCT and EDCVSL-LCT circuits, the operating regions of LCTs during pre-charge and evaluation phases are examined. In the precharge phase, both the OUT and OUTB are at V_{DD}. Under this condition, it can be observed that the transistor LCT2 is ON and LCT1 is in near cut off state. Thus, LCT1 offers more impedance along the path and reduces the leakage current. Similar behavior can be observed when a high voltage is obtained at the output in the evaluation phase.

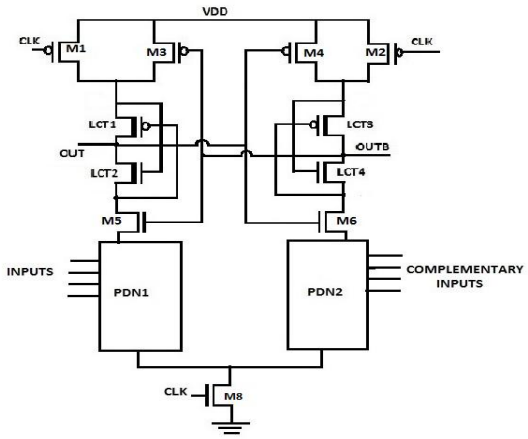

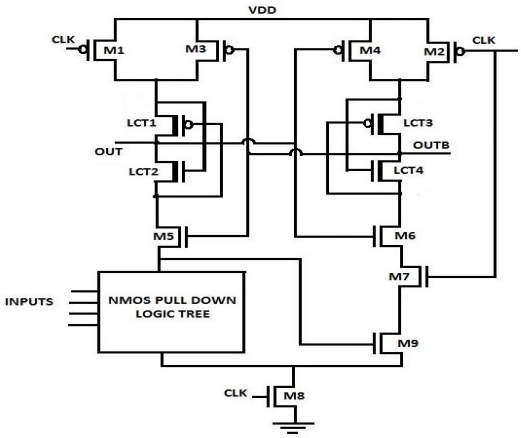

(a) (b)

Fig. 5 Proposed Architecture-2 for a) Dy-DCVSL-LCT circuits b) EDCVSL-LCT circuits

3.3 Proposed Architecture-3 (PA-3)

Proposed architecture 3 combines the features of proposed architectures 1 and 2. The resulting Dy-DCVSL and EDCVSL structures are called Dy-TG-DCVSL-LCT and TG-EDCVSL-LCT. The proposed architectures are shown in Fig. 6.

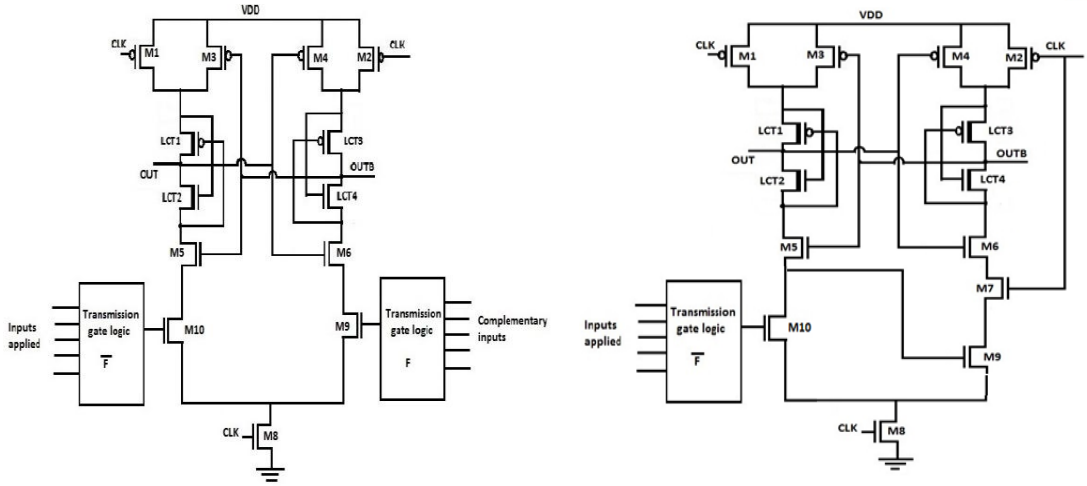

(a) (b)

Fig 6. Proposed architecture-3 based a)Dy-TG-DCVSL-LCT b) TG-EDCVSL-LCT circuits

4. Simulation Results

This section presents the simulation results for the new Dy-DCVSL circuits based on the proposed architectures. The simulations are performed using Symica tool and the PTM technology parameters for 90nm, 65nm and 45nm nodes. The frequencies of the inputs CLK, A, B and C are 50 MHz, 25 MHz, 12.5 MHz and 6.25 MHz respectively. A FO4 of inverters is maintained as the load in all the gates. The results are categorized into three sections according to the proposed architectures. The leakage power is computed on the basis of leakage current and the power supply.

4.1 Simulation results with PA-1

Dy-TG-DCVSL and TG-EDCVSL based two input AND-NAND (AND-NAND2), three input AND-NAND (AND-NAND3), two input exclusive-OR (XOR-XNOR2) and three input exclusive-OR (XOR-XNOR3) circuits are simulated using 90 nm CMOS technology parameters. The simulation waveform of the Dy-TG-DCVSL and TG-EDCVSL XOR-XNOR2 and XOR-XNOR3 gates are shown in Fig. 7. For all the gates it can be observed that for low value of the CLK signal, both the output nodes are precharged to V_{DD} (=1.8 V). The voltage changes in the

input signal A and B during this phase does not affect the potential of the output nodes. In the evaluation phase, for same value of the inputs A and B (Fig. 7a), the output node OUT remain low. Similarly, when the inputs differ, a high voltage level is obtained at the output node OUT. Thus, the XOR functionality is achieved in the proposed Dy-TG-DCVSL and TG-EDCVSL XOR2 gates. The simulation waveform for Dy-TG-DCVSL and TG-EDCVSL XOR-XNOR3 gate is shown in Fig. 7b. Similar waveforms were achieved for the other gates and are omitted for the sake of brevity.

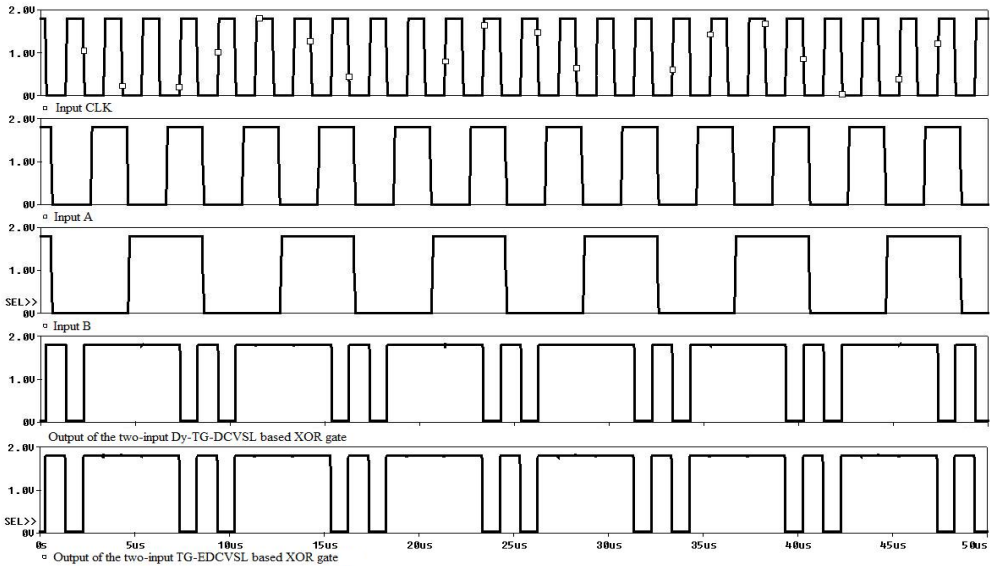

(a)

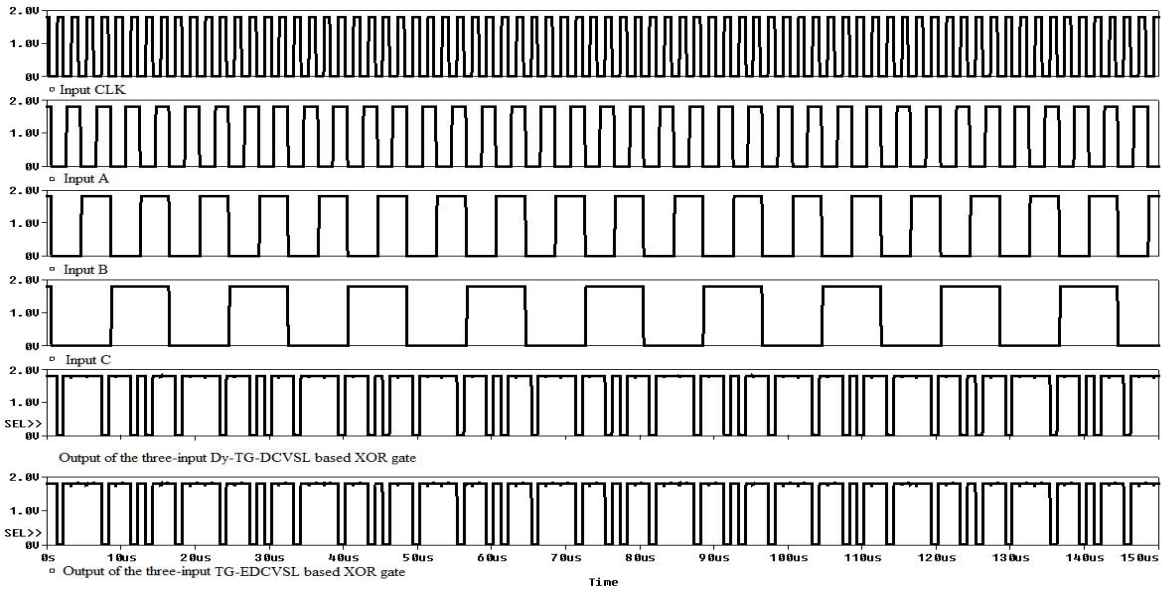

(b)

Fig. 7 Simulation waveform of Dy-TG-DCVSL and TG-EDCVSL based a) two input XOR-XNOR gate b) three input XOR-XNOR gate

The gates are also designed in Dy-DCVSL and EDCVSL styles to analyze the speed advantage. The corresponding delay results are noted and enlisted in Table I. The results clearly indicate the speed advantage of PA-1 based gates over the conventional counterparts. Also, the TG-EDCVSL gates are the fastest among all the logic styles. Lastly the PA-1 based gates show almost equal delay values irrespective of the implemented functionality.

Table I. Summary of delay results (ps)

style / Gate	Dy-DCVSL	EDCVSL	Dy-TG-DCVSL	TG-EDCVSL
AND-NAND2	500	480	350	340
AND-NAND3	570	530	355	345
XOR-XNOR2	500	480	350	341
XOR-XNOR3	550	490	355	345

4.2 Simulation results with PA-2

In this category, the leakage current reduction through incorporation of LECTOR technique in dynamic DCVSL circuits is demonstrated. A XOR-XNOR2 gate is chosen as the test bench due to its wide range of application. The conventional Dy-DCVSL, EDCVSL, Dy-DCVSL-LCT and EDCVSL-LCT XOR-XNOR2 gate circuits are simulated at various submicron technology nodes such as 90nm, 65 nm and 45 nm. Table II list the leakage power for the conventional Dy-DCVSL, EDCVSL, Dy-DCVSL-LCT and EDCVSL-LCT XOR-XNOR2 gate with V_{DD}=1.2V.

Following observations are made from Tables II:

1. The percentage reduction ranges in the leakage power is 30.4 % - 56.6 % in 90 nm, 32.2% - 61 % for 65 nm and 33.8 % - 74.3 % for 45 nm.
2. Leakage power tends to follow an increasing trend with the scaling down of the technology.
3. An increase in percentage reduction is seen as we dig down the lower technology nodes.

Table II: Leakage power (nW) for the conventional Dy-DCVSL, EDCVSL-LCT and PA-2 Dy-DCVSL-LCT, EDCVSL-LCT based XOR-XNOR2 gate topologies

Architecture / Inputs		Conventional		PA-2		Reduction w.r.t. conventional (%)	
A	B	Dy-DCVSL	EDCVSL	Dy-DCVSL-LCT	EDCVSL-LCT	Dy-DCVSL-LCT	EDCVSL-LCT
90 nm node							
0	0	9.27	8.9	4.02	4.06	56.6	54
0	1	0.23	0.21	0.16	0.14	30.4	33
1	0	0.23	0.21	0.16	0.14	30.4	33
1	1	9.27	8.9	4.02	4.06	56.6	54
65 nm node							
0	0	12.9	12.88	5.16	5	60	61
0	1	0.41	0.27	0.27	0.18	32.2	33.3
1	0	0.41	0.27	0.27	0.18	32.2	33.3
1	1	12.9	12.88	5.16	5	60	61

45 nm node							
0	0	22.48	22.48	5.79	5.79	74	74.3
0	1	0.41	0.28	0.28	0.18	33.8	35.7
1	0	0.41	0.28	0.28	0.18	33.8	35.7
1	1	22.48	22.48	5.79	5.79	74	74.3

4.3 Simulation results with PA-3

Dy-TG-DCVSL, TG-EDCVSL, Dy-TG-DCVSL-LCT and TG-EDCVSL-LCT two-input XOR2 and three input XOR3 gates are simulated at various technology nodes. Out of the two dynamic styles, the results pertaining to EDCVSL circuits are listed in Tables III- V for the leakage power and delay measurements. The delays reported in Table V are for 45 nm technology node. The findings can be summarized as follows:

1. A percentage reduction range of 27%-64% for 90nm, 30%-66% for 65nm and 38%-76% for 45nm in leakage power is observed.
2. The TG-EDCVSL-LCT XOR-XNOR2 gate show less leakage power with respect to Dy-TG-DCVSL counterpart.
3. Leakage power tends to follow an increasing trend with the scaling down of the technology.
4. The percentage reduction in the leakage power increases with the lower technology nodes.
5. The delay of the TG-EDCVSL-LCT XOR-XNOR2 gate is more than the Dy-TG-DCVSL due to the presence of the high resistance path for leakage current reduction. Thus exhibiting a trade-off between the speed and leakage power reduction.

Table III: Leakage power (nW) for TG-EDCVSL and TG-EDCVSL-LCT based XOR-XNOR2 gate topologies

Inputs \ Architecture		TG-EDCVSL	TG-EDCVSL-LCT	Reduction w.r.t. TG-EDCVSL (%)
A	B			
90 nm node				
0	0	8.8	4	55
0	1	0.18	0.13	27
1	0	0.18	0.13	27
1	1	8.8	4	55
65 nm node				
0	0	12.7	5	61
0	1	0.2	0.14	30
1	0	0.2	0.14	30
1	1	12.7	5	61
45 nm node				
0	0	22.24	5.7	74.3
0	1	0.21	0.13	38
1	0	0.21	0.13	38
1	1	22.24	5.7	74.3

Table IV. Leakage power (nW) in TG-EDCVSL and TG-EDCVSL-LCT three input XOR-XNOR gates

Inputs \ Architecture			TG-EDCVSL	TG-EDCVSL-LCT	Reduction w.r.t. TG-EDCVSL (%)
A	B	C			
90 nm node					

0	0	0	9.8	4	59
0	0	1	0.34	0.21	64
0	1	0	0.34	0.21	64
0	1	1	9.8	4	59
1	0	0	0.34	0.21	64
1	0	1	9.8	4	59
1	1	0	9.8	4	59
1	1	1	0.34	0.21	64
65 nm node					
0	0	0	14	5.07	63
0	0	1	0.38	0.26	66
0	1	0	14	5.07	63
0	1	1	0.38	0.26	66
1	0	0	0.38	0.26	66
1	0	1	14	5.07	63
1	1	0	14	5.07	63
1	1	1	0.38	0.26	66
45 nm node					
0	0	0	24.5	5.85	76
0	0	1	0.43	0.12	72
0	1	0	0.43	0.12	72
0	1	1	24.5	5.85	76
1	0	0	0.43	0.12	72
1	0	1	24.5	5.85	76
1	1	0	24.5	5.85	76
1	1	1	0.43	0.12	72

Table V: Delay measurement for the PA-1 based and the PA-3 based ED-CVSL XOR/XNOR gate

PA-1 based XOR gate				
Mode of Operation	**A**	**B**	**Output**	**Delay**
Evaluation	**1**	**1**	1->0	300ps
	0	**0**	1->0	299ps
precharge	**1**	**1**	0->1	184ps
	0	**0**	0->1	187ps
PA-3 based XOR gate				
Evaluation	**1**	**1**	1->0	355ps
	0	**0**	1->0	354ps
Precharge	**1**	**1**	0->1	598ps
	0	**0**	0->1	598ps

5. Conclusion

In this paper, three new architectures to enhance the performance of Dy-DCVSL and EDCVSL are proposed. The first improves the speed by using transmission gates through logic tree depth reduction. The second architecture is derived to reduce leakage power at lower technology nodes. The incorporation of leakage control by incorporating LECTOR technique is proposed. The third architecture merges the two proposed architectural modifications to analyze its combined effect on the performance. Extensive simulations are done at various CNOS submicron technology node such as 90 nm, 65 nm and 45 nm. It is observed that dynamic DCVSL gates based on first architecture are 1.6 to 1.4 times faster than the conventional dynamic CVSL circuits. The gates based on first architecture show almost equal delay values

irrespective of the implemented functionality. A maximum leakage power reduction of 78.43 % is achieved with second architecture based DCVSL gates. An increasing trend in the leakage power with the scaling down of the technology is observed in the proposed circuits. Lastly, the third architecture achieves the same leakage power reduction values as the second one but are not able to exhibit the same speed advantage as achieved with first architecture.

Conflict of interest

The authors declare that there is no conflict of interest regarding the publication of this paper.

References

[1] J. M. Rabaey, A. P. Chandrakasan, and B. Nikolic, *Digital integrated circuits: a design perspective*, Pearson Education, 2003

[2] N. Weste, and D. Harris, *CMOS VLSI Design: A Circuits and Systems Perspective*, Addison-Wesley Publishing Company, 2010

[3] C. Piguet, *Low-Power CMOS Circuits*, CRC Press, 2006

[4] L. Bisdounis, D. Goovetas, and O. Koufopavlou, "A comparative study of CMOS circuit design styles for low-power high-speed VLSI circuits," *International J. Electronics*, vol. 84, pp. 599-613, 1998

[5] K. M. Chu and D. L. Pulfrey, "A comparison of CMOS circuit techniques: differential cascode voltage switch logic versus conventional logic," *IEEE Journal of Solid-State Circuits*, vol. 22, no. 4, pp. 528–532, 1987.

[6] L. G. Heller, W. R. Griffin, J. W. Davis, and N. G. Thoma, "Cascode voltage switch logic: A differential CMOS logic family," *Proceedings of the IEEE International Solid-State Circuits Conference. Digest of Technical Papers*, pp. 16–17, 1984

[7] M. Stanisavljevic, A. Schmid, and Y. Leblebici, "Fault-tolerance of robust feedforward architecture using single-ended and differential deep-submicron circuits under massive defect density," *Proceedings of the International Joint Conference on Neural Networks*, pp. 2771–2778, 2006.

[8] R. F. Mirzaee, T. Nikoubin, K. Navi, and O. Hashemipour, "Differential Cascode Voltage Switch (DCVS) Strategies by CNTFET Technology for Standard Ternary Logic," *Microelectronics Journal*, Vol. 44, No. 12, pp. 1238–1250, 2013.

[9] S. Mathew, and R. Sridhar, "A data-driven micropipeline structure using DSDCVSL," *Proceedings of the IEEE 1999 Custom Integrated Circuits Conference*, pp. 295 – 298, 1999

[10] D. Z. Turker, S. P. Khatri, and E. Sanchez-Sinencio, "A DCVSL Delay Cell for Fast Low Power Frequency Synthesis Applications," *IEEE Transactions on Circuits and Systems I*, vol. 58, no. 6, pp. 1225-1238, 2011

[11] Priyanka, and A. K. Singh, "A low voltage high speed DCVSL based ring oscillator," *Annual IEEE India Conference (INDICON)*, pp. 1-5, 2015

[12] W. Y. Choi, "Miller effect suppression of tunnel field-effect transistors (TFETs) using capacitor neutralization," *Electronics Letters*, Vol. 52, No. 8, pp. 659-661, 2016

[13] D. W. Knng, and Y.B. Kim, "Design of Enhanced Differential Cascode Voltage Switch Logic (EDCVSL) Circuits for high fan-in Gate," *15th Annual IEEE International Conference on ASIC/SOC*, pp. 309-313, 2002

[14] N. Hanchate and N. Ranganathan, "LECTOR: A Technique for Leakage Reduction in CMOS Circuits," *IEEE Transactions on Very Large Scale Integration (VLSI) Systems*, Vol.12, No. 2, pp. 196-203, 2004

[15] P. Lakshmikanthan, and A. Nunez, "A Novel Methodology to Reduce Leakage Power In Differential Cascode Voltage Switch Logic Circuits", *3rd International Conference on Electrical and Electronics Engineering*, pp. 1-4, 2006

[16] W. Chen, W. Hwang, P. Kudva, G. D. Gristede, S. Kosonocky and R. V. Joshi "Mixed Multi Threshold Differential Cascode Voltage Switch (MT- DCVS) Circuit Styles and Strategies for Low Power VLSI Design" , *International Symposium on Low Power Electronics and Design*, pp. 263-266, 2001

Available online at www.ijapie.org

International Journal of Advanced
Production and Industrial Engineering

IJAPIE-SI-MM 515 (2017) 93–100

Special Issue on

MATERIALS
&
MANUFACTURING

Optimisation of Cutting Parameters on Surface Roughness in Turning: A Review

Yashwant Koli*, Prashant Kumar Singh ,Vipin, Ranganath M. S.
(Department of Mechanical Engineering, Delhi Technological University, Delhi110042, India)
**Email: yashwantkoli5@gmail.com*

Abstract : The literature review of these papers serves various goals. First it focuses on the work that has been done on turning during these recent years or the advancement that has been done in this field. Secondly it will helpful to the researcher who wishes to work further on this topic or wishes to know the effects of cutting parameters on SR in turning on different alloys. This analysis through this article will help the researcher to find the existing gap on this issue and outline the future direction for the researchers through this review analysis. Total 140 papers published were selected, categorized and analyse and gap in the work been identified to suggest for future analysis. The research will be helpful for researchers, academicians and practitioners for better understanding in the field of turning.

Keywords: Turning; surface roughness; cutting parameters

I. INTRODUCTION

Today economic machining with good dimensional accuracy has become the main concern for the production companies .The machining can be either on turning, milling, drilling In a turning operation Fig.1, it is significant task to select cutting constraints for achieving high cutting performance. However, this does not confirm that the selected cutting constraints have best or near best cutting performance for a specific machine and environment.(*B.Ackroyd*)[1]

Cutting constraints are imitated on roughness, surface quality and dimensional nonconformities of the product. Surface roughness is used to regulate and to estimate the quality of a product, is one of the chief quality characteristics of a turning product.

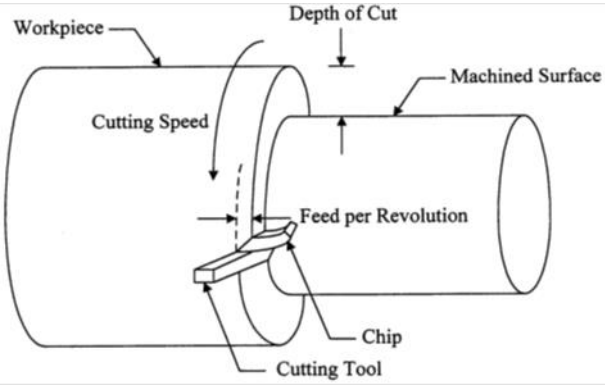

Fig.1. Basic turning operation(W.H. Yang et al.) [4]

According to (M.Nalbant et al.) [2]"Surface roughness can be defined as the measure of the quality of a product and also it is the factor that significantly effects manufacturing cost. It can further also be describes the geometry of the machined surfaces that combined with the texture of the surface".

In today's manufacturing industry, dimensional accuracy and surface finish are the very important point of concern. Thus, activity and characterizing the surface end is thought of because the predictor of the machining performance (Reddy and Rao) [3].

The papers review in this review paper has been selected form the journals and conference conducted. The papers are reviewed in this review paper has been selected as follow.

First the papers to be reviewed were selected from January 1995 to December 2015. Basic scholarly search engine 'Google Scholars' and 'Science Direct' were used. First the keywords 'surface roughness in turning' was used to search the papers. About 140 papers published from various journals and conferences were reviewed.

Fig.2, explains the experimental scheme for optimizing the surface roughness in turning operation. Initially, perform the basic turning operation on work piece with different cutting parameters then measure surface roughness with the help of surface measurement device. Then for enhancing the roughness both the cutting constraints and the measured surface roughness is inserted in the computer. With the assistance of different technique it gives the preferred optimal output.

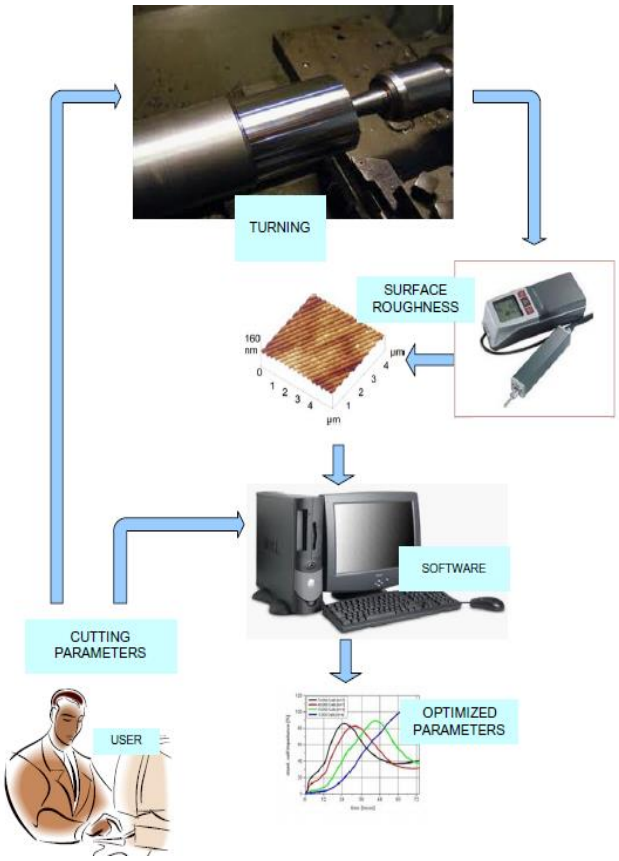

Fig.2. Experimental scheme (IlhanAsilturk et al.) [5]

I. SURFACE ROUGHNESS

Surface properties such as roughness are judicious to the purpose competence of machine components. Augmented understanding of surface generation instruments can be used to enhance machining process and to increase component function ability. Surface roughness is tougher to manage and track than physical dimensions are, because relatively many causes affect surface roughness. Some of these causes can be controlled and some cannot. Manageable process constraints include feed, cutting speed, tool geometry and tool setup. Other factors, such as tool, work piece, tool wear and degradation and tool material inconsistency cannot be controlled as easily.

TABLE I.
Cutting Parameters

Cutting parameters	Units
Cutting speed	(m/min)
Feed rate	(mm/rev)
Depth of cut	(mm)

II. TECHNIQUES

- TAGUCHI METHOD : Taguchi's parametric design is the operational tool for robust design it proposals a simple and organized qualitative ideal design to a comparatively low cost. The Taguchi method of off-line (Engineering) quality control encompasses all stages of product/process development. However the key component for attaining great value at low cost is Design of Experiments.

- ANOVA : Since there are a great number of variables governing the process, some mathematical simulations are required to represent the process. However, these models are to be developed using only the significant parameters influencing the process rather than including all the parameters. In order to achieve this, statistical analysis of the experimental results will have to be processed using the analysis of variance ANOVA is a computational method that allows the estimation of the comparative assistances of each of the control aspects to the overall calculated response. ANOVA can be beneficial for defining effect of any given input constraint from a series of experimental outcomes by design of experiments for machining process and it can be used to translate experimental data.

- ANN : ANN is an interconnected gathering of simple managing elements, units or nodes, whose functionality is loosely built on animal neuron. The processing capability of the network is kept in the inter-unit linking strengths, or weights, attained by a method of adaptation to, or learning from, a set of training patterns. In its most general form, ANN is a machine that is planned to model the way in which the brain implements a specific task or function of interest; the network is frequently executed by using electronic constituents or is simulated in software on a digital computer.

III. LITERATUREREVIEW

TABLE II

CLASSIFICATION AMONG DIFFERENT RESEARCHERS AND THEIR RESEARCH

Researchers	Tool Material	Work piece Material	Techniques	Key Findings
JANG.D.et al. [6]	Carbide	AISI 1020	On Line	The roughness along the work piece without chatter, has specific frequency components that are determined by the feed marks in the lower frequency range. They are narrowly related to the natural frequencies of a machine tool structure.
Davim. J et al. [7]	Cemented Carbide	Free Machining Steel	ANN	The roughness is highly sensitive to both cutting speed and feed rate whereas depth of cut has the least effect. The surface roughness has a tendency to reduce with the increase in cutting speed and also with the reduction in feed rate.
I.A. Choudhury et al.[8]	Uncoated Tungsten Carbide	EN 24T	Factorial Design	Effect of feed is much more pronounced than the effects of cutting speed and depth of cut, on the roughness. Though, a higher cutting speed improves the surface finish.
W.H. Yang et al. [4]	Uncoated Tungsten Carbide	S45C	Taguchi Method	The tool life and surface roughness from increases to about 250% from the initial cutting parameters to the optimal cutting parameters
M. Nalbant et al. [2]	TiN Coated	AISI 1030	Taguchi Method	Greater insert radius (1.2 mm), low feed rate (0.15 mm/rev) and low depth of cut (0.5 mm) leads to better surface roughness. The surface roughness improves to about 335% form initial cutting parameters to the optimal cutting parameters
IlhanAsilturk et al. [5]	Coated Carbide	AISI 4140	Taguchi Method	Optimum cutting conditions which correspond for the smaller surface roughness in hard turning method were found to be 120 m/min for the cutting speed, 0.18 mm/rev for the feed rate and 0.4 mm for the depth of cut.
HamdiAouici et al. [9]	CBN 7020	AISI H11	ANOVA	Feed rate and work piece hardness have major statistical influences on the surface roughness. Lower feed rate and the high cutting speed lead to best surface roughness.

S. Ramesh et al. [10]	Round Coated Carbide	Titanium Alloy (gr5)	ANOVA	The order of importance was feed, followed by depth of cut and cutting speed. Feed has a great effect on roughness.
Upadhyay.V et al. [11]	Uncoated Cemented Carbide	Ti–6Al–4V alloy	ANN	Surface roughness within reasonable accuracy.
Günay.M et al. [12]	CBN	High-alloy white cast iron (Ni-Hard)	Taguchi Method	The most significant variable for Ni-Hard with 62 HRC was found the feed rate while the variable that was the most significant for Ni-Hard with 50 HRC was the cutting speed.
Bouacha.K et al. [13]	CBN	AISI 52100	ANOVA	The surface roughness is highly affected by feed rate, whereas the cutting speed has a negative effect and the depth of cut a negligible influence.
N.R. Abburi et al. [14]	TiN-Coated Carbide	Mild Steel	ANN	Reducing the ranges and increasing the number of training data is expected to improve the accuracy of the surface roughness.
B.Y. Lee et al. [15]	Tungsten Carbide	S45C	Polynomial Network	The accuracy of the surface roughness can be predicted once the image of the turned surface and turning conditions (cutting speed, feed rate, and depth of cut) are given.
JanezKopac et al. [16]	Cermet	C15 E4	Taguchi Method	A higher cutting speed results in a smoother surface
P.V.S. Suresh et al. [17]	TiN-Coated tungsten carbide	Mild steel	GA	Surface quality can be greatly controlled using Genetic Algorithms
Shinn-Ying Ho et al. [18]	Tungsten Carbide	S45C	ANFIS	The advantages of the proposed method are non-contact measurements, ease of automation, and high accuracy
Tugrul Ozel et al. [19]	CBN	AISI 52100	ANN	The developed prediction system is found to be capable of accurate surface roughness prediction.

W.S. Lin et al. [20]	Carbide	S55C	Regression analysis	Feed rate is the significant factor that affects the roughness, where increasing feed rate will increase the roughness, while a regression multiplier proves that the cutting speed does not have a major impact on surface roughness.
O.B.Abouelatta et al. [21]	Cemented Carbide	Free cutting Steel	Mathematical Model	The maximum height roughness parameter depends greatly on the rotational cutting speed.
K.A. Risbood et al. [22]	TiN-Coated Carbide	Steel	ANN	Artificial neural networks can be used to find out the effective estimates of surface finish.
M.Y. Noordin et al. [23]	Coated Carbide	AISI 1045	ANOVA	The ANOVA revealed that feed is the most significant factor influencing the surface roughness.
D.I. Lalwani et al. [24]	Coated Ceramic	MDN250	ANOVA	Good surface roughness can be achieved when cutting speed and depth of cut are in range (93m/min and 0.2mm) and feed rate is at low level of (0.04mm/rev).
M. Anthony Xavior et al. [25]	Carbide	AISI 304	ANOVA	Coconut oil was found to be a better cutting fluid than the conventional mineral oils in reducing surface roughness.
Jeffrey D. Thiele et al. [26]	CBN	AISI 52100	ANOVA	The effect of work piece hardness and edge geometry interaction on the surface roughness was found to be very significant. The effect of edge hone on the surface roughness decreased with increase in work piece hardness
Davim. J et al. [27]	PCD	GFRP	ANOVA	The roughness increases with the feed rate and decreases with the cutting velocity. The feed rate has the highest physical and statistical effect on surface roughness.
A.Kohli et al. [28]	Carbide	Mild Steel	ANN	The experimental value is close to the most likely estimate and within the upper and lower estimates
Tugrul Ozel et al. [29]	CBN	AISI H13	ANOVA	Honed edge geometry and lower work piece surface hardness resulted in better surface roughness.

Eyup Bagci et al. [30]	MTT3000	GFRP	ANN	It was found that the maximum test errors were 6.30% and 6.36% by comparing roughness values predicted from ANN model with those predicted RSM.
Dilbag Singh et al. [31]	Ceramic	AISI 52100	ANOVA	Feed is the governing factor affecting the surface roughness.
Ahmet Hasçalhk et al. [32]	CNMG 12040-833	Ti-6Al-4V	Taguchi Method	Feed rate is the key factor that has the highest importance on the roughness and it is about 1.72 times more vital than depth of cut. The cutting speed does not seem to have much of an influence on the roughness.
Surjya K. Pal et al. [33]	HSS	Mild Steel	ANN	The predicted surface roughness from the neural network model is very close to the measured values.
Vishal S. Sharma et al. [34]	Coated Carbide	Adamite	ANN	Surface roughness is positively influenced with feed and it shows negative trend speed and depth of cut.
Hardeep Singh et al. [35]	Carbide	EN-8	Taguchi Method	The feed has the variable effect on surface roughness. It is interesting to note that spindle speed, feed rate and depth of cut for Material Removal Rate have increasing trend.
Ranganath M.S. et al. [41]	HSS	Aluminium 6061	ANOVA	The minimum surface roughness is obtained at 1.2mm depth of cut, 156rpm speed and 0.05mm/rev feed rate.
Ranganath M.S. et al. [42]	CNMG	Aluminium 6061	Taguchi Method	The optimal roughness is obtained at 1900rpm speed, 0.25mm depth of cut and 0.12mm/rev feed rate.
Ranganath M.S. et al. [43]	Carbide	Aluminium 6061	ANN	The surface roughness value increases as the feed and depth of cut increases and as spindle speed increases the roughness value decreases.

IV. ANALYSIS

The number of papers reviewed on turning is shown in fig 3. It shows in which year how many papers are published on turning which are reviewed.

Fig 4.gives the percentage distribution of the optimization technique used in the reviewed papers. With the help of the chart it can be stated that ANN, ANOVA and Taguchi techniques are used more than others.

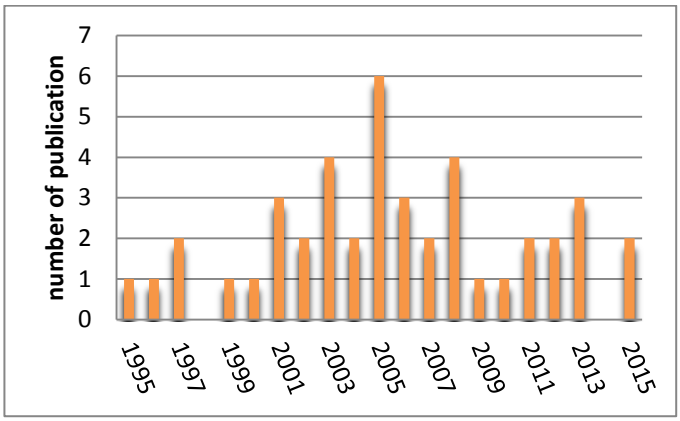

Fig 3. Total papers reviewed

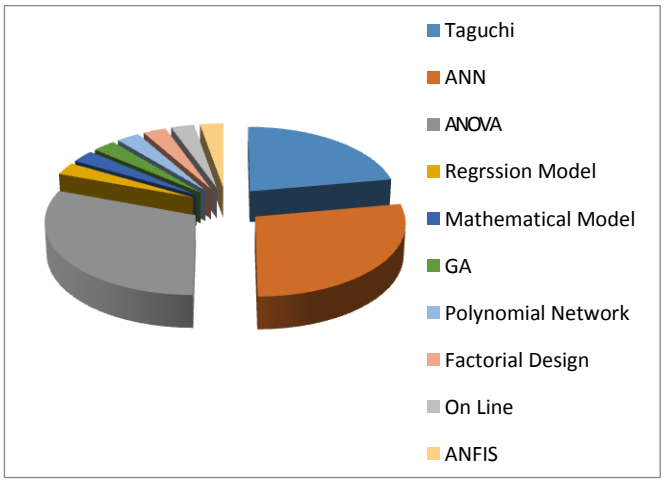

Fig 4. Percentage distribution of optimization technique

V. DİSCUSSİON AND CONCLUSİON

This literature review covers a brief literature of many areas of research; the current work presented a review of the different methodologies that are used for forecasting the surface roughness.

GAs and other optimization technique could be ideally used in conjunction with the developed models for the prediction of surface roughness(P.G. Benardos et al.) [36].

(Thomas M. et al.) [37] Concludes that the feed rate and also the tool nose radius square measure the variables that manufacture the foremost vital effects on surface roughness, followed by the cutting speed.

Dry machining of steel caused most tool wear and surface roughness and wet machining didn't show considerable improvement (N.R. Dhar et al.) [38].

It is observed that depth of cut and feed variables have a negative influence on the surface roughness average as increasing any of the two previous variables means increasing the roughness parameter. On the other hand, thereis an optimum value of cutting speed that provides a minimum value of surface roughness (I. Puertas Arbizu et al.) [39],(Davim. J et al.) [40].

This paper concludes that roughness increases with the feed rate and decreases with the cutting velocity. The best roughness was attained at the lower feed rate and the maximum cutting speed whereas depth of cut has negligible influence. This literature review not only presents the present scenario but also frame guideline for future research.

REFERENCES

[1] B.Ackroyd, (2001) Assessment of contact circumstances in machining , Accounts of the of Institution of Mechanical Engineers: Part B—Journal of Engineering Manufacture 215 (4) pp.493–507.

[2] M. Nalbant, H. Go¨kkaya, G. Sur; (2007) Presentation of Taguchi method in the optimization of cutting parameters for roughness in turning: Materials and Design 28 pp.1379–1385.

[3] Reddy, N.S., Rao, P.V., (2005) Selection of best tool geometry and cutting circumstances using a roughness calculation model for end milling. Int. J. Adv. Manuf. Technol. 26 pp.1202–1210.

[4] W.H. Yang, Y.S. Tarng; (1998) Strategy optimization of cutting constraints for turning operations based on the Taguchi method: Journal of Materials Processing Technology 84 pp.122–129.

[5] Ilhan Asilturk, Harun Akkus; (2011) Determining the effect of cutting constraint on roughness in hard turning using the Taguchi method: Measurement 44 pp.1697–1704.

[6] Jang.D., Young-Gu Choi, Hong-Gil Kim And Alex Hsiao (1996) Study of the relationship between roughness and cutting vibrations to develop an on-line roughness measuring process in hard turning: Int. J. Mach. Tools Manufact. Vol. 36, No. 4. pp.453-464.

[7] Davim. J , V.N. Gaitonde, S.R. Karnik; (2008) Inquiries into the effect of cutting circumstances on roughness in turning of free machining steel by ANN models: journal of materials administering technology 2 0 5 pp.16–23.

[8] I.A. Choudhury, M.A. EI-Baradie; (1997) Rroughness estimate in the turning of high-strength steel by factorial design of tests: Journal of Materials Processing Technology 67 pp.55-61.

[9] Hamdi Aouici, Mohamed Athmane Yallese, Kamel Chaoui, Tarek Mabrouki, Jean-François Rigal; (2012) Exploration of roughness and cutting force elements in hard turning with CBN tool: Prediction model and cutting conditions optimization: Measurement 45 pp.344–353.

[10] S. Ramesh, L. Karunamoorthy, K. Palanikumar; (2012) Dimension and investigation of roughness in turning of aerospace titanium alloy (gr5): Measurement 45 pp.1266–1276.

[11] Upadhyay.V, P.K. Jain, N.K. Mehta; (2013) In-process estimate of roughness in turning of Ti–6Al–4V alloy using

cutting constraints and vibration signals: Measurement 46 pp.154–160.
[12] Günay.M, Emre Yücel; (2013) Usage of Taguchi method for determining ideal roughness in turning of high-alloy white cast iron: Measurement 46 pp.913–919
[13] Bouacha.K, Mohamed Athmane Yallese, Tarek Mabrouki, Jean-François Rigal (2010) Statistical investigation of roughness and cutting forces using reaction surface approach in hard turning of AISI 52100 bearing steel with CBN tool: Int. Journal of Refractory Metals & Hard Materials 28 pp.349–361.
[14] N.R. Abburi, U.S. Dixit; (2006) A data -based system for the calculation of surface roughness in turning operation: Robotics and Computer-Integrated Manufacturing 22 pp.363–372.
[15] B.Y. Lee, Y.S. Tarng; (2001) Roughness assessment by computer visualization in turning processes: International Journal of Machine Tools & Manufacture 41 pp.1251–1263.
[16] Janez Kopac, Marko Bahor, Mirko Sokovic ; (2002) Finest machining constraints for attaining the desired roughness in fine turning of cold pre-formed steel workpieces: International Journal of Machine Tools & Manufacture 42 pp.707–716.
[17] P.V.S. Suresh e, P. Venkateswara Rao, S.G. Deshmukh; (2002) A genetic algorithmic method for optimization of surface roughness estimate model: International Journal of Machine Tools & Manufacture 42 pp.675–680.
[18] Shinn-Ying Ho, Kuang-Chyi Lee , Shih-Shin Chen, Shinn-Jang Ho; (2002) Perfect modeling and estimate of surface roughness by computer visualization in turning actions using an adaptive neuro fuzzy implication system: International Journal of Machine Tools & Manufacture 42 pp.1441–1446
[19] Tugrul Ozel, Yigit Karpat; (2005) Extrapolative modeling of roughness and tool wear in hard turning using regression and neural networks: International Journal of Machine Tools & Manufacture 45 pp.467–479.
[20] W.S. Lin, B.Y. Lee, C.L. Wu; (2001) Demonstrating the roughness and cutting force for turning: Journal of Materials Processing Technology 108 pp.286-293
[21] O.B.Abouelatta, J Madl ; (2001) Roughness estimate based on cutting parameters and tool vibrations in turning operations: Journal of Materials Processing Technology 118 pp.269-277.
[22] K.A. Risbood, U.S. Dixit, A.D. Sahasrabudhe; (2003) Estimate of dimensional deviation by measuring cutting forces and vibrations: Journal of Materials Processing Technology 132 pp.203–214.
[23] M.Y. Noordin, V.C. Venkatesh , S. Sharif, S. Elting , A. Abdullah; (2004) predicted the performance of coated carbide tools when turning of AISI 1045 steel: Journal of Materials Processing Technology 145 pp.46–58.
[24] D.I. Lalwani, N.K. Mehta, P.K. Jain; (2008) Experimental investigations of and influence on cutting forces and roughness in finish hard turning of MDN250 steel: journal of materials processing technology 2 0 6 pp.167–179.
[25] M. Anthony Xavior , M. Adithan; (2009) Influence of cutting fluids on tool wear and roughness on turning of AISI 304 austenitic stainless steel: journal of materials processing technology 2 0 9 pp.900–909.
[26] Jeffrey D. Thiele, Shreyes N. Melkote; (1999) Cutting edge geometry effect on surface generation in the finish hard turning of AISI 52100 steel: Journal of Materials Processing Technology 94 pp.216-226.
[27] Davim. J, Francisco Mata; (2004) Impact of cutting constraints on roughness in turning glass-fiber- strengthened plastics using geometric analysis: Industrial Lubrication and Tribology Volume 56 · Number 5 pp. 270–274.
[28] A. Kohli, U.S. Dixit; (2005) A neural-network-based practice for the calculation of roughness in a turning process: Int J Adv Manuf Technol 25: pp.118–129
[29] Tugrul Ozel, Tsu-Kong Hsu, Erol Zeren; (2005) Effects of cutting edge geometry, feed rate and cutting speed on roughness and forces in finishing of hardened AISI H13 steel: Int J Adv Manuf Technol 25: pp.262–269.
[30] Eyup Bagci, Birhan Işık; (2006) Examination of roughness in turning unidirectional GFRP syntheses by using RS approach and ANN: Int J Adv Manuf Technol 31: pp.10–17.
[31] Dilbag Singh, P. Venkateswara Rao; (2007) A roughness evaluation model for hard turning process: Int J Adv Manuf Technol 32: pp.1115–1124.
[32] Ahmet Hasçahk, Ulaş Çaydaş; (2008) Optimization of turning constraints for roughness and tool life centered on the Taguchi method: Int J Adv Manuf Technol 38: pp.896–903.
[33] Surjya K. Pal, Debabrata Chakraborty; (2005) Roughness calculation in turning using simulated neural network: Neural Comput & Applic 14: pp.319–324.
[34] Vishal S. Sharma , Suresh Dhiman, Rakesh Sehgal, S. K. Sharma; (2008) Assessment of cutting forces and roughness for hard turning using neural networks: J Intell Manuf 19: pp.473–483.
[35] Hardeep Singh, Rajesh Khanna, M.P. Garg; (2011) Consequence of Cutting Constraints on MRR and Roughness in Turning EN-8: Current Developments in Engineering Research Vol.1, No.1.
[36] P.G. Benardos, G.-C. Vosniakos; (2003) Expecting roughness in machining: a review: International Journal of Machine Tools & Manufacture 43 pp.833–844.
[37] Thomas M., Beauchamp Y., Youssef A.Y., Masounave J; (1996) Consequence of tool shakings on roughness during lathe dry turning process: Computers ind. Engng, Vol 31, No. 3/4, pp. 637 - 644
[38] N.R. Dhar, M. Kamruzzaman; (2007) Cutting temperature, tool wear, roughness and dimensional nonconformity in turning AISI-4037 steel under cryogenic circumstance: International Journal of Machine Tools & Manufacture 47 pp.754–759.
[39] I. Puertas Arbizu, C.J. Luis Pérez; (2003) Roughness estimate by factorial design of investigates in turning processes: Journal of Materials Processing Technology 143–144 pp.390–396.
[40] Davim. J, Francisco Mata; (2005) Optimisation of roughness on turning fiber- strengthened plastics (FRPs) with diamond cutting tools: Int J Adv Manuf Technol 26: pp.319–323.
[41] Ranganath M. S , Vipin , R. S. Mishra , Parshvam Jain , Sushil Kumar; (2015) Experiment Investigation of surface roughness and cutting force on conventional dry turning of aluminium (6061): International Journal of Modern Engineering Research (IJMER): vol 5; pp. 14-23.
[42] Ranganath M. S., Vipin, R. S. Mishra, Prateek; (2015) Optimization of surface roughness in CNC turning of Aluminium 6061 using Taguchi Techniqques: International Journal of Modern Engineering Research (IJMER): vol 5; pp. 1-9.
[43] Ranganath M.S., Vipin, R. S. Mishra; (2013) Neural Network process modeling for turning of aluminium (6061) using cemented carbide inserts: International Journal of Advance Research and Innovation: vol 1; pp. 211-219.

ResearchGate

See discussions, stats, and author profiles for this publication at: https://www.researchgate.net/publication/315207009

Quantum Transport in Two-Dimensional Group-IV monolayers and Topological Insulators

Conference Paper · March 2015

CITATIONS
0

READS
2

2 authors, including:

Gaurav Gupta
National University of Singapore
27 PUBLICATIONS **43** CITATIONS

SEE PROFILE

All content following this page was uploaded by Gaurav Gupta on 17 March 2017.

The user has requested enhancement of the downloaded file. All in-text references underlined in blue are added to the original document and are linked to publications on ResearchGate, letting you access and read them immediately.

Title: Quantum Transport in Two-Dimensional Group-IV monolayers and Topological Insulators

Gaurav Gupta* and Liang Gengchiau⬭
*Graduate Student ⬭Associate Professor
Computational Nanoelectronics and Nanodevices Lab (CNNL)
National University of Singapore
Singapore

Abstract

Graphene, the first two-dimensional (2D) material, since its realization in 2004 [1] has spawned new possibilities for physicists and device engineers alike [2]. The relativistic linear Dirac-bands with extremely high mobility of over 200000 $cm^2V^{-1}s^{-1}$ [3] and Klein tunneling in graphene makes it an excellent material for electron transport in THz high-speed [4, 5] and low-power atomically-thin devices [6, 7] of the future. The larger spin-orbit coupling (SOC), than in graphene, in later 2D-materials like Silicene and Germanene [8] provides an additional control over the spin of an electron, which can possibly be used for non-volatile logic and zero-standby power application [9]. Investigation of SOC in graphene [10] has, however, has taken a more prolific research direction with the recent discovery of topological insulating (TI) phase of matter in both 2D [11, 12] and three-dimensional (3D) [13, 14] systems. TI gets its unique advantage from having bulk band gap and SOC engendered spin-momentum locked helical Dirac 2D surface-states (1D edge-states) in 3D (2D) materials which are robust to non-magnetic impurities and disorders [15]. The suppression of backscattering in both 2D [16] and 3D [17] TIs and weak electron-phonon coupling [18] enables dissipationless surface (edge) transport. Therefore, topological insulators are posited to have gamut of applications ranging from interconnects [19] and spintronics [20] to optoelectronics [21], making them one of the most important contemporary material under investigation.
.

Biography

Dr. Gengchiau Liang is an Associate Professor in Department of Electrical and Computer Engineering at National University of Singapore. He received the B.S. and M.S. degrees in physics from National Tsinghua University, Hsinchu, Taiwan, in 1995 and 1997, respectively, and the Ph.D. degree in electrical and computer engineering from Purdue University, West Lafayette, IN, in 2005.
PLEASE ADD YOUR BIOGRAPHY.

Gaurav Gupta is a President Graduate Fellowship scholar pursuing PhD in Computational Nanoelectronics from Department of Electrical and Computer Engineering at National University of Singapore. He received his B.E. from Delhi College of Engineering, Delhi, India followed by three years in Freescale Semiconductors and Texas Instruments in Functional Verification, Embedded Software, Analog Validation and Circuit Design. Currently his research focuses on devising novel post-CMOS nano-devices that can meet the future product requirements of computing and storing information by investigating charge/spin state variable via quantum transport simulations.

References

[1] K. S. Novoselov, A. K. Geim, S. V. Morozov, D. Jiang, Y. Zhang, S. V. Dubonos, I. V. Grigorieva, and A. A. Firsov, "Electric field effect in atomically thin carbon films," *Science,* vol. 306, no. 5696, pp. 666-669, Oct 22, 2004.
[2] X. Huang, Z. Yin, S. Wu, X. Qi, Q. He, Q. Zhang, Q. Yan, F. Boey, and H. Zhang, "Graphene-Based Materials: Synthesis, Characterization, Properties, and Applications," *Small,* vol. 7, no. 14, pp. 1876-1902, 2011.
[3] A. S. Mayorov, R. V. Gorbachev, S. V. Morozov, L. Britnell, R. Jalil, L. A. Ponomarenko, P. Blake, K. S. Novoselov, K. Watanabe, T. Taniguchi, and A. K. Geim, "Micrometer-Scale Ballistic Transport in Encapsulated Graphene at Room Temperature," *Nano Letters,* vol. 11, no. 6, pp. 2396-2399, Jun, 2011.
[4] J. X. Zheng, L. Wang, R. G. Quhe, Q. H. Liu, H. Li, D. P. Yu, W. N. Mei, J. J. Shi, Z. X. Gao, and J. Lu, "Sub-10 nm Gate Length Graphene Transistors: Operating at Terahertz Frequencies with Current Saturation," *Scientific Reports,* vol. 3, Feb 19, 2013.
[5] N. Petrone, I. Meric, J. Hone, and K. L. Shepard, "Graphene Field-Effect Transistors with Gigahertz-Frequency Power Gain on Flexible Substrates," *Nano Letters,* vol. 13, no. 1, pp. 121-125, 2013/01/09, 2012.
[6] J. Heo, K.-E. Byun, J. Lee, H.-J. Chung, S. Jeon, S. Park, and S. Hwang, "Graphene and Thin-Film Semiconductor Heterojunction Transistors Integrated on Wafer Scale for Low-Power Electronics," *Nano Letters,* vol. 13, no. 12, pp. 5967-5971, 2013/12/11, 2013.
[7] J. A. Crosse, X. Xu, M. S. Sherwin, and R. B. Liu, "Low power ultra-broadband terahertz sideband generation in bilayer graphene," *arXiv:1401.1055 [cond-mat.mes-hall]*, 2014.
[8] G. Gupta, H. Lin, A. Bansil, M. B. Abdul Jalil, C.-Y. Huang, W.-F. Tsai, and G. Liang, "Y-shape spin-separator for two-dimensional group-IV nanoribbons based on quantum spin hall effect," *Applied Physics Letters,* vol. 104, no. 3, pp. 032410, 2014.
[9] M. Natsui, D. Suzuki, N. Sakimura, R. Nebashi, Y. Tsuji, A. Morioka, T. Sugibayashi, S. Miura, H. Honjo, K. Kinoshita, S. Ikeda, T. Endoh, H. Ohno, and T. Hanyu, "Nonvolatile logic-in-memory array processor in 90nm MTJ/MOS achieving 75% leakage reduction using cycle-based power gating." pp. 194-195.
[10] C. L. Kane, and E. J. Mele, "Quantum spin Hall effect in graphene," *Physical Review Letters,* vol. 95, no. 22, pp. 226801, Nov 25, 2005.
[11] C. L. Kane, and E. J. Mele, "Z(2) topological order and the quantum spin Hall effect," *Physical Review Letters,* vol. 95, no. 14, pp. 146802, Sep 30, 2005.
[12] B. A. Bernevig, T. L. Hughes, and S. C. Zhang, "Quantum spin Hall effect and topological phase transition in HgTe quantum wells," *Science,* vol. 314, no. 5806, pp. 1757-1761, Dec 15, 2006.
[13] L. Fu, C. L. Kane, and E. J. Mele, "Topological insulators in three dimensions," *Physical Review Letters,* vol. 98, no. 10, pp. 106803, Mar 9, 2007.

[14] Y. Xia, D. Qian, D. Hsieh, L. Wray, A. Pal, H. Lin, A. Bansil, D. Grauer, Y. S. Hor, R. J. Cava, and M. Z. Hasan, "Observation of a large-gap topological-insulator class with a single Dirac cone on the surface," *Nature Physics,* vol. 5, no. 6, pp. 398-402, Jun, 2009.

[15] L. A. Wray, S. Y. Xu, Y. Q. Xia, D. Hsieh, A. V. Fedorov, Y. S. Hor, R. J. Cava, A. Bansil, H. Lin, and M. Z. Hasan, "A topological insulator surface under strong Coulomb, magnetic and disorder perturbations," *Nature Physics,* vol. 7, no. 1, pp. 32-37, Jan, 2011.

[16] A. Roth, C. Brune, H. Buhmann, L. W. Molenkamp, J. Maciejko, X. L. Qi, and S. C. Zhang, "Nonlocal Transport in the Quantum Spin Hall State," *Science,* vol. 325, no. 5938, pp. 294-297, Jul 17, 2009.

[17] S. Kim, S. Yoshizawa, Y. Ishida, K. Eto, K. Segawa, Y. Ando, S. Shin, and F. Komori, "Robust Protection from Backscattering in the Topological Insulator Bi1.5Sb0.5Te1.7Se1.3," *Physical Review Letters,* vol. 112, no. 13, pp. 136802, 04/01/, 2014.

[18] Z. H. Pan, A. V. Fedorov, D. Gardner, Y. S. Lee, S. Chu, and T. Valla, "Measurement of an Exceptionally Weak Electron-Phonon Coupling on the Surface of the Topological Insulator Bi2Se3 Using Angle-Resolved Photoemission Spectroscopy," *Physical Review Letters,* vol. 108, no. 18, pp. 187001, May 3, 2012.

[19] X. Zhang, and S. C. Zhang, "Chiral interconnects based on topological insulators," *Micro- and Nanotechnology Sensors, Systems, and Applications IV,* vol. 8373, pp. 837309, 2012.

[20] D. Pesin, and A. H. MacDonald, "Spintronics and pseudospintronics in graphene and topological insulators," *Nature Materials,* vol. 11, no. 5, pp. 409-416, May, 2012.

[21] C. Jozwiak, C.-H. Park, K. Gotlieb, C. Hwang, D.-H. Lee, S. G. Louie, J. D. Denlinger, C. R. Rotundu, R. J. Birgeneau, Z. Hussain, and A. Lanzara, "Photoelectron spin-flipping and texture manipulation in a topological insulator," *Nat Phys,* vol. advance online publication, pp. 293–298, 03/10/online, 2013.

View publication stats

3rd International Conference on Innovative Trends in Science, Engineering and Management
YMCA, Connaught Place, New Delhi (ICITSEM-17)
7th January 2017 , www.conferenceworld.in ISBN: 978-93-86171-27-6

REVIEW ON PRODUCTION OF BIODIESEL FROM TRANSESTERIFICATION

Deepak Verma[1], Janmit Raj[2], Amit Pal[3], Manish Jain[4]

[1]Research Scholar, [2, 3, 4]Assistant Professor

[1, 2, 4] Department of Automobile Engineering, Rustam Ji Institute of Technology, Tekanpur, Gwalior (M. P.), (India)

[3]Department of Mechanical Engineering, Delhi Technological University, Bawana Road, Delhi, (India)

ABSTRACT

Biodiesel fuel produced by alcoholysis of edible, non-edible and waste cooking oil is viewed as a promising renewable fuel source. Diminishing petroleum reserves and increasing environmental regulations have made the search for renewable fuel. This paper focuses on review of a work carried out by researchers in the field of production of biodiesel from different types of oil. The raw oil used by researchers for production of biodiesel first briefly summarized followed by a description of biodiesel production method applied and yield percentage, FFA content, molar ratio and the reaction time of the biodiesel produced from the raw oil. The review is divided into three categories viz. production of biodiesel from edible oil, non-edible oil and waste cooking oil. This review paper contains the work of past researchers published between 2005 and 2015.

Keywords: Biodiesel, Transesterification, FFA Content, Reaction Time.

I. INTRODUCTION

With the increasing use of diesel fuel, many initiatives have become more attractive to search for alternate fuels to supply or replace fossil fuels. Biodiesel is synthesized from edible, non-edible and waste cooking oil or animal oil can be regarded as an alternative diesel fuel. The various alternative fuel options tried in place of hydrocarbon oils are mainly biogas, producer gas, ethanol, methanol and vegetable oils. Out of all these, biodiesel offers an advantage because of their comparable fuel properties with that of diesel. The emissions produced from biodiesel are cleaner compared to petroleum-based diesel fuel. Particulate emissions, soot, and carbon monoxide are lower since biodiesel is an oxygenated fuel. The biodiesel could be used as pure fuel or as blend with petro diesel, which is stable in all ratio. Alternative new and renewable fuels have the potential to solve many of the current social problems and concerns, from air pollution and global warming to other environmental improvements and sustainability issues.

II. BRIEF DESCRIPTION OF BIODIESEL

Biodiesel is an alternative fuel made from renewable biological sources such as vegetable oils both (edible and non-edible oil) and animal fats According to the US standard specification for biodiesel (American Society for Testing and materials (ASTM) 6751), biodiesel is defined as a fuel comprised of mono alkyl esters of long chain fatty acids from vegetable oils or animal fats [1]. The dominant bio-diesel production process, namely transesterification, typically involves the reaction of an alkyl-alcohol with a long chain ester linkage in the presence of a catalyst to yield mono-alkyl esters (bio-diesel) and glycerol [2, 3].

2.1 Production of Biodiesel by Transesterification

Generally, biodiesel is produced by means of transesterification. Transesterification is the reaction of a lipid with an alcohol to form esters and a byproduct, glycerol. It is, in principle, the action of one alcohol displacing another from an ester, referred to as alcoholysis (cleavage by an alcohol). In Transesterification mechanism, the carbonyl carbon of the starting ester ($RCOOR^1$) undergoes nucleophilic attack by the incoming alkoxide (R^2O^-) to give a tetrahedral intermediate, which either reverts to the starting material, or proceeds to the transesterified product ($RCOOR^2$). Transesterification consists of a sequence of three consecutive reversible reactions. The first step is the conversion of triglycerides to diglycerides, followed by the conversion of diglycerides to monoglycerides, and finally monoglycerides into glycerol, yielding one ester molecule from each glyceride at each step. The reaction is represented in equation 1. The reactions are reversible, although the equilibrium lies towards the production of fatty acid esters and glycerol. This reaction proceeds well in the presence of some homogeneous catalysts such as potassium hydroxide (KOH)/sodium hydroxide (NaOH). Depending on the undesirable compounds (especially FFA and water), each catalyst has its advantages and disadvantages. Sodium hydroxide is very well accepted and widely used because of its low cost and high product yield. The most common alcohols widely used are methyl alcohol and ethyl alcohol. Among these two, methanol found frequent application in the commercial uses because of its low cost.

$$\text{Triglycerides} + \text{ROH} \rightleftharpoons \text{Diglycerides} + R^1COOR$$

$$\text{Diglycerides} + \text{ROH} \rightleftharpoons \text{Monoglycerides} + R^2COOR$$

$$\text{Monoglycerides} + \text{ROH} \rightleftharpoons \text{Glycerol} + R^3COOR$$

Equation 1 Chemistry of transesterification

ISBN: 978-93-86171-27-6

III. PREVIOUS RESEARCHES

Previous work done on production of biodiesel from edible oil.

Over the last few years, there has been increasing amounts of research and interest in the different edible feedstocks that can be used to make biodiesel and the effects of the different feedstocks on the quality of the biodiesel. Currently, biodiesel is produced from different crops such as, Jojoba oil, palm oil, soybean oil, canola, rice bran, sunflower, coconut, rapeseed, soybean and sunflower oil [4, 5, 6]. The major difference between various edible oils is the type of fatty acids attached in the triglyceride molecule. Fatty acid composition effects the yield percentage, reaction temperature, FFA content and molar ratio of the biodiesel oil [7].

Leung D.Y.C and Guo Y. [8], compared the transesterification reaction conditions for fresh canola oil and used frying oil. Higher molar ratio (7:1, methanol/used frying oil), higher temperature (60° C) and higher amount of catalyst (1.1 wt% NaOH) was maintained in used frying oil when compared to fresh canola oil where optimal conditions maintained were 315-318 K, 1.0 wt% NaOH and 6:1 methanol/oil molar ratio. However, less reaction time (20 min) was observed for used frying oil when compared to fresh canola oil reaction time (60 min). The Fig. 1 shows the effect of temperature on the transesterification of (a) neat Canola oil; and (b) UFO. In the further work Lingfeng Cui *et al.* [9] developed biodiesel from cottonseed oil by using KF/γ-Al2O3 as heterogeneous catalysts for the transesterification of cottonseed oil with methanol. The operation variables used were methanol/oil molar ratio (6:1–18:1), catalyst concentration (1–5 wt %), temperature (50–68 °C), and catalyst type. The biodiesel with the best properties was obtained using a methanol/oil molar ratio of 12:1, catalyst (4%), and 65°C temperature with the catalyst KF/γ- Al2O3. Later Sinha Shailendra *et al.* [4] determined the optimum condition for transesterification of rice bran oil with methanol and NaOH as catalyst by mechanical stirring method. The condition was found at 55° C reaction temperature, 1 h reaction time, 9:1 molar ratio of rice bran oil to methanol and 0.75% catalyst (w/w). Further, the physical properties of rice bran methyl ester were tested and compared with other biodiesels and diesel. The result showed that characteristics of rice bran methyl ester were comparable to diesel.

ISBN: 978-93-86171-27-6

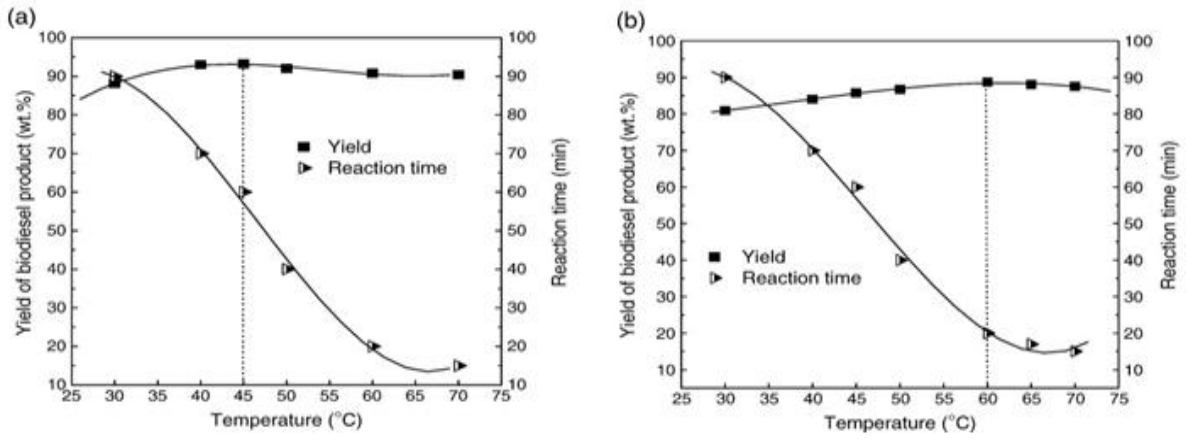

Figure 1: Effect of temperature on the transesterification of (a) neat Canola oil; and (b) UFO.

In an important research Georgogianni K.G. *et al.* [2] studied transesterification reaction of rapeseed oil with methanol, in the presence of homogeneous (NaOH) and heterogeneous (Mg MCM-41, Mg–Al Hydrotalcite, and K+ impregnated zirconia) using low frequency ultrasonication (24 kHz) and mechanical stirring (600 rpm) for the production of biodiesel fuel. The study concluded that that the homogeneous catalyst accelerated significantly the transesterification reaction, as compared to all heterogeneous catalysts, using both mechanical stirring (15 min vs. 24 h) and ultrasonication (10 min vs. 5 h). The table 1 shown below gives the Conversion of rapeseed oil in the presence of different catalysts using both mechanical stirring and ultrasonication. Further, Issariyakul Titipong and Dalai K. Ajay [5] carried out work on transesterification of canola oil and greenseed canola oil via KOH-catalyzed along with methanol, ethanol and a mixture of methanol and ethanol. The reaction was conducted at 60°C and a stirring speed of 600 rpm for 90 min. Prior to transesterification, greenseed canola oil was bleached to remove pigments using various adsorbents at different conditions. The result of the research work disclosed that Biodiesel derived from the treated greenseed canola oil showed an improvement in oxidative stability (induction time of 0.7 h) as compared to that derived from crude greenseed canola oil (induction time of 0.5 h).

Table 1: Conversion of rapeseed oil in the presence of different catalysts using both mechanical stirring and ultrasonication

	Time (h)	Yield (%)			
		Type of catalyst			
		Mg/MCM-41	MgAl hydrotalcite	$10K/ZrO_2$	$20K/ZrO_2$
Mechanical stirring	5	21	28	30	38
	10	43	54	37	42
	15	56	73	49	56
	20	73	89	61	69
	24	85	97	67	89
Ultrasonication	1	25	32	29	35
	2	48	58	39	48
	3	59	76	52	59
	4	75	89	63	73
	5	89	96	70	83

Afterwards Alamu J Oguntola et al. [10], produced the biodiesel from through transesterification 100g coconut oil, 20.0% ethanol (wt% coconut oil) and 0.8% potassium hydroxide catalyst at 65°C reaction temperature with 120 min. reaction time. Low yield of the biodiesel (10.4%) was obtained. While Tang Ying et al. [7], developed a new method catalyst, benzyl bromide-modified CaO for production of biodiesel from rapeseed. The improved catalytic activity was obtained by better fat diffusion to the surface of the benzyl bromide-modified CaO. Further, a 99.2% yield of fatty acid methyl esters in 3h was

obtained in comparison to by better fat diffusion to the surface of the benzyl bromide-modified CaO. The normal and modified CaO is shown in Fig.2. Further, Silva F. Giovanilton *et al.* [6], produced biodiesel from soybean oil by transesterification with ethanol. Optimum conditions for the production of ethyl esters were the following: mild temperature at

56.7 °C, reaction time in 80 min, molar ratio at 9:1 and catalyst concentration of 1.3 M. For esterification reaction, H*R2R*SO*R4R* was added as a catalyst and for transesterification KOH was added as the catalyst with methanol. In the investigation of Wakil Abdul Md. *et al.* [11], chosen Cottonseed oil, Mosna oil and Sesame oil for producing biodiesel. Biodiesel is produced by transesterifying the oil with an alcohol such as methanol under mild conditions in the presence of a base catalyst. Satisfactory amount of biodiesel is produced from

Cottonseed oil at 3:1 molar ratio of methanol and oil. Three types of oil (cottonsed oil, mosna oil, sesame oil) are extracted from the seeds and chemically converted via an alkaline transesterification reaction to fatty acid methyl ester. The optimum conditions established for the methanolysis of crude cotton seed oil in the investigation were recorded to be: 3:1 molar ratio of methanol to oil and 1.00% (w/w) catalyst. For Mosna oil the optimum conditions were recorded to be 3. 5:1 M ratio of methanol to oil and 1.00% (w/w) catalyst. But small amount of biodiesel was found from this oil and production cost is higher than cottonseed oil. And for Sesame oil the optimum conditions were recorded to be 3.5:1 M ratio of methanol to oil and 1.00% (w/w) catalyst.

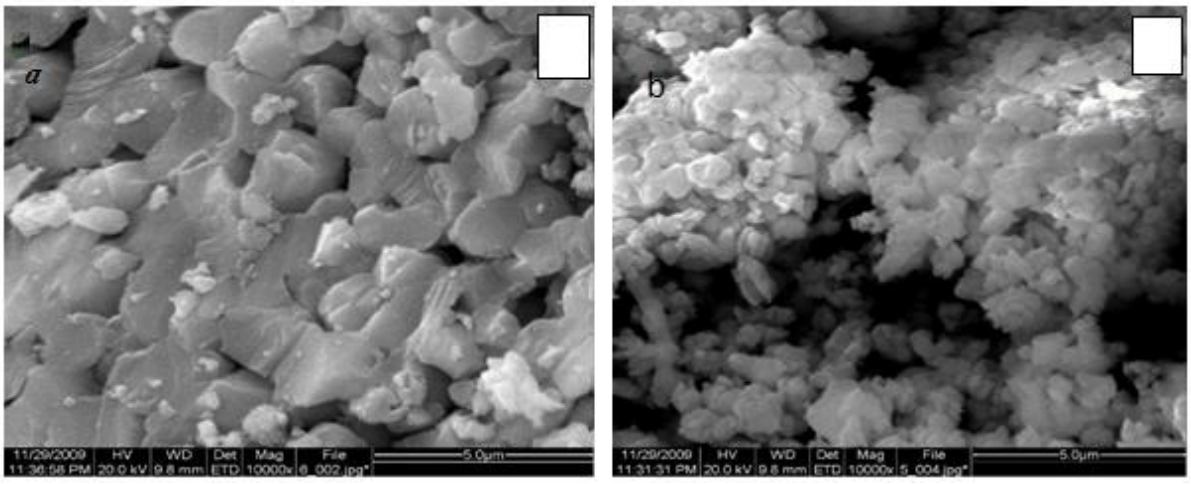

Figure 2: SEM Photo of (a) CaO and (b) Modified CaO

Ali N. Eman and Tay Isis Cadence [12], investigated characteristics of biodiesel produced from palm oil via base catalyst transesterification process. To find the optimum yield value of biodiesel, three important

ISBN: 978-93-86171-27-6

parameters were selected such as reaction temperature 40, 50, and 60°C, reaction time 40, 60 and 80 min. and methoxide ratio 4:1, 6:1 and 8:1. By conducting the experiments the optimum yield value 88% was achieved by the parameters such as reaction temperature 60°C, reaction time 40 minutes and methoxide ratio 6:1. From the optimum yield value, the physical properties were calculated like, density is 876.0 kg/m3, kinematic viscosity of 4.76 mm2/s, cetane number of 62.8, flash point of 170°C, cloud point of 13°C. The produced biodiesel had similar properties of ASTM D 6751, and EN 14214. In the important study

Banerjee Madhuchanda *et al.* [13], determined the catalytic activity of

bimetallic Gold–silver core–shell nanoparticles toward biodiesel production from Sunflower oil through transesterification. The structure of nanoparticles was examined by UV–vis spectroscopy, transmission electron microscopy (TEM) and energy dispersive X-ray (EDX) analysis. The result of studied showed that at certain catalyst concentration, temperature and reaction time, highest yield of biodiesel (86.9%) is attained. Further, the catalyst showed sustained activity for 3 cycles of transesterification. The effect of variable on the yield of biodiesel is shown in Fig. 3. In the most recent work Nikhom Ruamporn

and Tongurai Chakrit [14], examined the continuous deglycerolisation

(CD) for the production of ethyl ester biodiesel from palm oil. In this work, $KOCH_3$ was selected as the catalyst in transesterification and the reaction temperature was maintained at 60°C. The result showed that ethyl ester production using CD process could obtain good purity and yield in a single step transesterification. The ester content and yield were 98.0 wt.% and 93.1 wt.%, respectively at molar ratio of oil to ethanol of 1:5.5, $KOCH_3$ concentration of 1.2 wt.% and retention time of 30 min. The FFA content of palm oil and ethyl ester is shown in table

2 below.

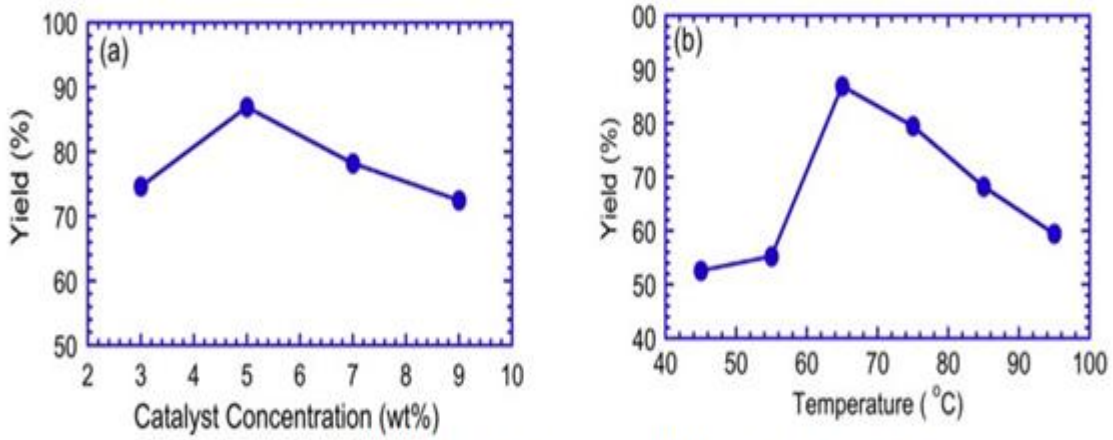

Figure 3: Effects of variables on biodiesel yield; (a) catalyst concentration and (b) temperature.

ISBN: 978-93-86171-27-6

Table 2: The fatty acid composition of palm oil raw material and Ethyl Ester product

Fatty Acid Composition	Wt. %	
	Palm Oil	Ethyl ester
Lauric acid (C12:0)	1.11	0.24
Myristic acid (C14:0)	1.23	0.97
Palmitic acid (C16:0)	36.58	37.95
Palmitoleic acid (C16:1)	1.39	0.16
Stearic acid (C18:0)	4.5	3.62
Oleic acid (C18:1)	43.38	45.95
Linoleic acid (C18:2)	11.81	11.10
Others	-	2.01

Previous work done on production of biodiesel from non-edible oil.

Azam Mohibbe M. *et al.* [15], found that FAME of Jatropha curcas were most suitable for use as bio- diesel and met the major specification of bio-diesel standards of the European, Germany and USA Standards Organization. Afterwards Sarin Rakesh *et al.* [16], made appropriate blends of Jatropha and palm bio-diesel to improve oxidation stability and low temperature properties because Jatropha bio-diesel has good low temperature property and palm bio-diesel has good oxidative stability. It was found that antioxidant dosage could be reduced by 80-90% when palm oil bio-diesel is blended with Jatropha bio-diesel at about 20-40%. Moreover, Tiwari Kumar Alok *et al.* [17], used response surface methodology to optimize three important reaction variables, including methanol quantity, acid concentration, and reaction time. The optimum the FFA of Jatropha oil from 14% to less than 1% was found to be 1.43% v/v sulphuric acid catalyst, 0.28 v/v methanol-to-oil ration and 88 min reaction time at 60 ºC. The properties of Jatropha oil bio- diesel conform to European and American standards.

ISBN: 978-93-86171-27-6

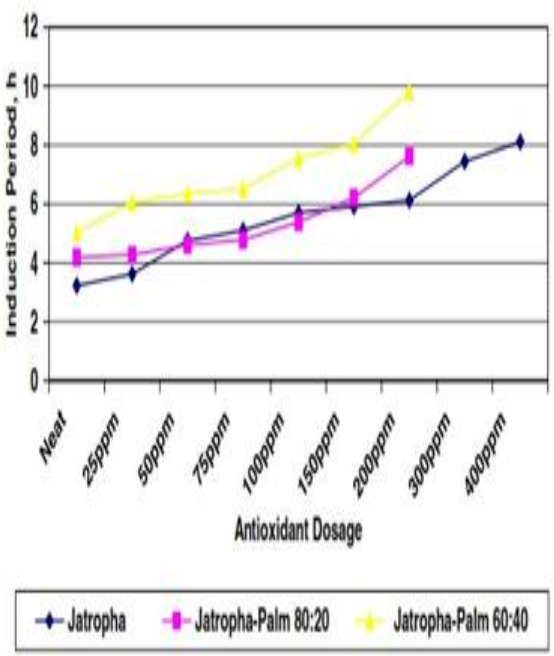

Figure 4: Antioxidant dose optimisation for Jatropha and Palm biodiesel.

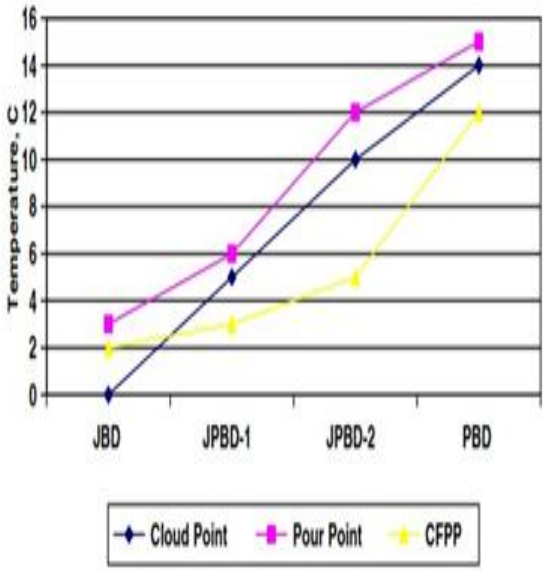

Figure 5: Low temperature property of Jatropha–Palm methyl ester blend

A year later Berchmans Johanes Hanny and Hirata Shizuko [18], developed a two-step pre-treatment process in which the high FFA (15%) of *Jatropha curcas* seed oil was reduced to less than 1%. In the first step, the reaction was carried out with 0.60 w/w methanol-to-oil ratio in the presence of 1 wt.% sulphuric acid as an acid catalyst in 1 h at 50ºC. In the second step, the transesterification reaction was performed using 0.24 w/w methanol-to-oil ratio and 1.4 wt% sodium hydroxide. While Chakrabarti H. Mohammed and Ahmad Rafiq [1], presented work on extraction of oil from castor bean and converting it into biodiesel from ransesterification. It was found that reaction mixture containing 65ml of methanol along with 2.4 g of catalyst (KOH) took a good start in half an hour at30°C. In this reaction, amount of glycerine removed as well as ester content produced was considerably increased with rise in temperature of mixture upto 70°C by extending time period (180-360 minutes). The removal of glycerine increased by two and half times and ester content by four times, respectively. When castor oil was subjected to acid esterification, prior to transesterification (a separate investigation), it was found that ester contents up to 95% could be obtained. The comparison of physical- chemical properties of castor oil and diesel done by them is shown in table 3.

ISBN: 978-93-86171-27-6

Table 3: Physical-chemical properties of mineral diesel, castor oil

Parameter	ASTM Test Method	ASTM Limits	Castor Oil	Diesel
Viscosity (mm^2/s)	ASTM D445	1.9 - 6.0	13.75	3.2
Sulfur (%)	ASTM D5453	0.0015, Max	0.0001	0.20
Density 15°C (g/cm^3)	ASTM D 1298	0.875 - 0.9	0.9279	0.8503
Density 20°C (g/cm^3)	ASTM D 1298	0.86	0.9245	0.8465
Flash point (°C)	ASTM D93	93°C Min.	120	37
Copper Corrosion	ASTM D130	No. 3, Max	1	1
Cetane index	ASTM D613	47, Min	50	45
Water and sediment (vol. %)	ASTM D2709	0.050, Max	0.05	Nil

In the further research work Kapilan N and Reddy R.P. [19], produced biodiesel from Mahua oil methyl esters (MOME) by transesterification using potassium hydroxide (KOH) as catalyst and tested the conversion of vegetable oil to biodiesel by nuclear magnetic resonance (NMR) testing method. Further, studied the performance characteristics fuelling with Mahua biodiesel in a diesel engine. They concluded that B20 gave higher thermal efficiency and lower specific fuel consumption then diesel fuel. The physical properties of Mahua oil prepared by them is shown in table 4. In another research work Kansedo Jibrail *et al.* [20], extracted oil from the seeds of C. odollam fruits. The transesterification of the extracted oil was done to form fatty acid methyl esters (FAME). The transesterification reactions were carried out using three different catalysts; sodium hydroxide (NaOH) as a homogenous catalyst, sulfated zirconia alumina and montmorillonite KSF as heterogeneous catalysts. The seeds were found to contain high percentage of oil up to 54% while the yield of FAME can reach up to 83.8% using sulfated zirconia catalyst. Further, Kafuku Gerald *et al.* [3], examined the feasibility of converting a non-edible oil source croton megalocarpus oil to methyl esters (biodiesel) using sulfated tin oxide with enchansed SiO_2 as super acid solid catalyst. At the following reaction condition 180°C, 2 h and 15:1 methanol to oil molar ratio, while keeping constant catalyst concentration and stirring speed at 3 wt.% and 350–360 rpm the yield up to 95% was obtained without any pre-treatment was obtained. The researcher Padhi S.K. and Singh R.K. [20] produced biodiesel from Mahua oil through the Esterification by varying different parameters. The conditions for produce biodiesel were 8% Sodium Methoxide, 0.33% v/v alcohol/oil ratio, 1 hr reaction time, 65°C temperature and 150% v/v excess alcohol. They concluded this was the best condition for biodiesel production. The results show that 4% H_2SO_4, 0.33% v/v alcohol/oil ratio, 1 hr reaction time and 65°C temperature are the optimum conditions for esterification. Optimum conditions for the production of biodiesel from Mahua oil are 8% Sodium Methoxide, 0.33% v/v alcohol/oil ratio, 1 hr reaction time, 65°C temperature and 150% v/v excess alcohol.

ISBN: 978-93-86171-27-6

Table 4: Properties of MOME and its blends with diesel

Property	MO	MOME	Diesel	B20
Flash point (°C)	212	129	65	103
Kinematic viscosity at 40 °C (cst)	28.58	5.10	2.4	4.04
Copper strip corrosion	1.5	1	1	1
Cloud point (°C)	17	4	−6	−3
Density at 15 °C (kg/m^3)	897	876	821	838
Calorific value (MJ/kg)	35.614	36.914	42.960	41.750

E.I Bello and A Makanju [22] analyzed castor oil methyl ester as possible alternative fuel for diesel engines. To overcome the high kinematic viscosity of the neat oil, a high molar ratio of 6:1 was used to produce the methyl ester. The viscosity of the ester was high and further reduced by blending with diesel fuel to reduce it to within the American Society for Testing and Materials (ASTM) D6751 limits for biodiesel. The biodiesel was characterized and tested in a single cylinder diesel engine. The results obtained gave properties, torque outputs and specific fuel consumption that are close to those of diesel fuel thus confirming that it can be used as alternative fuel for diesel engines. While Deshpande D.P. *et al.* [23], studied transesterification reaction on castor oil in a batch reactor using potassium hydroxide as a catalyst. The variables chosen for the study were reaction time, Oil to methanol ratio, catalyst concentration; and reaction temperature. The effects of these variables on the viscosity of biodiesel were studied, since this is one of the important specifications in ASTM standard. Apart from viscosity other properties like specific grravity, acid value, and sap value were also determined for the biodiesel product. From the study it was concluded that the optimum operating condition are oil to methanol mole ratio 1:9, temperature 30oC, catalyst concentration 1 wt % and run time 45 min. The variation of viscosity, specific gravity, acid value with time is shown in table 5.

Table 5: Variation of viscosity, specific gravity, acid value with time

Time of Run (min)	30	45	60	90
Kinematic viscosity, (cSt) for	16.56	11.28	12.44	13.93
Kinematic viscosity, (cSt) for Sodium Hydroxide as Catalyst	21.57	13.10	15.33	18.11
Specific gravity for Sulfuric Acid as	0.9018	0.9006	0.9012	0.9019
Specific gravity for Sodium	0.9106	0.889	0.9016	0.9039
Acid value for Sulfuric Acid as	0.90	0.58	0.562	0.541
Acid value for Sodium Hydroxide as Catalyst	0.92	0.37	0.40	0.52

Afterwards Widayat *et al.* [24], presented work on biodiesel from the rubber seed by situ method. The researcher focused on influence of reaction time, concentration of acid catalyst and ratio of raw material to methanol. This process took 120 minutes at 60°C with maximum yield of FAME 91.05% at HR2RSOR4R 0.25% (v/v) and ratio of raw material to methanol (1:3). Based on the results, ratio of raw material to methanol was quite important to increase yield of FAME significantly. The experimental setup used by the researcher is shown in Fig. 6.

Further, the team of researchers Ali Hasan Md. *et al.* [25] produced biodiesel from neem seeds, its properties were close to diesel. The methodology of esterification process was selected and carried out by

1000 ml raw neem oil, 300ml methanol and sodium hydroxide on mass basis as a catalyst usually kept in oven to form methyl ester, and initially to reach equilibrium condition at temperature 55-66°C. The ester and glycerine were separated by stimulating continuously and allow settling under gravity for 24 h. Thus the separated ester contains

3% to 6% methanol and soap agents. The methanol was removed by vaporization. The biodiesel had some catalyst; it was removed by warm water mix with ester. Kinematic viscosity lay between 1.9 to 6.0 according to the ASTM D6751 specification. Hence, 0.95 ltr. biodiesel was production from 1 ltr neem oil.

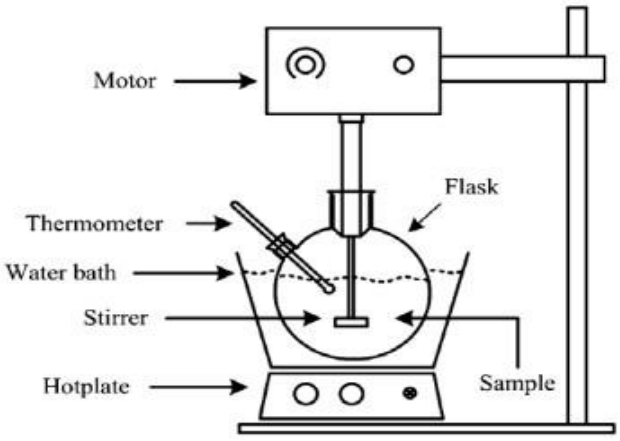

Figure 6: Experimental Setup

In an advance production method of biodiesel Riadi Lieke *et al.* [26], produced biodiesel from karanja oil by two step process. The first step process which was designed for 3 hours reaction time at 30°C and 5.8% of ozone using either 1 or 1.5 weight % KOH at various percent weight of supporting catalyst had proved simultaneous reaction for both ozonolysis and transesterification. The short chain methyl esters (methyl hexanoate, methyl octanoate and methyl nonanoate) were effectively produced for the first step process using 5.8% mole ozone at 30°C for 3 hours either for 1 or 1.5 weight % KOH at various percent weight of extracted supporting catalyst. From this reaction, the esters predicted by ozone reaction were sufficiently produced. The highest short chain methyl esters and long chain methyl esters produced in the first step process was 85.722 mg/litre and 655.286 mg/ltr respectively, which used 17.3 weight % ash and 1.5 weight % KOH. The presence of extracted ash in methanol as supporting catalyst enhanced the production of total methyl esters compared to that without the presence of ash in the first step process. Higher temperature (60°C) in the second step process without the presence of ozone gave enough vibration of energy, to increase rate of transesterification and decrease the viscosity.In the recent work Hotti R Siddalingappa and Hebbal D Omprakash [27], presented work on non-edible champaca seed oil biodiesel (CBD). The biodiesel was produced by two step process i.e. acid pretreatment process followed by base-catalyzed transesterification process as the free fatty acid (FFA) content found to be 5.30% (corresponding to acid value of 10.55, mg KOH/g). The first step of process was carried out with methanol and sulphuric acid as catalyst, followed by second step, base-catalyzed transesterification process with methanol and sodium hydroxide as catalyst the biodiesel yield was found to be 83.50 %.

Previous work done on production of biodiesel from waste cooking oil.

Zheng S. *et al.* [28] analyzed the reaction kinetics of acid-catalyzed transesterification of waste frying oil. They found that at the methanol/oil molar ratio of 250:1 at 70 ºC or in the range 74:1-250:1 at 80ºC, the reaction was a pseudo-first-order reaction. High yield of 99±1% could be achieved at both 70 ºC and 80 ºC temperatures while stirring at rate of 400 rpm, using a feed molar ratio oil:methanol:acid of 1:245:3.8. A year later Wang Yong *et al.* [29] investigated a two- step catalyzed processes for synthesis of bio-diesel by using WCO from Chinese restaurants. In the first step, ferric sulphate-catalyzed methanolysis was carried out,

while potassium hydroxide catalysis was performed in the second step. The authors concluded that compared with one-step sulphur acid catalysis the two-step catalyzed process provided a simpler and more economic method to produce bio-diesel from WCO. The conversion rate is shown in fig. 7. In the further research work Issariyakul Titipong *et al.* [30] also used the two-step process to transesterify waste cooking oil, except that sulphuric acid was selected as acid catalyst and mixtures of methanol and ethanol were used for transesterification in order to use the better solvent properties of ethanol and a more rapid equilibrium using methanol. More than 90% ester was obtained by using the two-stage method compared with yield of ~50% ester by using the single stage alkaline catalyst.

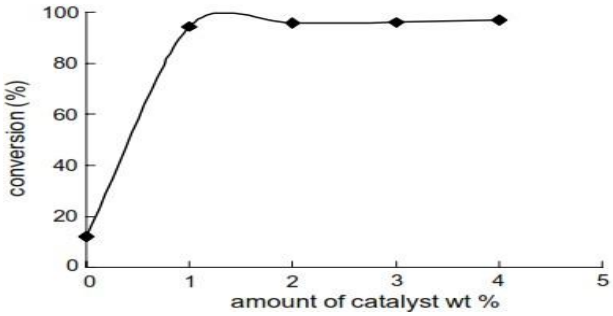

Figure 7: Conversion of FFA VS. Amount of Catalyst

Lin Fen-Ya *et al.* [31] also used WCO to prepare bio-diesel and then conducted a study in which the exhaust tail gas of bio-diesels was compared when the engine was operated using different fuel types, including neat bio-diesel, bio-diesel/diesel blends, and normal diesel fuels. Among the collected data, the authors found that B20 and B50 were the optimum fuel blends. The properties of diesel and biodiesel used by the researcher is shown in table 6. Later Hossain A.B.M.S. and Boyce A.N. [32] in their work compared optimum conditions of alkaline- catalyzed transesterification process for biodiesel production from pure sunflower cooking oil (PSCO) and waste sunflower cooking oil (WSCO) through transesterification process. The highest approximately 99.5% biodiesel yield acquired under optimum conditions of 1:6 volumetric oil-to-methanol ratio, 1% KOH catalyst at 40ºC reaction temperature and 320 rpm stirring speed. Result of the test showed that the biodiesel production from PSCO and WSCO exhibited no considerable differences. Afterwards Bakir T. Emaad and Fadhil B. Abdelrahman [33] presented work on single step transesterification and two step transesterification, namely acid-base and base–base catalyzed transesterification process for production of biodiesel from Chicken fried oil. For this purpose, hydrochloric acid and potassium hydroxide with methanol were used. The results disclosed that two step base catalyzed transesterification was better compared to other methods. It resulted in higher yield and better fuel properties.

Table 6: Major properties of premium diesel and biodiesel used

ISBN: 978-93-86171-27-6

	Premium diesel	B100	Test method
Density at 20 °C (g/mL)	0.826	0.86	ASTM D 1298
Kinematic viscosity at 40 °C (cSt)	2.73	4.49	ASTM D 445
Cetane index	46.2	44.28 48.05	ASTM D 976 EN ISO 4264
Flash point (°C)	89	122	ASTM D 93
Water and sediment (vol.%)	<1	0.22	ASTM D 2709
Gross Heating Value (cal/g)	11411.4	9850.6	ASTM D 240

Prafulla D. Patil *et al.* [34] carried out comparative study on biodiesel production from waste cooking oil using sulfuric acid (Two-step) and microwave-assisted transesterification (One-step). The two-step transesterification process was used to produce bio-diesel (alkyl ester) from high free fatty acid (FFA) waste cooking oil. While Microwave- assisted transesterification was done by using catalytic BaO and KOH in biodiesel production from waste cooking oil. The study shown that that the microwave-heating method consumes less than 10% of the energy to achieve the same yield as the conventional heating method. Further, fuel properties of biodiesel produced were compared with ASTM Standards for biodiesel and regular diesel. In important study Suvendu Mohanty *et al.* [35] observed that from Waste cooking oil CO emissions are increased with increase in engine load. Further it was found that volume of CO initially decreases but increase at full load indicating better burning conditions at higher temperature assisted by improved spraying qualities with uniform charge preparations of biodiesel. The emissions of unburnt hydrocarbon for biodiesel exhaust due to lower than that of diesel fuel the increased gas temperature and higher cetane number of biodiesel could be responsible for this decrease. Higher temperature of burnt gases in biodiesel fuel helps in preventing condensation of higher hydrocarbon reducing. While Canesin Antonio Edmilson *et al.* [36] produced biodiesel from Residual oils and also check the viability and degradation level of production process. Residual bovine, chicken and soybean oils were used for biodiesel production process. They used four transesterification methods, using acidic and basic catalysis and, gas chromatography with flame ionization detector (GC–FID). They concluded use of acidic catalysis at a lower temperature were the most efficient in the biodiesel production process. In the recent study Farooq Muhammad and Ramli Anita [37] prepared catalysts from raw chicken bones for transesterification reaction of waste cooking oil for biodiesel production. The study revealed that heterogeneous catalyst calcined at

900°C exhibited good catalytic activity in the transesterification of WCO, providing maximum biodiesel yield of 89.33% at 5.0 g of catalyst loading, 15:1 methanol to oil molar ratio at temperature of 65°C in reaction time of 4 h. The effect of molar ratio, catalyst amount and temperature observed by the researcher on the yield of biodiesel is shown in fig. 8.

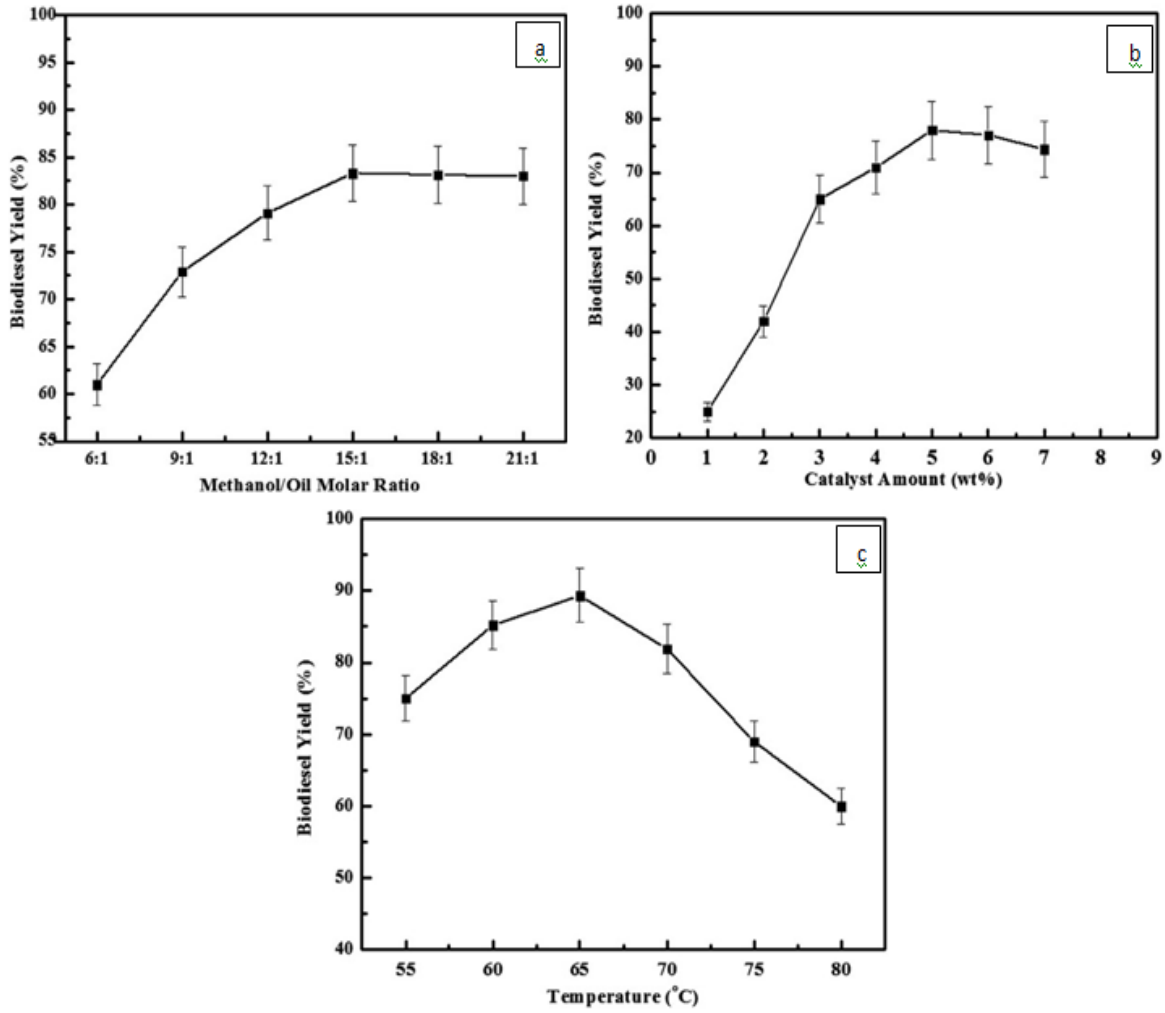

Figure 8: Effect Of (A) Molar Ratio (B) Catalyst Amount And (C) Temperature On Biodiesel Yield

IV. CONCLUSION

This work has provided a comprehensive literature review of the previous research work carried out in past years on production of biodiesel from edible, non-edible and waste cooking oil. An effort has been made to comprise all the important contributions and highlighting the most pertinent literature available for investigating the feedstocks of biodiesel. The conclusion from the current literature survey are as follows: -

a) Biodiesel is an important alternative transportation fuel and it possess properties like renewability, biodegradability, non- toxicity and environmentally friendly benefits.
b) Biodiesel can be produced from different feedstock containing fatty acids such as animal fats, edible oils, non-edible oils, and waste cooking oils and by products of the refining vegetables oils.
c) Transesterification is a commonly employed method for its production. The purpose of this method is to reduce the viscosity of oil or fat using acid or base catalyst in the presence of methanol or ethanol.
d) Transesterification with alkali catalyst (KOH and NaOH) is more economical than acid catalyst and enzyme catalyst.

e) The biodiesel production is strongly affected by parameters such as molar ratio of alcohol, reaction temperature, reaction time and catalyst concentration.

V. ACKNOWLEDGMENT

The review presented in this work is by no means complete but it gives a comprehensive review of production of biodiesel from various feedstocks. The author wishes to apologize for the unintentional exclusions of missing references and would appreciate receiving comments and pointers to other relevant literature for a future update.

REFERENCES

[1] Mohammed H. Chakrabarti, Rafiq Ahmad. Trans esterification studies on castor oil as a first step towards its use in bio diesel production. Pakistan Journal of Botany 2008;40:1153-1157.

[2] Georgogianni K.G., Katsoulidis A.K., Pomonis P.J., Manos G., Kontominas M.G. Transesterification of rapeseed oil for the production of biodiesel using homogeneous and heterogeneous catalysis. Fuel Processing Technology. 2009;90(7-8):1016-1022.

[3] Gerald Kafuku, Man Kee Lam, Jibrail Kansedo, Keat Teong Lee, Makame Mbarawa. *Croton megalocarpus* oil: A feasible non-edible oil source for biodiesel production. Bioresource Technology. 2010;101(18):7000-7004.

[4] Sinha Shailendra, Agarwal Kumar Avinash, and Garg Sanjeev. Biodiesel development from rice bran oil: transesterification process optimization and fuel characterization. Energy Conversion and Management. 2008; 49):1248–1257.

[5] Issariyakul Titipong and Dalai K. Ajay. Biodiesel production from greenseed canola oil. Energy Fuels 2010;24: 4652–4658.

[6] Giovanilton F. Silva, Fernando L. Camargo, Andrea L.O. Ferreira. Application of response surface methodology for optimization of biodiesel production by transesterification of soybean oil with ethanol. Fuel Processing Technology 2011;92:407–413.

[7] Ying Tang, Gang Chen, Jie Zhang, Yong Lu. Highly active CaO for the transesterification to biodiesel production from rapeseed oil. Bulletin of the Chemical Society of Ethiopia 2011;25(1):37-42.

[8] D.Y.C. Leung, Y. Guo. Transesterification of neat and used frying oil:Optimization for biodiesel production. Fuel Processing Technology 2006;87:883-890.

[9] Lingfeng Cui, Guomin Xiao, Bo Xu, and Guangyuan Teng. Transesterification of cottonseed oil to biodiesel by using heterogeneous solid basic catalysts. Energy & Fuels 2007;21:3740–3743.

[10] Oguntola J ALAMU, Opeoluwa DEHINBO, Adedoyin M SULAIMA. Production and testing of coconut oil biodiesel fuel and its blend. Leonardo Journal of Sciences 2010;16:95-104.

[11] Md. Abdul Wakil, Z.U. Ahmed, Md. Hasibur Rahman, Md. Arifuzzaman. Study on fuel properties of various vegetable oil available in Bangladesh and biodiesel production. International Journal of Mechanical Engineering 2012;2(05):10-17.

[12] Eman N. Ali, Cadence Isis Tay. Characterization of biodiesel produced from palm oil via base catalyzed transesterification. Procedia Engineering 2013;53:7-12.

[13] Madhuchanda Banerjee, Binita Dey, Jayanta Talukdar, Mohan Chandra Kalita. Production of biodiesel from sunflower oil using highly catalytic bimetallic gold-silver core-shell nanoparticles. Energy. 2014;30:1-5.

[14] Ruamporn Nikhom, Chakrit Tongurai. Production development of ethyl ester biodiesel from palm oil using a continuous deglycerolisation process. Fuel 2014;117:926-931.

[15] Azam Mohibbe M., Amtul Waris, N.M. Nahar. Prospects and potential of fatty acid methyl esters of somenon-traditional seed oils for use as biodiesel in India. Biomass and Bioenergy 2005;29:293–302.

[16] Rakesh Sarin, Meeta Sharma, S. Sinharay, R.K. Malhotra. Jatropha–Palm biodiesel blends: An optimum mix for Asia. Fuel 2007;86: 1365–1371.

[17] A.K. Tiwari, A. Kumar, H. Raheman. Biodiesel production from Jatropha (*Jatropha curcas*) with high free fatty acids: an optimized process. Biomass and Bioenergy 2007;31:569-575.

[18] Hanny Johanes Berchmans, Shizuko Hirata. Biodiesel production from crude *Jatropha curcas* L. seed oil with a high content of free fatty acids. Bioresource Technology 2008;99:1716–1721.

[19] Kapilan N, Reddy R.P. Evaluation of methyl esters of Mahua oil (*Madhuca indica*) as Diesel Fuel. Journal of American Oil Chemists Society. 2008;85:185-188.

[20] Kansedo Jibrail, Lee Teong Keat and Bhatia Subhash. *Cerbera odollam* (Sea Mango) oil as a promising non-edible feedstock for biodiesel production. Fuel 2009;88:1148-1150.

[21] Padhi S.K and Singh R.K. Optimization of esterification and transesterification of Mahua (*Madhuca indica*) oil for production of biodiesel. Journal of Chemical and Pharmaceutical Research. 2010;5: 599-608.

[22] Bello E.I., A. Makanju. Production, characterization and evaluation of castor oil biodiesel as alternative fuel for diesel engines. Emerging Trends in Engineering and Applied Science 2011;2:525-530.

[23] Deshpande D.P., Urunkar Y.D., Thakare P.D. Production of Biodiesel from Castor Oil using acid and Base catalysts. Research Journal of Chemical Sciences 2012;2:51-56.

[24] Widayat, Agam Duma Kalista Wibowo, Hadiyanto. Study on production process of biodiesel from rubber seed (hevea brasiliensis) by in situ (trans) esterification method with acid catalyst. Energy Procedia. 2013;32:64-73.

[25] Hasan Ali Md., Mohammad Mashud, Rowsonozzaman Rubel Md., Rakibul Hossain Ahmad. Biodiesel from Neem oil as an alternative fuel for Diesel engine. ,Procedia Engineering 2013; 56:625- 630.

[26] Lieke Riadi, Edy Purwanto, Hendrik Kurniawan and Ria Oktaviana. Effect of Bio-Based Catalyst in Biodiesel Synthesis. Procedia Chemistry, 2014; 9:172-181.

[27] Hotti R Siddalingappa and Hebbal D Omprakash). Biodiesel production and fuel properties from non-edible Champaca (*Michelia champaca*) seed oil for use in diesel engine. Journal of Thermal Engineering. 2015;1330-336.

[28] S. Zheng, M. Kates, M.A. Dube, D.D. McLean. Acid-catalyzed production of biodiesel from waste frying oil. Biomass and Bioenergy 2006;30:267–272.

ISBN: 978-93-86171-27-6

[29] Yong Wang, Shiyi Ou, Pengzhan Liu, Zhisen Zhang. Preparation of biodiesel from waste cooking oil via two-step catalyzed process. Energy Conversion and Management 2007;48:184–188.

[30] Issariyakul, T., Kulkarni, M.G., Dalai, A.K., Bakhshi, N.N. Production of biodiesel from waste fryer grease using mixed methanol/ethanol system. Fuel Process Technol 2007;88:429-436.

[31] Ya-fen Lin, Yo-ping Greg Wu, Chang-Tang Chang. Combustion characteristics of waste-oil produced bio-diesel/diesel fuel blends. Fuel 2007;86:1772-1780.

[32] Hossain A.B.M.S. and Boyce A.N. Biodiesel production from waste sunflower cooking oil as an environmental recycling process and renewable energy. Bulgarian Journal of Agricultural Science. 2009;15: 312-317.

[33] Bakir T. Emaad, Fadhil B. Abdelrahman. Production of biodiesel from chicken frying oil. Pak. J. Anal. Environ. Chem. 2011;12: 95-101.

[34] Patil D. Prafulla, Gude Gnaneswar Veera, Reddy K. Harvind, Muppaneni Tapaswy and Deng Shuguang . Biodiesel production from waste cooking oil using sulfuric acid and microwave irradiation processes. Journal of Environmental Protection. 2012;3107-113.

[35] Suvendu Mohanty, Dr. Om Prakash. Analysis Of Exhaust Emission Of Internal Combustion Engine Using Biodiesel Blend. International Journal of Emerging Technology and Advanced Engineering 2013;3(05):731-742.

[36] Edmilson Antonio Canesin, Cláudio Celestino de Oliveira, Makoto Matsushita, Lucia Felicidade Dias, Mayka Reghiany Pedrao, Nilson Evelazio de Souza. Characterization of residual oils for biodiesel production. Electronic Journal of Biotechnology 2014;17:39-45.

[37] Farooq Muhammad and Ramli Anita. Biodiesel production from low FFA waste cooking oil using heterogeneous catalyst derived from chicken bones. Renewable Energy. 2015;76:362-368.

Materials Science and Engineering C 75 (2017) 1206–1213

Contents lists available at ScienceDirect

Materials Science and Engineering C

journal homepage: www.elsevier.com/locate/msec

Role of cellulose functionality in bio-inspired synthesis of nano bioactive glass

Nidhi Gupta, Deenan Santhiya *

[a] Delhi Technological University, Department of Applied Chemistry and Polymer Technology, Bawana Road, Delhi 110 042, India

ARTICLE INFO

Article history:
Received 7 December 2016
Received in revised form 8 February 2017
Accepted 3 March 2017
Available online 07 March 2017

Keywords:
Cellulose
Methyl cellulose
Bioactive glass
In situ nanoparticulate composite

ABSTRACT

In search of abundant cheaper natural polymer for bio-inspired bioactive glass nanoparticles synthesis, cellulose and its derivatives have been considered as a template. Different templates explored in the present studies are pure cellulose, methyl cellulose and amine grafted cellulose. To the best of our knowledge, for the first time of the considered templates, pure cellulose and amine grafted cellulose results in *in situ* nano particulate composite formation while interestingly methyl cellulose proves to be an excellent sacrificial template for the synthesis of uniform bioglass nanoparticles of diameter in the range of 55 nm. Further, viscoelastic measurements were carried out using dynamic mechanical analyzer. Herein, an attempt has been made to establish structure-mechanical relationship based on the templates. Moreover, *in vitro* bioactivity is also observed to be affected by the nature of the template molecule used for the synthesis of bioactive glass.

© 2017 Elsevier B.V. All rights reserved.

1. Introduction

Bioactive glass, recently known third generation adhesive biomaterial [1], is well-known bone regenerative material. Since, its discovery by Hench [2] bioglass is known for the formation of bone-like hydroxyapatite on its surface which eases in healing of the fractured bone sites. In our previous investigations, different organic templates have been explored for the bio-inspired synthesis of bioactive glass materials [3,4,5]. To the best of our knowledge, first time an attempt has been made to utilize the natural, cheaper and abundant organic molecule, cellulose and its derivatives as a template. Cellulose, a versatile biopolymer is widely used in the bio-medical field owing to its abundancy, mechanical strength, good potential for chemical modification and biocompatibility [6]. Cellulose finds wider application in the field of wound healing, blood vessel replacement and skin tissue engineering [6]. Recently, it has gained attention in the area of bone tissue engineering too. Luo et al. investigated bacterial cellulose as a template for the construction of bioactive 3D nanofibrous bioglass scaffold [7]. Various research groups have also attempted for 45S5 bioactive-glass scaffolds coating with wood pulp based microcrystalline cellulose nanowhiskers [8], PVA/microfibrillated cellulose composite [9] for bone tissue engineering. Even electrophoretic deposition of microcrystalline cellulose nanocrystals-45S5 bioactive glass nanocomposite coating on stainless steel for biofunctionalization of metallic orthopedic implants have also been proposed [10].

Unlike the previously reported synthesis procedure, wherein cellulose and bioglass composites have been prepared using pre-synthesized bioglass particles dispersion in cellulose suspensions, herein cellulose has been utilized as a template for the synthesis of highly bioactive glass particles in environmentally friendly processing conditions (at room temperature and using aqueous solvent). However, due to its high molecular weight and crystalline structure, cellulose is insoluble in water and has a poor ability to absorb water. In order to overcome this issue, different functionalized cellulose molecules have been explored as a template. Such as methyl cellulose and amine grafted cellulose to make it readily soluble in water and utilize in bioglass synthesis with the template assisted bio-inspired route. In the present investigation, role of template functionality in the end-product synthesis (bioactive glass) has been intensively evaluated. Structure-mechanical function relationship has been established based on the template (cellulose) functionality.

Earlier often positively charged template such as PAMAM dendrimer [4] and CTAB [5] has been explored as a template for the bioglass synthesis on the basis of electrostatic nucleation of negatively charged network former (TEOS and TEP) precursors of bioglass. However, a negatively charged template has been seldom used [3,10] for bioglass synthesis. In the present piece of study, to the best of our knowledge first time an attempt has been made, wherein both negatively and positively charged templates originating from same parent molecule (cellulose) has been explored. Herein negatively charged cellulose (C) and methyl cellulose (MC) as well as positively charged grafted

* Corresponding author.
E-mail address: deenan.santhiya@dce.ac.in (D. Santhiya).

http://dx.doi.org/10.1016/j.msec.2017.03.026
0928-4931/© 2017 Elsevier B.V. All rights reserved.

cellulose (GC) has been investigated as a template for the bioglass synthesis through bio-inspired route. Although various procedures also been reported for the amination of cellulose using glycidyl methacrylate (GMA) grafting but suffers from the limitation of gamma irradiation requirement [11] and atom transfer radical polymerization [12]. However, the chosen procedure [13] utilizes the versatility of GMA, though hydrophobic is overcome by crosslinker like *N*,*N*′-methylene-bis-acrylamide (MBA) being hydrophilic, increases water uptake by the copolymers [14]. Thus it was also supposed to resolve the issue of cellulose insolubility. Present work concerns the graft polymerization reaction of cellulose as reported earlier [13] with GMA using MBA as a cross linker and benzoyl peroxide as an initiator, followed by amination with dimethyl amine and acid treatment. The objective of the present investigation is to thoroughly explore the effect of different cellulose functionalized templated bioglass material on the bioactivity and damping of the particular material for bone regeneration.

2. Materials and methods

2.1. Materials

Different precursors used for the bioactive glass synthesis, namely tetraethyl orthosilicate (TEOS), triethyl phosphate (TEP), sodium acetate and calcium acetate were procured from Sigma-Aldrich with purity of 99%. Moreover, the different templates considered in the present work such as microcrystalline cellulose (M.W. ~ 36 KDa) and methyl cellulose (M.W. 17 KDa) were procured from Sigma Aldrich. While chemicals for the amine grafting over cellulose (M.W. ~>36 KDa) such as glycidyl methacrylate (GMA) from sigma Aldrich and benzoyl peroxide, *N*,*N*′-methylene-bis-acrylamide (MBA) and dimethylamine from Central Drug House. Milli-Q water was used for all experimental work and all other reagents used were of analytical reagent (AR) grade.

2.2. Methods

2.2.1. Bioactive glass synthesis

Bio-inspired synthesis of bioactive glass was carried out with different cellulose and its derivatives as templates in reference to our previously reported procedure [4]. In brief, template solution was prepared in 10 mM pH 8 TRIZMA buffer. To the continuously stirred template solution at 37 °C in a silicone oil bath, different precursors of bioglass were added in the sequential order of tetraethyl orthosilicate (TEOS) (92.9 g/l), triethyl phosphate (TEP) (10 g/l), sodium acetate (63.6 g/l) and calcium acetate (42.1 g/l) at an interval of half an hour. After 24 h of stirring a white precipitate was formed, centrifuged and washed with 7 wt% NaOH/12 wt% urea/81 wt% water mixture [13] followed by pure milli-Q water and dried at 40 °C in an air oven for 48 h and preserved in desiccator. The different templates explored in the present investigation were cellulose, methyl cellulose and amine grafted cellulose. Amine grafted cellulose was synthesized in accordance with the reported literature [13].

2.2.2. Characterization of bioactive glass

2.2.2.1. XRD. Powder X-ray diffraction experiments were performed for various cellulose templated bioglass particles with Bruker D4 X-ray diffractometer operating at 30 kV and 15 mA using CuKα radiation. XRD patterns were collected in the 2θ range of 10° to 70° with step sizes of 0.02° and a counting time of 6 s per step.

2.2.2.2. FTIR recording. Fourier transform infrared (FTIR) spectra were recorded for the bioactive glass samples. Dried samples were ground and mixed thoroughly with potassium bromide at the ratio of 1:100 and pelleted. The IR spectra of the pellets were then recorded using the NICOLET 380 FTIR operating in the range of 400–4000 cm^{-1} with the resolution of 4 cm^{-1}.

2.2.2.3. Morphology study. The surface morphology of different cellulose templated bioactive glass materials before and after interaction with SBF was characterized by scanning electron microscope (HITACHI-S-3700N). The samples were gold coated and then observed at an accelerating voltage of 12 KeV. The elemental analysis of bioglass sample was carried out by energy dispersive X-ray detector (Thermo Scientific (Ultradry)) and results were collected at 20 keV. Morphology was also studied by transmission electron microscope (TECNAI) operating at 200 KeV.

2.2.2.4. TGA. TGA analysis for all the fabricated bioglass samples was carried out using Perkin Elmer, Pyris Diamond TGA/DTA at the heating rate of 5 °C/min.

2.2.2.5. Zeta potential measurement. Zeta-potential of nanobioglass particles was monitored in trizma buffer pH 8 using ZetasizerNano ZS (Malvern Instruments, UK) instrument. A minimum of 3 readings were recorded for the sample.

2.2.2.6. NMR study. To evaluate the purity and structure of the pure cellulose and tertiary amine grafted cellulose, a ^{13}C NMR spectrum was recorded as reported by Song et al. [15]. First 0.287 g of NaOH, 0.5 g of urea and 3.375 ml of distilled water was frozen for 2–3 h and then 0.125 g of cellulose/amine grafted cellulose was dissolved in the pre-cooled solvent and then was kept in ice-bath for 1 h. After this, it was refrigerated. Each sample (300 μl) was dissolved in 200 μl of deuterium oxide (D_2O) followed by ^{13}C NMR record through the NMR instrument Bruker Avance III at the resonant frequency of 125.7 MHz and 295.7 K temperature.

2.2.2.7. Bioactivity test. For *in vitro* evaluation of the bioactivity of as synthesized bioglass samples, they were incubated in simulated body fluid (SBF) medium as per the procedure described by Kokubo [16] for 4 and 7 days. The SBF solution was refreshed/replaced twice a week because during the course of the experiment the cation concentration decreases, as a result of the changes in the chemistry of the sample [3,17]. The formation of bone-like hydroxyapatite was monitored on samples surface, for evaluating bone forming activity of the sample.

2.2.2.8. DMA study. For characterizing the mechanical features of biomaterials, dynamic mechanical analyzer (DMA) [18], a non-destructive tool was utilized. All viscoelastic measurements were performed using a Perkin Elmer DMA 8000 analyzer, equipped with a material pocket. The measurements were carried out at 37 °C. In brief, powder samples were filled into a material pocket of DMA with 0.27 mm thickness and 6 mm width. The geometry of the sample within the material pocket was then measured by a micrometer and the pocket was clamped in the DMA apparatus (the distance between the clamps was 10 mm) in a single point bending mode. After equilibration at 37 °C, the DMA spectra were obtained during a frequency scan between 0.1 and 10 Hz. The experiments were performed under constant strain amplitude (0.03 mm) and a strain of 5%. Three specimens were tested for each condition.

3. Result and discussion

3.1. Morphological, structural and textural characterization

The chemical shift (δ) of ^{13}C could be clearly observed at 162.7 ppm in the pure urea spectra. A downfield shift in the urea–NaOH spectra could be clearly observed indicating that NaOH interact as an electron acceptor to urea, and the shielding effect is weakened. (Fig not shown) However, the signal of urea–cellulose–NaOH shifted upfield to 166.7 ppm compared with urea–NaOH, indicates that cellulose plays a role as an electron donor. The

recorded spectra are in accordance with the previously reported observation [15]. Interestingly, the addition of urea does not change the ^{13}C resonance of cellulose. A similar chemical shift is observed in the ^{13}C spectra of the cellulose as reported previously [19]. The different carbon positions are marked in the Fig. 1. However, for aminated cellulose, the weaker intensity of the ^{13}C peaks is observed with emergence of new peaks, upfield to the carbon positions. These observations indicate that amine grafting over cellulose essentially a surface derivatization does not disturb the microfibrillar nature of cellulose, in line with ^{13}C NMR results. The new ^{13}C peaks in the tertiary amine grafted cellulose could be attributed to the amination of the sample. Herein, value of δ at 30 and 18 ppm could be assigned to CH_2-NH^+ and $-CH_3$, respectively. Moreover, value of δ at 58 ppm could be attributed to $-CH_2$, –CH present in the backbone of GMA and MBA. Grafting percentage was found to be consistent with reported literature [13]. It is worth mentioning that non-existence of undesirable NMR signals reflects the purity of the synthesized GC.

It is interesting to note that the XRD pattern of naïve cellulose (C) and grafted cellulose (GC) (Fig. S1) is comparable to cellulose based bioglass (CBG) and grafted cellulose based bioglass (GCBG) (Fig. 2(a3, b3)). This indicates the presence of template molecule in the synthesized BG samples. The observed peaks at $2\theta = 15$, 22 and 35 corresponding to miller indices $1\bar{1}0$, 200 and 004 is in good agreement with the XRD spectrum of naïve cellulose reported literature with the JCPDS file no. 00-056-1718 [20,21]. However, the increase in the broadness of the peak pattern for methyl cellulose bioglass (MCBG) (Fig. 2c3) in comparable to naïve methyl cellulose (Fig. S1) indicates the sacrificial role of methyl cellulose template. The microcrystalline cellulose used in the present investigation was observed to possess 78% crystallinity according to peak height method as described by Terinte et al. [22].

Fig. 3(a–c) portrays the powder FTIR spectrum of CBG, GCBG and MCBG along with their corresponding template molecules C, GC and MC respectively. In Fig. 3a, it is pertinent to observe the remnants of cellulose in CBG are clearly reflected *via* retention of similar IR peaks. In detail, FTIR peaks for cellulose molecules assigned to —OH (3418, 2900 cm^{-1}), C—H stretching of CH_2 and CH_3 (1430, 1373, 1320 and 900 cm^{-1}) were observed as a weak peaks in CBG spectra. Interestingly, though peak at 1100 cm^{-1}, characteristic of Si—O—Si bond exists but it is overlapped by characteristic glycosidic bond (C—O—C) symmetric stretching of cellulose. The as synthesized grafted cellulose FTIR spectra is shown in Fig. 3b. Herein peak at 3344 cm^{-1} and 2900 cm^{-1} could be attributed to hydrogen bonded —OH group and —CH stretching from the $—CH_2$ group. A band at 1625 and 1725 cm^{-1} (carbonyl group of ester) provides evidence that GMA has been incorporated on the cellulose backbone with a weak peak at 894 cm^{-1} (epoxy group) indicating that some unopened epoxy rings remains in GC. Most importantly, peaks at 2720, 1470 and 1280 cm^{-1} indicates the presence of $—CH_2—NHR_2$ type nitrogen and aliphatic —CN group, respectively, validating the proper amine grafting of cellulose in consistent with previous results [13].

It is pertinent to observe that for GCBG peak at 1470 and 1280 cm^{-1}, characteristic of C—N bond in GC (Fig. 3b) is observed to get weaker after interaction with precursors. At the end, only a shoulder is observed in the IR spectra along with the retention of $—CH_3$ bond (1373 cm^{-1}). This reveals that $—NH—(CH_3)_2$ moiety remains concealed in the bioglass network which further enhances the positive charge density on GCBG along with other network modifiers as confirmed by zeta (Fig. 4). However, it is pertinent to note that GMA remains in the main chain of grafting and provides the nucleation site to TEOS precursor of bioglass through its C═O coordinate bond and epoxy group. Further, it is noteworthy that under alkaline condition (pH 8), the protonation on the amino group is considerably reduced, thus most probable site for nucleation could be C═O coordinate bond and epoxy group. As also evident from the IR spectra, the doublet peak of C═O at 1635 and 1725 cm^{-1} and epoxy group at 894 cm^{-1} is observed to decrease in

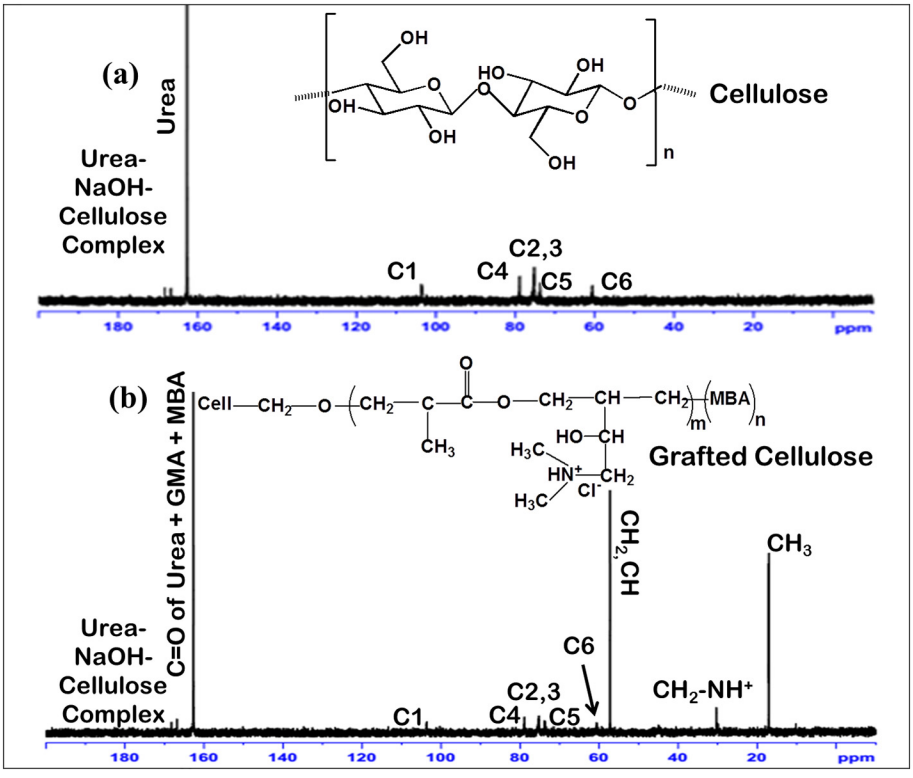

Fig. 1. Represents ^{13}C NMR for (a) Pure cellulose and (b) Grafted cellulose.

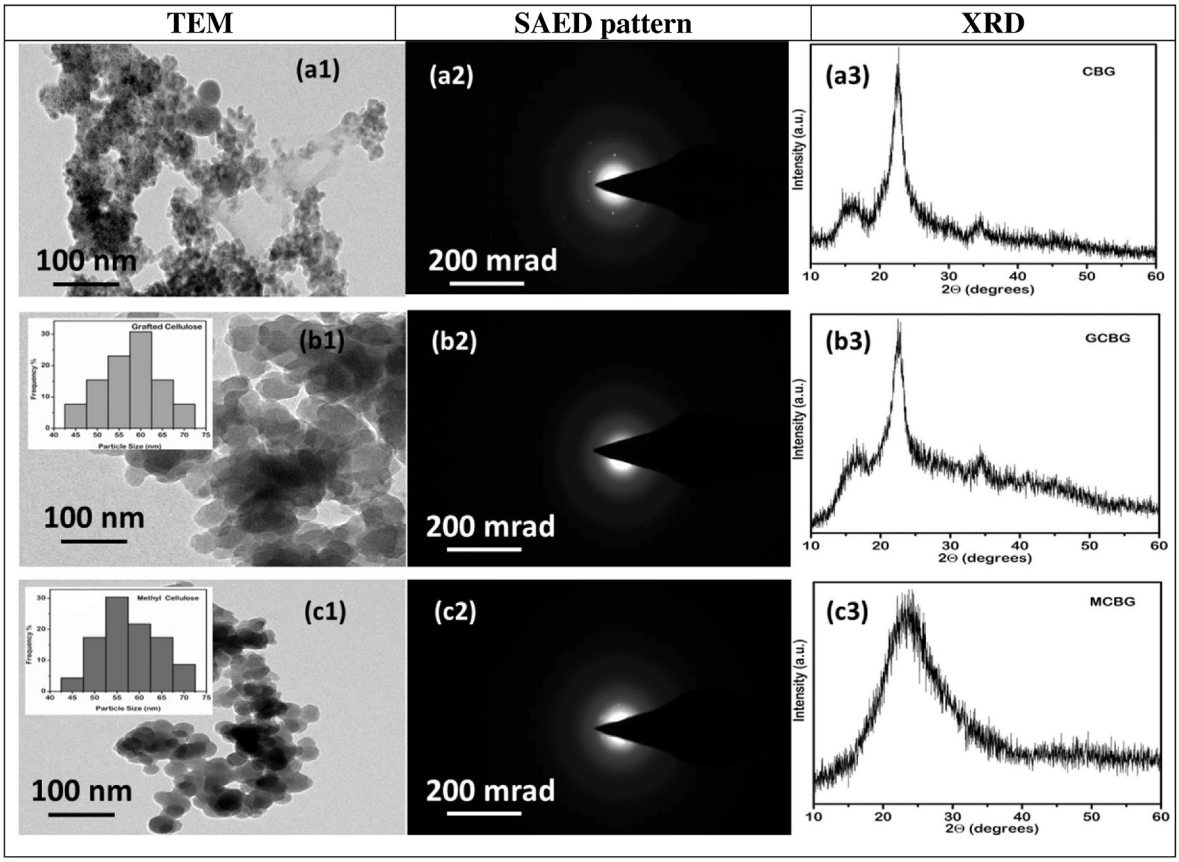

Fig. 2. Represents TEM, SAED pattern and XRD for (a) CBG (b) GCBG and (c) MCBG. Inset shows the particle size distribution according to Image J analysis for (b) GCBG and (c) MCBG.

intensity along with the emergence of new peak at 1155 cm^{-1} corresponding to Si—O bond. Throughout this spectrum study, peak at 1033 cm^{-1} characteristic of C—O—C bond of cellulose backbone is retained as such.

Interestingly, for methyl cellulose, characteristic peak for methyl group (—CH_3) at 1375 cm^{-1} disappears in MCBG, clearly indicates that the site of nucleation in methyl cellulose templated bioglass remains to be —OCH_3. It is evident from the FTIR spectra (Fig. 3c), none

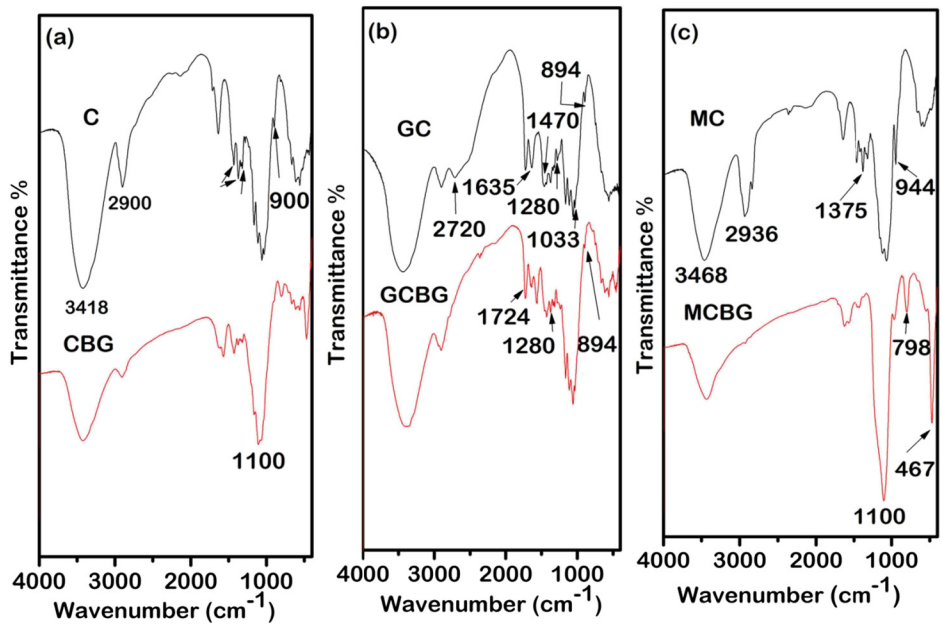

Fig. 3. Represents FTIR spectra for (a) CBG, (b) GCBG and (c) MCBG along with respective parent molecule (a) C, (b) GC and (c) MC.

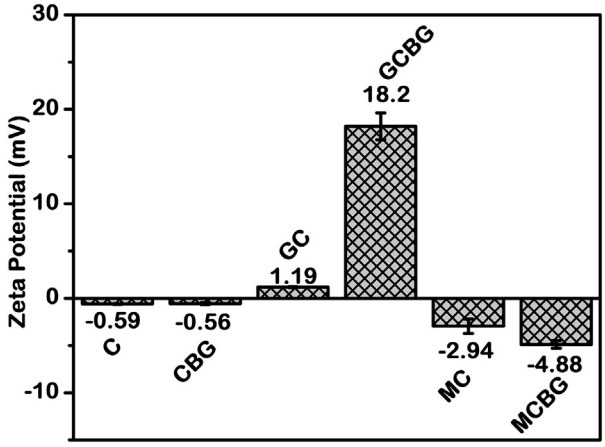

Fig. 4. Represents Zeta Potential for C, CBG, GC, GCBG, MC and MCBG in TRZIMA Buffer (10 mM, pH 8).

of the characteristics peaks of methyl cellulose are visualized. However, within the spectrum of MCBG broad intense peak at 1100 cm^{-1} and a small sharp peak at 467 cm^{-1} attributed to Si—O—Si asymmetric stretching and bending vibrations respectively were observed. A small shoulder at 960 cm^{-1} assigned to non-bridging oxygen together with the surface active silanol (Si—OH) groups, which enhances the rate of apatite formation were observed. The peak at 798 cm^{-1} characteristic of the ring structures of the silicate network was observed [23] attributed to bioglass, strongly supports the fact that methyl cellulose acts as a sacrificial template.

In order to validate the interaction between chosen templates (C, GC and MC) and bioglass precursors, liquid FTIR spectrum (Fig. S2a) was recorded as per the synthesis procedure at various stages of precursor addition for studying the interaction mechanism. It is noteworthy that template peaks disappears due to reduction in their abundancy in the presence of buffer. Moreover, with the sequential interaction of the cellulose template with the aforementioned precursors (Fig. S2a), the characteristic peak of cellulose at 1637 cm^{-1} assigned for —OH bending gets transformed to a doublet at 1637 cm^{-1} and 1552 cm^{-1} suggesting that the template has interacted with the precursors through hydrogen bonding between OH group of cellulose and Si—O^- bond of TEOS Cell-OH——O-Si. TEOS hydrolysis in template solution could be confirmed from the emergence of IR peak at 1442 cm^{-1}. During liquid FTIR spectrum recording, on interaction TEOS at step 1 with the template, formation of Si—O—Si asymmetric stretching at 1074 cm^{-1} is observed which gets lower in intensity and shifts to 1026 cm^{-1} with the subsequent addition of network modifiers *i.e.* sodium acetate and calcium acetate. This indicates the distortion in silica network of CBG on subsequent interaction with network modifiers.

Interestingly, the characteristic peak of cellulose backbone in grafted cellulose (GC) at 1641 cm^{-1} (Fig. S2b) assigned for —OH bending is also overlapped by C═O as it gets transformed to a doublet at 1641 cm^{-1} and 1543 cm^{-1} along with emergence of new peaks suggesting that the template has interacted with the precursors through different bonding such as hydrogen bonding between OH group of cellulose backbone of GC and Si—O^- bond of TEOS as well as carbonyl or epoxy group of GMA present in GC and Si—O—Si of TEOS (C = O–Si, C-O——Si). It is pertinent to recall the structure of GC [Fig. 1b], wherein presence of both —OH and C═O groups could be observed. Remaining similar pattern of interactions was observed as in case of CBG.

Further, in order to understand site of bioglass precursor interaction on the methyl cellulose, the liquid FTIR spectrum (Fig. S2c) was reported. The recorded spectrum was found to be consistent with the previously explored templates (C and GC) precursor interaction studies.

Surface charge for various synthesized bioglass materials along with respective template molecules was analyzed through zeta potential measurement in trizma buffer (pH 8) as depicted in Fig. 4. Interestingly for negatively charged template molecules *i.e.* cellulose and methyl cellulose, corresponding negative charge on CBG and MCBG was recorded in consistent with the previously reported findings on the negative charge possession by the bioglass [4,5]. However, it is pertinent to note that for positively charged template *i.e.* GC, enhancement in the positive charge of GCBG was observed due to the —NH—$(CH_3)_2$ moiety concealment in the bioglass network along with other network modifiers as confirmed by FTIR (Fig. 3).

It is pertinent to observe the remnant cellulose template in CBG through TEM images (Fig. 2 a1). Whereas in the case of GCBG, the remnant GC in not prominently visible, though it might be concealed in the bioglass network as revealed by XRD (Fig. 2b3) and FTIR (Fig. 3b). GCBG particles in the range of 85 nm were observed through Image J analysis. Interestingly, for MCBG remnants of template were not visualized in TEM micrographs, in concurrent with the XRD (Fig. 2c3) and FTIR data (Fig. 3c). MCBG nanoparticles of uniform diameter in the range of 55 nm were observed through Image J analysis. Interestingly, the SAED pattern for all the samples was consistent with the XRD pattern. Furthermore, the EDX results (not shown) confirm that the compositions of the as prepared glasses are in accordance with the theoretical calculations.

Further, the existence of template in the corresponding bioglass was investigated through phenol sulfuric acid chemical analysis test for cellulose as per the standard procedure [24]. It is pertinent to note that for the CBG and GCBG samples, significant remaining of corresponding cellulose templates could be confirmed *via* reported characteristic absorbance at 480 nm through UV–Vis spectra (Fig. 5). However, for MCBG samples such absorbance was found to be insignificant. It is important to recall that molecular weight of C and GC is very high in comparison with MC, thus the removal of C and GC is difficult from CBG and GCBG using the urea–NaOH solution for all the cases as mentioned in Section 2.2.1.

It was interesting to observe that naïve template molecules were stable during TGA analysis (Fig. 6) with negligible weight loss in comparison to respective bioglass synthesized samples except for grafted cellulose wherein, a sharp dip in weight loss percentage at 225 °C is recorded. This could be attributed to the release of chemically absorbed water which is further validated by DMA studies. Of the various cellulose and its derived templated bioglass, for CBG and GCBG upto 150 °C loss of surface water could be observed while beyond 150 °C the loss in weight percentage could be attributed to the loss in chemically absorbed water. However, no such observations could be visualized for MCBG. Thus, it could be concluded that MCBG remained stable throughout TGA analysis and there was no water retention in the sample.

Morphological changes before and after soaking in simulated body fluid (SBF) for bioactivity evaluation was observed through SEM as

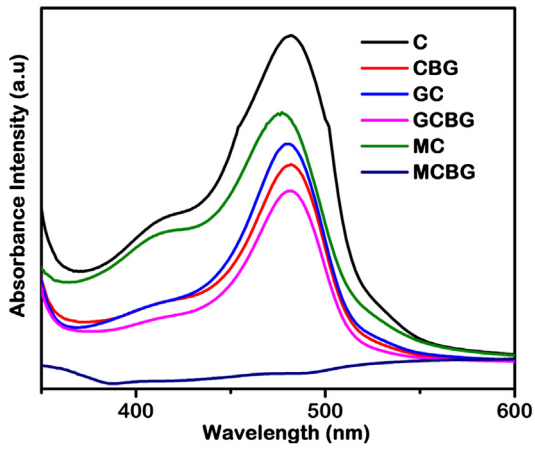

Fig. 5. Represents UV–Vis analysis data for phenol sulfuric acid test.

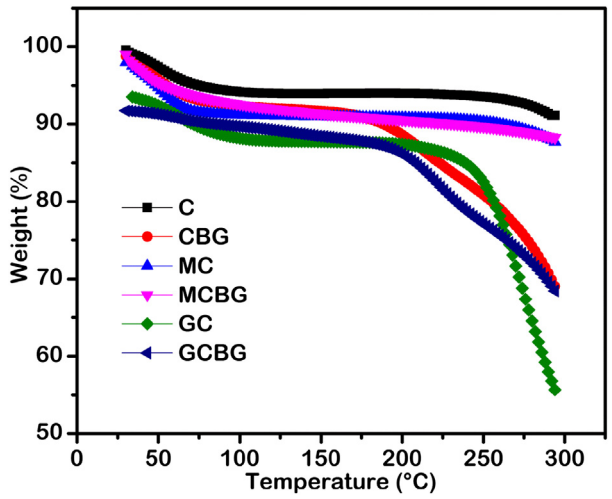

Fig. 6. TGA graph.

displayed in Fig. 7. It was observed that after soaking in SBF, a layer of lath-like apatite microcrystals were formed on the surface of CBG (Fig. 7a1–a3). While in case of MCBG (Fig. 7c1–c3), larger surface area coverage with hydroxyapatite was observed in comparison with GCBG (Fig. 7b1–b3). The SEM image for the synthesized grafted cellulose was similar to reported micrograph by Anirudhan et al. [13]. As observed in Fig. S3, interestingly, the formation of crystalline hydroxyapatite phase formed on interaction with SBF is expected to increase the bone bonding ability. It is pertinent to note that for the diffraction peaks of the SBF soaked CBG and GCBG samples are indexed as the carbonated hydroxyapatite ($Ca_{10}(PO_4)_3(CO_3)_3(OH)_2$) phase [JCPDS-00-019-0272] while SBF soaked MCBG samples corresponds to hydroxyapatite ($Ca_5(PO_4)_3(OH)$) phase [JCPDS-01-073-1731]. Several typical reflections of the SBF soaked samples are indexed and corresponding hkl values are marked in Fig. S3.

Interestingly, after immersing the samples into SBF for 4 days, a peak at 1638 cm^{-1} corresponding to hydroxyl groups for the deposited sample was observed in the FTIR spectra (Fig. S4). In addition to this, the appearance of new peaks corresponding to phosphate group absorption bands with a broad peak centered at 1133 cm^{-1}, a sharp peak at 800 cm^{-1} containing a shoulder at 954 and 569 cm^{-1} were recorded. It is worth to note that the peak at 800 cm^{-1} corresponding to phosphate group is comparatively more intensified for MCBG, thus validating the formation of hydroxyapatite, in consistent with XRD (Fig. S3). Interestingly, for CBG and GCBG presence of carbonate group (small sharp peaks at 1478, 1424 (weak shoulder) and 878 cm^{-1}) was also observed. The presence of phosphate, carbonate and hydroxyl moieties in case of CBG and GCBG indicates that the formed hydroxyapatite was carbonated hydroxyapatite [25] in consent with XRD data (Fig. S3).

Above reported XRD, FTIR and TGA data confirms retention of cellulose and GC templates in their respective CBG and GCBG synthesis. For CBG and GCBG it could be envisaged that within the template matrix the dispersion of *in situ* synthesized nano bioglass particles takes place resulting in particulate composite formation. Pertinently due to interfacial interaction at the interface of bioglass and template, bioglass particles act as a reinforcing material in C and GC template as revealed by viscoelastic property measurement through DMA (Fig. 8a). Herein, for CBG and GCBG a significant increase in storage modulus (E′) with

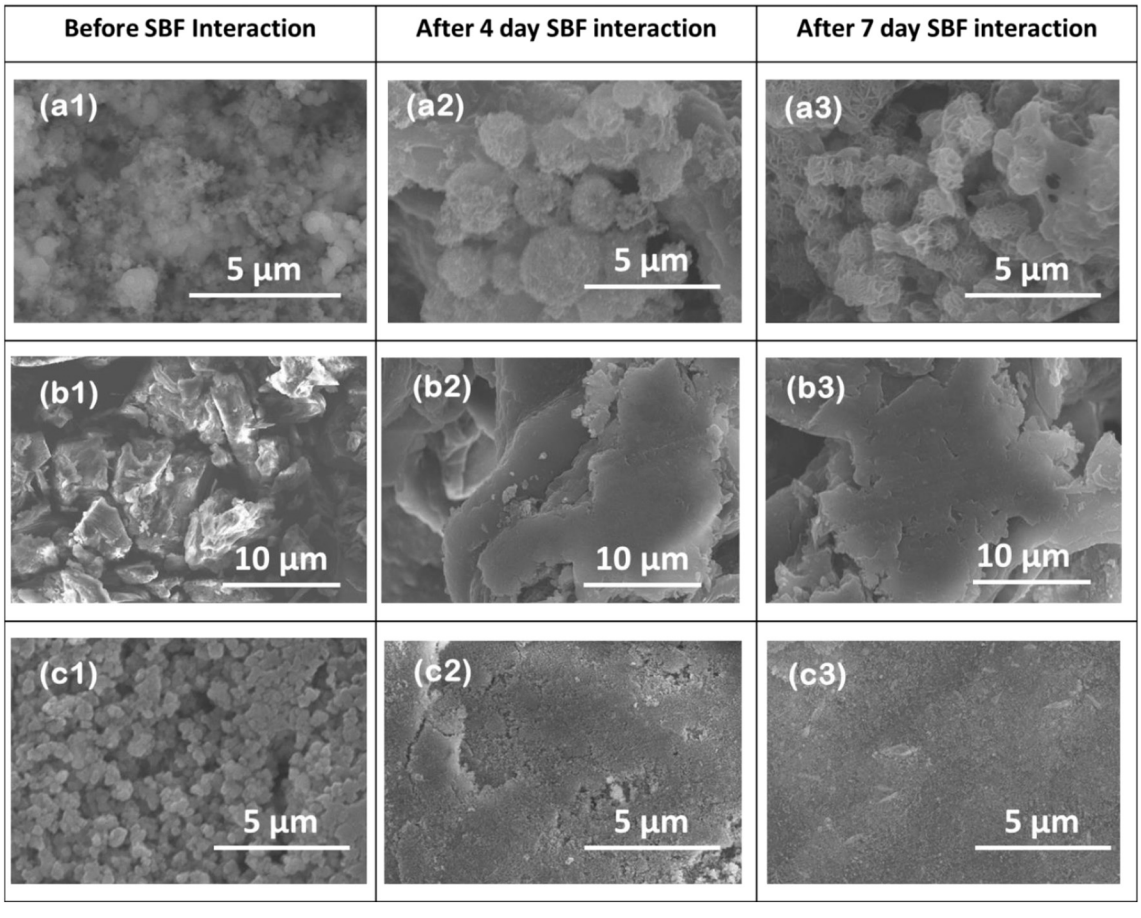

Fig. 7. Represents SEM for (a) CBG (b) GCBG and (c) MCBG before and after interaction with SBF for 4 and 7 days.

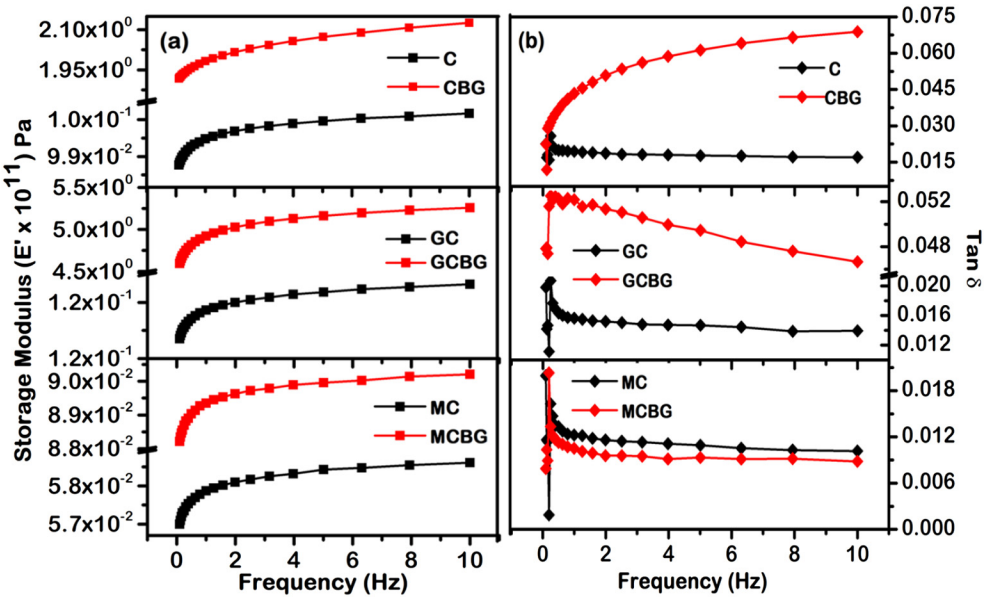

Fig. 8. Represents (a) storage modulus and (b) tan δ for CBG, GCBG and, MCBG with corresponding naïve C, GC and MC, respectively obtained from DMA.

frequency in comparison to respective C and GC was observed thus conforming induction of stiffness to the material. However due to solvent retention in CBG and GCBG network as observed from TGA (Fig. 6), viscous nature is imparted to the material which results in increase in tan delta with frequency (Fig. 8b) in case of CBG and though tan delta decreases with frequency in case of GCBG but in comparison to GC a significant increase in tan delta with frequency is observed *i.e.* damping property decreases with respect to respective templates C and GC. Overall considering the uniformity in *in situ* mineralization of bioglass in GCBG template is more with respect to CBG in which clusters of bioglass nanoparticles are observed (Fig. 2a1), thus suggesting the superiority of GCBG as an *in situ* nano particulate composite for bone regeneration.

Interestingly for MCBG above discussion clearly indicates the complete removal of template MC from MCBG, thus resulting in the formation of pure methyl cellulose templated bioglass nanoparticle synthesis. Viscoelastic measurement for MCBG indicates a comparatively higher value of E′ confirming the stiffness of the material with respect to MC template. In general, it is observed that the value of tan delta decreases with the increase in frequency (Fig. 8b) in comparison to MC suggesting that the damping property was improved by becoming less viscous and more elastic. Moreover, higher capacity to dissipate mechanical energy is imparted by the uniform nano nature of the material. This property will ease to prevent bone bonding material breaking. In this way, MCBG can act as an impact modifier by providing an effective uniform gradient of stress transfer from bone to implant. Possession of aforementioned interesting mechanical damping property makes it a superior material of choice for bone-joint replacement over cellulose and its other derivative templated bioglass. This study clearly highlights the important role played by the template in designing of the bioglass material and directing its properties.

4. Conclusion

The result discussed shows that template plays crucial role in the microstructure of nano bioactive glass synthesis. Interestingly considering cellulose based three different templates, two important aspects has been explored. Firstly, for cellulose and amine grafted cellulose, *in situ* uniform mineralization of bioactive glass within the template matrix leading to nano particulate composite formation takes place. Secondly, methyl cellulose role as a sacrificial template results in uniform nano bioactive glass synthesis with superior bioactivity, mechanical stiffness and damping property leading to a cheaper template assisted synthesis for large scale production. Depending on the type of template, hydroxyapatite of various phases by SBF treatment has been observed to be crystalline in nature indicating their strong bone bonding ability.

Acknowledgement

Authors acknowledge Dr. Ajai Kumar of AIRF, JNU for NMR recordings, Sophisticated Analytical Instrumentation Facility of AIIMS for lending facility to record TEM and Mr. Aman Verma of DTU for the mechanical measurement. Special thanks to Mr. Om Prakash Yadav and Shashank Gupta of Department of Chemistry and Polymer Technology, DTU for NMR analysis and experimental support from time to time, respectively.

Appendix A. Supplementary data

Supplementary data to this article can be found online at http://dx.doi.org/10.1016/j.msec.2017.03.026.

References

[1] L.L. Hench, Chronology of bioactive glass development and clinical applications, New J. Glas. Ceram. 3 (2013) 67–73.
[2] L.L. Hench, The story of bioglass®, J. Mater. Sci. – Mater. Med. 17 (2006) 967–978.
[3] D. Santhiya, H.K. Alajangi, F. Anjum, S. Murugavel, M. Ganguli, Bio-inspired synthesis of microporous bioactive glass-ceramic using CT-DNA as a template, J. Mater. Chem. B 1 (2013) 6329–6338.
[4] N. Gupta, D. Santhiya, A. Aditya, K. Badra, Dendrimer templated bioactive glass-ceramic nanovehicle for gene delivery applications, RSC Adv. 5 (2015) 56794–56807.
[5] N. Gupta, D. Santhiya, A. Aditya, Tailored smart bioactive glass nanoassembly for the dual antibiotic *in vitro* sustained release against osteomyelitis, J. Mater. Chem. B 4 (2016) 7605–7619.
[6] K.C. Wojciech, J.Y. David, K. Marek, R.M. Brown, The future prospects of microbial cellulose in biomedical applications, Biomacromolecules 8 (1) (2007) 1–12.
[7] L. Honglin, J. Dehui, L. Wei, X. Jian, L. Chunzhi, X. Guangyao, Z. Yong, W. Yizao, Constructing a highly bioactive 3D nanofibrous bioglass scaffold via bacterial cellulose-templated sol-gel approach, Mater. Chem. Phys. 176 (2016) 1–5.
[8] Wei L., Nere G., Uxua P. de L., Yaping D., Rainer D., Alina G., Judith A. R., Dirk W.S., A.R. Boccaccini, 45S5 bioactive glass-based scaffolds coated with cellulose nanowhiskers for bone tissue engineering, RSC Adv. 4 (2014) 56156–56164.
[9] L. Bertolla, I. Dlouhý, A. Philippart, A.R. Boccaccini, Mechanical reinforcement of Bioglasss-based scaffolds by novel polyvinyl alcohol/microfibrillated cellulose composite coating, Mater. Lett. 118 (2014) 204–207.

[10] Q. Chen, Y. Yang, U. Pérez de Larraya, N. Garmendia, S. Virtanen, A.R. Boccaccini, Electrophoretic co-deposition of cellulose nanocrystals-45S5 bioactive glass nanocomposite coatings on stainless steel, Appl. Surf. Sci. 362 (2016) 323–328.
[11] M. Barsbay, O. Güven, Y. Kodama, Amine functionalization of cellulose surface grafted with glycidyl methacrylate by γ-initiated RAFT polymerization, Radiat. Phys. Chem. 124 (2016) 140–144.
[12] C. Lin, S. Qiao, D. Liu, M. Liu, Cellulose functionalization via ATRP grafting of glycidyl methacrylate for Cr (VI) adsorption, Chin. J. Chem. 31 (2013) 1551–1556.
[13] T.S. Anirudhan, S. Jalajamony, Cellulose-based anion exchanger with tertiary amine functionality for the extraction of arsenic (V) from aqueous media, J. Environ. Manag. 91 (2010) 2201–2207.
[14] Y.A. Aggour, Thermal decomposition behavior of ethyl cellulose grafted copolymers in homogeneous media, J. Mater. Sci. 35 (2000) 1623–1627.
[15] J. Song, H. Ge, M. Xu, Q. Chen, L. Zhang, Study on the interaction between urea and cellulose by combining solid-state ^{13}C CP/MAS NMR and extended Hückel charges, Cellulose 21 (2014) 4019–4027.
[16] T. Kokubo, Bioactive glass ceramics: properties and applications, Biomaterials 12 (1991) 155–163.
[17] Q.Z. Chen, I.D. Thompson, A.R. Boccaccini, 45S5 bioglass®-derived glass–ceramic scaffolds for bone tissue engineering, Biomaterials 27 (2006) 2414–2425.
[18] S.G. Caridade, E.G. Merino, N.M. Alves, V.Z. Bermudez, A.R. Boccaccini, J.F. Mano, Chitosan membranes containing micro or nano-size bioactive glass particles: evolution of biomineralization followed by in situ dynamic mechanical analysis, J. Mech. Behav. Biomed. Mater. 20 (2013) 173–183.
[19] B. Xiong, P. Zhao, K. Hu, L. Zhang, G. Cheng, Dissolution of cellulose in aqueous NaOH/urea solution: role of urea, Cellulose 21 (2014) 1183–1192.
[20] A.W. Morawski, E.K. Nejman, J. Przepiórski, R. Kordala, J. Pernak, Cellulose TiO_2 nanocomposite with enhanced UV–Vis light absorption, Cellulose 20 (3) (2013) 1293–1300.
[21] L. Cabrales, N. Abidi, F. Manciu, Characterization of developing cotton fibers by confocal Raman microscopy, Fibers 2 (2014) 285–294.
[22] N. Terinte, R. Ibbett, K.C. Schuster, Overview on Native Cellulose and Microcrystalline Cellulose I Structure Studied by X-ray diffraction (WAXD): Comparison Between Measurement Techniques, 89, Lenzinger Berichte, 2011 118–131.
[23] A.S. Herman, Infrared Hand Book, Plenum, New York, 1963.
[24] M. DuBois, K.A. Gilles, J.K. Hamilton, P.A. Rebers, Fred Smith, Colorimetric method for determination of sugars and related substances, Anal. Chem. 28 (3) (1956) 350–356.
[25] B. Lei, X. Chen, Y. Wang, N. Zhao, C. Du, L. Fang, Influence of sintering temperature on pore structure and apatite formation of a sol–gel-derived bioactive glass, J. Am. Ceram. Soc. 93 (1) (2010) 32–35.

Accepted Manuscript

Single NUV band pumped PbO-GeO_2-TeO_2:Tb^{3+} yellowish green emitting glass material for tricolor white LEDs

M. Jayasimhadri, Kaushal Jha, B.V. Ratnam, Hyun-Joo Woo, Kiwan Jang, A.S. Rao, D. Haranath

PII: S0925-8388(17)31044-7

DOI: 10.1016/j.jallcom.2017.03.252

Reference: JALCOM 41290

To appear in: *Journal of Alloys and Compounds*

Received Date: 13 September 2016

Revised Date: 16 February 2017

Accepted Date: 19 March 2017

Please cite this article as: M. Jayasimhadri, K. Jha, B.V. Ratnam, H.-J. Woo, K. Jang, A.S. Rao, D. Haranath, Single NUV band pumped PbO-GeO_2-TeO_2:Tb^{3+} yellowish green emitting glass material for tricolor white LEDs, *Journal of Alloys and Compounds* (2017), doi: 10.1016/j.jallcom.2017.03.252.

This is a PDF file of an unedited manuscript that has been accepted for publication. As a service to our customers we are providing this early version of the manuscript. The manuscript will undergo copyediting, typesetting, and review of the resulting proof before it is published in its final form. Please note that during the production process errors may be discovered which could affect the content, and all legal disclaimers that apply to the journal pertain.

ACCEPTED MANUSCRIPT

Single NUV Band Pumped PbO-GeO_2-TeO_2:Tb^{3+} Yellowish Green Emitting Glass Material for Tricolor White LEDs

M. Jayasimhadri[1], Kaushal Jha[1], B.V. Ratnam[2], Hyun-Joo Woo[2], Kiwan Jang*[,2], A.S. Rao[1], D. Haranath[3]

[1]*Luminescent Materials Research Lab (LMRL), Department of Applied Physics, Delhi Technological University, Delhi - 110 042, India*

[2]*Department of Physics, Changwon National University, Changwon, Korea 641-773*

[3]*CSIR-National Physical Laboratory, Dr. K.S. Krishnan Road, New Delhi 110012, India*

Abstract

In this work, Tb^{3+} ions doped lead-germanate-tellurite (LGT) glasses were prepared by conventional melt quenching technique with different dopant concentrations ranging from 0.5 to 3.5 mol %. X-ray diffraction (XRD) and FT-IR analysis were carried out to analyze the structural properties of LGT glass. The excitation spectra revealed a single band centered in the NUV region at 380 nm by monitoring emission at 545 nm. The emission spectra consist of four bands, which are attributed to the $^5D_4 \rightarrow {}^7F_J$ (J= 3-6) transitions. Among these transitions, the strong emission band was observed at 545 nm corresponding to the $^5D_4 \rightarrow {}^7F_5$ transition and the optimized doping concentration of Tb^{3+} ions was 2 mol %. The Huang's theory and I-H model indicate the possibility of energy transfer via electric dipole-dipole interaction between Tb^{3+} ions. The CIE chromaticity coordinates were (x = 0.282 and y = 0.614) and emits intense yellowish green light. The decay curves measured for $^5D_4$ level for the samples with different doping concentrations and the lifetime for the optimized sample was 548 µs. The results indicated that these glasses have potential applications in solid state lighting and display devices.

Keywords: Rare earths, Glasses, Photoluminescence Spectra, CIE Chromaticity Coordinates

*Corresponding Author: E-mail: kwjang@changwon.ac.kr (Kiwan Jang),
Tel.: +82-55-3427, Fax: +82-55-267-0264

1. Introduction

Solid state lighting (SSL) in the form of white light emitting diodes (w-LEDs) have emerged as a highly competent and viable lighting technology as an alternative to incandescent and fluorescent lamps due to higher efficiency, longer lifetime and environment-friendly characteristics [1]. Phosphor based w-LEDs have received enormous attention in the field of SSL and are fabricated by different approaches. The commercial approach utilizes blue emitting InGaN LED chip in combination with yellow emitting phosphor (YAG:Ce^{3+}). However, this method suffers from the halo effect of blue/yellow color separation and poor color rendering index (CRI) due to lack of red component. Also, the blue InGaN LED chip gets deteriorated by temperature and drive current. To overcome the mentioned shortcomings, the second approach employs the combination of near ultra-violet (NUV) LEDs with RGB phosphors which significantly improves CRI and reduces halo effect [2, 3]. However, in both the approaches phosphor is suspended in the form of powder in an epoxy resin which is made of organic material. The epoxy resin gets damaged at high temperatures and by high energy/power excitation light sources, which affects luminous efficiency and CRI adversely. Therefore, the requirement of a monolithic material having high durability along with superior emission property is required for futuristic applications, which suggested us to propose inorganic glasses as a potential phosphor candidate. The added advantage of glass as phosphor candidate results in a decrement of re-absorption of light. Also, glasses exhibit excellent thermal, mechanical and chemical stability, homogenous light emission, lower production cost and simpler manufacturing technique [4, 5].

Lead germanate glasses doped with rare earth ions have been receiving great interest due to high ion solubility and are promising candidates for applications in optical recorders, optical

amplifiers, infrared to visible converters and laser materials [6-8]. LGT glasses have low phonon energy (~800 cm^{-1}) as compared with heavy oxide glasses based on silicate, phosphates and borates. The low phonon energy results in low non-radiative relaxation rates. These glasses also offer unique characteristics such as high transparency, low melting temperature, high solubility for rare earth ions, good chemical and mechanical stability [9-11]. Recently, Jayasimhadri et al. have reported Sm^{3+} doped lead germanate glasses for laser applications [8]. Among various trivalent rare earth ions, terbium (Tb^{3+}) with $4f^8$ configuration is an important activator ion for luminescent materials due to the emissions mainly originating from $^5D_4 \rightarrow {}^7F_J$ (J= 3-6) transition levels [12]. Chen et al. studied the effect of Tb^{3+} in different heavy germanate glasses and Zur et al. investigated the influence Tb^{3+} on different glass formers with lead oxide [13, 14].

In the present investigation, Tb^{3+} ions doped LGT glasses were prepared for the first time with an aim to develop this glass as one of the components for w-LED fabrication based on RGB approach with NUV excitation. Emission spectra were studied as a function of Tb^{3+} ion concentration and concentration quenching mechanism has been discussed based on Huang theory. CIE chromaticity coordinates were calculated from the emission spectra, which explore the utility of LGT glasses in lighting and display applications.

2. Experimental Work

Glasses with the molar compositions (50-x) PbO + 30 GeO_2 + 20 TeO_2 + x Tb_4O_7 (x = 0.5, 1, 2, 3 and 3.5 mol %) were prepared by conventional melt-quenching technique. The appropriate amounts of oxides were weighed by using an electronic balance having an accuracy of 0.0001 g. The weighed chemicals were mixed by using a pestle mortar for 30 min to obtain homogeneous mixtures. The well-mixed batches were placed in an alumina crucible and then

melted in an electric furnace at the temperature of 1150 ^{o}C for about 1 h. The colorless and transparent melt was then poured onto a pre-heated brass plate and pressed with another brass plate. The prepared glasses were annealed around 330 ^{o}C for 4 h to remove the thermal strains and polished to obtain maximum flatness before measuring spectral properties [15].

The XRD analysis was performed by using X-ray powder diffractometer (Philips X'pert, MPD 3040) with Cu K_{α} radiation (λ = 1.5406 Å). The microstructure of the samples was studied by FE-SEM (Tescan, MIRA II LMH). Fourier-transform infrared (FTIR) measurements were performed with FT/IR-6300 spectrometer in the range 400 to 4000 cm^{-1}. The photoluminescence excitation and emission spectra were measured by Shimadzu, RF 5301PC (150 W xenon lamp) spectrofluorophotometer. The decay analysis was performed using an Edinburgh FLSP900, where a xenon lamp was used as an excitation source. The slit width for excitation and emission measurement was kept at 3 nm and the spectra measured with the step size of 0.2 nm.

3. Results and discussion

3.1. Structural and Morphological Properties

All the prepared glasses were highly transparent. Fig.1 shows the X-ray diffraction pattern of the 1 mol % Tb^{3+} ions doped LGT glass in the range of $10^{o} < 2\theta < 70^{o}$. The XRD pattern represents a broad hump for the prepared glass without any crystalline features indicating the amorphous nature of the glass. Inset of Fig. 1 represents the FE-SEM image of the LGT glass surface, which suggests the homogenous distribution of glassy phase. The XRD spectrum along with FE-SEM image with confirms the amorphous nature of LGT glass.

Infrared spectroscopy was effectively used to investigate the vibrational features in these glasses. The infrared absorption spectrum of 1 mol % Tb^{3+} ions doped LGT glass measured in

the wave number range 400 to 4000 cm^{-1} is shown in Fig. 2. The FT-IR spectrum represents different peaks in the range 400-500 cm^{-1} which is represented in the inset of Fig. 2. In addition to this, there are several peaks centered at 720, 1636, 2354, 2930 cm^{-1} and a broad band in the range 3200 to 3650 cm^{-1}. The band in the range 400-500 cm^{-1} may be attributed to the bending vibrations of Te-O-Te, O-Te-O linkage along with the bending vibration of Pb-O-Pb linkage in PbO_4 tetragonal structural units [16]. The peak located at 470 cm^{-1} may be related to PbO covalent bond, suggesting that the Pb can act as a network former in the glassy host. The band centered at 720 cm^{-1} arises due to the stretching vibration of the Ge-O-Ge in the octahedral structural units of rutile GeO_2 [17]. The peak located around 1636 cm^{-1} is ascribed to the bending vibrations of O-H bonds incorporated by air mixture during preparation of KBr pellets for FT-IR measurements [18]. The bands located near 2354 and 2930 cm^{-1} are due to the asymmetric stretching of the water molecule, while the band located in the range 3200 to 3650 cm^{-1} is ascribed to the symmetric stretching of the water molecule [19].

3.2. Luminescent Properties

Fig. 3 represents the excitation spectra of LGT glasses doped with different Tb^{3+} concentration in the wavelength range from 300 to 450 nm by monitoring the green emission at 545 nm. The spectra revealed only one excitation band of Tb^{3+} ions at 380 nm, which is associated with the transition from ground state $^7F_6$ to $^5G_6$ excited state. This band corresponds to f-f transitions of Tb^{3+} ions with $4f^8$ configuration [20]. The most intense excitation band is observed for 2 mol% of Tb^{3+} concentration. Fig. 4 represents the emission spectra of LGT glasses doped with different Tb^{3+} concentrations from 0.5 to 3.5 mol % by monitoring the excitation at 380 nm. The emission spectra exhibit the well-known characteristic emission bands of Tb^{3+} ions assigned to $^5D_4 \rightarrow {}^7F_J$ (J= 3-6). The intense emission peak was centered at 545 nm

corresponding to the $^5D_4 \rightarrow {}^7F_5$ transition and the remaining three emission bands were centered at 490, 586 and 624 nm corresponding to $^5D_4 \rightarrow {}^7F_6$, $^5D_4 \rightarrow {}^7F_4$ and $^5D_4 \rightarrow {}^7F_3$ transitions, respectively. The peak at 545 nm splits into two peaks due to crystal field splitting. The emission bands cover the range from blue to red region as a result of transitions to different ^7F_j levels [21, 22]. The intense transition $^5D_4 \rightarrow {}^7F_5$ obeys the magnetic dipole selection rule ($\Delta J = \pm 1$) and the transition $^5D_4 \rightarrow {}^7F_6$ is forced electric dipole in nature governed by the selection rule ($\Delta J = 2$) [23, 24]. The inset of Fig. 4 represents the integrated emission intensity of $^5D_4 \rightarrow {}^7F_5$ transition with varying concentration of Tb^{3+} ions. It is evident from both Fig. 4 and its inset that the optimized doping concentration of Tb^{3+} ions is 2 mol % and the emission intensity decreases beyond this concentration. This decrease in emission is termed as concentration quenching phenomenon [22]. The emission spectra does not reveal any emission peak originating from higher excited $^5D_3$ level, which indicates very efficient non-radiative transition to the lower excited $^5D_4$ level [20]. The cross-relaxation process is dominant for not observing any emission peak from $^5D_3$ level. However, at higher concentrations of Tb^{3+}, the quenching of emission at $^5D_4$ level is observed may be due to energy migration and/or cooperative energy transfer to the upper levels as shown in Fig. 5. The channels for the cooperative energy transfer may be possible from $^5D_4$ to ^7D (upper levels). The $^5D_4 \rightarrow {}^7F_J$ transitions are in resonance with $^5D_4 \rightarrow {}^7D$ transitions of Tb^{3+} ions [25, 26]. Therefore, it may be assumed that the energy migration and cooperative energy transfer processes represented in Fig. 5 are playing key role in quenching of emission from $^5D_4$ level. The Huang theory gives the relationship between the integrated luminescent intensity (I) and the activator ion molar concentration (c) which is [27].

$$I \propto \alpha^{\left(1-\frac{s}{d}\right)} \Gamma\left(1+\frac{s}{d}\right) \qquad (1)$$

$$\alpha = c\Gamma(1-\frac{d}{s})\,[X_0\,\frac{(1+A)}{\gamma}]^{\frac{d}{s}} \qquad (2)$$

where γ is the intrinsic transition probability of sensitizer, d is the sample dimension, A and X_0 are constants, s is index of electric multi-pole interaction: which is 6, 8 and 10 for electric dipole-dipole, electric dipole-quadrupole, and electric quadrupole-quadrupole, respectively. If the value of s = 3, the interaction type is an exchange interaction and Γ(1 + s/d) is a gamma function. From equations 1 and 2 it can be derived that:

$$log\left(\frac{I}{c}\right) = -\frac{s}{d}\log c + logf \qquad (3)$$

where *f* is independent of doping concentration. The plot of log (I/c) v/s log(c) for the $^5D_4 \rightarrow {}^7F_5$ transition level is represented in Fig. 6. To obtain the value of the slope, the experimental data was linearly fitted. The calculated value of slope parameter (-s/d) was determined to be -1.67. The slope parameter was multiplied with dimension (d=3) of the sample and the value of s was found to be 5.01, which can be approximated to 6. This value (s) confirmed the energy transfer between Tb^{3+} ions via electric dipole-dipole interaction. Fig. 5 represents the partial energy level diagram for Tb^{3+} ions in LGT glass. When the Tb^{3+} ions in LGT glasses are excited by near ultraviolet excitation of 380 nm, the electrons are excited to the higher $^5G_6$ level and then decay non-radiatively to the $^5D_4$ level. The radiative emission takes place from $^5D_4$ electronic level to different transition levels $^7F_3$, $^7F_4$, $^7F_5$ and $^7F_6$ [22]. Fig. 7 represents the Commission International de l'Eclairage (CIE) chromaticity coordinates of LGT glass for the optimized Tb^{3+} ion concentration on the CIE 1931 chromaticity diagram. The chromaticity coordinates were calculated based on the emission spectrum and found to be (*x*=0.282, *y*=0.614), which falls into the yellowish green region.

Fig. 8 represents the luminescence decay curve for the optimized concentration of Tb^{3+} ions doped LGT glass measured for $^5D_4$ excited level by monitoring the emission at 545 nm under 380 nm excitation. The decay curve was well fitted by bi-exponential function which is given by the relation [28]:

$$I = A_0 + A_1 e^{-t/\tau_1} + A_2 e^{-t/\tau_2}$$

The average lifetime in case of bi-exponential curve is calculated by using relation:

$$\tau_{avg} = \frac{A_1\tau_1^2 + A_2\tau_2^2}{A_1\tau_1 + A_2\tau_2}$$

The average lifetimes for the glass samples containing 0.5, 1.0, 2.0, 3.0 mol% Tb^{3+} dopant concentrations were found to be 752, 721, 548 and 510 µs, respectively. The bi- exponential curve and the decrease in the lifetime with increasing doping concentration indicate the existence of energy transfer process between Tb^{3+}- Tb^{3+} ions. A deeper insight on the type of multipolar interaction involved in energy transfer process can be estimated by using Inokuti-Hirayama (I-H) model on the decay curves. The decay of the luminescence of a donor - acceptor is given by the equation [29, 30]

$$I_t = I_0 \exp\left\{\frac{-t}{\tau_0} - Q\left(\frac{t}{\tau_0}\right)^{\frac{3}{s}}\right\}$$

where, I_t is the luminescence intensity at time t, t is time after excitation, τ_0 is the intrinsic decay time of the donors in the absence of the acceptors. Q is the energy transfer parameter, s is the multipolar interaction parameter and takes the value 6, 8 and 10 for dipole-dipole, dipole-quadrupole and quadrupole-quadrupole interaction, respectively. The decay curves were fitted with I-H model for S=6, as represented in Fig. 9 (a) for different concentrations of Tb^{3+}. For comparison, I-H model fitting for S=6, 8 and 10 of 2 mol% Tb^{3+} doped LGT glass were shown in

Fig. 9 (b). Form Fig. 9 (a) & (b), it is evident that the best fit was obtained for S=6, which confirms the dipole-dipole interaction among Tb^{3+} ions in the LGT glasses. The results of Huang's theory are in agreement with the I-H model.

4. Conclusions

In summary, Tb^{3+} ions doped colorless and optically transparent LGT glasses were successfully synthesized by the melt quenching method. The XRD analysis and SEM micrograph confirmed the amorphous nature of LGT glasses. FT-IR analysis was carried out to analyze the vibrational features present in the glass and the results indicated the role of Pb as a glass former. The excitation spectra has been measured by monitoring emission at 545 nm, which depicted only one band centered at 380 nm in the NUV region. The emission spectra consisted of several emissions bands, which originated from $^5D_4$ to different ^7F_J (J= 3-6) transition levels. The intense emission band corresponds to $^5D_4 \rightarrow {}^7F_4$ transition in the green region centered at 545 nm. The optimized doping concentration of Tb^{3+} ions was 2 mol % and the Huang's theory and I-H model confirms the energy transfer between Tb^{3+} ions via electric dipole-dipole interaction. The CIE chromaticity coordinates (x=0.282, y=0.614) for optimized concentration were falling in the yellowish green region and the lifetime values obtained from the decay curves indicate the existence of energy transfer with increasing Tb^{3+} concentration. The above results clearly indicates the potential applicability of the Tb^{3+} ions doped LGT glasses for solid state lighting and display applications under NUV excitation.

Acknowledgements

This work was financially supported by the National Research Foundation of Korea funded by the Ministry of Education, Science and Technology (NRF–2015–056886). One of the authors

(Dr. M. Jayasimhadri) would like to thank DST-SERB, Govt. of India for sanctioning the research project (No. SB/FTP/PS-082/2014, dt. 02/03/2015).

References:

[1] M. Jayasimhadri, K. Jang, H.S. Lee, B. Chen, S.S. Yi, J.H Jeong, White light generation from Dy^{3+} doped $ZnO-B_2O_3-P_2O_5$ glasses, J. Appl. Phys. 106 (2009) 013105.

[2] S.P. Lee, S.D. Liu, T.S. Chan, T.M. Chen, Synthesis and luminescence properties of novel Ce^{3+}-and Eu^{2+}-doped lanthanum bromothiosilicate $La_3Br(SiS_4)_2$ phosphors for white LEDs, ACS Appl. Mater. Interfaces 8 (2016) 9218-9223.

[3] H. Daicho, T. Iwasaki, K. Enomoto, Y. Sasaki, Y. Maeno, Y. Shinomiya, S. Aoyagi, E. Nishibori, M. Sakata, H. Sawa, S. Matsuishi, H. Hosono, A novel phosphor for glareless white light-emitting diodes, Nat. Commun. 3 (2012) 1132.

[4] H. Masai, Y.Yamada, Y. Suzuki, K. Teramura, Y. Kanemitsu, T. Yoko, Narrow energy gap between triplet and singlet excited states of Sn^{2+} in borate glasses, Sci. Rep. 3 (2013) 3541.

[5] Y.G. Zhao, D.M. Shi, X.F. Wang, J. Liu, Role of B2O3 substitution by SiO_2 on Luminescence properties of Tb^{3+} doped $SiO_2-B_2O_3-Na_2O-BaO$ glass, Phys Procedia 48 (2013) 165-171.

[6] Z. Pan, S. H. Morgan, A. Loper, V. King, B. H. Long, W. E. Collins, Infrared to visible upconversion in Er^{3+} doped lead germinate glass: Effects of Er^{3+} ion concentration, J. Appl. Phys. 77 (1995) 4688.

ACCEPTED MANUSCRIPT

[7] J. Wang, J.R. Lincoln, W.S. Brocklesby, R.S Doel, C.J. Mackechnie, A. Pearson, A.C Topper, D.C Hanna, D.N Payne, Fabrication and optical properties of lead-germanate glasses and a new class of optical fibers doped with Tm^{3+}, J. Appl. Phys. 73 (1993) 8066.

[8] M Jayasimhadri, Eun-Jin Cho, Ki-Wan Jang, Ho Sueb Lee, Sun Il Kim, Spectroscopic properties and judd-ofelt analysis of Sm^{3+} doped lead-germanate-tellurite glasses, J. Phys. D: Appl. Phys. 41 (2008) 175101.

[9] M. Wachtler, A. Speghini, K. Gatterer, H.P. Fritzer, D. Ajo, M. Bettinelli, Optical properties of rare earth ions in lead germinate glasses, J. Am. Ceram. Soc. 81 [8] (1998) 2045-52.

[10] D.S. da Silva, T.A.A. de Assumpção, L.R.P. Kassab, C. B. de Araújo, Frequency upconversion in Nd^{3+} doped PbO-GeO_2 glasses containing silver nanoparticles, J. Alloys Compd. 586 (2014) S516-S519.

[11] L.R.P. Kassab, W.G. Hora, Whualkuer Lozano B., Marcos A.S. de Oliveira b, Glauco S. Maciel, Optical properties of Er^{3+} doped GeO_2-PbO glass: Effect of doping with Bi_2O_3 Opt Commun. 269 (2007) 356-361.

[12] B.C. Jamalaiah, J.S. Kumar, A.M. Babu, T. Sasikala, L.R. Moorthy, Study on spectroscopic and fluorescence properties of Tb^{3+}-doped LBTAF glasses, Physica B 404 (2009) 2020-2024.

[13] G. Chen, Y. Yang, D. Zhao, F. Xia, S. Baccaro, A. Cecilia, M. Nikl, Composition Effects on Optical Properties of Tb^{3+}-Doped Heavy Germanate Glasses, J. Am. Ceram. Soc. 88 (2005) 293-296

[14] L. Żur, M. Sołtys, J. Pisarska, W. A. Pisarski, Absorption and luminescence properties of terbium ions in heavy metal glasses, J Alloy Compd. 578 (2013) 512-516

ACCEPTED MANUSCRIPT

[15] S.K. Mahmuda, K. Swapna, A. Srinivasa Rao, M. Jayasimhadri, T. Sasikala, K. Pavani, L. Rama Moorthy, Spectroscopic properties and luminescence behavior of Nd^{3+} doped zinc alumino bismuth borate glasses, J. Phys. Chem. Solids 74 (2013) 1308-1315.

[16] S. Rada, A. Dehelean, E. Culea, FTIR and UV-VIS spectroscopy investigations on the structure of the europium-lead-tellurate glasses, J. Non-Cryst Solids 357 (2011) 3070-3073.

[17] H. Bahari, S.H.A Aziz, H M. Kamari, W.M.M. Yunus, F.R.M Adikan, The effect of bismuth on the structure and mechanical properties of GeO_2-PbO-Bi_2O_3 ternary bulk glass system, J. Ceram. Soc. Jpn. 120 [7] (2012) 280-285.

[18] Y.B. Saddeek, Network structure of molybdenum lead phosphate glasses: Infrared spectra and constants of elasticity, Physica B 406 (2011) 562-566.

[19] A.M. Efimov, V.G. Pogareva, Water-related IR absorption spectra for some phosphate and silicate glasses, J. Non-Cryst. Solids 275 (2000) 189-198.

[20] J. Liao, B. Qiu, H. Lai, Synthesis and luminescence properties of Tb^{3+}: $NaGd(WO_4)_2$ novel green phosphors, J. Lumin. 129 (2009) 668-671.

[21] F.S. Kao, T.M. Chen, A study on the luminescent properties of new green-emitting terbium activated $CaIn_2O_4$:xTb phosphors, J. Lumin. 96 (2002) 261-267.

[22] J.B. Prasannakumar, Y.S. Vidya, K.S. Anantharaju, G. Ramgopal, H. Nagabhushana, S.C. Sharma, B.D. Prasad, S.C. Prashantha, R.B. Basavaraj, H. Rajanaik, K. Lingaraju, K.R. Prabhakara, H.P. Nagaswarupa, Bio-mediated route for the synthesis of shape tunable Y2O3: Tb^{3+} nanoparticles: Photoluminescence and antibacterial properties, Spectrochim Acta A 151 (2015) 131-140.

[23] Y.C. Fang, X.R. Huang, Y.D. Juang, S.Y. Chu, Color-tunable blue to green $Ca_{4-1.5x}Ta_2O_9:xTb^{3+}$ phosphor: Cross-relaxation mechanism and thermal stability, J. Am. Ceram. Soc., 95 [5] (2012) 1613-1618.

[24] B.V. Ratnam, M. Jayasimhadri, G.B. Kumar, K. Jang, S.S. Kim, Y.I. Lee, J.M. Lim, D.S. Shin, T.K. Song, Synthesis and luminescent features of $NaCaPO_4:Tb^{3+}$ green phosphor for near UV-based LEDs, J Alloy Compd. 564 (2013) 100-104.

[25] A.D. Sontakke, K. Biswas, K. Annapurna, Concentration-dependent luminescence of Tb^{3+} ions in high calcium aluminosilicate glasses, J. Lumin. 129 (2009) 1347-1355.

[26] Y.Y. Choi, K.S. Sohn, H.D. Park, S.Y. Choi, Luminescence and decay behaviors of Tb-doped yttrium silicate, J Mater Res. 16 (2001) 881-889.

[27] Xin-yuan Sun, Shi-ming Huang, Xiao-san Gong, Qing-chun Gao, Zi-piao Ye, Chun-yan Cao, Spectroscopic properties and simulation of white-light in Dy^{3+}-doped silicate glasses, J Non-Cryst. Solids 356 (2010) 98-101.

[28] S.K. Gupta, P.S. Ghosh, N. Pathak, A. Aryab, V. Natarajana, Understanding the local environment of Sm^{3+} in doped $SrZrO_3$ and energy transfer mechanism using time-resolved luminescence: a combined theoretical and experimental approach, RSC Adv. 4 (2014) 29202-29215.

[29] M. Inokuti, F. Hirayama, Influence of Energy Transfer by the Exchange Mechanism on Donor Luminescence, J. Chem. Phys. 43 (1965) 1978.

[30] S.N Rasool, L.R Moorthy, C.K. Jayasankar, Spectroscopic Investigation of Sm^{3+} doped phosphate based glasses for reddish-orange emission, Opt. Commun. 311 (2013) 156–162.

Figure captions:

Fig: 1. X-ray diffraction pattern of 1 mol% Tb^{3+} ions doped LGT glass [Inset: Represents the SEM micrograph of 1 mol % Tb^{3+} LGT glass].

Fig: 2. FT-IR spectrum of 1 mol % Tb^{3+} ions doped LGT glass.

Fig: 3. Excitation spectra of LGT glasses for different concentrations of Tb^{3+} ions.

Fig: 4. Emission spectra of LGT glasses for different concentration of Tb^{3+} ions [Inset: Shows the dependence of $^5D_4 \rightarrow {}^7F_5$ peak intensity at different Tb^{3+} ions]

Fig: 5. Partial energy level diagram for Tb^{3+} ions in LGT glass.

Fig. 6. Relationship of log (I/c) with log(c) for $^5D_4 \rightarrow {}^7F_5$ transition of LGT glasses.

Fig: 7. CIE chromaticity coordinates of 2 mol % Tb^{3+} ions doped LGT glass.

Fig: 8. Decay curves for LGT glasses with different Tb^{3+} concentrations.

Fig. 9. (a) Decay curves for LGT glasses with different concentrations of Tb^{3+} fitted with I-H model for S=6 and (b) Decay curves for 2 mol% Tb^{3+} doped LGT glass fitted for S=6, 8 and 10.

ACCEPTED MANUSCRIPT

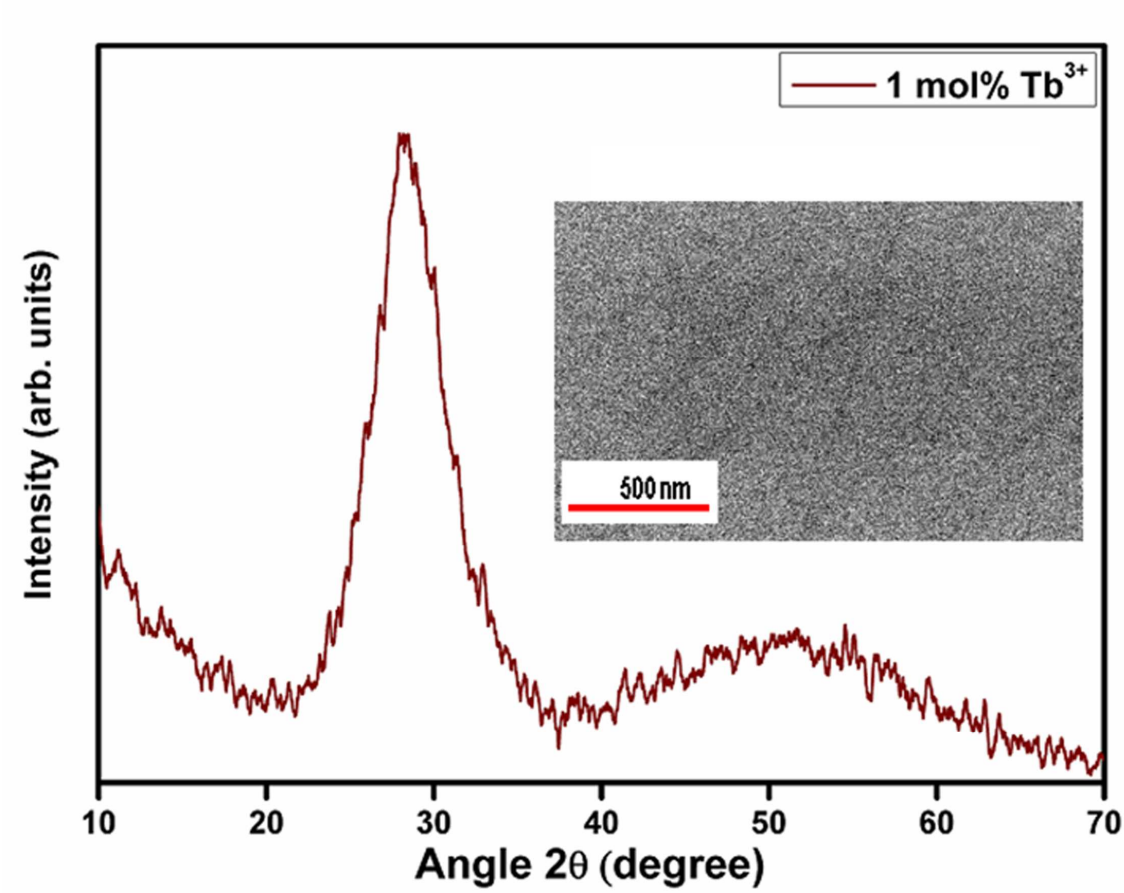

ACCEPTED MANUSCRIPT

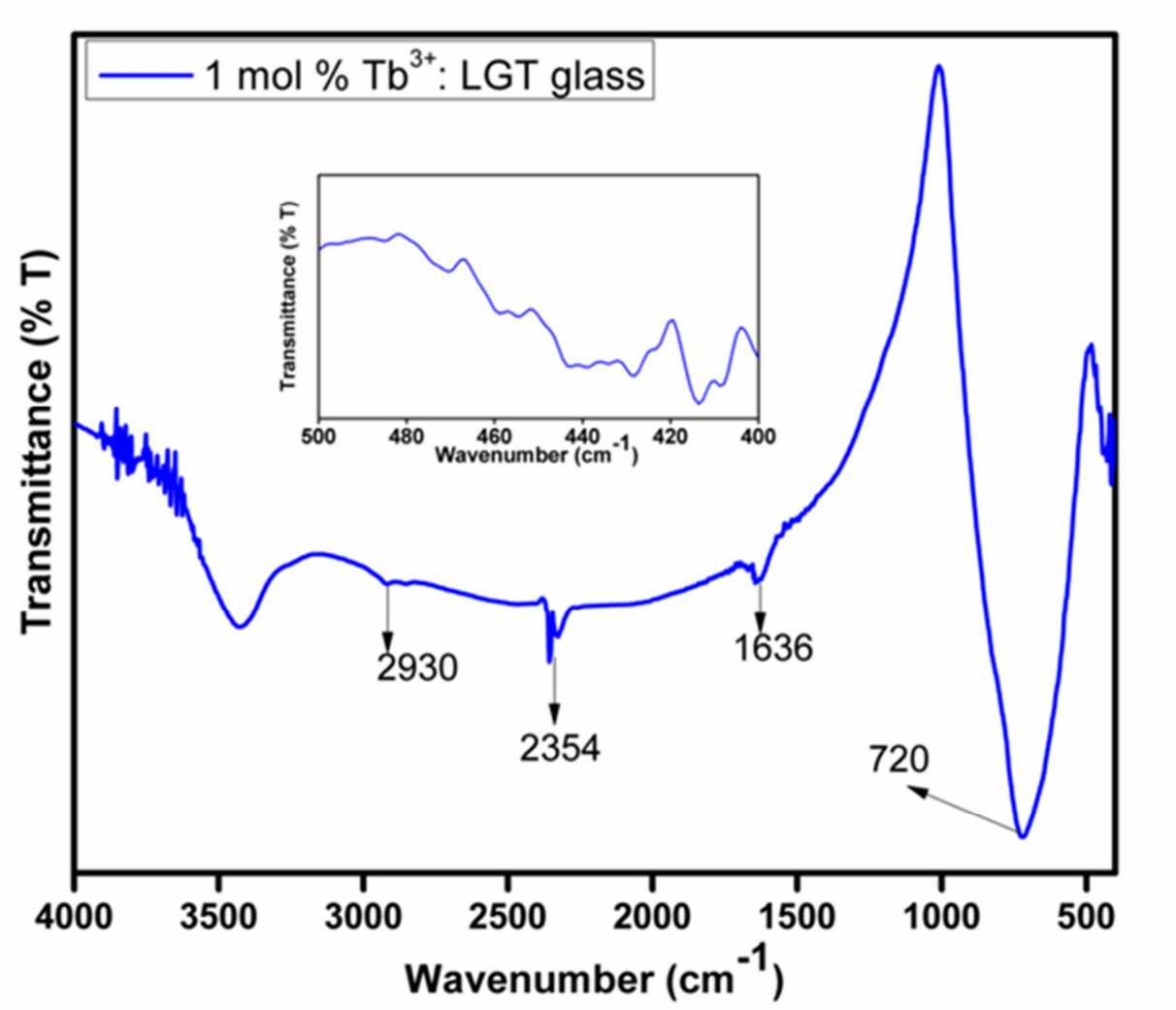

ACCEPTED MANUSCRIPT

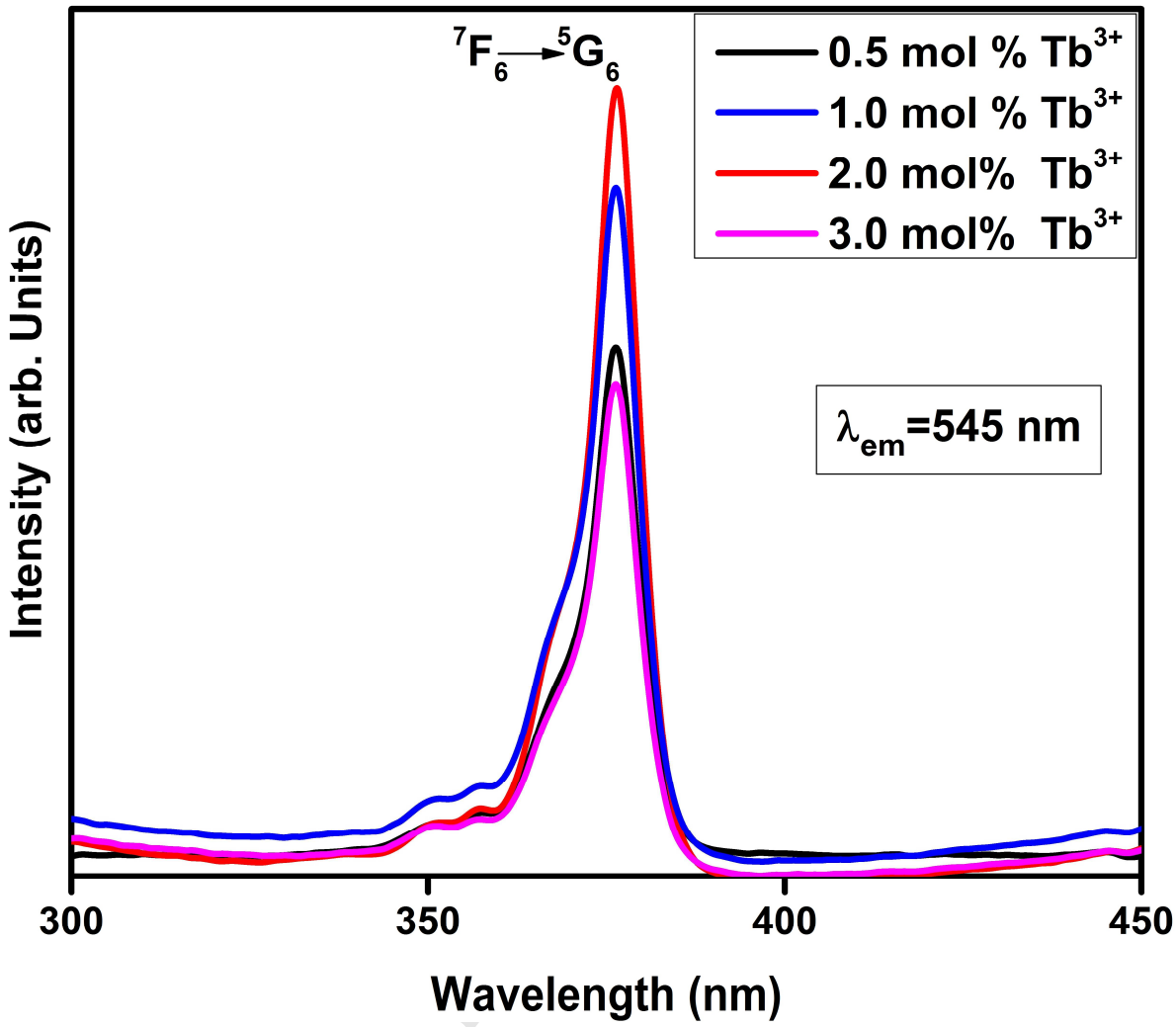
$^7F_6 \rightarrow {}^5G_6$
0.5 mol % Tb^{3+}
1.0 mol % Tb^{3+}
2.0 mol% Tb^{3+}
3.0 mol% Tb^{3+}
λ_{em}=545 nm
Intensity (arb. Units)
300
350
400
450
Wavelength (nm)

ACCEP

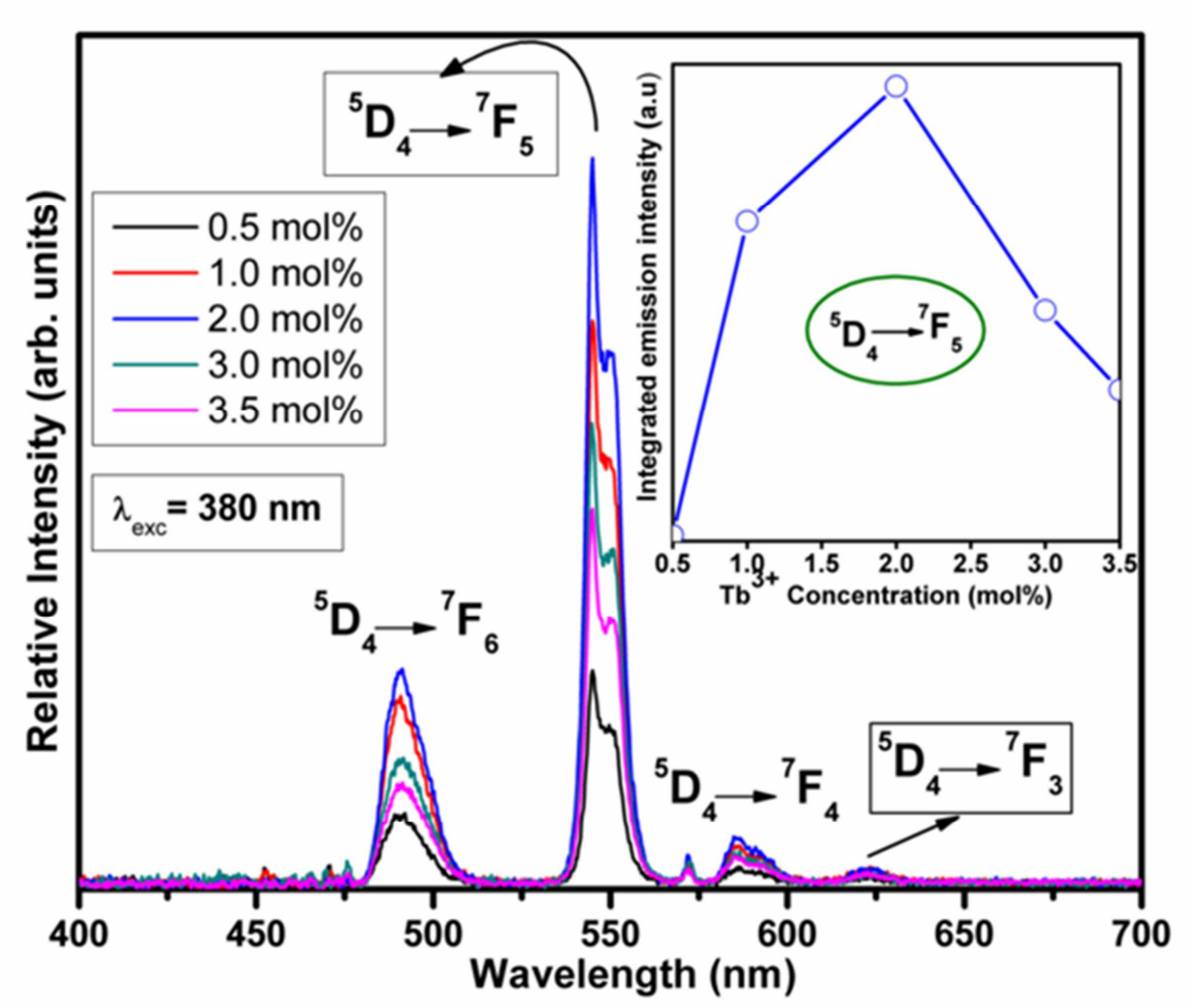
$^5D_4 \rightarrow {}^7F_5$
0.5 mol%
1.0 mol%
2.0 mol%
3.0 mol%
3.5 mol%
λ_{exc} = 380 nm
$^5D_4 \rightarrow {}^7F_6$
$^5D_4 \rightarrow {}^7F_4$
$^5D_4 \rightarrow {}^7F_3$
Relative Intensity (arb. units)
Wavelength (nm)
400
450
500
550
600
650
700
Integrated emission intensity (a.u)
Tb^{3+} Concentration (mol%)
0.5
1.0
1.5
2.0
2.5
3.0
3.5
$^5D_4 \rightarrow {}^7F_5$

ACCEPTED

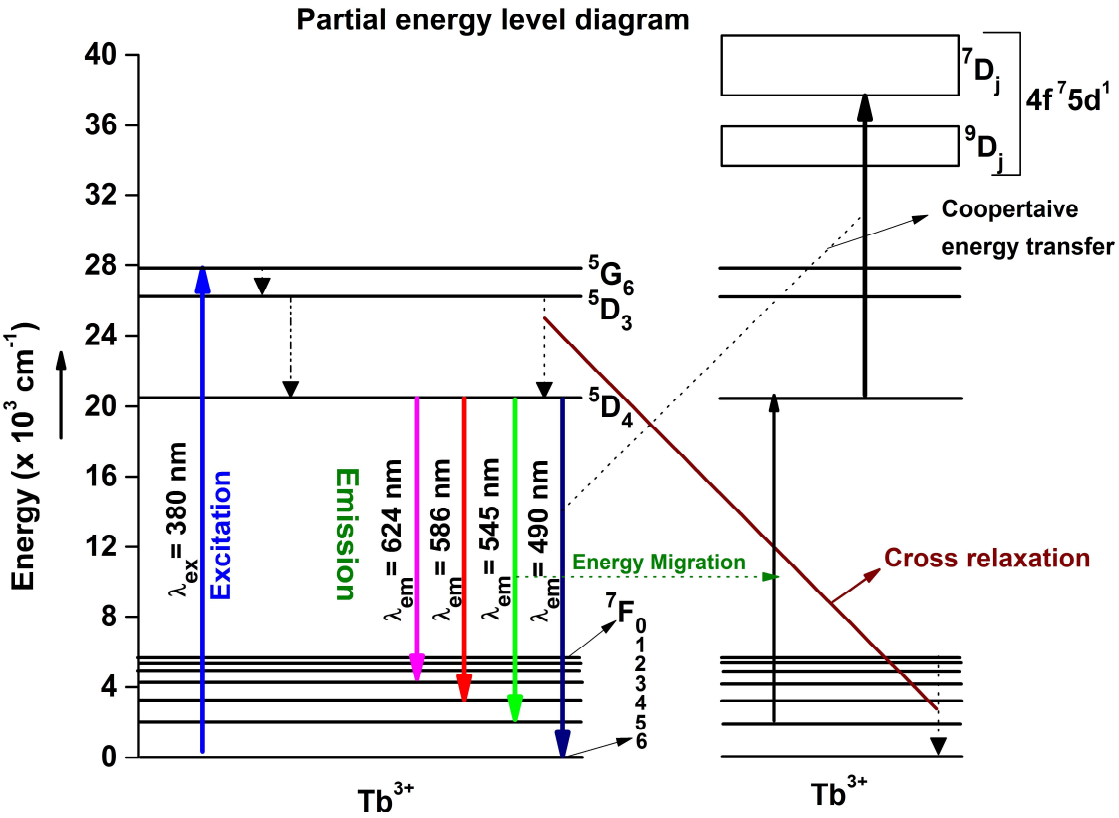

ACCEPTED MANUSCRIPT

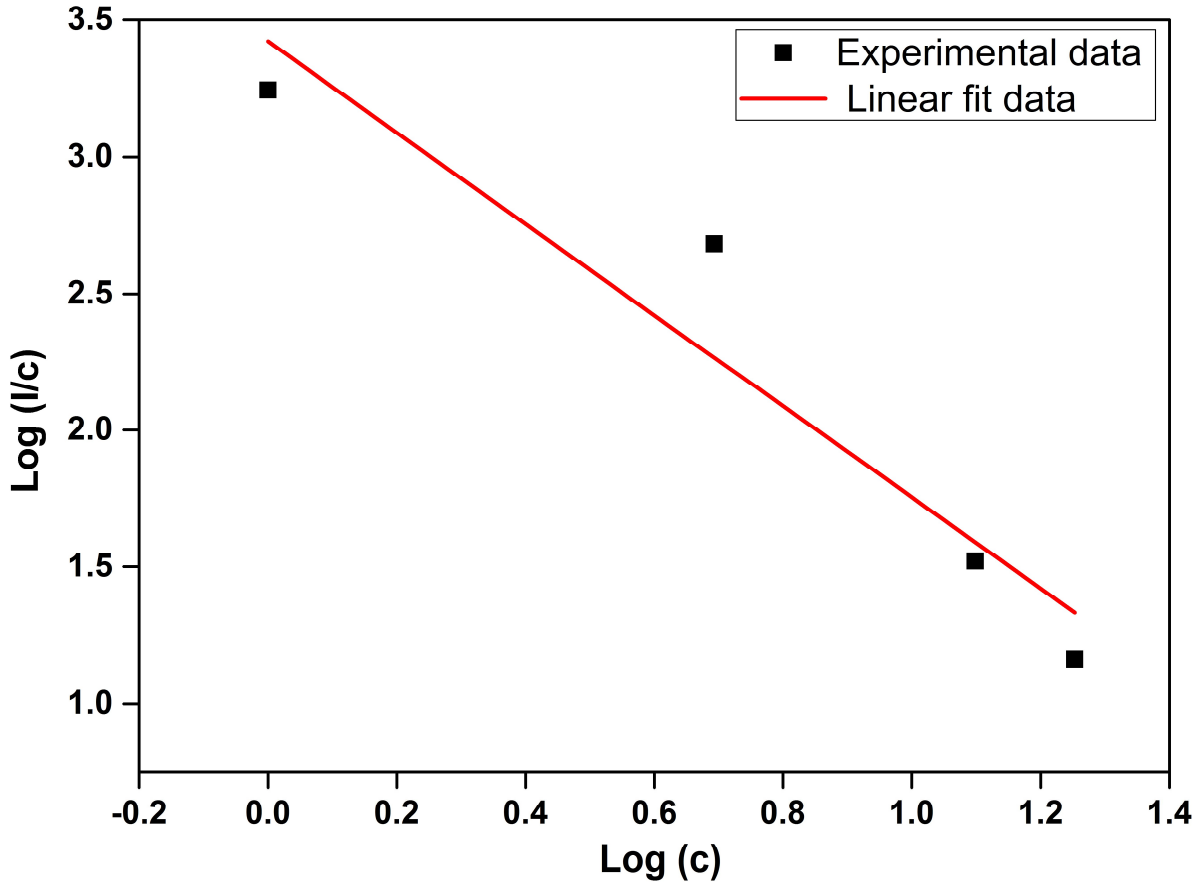
Experimental data
Linear fit data
Log (I/c)
Log (c)
3.5
3.0
2.5
2.0
1.5
1.0
-0.2
0.0
0.2
0.4
0.6
0.8
1.0
1.2
1.4

ACCEPTED

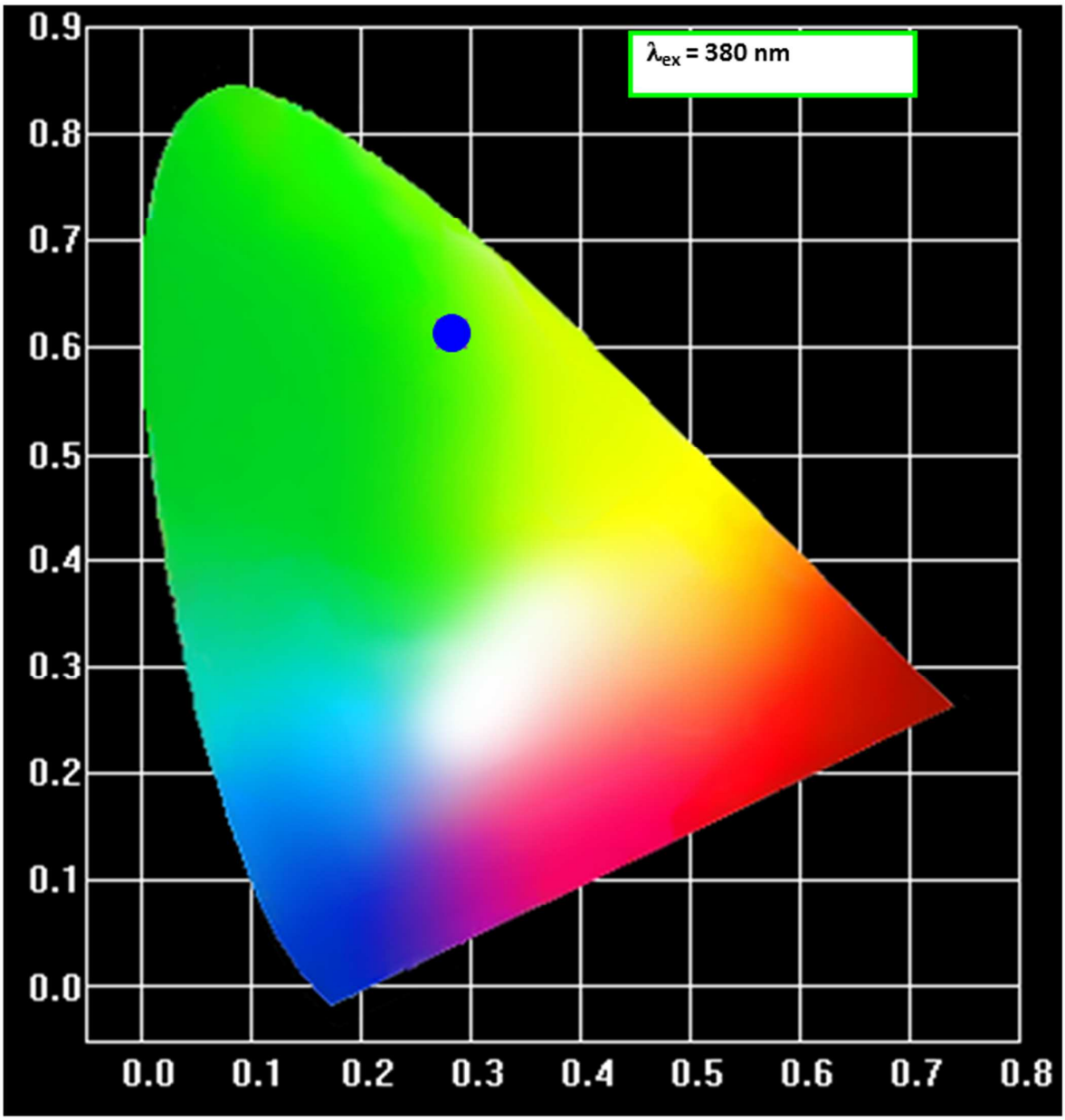
λex = 380 nm
0.9
0.8
0.7
0.6
0.5
0.4
0.3
0.2
0.1
0.0
0.0
0.1
0.2
0.3
0.4
0.5
0.6
0.7
0.8

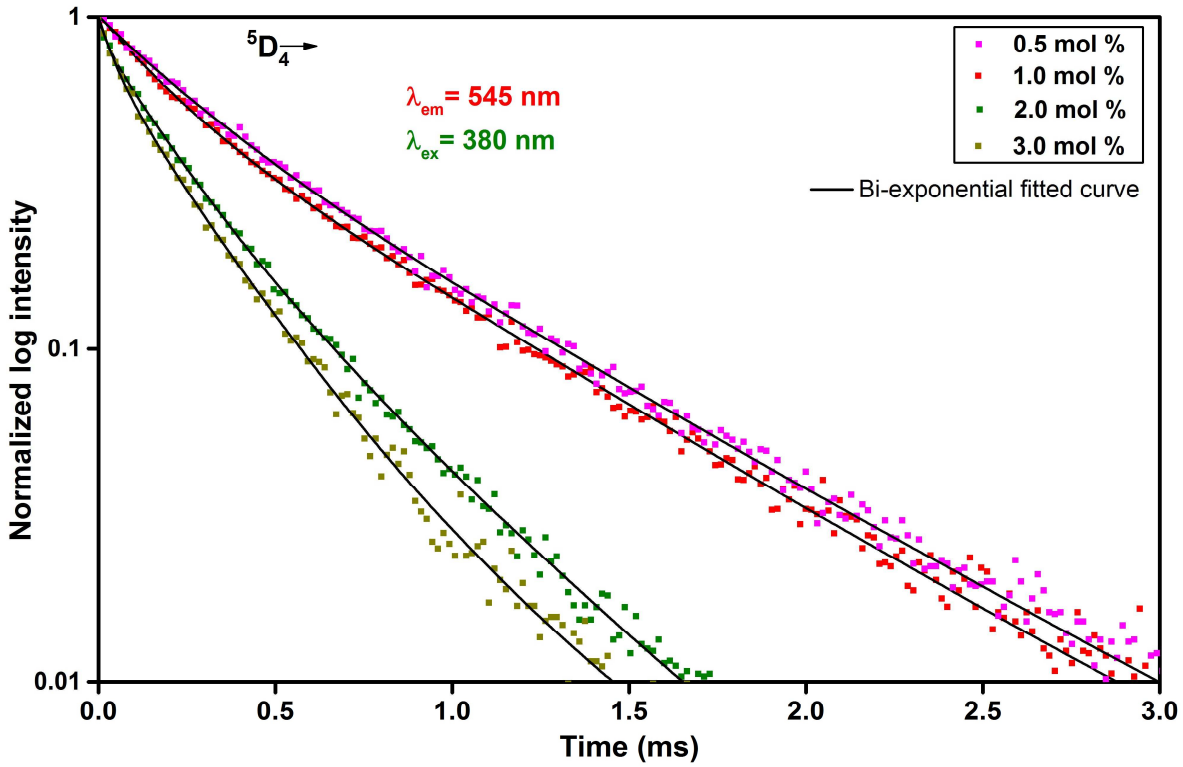

ACCEPTED MANUSCRIPT

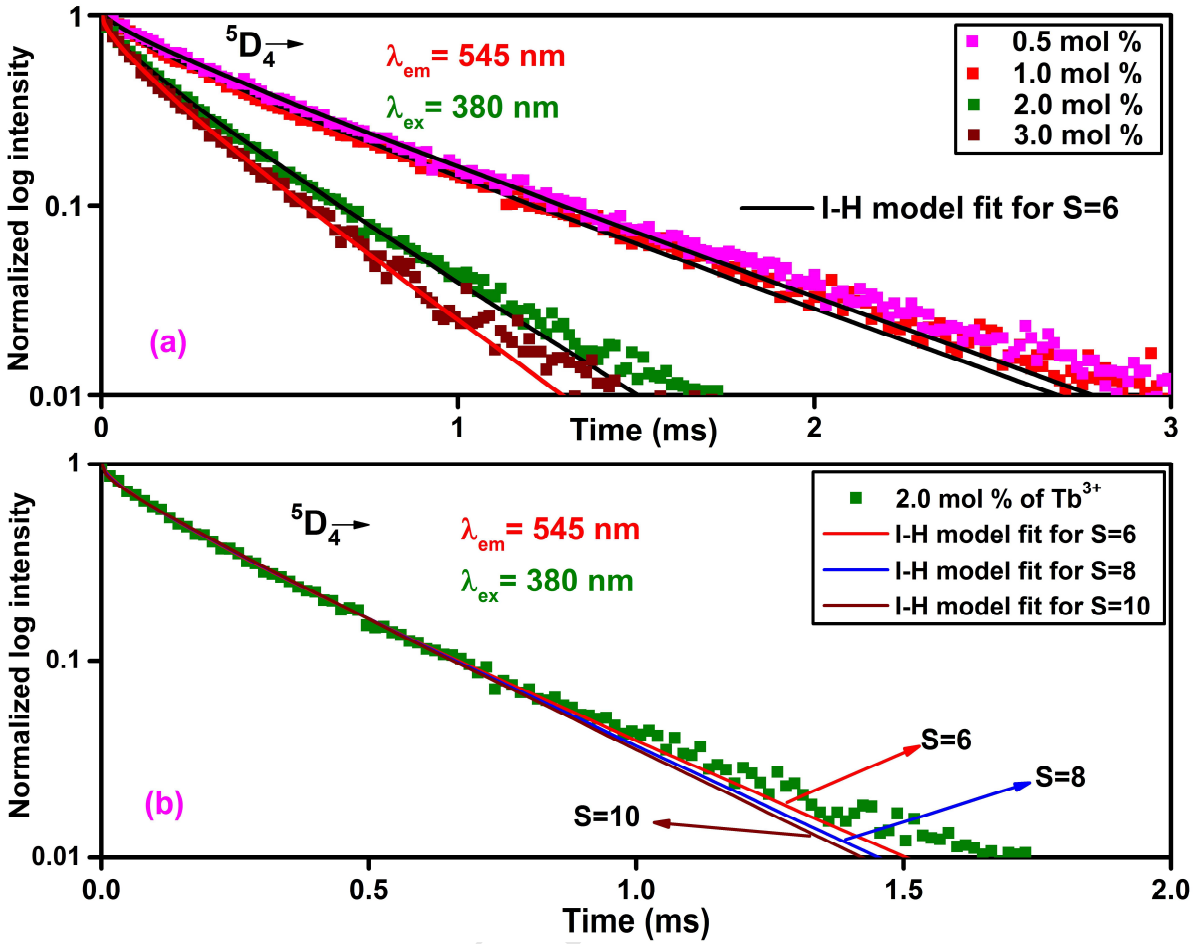
Normalized log intensity
1
0.1
0.01
$^5D_4$
λ_{em}= 545 nm
λ_{ex}= 380 nm
0.5 mol %
1.0 mol %
2.0 mol %
3.0 mol %
I-H model fit for S=6
(a)
0
1
2
3
Time (ms)
Normalized log intensity
1
0.1
0.01
$^5D_4$
λ_{em}= 545 nm
λ_{ex}= 380 nm
2.0 mol % of Tb^{3+}
I-H model fit for S=6
I-H model fit for S=8
I-H model fit for S=10
S=6
S=8
S=10
(b)
0.0
0.5
1.0
1.5
2.0
Time (ms)

ACCEPTED

ACCEPTED MANUSCRIPT

HIGHLIGHTS

- Optically transparent Tb^{3+} doped PbO-GeO_2-TeO_2 (LGT) glasses have been prepared.
- Excitation spectrum consists of single band in the NUV region at 380 nm
- CIE coordinates indicate that Tb^{3+} doped LGT glass emits yellowish green light
- Huang's theory applied to reveal the energy transfer process between Tb^{3+} ions
- This glass may be potential to use in fabricating GaN based WLEDs.

ACCEPTED MANUSCRIPT

A | T | C | T
Application and Theory of Computer Technology

ARCHYWORLD

Article

Software Defined Millimeter Wave 5th Generation Communications System

S. K. Agrawal[1*] and Dr. Kapil Sharma [2]

[1] CS Dept., Delhi Technological University, Delhi, India. Email : sachin.ecin@gmail.com
[2] CS Dept., Delhi Technological University, Delhi, India. Email : kapil@ieee.org
* Correspondence: sachin.ecin@gmail.com

Received: 24-December-2016; Accepted: 22-January-2017 date; Published: 25-January-2017

Abstract: A row column Diagonal (RCD) based data security method has been disused here for software defined millimeter wave (SDMW) based 5th generation (5G) millimeter wave (MW) communication system. The RCD based security method in this research paper discusses encryption and decryption technique for 5G SDMW based cloud computing environment (CCE) and fog computing environment (FCE). The Fog computing is an emerging technology trend and complementing along with Cloud computing. Fog Computing along with Cloud computing considers various emerging applications of ubiquitous computing, Internet of Flying-Things (IoT) and 5G millimeter wave (MW) communication system. FCE also provides data storage for user and groups at personal and professional level along with the application services. In this paper we are discussing, data security need and demand for Fog computing and Cloud computing. RCD based encryption and decryption module is very secure and useful. This proposed security method is easy to develop and integrate in SDMW based 5G millimeter wave (MWe) communications system. This research is promising high quality security for the 5G MW communications system to provide efficient and optimum security.

Keywords: Millimeter Wave (mmWave), Software Defined Radio (SDR), Software Defined Millimeter Wave (SDMW), 5th Generation (5G), Cloud Computing Environment (CCE), Fog Computing Environment (FCE), Row Column Diagonal (RCD), Internet of Flying-Things (IoT)

1. Introduction

5th Generation millimeter wave communications system is emerging as promising and potential wireless communication system having along with technologies like Cloud Computing, green communications, Internet of Things, Fog Commuting, device- to-device communications, Software defined millimeter wave and etc. 5th Generation millimeter wave communication system along with these technologies will provide high efficiency long term wireless communications system [1-3]. 5G millimeter wave communication system will fulfill the requirement of high data rates, low latency, low energy consumption, improved connectivity and reliability, High scalability and etc. 5G millimeter wave communication system still requires improved security mechanism and there is demand and need for efficient and optimum security in 5G communication system. To full-fill the demand and need of the 5G millimeter wave communication system in a flexible manner; several research has proposed to use flexible system where SDMW based technology can support in desirable and easy way [3-5]. SDMW provides programmable hardware as per access control and standards. Such type of programmable system flexibly supports our proposed security mechanism [4-5].

Fog Computing Environment (FCE) is an emerging trend to provide user or group data processing among number of Internet of Flying-Things (IoT) based connected devices along with the link in Cloud Computing Environment (CCE) [4-7]. The FCE and CCE is situated under software defined millimeter wave (SDMW) based 5G millimeter wave (MW) wireless communication system. The system allows to share and process data among the devices through FCE and CCE environment. It also provides connectivity interfaces among devices through Device to Device Communication (D2DC) user SDMW based 5G wireless communication system [7-11]. CCE is a data sharing and accessing shared network system. It is attracting users, groups and organizations to share data among themselves. CCE requires highly secure and efficient architectures and systems. CCE condenses the load among the devices in the shared network environment and reduces complexity. Such CCE architecture adds user simplicity and reduces complexity and improves the likeness factor among the users [11-16]. FCE provides services which can be hosted at user devices or access points (AP). FCE allows user applications to run and execute in a close environment to the related sensed data which means most of the processing takes place locally. The CCE requires secure environment and some places require very high level security mechanism. The secured CCE is becoming popular for normal or individual user and beneficial for group users or organizations [16-19].

CCE requires strong security mechanism in SDMW based 5G MW wireless communication system and there is a need for innovative and dynamic security systems. CCE is user involved system and as well as several servers are interlinked. Secure cancelable fingerprint key and Cryptographic Primitives techniques are discussed in literature for Multimedia Security and data security. In this paper we are discussing basics of Fog Computing Environment (FCE) and Cloud Computing Environment (CCE) and discussing about security in CCE and FCE perspective. Further this paper discusses, about Row Column Diagonal (RCD) based security engine for Fog Computing Data (FCD) and Cloud Computing Data (CCD) [4-10, 17-25].

2. Cloud Computing Environment (CCE)

CCE provides services for user and groups. Users in CCE are basically individuals or personal devices which are using CCE. Groups in CCE are basically organizations or industries or academics or various types of groups which are using CCE. Through CCS users or groups can obtain data storage on the network and can use or access other computing applications or resources in CCE [4-7]. The CCE provides major deployment models:

- Private Cloud Computing Environment (PCCE)
- Public Cloud Computing Environment (PCCE)
- Community Cloud Computing Environment (CCCE)
- Hybrid Cloud Computing Environment (HCCE)

The CCE has three major services for users and groups like:

- Infrastructure-as-a-Service (IaaS),
- Platform-as-a-Service (PaaS) and
- Software-as-a-Service (SaaS)

The CCE accommodates large users' data and group users data and as well as organizations data. CCE is distributed network by considering various servers and data centers. The CCE needs tight security to provide

Appl. Theory Comput. Technol.2017, 2,1; doi: 10.22496/atct20161224118

efficient CCE services [11-13]. The CCE allows users, group users and organizations to access data at any time from any place using any terminal in a simple and easy manner. The CCE avoids the need of same physical location or same user device to access data or files. The CCE run users defined applications in the user defined control. CCE is useful for saving users, group users and organizations data and saves the cost and time. CCE allows user to access the files smoothly and allows organizations to function much simpler and easy manner by providing facility to access the data from anywhere in personal or public or group mode [1-10].

3. Fog Computing Environment (FCE)

Fog Computing Environment (FCE) is a concept where most of the data processing takes place in a close or local environment by considering local sensed data or related data. FCE is a structured, extremely virtual and network-integrated framework for providing data services, storage and networking services among the users, group users and organizations [16-17].

The FCE is structured below the CCE to serve as efficient data and service mediator as shown in figure 1. In this environment users, group users and organizations are linked with one of the FCE and majorly each specially, each user, group user and organization is attached to one of the FCE. FCE is also connected among themselves and connected with CCE. The FCE is external to CCE and provides Cloud services, Cloud Data, Cloud Storage, Cloud applications from any node or terminal to allows users, group users and organizations. FCE controls data flow, data access among users, group users and organizations and there is a need for secure system and mechanism [13-18].

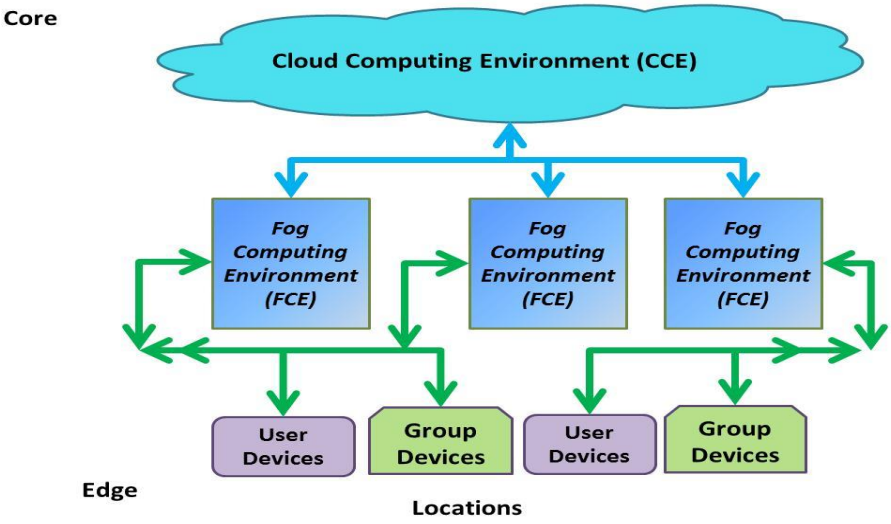

Figure 1. Fog Computing Environment (FCE) and Cloud Computing Environment (CCE)

Appl. Theory Comput. Technol.2017, 2,1; doi: 10.22496/atct20161224118

FCE and CCE provide user data, group data, computation, processing, storage, services and applications for the users or groups. The CCE is sometimes time consuming for many users, group users and organizations. FCE provides quick and fast data services for the users, group users and organizations by providing local Computing Environment (CE) i.e. called Fog Computing Environment (FCE). CCE collects ad stores data locally and provides fast and efficient processing [15-19].

FCE manages data, services and applications for users, group users and organizations in a fast and efficient manner. FCE provides fast local processing, better support and also uses networks in mass to monitor the processing. The FCE facilitates Internet of Flying-Things (IoT) development, Ubiquitous Computing and 5G millimeter wave (MW) communications systems by encompassing CCE services to include smart transducers, smart devices and smart data [14-19]. FCE provides real-time data analytics and considers interactive applications and also improves user, group and organization performance, quality of service (QOS), security and privacy issues. FCE resources are highly dynamic and heterogeneous at different levels of network hierarchy to support data, services and applications. FCE components are intelligent and smart to have seamless support of streaming services [13-19].

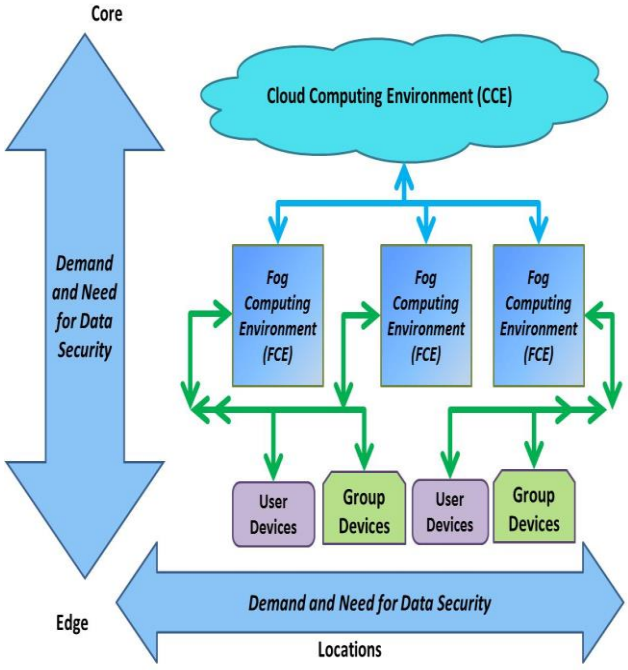

Figure 2. Demand and Need for Data Security FCE and CCE

4. Software Defined Millimeter Wave (SDMW) 5th Generation (5G) Communication System

Software defined millimeter wave 5G communication system can be designed and developed in a flexible architecture mode. Software defined millimeter wave provides flexible architecture to have more

Appl. Theory Comput. Technol.2017, 2,1; doi: 10.22496/atct20161224118

flexible control and updating options along with real time adaptive features. Software defined millimeter wave 5G communication system provides following features [3-7]:

- Highly Flexible
- Adaptive System reconfiguration
- Quick and Easy
- Seamless Incorporation
- Efficient Resource Utilization and more

Software defined millimeter wave 5G communication system along with proposed security mechanism will be very useful for upcoming system. Due to the flexibility of Software defined millimeter wave 5G communication system proposed solution will give high secure system as per demand and need [3-7].

5. Demand and Need for Data Security in Fog Computing Environment (FCE)

Security issues are not much explored were not studied in the context of fog computing. There is demand and need for security solutions which can be accommodated in FCE and CCE. There shall be security engine to provide data security for users, group users and organizations. Man-in-middle (MIM) attack carrier strong potential for attacks in Fog Computing Environment (FCE). In MIM attack gateways serving as Fog nodes are replaced by fake nodes. In such MIM cases users, group users and organizations are connecting to malicious access points. Secure cancelable fingerprint key and Cryptographic Primitives techniques are discussed in literature for Multimedia Security and data security. An attack in FCE consumes a fraction amount of resources or nodes. There is demand and need for data security in high altitude platforms systems as well which can provide dynamic or temporary networks in FCE [14-23].

5G millimeter wave communication system still requires improved security mechanism. There is demand and need for efficient and optimum security in 5G communication system and requirements are summarized in below Table 1. 5G millimeter wave communication system security with related demand and need, specifications and the enabling technologies are given below. As per proposed security mechanism for 5G millimeter wave communication system; users data, group users data and organizations data will be efficiently processed [1-7].

Table 1: Demand and Need

Demand &Need	Specifications	Enabling Technologies
Efficient security for users' data, group users' data and organizations data	Optimum process and system having authentication, authorization and accounting	Software defined millimeter wave, fog computing, mobile cloud computing and etc.

Appl. Theory Comput. Technol.2017, 2,1; doi: 10.22496/atct20161224118

In order to save users data, group users data and organizations data; Row Column Diagonal Security Engine (RCDSE) can provide secure user data by having multiple topologies and structures which can be used as per demand and need. The man-in-the-middle attack requires to control the data communication between the users, group users and organizations while nodes or users are connected in ubiquitous computing, Internet of Flying-Things (IoT) and 5G millimeter wave (MW) communication system. In the practical world, it is very difficult to protect Fog data for users, group users and organizations. As shown below in figure 2 demand and need for data security in FCE and CCE in the context of users, group users and organizations nodes or devices it requires multiple directions, multiple level for data downloading, data uploading. The security is required in central fashion, distributed fashion or scattered manner based on the user or groups need to accommodate the various applications [13-17].

At present Encrypted data communication engines are not much perfect to protect users, group users and organizations data. The encryption engines and decryption engines consume lots of power, resources. Practically complex encryption engine and decryption engine techniques may not be useful for FCE and CCE [14-19].

6. Row Column Diagonal Security Engine (RCDSE) In Fog Computing Environment (FCE) And Cloud Computing Environment (CCE)

With the growing demand of data and applications sharing in FCE and CCE; Data security becomes important so that users, group users and organizations can share data among themselves in a safe environment. Row Column Diagonal Security Engine (RCDSE) provides security in multiple directions, multiple level for data downloading, data uploading for users, group users and organizations as shown in figure 3. Row Column Diagonal Security Engine (RCDSE) provides data security, in multiple architecture like central fashion, distributed fashion or scattered manner based on the user or groups need to accommodate the various applications [13-17].

Appl. Theory Comput. Technol.2017, 2,1; doi: 10.22496/atct20161224118

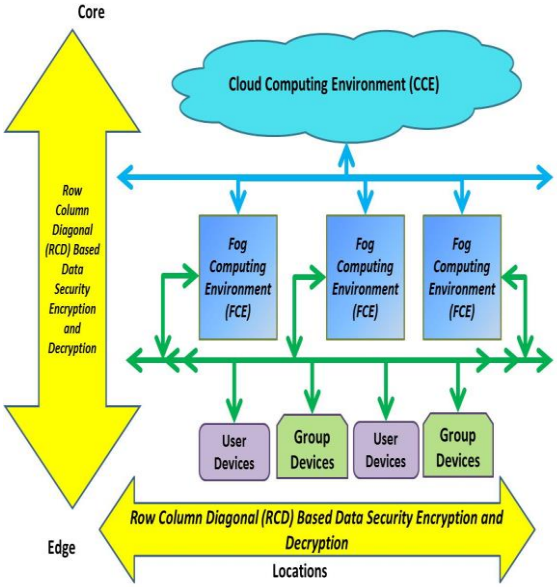

Figure 3. Row Column Diagonal (RCD) Based Data Security Encryption and Decryption in FCE and CCE

Proposed innovative Row Column Diagonal Security Engine (RCDSE) is a system and method to encode the data in 2D or 3D format. The Row Column Diagonal Security Engine (RCDSE) is secure and provides the high level data security for users' data, group users data and organizations data. Row Column Diagonal Security Engine (RCDSE) is uses one of the Row Column and Diagonal processing on the data by considering RCD bits (RCD_SUP) given by RCD Supervisor. Row Column and Diagonal RCD Bits contain the data regarding the processing set. The processing should be performed on Either Row, Column or Diagonal of Matrix or Transpose of the Matrix. RCD_Seed is processed on Either Row, Column or Diagonal of the Matrix and if the processing is whether Addition or Subtraction [13-18].

RCD EDM performs all encryption and Decryption process for the DATA that will be send and received using processing specified by RCD bits. RCD bits specifies which processing has to be performed on Row, Column or Diagonal while Uploading or Downloading on DATA Matrix. Whether to transpose the Matrix or not, this information is also specified by RCD Bits. RCD_SUP are RCD Bits generated by RCD_Supervisor which informs Row Column Diagonal Security Engine (RCDSE) about the processing which has to be performed on the Row, Column, Diagonal or transpose of the DATA Matrix which has to be encrypted or decrypted [13-17]. The basic used terms and definitions are given below and shown in figure 4:

Appl. Theory Comput. Technol.2017, 2,1; doi: 10.22496/atct20161224118

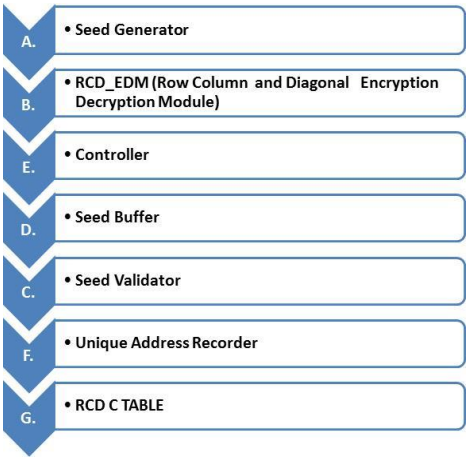

Figure 4. Row Column Diagonal Security Engine (RCDSE) Basic Terms

Row Column Diagonal Security Engine (RCDSE) basic terms and definitions are given below:

- Seed Generator: Row Column Diagonal Security Engine (RCDSE) Supervisor uses Seed Generator at the beginning of every operation (Upload/Download) to create RCD_SUP, RCD_Seed in FCE and CCE.
- RCD_EDM (Row Column and Diagonal Encryption Decryption Module): Row Column Diagonal Security Engine (RCDSE) EDM performs all encryption and Decryption and applies on data or files based on RCD bits.
- Controller: The Row Column Diagonal Security Engine (RCDSE) Supervisor Controller controls transmission for SCL (Secured Control Line) and Secured Data Line(SCL). DATA transmission takes place by SDL. RCD REPLY, Seed Values, Row Column Diagonal Security Engine (RCDSE) bits and Control transfer signals are transmitted by SCL.
- Seed Buffer: The devices use Seed Buffer to Store all the Seeds, RCD bits and Validation DATA (explained Later) which will be used in FCE and CCE.
- Seed Validator: The devices ST uses Seed Validator to validate the Row Column Diagonal Security Engine (RCDSE) _REPLY (from Cloud Side contains Unique Address in FCE and CCE.) using the Validation DATA received and stored in Seed Buffer.
- Unique Address Recorder: The devices use Unique Address Recorder to give its own Unique Address (IMEI/MAC/IPv6 etc....) in FCE and CCE to EDM Module/ Row Column Diagonal Security Engine (RCDSE) Supervisor for generating Validation information / RCD Reply.
- RCD_C TABLE: Row Column Diagonal Security Engine (RCDSE)_C table is used in FCE and CCE includes details about the sub-clouds, fog layers, their status (Available space, Load and other parameters) and the files stored in them. Status Info is used when upload request is encountered, Central Cloud chooses a sub-cloud for Uploading file and Update the Table accordingly.

Appl. Theory Comput. Technol.2017, 2,1; doi: 10.22496/atct20161224118

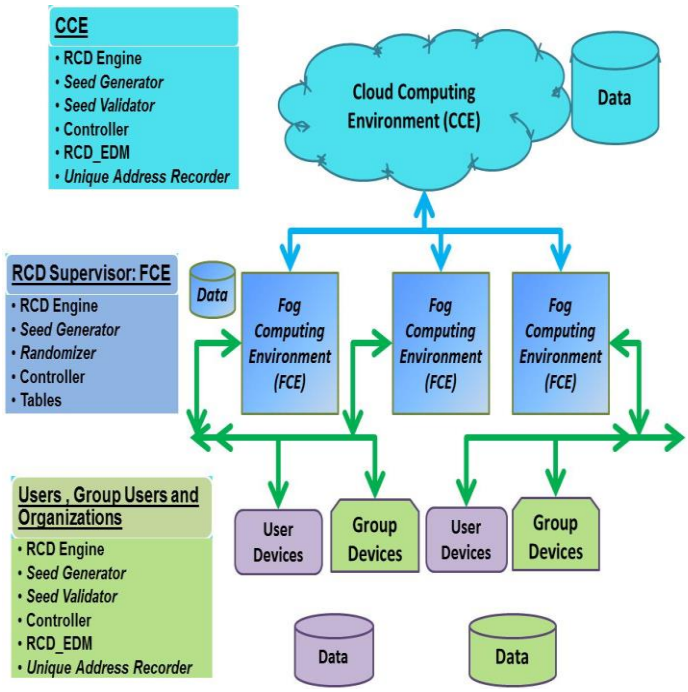

Figure 5. Row Column Diagonal Security Engine (RCDSE) in FCE and CCE

In figure 5, Row Column Diagonal Security Engine (RCDSE) Service Provider performs first Authentication with the users' data, group users' data and organizations data after this the validation data and key exchanges takes place between RCD Supervisor and users data, group users data and organizations data and RCD supervisor decide the cloud address for Upload/Download and the HOST Upload/Download the encrypted/decrypt data with the keys and Seed to specified cloud address.

In FCE and CCE, communication takes place between RCD at HOST, Cloud and RCD Supervisor to transfer data between Host and Cloud in a random secured manner Row Column Diagonal Security Engine (RCDSE) is based on Row, Column and Diagonal processing on the data based on the RCD bits (RCD_SUP) given by RCD Supervisor. RCD Bits contains the information regarding the processing set which has to be performed on Either Row, Column or Diagonal of Matrix or Transpose of the Matrix. There is also another data, RCD_Seed which is operated on Either Row, Column or Diagonal of the Matrix if the processing is Either Addition or Subtraction [12-19].

As FCE or fogging is a distributed computing infrastructure in which some application services as handles at the network edge for smart devices and some are handled at remote data centers in the cloud. So the RCD Supervisor's functionality will be handles at remote data centers which contains the complexity for handling the RCD_Seed generation and user authentication before the downloading or uploading of the data this will directly result in improving the efficiency and reduces the amount of data need to be transported to the cloud at remote end for processing, analysis and storage.

In this architecture of FCE and CCE, fogging the computation power that is required for processing at network edge can be done by smart mobile computing device, smart routers or other gateway devices. In

Fog architecture the fog system RCD Supervisor unit will work as it works in the normal cloud architecture with RCD Engine, Seed generator and Randomizer while the central cloud will be connected to other FOG in the meantime the address details of FOG and central cloud are stored in the unique address tables. While at user end i.e the computing ends or mobile device end will behave same system irrespective of FCE or normal cloud architectures. The main component RCD_EDM is generally at main cloud and at Device end for encryption and decryption of user data while uploading and downloading.

7. Conclusion

This paper discusses about the expanding Row Column Diagonal security engine (RCDSE) and integration with Fog Computing Environment (FCE) and Cloud Computing Environment (CCE) for efficient and more secured data in SDMW based 5G wireless communication system. RCD based security mechanism provides quick and secured services. It allows users to share data in a secure manner as per demand and need in Internet of Flying-Things (IoT) environment. We have presented and discussed that Row Column Diagonal security engine (RCDSE) based data sharing in FCE reduces load of the CCE. Due to the flexibility of Software defined millimeter wave 5G communication system; proposed solution will give high security as per demand and need. It also helps by providing various systems to create better services more efficiently in FCE. The extended work could be on performance evaluation under various attacks in FCE and CCE.

1. Acknowledgement

This paper is specifically meant for research growth purpose and educational purpose. The authors are very much thankful to Samsung Electronics India. This paper is specifically meant for academic research and progress.

References

1. Rabi Prasad Padhy and Manas Ranjan Patra, “Evolution of Cloud Computing and Enabling Technologies”, International Journal of Cloud Computing and Services Science (IJ-CLOSER) Vol.1, No.4, October 2012, pp. 182-198
2. Marinela Mircea and Anca Ioana Andreescu , “Using Cloud Computing in Higher Education: A Strategy to Improve Agility in the Current Financial Crisis” , IBIMA Publishing Communications of the IBIMA ,Vol. 2011 (2011), Article ID 875547, 15 pages
3. Ian F. Akyildiz , Shuai Nie, Shih-Chun Lin and Manoj Chandrasekaran , “5G Roadmap: 10 Key Enabling Technologies,” Computer Networks (Elsevier) Journal, vol. 106, pp. 17-48, Sept. 2016
4. I. F. Akyildiz, P. Wang, and S.-C. Lin, “SoftAir: A Software Defined Networking Architecture for 5G Wireless Systems”, Computer Networks (Elsevier) Journal, vol. 85, pp. 1-18, Jul. 2015
5. Ian F. Akyildiz, Shih-Chun Lin and Pu Wang, “Wireless Software-Defined Networks (W-SDNs) and Network Function Virtualization (NFV) for 5G Cellular Systems: An Overview and Qualitative Evaluation,” Computer Networks (Elsevier) Journal, vol. 93, pp. 66-79, Dec. 2015
6. Mugen Peng, Senior Member, IEEE, Shi Yan, Kecheng Zhang, Chonggang Wang,” Fog Computing based Radio Access Networks: Issues and Challenges”,2015

7. Seng W. Lok, "The Internet of Flying-Things: Opportunities and Challenges with Airborne Fog Computing and Mobile Cloud in the Clouds", Internet of Things Journal, VOL. X, NO. X, XXX 20
8. R. Buyya et al., "Cloud computing and emerging IT platforms: Vision, hype, and reality for delivering computing as the 5th utility", Elsevier, Future Generation Computer Systems 25 (2009) 599 616
9. Tuncay Ercan , Effective use of cloud computing in educational institutions", Elsevier, Procedia Social and Behavioral Sciences 2 (2010) 938–942
10. S. K. Agrawal and K. Sharma, "5G Millimeter Wave (mmWave) Communications System: Vision and Challenges", IEEE Proceedings of INDIACom-2016, Date of Conference: 16-18 March 2016
11. S. K. Agrawal and K. Sharma, "5G Millimeter Wave (mmWave) Communication System with Software Defined Radio (SDR)", International Conference on Recent Trends in Engineering & Science (ICRTES-16), 29th-30th September 2016, ISBN: 978-93-86171-06-1
12. ACMqueue, "Cloud Computing: An Overview", 2009 ACM 1542-7730/09/0600
13. Won Kim, "Cloud Computing: Today and Tomorrow", journal ofobject technology, vol. 8, no. 1, january-february 2009
14. Dimitris zegini and et. al. "A User-Centric Multi-Paas Application Management Solution For Hybrid Multi-Cloud Scenarios", Scalable Computing: Practice and Experience Volume 14, Number 1, pp. 17–32
15. Rainer Poisel,, Erich Malzer, and Simon Tjoa, "Evidence and Cloud Computing: The Virtual Machine Introspection Approach", Evidence and Cloud Computing: The VMI Approach, Journal of Wireless Mobile Networks, Ubiquitous Computing, and Dependable Applications, volume: 4, number: 1, pp. 135-152
16. Kim Khoa Nguyen and Mohamed Cheriet, "Enabling Infrastructure as a Service (IaaS) on IP Networks: From Distributed to Virtualized Control Plane", IEEE Communications Magazine, December 2012
17. Pragya Gupta, Sudha Gupta," Mobile Cloud Computing: The Future of Cloud", International Journal of Advanced Research in Electrical, Electronics and Instrumentation Engineering, Vol. 1, Issue 3, September 2012
18. David Chappell, "The Benefits and Risks of Cloud Platforms, A Guide for Business Leader", Sponsored by Microsoft Corporation
19. Karthik Sukumar and et. al., "The Structure of the New IT Frontier: Aneka Platform for Elastic Cloud Computing Applications – Part III"
20. S. K. Agrawal, S. Joshi and B.M. Purohit, "Secure Data Communication In A Cloud Environment using Row Column Diagonal (RCD) ", International Conference on Soft Computing Techniques and Implementations (ICSCTI), Oct 8-10, 2015, p-p: 120 – 126, Print ISBN: 978-1-4673-6790-5, INSPEC No.: 16072400, IEEE International Conference, India
21. M. Hajibaba and S.Gorgin, "A Review on Modern Distributed Computing Paradigms: Cloud Computing, Jungle Computing and Fog Computing",Journal of Computing and Information Technology - CIT 22, 2014, 2, 69–84
22. M. Aazam and, E. N. Huh, "Fog Computing and Smart Gateway Based Communication for Cloud of Things",2014 International Conference on Future Internet of Things and Cloud, 2014
23. S. J. Stolfo, M. B. Salem and A.s D. Keromytis,"Fog Computing: Mitigating Insider Data Theft Attacks in the Cloud", 2012 IEEE Symposium on Security and Privacy Workshop, 2012
24. A. Bhatega, K. Sharma, "Secure Cancelable Fingerprint Key Generation", Power India International Conference (PIICON) IEEE, Dec. 2014, pp-1-3
25. S. Dhall Sakshi, K. P. Saibal, K. Sharma, "Cryptographic Primitives for Multimedia Security", INROADS-An International Journal of Jaipur National University, 2014, Volume: 3, pp- 335- 339

© 2016 by the authors. Submitted for possible open access publication under the terms and conditions of the Creative Commons Attribution (CC-BY) license (http: //creativecommons.org/licenses/by/4.0/)

Author's Accepted Manuscript

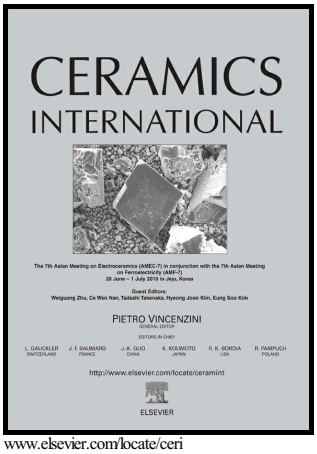

www.elsevier.com/locate/ceri

Spectroscopic and Photoluminescence Characteristics of Sm^{3+} doped Calcium Aluminozincate Phosphor for Applications in w-LEDs

Sumandeep Kaur, A.S. Rao, M. Jayasimhadri

PII: S0272-8842(17)30332-2
DOI: http://dx.doi.org/10.1016/j.ceramint.2017.02.129
Reference: CERI14745

To appear in: *Ceramics International*

Received date: 3 January 2017
Revised date: 22 February 2017
Accepted date: 24 February 2017

Cite this article as: Sumandeep Kaur, A.S. Rao and M. Jayasimhadri Spectroscopic and Photoluminescence Characteristics of Sm^{3+} doped Calciur Aluminozincate Phosphor for Applications in w-LEDs, *Ceramics Internationa* http://dx.doi.org/10.1016/j.ceramint.2017.02.129

This is a PDF file of an unedited manuscript that has been accepted fo publication. As a service to our customers we are providing this early version o the manuscript. The manuscript will undergo copyediting, typesetting, an review of the resulting galley proof before it is published in its final citable form Please note that during the production process errors may be discovered whic could affect the content, and all legal disclaimers that apply to the journal pertain

ACCEPTED MANUSCRIPT

Spectroscopic and Photoluminescence Characteristics of Sm^{3+} doped Calcium Aluminozincate Phosphor for Applications in w-LEDs

Sumandeep Kaur, A.S.Rao*, M. Jayasimhadri*

Department of Applied Physics, Delhi Technological University, Bawana Road, New Delhi-110 042, India.

drsrallam@gmail.com

jayaphysics@yahoo.com

**Corresponding authors*: Tel.: +91-85860 39007
**Corresponding authors:* Tel.: +91-9013553360

Accepted manuscript

Abstract

Monophase Calcium Aluminozincate ($Ca_3Al_4ZnO_{10}$) phosphor doped with Sm^{3+} ions with varying concentrations have been prepared at 1300 °C by conventional solid state reaction technique. The crystal structure and phase analysis of the as-prepared phosphor has been carried out by X-ray Diffraction (XRD) studies. Morphology and functional groups present in the phosphor have been investigated thoroughly by using Scanning Electron Microscope (SEM) and Fourier Transform Infrared (FT-IR) spectral measurements, respectively. Under 401 nm excitation, the as-prepared phosphor exhibit intense visible orange emission at 601 nm. It has been observed that 1.0 mol% of Sm^{3+} ions concentration is optimum to give intense visible orange emission. The PL analysis reveals that the dipole-dipole interaction is primarily responsible for the concentration quenching observed beyond 1.0 mol% of Sm^{3+} ions. The TR-PL study reveals a bi-exponential behavior of decay curves with an average lifetime of the order of microseconds. The CIE coordinates (x= 0.574 and y= 0.424) measured for the optimized phosphor are very close to the intense orange emission coordinates specified by Nichia Corporation developed Amber LED NSPAR 70BS (0.570, 0.420). The

ACCEPTED MANUSCRIPT

spectroscopic, PL and TR-PL studies suggest the potential use of Sm^{3+} doped calcium aluminozincate phosphors for display and white light emitting devices.

Keywords: XRD, Calcium Alumino Zincate Phosphor, PL, TR-PL, FT-IR, Solid State Reaction

1. Introduction.

In recent years, conventional light sources such as incandescent and fluorescent lamps have been replaced by solid state lighting (SSL) technology. SSL technology involves white Light Emitting Diodes (w-LEDs), which are globally used for wide spread applications in consumer electronics and general illumination [1,2]. It offers many scientific and technological patronages such as environmental friendliness, lower operating temperature and effective energy utilization by saving 80% of energy consumption over conventional lighting devices. In the light of the aforementioned advantages, w-LEDs are considered to be the next generation lighting sources [3–6]. Indium Gallium Nitride (InGaN) or Gallium Nitride (GaN) chip based w-LEDs are gaining paramount attention because of their longevity, high luminous efficiency, high energy efficiency, smaller size, faster switching, excellent reliability with reduced operating expenses and capable of replacing conventional light sources [2,5–10]. The current strategy of achieving white light is based on yellow phosphor encapsulated over UV/blue LED chip, which utilizes UV/blue light for excitation. However, this strategy suffers from several drawbacks such as lower color rendering index (CRI), high correlated color temperature (CCT), thermal quenching, narrow visible range and hence cannot meet the demand of warm white light needed for indoor and artificial lighting [11,12]. To circumvent the problem, red phosphors can be introduced to improve CRI and CCT. However, commercial red phosphor Y_2O_2S: Eu^{3+} has some shortcomings such as inimical

Accepted manuscript

ACCEPTED MANUSCRIPT

decomposition products, chemical instability which degrades its luminescence efficiency over a period. This necessitate the development of a new orange-red emitting phosphor that can be excited by n-UV or blue LED [13,14].

Rare earth (RE) ions play a vital role in display devices and lighting fields due to f-f and f-d transitions, which give narrow and broad emission, respectively. At present, Sm^{3+} doped phosphors are studied for the development of an orange-red phosphor due to their potential applications for color display, plasma display panels and solid state lighting [10,15–17]. For efficient white light emission with improved CRI and CCT, a new combination of cyan plus orange can be realized, where orange emission can be accomplished from Sm^{3+} ions doped phosphors [18]. Therefore, Sm^{3+} serves as one of the best activator/dopant for orange-red emission to augment the efficiency of w-LEDs [19].

Inorganic oxide based compounds, including zincates, aluminates [20-26] doped with RE ions are better luminescent materials over sulfide and nitride based compounds, because of easiness in their synthesis and structural viability for doping with different RE ions. Zincates possesses excellent structural, optical, magnetic, dielectric, superconducting properties along with high thermal, physical and chemical stability [21–23]. Quite recently, Zincates based compounds have attracted researchers to explore their properties as luminescent materials.[23–25]. These luminescent materials have applications in dye sensitized solar cells, high performance display devices such as plasma display devices (PDPs), field emission displays (FEDs), cathode ray tubes (CRTs), electroluminescent displays (ELs), laser generation apparatus, white Light Emitting Diodes (w-LEDs), thin film electroluminescence devices, thermographic sensors and biomedical fields [26]. This motivates researchers to develop new phosphors suitable for the aforementioned applications [19,27–32]. Quite recently, we investigated the photoluminescence spectral studies of Eu^{3+} doped calcium aluminozincate ($Ca_3Al_4ZnO_{10}$) phosphor to understand its utility in w-LEDs [33]. The

Accepted manuscript

ACCEPTED MANUSCRIPT

interesting results obtained have prompted us to investigate the potentiality of the same host lattice doped with Sm^{3+} ions at different concentrations. To the best of our knowledge, luminescent properties of Sm^{3+} doped $Ca_3Al_4ZnO_{10}$ (CAZ) phosphor has not been studied so far.

This paper reports the synthesis of Sm^{3+} ions doped calcium alumino-zincate phosphors using traditional solid state reaction technique. The as-synthesized phosphors have been used to study structural, morphological, luminescent, colorimetric properties and energy transfer processes in detailed for their utility in w-LEDs.

2. Sample Preparation.

Samarium doped CAZ phosphors at different concentrations of Sm^{3+} ions (i.e., 0.5, 1.0, 1.5, 2.0 and 2.5 mol%) are prepared by using conventional solid state reaction technique. The analar grade chemicals CaO, ZnO, Al_2O_3 and Sm_2O_3 have been taken as raw material in stoichiometric ratio. All the chemicals have been weighed, dispersed in acetone and grinded thoroughly by using an agate mortar for an hour. The grinded sample has been kept in an alumina crucible at 1300 ^oC for five hours in a high temperature programmable muffle furnace and then allowed to cooled down to the room temperature naturally. The sintered samples have been grinded again to obtain fine powder and taken for different characterizations.

Crystalline structure of the as-prepared powder phosphor has been analyzed by high resolution X-ray bruker D8 Advance Diffractometer operating with nickel filtered CuKα radiation (λ = 1.5406 Å) under operating conditions at 40 kV and 40 mA employing a scan rate of 0.02 $^\circ s^{-1}$, where Bragg's diffraction angle ranges from 20° to 70°. To estimate the particle size and morphology of the crystalline powder, Hitachi 3700N SEM has been used. The FT-IR spectrum has been recorded by Perkin Elmer's Frontier FT-IR spectrometer and

Accepted manuscript

ACCEPTED MANUSCRIPT

the pellet has been prepared by mixing the 1.0 mol% of Sm^{3+} doped CAZ phosphor with KBr pellet and then compressed mechanically at 1.5 ton. The luminescent spectra have been recorded with a Shimadzu spectrofluorophotmeter (RF-5301PC) fitted with a Xenon flash lamp as source of excitation and having spectral resolution of 0.2 nm. The Time Resolved Photoluminescence (TR-PL) spectral recordings have been carried out using an Edinburgh FLSP 900 spectrofluorophotometer with spectral resolution of 0.1 nm, where Xenon lamp acts as source of excitation. All characterizations have been performed at room temperature.

3. Result Analysis.

3.1. Phase Analysis and Crystal Structure:

The X-ray diffraction patterns of calcium aluminozincate phosphor doped with different concentration of Sm^{3+}, $Ca_{3-x}Al_4ZnO_{10}$: xSm^{3+} (0.0, 0.5, 1.0, and 2.0 mol%) has been examined and compared with the International Crystallographic Diffraction Database (ICDD card no. 04-009-7304) of $Ca_3Al_4ZnO_{10}$ to verify the crystal structure, effect of doping concentration and to identify the phase as shown in Fig. 1a. All the observed diffraction peaks are in complete agreement with the standard data and (h k l) planes have been well indexed as shown in Fig. 1a. The sharp XRD patterns without any additional peak confirm the formation of pure orthorhombic crystalline phase of calcium aluminozincate phosphor. The results suggest that, the incorporation of Sm^{3+} ions in calcium aluminozincate phosphor does not lead to noteworthy changes in the host crystal structure. As the ionic radius of samarium is close to calcium (r_{sm3+} = 109.8 pm, r_{ca2+} = 114 pm with coordination number = 6) rather than aluminium (r_{Al3+} = 67.5 pm) and zinc (r_{zn2+} = 88 pm), it can incorporate into Ca^{2+} sites.

To determine average crystallite size, the following Debye-Scherrer relation has been used:

$$D = k\lambda/\beta cos\theta \qquad \text{(A)}$$

Accepted manuscript

ACCEPTED MANUSCRIPT

in which, k is the shape factor (= 0.94), λ is the wavelength of X-ray used (0.154 nm), β is the full width at half maximum of the diffraction peak (FWHM), θ is the Bragg's diffraction angle, D is the crystallite size [7]. The average crystallite size found to be in the range 61-110 nm for all the characterized CAZ phosphors. Since, the FWHM is a combination of micro strain and the crystallite size [34], the Williamson-Hall (W-H) method has been employed to estimate the effect of FWHM on strain and the crystallite size [35] by using the following equation:

$$\beta cos\theta = \frac{k\lambda}{D} + 4\varepsilon sin\theta \qquad \text{(B)}$$

where, ε is the lattice strain and other symbols have their usual meanings. W-H graph has been plotted between βcosθ versus sinθ as shown in Fig. 1b. From the intercept and slope of the plot, the average crystallite size (D) and the value of lattice strain (ε) can be estimated, respectively. The average crystallite size is found to be in the range 52-75 nm and strain (%) is 0.006–0.03 for all the characterized CAZ phosphors.

3.2. Particle Morphology:

To investigate morphology and particle size, SEM analysis has been carried out for the optimized $Ca_{2.99}Al_4ZnO_{10}$: $0.01Sm^{3+}$ phosphor as shown in Fig. 2. The phosphor exhibit solid microcrystalline structure with some agglomeration among crystalline grains produced by high temperature solid state reaction technique. The average size of particles for $Ca_{3-x}Al_4ZnO_{10}$: xSm^{3+} (x = 1.0 mol%) sample is found to be in the range of 2-15 μm. Most of the commercial phosphors currently available in the market contain particle size of the order of few micrometers [1].

3.3. FT-IR Analysis:

Accepted manuscript

ACCEPTED MANUSCRIPT

Fig. 3 shows the FT-IR spectrum of the $Ca_{2.99}Al_4ZnO_{10}$: $0.01Sm^{3+}$ sample characterized into several peaks in the range 400-3600 cm^{-1}; of which some are broad and others are moderate in bandwidth. The broad bands are formed due to highly degenerate vibrational states, thermal broadening of lattice dispersion and mechanical scattering [36,37]. The low intensity peaks in the region 400 – 650 cm^{-1} are ascribed to metal-oxygen bond vibrations Ca-O, Al-O [38]. The spectra reveal characteristics absorption centered at 440 cm^{-1} Zn-O stretching vibration. The peaks centered at 510 and 580 cm^{-1} can also be assigned to Zn-O symmetric stretching vibration of ZnO_4 units. The peak at around 638 and 691 cm^{-1} assigned to Al-O bond vibration of AlO_4 units [39,40]. The broad peaks centered at around 764 cm^{-1} due to AlO_4 tetrahedral units [41]. The peaks centered at about 1376 cm^{-1} due to –OH vibrations [42].The peaks centered at about 1641 cm^{-1} accredited to crystal water with H-O-H bending mode [43]. The peak at 2354 cm^{-1} ascribed to antisymmetric stretching of adsorbed water molecules [36]. The peaks center at 2918 cm^{-1} confirms the presence of hydrogen bonding [37]. The band at about 3436 cm^{-1} accredited to fundamental –O-H stretching vibrations disclose the presence of hydroxyl group [44].

3.4. Luminescent Properties:

Fig. 4a and 4b shows the photoluminescence excitation (PLE) and photoluminescence (PL) spectra of $Ca_{3-x}Al_4ZnO_{10}$: xSm^{3+} phosphor monitoring characteristic emission of Sm^{3+} at 601 nm and excitation at 403 nm respectively. The concentration of trivalent samarium ion in $Ca_{3-x}Al_4ZnO_{10}$: xSm^{3+} is varied from x = 0.5 to x = 2.5 mol%. The excitation spectra manifests various sharp peaks at 343, 359, 373, 401, 412, 422, 439, 448, 461, 470, 480, 500 and 525 nm which are accredited to the intra configurational f-f transitions from ground state $^6H_{5/2}$ to various excited states $(^4K, ^4L)_{17/2}$, $(^4D, ^6P)_{5/2}$, $^4L_{17/2}$, $^4F_{7/2}$, $^4L_{13/2}$, $^4M_{19/2}$, $^4G_{9/2}$, $^4M_{17/2}$, $^4I_{13/2}$, $^4I_{11/2}$, $^4M_{15/2}$, $^4G_{7/2}$, and $^4F_{3/2}$, respectively [45–47]. Out of these transitions, the band corresponding to the $^6H_{5/2} \rightarrow ^4F_{7/2}$ transition is the most intense one, which suggests that the

Accepted manuscript

ACCEPTED MANUSCRIPT

$^4F_{7/2}$ level is highly populated by 401 nm excitation, indicating the effective excitation of these phosphors using n-UV LEDs. Therefore, the emission spectra of $Ca_{3-x}Al_4ZnO_{10}$: xSm^{3+} has been recorded under 401 nm excitation. As shown in Fig. 4b, the PL spectra exhibit three emission bands centered at 564, 601, and 651 nm owing to $^4G_{5/2} \rightarrow {}^6H_{5/2}$, $^6H_{7/2}$, and $^6H_{9/2}$ transitions, respectively [1]. Fig. 5 shows the partial energy level diagram of Sm^{3+} doped $Ca_3Al_4ZnO_{10}$ phosphor showing the radiative and non-radiative emissions. All the excitation levels above $^4G_{5/2}$ quickly undergo cascade non-radiative relaxation to this state due to small energy difference in their energy levels as shown in Fig. 5. The $^4G_{5/2}$ state undergoes radiative relaxation to the lower levels $^6H_{5/2}$, $^6H_{7/2}$, and $^6H_{9/2}$ because of the presence of sufficient energy difference between them [48]. The non-radiative energy transfer mechanism might have occurred through the various possible cross relaxation channels between Sm^{3+} ions from $^4G_{5/2}$ state to the nearby Sm^{3+} sites in the ground state. The possible cross relaxation channels are ($^4G_{5/2} \rightarrow {}^6F_{5/2}$; 10793 cm^{-1}) ≈ ($^6H_{5/2} \rightarrow {}^6F_{11/2}$; 10471 cm^{-1}) , ($^4G_{5/2} \rightarrow {}^6F_{7/2}$; 9947 cm^{-1}) ≈ ($^6H_{5/2} \rightarrow {}^6F_{9/2}$; 9090 cm^{-1}), ($^4G_{5/2} \rightarrow {}^6F_{9/2}$; 7784 cm^{-1}) ≈ ($^6H_{5/2} \rightarrow {}^6F_{7/2}$; 7931 cm^{-1}), ($^4G_{5/2} \rightarrow {}^6F_{11/2}$; 7407 cm^{-1}) ≈ ($^6H_{5/2} \rightarrow {}^6F_{5/2}$; 7085 cm^{-1}) referred as CRC1, CRC2, CRC3, and CRC4 respectively as shown in Fig. 5 [49,50].

Among all the emission transitions shown in Fig. 4b, $^4G_{5/2} \rightarrow {}^6H_{7/2}$ observed in visible orange region (601 nm) is more intense than the remaining two. The first transition at 564 nm assigned to $^4G_{5/2} \rightarrow {}^6H_{5/2}$ is purely magnetic dipole (MD) transition and is independent of crystal field obeying the selection rules ($\Delta J = 0, \pm 1$; J is angular momentum); the second one $^4G_{5/2} \rightarrow {}^6H_{7/2}$ at 601 nm obeys the selection rule ($\Delta J = \pm 1$) is a magnetic dipole (MD) transition but here forced electric dipole transition dominates. Therefore, it is partially magnetic and partially forced electric dipole (ED) transition. The third one $^4G_{5/2} \rightarrow {}^6H_{9/2}$ at 651 nm is purely forced electric dipole (ED) crystal field sensitive transition according to the selection rules ($\Delta J \leq 6$; J or J' = 0, when J = 2, 4, 6) [50,51]. The intensity ratio of ED to MD

Accepted manuscript

ACCEPTED MANUSCRIPT

transition describes the asymmetric nature of the local environment of the luminescent center in the host system. Lower the intensity ratio of ED to MD transition, lesser is the distortion from the inversion symmetry. The calculated value of intensity ratio is found to be in the range 0.29 to 0.33. The lower values of intensity ratio suggests the higher environmental symmetry of luminescent ion in the host lattice; which implies that Sm^{3+} ions have been substituted into symmetric nature [52].

3.5. Effect of Sm^{3+} concentration on emission:

It is observed from Fig. 4b that all the prepared phosphors have insignificant change in spectral profile except the intensity variation with the increasing concentration of Sm^{3+} in $Ca_{3-x}Al_4ZnO_{10}$: xSm^{3+} (x= 0.5, 1.0, 1.5, 2.0, and 2.5 mol%) phosphors. Intensity increases up to 1.0 mol% of Sm^{3+} ions and beyond concentration quenching is observed. Thus, the optimized concentration of Sm^{3+} in the as prepared phosphor is 1.0 mol%. The emission intensity variation with Sm^{3+} ion concentration is shown in the inset of Fig. 4b. Fundamentally, the concentration quenching is a phenomenon observed at higher doping concentration due to energy transfer among the activator ions i.e., Sm^{3+} to Sm^{3+}. At higher concentration, the distance between Sm^{3+} ions decrease with increase in concentration. The energy states of these ions are close enough that energy migration from these states to quenching centers occurs with increasing concentration. The occurrence of non-radiative energy transfer from one luminescent center to another at different sites in the host lattice leads to decrease in luminous intensity. The exchange interaction, radiation re-absorption, multipole-multipole interaction are the three possible methods for non-radiative energy transfer [15]. The exchange interaction in short range order can occur up to a critical transfer distance, R_c of 5 Å which cannot be attributed for concentration quenching at very low concentration, since the distance between the two luminescent centers at low concentration will be sufficiently large. The mechanism of radiation re-absorption occurs when there is a

Accepted manuscript

ACCEPTED MANUSCRIPT

broad overlap of excitation and emission spectra, which is not observed for the as prepared phosphors. Therefore, the multipole-multipole interaction account for the quenching phenomenon. The multipole-multipole interaction mechanism is mainly affected by the critical transfer distance (R_c) defined as the distance at which the probability of energy transfer equals the probability of radiative emission and approximately equals to twice the radius of the sphere with this volume [53]. The critical transfer distance [54] can be expressed as:

$$R_c \approx 2\left[\frac{3V}{4\pi X_c N}\right]^{\frac{1}{3}} \quad \text{(C)}$$

where, N is the number of cations per unit cell (N = 4), V is the volume of the unit cell (V = 923.438 $Å^3$), and X_c is the critical concentration (X_c =0.01 mole). The value of R_c is calculated to be 35.33 Å much greater than 5 Å. Hence the energy transfer due to multipole-multipole interaction causes the concentration quenching [15,55].

Then according to the Dexter theory [56], the emission intensity per activator ion can be described by the following relation:

$$\frac{I}{x} = K\{1 + \beta(x)^{\frac{Q}{3}}\}^{-1} \quad \text{(D)}$$

where x is the activator ion concentration, K and β are some constants for the same excitation for a given host lattice. The value of Q defines the type of interaction among the nearest neighbor ions, Q = 3, 6, 8, and 10 for exchange interaction, dipole-dipole, dipole-quadrupole, quadrupole-quadrupole interaction, respectively.

Assuming that $\beta x^{Q/3} >> 1$, the above equation can be reduced to [54]:

$$log\frac{I}{x} = K' - \frac{Qlog(x)}{3}; \quad where\ (K' = logk - log\beta) \quad \text{(E)}$$

Accepted manuscript

ACCEPTED MANUSCRIPT

Therefore, to get the correct the value of Q for Sm^{3+} sites in the host lattice, the graph between log(I/x) and log (x) has been plotted as shown in Fig. 6 that yields a straight-line plot having slope -Q/3. In the present study, the slope comes out to be -1.714, which gives Q = 5.142 close to 6, implying dipole-dipole interaction is the underlying mechanism for quenching of Sm^{3+} site emission centers in the host lattice [55].

3.6. Color chromaticity coordinates:

From the recorded emission spectra of CAZ phosphors, CIE chromaticity coordinates have been calculated and found to be (0.571, 0.426), (0.574, 0.424), (0.576, 0.422), (0.575, 0.423), (0.577, 0.421) for 0.5, 1.0, 1.5, 2.0, and 2.5 mol% of Sm^{3+} concentration, respectively. Fig. 7 shows the CIE coordinates (0.574, 0.424) for the optimized sample $Ca_{2.99}Al_4ZnO_{10}$: $0.01Sm^{3+}$. From the CIE diagram, it is observed that $Ca_3Al_4ZnO_{10}$: Sm^{3+} phosphor exhibit pure orange color. The calculated CIE coordinates for all the samples are in close proximity to Nichia Corporation developed Amber LED NSPAR 70BS (0.570, 0.420) [47]. The correlated color temperature (CCT) has been calculated empirically from the equation:

$$CCT = -437\left[\frac{x-x_e}{y-y_e}\right]^3 + 3601\left[\frac{x-x_e}{y-y_e}\right]^2 - 6861\left[\frac{x-x_e}{y-y_e}\right] + 5514.31 \qquad \text{(F)}$$

given by McCamy [54], where (x,y) are the chromaticity coordinates of $Ca_3Al_4ZnO_{10}$: Sm^{3+} phosphor and and (x_e, y_e) is the chromaticity epicenter (0.338, 0.186) respectively) [58]. The CCT values are found to be 1829.81, 1811.25, 1798.91, 1804.33, and 1792.95 K for $Ca_{3-x}Al_4ZnO_{10}$: xSm^{3+} where, x= 0.5, 1.0, 1.5, 2.0, and 2.5 mol% respectively. Therefore, it is expected that the samarium doped CAZ phosphors show favorable properties for n-UV excited LED driven orange component for warm white light display devices with low CCT.

3.7. **Time Resolved Photoluminescence analysis:**

Accepted manuscript

ACCEPTED MANUSCRIPT

The room temperature decay profile for CAZ phosphors have been recorded for $^4G_{5/2}$ level of Sm^{3+} ions under 401 nm excitation. Fig. 8 represents the decay curves well fitted with a double exponential function:

$$I_t = I_0 + A_1 \exp\left(-\frac{t}{\tau_1}\right) + A_2 \exp\left(-\frac{t}{\tau_2}\right) \quad \text{(G)}$$

for all the samples, where I_t and I_0 are the emission intensities at time t and 0 respectively; A_1, and A_2 are constants; τ_1 and τ_2 are the rapid and slow lifetimes for exponential components respectively. The average lifetime (τ) has been calculated for the series of CAZ phosphor by using the formula [50]:

$$\tau = \frac{A_1\tau_1^2 + A_2\tau_2^2}{A_1\tau_1 + A_2\tau_2} \quad \text{(H)}$$

The lifetime values are found to be 1.64, 1.49, 1.44, 1.38, and 1.33 μs for 0.5, 1.0, 1.5, 2.0, and 2.5 mol% of Sm^{3+} in CAZ phosphor, respectively. It can be observed that the average lifetime decreases with increase in Sm^{3+} concentration due to the energy transfer among Sm^{3+} ions at shorter distances. The decrease in lifetime with increasing Sm^{3+} concentration is plotted and shown in the inset of Fig. 8.

4. Conclusions.

Sm^{3+} doped monophasic $Ca_3Al_4ZnO_{10}$ powder phosphor has been synthesized by high temperature solid state reaction technique. The XRD profile confirms the phase purity of the as prepared phosphor with average crystallite size in 60-110 nm range calculated by Debye-Scherer's method, which are in close proximity with the result obtained from W-H method. The SEM micrographs reveal inhomogeneous, irregular morphology with some agglomeration in the samples. The PL study reveals that the as synthesized phosphors have three emission bands with the intense emission at 601 nm for $^4G_{5/2} \rightarrow {}^6H_{7/2}$ transition when

Accepted manuscript

ACCEPTED MANUSCRIPT

pumped from $^6H_{5/2} \rightarrow {}^4F_{7/2}$ at 401 nm wavelength. The concentration quenching has been obtained beyond 1.0 mol% of Sm^{3+}. The calculated result reveals that the dipole-dipole interaction plays a major role in the quenching phenomenon. The calculated CIE chromaticity coordinates for all the samples lie in the orange region and the chromaticity values for the optimized sample are (0.574, 0.424) showing insignificant deviation from the coordinates specified by Nichia Corporation developed Amber LED NSPAR 70BS (0.570, 0.420). The TR-PL study reveals the bi-exponential behavior of the decay curves with decay time in 1.64-1.33 μs range. All these results indicate that the prepared $Ca_{3-x}Al_4ZnO_{10}$: xSm^{3+} powder phosphor serve as an efficient orange emitting phosphor for display and solid-state lighting devices.

Acknowledgement

One of the authors Ms. Sumandeep Kaur is grateful to University Grants Commission (UGC) for providing financial support in the form of Junior Research Fellowship (JRF) to her. The author (M. Jayasimhadri) also grateful to DST-SERB, Govt. of India for the sanction of a research project (No. SB/FTP/PS-082/2014, dt. 02/03/2015).

References

[1] Yu R, Guo Y, Wang L, Noh HM, Moon BK, Choi BC, et al. Characterizations and optical properties of orange-red emitting Sm^{3+}-doped Y_6WO_{12} phosphors. J Lumin 2014;155:317–21. doi:10.1016/j.jlumin.2014.06.041.

[2] Chen X, Zhao J, Yu L, Rong C, Li C, Lian S. A white light emitting phosphor $Sr_{1.5}Ca_{0.5}SiO_4$:Eu^{3+}, Tb^{3+}, Eu^{2+} for LED-based near-UV chip: Preparation, characterization and luminescent mechanism. J Lumin 2011;131:2697–702. doi:10.1016/j.jlumin.2011.06.056.

Accepted manuscript

ACCEPTED MANUSCRIPT

[3] Rao GM, Hussain SK, Seeta Rama Raju G, Subba Rao PSV, Yu JS. Synthesis and characterizations of novel $Sr_2Gd_8(SiO_4)_6O_2:Eu^{3+}$ oxyapatite phosphors for solid-state lighting and display applications. J Alloys Compd 2016;660:437–45. doi:10.1016/j.jallcom.2015.11.109.

[4] Bondzior B, Stefańska D, Kubiak A, Dereń PJ. Spectroscopic properties of $K_4SrSi_3O_9$ doped with Sm^{3+}. J Lumin 2016;173:38–43. doi:10.1016/j.jlumin.2015.12.031.

[5] Yang F, Yang Z, Yu Q, Liu Y, Li X, Lu F. Sm^{3+}-doped $Ba_3Bi(PO_4)_3$ orange reddish emitting phosphor. Spectrochim Acta-Part A Mol Biomol Spectrosc 2013;105:626–31. doi:10.1016/j.saa.2013.01.010.

[6] He G, Mei L, Wang L, Liu G, Li J. Synthesis and Luminescence Properties of Nano- / Microstructured $Y_3Al_5O_{12}$: Ce^{3+} Microspheres by Controlled Glass Crystallization. Cryst Growth Des 2011;11:5355–61.

[7] Bedekar V, Dutta DP, Mohapatra M, Godbole S V, Ghildiyal R, Tyagi a K. Rare-earth doped gadolinia based phosphors for potential multicolor and white light emitting deep UV LEDs. Nanotechnology 2009;20:125707. doi:10.1088/0957-4484/20/12/125707.

[8] Yang Z, Dong H, Liu P, Hou C, Liang X, Wang C, et al. Photoluminescence properties of Sm^{3+}-doped $LiY(MoO_4)_2$ red phosphors. J Rare Earths 2014;32:404–8. doi:10.1016/S1002-0721(14)60085-5.

[9] Wang Z, Li P, Yang Z, Guo Q. A novel red phosphor $BaZn_2(PO_4)_2:Sm^{3+}$, R^+ (R=Li, Na, K). J Lumin 2012;132:1944–8. doi:10.1016/j.jlumin.2012.03.022.

[10] Wang L, Noh HM, Moon BK, Choi BC, Jeong JH, Shi J. Luminescent properties and energy transfer of Sm^{3+} doped $Sr_2CaMo_{1-x}W_xO_6$ as a potential phosphor for white LEDs. J Alloys Compd 2016;663:808–17. doi:10.1016/j.jallcom.2015.12.179.

Accepted manuscript

ACCEPTED MANUSCRIPT

[11] Choi NS, Park KW, Park BW, Zhang XM, Kim JS, Kung P, et al. Eu^{2+}-Mn^{2+} energy transfer in white-light-emitting T-phase $(Ba,Ca)_2SiO_4:Eu^{2+}$, Mn^{2+} phosphor. J Lumin 2010;130:560–6. doi:10.1016/j.jlumin.2009.10.031.

[12] Zhu G, Wang Y, Ci Z, Liu B, Shi Y, Xin S. $Ca_8Mg(SiO_4)_4Cl_2:Ce^{3+}$, Tb^{3+}: A potential single-phased phosphor for white-light-emitting diodes. J Lumin 2012;132:531–6. doi:10.1016/j.jlumin.2011.09.029.

[13] Yu R, Mi Noh H, Kee Moon B, Chun Choi B, Hyun Jeong J, Sueb Lee H, et al. Photoluminescence characteristics of Sm3+-doped Ba_2CaWO_6 as new orange-red emitting phosphors. J Lumin 2014;152:133–7. doi:10.1016/j.jlumin.2014.01.074.

[14] Yu R, Mi Noh H, Kee Moon B, Chun Choi B, Hyun Jeong J, Sueb Lee H, et al. Photoluminescence characteristics of Sm^{3+} doped $Ba_3La(PO_4)_3$ as new orange-red emitting phosphors. J Lumin 2014;145:717–22. doi:10.1016/j.jlumin.2013.08.049.

[15] Maheshwary, Singh BP, Singh RA. Color tuning in thermally stable Sm^{3+} -activated $CaWO_4$ nanophosphors. New J Chem 2015;39:4494–507. doi:10.1039/C4NJ01911C.

[16] Xu J, Ju Z, Gao X, An Y, Tang X, Liu W. $Na_2CaSn_2Ge_3O_{12}$: A Novel Host Lattice for Sm^{3+}-Doped LongPersistent Phosphorescence Materials Emitting Reddish Orange Light. Inorg Chem 2013;52:13875–81.

[17] Kiran N, Baker AP, Wang G. Synthesis and luminescence properties of MgO : Sm^{3+} phosphor for white light-emitting diodes. J Mol Struct 2017;1129:211–5. doi:10.1016/j.molstruc.2016.09.046.

[18] Vishwakarma AK, Jayasimhadri M. Pure orange color emitting Sm^{3+} doped $BaNb_2O_6$ phosphor for solid - state lighting applications. J Lumin 2016;176:112–7. doi:10.1016/j.jlumin.2016.03.025.

Accepted manuscript

ACCEPTED MANUSCRIPT

[19] Li Q, Yuan Y, Wei T, Li Y, Chen Z, Jin X, et al. The origin of efficiency enhancement of inorganic/organic Hybrid solar Cells by robust samarium phosphate nanophosphors. Sol Energy Mater Sol Cells 2014;130:426–34. doi:10.1016/j.solmat.2014.07.033.

[20] Liu Q, Li X, Zhang B, Wang L, Zhang Q, Zhang L. Structure evolution and delayed quenching of the double perovskite $NaLaMgWO_6$: Eu^{3+}phosphor for white LEDs. Ceram Int 2016;42:15294–300. doi:10.1016/j.ceramint.2016.06.169.

[21] Li F, Li L, Guo C, Li T, Noh HM, Jeong JH. Up-conversion luminescence properties of Yb^{3+}–Ho^{3+} co-doped $CaLa_2ZnO_5$. Ceram Int 2014;40:7363–6. doi:10.1016/j.ceramint.2013.12.080.

[22] Li L, Guo C, Jiang S, Agrawal DK, Li T. Green up-conversion luminescence of Yb^{3+}-Er^{3+} co-doped $CaLa_2ZnO_5$ for optically temperature sensing. RSC Adv 2014;5:6391–6. doi:10.1039/c3ra47264g.

[23] Xu D, Haranath D, He H, Mishra S, Bharti I. Studies on phase stability, mechanical, optical and electronic properties of a new Gd 2 CaZnO 5 phosphor system for LEDs †. Crystengcomm 2014:1652–8. doi:10.1039/c3ce42194e.

[24] Shih H, Tsai Y, Liu K, Liao Y, Chang Y. The luminescent properties of Pr^{3+} ion-doped BaY_2ZnO_5 phosphor under blue light irradiation. Opt Mater 2013;35:2654–7. doi:10.1016/j.optmat.2013.08.007.

[25] Dalal M, Taxak VB, Chahar S, Dalal J, Khatkar A, Khatkar SP. Judd-Ofelt and structural analysis of colour tunable BaY_2ZnO_5:Eu^{3+} nanocrystals for single-phased white LEDs. J Alloys Compd 2016;686:366–74. doi:10.1016/j.jallcom.2016.06.040.

[26] Wei D, Qin L, Huang Y, Seo HJ. Photoluminescence properties of Eu^{2+}-activated $BaCa_2Al_8O_{15}$ nanophosphors. Ceram Int 2013;39:2383–7.

Accepted manuscript

ACCEPTED MANUSCRIPT

doi:10.1016/j.ceramint.2012.08.090.

[27] Liang C-H, Teoh L-G, Liu KT, Chang Y-S. Near white light emission of BaY_2ZnO_5 doped with Dy^{3+} ions. J Alloys Compd 2012;517:9–13. doi:10.1016/j.jallcom.2011.11.088.

[28] Liang Z, Qin F, Zheng Y, Zhang Z, Cao W. Noncontact thermometry based on downconversion luminescence from Eu^{3+} doped $LiNbO_3$ single crystal. Sensors Actuators A Phys 2016;238:215–9. doi:10.1016/j.sna.2015.12.018.

[29] Wang F, Chen K, Chien Y, Chang C, Chuang M. Enhanced luminance for inorganic electroluminescent devices with a charged electret. J Lumin 2013;141:106–10. doi:10.1016/j.jlumin.2013.03.020.

[30] Holst G, Grunwald B. Luminescence lifetime imaging with transparent oxygen optodes. Sensors Actuators, B Chem 2001;74:78–90. doi:10.1016/S0925-4005(00)00715-2.

[31] Zhang J, Chen G, Zhai Z. Investigations on luminescence of $CaLa_4Si_3O_{13}$ -based phosphors for multifunctional applications. J Alloys Compd 2016;682:618–26. doi:10.1016/j.jallcom.2016.05.046.

[32] Sawala NS, Omanwar SK. Downconversion from ultra violet to near infer red region in novel Yb^{3+} doped $LiSrVO_4$ phosphor. J Alloys Compd 2016;686:287–91. doi:10.1016/j.jallcom.2016.05.275.

[33] Kaur S, Jayasimhadri M, Rao AS. A novel red emitting Eu3+ doped calcium aluminozincate phosphor for applications in w-LEDs. J Alloys Compd 2017;697:367–73. doi:10.1016/j.jallcom.2016.12.150.

Accepted manuscript

ACCEPTED MANUSCRIPT

[34] Naik R, Prashantha SC, Nagabhushana H, Sharma SC, Nagaswarupa HP, Anantharaju KS, et al. A single phase, red emissive $Mg_2SiO_4:Sm^{3+}$ nanophosphor prepared via rapid propellant combustion route. Spectrochim Acta A Mol Biomol Spectrosc 2015;140C:516–23. doi:10.1016/j.saa.2015.01.011.

[35] Vishwakarma AK, Jha K, Jayasimhadri M, Sivaiah B, Gahtori B, Haranath D. Emerging cool white light emission from Dy^{3+} doped single phase alkaline earth niobate phosphors for indoor lighting applications. Dalt Trans 2015;44:17166–74. doi:10.1039/c5dt02436f.

[36] Swapna K, Mahamuda S, Rao AS, Shakya S, Sasikala T, Haranath D, et al. Spectrochimica Acta Part A : Molecular and Biomolecular Spectroscopy Optical studies of Sm^{3+} ions doped Zinc Alumino Bismuth Borate glasses. Spectrochim acta part A Mol Biomol Spectrosc 2014;125:53–60. doi:10.1016/j.saa.2014.01.025.

[37] Mahamuda S, Swapna K, Venkateswarlu M, Rao AS, Shakya S, Prakash GV. Spectral characterisation of Sm^{3+} ions doped Oxy- fluoroborate glasses for visible orange luminescent applications. J Lumin 2014;154:410–24. doi:10.1016/j.jlumin.2014.05.017.

[38] Kumar JS, Pavani K, Babu AM, Kumar N, Rai SB, Moorthy LR. Fluorescence characteristics of Dy^{3+} ions in calcium fluoroborate glasses. J Lumin 2010;130:1916–23. doi:10.1016/j.jlumin.2010.05.006.

[39] Singh GP, Kaur S, Kaur P, Singh DP. Modification in structural and optical properties of ZnO, CeO_2 doped Al_2O_3-PbO-B_2O_3 glasses. Phys B Phys Condens Matter 2012;407:1250–5. doi:10.1016/j.physb.2012.01.114.

[40] Tarafder A, Rahaman A, Mukhopadhyay S, Karmakar B. Fabrication and enhanced

Accepted manuscript

ACCEPTED MANUSCRIPT

photoluminescence properties of Sm^{3+}-doped $ZnO–Al_2O_3–B_2O_3–SiO_2$ glass derived willemite glass – ceramic nanocomposites. Opt Mater 2014;36:1463–70. doi:10.1016/j.optmat.2014.03.035.

[41] Mohini GJ, Krishnamacharyulu N, Baskaran GS, Rao PV, Veeraiah N. Applied Surface Science Studies on influence of aluminium ions on the bioactivity of $B_2O_3–SiO_2–P_2O_5–Na_2O–CaO$ glass system by means of spectroscopic studies. Appl Surf Sci 2013;287:46–53. doi:10.1016/j.apsusc.2013.09.055.

[42] Pappas CS, Tarantilis PA, Harizanis PC, Polissiou MG. New Method for Pollen Identification by FT-IR Spectroscopy. Appl. Spectrosc. 2003;57:23–7.

[43] Balachander L, Ramadevudu G, Sayanna R, Venudhar YC. IR analysis of borate glasses containing three alkali oxides. Sci Asia 2013;39:278–83. doi:10.2306/scienceasia1513-1874.2013.39.278.

[44] Wang PF, Li ZH, Li J, Zhu YM. Effect of ZnO on the interfacial bonding between $Na_2O–B_2O_3–SiO_2$ vitrified bond and diamond. Solid State Sci 2009;11:1427–32. doi:10.1016/j.solidstatesciences.2009.04.026.

[45] Xu Q, Xu D, Sun J. Preparation and luminescence properties of orange – red $Ba_3Y(PO_4)_3$: Sm^{3+} phosphors. Opt Mater 2015;42:210–4. doi:10.1016/j.optmat.2014.12.035.

[46] Jayasankar CK, Babu P. Optical properties of Sm^{3+} ions in lithium borate and lithium fluoroborate glasses. J. Alloys Compd. 2000;307:82–95.

[47] Xiguang GU, Renli FU, Weina J, Pengfei Z, Ye T. phosphor prepared by the Pechini-type sol-gel process. J Rare Earths 2015;33:954–60. doi:10.1016/S1002-0721(14)60511-1.

Accepted manuscript

ACCEPTED MANUSCRIPT

[48] Jamalaiah BC, Kumar JS, Babu AM, Suhasini T, Ã LRM. Photoluminescence properties of Sm^{3+} in LBTAF glasses. J Lumin 2009;129:363–9. doi:10.1016/j.jlumin.2008.11.001.

[49] Karthikeyan P, Arunkumar S, Basavapoornima C, Marimuthu K. Modifier effect on the spectroscopic properties of telluro fluoroborate glasses containing Sm^{3}+ ions. J Lumin 2016;178:43–53. doi:10.1016/j.jlumin.2016.05.037.

[50] Wang L, Noh HM, Moon BK, Park SH, Kim KH, Shi J, et al. Dual-Mode Luminescence with Broad Near UV and Blue Excitation Band from Sr_2CaMoO_6:Sm^{3+} Phosphor for White LEDs. J Phys Chem C 2015;119:15517–25. doi:10.1021/acs.jpcc.5b02828.

[51] Zhang W, Zhang Y, Ouyang S, Zhang Z, Xia H. Enhanced luminescent properties of Sm^{3+} doped glass ceramics – as potential red–orange phosphor for white light-emitting diodes. Mater Lett 2015;160:459–62. doi:10.1016/j.matlet.2015.08.002.

[52] Mariyappan M, Arunkumar S, Marimuthu K. Effect of Bi_2O_3 on the structural and spectroscopic properties of Sm^{3+} ions doped sodium fluoroborate glasses. J Mol Struct 2016;1105:214–24. doi:10.1016/j.molstruc.2015.10.043.

[53] Som S, Kumar V, Kumar V, Gohain M, Pandey A, Duvenhage MM, et al. Ultrasonics Sonochemistry Dopant distribution and influence of sonication temperature on the pure red light emission of mixed oxide phosphor for solid state lighting. Ultrason Sonochem 2016;28:79–89. doi:10.1016/j.ultsonch.2015.07.003.

[54] Darshan GP, Premkumar HB, Nagabhushana H, Sharma SC, Prashanth SC, Prasad BD. Effective fingerprint recognition technique using doped yttrium aluminate nano phosphor material. J Colloid Interface Sci 2016;464:206–18.

Accepted manuscript

ACCEPTED MANUSCRIPT

doi:10.1016/j.jcis.2015.11.025.

[55] Ce BSO, Xia Z, Liang Y, Yu D, Zhang M, Huang W. Optics & Laser Technology Photoluminescence properties and energy transfer in color tunable. Opt Laser Technol 2014;56:387–92. doi:10.1016/j.optlastec.2013.09.014.

[56] Dexter DL. A Theory of Sensitized Luminescence in Solids. J Chem Phys 1953;21:836. doi:10.1063/1.1699044.

[57] McCamy CS. Correlated Color Temperature as an Explicit Function of Chromaticity Coordinates. Color Res Appl 1992;17:142–4.

[58] Jha K, Jayasimhadri M. Spectroscopic investigation on thermally stable Dy^{3+} doped zinc phosphate glasses for white light emitting diodes. J Alloys Compd 2016;688:833–40. doi:10.1016/j.jallcom.2016.07.024.

Fig. 1(a): XRD pattern of $Ca_{3-x}Al_4ZnO_{10}$: xSm^{3+} (x = 0.0, 0.5, 1.0 and 2.0 mol %) along with standard diffraction pattern of $Ca_3Al_4ZnO_{10}$. **(b):** W-H plot of $Ca_{3-x}Al_4ZnO_{10}$: xSm^{3+} (x = 0.0, 0.5, 1.0 and 2.0 mol%).

Fig. 2: SEM image of $Ca_{3-x}Al_4ZnO_{10}$; xSm^{3+} (x = 1.0 mol%).

Fig. 3: FT-IR analysis of $Ca_{3-x}Al_4ZnO_{10}$; xSm^{3+} (x = 1.0 mol%).

Fig. 4(a): The excitation spectra of $Ca_{3-x}Al_4ZnO_{10}$: xSm^{3+} (x = 0.5, 1.0, 1.5, 2.0 and 2.5 mol%) λ_{em} = 601 nm. **(b):** The emission spectra of $Ca_{3-x}Al_4ZnO_{10}$: xSm^{3+} (x = 0.5, 1.0, 1.5, 2.0 and 2.5 mol%) λ_{ex} = 401 nm. (Inset: Plot of Intensity vs Concentration)

Fig. 5: Partial Energy level diagram and possible cross-relaxation channels of Sm^{3+} ion doped CAZ phosphor.

Fig. 6: Plot of log (I/x) vs log (x).

Fig. 7: CIE Chromaticity diagram of CAZ phosphor doped with 1.0 mol% of Sm^{3+} ions (λ_{ex} =

Accepted manuscript

ACCEPTED MANUSCRIPT

401 nm).

Fig. 8: Decay curves of $Ca_{3-x}Al_4ZnO_{10}$: xSm^{3+} (x = 0.5, 1.0, 1.5, 2.0 and 2.5 mol%) λ_{ex} = 401 nm and λ_{em} = 601 nm. (Inset: Plot of lifetime of Sm^{3+} doped CAZ phosphor vs concentration of Sm^{3+}).

Accepted manuscript

ACCEPTED MANUSCRIPT

Fig. 1(a).

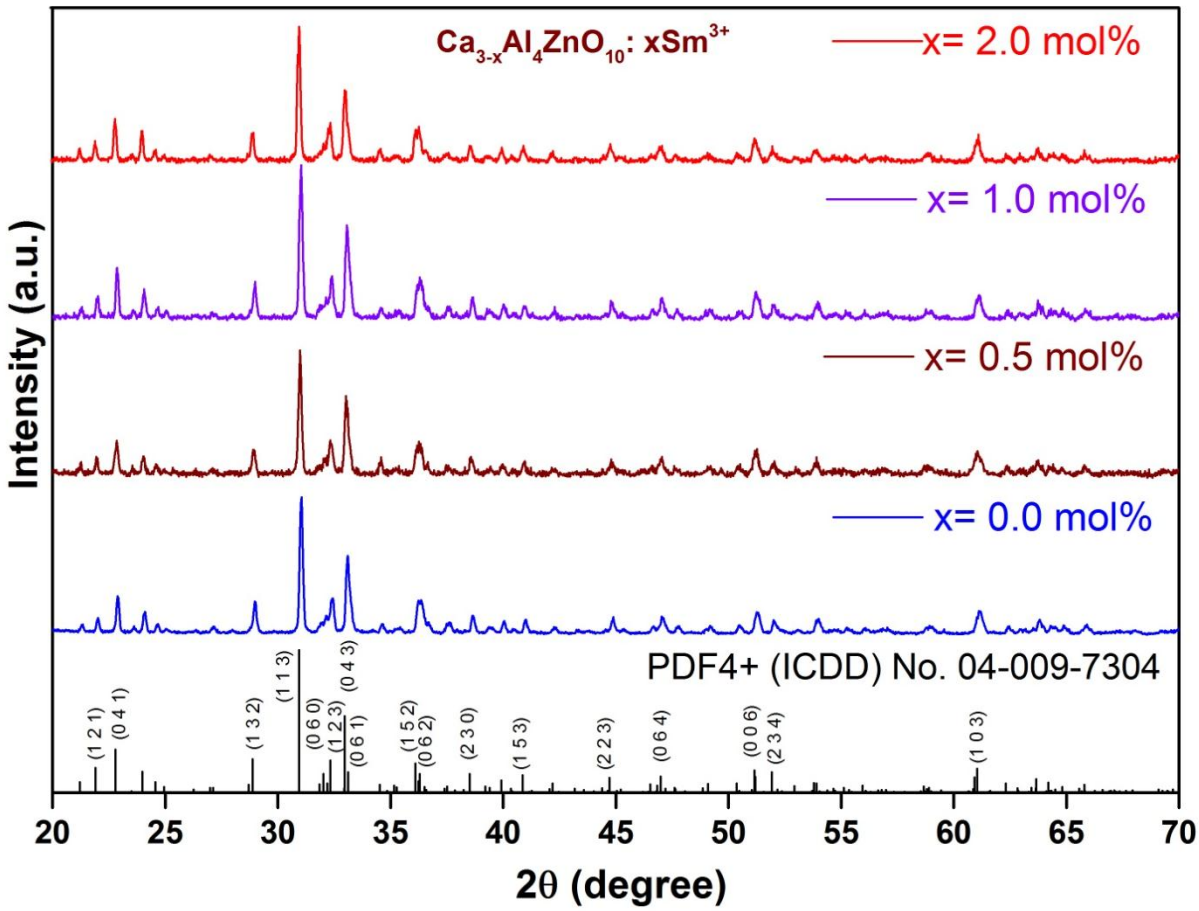

Accep

ACCEPTED MANUSCRIPT

Fig. 1(b).

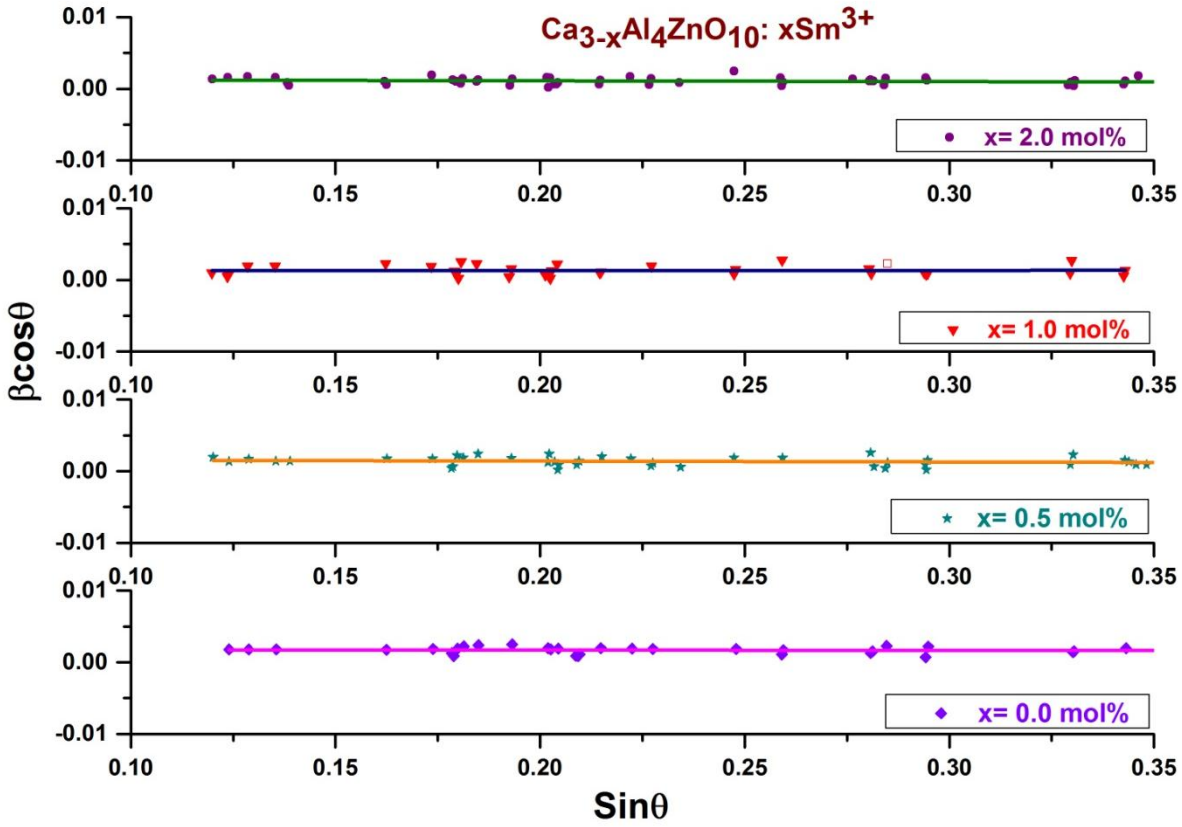

Accepte

ACCEPTED MANUSCRIPT

Fig. 2.

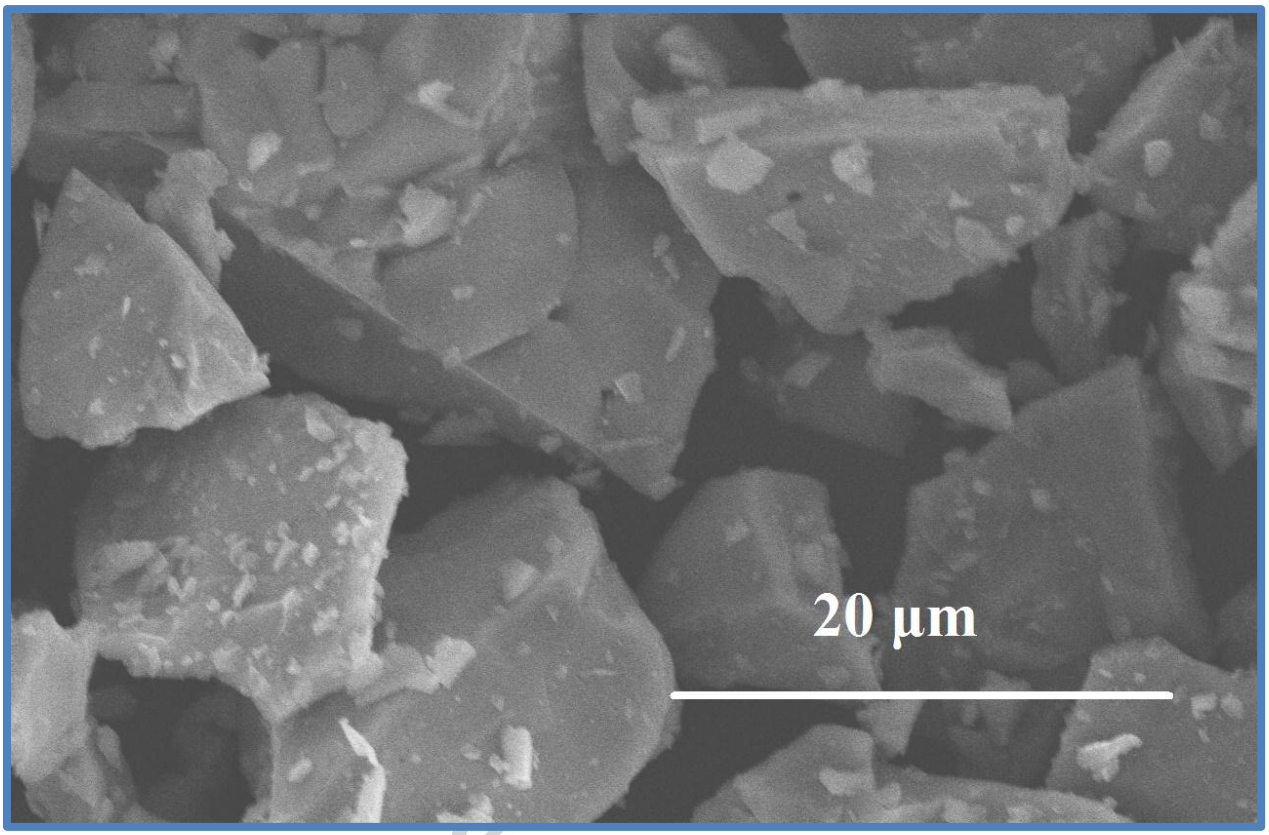

Accepte

ACCEPTED MANUSCRIPT

Fig. 3.

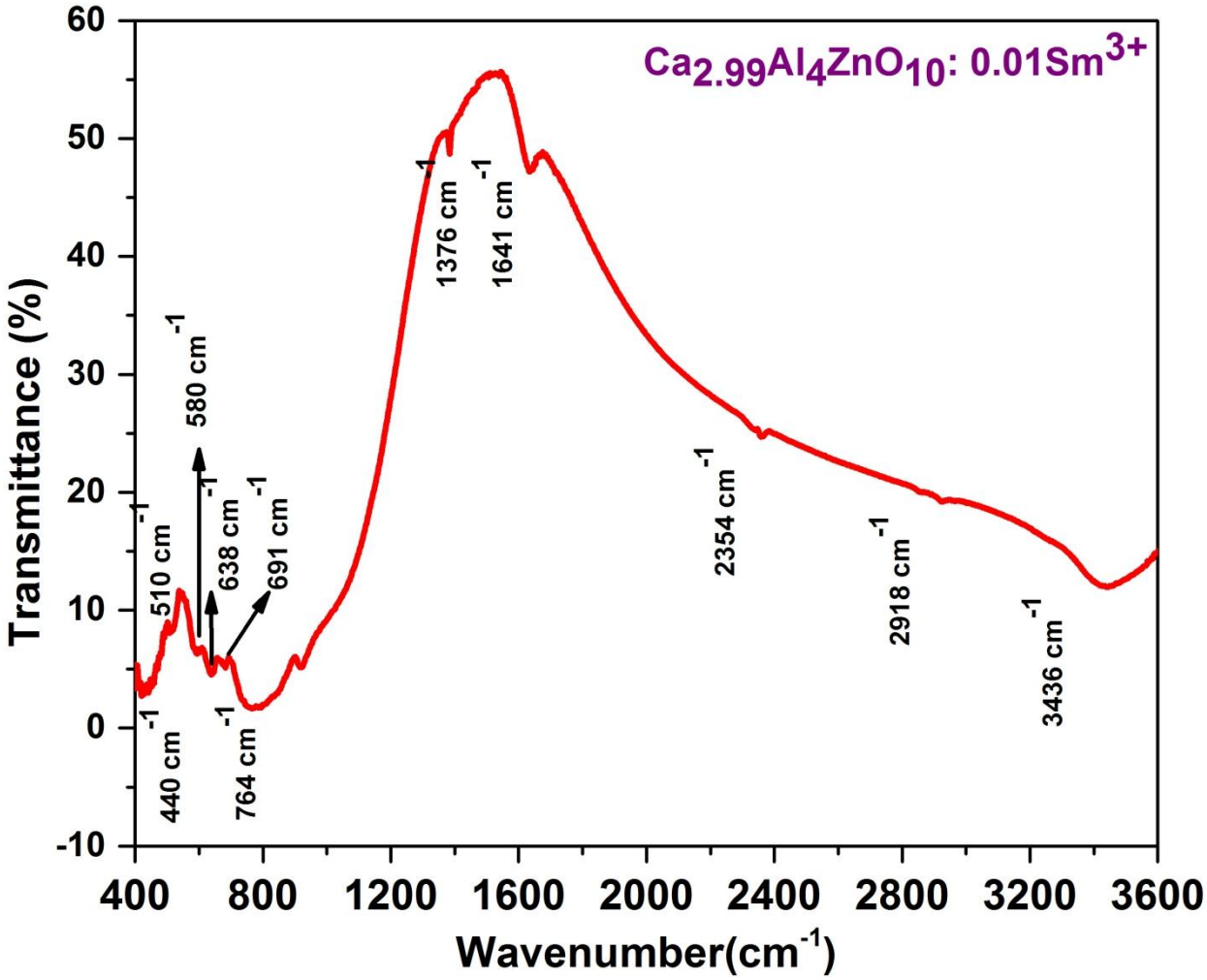

ACCEPTED MANUSCRIPT

Fig. 4(a).

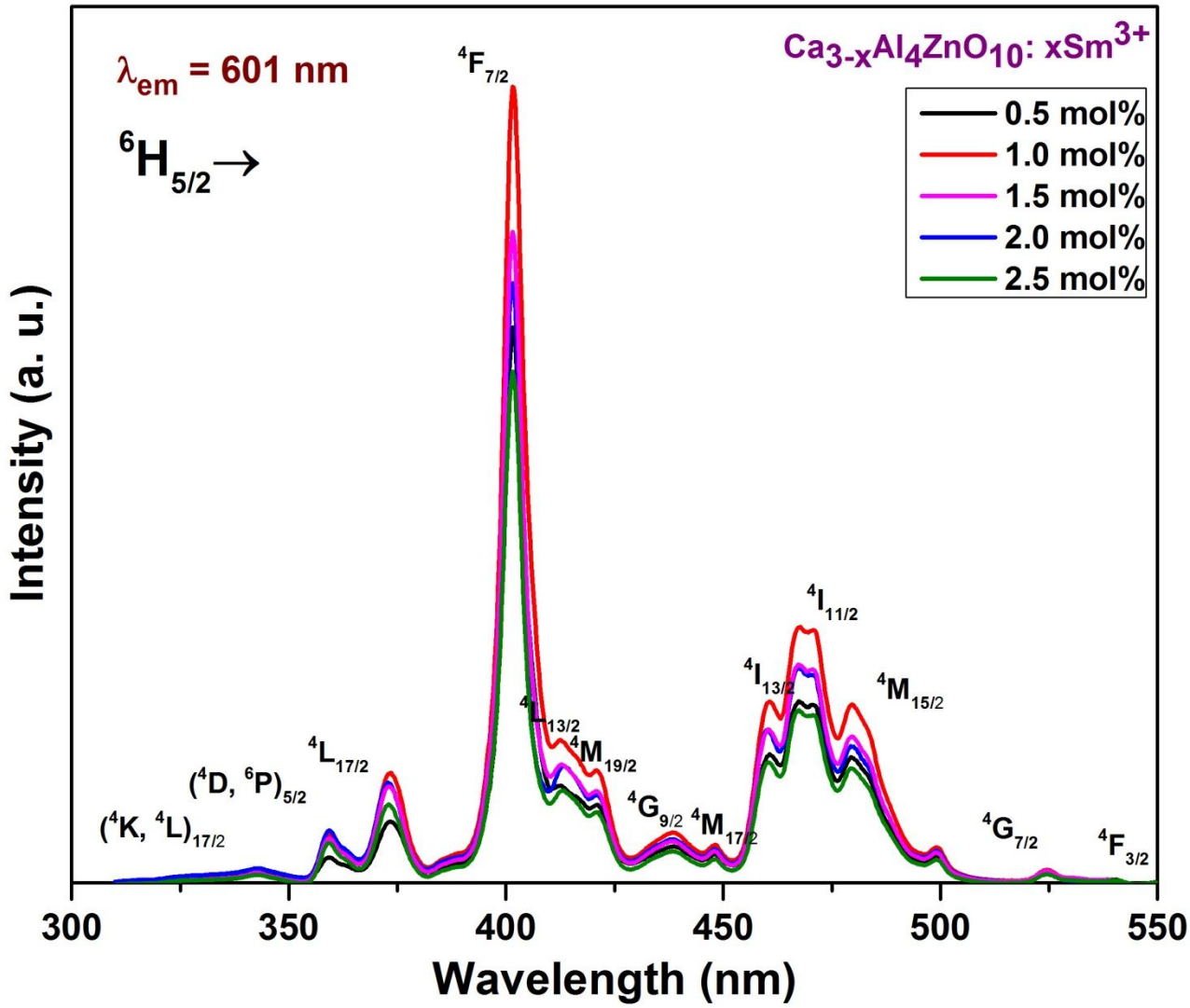

ACCEPTED MANUSCRIPT

Fig. 4(b)

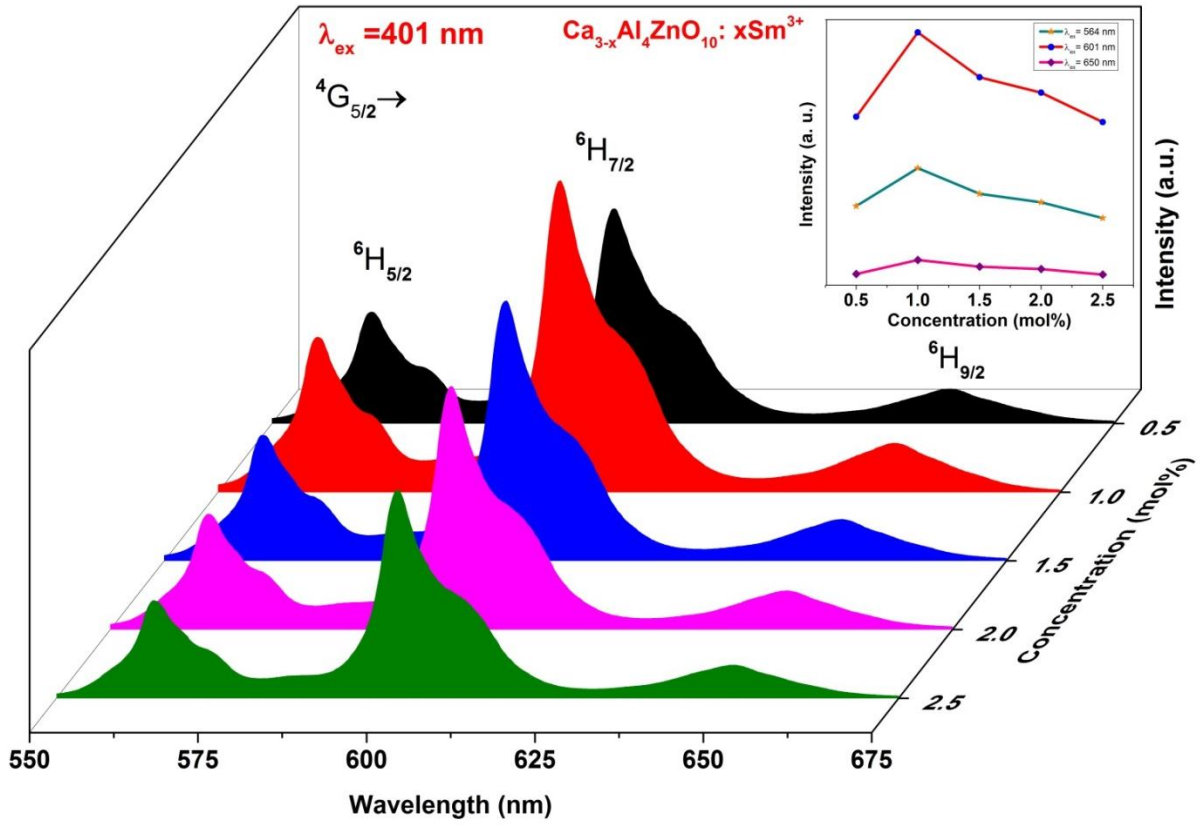

Fig. 5.

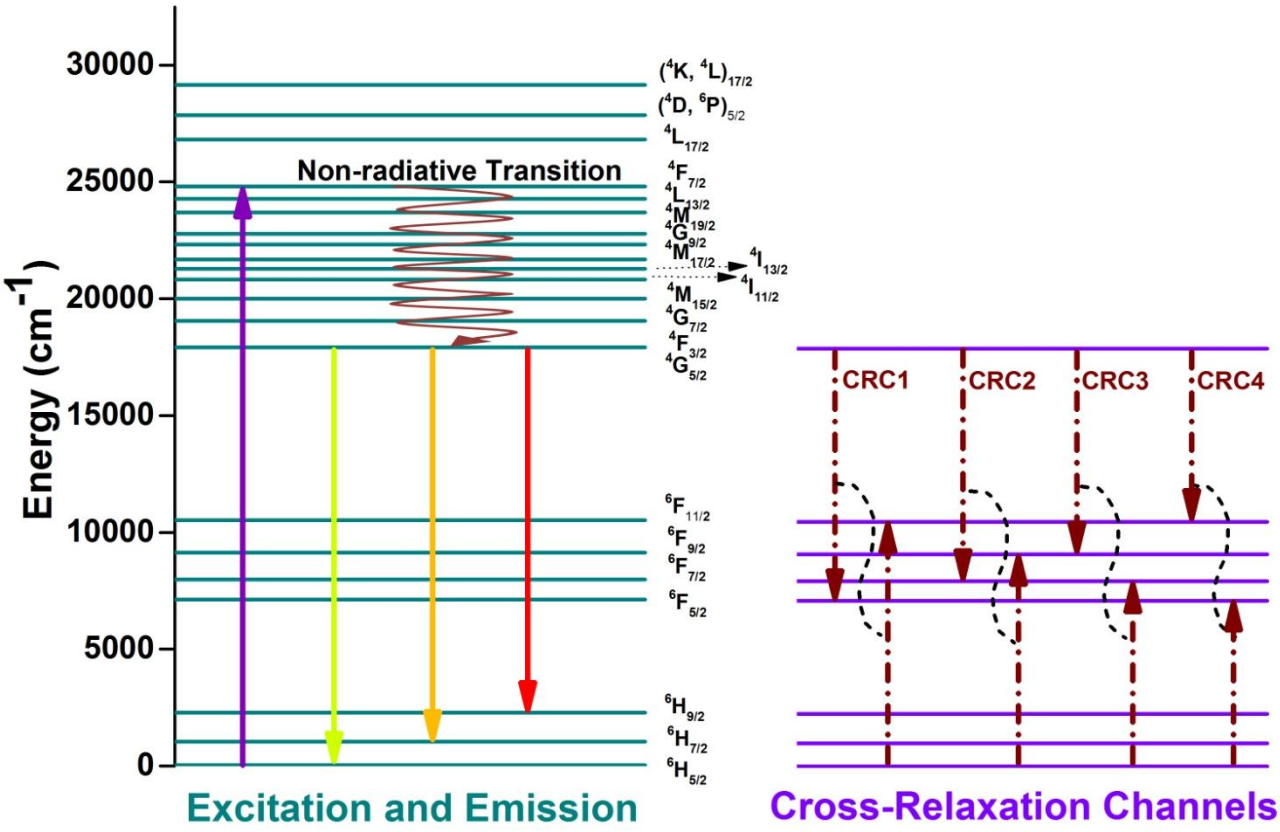

Accepted

ACCEPTED MANUSCRIPT

Fig. 6.

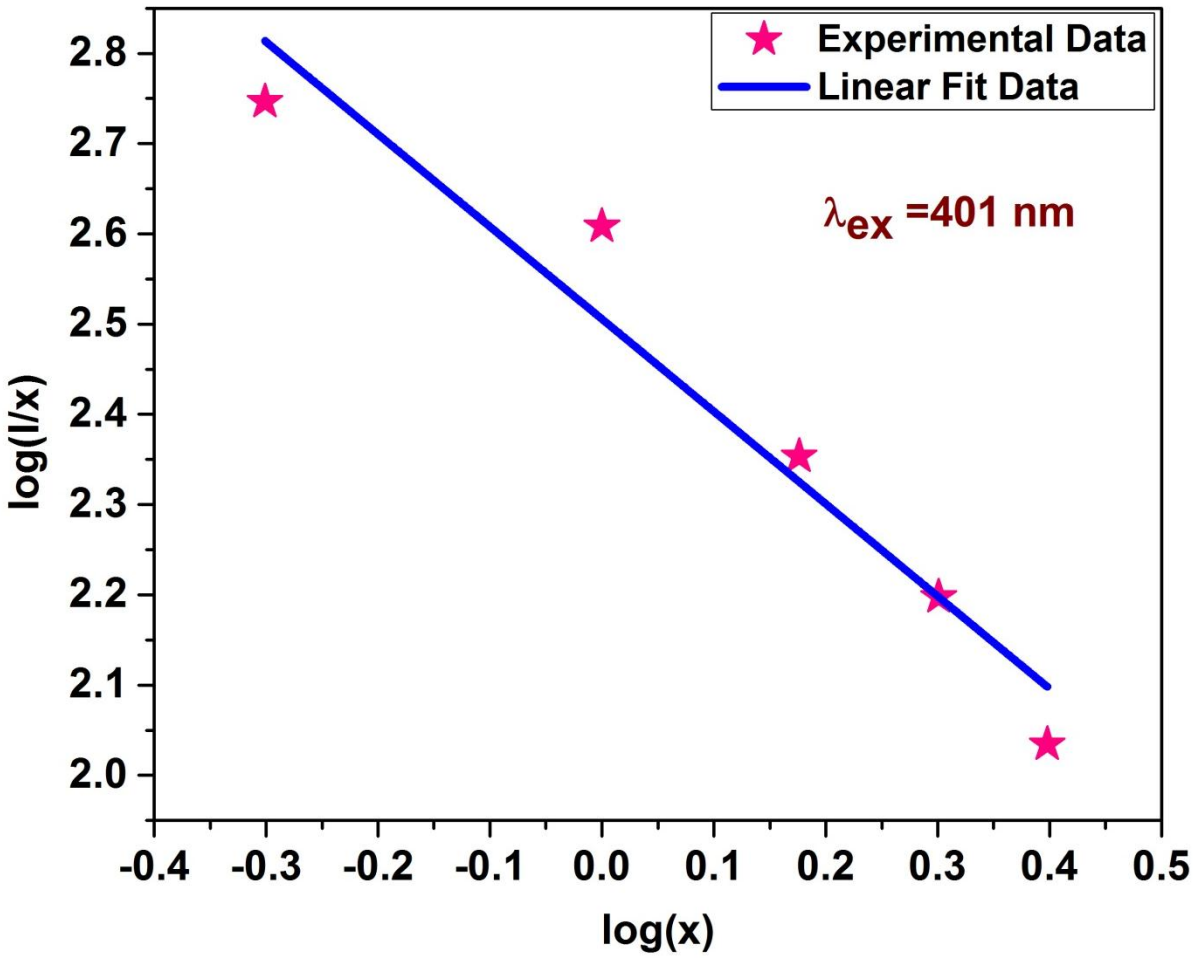

Fig. 7.

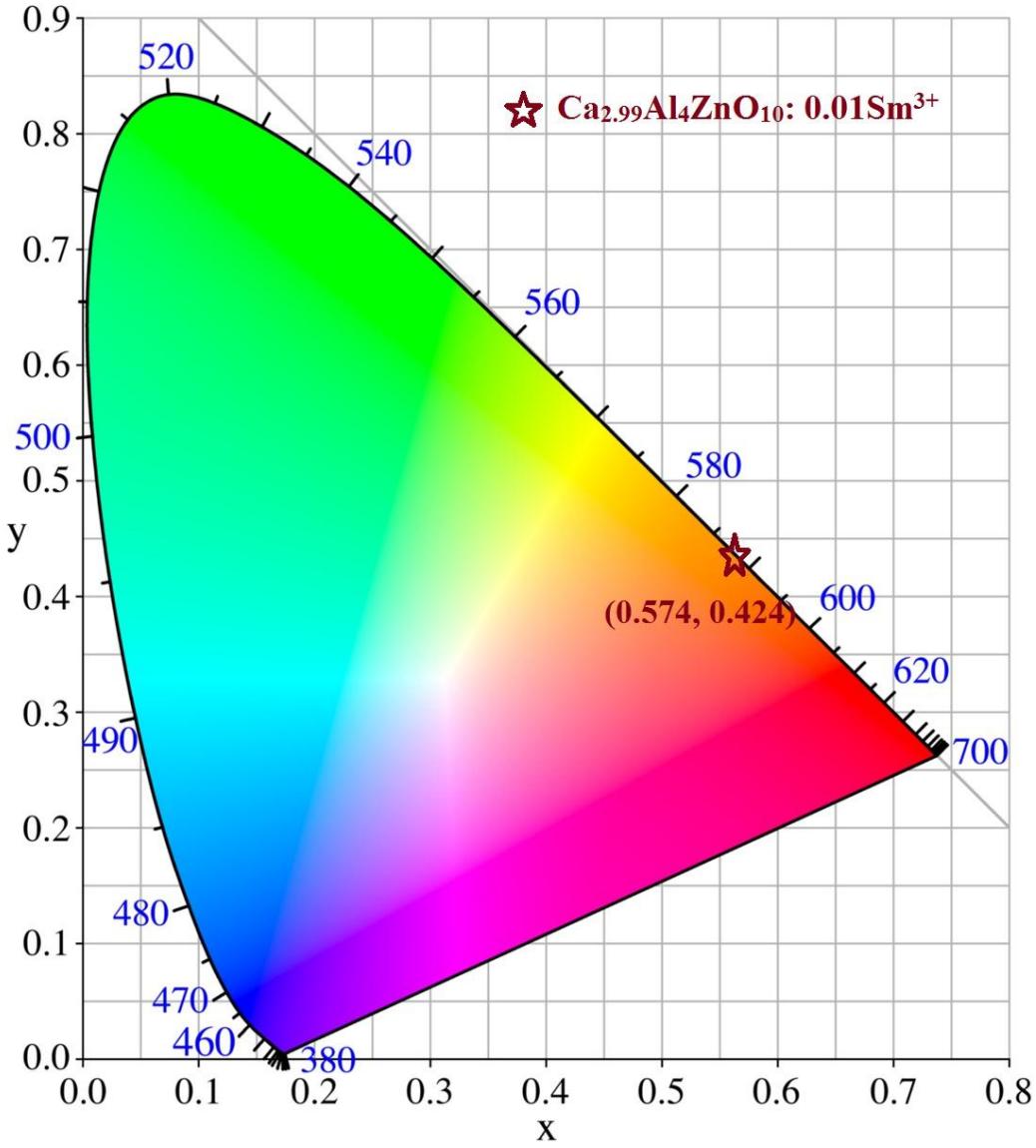
Ca2.99Al4ZnO10: 0.01Sm3+
(0.574, 0.424)
520
540
560
580
600
620
700
500
490
480
470
460
380
0.9
0.8
0.7
0.6
0.5
0.4
0.3
0.2
0.1
0.0
y
0.0
0.1
0.2
0.3
0.4
0.5
0.6
0.7
0.8
x

ACCEPTED MANUSCRIPT

Fig. 8.

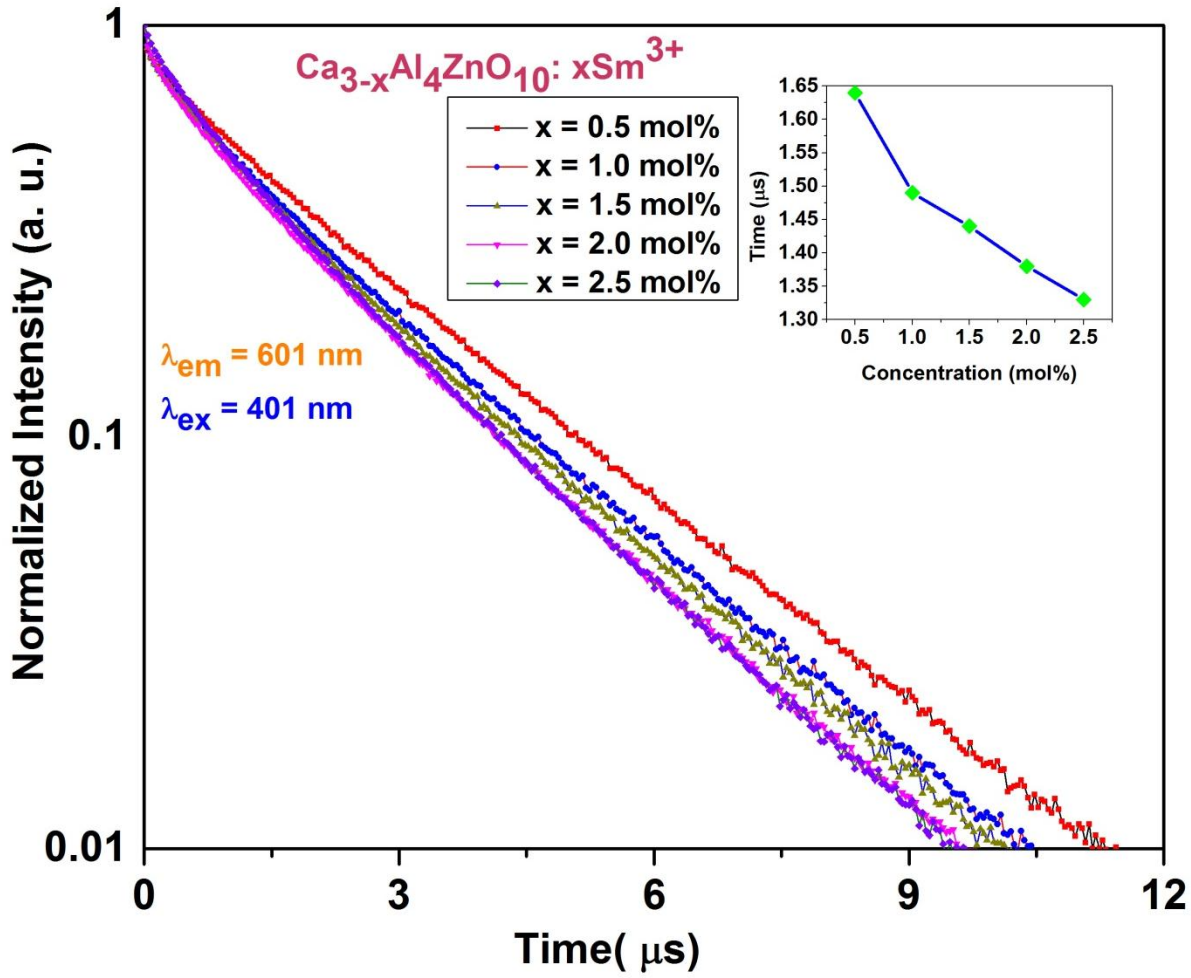

Accepted Manuscript

Spectroscopic studies of Pr^{3+} doped lithium lead alumino borate glasses for visible reddish orange luminescent device applications

Nisha Deopa, A.S. Rao, Sk. Mahamuda, Mohini Gupta, M. Jayasimhadri, D. Haranath, G. Vijaya Prakash

PII: S0925-8388(17)30789-2

DOI: 10.1016/j.jallcom.2017.03.020

Reference: JALCOM 41058

To appear in: *Journal of Alloys and Compounds*

Received Date: 1 December 2016

Revised Date: 28 February 2017

Accepted Date: 4 March 2017

Please cite this article as: N. Deopa, A.S. Rao, S. Mahamuda, M. Gupta, M. Jayasimhadri, D. Haranath, G.V. Prakash, Spectroscopic studies of Pr^{3+} doped lithium lead alumino borate glasses for visible reddish orange luminescent device applications, *Journal of Alloys and Compounds* (2017), doi: 10.1016/j.jallcom.2017.03.020.

This is a PDF file of an unedited manuscript that has been accepted for publication. As a service to our customers we are providing this early version of the manuscript. The manuscript will undergo copyediting, typesetting, and review of the resulting proof before it is published in its final form. Please note that during the production process errors may be discovered which could affect the content, and all legal disclaimers that apply to the journal pertain.

Graphical Abstract

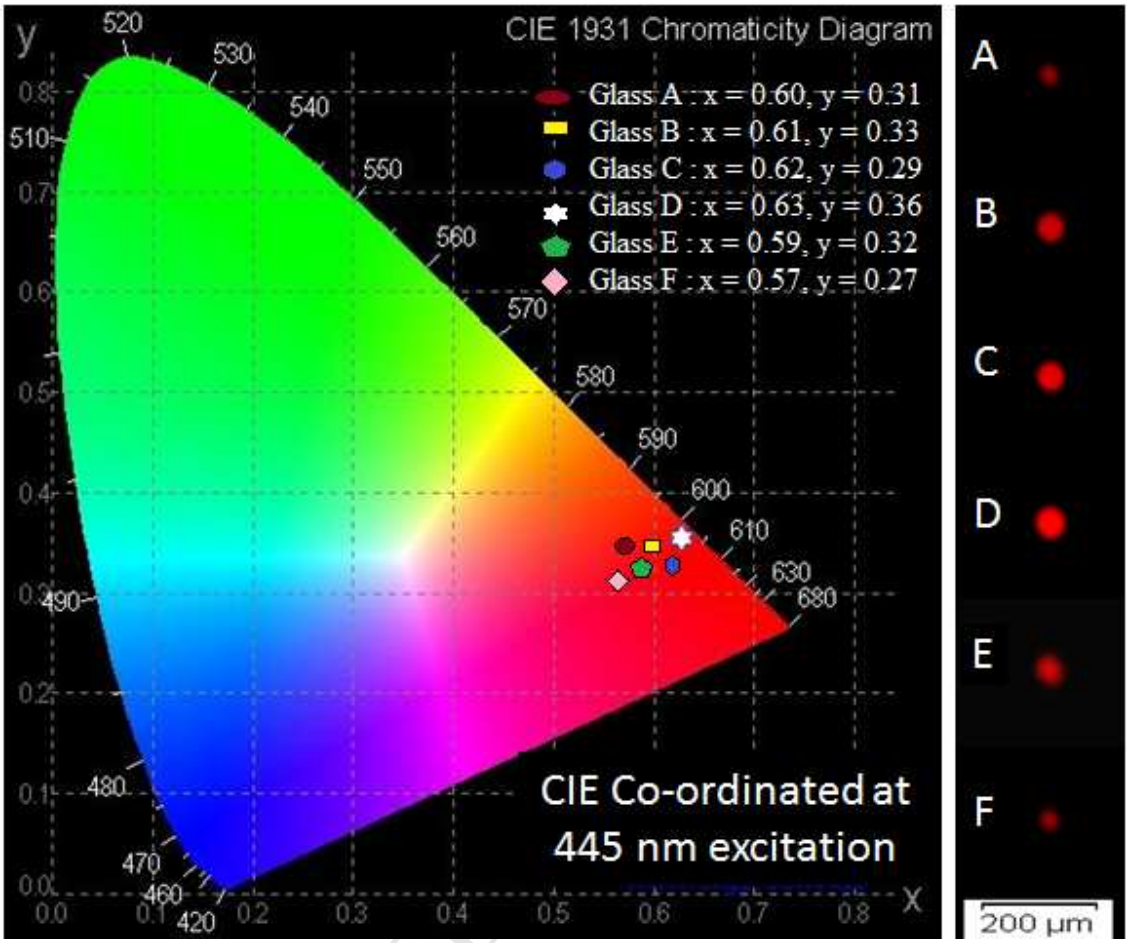

ACCEPTED

ACCEPTED MANUSCRIPT

Spectroscopic studies of Pr^{3+} doped lithium lead alumino borate glasses for visible reddish orange luminescent device applications

Nisha Deopa[1], A. S. Rao*[1], Sk. Mahamuda[2], Mohini Gupta[3], M. Jayasimhadri[1], D. Haranath[4] and G. Vijaya Prakash[3]

[1]Department of Applied Physics, Delhi Technological University, Bawana Road, New Delhi-110 042, India.
[2]Department of Physics, K L University, Green Fields, Vaddeswaram-522 502, Guntur (Dt), A.P, India.
[3]Nanophotonics Lab, Department of Physics, Indian Institute of Technology-Delhi, Hauz Khas, New Delhi-110016, India
[4]CSIR-National Physical Laboratory, Dr. K.S. Krishnan Marg, Pusa Road, New Delhi-110012, India

Abstract

Lithium Lead Alumino Borate (LiPbAlB) glasses doped with Pr^{3+} ions were prepared via melt quenching technique to study their luminescence behavior using absorption, excitation, photoluminescence (PL) and decay spectral studies. A broad hump observed in XRD confirms the amorphous nature of the as-prepared glass. The glass transition temperature (T_g) and thermal stability (ΔT) were measured from Differential Scanning Calorimetry (DSC). FT-IR and Raman studies were performed to understand the network functional groups involved in the host glass. Various radiative parameters for the prominent fluorescent levels of Pr^{3+} were evaluated with in the frame work of Judd-Ofelt theory. PL and confocal images recorded under 445 nm Continuous Wave (CW) diode laser excitation were used to understand the visible emission characteristic features of the as-prepared glasses. The decay profiles of $^1D_2 \rightarrow {}^3H_4$ show single exponential for lower concentration and non-exponential for higher concentration resulting decrease in experimental lifetime (τ_{exp}) with increase in concentration. Such decrease in τ_{exp} and decay conversion from single to non-exponential with increase in rare earth ion concentration has been attributed to the cross-relaxation processes and subsequent concentration quenching observed. From the emission cross-sections, branching ratios, quantum efficiency, CIE coordinates and confocal images, it was concluded that 1 mol % Pr^{3+} ion concentration is optimum in LiPbAlB glasses to develop visible reddish orange luminescent devices.

Keywords: Praseodymium, Glasses, Raman spectra, Judd-Ofelt parameters, Photoluminescence, Confocal images.

Corresponding author, **E-mail: drsrallam@gmail.com, Tel: +91 85860 39007, Fax: +91 01127871023.*

ACCEPTED MANUSCRIPT

ACCEPTED MANUSCRIPT

1. Introduction

Nowadays, Rare Earth (RE) doped glasses have attracted a great deal of attention among the researchers because of their versatile use and potential applications in diversified fields of Science and Technology [1–4]. The advancement in optical glasses doped with RE ions has caused revolution in optical communication and electronic industries. To elucidate the effect of host glass on lasing potentialities of the doped RE ions, various glassy materials such as borates, fluoroborates, phosphates, tellurites and fluorophosphates etc. were investigated [5–8]. Quite recently, glasses doped with RE ions are said to be superior over phosphors owing to their special characteristic features such as broad inhomogeneous band widths, simple manufacturing process, cheap production cost, good thermal stability and high doping capacity [9,10]. The spectroscopic characteristic of RE ions depends on its concentration, ambient temperature and composition of the host glass [11]. A host glass having low phonon energy is aptly suitable in designing the luminescent materials capable of reducing the non-radiative decay rates and thereby to enhance quantum efficiency to a greater extent [12].

Among all the conventional glass formers, boric acid (B_2O_3) is said to be one of the best glass formers, owing to its superior characteristic features such as good transparency, lower melting point, thermal stability, chemical durability and high RE ion solubility [13]. Nevertheless, in borate glasses, the presence of stretching vibrations of network forming oxides usually makes them to possesses high phonon energies around 1300 cm^{-1} resulting in enhancing the non-radiative decay processes there by reducing the luminescence efficiency drastically [14]. However such redundant phonon energies possessed by borate glasses can be effectively reduced by adding Heavy Metal Oxides (HMO) such as lead and bismuth [15,16]. Further glasses containing HMOs are extremely robust in shielding the radioactive radiation penetration because

of their high density and atomic number. Addition of lead oxide to a borate glass not only reduces the redundant phonon energies, but also enhances its transparent window from visible to near infrared regions. It is well known that, the presence of PbO in glasses enhances the chemical durability, resistance against devitrification and lowers the melting temperature [17]. In literature it was reported that, PbO can act as a network former or modifier depending on its content in glass [18]. The presence of Al_2O_3 in RE doped glasses not only improves chemical durability, mechanical strength and emission properties, but also works as network modifier [19]. It is worth to note that Al^{3+} ions can improve the optical response of the material by occupying tetrahedral and octahedral sites in the host glass [20]. Recently, borate glasses containing lithium oxides are showing immense scientific interest because of its network forming ability as well as best chemical durability [21]. There are only three coordinated boron atoms present in B_2O_3 vitreous and addition of alkali oxide (Li_2O) to this form changes it into four coordinated tetrahedral. Therefore an alkali metal oxide in B_2O_3 forms non bridging oxygen and modifies physical and chemical properties [22]. The aforementioned various scientific patronages offered by B_2O_3, PbO, Al_2O_3 and Li_2O have prompted us to prepare a germane system namely Lithium Lead Alumino Borate (LiPbAlB) glass to study the luminescence properties possessed by RE ions doped in them. The prime aim of the present work is to develop chemically and thermally more stable RE doped glassy system preferably with less phonon energies and better suited for fabricating a visible luminescent device with relatively good emission cross-section and quantum efficiency.

RE elements are attracting scientists continuously because of the special spectroscopic characteristic feature possessed by electrons present in 5f and 4d orbitals, which makes them as promising candidates in designing the luminescence devices. Among the RE elements, praseodymium is the most preferred one because of the presence of various metastable states like $^3P_{0,\,1,\,2,}$ $^1D_2$, $^1G_4$ in its energy level structure, which results emission in UV and infrared regions. Pr^{+3} doped glasses are also useful in up-conversion laser processes and suitable to develop

ACCEPTED MANUSCRIPT

1.3 µm optical communication window [23]. Further, some energy levels of Pr^{+3} ions shows concentrating quenching with increase in the doped RE ion content. It has been investigated that, Pr^{+3} doped glasses possess lasing action from $^1D_2 \rightarrow {}^3H_4$ transition around 600 nm [24,25]. In the backdrop of the aforementioned reasons, Pr^{+3} doped glasses with low phonon energies are said to be potential candidates for solid state lasers in visible region. The absorption spectra of RE doped glassy matrices have been analyzed with the help of Judd-Ofelt (J-O) theory [26,27]. Recently much work has been done in the field of RE doped glasses for the luminescent device application using J-O theory [28–31]. Due to small energy difference between ground ($4f^2$) and excited states (4f 5d) of Pr^{3+}, sometimes the J-O theory fails to explain intensity measurements successfully. To overcome this difficulty Goldner and Auzel [32] have used the standard J-O theory and adopted the normalization method for getting reliable J-O intensity parameters with proper scaling of intensity measurement by keeping hypersensitive transition ($^3H_4 \rightarrow {}^3P_2$) aside in the fitting procedure.

In the present study, LiPbAlB glasses doped with different concentration of Pr^{+3} were synthesized. Different spectroscopic characterization tools like XRD, DSC, FT-IR and Raman were used to understand glassy nature, thermal and structural properties of the as-prepared glass. Absorption, excitation, PL, confocal images and Time Resolved Photoluminescence (TR-PL) spectral profiles were used to understand the suitability of the as-prepared glasses along with optimization of the doped praseodymium ion concentration for better luminescence efficiency.

2. Experimental

Pr^{3+} doped LiPbAlB glasses were synthesized by using conventional melt quenching technique using the following chemical composition.

$10Li_2O - 10PbO - (10\text{-}x)\,Al_2O_3 - 70B_2O_3 - xPr_6O_{11}$

where, x = 0.05, 0.1, 0.5, 1.0, 1.5, 2.0 mol % ; these glasses are designated as glass A, B, C, D, E and F. Analar grade chemicals of Li_2O, PbO, Al_2O_3, B_2O_3 and Pr_6O_{11} were purchased from Sigma Aldrich and about 8g of these samples were mixed and crushed in an agate mortar until homogeneous mixture is obtained. Such mixture was collected into a silica crucible and heated at 1100^0 C in an electrical furnace for about 5 hours and desired melts were prepared. Such melts removed from the furnace were quenched quickly between two pre-heated brass plates to form glass sample of uniform thickness. The glass samples thus prepared are annealed for 4 hours in another electrical furnace at 350^0C to eliminate thermal strains. Finally, Pr^{3+} doped LiPbAlB glass samples were obtained to study their luminescent properties.

Refractive indices of the as-prepared glasses were measured with the help of Brewster's angle method by using He-Ne laser (650 nm line) with ± 0.01 accuracy. Archimedes principle was employed to determine the density of the glasses taking water as an immersion liquid with an accuracy of ±0.01 gm/cm^3. XRD measurement for an un-doped glass was recorded by using high-resolution X-ray diffractometer (Bruker; Model D8 advance) in the 2θ range from 10º to 70º using nickel-filtered CuKa radiation (λ=1.5406 Å). The FT-IR spectra was recorded by using Perkin Elmer's Frontier FT-IR Spectrometer and the pellet was prepared by mixing an un-doped glass in powdered form with KBr pellet and then compressed mechanically at 1.5 ton. Raman spectral studies were performed with the help of Renishaw Invia Raman Microscope. Thermal analysis was recorded by using Perkin Elmer Differential Scanning Calorimetry (DSC) equipment with a heating rate of 10^0C/min starting from the ambient temperature to 500^0C in presence of N_2 atmosphere.

The optical absorption spectrum was recorded by using Shimadzu 3600 UV-vis-NIR spectrophotometer having a spectral resolution of 0.1 nm. The excitation spectrum for glass D was recorded using Shimadzu RF-5310 PC-Spectrofluorophotometer with a spectral resolution of 0.5 nm. The steady state PL spectra for all the LiPbAlB glasses were recorded by using a

ACCEPTED MANUSCRIPT

home build setup with 445 nm CW diode laser as an excitation source. The emission was dispersed into a monochromator (Acton SP2300) coupled to a PMT through appropriate lenses and filters. TR-PL spectral recordings were done using an Edinburgh FLSP900 Fluorescence Spectrometer with a spectral resolution of 0.1 nm, where xenon lamp is used as an excitation source and data was analyzed by using origin 9 software. The confocal images were recorded by using a modified laser scanning confocal microscope (Olympus BX51) equipped with XY piezo state under 445 nm CW diode laser excitation.

3. Results and discussion

3.1 XRD spectral measurement analysis

In order to check the amorphous nature of the un-doped LiPbAlB glass, XRD spectral analysis was carried out and it was shown in Fig. 1(a). As shown in Fig. 1(a), a broad hump observed in the XRD spectrum without any sharp peaks confirms the amorphous nature of the as-prepared glass.

3.2 Thermal characterization

The DSC curve recorded for an un-doped glass is shown in Fig. 1(b). The DSC curve shows three peaks at 325 °C, 352 °C and 452 °C corresponding to glass transition temperature (T_g), onset crystallization temperature (T_x) and peak crystallization temperature (T_p) respectively. The thermal stability of glass was evaluated by using following expression [33].

$$\Delta T = T_X - T_g \quad (1)$$

For better thermal stability, the ΔT value should be relatively large for a given glass. In the present work for an un-doped LiPbAlB glass the value of ΔT was observed to be around 27°C.

ACCEPTED MANUSCRIPT

Thermal stability of a glassy material can also be estimated using Hurby's parameter using following equation [34].

$$K_H = \frac{T_X - T_g}{T_m - T_g} \quad (2)$$

where, K_H is Hruby's parameter of the glass. The higher the value of Hruby's parameter for a given glass the better will be the thermal stability. For better thermal stability the value of K_H should be greater than 0.1 [33, 34]. In the present work for an un-doped LiPbAlB glass, the value of K_H was found to be 0.15, which confirms that the as-prepared glass is relatively stable thermally.

3.3 Physical properties characterization

From the experimentally calculated density and refractive index values, various other physical properties were evaluated using suitable expression that are given in literature [35] and are presented in Table 1. The physical properties of the as-prepared glasses changing with increase in Pr^{3+} ions concentration indicates the transformed environment around the doped RE ion. From Table 1 it can be observed that with increasing the RE ion concentration from glass A to F, the average molecular weight, mean atomic volume, molar refraction, field strength, reflection losses and optical dielectric constant values are increasing and on the other hand the physical properties such as polaron radius, optical basicity, inter atomic distance and molecular electronic polarizability are decreasing. The low field strength values observed for the present glasses shows high RE ion solubility in these glasses. Further, optical basicity of the titled glasses denotes the capacity of the host glass to donate negative charges to the doped RE ion. It is observed form the Table 1 that the titled glasses possess low molecular electronic polarizability that makes them more stable.

3.4. FT-IR and Raman spectral studies

To identify the functional groups present and local structure, FT-IR and Raman spectra of an un-doped LiPbAlB glass have been recorded and are shown in Fig. 2 and Fig. 3 respectively. The proper assignment of different function groups corresponding to the wavenumbers are given in Table 2. The FT-IR spectral vibrations of an un-doped glass consists of six infrared active modes around 3483, 2853, 2929, 2664, 544 and 462 cm^{-1}. It is reported that the presence of broad band in the FT-IR spectra is because of the mixture of high degeneracy vibrational states, mechanical scattering and thermal broadening of the lattice dispersion within the sample [36]. A broad band around 3483 cm^{-1} arises due to symmetric stretching of the O-H bond. The bands observed at 2853 cm^{-1} and 2929 cm^{-1} shows the presence of organic contaminants and existence of hydrogen bonding respectively. The band present at 544 cm^{-1} attributes to B-O-B bond bending vibrations mixed with covalent Pb-O vibrations. The peak position around 462 cm^{-1} assigned for O-B-O bond bending vibrations Li-O bond vibrations. These FT-IR assignments are in good agreement with the reported once in borate glasses [17,37]. FT-IR spectral studies are also useful in evaluating the OH content present in the glass [38]. Estimation of OH content present in a glass is important because, its presence in a glass can reduce radiative decay process, resulting decrease in quantum efficiency. The OH content in an amorphous matrix can be evaluated by using the following expression

$$\alpha_{OH} = \frac{\ln(\frac{T_0}{T_D})}{l} \quad (3)$$

here, T_0 is highest transmission, T_D is the glass transmission at 3,000 cm^{-1} and l is thickness of glass sample. For the present glass, the estimated OH content is 58.79 ppm which is lower than ZnAlBiB glass (65.48 ppm) [20], GeS_2 (175.5 ppm) [39], LHG-8L (128 ppm) [40], KBS (133 ppm) [41] and LBTAF glass (120.00 ppm) [42]. Relatively smaller amount of OH content

present in the as-prepared glass speaks its superiority in acting as an efficient luminescent device.

The Raman spectrum is a very significant tool for identifying the presence of different functional groups involved in a glassy matrix. The Raman spectrum of an un-doped glass was recorded in the wavelength range 400-1600 cm^{-1} and is shown in Fig. 3. The spectrum represents one dominant band corresponding to 801 cm^{-1}, which is assigned for symmetric breathing vibrations of boroxol rings. In addition to this dominant band, seven more peaks with one small shoulder of lower intensity also observed and presented in Table 2. The peak observed at 1094 cm^{-1} ascribed to di-borate group while 1206 cm^{-1} to pyro-borate group. The peak located at 1452 cm^{-1} and 1508 cm^{-1} ascribed to BO_2O triangle linked to BO_4 units and BO_2O triangle linked to other borate triangular units respectively. Further, the peak positioned at 780 cm^{-1} indicates the symmetric breathing vibrations of six-member rings with one or two BO_3 triangle replaced by BO_4 tetrahedral. A band observed at 662 cm^{-1} indicates the presence of ring type metaborate units and the in plane bending mode of BO_3 units while band located at 486 cm^{-1} ascribed to isolated di-borate groups as well as Li-O and Pb-O bond vibrations. These Raman peaks matches well with some of the reported values of borate glasses in literature [43,44].

3.5. *Absorption spectral studies*

Optical absorption spectra of LiPbAlB glasses doped with different concentration of Pr^{+3} were recorded at room temperature in UV-vis-NIR region is shown in Fig. 4. The spectra shows seven absorption peaks centered around 444, 470, 482, 590, 1436, 1514 and 1926 nm. Each absorption spectrum consists three peaks in the blue region arising from $^3H_4 \rightarrow {}^3P_{2,1,0}$ transitions, single intense peak corresponds to visible region from $^3H_4 \rightarrow {}^1D_2$ transition while three peaks in near infra-red region from $^3H_4 \rightarrow {}^3F_{4,3,2}$ transitions. Identification and assignment of bands observed in the present work are done as per the procedure outlined by Carnall et al. [45]. Transition

observed in ultra violet to blue ($^3H_4 \rightarrow {}^3P_2$) region is hypersensitive, which strongly depends on the local environment of the RE ions and affects the J-O intensity parameters. Such

hypersensitive transitions are governed by a selection rules $|\Delta S|=0$, $|\Delta L| \leq 2$, and $|\Delta J| \leq 2$ [46]. It is shown in the Fig. 4 that with increase in the RE ion concentration, the peak position of the hypersensitive transition shifts slightly toward shorter wavelength side and this may be due to nephelauxetic effect [47]. In order to know nature of bonding in the as-prepared glasses, nephelauxetic ratio ($\bar{\beta}$) and bonding parameters (δ) were evaluated using the relevant expression given in literature [48, 49]. The bonding parameter (δ) thus evaluated for all the glasses are given in Table 3. Depending on the ligand field distribution around the RE ions, the bonding parameter may be positive or negative indicating covalent or ionic bonding respectively. From Table 3, it is conspicuous that, the magnitude of bonding parameter (δ) is negative for all the glasses indicating the bonding nature predominantly ionic. Such ionic nature of bonding decreases with increase in Pr^{3+} ion concentration in these glasses.

The energies of the absorption bands are calculated in terms of experimental oscillator strength (f_{exp}) using the area under the absorption curve employing the equation given in literature [50] and are given in Table 3. From the experimental oscillator strengths (f_{exp}) the J-O intensity parameters (Ω_2, Ω_4, Ω_6) and calculated oscillator strengths (f_{cal}) are evaluated by least square fit method using the J-O theory [26,27]. Root mean square deviation (δ_{rms}) was used to evaluate the quality of fit between calculated and experimental oscillator strength by using the following expression.

$$\delta_{rms} = \left[\frac{\sum(f_{ex} - f_{cal})^2}{p}\right]^{\frac{1}{2}} \quad (4)$$

here, p represents the total number of energy levels present in the fitting procedure.

The experimental and calculated oscillator strengths along with δ_{rms} are given in Table 3. From Table 3, it can be observed that, exclusion of hypersensitive transition gives more reasonable δ_{rms} between calculated and experimental oscillator strengths. Hence, the J-O intensity parameters have been calculated by excluding hypersensitive transition and are given in Table 4 along with the values reported in literature [4,6,14,37–39,42,44,51–54].

From Table 4, it can be seen that the J-O parameters follows the same trend ($\Omega_4 > \Omega_6 > \Omega_2$) for all the glasses. The Ω_2 J-O parameter represents covalent nature between Pr^{3+} ions and ligand anions because this parameter directly connects to the asymmetry of the local environment around the trivalent RE ions (Pr^{3+} ions). In the present series of glasses, the Ω_2 parameter values are small when compared with Ω_4 and Ω_6. The small values of Ω_2 parameter show the asymmetrical behavior of ion site i.e., the ionic nature is dominating the covalent nature between the ligands. The degree of covalency present in a glass can be evaluated using the following expression [55].

$$C_{covalent}\% = \exp[-25\,(\Delta\aleph)^2] \times 100 \quad . \tag{5}$$

where, $\Delta\aleph$ is the host glass's electro negativity value which is nothing but the difference between the anion's and cation's electronegativity values. For the present series of glasses, the estimated value of covalent character is 35.24% and ionic character is approximately 65%. The lowest percentage value of covalent character is an evidence for the low values of Ω_2 parameter. Hence in the present series of glasses, the ionic nature is more predominant when compared with the covalent nature. This is also well confirmed by the higher values of Ω_4 and Ω_6 parameters. Moreover, this result is also in consistent with the bonding nature (δ) evaluated from the nephelauxetic ratio ($\bar{\beta}$). The Ω_4 and Ω_6 parameters represent the rigidity of the host material in which RE ions are situated. Binnemans et al. [56] reported that increase in Ω_6 J-O parameter with increasing RE ion concentration may be due to tightening of the structure along with the

formation of BO_4 units in the matrix. The spectroscopic quality factor ($\chi = \frac{\Omega_4}{\Omega_6}$) is also evaluated for the present series of glasses and are presented in Table 4 along with the reported values for other glasses. From Table 4, it can be observed that, the "χ" values are in comparable with other reported values. In the present series, Glass D possesses maximum value of "χ" indicating the superiority of that glass in giving higher stimulated emission cross-sections than the others [57].

3.6. Photoluminescence spectral studies

In order to analyze the PL spectra, it is very much essential to know about the suitable excitation wavelength. For this reason, the excitation spectrum for glass D was recorded in the wavelength range 420-500 nm by fixing the emission at 602 nm and is shown in Fig. 5. As shown in Fig. 5, the excitation spectra consists of three excitation bands 445, 470 and 485 nm corresponding to the transition $^3H_4 \rightarrow {}^3P_2$, $^3P_1$ $^3P_0$ respectively. Among them, $^3H_4 \rightarrow {}^3P_2$ transition observed at 445 nm is very intense and is more suitable as an excitation wavelength to record the emission spectra of the titled glasses. We have recorded PL spectra for all the LiPbAlB glasses by using 445 CW diode laser as an excitation source as it can effectively excite more number of atoms to the desired metastable state than the conventional excitation source. Fig. 6 shows the PL spectra recorded for the titled glasses using 445 nm CW diode laser as an excitation source. From Fig. 6, it is observed that the PL spectra consists of three bands at 572, 602, 644 nm corresponding to $^3P_1 \rightarrow {}^3F_2$, $^1D_2 \rightarrow {}^3H_4$ and $^3P_1 \rightarrow {}^3F_3$ transitions respectively. Among all, $^1D_2 \rightarrow {}^3H_4$ observed in reddish orange region of the electromagnetic spectrum (602 nm) is very intense than the remaining two. The intensity of $^1D_2 \rightarrow {}^3H_4$ transition increases with Pr^{3+} ions concentration up to 1 mol % and decreases beyond showing concentration quenching. The feasible cross-relaxation channels for concentration quenching are given below [58].

Cross relaxation channels	Donor emission channels	Acceptor absorption channels
CR1 ($^3P_0$)	$^3P_0 \rightarrow {}^1D_2$ (3910 cm^{-1})	$^3H_4 \rightarrow {}^3H_6$ (4300 cm^{-1})
	$^3P_0 \rightarrow {}^1G_4$ (10850 cm^{-1})	$^3H_4 \rightarrow {}^1G_4$ (9700 cm^{-1})
	$^3P_0 \rightarrow {}^3H_6$ (16250 cm^{-1})	$^3H_4 \rightarrow {}^1D_2$ (16640 cm^{-1})
CR2 ($^3P_1$)	$^3P_1 \rightarrow {}^1D_2$ (4460 cm^{-1})	$^3H_4 \rightarrow {}^3F_2$ (5000 cm^{-1})
CR3 ($^1D_2$)	$^1D_2 \rightarrow {}^1G_4$ (6940 cm^{-1})	$^3H_4 \rightarrow {}^3F_2$ (6300 cm^{-1})
	$^1D_2 \rightarrow {}^3F_4$ (9890 cm^{-1})	$^3H_4 \rightarrow {}^1G_4$ (9700 cm^{-1})
ET ($^1D_2$)	$^1D_2 \rightarrow {}^3H_4$ (16640 cm^{-1})	$^3H_4 \rightarrow {}^1D_2$ (16640 cm^{-1})

The above cross relaxation channels are depicted in energy level diagram shown in Fig. 7 along with excitation and emission wavelengths observed for glass D. Dexter's theory [59, 60] explains the role of cross relaxation channels in emission quenching and lifetime shortening. According to this theory, emission and absorption spectra of doped glasses should have an overlap. Fig. 8 shows the perfect spectral overlap between emission and absorption spectra of $^1D_2$ transition in visible region along with cross relaxation channel. Such spectral overlap observed helps to us understand the energy migration produced from excited to unexcited Pr^{3+} ions through resonant energy transfer process.

The PL performance of titled glasses can be further understood with the help of radiative parameters like radiative transition probability (A_R), total transition probability (A_T), luminescence branching ratio (β_R) and radiative lifetime (τ_R) for all the fluorescent levels observed in the PL spectra using the expressions given literature [4,61]. Stimulated emission cross-section (σ_{se}) is another significant parameter for a glassy material to act as a good host for laser. The "σ_{se}" for a transition from an initial to final manifold can be evaluated by using the following expression [62,63].

$$\sigma_{se}(a_j, b_{j'}) = \left[\frac{\lambda_p{}^4}{8\pi c n^2 \Delta\lambda_p}\right] A_R(a_j, b_{j'}) \quad (6)$$

here, λ_P is wavelength of emission peak, $\Delta\lambda_p$ is the effective line-width (FWHM) of the transition.

A_R, A_T, β_R and τ_R values evaluated for all the emission transitions of Pr^{3+} ions in LiPbAlB glasses are given in Table 5. The emission peak wavelength (λ_P), effective band widths ($\Delta\lambda_P$), radiative and experimental branching ratios (β_R & β_{exp}), σ_{se}, gain band width (σ_{se} x $\Delta\lambda_p$) and

optical gain parameter (σ_{se} x τ_R) for the intense $^1D_2 \rightarrow {}^3H_4$ emission transition of Pr^{3+} ions doped LiPbAlB glasses are given in Table 6. Luminescence branching ratio (β_R) is another important parameter and for best lasing potentiality its value should be higher (around 0.5). From Table 6 it is observed that the value of β_R for $^1D_2 \rightarrow {}^3H_4$ transition in LiPbAlB glasses increases with increasing Pr^{3+} ion concentration up to 1 mol % and beyond deceases. This might be due to fluorescence quenching of the $^1D_2 \rightarrow {}^3H_4$ transition beyond 1 mol% of Pr^{3+} ions. The values of β_R obtained for all the glasses in the present work are in good agreement with the reported values [4,46,57,64]. The β_{exp} values are evaluated by measuring the relative areas of the emission transitions and these values are found to be in good agreement with β_R. From Table 6, it is observed that glass D with 1 mol% of Pr^{3+} ions in LiPbAlB glass is having highest radiative as well as experimental branching ratios suggests that this glass can act as a best luminescent device under 445 nm excitation. Stimulated emission cross-section, gain band width and optical gain parameter are another set of important parameters for a better luminescent material. From Table 6, it can be seen that these parameters are highest for glass D indicating the superior nature of glass D over the other glasses studies in the present investigation.

3.7.Time resolved photoluminescence spectral studies

The Time Resolved Photoluminescence (TR-PL) decay profiles for $^1D_2 \rightarrow {}^3H_4$ emission transition of Pr^{3+} ions in LiPbAlB glasses under 445nm excitation are shown in Fig. 9. From Fig. 9 it can be observed that, the decay profile is single exponential for lower concentration and non-exponential for higher concentration. The experimental lifetimes (τ_{exp}) measured from the decay curves for all the glasses under investigation are given in Table 7 along with radiative

ACCEPTED MANUSCRIPT

ACCEPTED MANUSCRIPT

lifetimes (τ_R). From Table 7, it can be observed that, the τ_{exp} values are decreasing with increase in Pr^{3+} ion concentration in these glasses. This decrease in τ_{exp} and conversion of decay curves from exponential to non-exponential with increase in RE ion concentration can be attributed to

the cross-relaxation processes (As shown in Fig. 7) and the subsequent concentration quenching observed. From Table 7 it can also be observed that, the τ_{exp} are less than τ_R. This small inconsistency between τ_{exp} and τ_R can be attributed to the multi photon relaxation processes observed. In such a case, the τ_{exp} of an emitting state relates with τ_R and non-radiative decay rate (W_{NR}) through

$$\frac{1}{\tau_{exp}} = \frac{1}{\tau_R} + W_{NR} \qquad (7)$$

The W_{NR} thus calculated by using the above expression are placed in Table 7.

The quantum efficiency (η %) is another important parameter used to evaluate the luminescence efficiency of a material under investigation. The value of η% can be evaluated by taking the ratio between τ_{exp} and τ_R. The value of η % increases with increase in Pr^{3+} ion concentrations up to 1 mol % (glass D) and deceases beyond. The η% values measured for all the titled glasses are presented in Table 7. Among all the glasses studied in the present work, glass D with 1 mol % of Pr^{3+} ions possesses highest quantum efficiency than the other glasses. Hence glass D is best suitable for lasing emission in reddish orange region under 445 nm excitation.

An amorphous material doped with RE ions can also acts as a good optical fiber, if the gain band width (σ_{se} x $\Delta\lambda_p$) and optical gain parameters (σ_{se} x τ_R) are having relatively higher values. Particularly gain band width parameter is more important to achieve a highly stable laser host material. From Table 6 it is observed that glass D (1 mol % Pr^{3+}) possesses highest values of gain band width and optical gain parameter among all the glasses. Hence glass D with 1 mol %

Pr^{3+} ions in LiPbAlB glass is best suited for optical fiber amplification as well as visible reddish orange laser emission at 602 nm.

3.8. Inokuti-Hirayama modal analysis

It is well known that the lifetime of a molecule or ion is the average time that it can spend in the excited state prior to its return to the ground state with the emission of a photon [49]. A molecule /ion in the excited state (donor ion) can relax to the lower energy states via two different mechanisms. Firstly donor ions/molecules can migrate energy between the donor ions prior to the energy reaches to the acceptor ions (un excited molecule/ion); secondly they can transfer energy directly to the acceptor ions [65]. In some cases, when donor and acceptor ions are distributed homogeneously in host matrix and if energy migration between the donor ions are negligible, then the decay curves obtained can be fitted well with the help of Inokuti-Hirayama (I-H) modal [66] to understand the predominant energy transfer mechanism. Hence I-H modal can be applicable when the energy transfer between donor and acceptor ions is faster than the energy migration between donor ions. The luminescence intensity decay in such a case is given by

$$I_t = I_0 \exp\{-\frac{t}{\tau_0} - Q(\frac{t}{\tau_0})^{\frac{3}{S}}\} \quad (8)$$

where, t is time after excitation, τ_0 is intrinsic decay time of donors in absence of acceptors and Q is energy transfer parameter which can be expressed as follows

$$Q = \frac{4\pi}{3} \Gamma(1-\frac{3}{S}) N_0 R_0^3 \quad (9)$$

here, N_0 is concentration of acceptor ions, R_0 is critical energy transfer distance which can be obtained as the distance between donor and acceptor when energy transfer rate is equal to rate of intrinsic decay. Interactions involved in the mechanism can be of different types depending on the values of S and gamma function Γ(X). It can be dipole-dipole(S=6, Γ(X)=1.77) dipole-

quadrupole (S=8, Γ(X)=1.43) and quadrupole-quadrupole interactions (S=8, Γ(X)=1.3) .The energy transfer probability and donor acceptor interaction parameter can be evaluated by using the following expression.

$$C_{DA} = R_0^{(S)} \tau_0^{-1} \text{ and } W_{ET} = C_{DA} R_0^{(S)} \quad (10)$$

In the present work, non-exponential decay curves were fitted to I-H model by taking S=6 as show in Fig. 9; which confirms dipole-dipole interaction between Pr^{3+} ions. As the concentration increases, distance between donor and acceptors decreases and there may be a chance for increased energy transfer due to instant fluorescence decay [67]. From Table 8 it is observed that energy transfer parameter increases while critical distance between donor and acceptor decreases with increase in Pr^{3+} ions concentration. This is because of the enhanced energy transfer between Pr^{3+} ions via Cross relaxation. Fig.10 shows the variation of energy transfer parameter (Q) and τ_{exp} with increase in Pr^{3+} ion concentration. From Fig.10 it is conspicuous that, as Pr^{3+} ion concentration increases, the magnitude of Q increases while τ_{exp} decreases.

3.9. CIE chromaticity co-ordinates

The chromaticity coordinates which are useful to know the color emitted by the material can be calculated from PL spectra shown by the material under suitable excitation wavelength by using Commission International de I'Eclairage France CIE system [68]. The PL spectra of the as-prepared glasses consist of three parts which is yellow to orange, orange to red, and pure red. Fig. 11 shows CIE chromaticity co-ordinates evaluated for Pr^{3+} doped LiPbAlB glasses under 445 nm CW diode laser excitation along with confocal PL images recorded for all the LiPbAlB glasses under the same excitation wavelength. CIE color co-ordinates for all the glass samples were found to be in orange red to red regions. Among all the glasses, the color co-ordinates evaluated for glass D (x=0.630, y=0.360) falls exactly in the reddish orange region of CIE chromaticity diagram. Therefore glass D with 1 mol% of Pr^{3+} concentration in LiPbAlB glass is

more suitable for reddish orange light emission under 445 nm excitation. This result is also in consonance with the confocal PL images recorded for glass D emitting intense Reddish Orange light than the other glasses under investigation.

4. Conclusions

Lithium Lead Aumino Borate glasses doped with different concentrations of Praseodymium ions were synthesized using conventional melt quenching techniques to understand their structural as well as luminescence behavior using spectroscopic techniques such as XRD, FT-IR, Raman, absorption, excitation, PL, confocal images and TR-PL spectral profiles. The best fit J-O parameters evaluated from the absorptions spectral features allowed us to evaluate various radiative parameters for the observed fluorescent levels of Pr^{3+} ions in LiPbAlB glasses. Under 445 nm CW diode laser excitation, the titled glasses show three emission bands, of which $^1D_2 \rightarrow {}^3H_4$ emission is more intense and for which the emission cross-section and branching ratios are evaluated. The intensity of $^1D_2 \rightarrow {}^3H_4$ transition increases with Pr^{3+} ion concentration up to 1 mol % and decreases beyond showing concentration quenching. The decay profiles of $^1D_2 \rightarrow {}^3H_4$ transition shows single exponential for lower concentration and non-exponential for higher concentration resulting decrease in experimental lifetimes with increase in concentration. Such decrease in experimental lifetimes and conversion of decay curves from exponential to non-exponential with increase in RE ion concentration has been attributed to the cross-relaxation processes and subsequent concentration quenching observed. From the observed branching ratios, spectroscopic quality factor, stimulated emission cross-section, CIE chromaticity co-ordinates and quantum efficiency, it was finally concluded that LiPbAlB glasses doped Pr^{3+} ions are quite suitable for the development of visible reddish orange luminescent devices. Among all, glass D with 1 mol% of Pr^{3+} ion concentration in LiPbAlB glass is superior in all respects to act as a best visible orange luminescent device to operate at 602 nm. This result is also in consistent

ACCEPTED MANUSCRIPT

with the confocal PL image captured for glass D showing more bright reddish orange emission than the other titled glasses.

Acknowledgement:

This work is partly supported by High Impact Research Initiative of IIT-Delhi, UK-India Education Research Initiative (UKIERI) and Department of Science and Technology (DST), Govt. of India, New Delhi. Two of the authors, Dr.A.S.Rao and Dr.Sk.Mahamuda are thankful to DST, Govt. of India, New Delhi for the award of a major research project to them (File Number: ECR/2016/000376).

ACCEPTED MANUSCRIPT

References

[1] Z. Wang, H. Guo, X. Xiao, Y. Xu, X. Cui, M. Lu, B. Peng, A. Yang, Z. Yang, S. Gu, Synthesis and spectroscopy of high concentration dysprosium doped GeS_2-Ga_2S_3-CdI_2 chalcohalide glasses and fiber fabrication, J. Alloys Compd. 692 (2017) 1010–1017.

[2] K. Jha, M. Jayasimhadri, Structural and emission properties of Eu^{3+}-doped alkaline earth zinc-phosphate glasses for white LED applications, J. Am. Ceram. Soc. (2017) 1–10. doi:10.1111/jace.14668.

[3] Ch.B. Annapurna, Sk. Mahamuda, M. Venkateswarlu, K. Swapna, A.S. Rao, G. Vijaya Prakash, Dy^{3+} ions doped single and mixed alkali fluoro tungsten tellurite glasses for LASER and white LED applications, Opt. Mater. 62 (2016) 569–577.

[4] Sk. Mahamuda, K. Swapna, A.S. Rao, T. Sasikala, L.R. Moorthy, Reddish-orange emission from Pr^{3+} doped zinc alumino bismuth borate glasses, Physica B 428 (2013) 36–42.

[5] S. Kang, X. Wang, W. Xu, X. Wang, D. He, L. Hu, Effect of B_2O_3 content on structure and spectroscopic properties of neodymium-doped calcium aluminate glasses, Opt. Mater. 66 (2017) 287–292.

[6] J.S. Kumar, K. Pavani, T. Sasikala, A.S. Rao, N.K. Giri, S.B. Rai, L.R. Moorthy, Photoluminescence and energy transfer properties of Sm^{3+} doped CFB glasses, Solid State Sci. 13 (2011) 1548–1553.

[7] W.A. Pisarski, J. Pisarska, G. Dominiak-Dzik, W. Ryba-Romanowski, Transition metal (Cr^{3+}) and rare earth (Eu^{3+} , Dy^{3+}) ions used as a spectroscopic probe in compositional-dependent lead borate glasses, J. Alloys Compd. 484 (2009) 45–49.

ACCEPTED MANUSCRIPT

[8] G. Lakshminarayana, J. Qiu, Photoluminescence of Pr^{3+}, Sm^{3+} and Dy^{3+} doped SiO_2 – Al_2O_3 – BaF_2 – GdF_3 glasses, J. Alloys Compd. 476 (2009) 470–476.

[9] S. Liu, G. Zhao, X. Lin, H. Ying, J. Liu, J. Wang, G. Han, White luminescence of Tm – Dy ions co-doped aluminoborosilicate glasses under UV light excitation, J. Solid State Chem. 181 (2008) 2725–2730.

[10] H.J. Lozykowski, W.M. Jadwisienczak, I. Brown, Cathodoluminescence of GaN doped with Sm and Ho, Solid State Commun. 110 (1999) 253–258.

[11] H.J. Lozykowski, W.M. Jadwisienczak, I. Brown, Photoluminescence and cathodoluminescence of GaN doped with Pr, J. Appl. Phys. 88 (2000) 210–222.

[12] Y.G. Choi, J. Heo, 1.3 μm emission and multiphonon relaxation phenomena in PbO-Bi_2O_3-Ga_2O_3 glasses doped with rare-earths, J. Non Cryst. Solids. 217 (1997) 199–207.

[13] G. Lakshminarayana, S. Buddhudu, Spectral analysis of Eu^{3+} and Tb^{3+} : B_2O_3–ZnO – PbO glasses, Mater. Chem. Phys. 102 (2007) 181–186.

[14] S. Arunkumar, K. Marimuthu, Concentration effect of Sm^{3+} ions in B_2O_3 – PbO – PbF_2 – Bi_2O_3 – ZnO glasses-structural and luminescence investigations, J. Alloys Compd. 565 (2013) 104–114.

[15] M. Peng, L. Wondraczek, Photoluminescence of $Sr_2P_2O_7$: Bi^{2+} as a red phosphor for additive light generation, Opt. Lett. 35 (2010) 2544–2546.

[16] M. Peng, C. Zollfrank, L. Wondraczek, Origin of broad NIR photoluminescence in bismuthate glass and Bi-doped glasses at room temperature, J. Phys-Condens Mat. 21 (2009) 285106–285112.

ACCEPTED MANUSCRIPT

[17] R.C. Lucacel, C. Marcus, V. Timar, I. Ardelean, FT-IR and Raman spectroscopic studies on B_2O_3-PbO-Ag_2O glasses dopped with manganese ions, Solid State Sci. 9 (2007) 850–854.

[18] M. Ganguli, K.J. Rao, Structure role of PbO in Li_2O – PbO – B_2O_3 glasses, J. Solid State Chem. 145 (1999) 65–76.

[19] G. Lakshminarayana, R. Yang, M. Mao, J. Qiu, Spectral analysis of RE^{3+} (RE = Sm , Dy , and Tm): P_2O_5 – Al_2O_3 – Na_2O glasses, Opt. Mater. 31 (2009) 1506–1512.

[20] K. Swapna, Sk. Mahamuda, A.S. Rao, S. Shakya, T. Sasikala, D. Haranath, G. Vijaya Prakash, Optical studies of Sm^{3+} ions doped zinc alumino bismuth borate glasses, Spectrochim. Acta - Part A Mol. Biomol. Spectrosc. 125 (2014) 53–60.

[21] A. Pan, A. Ghosh, Dynamics of lithium ions in bismuthate glasses, J. Chem. Phys. 112 (2000) 1503–1509.

[22] D. L. Griscon, Borate glasses, structure, properties, application, Ed: I. D. Pye, V. D. Frechette and N. J. Kreidl (Plenum, New York, 1978).

[23] K. Wei, D.P. Machewirth, J. Wenzel, E. Snitzer, G.H.S. Jr, Pr^{3+}-doped Ge-Ga-S glasses for 1.3 μm optical fiber amplifiers, J. Non Cryst. Solids. 182 (1995) 257–261.

[24] F. Varsanyi, Surface Lasers, Appl. Phys. Lett. 19 (1971) 169–171.

[25] J. Hegarty, D.L. Huber, W.M. Yen, Fluorescence quenching by cross relaxation in LaF_3:Pr^{3+}, Phys. Rev. B. 25 (1982) 5638–5645.

[26] B.R. Judd, Optical absorption intensities of rare-earth ions, Phys. Rev. 127 (1962) 750–761.

ACCEPTED MANUSCRIPT

[27] G.S. Ofelt, Intensities of crystal spectra of rare earth ions, J. Chem. Phys. 37 (1962) 511–520.

[28] Sk. Mahamuda, K. Swapna, A.S. Rao, M. Jayasimhadri, T. Sasikala, K. Pavani, L.R. Moorthy, Spectroscopic properties and luminescence behavior of Nd^{3+} doped zinc alumino bismuth borate glasses, J. Phys. Chem. Solids. 74 (2013) 1308–1315.

[29] Sk. Mahamuda, K. Swapna, P. Packiyaraj, A.S. Rao, G. Vijaya Prakash, Visible red, NIR and Mid-IR emission studies of Ho^{3+} doped ainc alumino bismuth borate glasses, Opt. Mater. 36 (2013) 362–371.

[30] K. Swapna, Sk. Mahamuda, A.S. Rao, T. Sasikala, P. Packiyaraj, L.R. Moorthy, G. Vijaya Prakash, Luminescence characterization of Eu^{3+} doped zinc alumino bismuth borate glasses for visible red emission applications, J. Lumin. 156 (2014) 80–86.

[31] K. Swapna, Sk. Mahamuda, A.S. Rao, T. Sasikala, L.R. Moorthy, Visible luminescence characteristics of Sm^{3+} doped zinc alumino bismuth borate glasses, J. Lumin. 146 (2014) 288–294.

[32] P. Goldner, F. Auzel, Application of standard and modified Judd-Ofelt theories to a praseodymium-doped fluorozirconate glass, J. Appl. Phys. 79 (1996) 7872–7877.

[33] R.T. Karunakaran, K. Marimuthu, S.S. Babu, S. Arumugam, Structural, optical and thermal investigations on Dy^{3+} doped $NaF–Li_2O – B_2O_3$ glasses, Physica B 404 (2009) 3995–4000.

[34] A. Hruby, Evaluation of glass-forming tendency by means of DTA, Czechoslovak Journal of Physics 22 (1972) 1187-1193.

[35] A.S. Rao, Y.N. Ahammed, R.R. Reddy, T.V.R. Rao, Spectroscopic studies of Nd^{3+}-doped alkali fluoroborophosphate glasses, Opt. Mater. 10 (1998) 245–252.

ACCEPTED MANUSCRIPT

[36] K. Jha, M. Jayasimhadri, Spectroscopic investigation on thermally stable Dy^{3+} doped zinc phosphate glasses for white light emitting diodes, J. Alloys Compd. 688 (2016) 833–840.

[37] K. Annapoorani, C. Basavapoornima, N.S. Murthy, K. Marimuthu, Investigations on structural and luminescence behavior of Er^{3+} doped lithium zinc borate glasses for lasers and optical amplifier applications, J. Non Cryst. Solids. 447 (2016) 273–282.

[38] H.E. Heidepriem, W. Seeber, D. Ehrt, Dehydration of phosphate glasses, J. Non Cryst. Solids. 163 (1993) 74–80.

[39] B.B. Kale, A. Jha, S.K. Apte, P. V. Adhyapak, D.P. Amalnerkar, Removal of OH impurities from GeS_2 by reactive atmosphere and its glass preparation, Mater. Chem. Phys. 78 (2002) 330–336.

[40] T.I. Suratwala, R.A. Steele, G.D. Wilke, J.H. Campbell, K. Takeuchi, Effects of OH content , water vapor pressure and temperature on sub-critical crack growth in phosphate glass, J. Non Cryst. Solids. 264 (2000) 23–227.

[41] T. Som, B. Karmakar, Nephelauxetic effect of low phonon antimony oxide glass in absorption and photoluminescence of rare-earth ions, Spectrochim. Acta - Part A Mol. Biomol. Spectrosc. 79 (2011) 1766–1782.

[42] T. Suhasini, B.C. Jamalaiah, T. Chengaiah, J.S. Kumar, L.R. Moorthy, An investigation on visible luminescence of Ho^{3+} activated LBTAF glasses, Physica B 407 (2012) 523–527.

[43] S. Saravanan, S. Rajesh, R. Palani, Thermal and structural properties of mixed alkali and transition metal ions in sodium borate glass, Int. J. Recent Res. Rev. 8 (2015) 1–9.

[44] G. Padmaja, P. Kistaiah, Infrared and Raman spectroscopic studies on alkali borate glasses : evidence of mixed alkali effect, J. Phys. Chem. A. 113 (2009) 2397–2404.

ACCEPTED MANUSCRIPT

[45] W.T. Carnall, P.R. Fields, K. Rajnak, Electronic energy levels in the trivalent lanthanide aquo ions. I. Pr^{3+}, Nd^{3+}, Pm^{3+}, Sm^{3+}, Dy^{3+}, Ho^{3+}, Er^{3+}, and Tm^{3+}, J. Chem. Phys. 49 (1968) 4424–4442.

[46] M. Venkateswarlu, M.V.V.K.S. Prasad, K. Swapna, Sk. Mahamuda, A.S. Rao, A.M. Babu, D. Haranath, Pr^{3+} doped lead tungsten tellurite glasses for visible red lasers, Ceram. Int. 40 (2014) 6261–6269.

[47] C.K. Jorgensen, The nephelauxetic series, Prog. Inorg. Chem. 4 (1962) 73.

[48] M.B. Saisudha, J. Ramakrishna, Optical absorption of Nd^{3+}, Sm^{3+} and Dy^{3+} in bismuth borate glasses with large radiative transition probabilities, Opt. Mater. 18 (2002) 403–417.

[49] Sk. Mahamuda, K. Swapna, M. Venkateswarlu, A.S. Rao, S. Shakya, G. Vijaya Prakash, Spectral characterisation of Sm^{3+} ions doped oxy-fluoroborate glasses for visible orange luminescent applications, J. Lumin. 154 (2014) 410–424.

[50] P. Babu, C.K. Jayasankar, Spectroscopic properties of Dy^{3+} ions in lithium borate and lithium fluoroborate glasses, Opt. Mater. 15 (2000) 65-79.

[51] H. Takabe, Y. Nageno, K. Morinaga, Compositional dependence of Judd-Ofelt parameters in silicate, borate, and phosphate glasses, J. Am. Ceram. Soc. 78 (1995) 1161–1168.

[52] K. Brahmachary, D. Rajesh, S. Babu, Y.C. Ratnakaram, Investigations on spectroscopic properties of Pr^{3+} and Nd^{3+} doped zinc-alumino-sodium-phosphate (ZANP) glasses, J. Mol. Struct. 1064 (2014) 6–14.

[53] K.K. Mahato, D.K. Rai, S.B. Rai, Optical studies of Sm^{3+} doped oxyfluoroborate glass, Solid State Commun. 108 (1998) 671–676.

[54] F.B. Xiong, Z.D. Luo, Y.D. Huang, Spectroscopic properties of Pr^{3+} in anisotropic $PbWO_4$ crystal, Appl. Phys. B Lasers Opt. 80 (2005) 321–328.

[55] M.V. V. Kumar, K.R. Gopal, R.R. Reddy, G.V.L. Reddy, N.S. Hussain, B.C. Jamalaiah, Application of modified Judd-Ofelt theory and the evaluation of radiative properties of Pr^{3+}-doped lead telluroborate glasses for laser applications, J. Non Cryst. Solids. 364 (2013) 20–27.

[56] K. Binnemans, R.V. Deun, C.G. Walrand, J.L. Adam, Spectroscopic properties of trivalent lanthanide ions in fluorophosphate glasses, J. Non Cryst. Solids. 238 (1998) 11–29.

[57] D.V.R. Murthy, B.C. Jamalaiah, T. Sasikala, L.R. Moorthy, M. Jayasimhadri, K. Jang, H.S. Lee, S.S. Yi, J.H. Jeong, Optical absorption and emission characteristics of Pr^{3+} doped RTP glasses, Physica B 405 (2010) 1095–1100.

[58] V. Naresh, B.S. Ham, Influence of multiphonon and cross relaxations on $^3P_0$ and $^1D_2$ emission levels of Pr^{3+} doped borosilicate glasses for broad band signal amplification, J. Alloys Compd. 664 (2016) 321–330.

[59] D.L. Dexter, Theory of sensitized luminescence in solids, J. Chem. Phys. 21 (1953) 836-850.

[60] D.L. Dexter, J.H. Schulman, Theory of concentration quenching in inorganic phosphors, J. Chem Phys. 22 (1954) 1063-1070.

[61] R. Cases, M.A. Chamarro, R. Alcala, V.D. Rodriguez, Optical properties of Nd^{3+} and Dy^{3+} ions in ZnF_2-CdF_2 based glasses, J. Lumin. 48 (1991) 509-514.

[62] R.D. Peakcock, The intensities of lanthanide f-f transitions, Struct-Bond 22 (1975) 83-122.

ACCEPTED MANUSCRIPT

[63] W.Krupke, Induced-emission cross sections in neodymium laser glasses, IEEE J.Quant.Electron. 10 (1974) 450.

[64] G. Lakshminarayana, K.M. Kaky, S.O. Baki, S. Ye, A. Lira, I. V Kityk, M.A. Mahdi, Concentration dependent structural, thermal and optical features of Pr^{3+}-doped multicomponent tellurite glasses, J. Alloys Compd. 686 (2016) 769–784.

[65] B.C. Jamalaiah, M.V. V. Kumar, K.R. Gopal, Fluorescence properties and energy transfer mechanism of Sm^{3+} ion in lead telluroborate glasses, Opt. Mater. 33 (2011) 1643–1647.

[66] M. Inokuti, F. Hirayama, Influence of energy transfer by the exchange mechanism on donor luminescence, J. Chem. Phys. 43 (1965) 1978-1988.

[67] K.S. Lim, N. Vijaya, C.R. Kesavulu, C.K. Jayasankar, Structural and luminescence properties of Sm^{3+} ions in zinc fluorophosphate glasses, Opt. Mater. 35 (2013) 1557–1563.

[68] F.W. Billmeyer, M. Saltzman Jr., Principles of colour technology, Wiley, New York, 1981.

ACCEPTED MANUSCRIPT

ACCEPTED MANUSCRIPT

Table 1

Various physical properties of Pr^{3+} ions in LiPbAlB glasses.

S.No	Physical Property	Glass A	Glass B	Glass C	Glass D	Glass E	Glass F
1	Refractive index (n_d)	2.13	2.24	2.38	2.49	2.59	2.68
2	Density (gm/cm^3)	3.32	3.33	3.34	3.36	3.38	3.41
3	Average molecular weight (g)	85.32	85.49	86.92	88.7	90.48	92.25
4	Pr^{3+} ion concentration, N(10^{22} ions/cm^3)	0.12	0.22	1.16	2.28	3.38	4.45
5	Mean atomic volume (g/cm^3/atom)	5.71	5.72	5.73	5.76	5.79	5.81
6	Dielectric constant (ϵ)	4.52	5.03	5.68	6.24	6.71	7.17
7	Optical dielectric constant ($\epsilon - 1$)	3.52	4.03	4.68	5.24	5.71	6.17
9	Reflection losses (R %)	12.96	14.69	16.71	18.34	19.63	20.81
10	Molar refraction (R_m)(cm^{-3})	13.86	14.75	15.85	16.77	17.53	18.23
11	Polaron radius (r_p) (Å)	3.82	3.04	1.78	1.42	1.25	1.14
12	Inter-atomic distance (r_i) (Å)	9.48	7.53	4.42	3.53	3.09	2.82
13	Molecular electronic polarizability (10^{-23}cm^3)	10.99	5.847	1.257	0.665	0.463	0.361
14	Field Strength F (x10^{15} cm^{-2})	2.05	3.26	9.45	14.86	19.30	23.18
15	Optical basicity (Λ_{th})	0.448	0.447	0.446	0.436	0.434	0.429

ACCEPTED MANUSCRIPT

ACCEPTED MANUSCRIPT

Table 2

Assignment of FT-IR and Raman peaks for an un-doped LiPbAlB glass.

FT-IR Wavenumber (cm^{-1})	**FT-IR assignments**	**Raman Wavenumber (cm^{-1})**	**Raman assignments**
462	O-B-O bond Bending vibrations Li-O bond vibrations	486	Isolated diborate groups, Li-O, Pb-O bond vibrations
544	B-O-B bond Bending vibrations mixed with covalent Pb-O vibrations	662	Presence of ring type metaborate units and the in plane bending mode of BO_3 units, Pentaborate groups
2664	Symmeytric stretching of the O-H bond , molecular water	780	Symmetric breathing vibrations of six-member rings with one or two BO_3 triangle replaced by BO_4 tetrahedra
2853, 2929	Presence of organic contaminants	801,913	Symmetric breathing vibrations of boroxol rings
3483	Symmeytric stretching of the O-H bond , molecular water	1094	Diborate group
		1206	Pyroborate group
		1452	BO_2O-triangle linked to BO_4- units
		1508	BO_2O-triangle linked to other borate Triangular units

ACCEPTED MANUSCRIPT

Table 3

Experimental oscillator strengths (f_{exp}) (10^{-6}), calculated oscillator strengths (f_{cal}) (10^{-6}) along with rms deviation (δ_{rms}) and bonding parameter (δ) of Pr^{3+} ions in LiPbAlB glasses.

Transition	**Glass A**		**Glass B**		**Glass C**		**Glass D**		**Glass E**		**Glass F**	
$^3H_4 \rightarrow$	**(0.05 mol %)**		**(0.1 mol %)**		**(0.5 mol %)**		**(1 mol %)**		**(1.5 mol %)**		**(2 mol %)**	
	f_{exp}	f_{cal}	f_{exp}	f_{cal}	f_{exp}	f_{cal}	f_{exp}	f_{cal}	f_{exp}	f_{cal}	f_{exp}	f_{cal}
$^3P_2$*	5.97	2.44	6.85	2.82	7.19	3.03	8.19	3.58	6.81	2.61	5.63	1.71
$^3P_1$	1.31	2.84	1.33	3.08	1.84	3.19	2.30	3.94	2.08	2.97	1.71	2.75
$^3P_0$	1.18	2.79	1.36	3.03	1.59	3.14	1.81	3.88	1.65	2.93	1.31	2.71
$^1D_2$	2.05	0.76	3.00	0.87	3.91	0.93	2.38	1.11	1.46	0.80	0.32	0.53
$^3F_4$	1.10	2.31	1.35	2.69	1.72	2.91	1.98	3.42	1.55	2.46	0.48	1.47
$^3F_3$	5.17	4.61	5.80	5.22	6.03	5.58	7.31	6.66	5.17	4.84	3.74	3.34
$^3F_2$	2.93	2.96	2.98	3.00	3.18	3.19	3.97	3.99	2.69	2.69	1.82	1.82
$\delta_{rms}(10^{-6})$	± 1.73[a]		± 2.03[a]		± 2.14[a]		± 2.15[a]		± 1.75[a]		± 1.70[a]	
	± 1.20[b]		± 1.46[b]		± 1.58[b]		± 1.37[b]		± 0.81[b]		± 0.85[b]	
δ	-0.89		-0.86		-0.66		-0.57		-0.54		-0.49	

*hypersensitive transition.

[a] including hypersensitive transition ($^3H_4 \rightarrow {}^3P_2$).

[b] excluding hypersensitive transition ($^3H_4 \rightarrow {}^3P_2$).

ACCEPTED MANUSCRIPT

Table 4

Judd-Ofelt intensity parameters [Ω_2, Ω_4 and Ω_6 (10^{-20} cm^2)] for Pr^{3+} ions in LiPbAlB glasses.

Glass System	Ω_2	Ω_4	Ω_6	χ	Trend	References
Glass A	1.42	2.96	2.21	1.33	$\Omega_4 > \Omega_6 > \Omega_2$	present work
Glass B	1.09	2.91	2.36	1.23	$\Omega_4 > \Omega_6 > \Omega_2$	present work
Glass C	1.07	2.69	2.15	1.24	$\Omega_4 > \Omega_6 > \Omega_2$	present work
Glass D	1.29	3.01	1.99	1.51	$\Omega_4 > \Omega_6 > \Omega_2$	present work
Glass E	0.62	2.12	1.51	1.40	$\Omega_4 > \Omega_6 > \Omega_2$	present work
Glass F	0.05	1.83	1.74	1.05	$\Omega_4 > \Omega_6 > \Omega_2$	present work
ZnAlBiB	7.36	4.46	4.17	1.06	$\Omega_2 > \Omega_4 > \Omega_6$	[4]
CFBSm10	1.92	6.35	3.44	1.84	$\Omega_4 > \Omega_6 > \Omega_2$	[6]
PbFB	0.13	3.289	1.92	1.71	$\Omega_4 > \Omega_6 > \Omega_2$	[14]
Li–P–Al	2.41	5.89	5.60	1.41	$\Omega_4 > \Omega_6 > \Omega_2$	[37]
ZANP10	12.28	13.69	10.89	1.25	$\Omega_4 > \Omega_6 > \Omega_2$	[38]
OXFB	1.14	2.28	1.33	1.71	$\Omega_4 > \Omega_6 > \Omega_2$	[39]
ZBLAN	2.9	6.4	5.5	1.16	$\Omega_4 > \Omega_6 > \Omega_2$	[40]
MgTP	2.69	11.87	8.39	1.41	$\Omega_4 > \Omega_6 > \Omega_2$	[42]

ACCEPTED MANUSCRIPT

Table 5

Transition probability (A_R) (s^{-1}), total transition probability (A_T) (s^{-1}), branching ratio (β_R) and radiative lifetimes (τ_R) (μs) for the observed emission transitions of Pr^{3+} ions in LiPbAlB glasses.

Name	Transition	A_R	A_T	β_R	τ_R
Glass A	$^3P_1 \rightarrow {}^3F_2$	3831.16	54628.14	0.0701	18
	$^1D_2 \rightarrow {}^3H_4$	1166.92	4013.99	0.2907	230
	$^3P_1 \rightarrow {}^3F_3$	10934.67	54628.14	0.2001	18
Glass B	$^3P_1 \rightarrow {}^3F_2$	3559.08	63913.24	0.0556	15
	$^1D_2 \rightarrow {}^3H_4$	1386.92	4543.92	0.3272	202
	$^3P_1 \rightarrow {}^3F_3$	11474.62	63913.24	0.1795	15
Glass C	$^3P_1 \rightarrow {}^3F_2$	4469.67	76005.48	0.0588	13
	$^1D_2 \rightarrow {}^3H_4$	1902.14	5499.22	0.3277	167
	$^3P_1 \rightarrow {}^3F_3$	13911.10	76005.48	0.1830	130
Glass D	$^3P_1 \rightarrow {}^3F_2$	6544.64	103585.76	0.0631	9
	$^1D_2 \rightarrow {}^3H_4$	2951.41	7530.50	0.4122	122
	$^3P_1 \rightarrow {}^3F_3$	19656.71	103585.76	0.1897	9
Glass E	$^3P_1 \rightarrow {}^3F_2$	3491.74	78758.73	0.0443	13
	$^1D_2 \rightarrow {}^3H_4$	1831.02	5348.68	0.3423	171
	$^3P_1 \rightarrow {}^3F_3$	12996.95	78758.73	0.1650	13
Glass F	$^3P_1 \rightarrow {}^3F_2$	6966.36	64905.50	0.1099	15
	$^1D_2 \rightarrow {}^3H_4$	1282.21	3432.08	0.3735	262
	$^3P_1 \rightarrow {}^3F_3$	7392.65	64905.50	0.1138	15

ACCEPTED MANUSCRIPT

Table 6

Emission peak wavelength (λ_P) (nm), effective band width ($\Delta\lambda_P$) (nm), measured and experimental branching ratios (β_R & β_{exp}), stimulated emission cross-section (σ_{se}) (cm^2), gain band width ($\sigma_{se} \times \Delta\lambda_P$) ($cm^3$) and optical gain parameter ($\sigma_{se} \times \tau_R$) ($cm^2$ s) for $^1D_2 \rightarrow {}^3H_4$ emission transition of Pr^{3+} ions in LiPbAlB glasses.

Spectral Parameters	**Glass A**	**Glass B**	**Glass C**	**Glass D**	**Glass E**	**Glass F**
			$^1D_2 \rightarrow {}^3H_4$ (Reddish Orange)			
λ_P= 602 nm						
$\Delta\lambda_P$	15.13	15.52	17.28	18.09	20.03	23.06
β_R	0.29	0.33	0.33	0.41	0.34	0.37
β_{exp}	0.33	0.32	0.45	0.51	0.45	0.54
σ_{se}(x 10^{-22})	30.1	31.3	34.2	46.1	23.9	13.6
$\sigma_{se} \times \Delta\lambda_P$ (x 10^{-26})	0.46	0.49	0.59	0.83	0.48	0.31
$\sigma_{se} \times \tau_R$ (x 10^{-25})	6.93	6.89	6.19	7.50	4.44	3.96

ACCEPTED MANUSCRIPT

ACCEPTED MANUSCRIPT

Table 7

Experimental (τ_{exp}) (μs), radiative (τ_R) (μs) lifetimes, quantum efficiencies (η) and non-radiative decay rates (W_{NR}) for $^1D_2 \rightarrow {}^3H_4$ transition of Pr^{3+} in LiPbAlB glasses.

Name of sample	τ_{exp}	τ_R	η (%)	W_{NR}
Glass A	165	230	71	1713
Glass B	160	202	79	1300
Glass C	136	167	81	1365
Glass D	106	122	86	1237
Glass E	101	171	58	4053
Glass F	94	262	38	6822

ACCEPTED MANUSCRIPT

ACCEPTED MANUSCRIPT

Table 8

Energy transfer parameter (Q), critical transfer distance (R_0) (Å), donor acceptor interaction parameters ($C_{DA,}$ 10^{-41} cm^6 s^{-1}) of Pr^{3+} ions in LiPbAlB glasses.

Name of glass	Q	R_0	C_{DA}
Glass A	----	----	----
Glass B	----	----	----
Glass C	3.29	3.95	2.97
Glass D	3.58	3.25	0.91
Glass E	3.85	2.92	0.47
Glass F	4.69	2.85	0.42

ACCEPTED MANUSCRIPT

Figure captions

Fig. 1 (a): XRD spectrum of an un-doped LiPbAlB glass.

Fig. 1 (b): DSC spectrum of an un-doped LiPbAlB glass.

Fig. 2: FT-IR spectrum of an un-doped LiPbAlB glass.

Fig. 3: Raman spectrum of an un-doped LiPbAlB glass along with glass D.

Fig. 4: Absorption Spectra of Pr^{3+} ions doped LiPbAlB glasses in UV-vis-NIR regions.

Fig. 5: Excitation spectrum of 1 mol% of Pr^{3+} ions in LiPbAlB glass (Glass D).

Fig. 6: PL spectra of LiPbAlB glasses under 445 nm CW diode laser excitation.

Fig. 7: Energy level diagram of 1 mol% of Pr^{3+} ions in LiPbAlB glass (glass D) with excitation, emission and cross-relaxation channels.

Fig. 8: Spectral overlap of emission and absorption spectra of $^1D_2$ transitions of Pr^{3+} ions in LiPbAlB glasses.

Fig. 9: Decay spectral profiles of $^1D_2 \rightarrow {}^3H_4$ (602) nm emission transition of Pr^{3+} ions in LiPbAlB glasses under 445 nm excitation along with I-H Fitting.

Fig. 10: Variation of energy transfer parameter (Q) and experimental lifetime (τ_{exp}) with increasing Pr^{3+} ions concentration in LiPbAlB glasses.

Fig. 11: CIE chromaticity coordinates and confocal images of Pr^{3+} ions in LiPbAlB glasses.

ACCEPTED MANUSCRIPT

ACCEPTED MANUSCRIPT

Fig. 1(a)

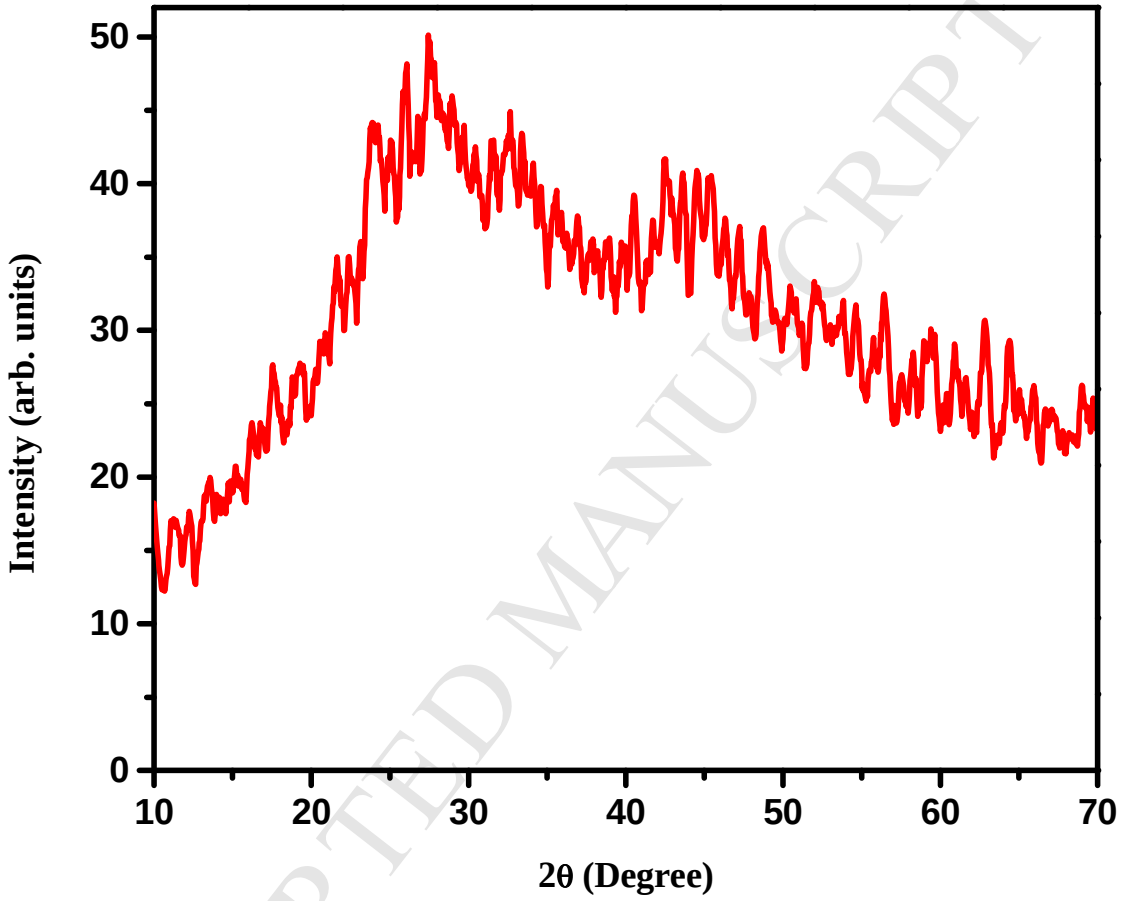

ACCEPTED MANUSCRIPT

Fig. 1(b):

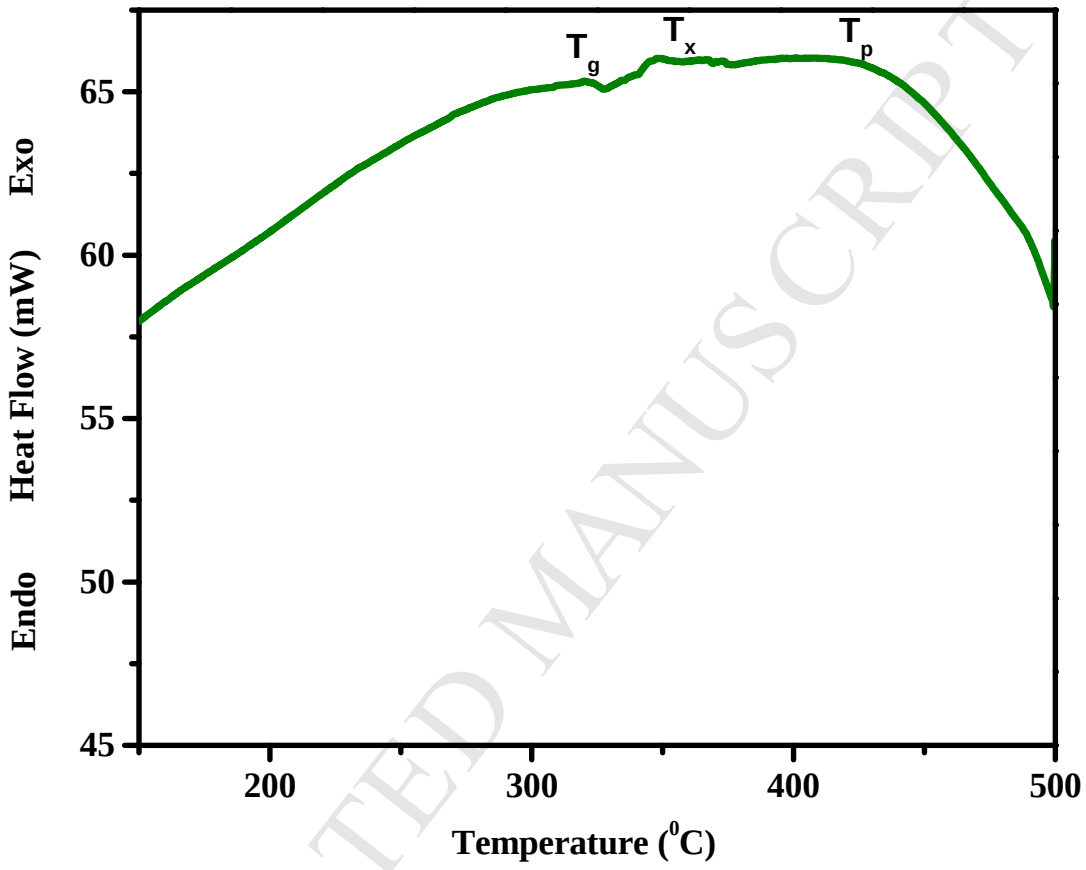

ACCEPTED MANUSCRIPT

Fig. 2:

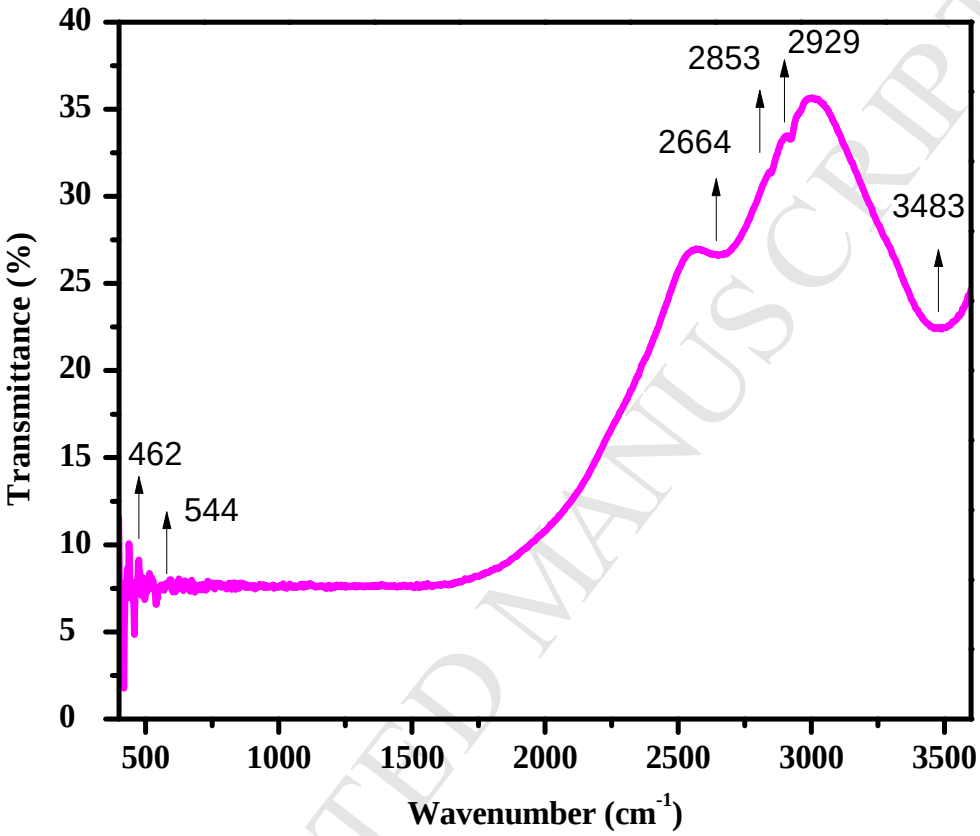

ACCEPTED MANUSCRIPT

Fig. 3:

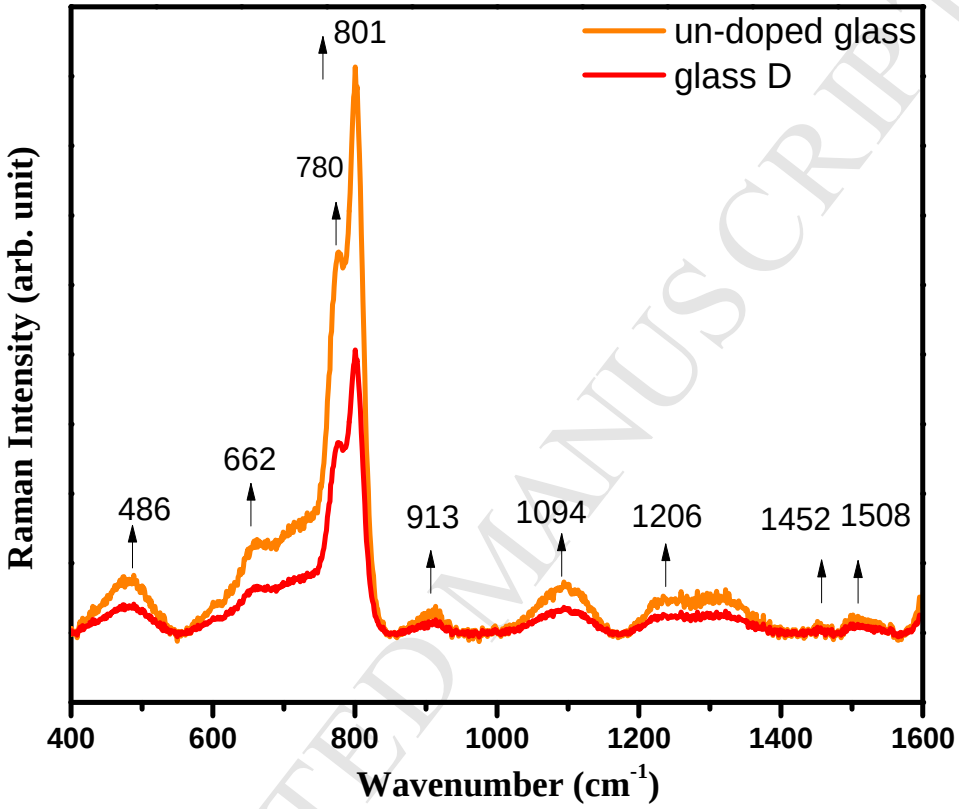

ACCEPTED MANUSCRIPT

Fig. 4:

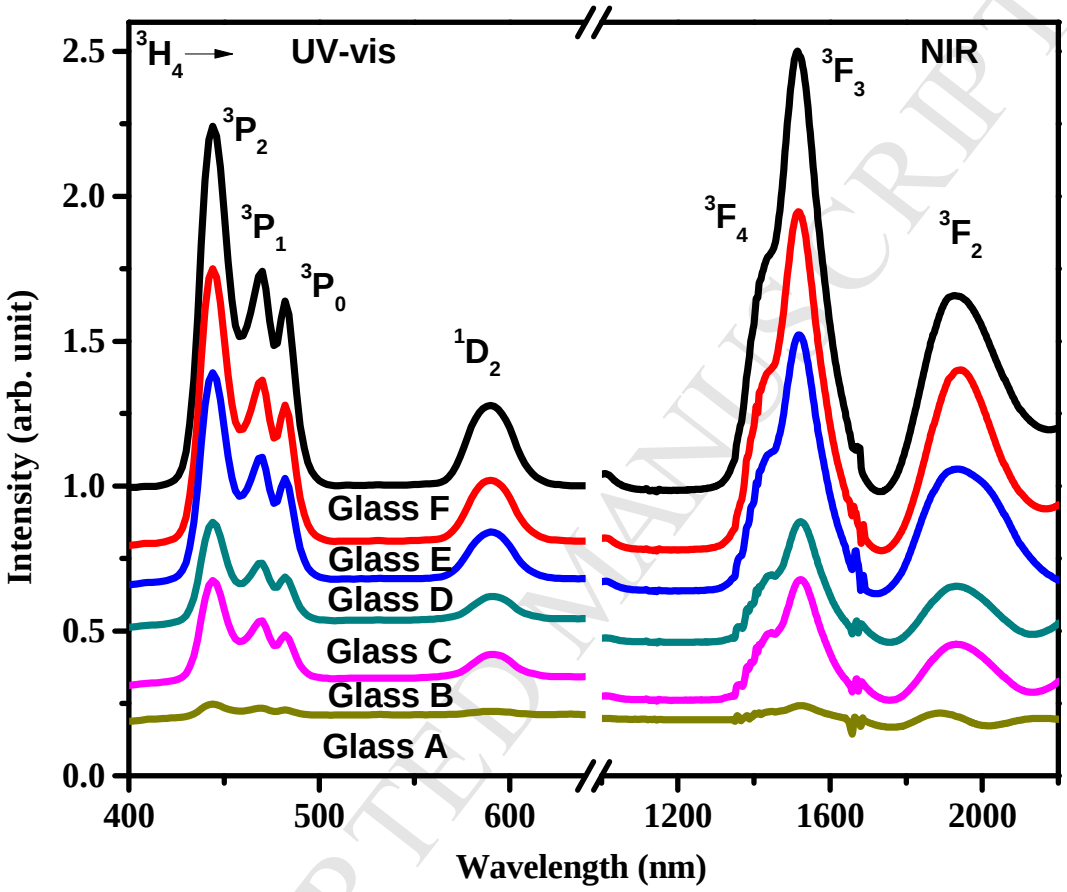

ACCEPTED MANUSCRIPT

Fig. 5:

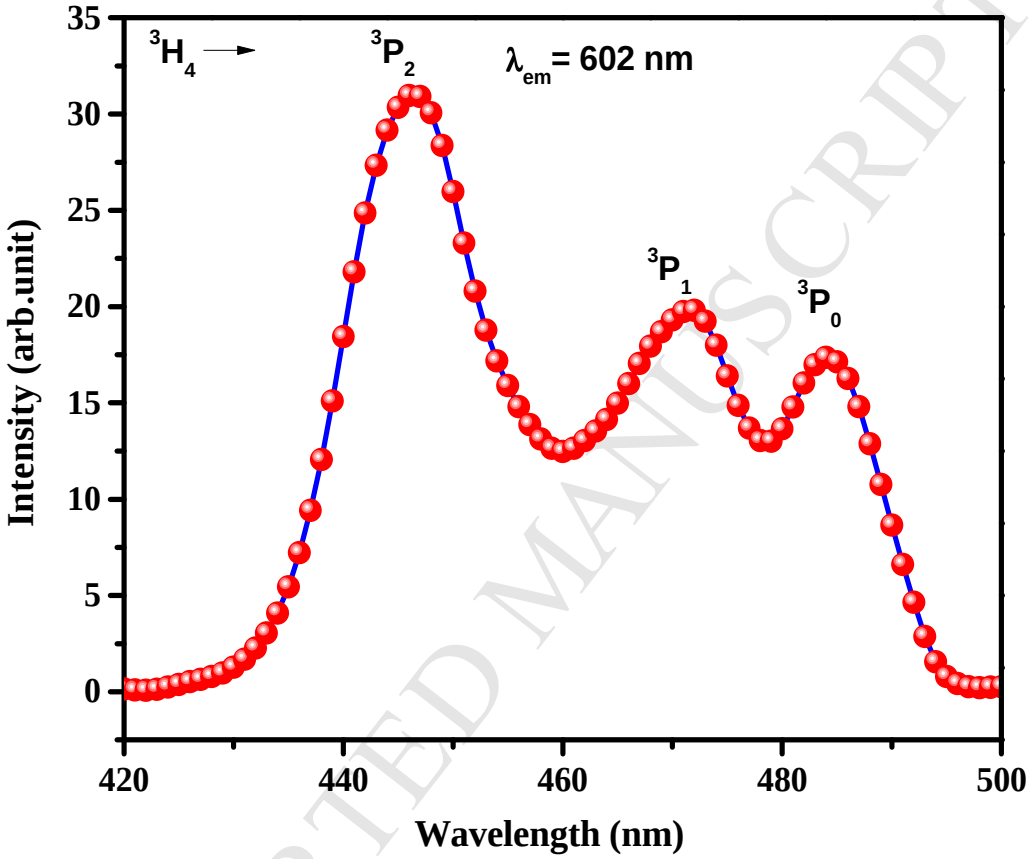

ACCEPTED MANUSCRIPT

Fig. 6:

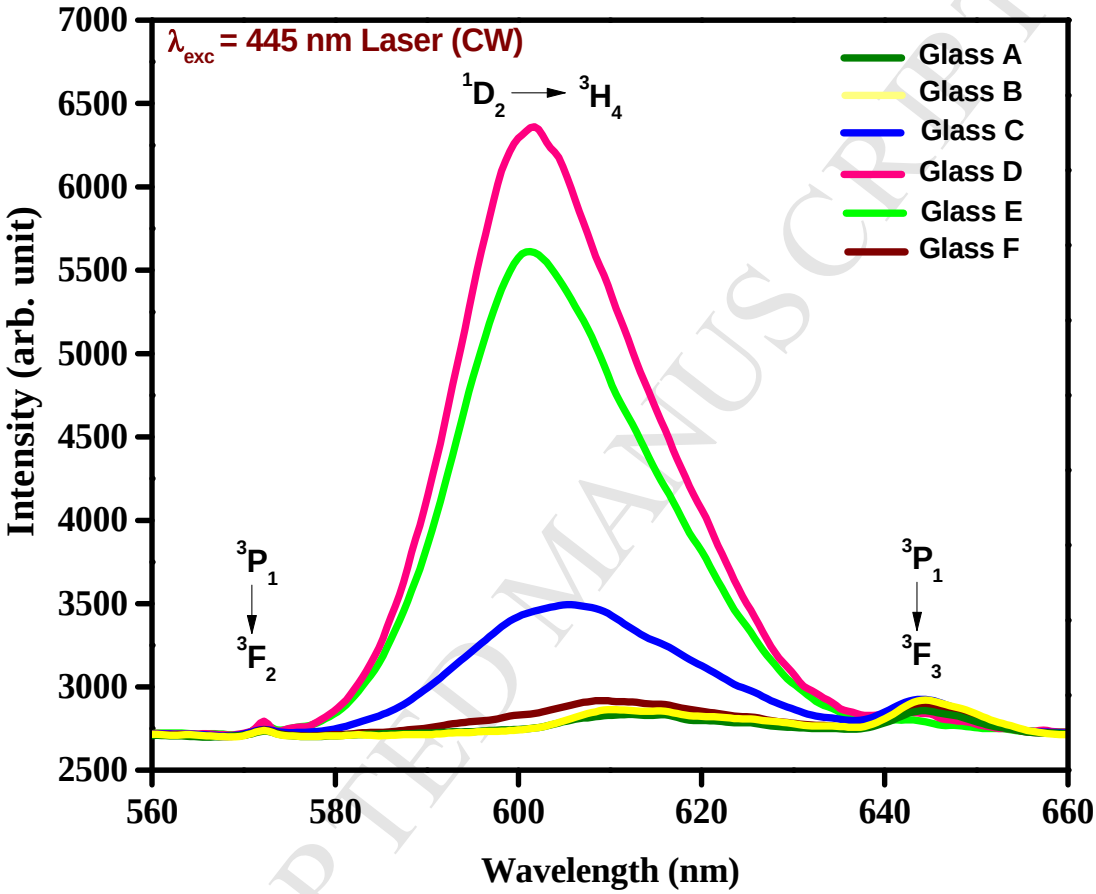

ACCEPTED MANUSCRIPT

Fig. 7:

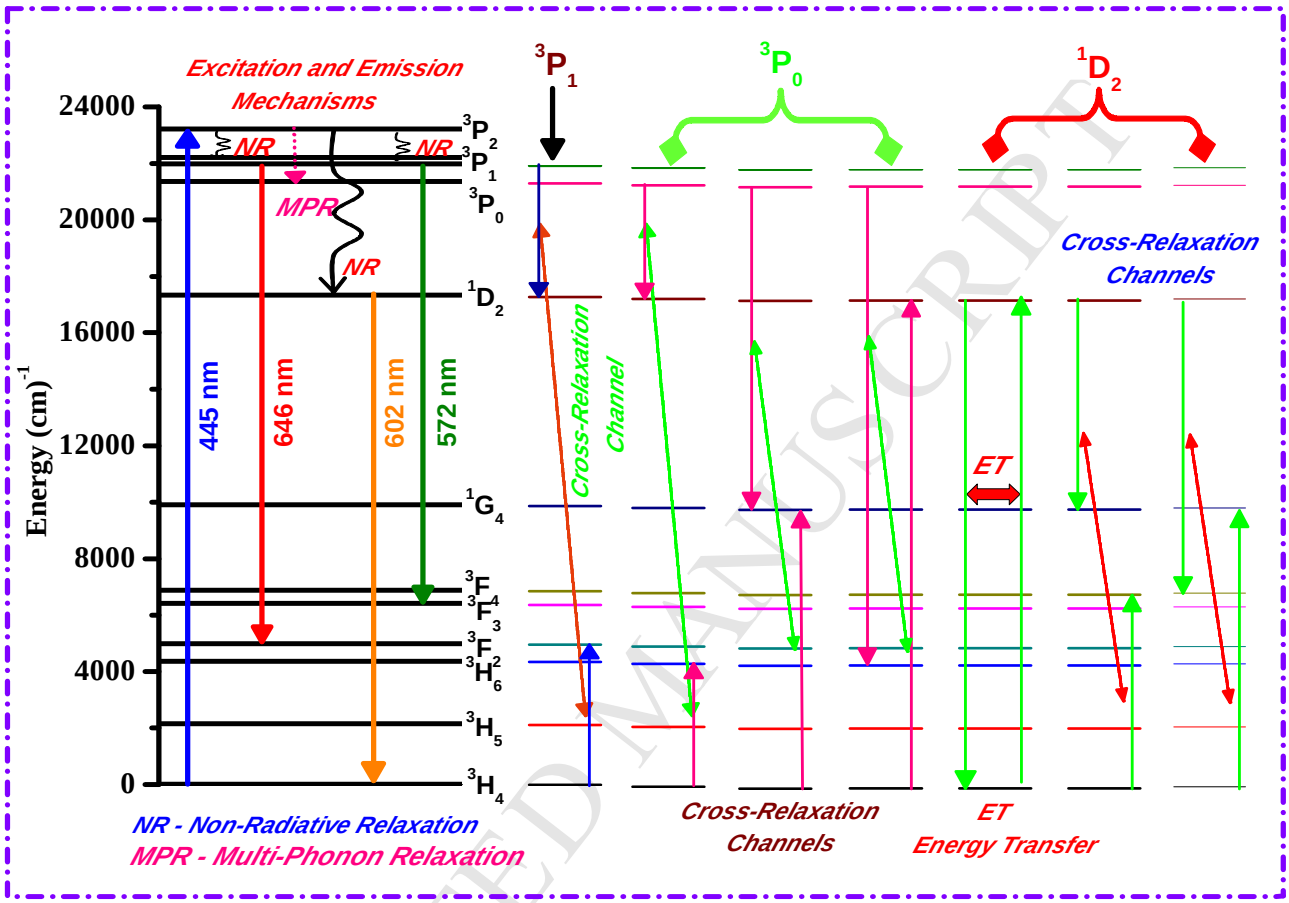

ACCEPTED MANUSCRIPT

Fig. 8:

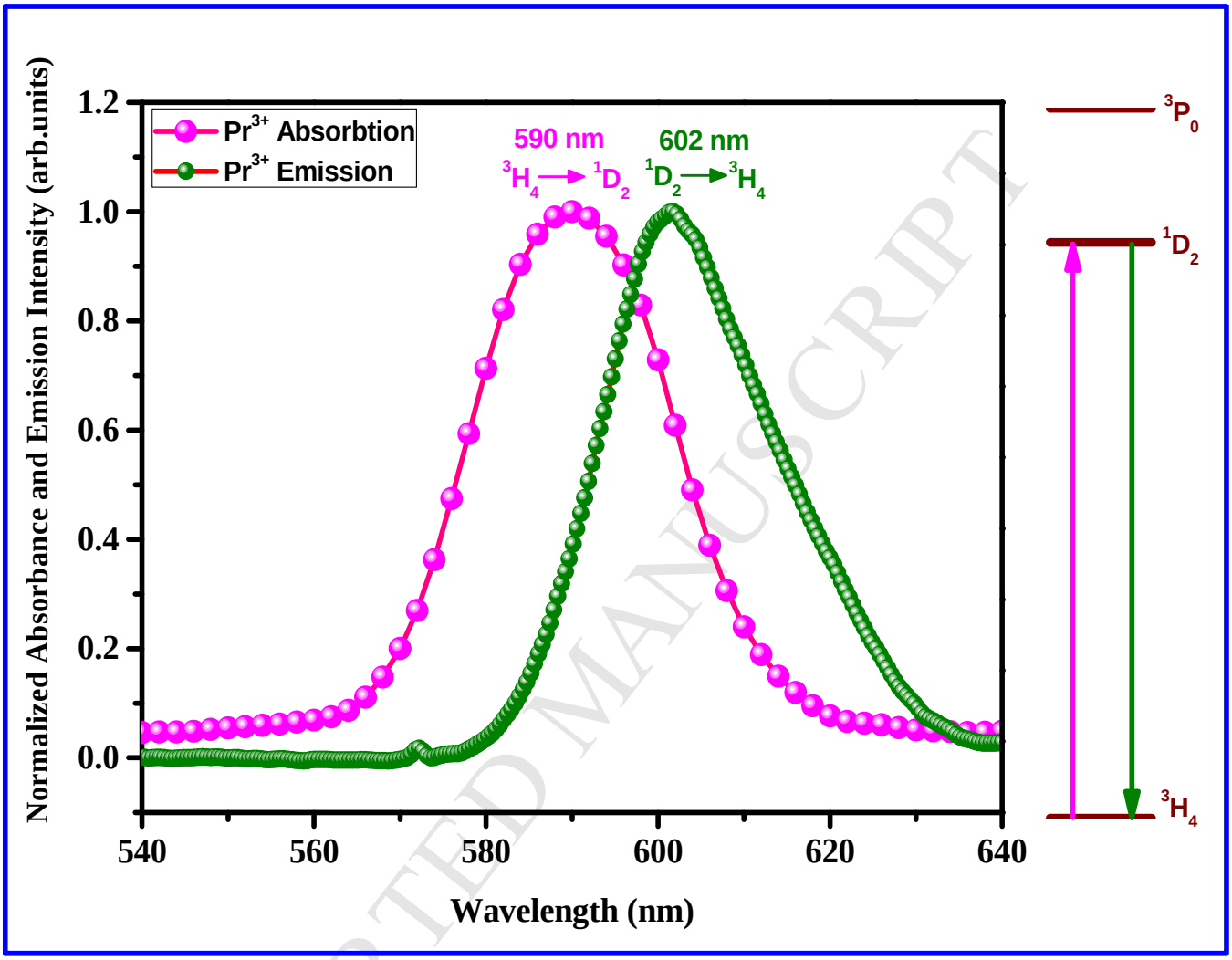

ACCEPTED MANUSCRIPT

Fig. 9:

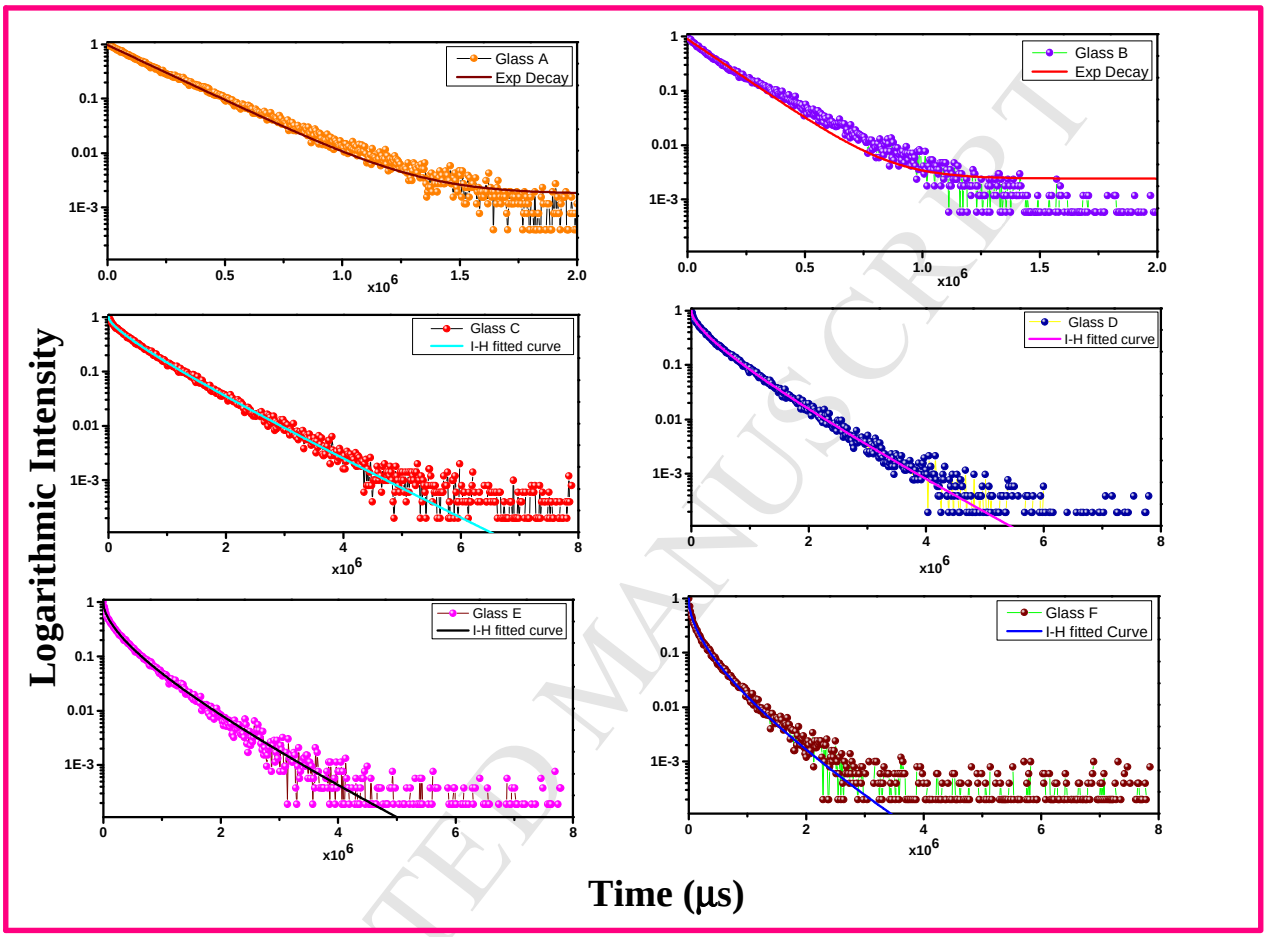

ACCEPTED MANUSCRIPT

Fig. 10:

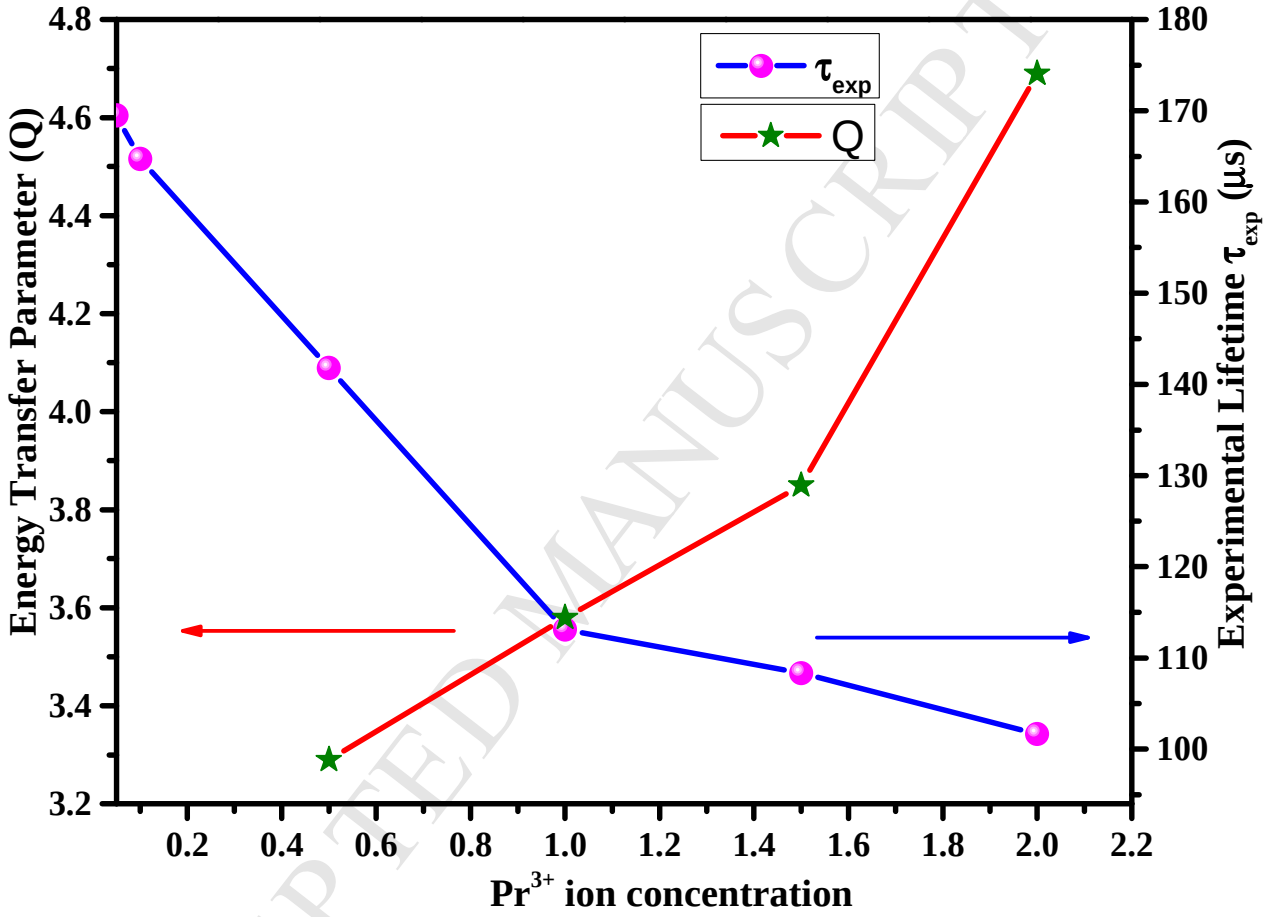

ACCEPTED MANUSCRIPT

Fig. 11:

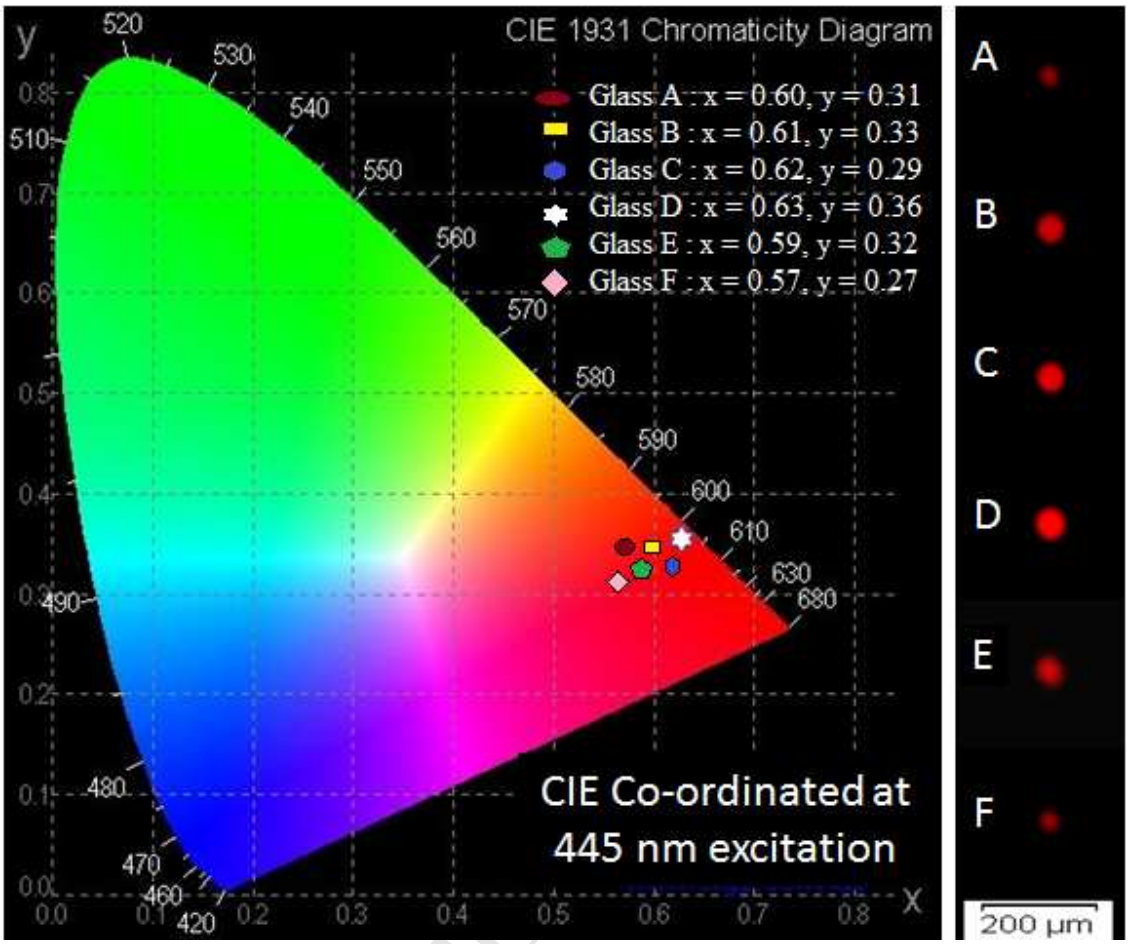

ACCEPTED MANUSCRIPT

ACCEPTED MANUSCRIPT

Highlights

- LiPbAlB glasses with Pr^{3+} were prepared by using sudden melt quenching technique.
- FT-IR and Raman studies reveal the functional groups present in the titled glass.
- Under 445nm CW laser excitation LiPbAlB glasses show reddish orange luminescence.
- CIE coordinates and confocal images also reiterate visible reddish orange emission.
- 1mol% Pr^{3+} concentration is apt in these glasses for reddish orange luminescence.

ACCEPTED MANUSCRIPT

International Journal of Scientific Engineering and Technology ISSN:2277-1581
Volume No.5 Issue No.8, pp: 400-405 01 August 2016

Study of Compilation and Heap Tuning Parameters across Virtual Machines for the Application Performance Improvements

Vijayanand Kumar[1], Ankit Babbar[2,] Vikas Kala[3], Mudit Khare[4], Amitesh Anand[5]
Department of Computer Sc & Engineering
[3] IIIT, Gwalior, India
[2] Thapar University, Patiala, India
[1] Delhi Technological University, Delhi, India
[4] Bundelkhand Institute of Engineering & Technology, Jhansi, India
[5] Calcutta Institute of Engineering and Management, Kolkata, India
1vijayanand033@gmail.com , 2ankitbabbar89@gmail.com, 3vikaskala189@gmail.com,
4khare.mudit@gmail.com ,5amitesh.unique@gmail.com

Abstract : Virtual Machines are the programs for supporting platform independence, network mobility and scalability for different underlying machine architectures such as x86 and ARM etc for JAVA based framework. VM main functions are Compilation of bytecode to the native code, Memory Management and Garbage Collector Management etc. Java architecture is a stack based architecture where as Dalvik and ART possesses register based architecture. All mentioned Virtual Machines are run on battery driven devices such as laptop and mobile. So the goal of VM must be to improve performance by consuming less battery power and faster execution of programs. It is also important to maximize the throughput of the CPU cycles. CPU cycles are one more major factor to consider which impact the battery life. Many enhancements have been observed in VM evolution from JAVA VM to ART VM.JAVA Code compilation has been taken care by interpreter and just in time compilation technique which convert per java class to native code where as dalvik bytecode per application forms Dex executable and further conversion of Dex to native by using JIT compilation in runtime. ART uses new Ahead of Time compilation technique which creates executable and linkable format. ART compilation done during boot or upgrade time and overcome the runtime compilation.

So far ART Virtual Machine has been considered as best VM in terms of performance and better user experience for android system under command of linux operating system. Tradeoffs took place for performance over higher installation time for application in case of ART (Android Runtime) [14, 15, 16, 17].

Virtual Machines also evolved and experimented with different memory management techniques for fast allocation and aim to achieve parallelism and concurrency. Allocation technique used for JAVA and Dalvik VM is through dlmalloc library whereas rosalloc technique used for Android Runtime to boost performance in allocation [2, 5].Garbage collection runs as daemon in each VM for reclaiming the memory and causes application performance to go low. Several GC techniques have been experimented on VM's among which Concurrent Mark and Sweep and Generational are most famous one. Goal of GC must be lesser pause time, GC time and to overcome UI frame drops [1, 13]. This paper presents different compilation and heap tuning parameters for different virtual machine. Experimentation results discuss about the trade-off with tuning.

Keywords : **Virtual Machine, Android, Dalvik, Android RunTime, Garbage Collection**.

NOMENCLATURE:

GC – Garbage Collector
VM – Virtual Machine
UI – User Interface
ART – Android Runtime
Dex – Dalvik Executable
OAT – Optimized art
ODEX – Optimized Dalvik Executable
JIT – Just in Time
AOT – Ahead of Time
CGC – Concurrent GC
AGC – GC for Alloc
CSB – Concurrent Start Bytes
S.L. – Soft Limit
TU – Target Utilization
HSS – Heap Start Size
HMF – Heap Max Free

1. Introduction

Java, Dalvik and ART offer several tuning parameters to optimize the performance in terms of compilation and heap. These tuning varies with the device configuration such as RAM size and density pixel used [2]. For different mobile devices tuning parameter varies and scope for optimum tuning exists.

(a) Compilation Tuning:-

Interpreter, JIT, AOT and mix of compilation techniques with profiling of methods and bytecodes are available for different virtual machines [14-17].

For Java Applications, compilation tuning parameters relies on profiling the hot methods and taken care by the interpreter and JIT compiler itself [18, 19]. Bytecode optimization using _quick instruction improves the performance by using caching technique [8, 9]. Similar case is with the dalvik which uses JIT framework for compilation in runtime. Dalvik executable with optimization (dexopt) takes place before converting bytecode to

ISSN:2277-1581
01 August 2016

the native code. Only tuning associated with it is the number of methods or code needs the compiler during profiling at runtime. For dalvik and android runtime, bytecode representations are register based which is more approximated to machine architecture (x86 and ARM) and hence faster execution of bytecode takes place [3]. Compilation tuning for ART has scope to improve performance [21]. Dex2oat is the tool which converts dex bytecode to native code and there are associated tuning parameters including profiling for methods [22, 23].

ART Compilation Tuning:-

dalvik.vm.profiler [0/1]
dalvik.vm.dex2oat-Xms : [64m]
dalvik.vm.dex2oat-Xmx : [256m]
dalvik.vm.image-dex2oat-Xms:[64m]
dalvik.vm.image-dex2oat-Xmx:[64m]
dalvik.vm.dex2oat - filter
dalvik.vm.image -dex2oat - filter

Filter Options:

- everything - compiles almost everything, excluding class initializers and some rare methods that are too large to be represented by the compiler's internal representation.
- speed - compiles most methods and maximizes runtime performance, which is the default option.
- balanced - attempts to get the best performance return on compilation investment.
- space - compiles a limited number of methods, prioritizing storage space.
- interpret-only - skips all compilation and relies on the interpreter to run code.
- verify-none - special option that skips verification and compilation, should be used only for trusted system code.

Threshold Limits on the methods:-

- kDefaultHugeMethodThreshold
- kDefaultLargeMethodThreshold
- kDefaultSmallMethodThreshold
- kDefaultTinyMethodThreshold
- kDefaultNumDexMethodsThreshold
- kDefaultTopKProfileThreshold

ART uses AOT compilation and above are important parameters to control the compilation and performance. Most of the code can be compiled using "everything" filter option with more memory footprint with trade-off with runtime performance improvements.

Heap Tuning:-

Performance impact for the application can be observed with the heap tuning parameters. This tuning mainly impacts the GC work functionality. Running the GC daemon for memory reclaim for the applications is bounded by the memory tuning parameters.

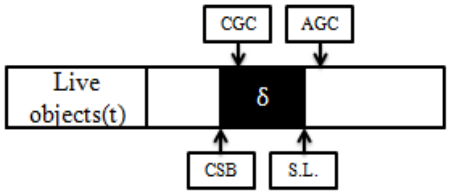

Figure 1: Concurrent GC and Allocation GC on heap

Running concurrent GC depends when concurrent start byte gets hit and allocation GC is being triggered when soft limit footprint crossover while object allocation [1]. Figure 1 is the theory behind dalvik and ART garbage collection with heap configuration for each application. One parent zygote process forks several children as application with the copy of same heap tuning configurations. Heap tuning changes system wide and overall performance impact can be observed. For the Java serial and parallel GC runs automatically when the soft limit threshold reached on allocation for each application. Figure 1 also represents the heap with live objects present and adjusted CSB and S.L corresponding to it. Concurrent start bytes and soft limit is likely to change on each allocation [1] and shows the piston behaviour which moves to and fro on allocation and collection.

For Java VM three heap parameters are essential for the tuning [25].

Parameters	**Description**	**JVM Option(Kaffe-VM)**	**Default**
Initial Heap Size	VM requests this amount of memory from operating system and add it to heap it manages	-ms	5MB
Maximum Heap Size	VM never requests more than this amount of memory	-mx	64MB
Heap Increment Size	Memory will be allocated when VM decides to postpone GC and increase heap by this amount of memory.	-as	1MB

Table 1: JVM Heap Tuning Parameters

Parameters	Limits
dalvik.vm.heapstartsize	5MB-16MB
dalvik.vm.heapgrowthlimit	64MB -96MB
dalvik.vm.heapsize	96MB -128MB
dalvik.vm.heaptargetutilization	0.75-.90(%)
dalvik.vm.heapminfree	512KB-2MB
dalvik.vm.heapmaxfree	8MB-16MB

Table 2: Android Dalvik/ART VM Heap Tuning Parameters

Table 1 and 2 describes some of the tuning parameters associated to the heap. Garbage collector runs as GC daemon for concurrent GC and normal collection while allocation occurs for other types of GC.

Section II explains about the relative work based on experiments conducted by hardware manufacturer. Section III describes the proposed methodology of tuning for optimum performance. Section IV deals with simulation environment and results and the conclusion has been made in Section V.

2. Related Work

Java performance for different virtual machine depends on benchmarking tool such as dacapo, jprofiler and jRockit etc. In the case of finding the best VM, machine consistency must be maintain and tuning must be set as default or described by the VM vendor. Different machines with different architecture or memory footprint have different tunings. These tuning are variables and left to the vendor for further optimization which uses VM. For the Dalvik and ART case combination of compilation tuning and heap tuning can give optimum performance in terms of better battery life and CPU usage. Techniques such as compilation of mixed AOTC and JITC [14-17] can optimize performance. Garbage collections such as including the generational collection [1] also help improving performance. ART has such configuration which uses AOTC and JITC framework with generational collection. ART also achieve parallelism by using new memory management techniques. Evolution of virtual machine is resulting in better performance by changing the VM framework. VM Vendors provide options for tuning and VM are in the generic form which later on configured by device vendor which uses the VM.

dalvik.vm.parameters	Xhdpi 1GB	Xhdpi 2GB	Mdpi 1GB
heapstartsize	8MB	16MB	8MB
heapgrowthlimit	128MB	200MB	64MB
heapsize	174MB	348MB	174MB
heaptargetutilization	0.75	0.75	0.75
heapminfree	512KB	512KB	512KB
heapmaxfree	8MB	8MB	8MB

Table3: Experimental Tuning by Vendor (Intel)

Table 3 is the experimental result [2] from the Intel which varies for different devices which are variable in density pixel and RAM footprint. Claim here is that these tuning are optimum with such specification mentioned in table 3.This conclude that there is scope for further tuning for different upcoming specifications with current tuning parameters. Further modification scope is present to find optimum tuning with current specification. Proposed work and experimentation results are discussed with respect to finding optimum tuning parameters for specific device configuration.

3. Proposed Work

Programming language such as C,C++,JAVA or supported framework using these language such as C based platform for mobile development or Java based android development compilation optimization is done based on the coding construct defined. In other word making code to compile and converting code to the native or machine understandable also affected by coding done for the application. Best coding guidelines supports optimum compilation and fast execution [26-28]. Virtual machine interpretations for compilation is either stack based [C, C++, Java] or register based [Android Dalvik or ART]. For the Android system google provide tuning [29] for low ram and enabling or disabling the JIT compilation. Vendors such as google a provide specification and support list of features tuned for the device configuration [2, 3].

Tuning Area for Performance	Parameters
Density Pixels	Ram Requirements
Garbage Collection	Pause Time GC Time GC Count Type of GC run on heap space(ART)
OS support	32 bit or 64 bit support
Kernel Memory Optimization	Swap space size Swappiness
Low Memory Killer OOM Adjustment Low Ram Flag	RAM based configuration

Table 4: Device Tuning Parameters

Apart from compilation and heap tuning, table 4 describes other tuning for the device for performance optimization [2].Till now mentioned parameters are configurable with respect to device configuration and scope for further tuning for specific device. For finding optimum tuning tools such as benchmarking for JAVA, Android specific virtual machines, GC benchmarking for performance are available [2]. For android case google code base can be tested for different applications with change in tuning parameters with specific device configuration. Tools provided by google for android such as sys trace analysis, heap dump profiler and cpu analysis tools in built with eclipse can support the analysis for the performance for particular application as well as for all the applications. Logs are enabled for virtual machine to analyze the garbage collector which can help finding GC time, GC Pause time and GC Counts. Compilation logs can be

International Journal of Scientific Engineering and Technology
Volume No.5 Issue No.8, pp: 400-405
ISSN:2277-1581
01 August 2016

enabling to analyze the initialization of the class, time taken for verification of the class and loading of the class. Tuning does have system wide impacts. Automation, Manual and monkey tests are also useful in analyzing system wide impacts. Experimentation performed uses all the methodology for analyzing system performance. Implementation has been to parse the GC logs for the system.

GCType	Count	Pause Time	Total Time
Explicit concurrent mark sweep	1008	2533.795	108293.5
Background concurrent mark sweep	5	7.78	497.617
Explicit marksweep + semispace	146	6324.298	6410.48
Background sticky concurrent mark sweep	271	2829.847	25699.85
Background partial concurrent mark sweep	184	1185.853	25307.44
Explicit	1154	8858.093	114704
Background	460	4023.48	51504.91
Total(Explicit+BG)	1614	12881.573	166208.9

Table5: ART GC Types versus Time

GCType	Freed Obj Count	Freed Obj Size
Explicit concurrent mark sweep	11459443	782.400MB
Background concurrent mark sweep	3930	165KB
Explicit marksweep + semispace	2100211	126.0MB
Background sticky concurrent mark sweep	4918594	254.232MB
Background partial concurrent mark sweep	3290614	172.0MB
Explicit	13559654	909.400MB
Background	8213138	427.232MB
Total(Explicit+BG)	21772792	1336.632MB

Table6: ART GC Types versus Objects

GCType	Freed L Obj Count	Freed L Obj Size
Explicit concurrent mark sweep	1704	243.0MB
Background concurrent mark sweep	0	0B
Explicit marksweep + semispace	33	3.0MB
Background sticky concurrent mark sweep	2473	80.0MB
Background partial concurrent mark sweep	2316	339.0MB
Explicit	1737	246.0MB
Background	4789	419.0MB
Total(Explicit+BG)	6526	666.0MB

Table7: ART GC Types versus Large Objects

Table 5, 6 and 7 are the parsed log for android runtime garbage collection for analysis. Comparison reports can be prepared based on log analysis for particular test suite on android. Table 5, 6 and 7 prepared after tuning the heap parameter for comparison analysis with the default heap tuning.

4. Simulation Results

Experimentation has been done on Java virtual machine (Kaffe-VM), Dalvik VM and ART VM.

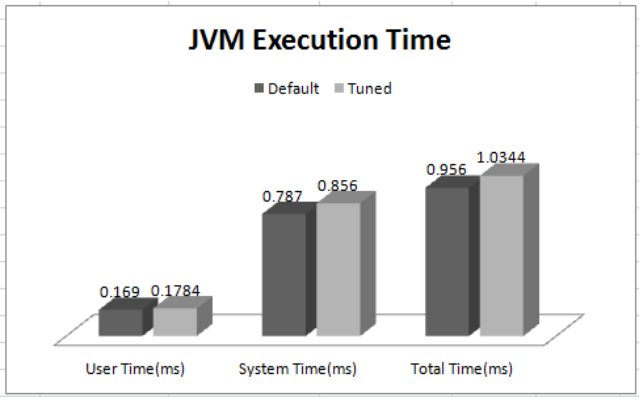

Figure 2: Execution Time Kaffe-VM

Configuration	Default: Initial Heap Size=5M, Maxheap Size=64M, Increment Size=1M Tuned: Initial Heap Size=8M, Maxheap Size=12M, Increment Size=3M
Inference	Tuning the parameters, the performance of the app is similar but consumes less memory resources, as max heap memory has been reduced; but as a trade-off initial & incremental size of heap is increased.

Table 8: Java VM Heap Tuning

Figure2 and table 8 describe the results and impact for specific application with average 12M ram usage.

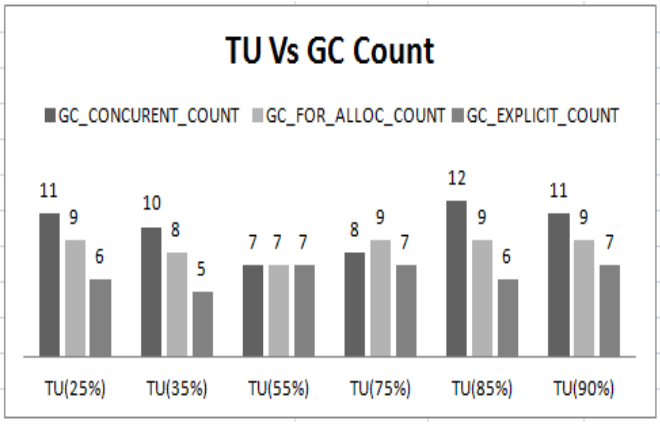

Figure 3: Dalvik VM heap tuning for target utilization

International Journal of Scientific Engineering and Technology
Volume No.5 Issue No.8, pp: 400-405
ISSN:2277-1581
01 August 2016

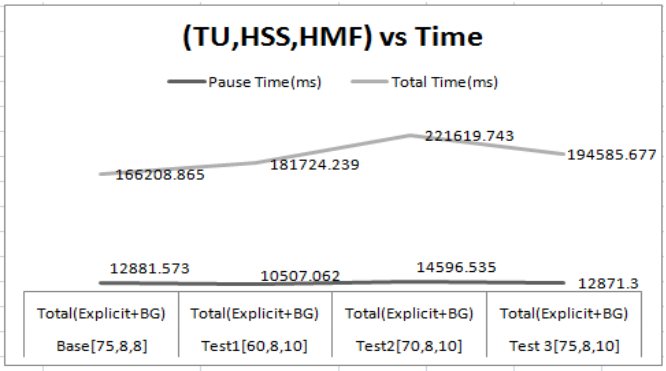

Figure 4: ART VM heap tuning versus time

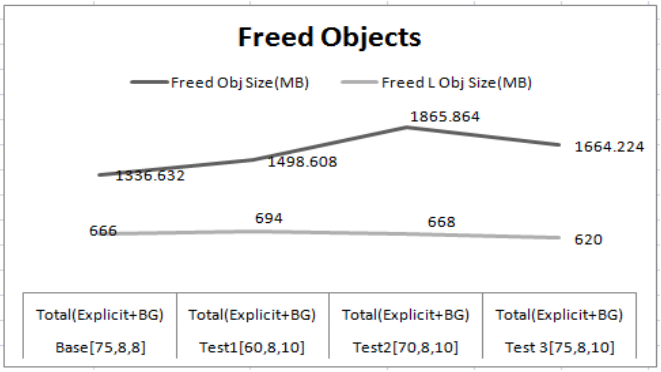

Figure 5: ART VM heap tuning versus Objects

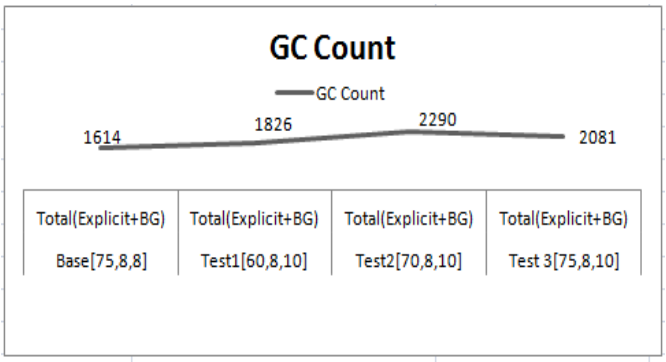

Figure 6: ART VM heap tuning versus GC counts

Figure 3, 4, 5 and 6 demonstrate the heap tuning results for specific test suit for 1GB RAM configuration.

Figure	Inferences
3	Heap target utilization varied and compared to default (75%). GC Count has been reduced.
4	Optimum GC time for [78,8,8] (166 sec) and optimum paused time at [60,8,10] (105 sec)
5	Less freed object for [78,8,8] , highest at [70,8,10]
6	Less GC count at [75,8,8]

Table 9: Android VM Analysis

Table 9 suggests that heap tuning with target utilization of 75%, heap start size with 10MB and heap max free with 8MB provides optimum GC performance for ART with configuration for Xhdpi with 1GB RAM.

For runtime improvements setting dex2oat filter in device.mk with product property configuration for 1GB RAM(Xhdpi) native application ROM footprint increased by 4MB and overall more than >15MB in size with native and downloaded applications i.e. code has been optimised with below configuration and provide >200ms average application entry time improvement(140 application's oat were present in the device)

PRODUCT_PROPERTY_OVERRIDES += \
dalvik.vm.dex2oat-filter=**everything** \
dalvik.vm.image-dex2oat-filter=**everything**

5. Conclusion

Goal was to find optimum tuning for different devices with different configuration so that performance boost can be realized. Introduction and related work section provide the study related to tuning parameters which is configurable for different devices for different configurations. There is vast scope for improvement through tuning parameters provided by different virtual machine vendors. These tuning will change with the change in configuration for future devices. Compilation and Garbage collector for android systems are major area for improvements. Memory management such as ROSALLOC over DLMALLOC techniques has been used for fast allocation in case of android runtime. ART provided pre-compilation technique which provide runtime performance boost over higher install time and increased ROM footprint where as DALVIK relies on interpreter and JIT compilation techniques with caching the hot methods of code for performance boost.

References

i.Ahmed Hussein, Mathias Payer et. al. Impact of GC Design on Power and Performance for Android.

ii. https://nebelwelt.net/publications/files/15SYSTOR.pdf

iii.Android Memory Tuning for Android 5.0 and 5.1. https://01.org/android-ia/user-guides/android-memory-tuning-android-5.0-and-5.1

iv.http://source.android.com/compatibility/android-cdd.pdf . Google CDD for Android 5.1

v.http://developer.android.com/tools/debugging/debugging-memory.html. Investigating Your RAM Usage

vi.http://dubroy.com/memory_management_for_android_apps.pdf and associated video at

vii. http://dubroy.com/blog/google-io-memory-management-for-android-apps/

viii.https://source.android.com/devices/tech/ram/low-ram.html Google's discussion of low-ram configuration.

ix.http://source.android.com/devices/tech/dalvik/configure.html Google's discussion on configuring ART.

x.Inside the Java Virtual Machine by Bill Venners.

xi.https://conference.hitb.org/hitbsecconf2014ams/materials/D1T2-State-of-the-Art-Exploring-the-New-Android-KitKat-Runtime.pdf.

xii.https://anatomyofandroid.com/.

xiii.http://www.cubrid.org/blog/dev-platform/understanding-java-garbage-collection/

xiv.http://NewAndroidBook.com/

xv. A Generational Mostly Concurrent Garbage Collection. Tony Printezis, David Detlefs.

xvi. On Real-Time Performance of Ahead-of-Time Compiled Java. Anders Nilsson and Sven

a. Gestegard Robertz

xvii. Design and Optimization of a Java Ahead-of-Time Compiler for Embedded Systems, Dong-Heon Jung, Soo-Mook Moon, Sung-Hwan Bae.

xviii. A Method-Based Ahead-of-Time Compiler for Android Applications. Chih-Sheng Wang, Guillermo A. Perez et. al.

xix. A Selective Ahead-Of-Time Compiler on Android Device. Yeong-Kyu Lim, Sharfudheen Parambil,See-Hyung Lee et.al.

xx. http://www.javaworld.com/article/2078635/enterprise-middleware/jvm-performance-optimization-part-2-compilers.html

xxi. http://www.ibm.com/support/knowledgecenter/SSAW57_7.0.0/com.ibm.websphere.nd.doc/info/ae/ae/tprf_tunejvm_v61.html

xxii. http://www.ibm.com/support/knowledgecenter/SSAW57_7.0.0/com.ibm.websphere.nd.doc/info/ae/ae/tprf_hotspot_jvm.html

xxiii. https://source.android.com/devices/tech/dalvik/configure.html

xxiv. http://newandroidbook.com/files/Andevcon-ART.pdf

xxv. https://conference.hitb.org/hitbsecconf2014ams/materials/D1T2-State-of-the-Art-Exploring-the-New-Android-KitKat-Runtime.pdf

xxvi. http://www.kaffe.org/

xxvii. http://www.oracle.com/webfolder/technetwork/tutorials/obe/java/gc01/index.html

xxviii. https://software.intel.com/en-us/articles/how-to-optimize-java-code-in-android-marshmallow

xxix. http://www.vogella.com/tutorials/AndroidApplicationOptimization/article.html

xxx. http://developer.android.com/training/articles/perf-tips.html

xxxi. https://source.android.com/devices/tech/config/low-ram.html

Available online at www.ijapie.org

International Journal of Advanced
Production and Industrial Engineering

IJAPIE-SI-MM 512 (2017) 81–84

Special Issue on

MATERIALS
&
MANUFACTURING

Synthesis and Wear Behaviour of $(Al, Cu)_3Ti$ Powder Blend by Mechanical Alloying

Shailesh Kumar Singh*[1], Satyajeet Kumar[1], Jay Shankar kumar[1], Sitikantha Behera[1], Shailesh Mani Pandey[2]

[1]*(Department of mechanical Engineering, Krishna Engineering College, Ghaziabad 201007, India)*
[2]*(Department of mechanical Engineering, Delhi Technological University, Delhi110042, India)*
**Email:* shaileshsonu10@gmail.com

Abstract : In the present investigation, an attempt has been made to study the formation of intermetallic compound for $Al_{70}Cu_{22}Ti_8$ alloy composition by mechanical alloying. Elemental powder of $Al_{70}Cu_{22}Ti_8$(all in wt. %) composition was milled in a Fritsch pulverisette planetary mill for 50h under toluene. Powder of 1wt. % Y_2O_3 and 1wt. % TiO_2 were added separately to the 50 h milled base alloy powder to study the effect of oxide dispersion. A maximum of 81% theoretical density was obtained for the composite powder mixture sintered at 1100^0C for 1h. A maximum Vickers microhardness of 449, 649, 872HV were obtained for base alloy, Y_2O_3 and TiO_2 dispersed alloy sintered at 1100^0C for 1h respectively. It was also found that TiO_2 and Y_2O_3 dispersed base alloy have higher wear resistance than base alloy.

Keywords: Synthesis and wear behaviour , $(Al, Cu)_3Ti$ powder blend, mechanical alloying

INTRODUCTION

In earth crust aluminium is present in hydrated oxide form of which bauxite is the primary ore. The aluminium alloys are light weight ($2.77g/m^3$) and easy to manufacture. Aluminium alloys have high specific strength approximately 3 times that of structural steel. So, aluminium alloys are primary used for consumption and production after steel [1].But today's modern world calls for materials with a combination of properties that cannot be met by single metal like polymer, ceramic and metal alloys. This combination of material properties is achieved by the development of intermetallic [2].Intermetallic is new class of most advanced materials. Intermetallic has different crystal structure than that of the parent materials. The intermetallic compound formation occurs when the bond strength of similar atoms (Al-Al) is less than that of bond strength of unlike atoms (Al-Ti).Intermetallic have properties between metal and ceramics because they have order distribution of atom [3].

Intermetallics have high structural material because they have high oxidation resistance, low density and high melting point temperature etc. [4-9]. Intermetallic can replace the super alloy and stainless steel as they process high melting point [10]. Intermetallic widely applied for high temperature structural application so they generally used in jet engine to withstand the operating temperature and reduce the weight of the engine.At room temperature most of intermetallichas less toughness and the manufacturing cost of intermetallic compound is too high. Due to extrinsic factor the ductility of intermetallic is less but exception is FeAl intermetallic.Al_3Ti intermetallic has low density i.e. $3.31g/cm^3$ and high oxidation resistance [11]. At room temperature the Al_3Ti intermetallic shows 216 GPA of young's modulus which is more than other titanium aluminaides. Most super alloys have this range of young's modulus hence it can substitute super alloy. As Al_3Ti intermetallic is light weight it is used in aerospace application [12]. At low temperature Al_3Ti intermetallic is brittle but when exposed to air Al_2O_3 layer formation occurs as a result oxidation resistance increases [10, 11].

MATERIALS AND METHOD

Synthesis of $(Al,Cu)_3Ti$ powder blend

Synthesis of $(Al, Cu)_3Ti$ powder blend were performed by mechanical alloying followed by conventional pressure less sintering.

Table-1 Milling parameters used for planetary milling of $(Al ,Cu)_3Ti$

Milled parameter	Value
Rotation speed (rpm)	300
Ball-power weight ratio	5:1
Al: Cu: Ti (wt %)	70:22:8
Type of ball	steel
Milling time (h)	0 , 10 , 20 , 30 , 40 , 50
Grinding medium	toluene
Cointainer volume (ml)	250
Steel ball size (mm)	15 , 10

Elemental powder of the composition $Al_{70}Cu_{22}Ti_8$ (all in wt. %) were milled for 0, 10, 20, 30, 40 and 50 h in a Fritsch pulverisette planetary mill. To avoid oxidation of powders during milling toluene ($C_6H_5CH_3$) was used to fill to just pass over the balls and powders. The details of milling parameters are mentioned in Table 1.

Fifty hours milled base powders were mixed separately with 1 wt. % of Y_2O_3 and TiO_2 powders by pestle and mortar for 1 hour. Then the mixed powders were cold compacted by hydraulic press using a load of 450MPa. Pellets of 15mm diameters were prepared by cold compaction. The cold compacted pellets were then sintered in a tubular furnace at 900°C, 1000°C and 1100°C for different times under a flowing argon gas. The different sintering parameters used are represented in Table 2.

Table-2 Sintering parameters used for different pellets

Elemental power	Compaction pressure (MPa)	Sintering temp (°C)	Holding time (h)	atmosphere
$Al_{70}Cu_{22}Ti_8$	450	900	2	argon
	450	1000	1	argon
	450	1100	1	argon
$Al_{70}Cu_{22}Ti_8$ -TiO_2(1 wt. %)	450	900	2	argon
	450	1000	1	argon
	450	1100	1	argon
$Al_{70}Cu_{22}Ti_8$ -Y_2O_3 (1 wt. %)	450	900	2	argon
	450	1000	1	argon
	450	1100	1	argon

RESULTS AND DISCUSSIONS

Hardness measurement

Figure-1 shows the hardness of $Al_{70}Cu_{22}Ti_8$ (base alloy), Y_2O_3 and TiO_2 dispersed base alloy sintered at 900, 1000 and 1100°C respectively. It is shown from the graph that hardness of base alloy and Y_2O_3 and TiO_2 dispersed base alloys increases with temperature. However, the rate of increase of hardness of base alloy is less as compared to Y_2O_3 and TiO_2 dispersed base alloy. The hardness values of base alloy increases from 409 to 449 as sintering temperature increases from 900 to 1100°C. With the addition of 1 wt. % nanoY_2O_3 and TiO_2 hardness drastically increases. The hardness values of Y_2O_3 dispersed base alloy are 421, 442 and 649 at 900, 1000 and 1100°C respectively. Similarly, the hardness value of TiO_2 dispersed base alloy are 572, 593 and 872 at 900, 1000 and 1100°C respectively. From the hardness data it is clear that hardness is highest for TiO_2 dispersed alloy and lowest for base alloy. The hardness increases drastically with the addition of hard and brittle TiO_2 and Y_2O_3 particles. Another reason of high hardness after addition of TiO_2 and Y_2O_3 particles is due to the formation of hard and brittle Al_2O_3 phase as evident from XRD spectrum.

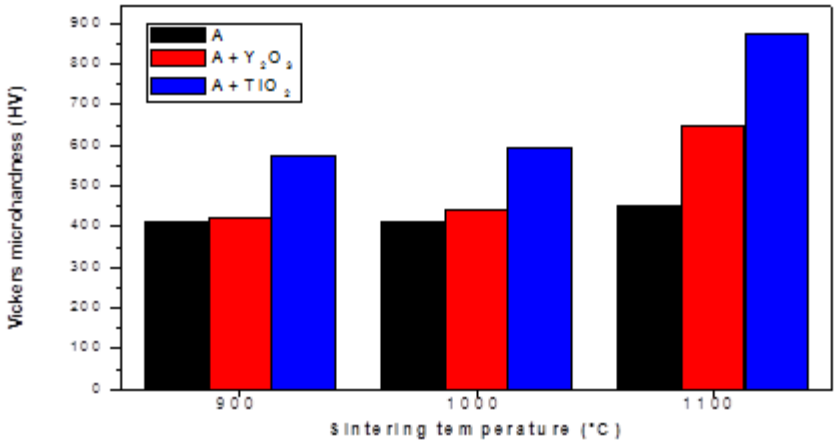

Figure-1 Bar chart of Vickers micro-hardness of $Al_{70}Cu_{22}Ti_8$ (base alloy), TiO_2 and Y_2O_3 dispersed base alloy sintered at different temperature

Wear study

From 2 (a, b) shows the variation of wear depth with sliding time of $Al_{70}Cu_{22}Ti_8$ (base alloy), Y_2O_3 and TiO_2 dispersed base alloy sintered at 900 and 1100°C respectively. It is observed from both graphs that the wear depth decreases with the addition of Y_2O_3 and TiO_2 to the base alloy. The reason is that hard and brittle TiO_2 and Y_2O_3 spread all over the intermetallic uniformly and reduces the pores and providing strong interfacial bond. Watanabe et al. studied the wear behaviour of Al-Al_3Ti composite and showed that wear resistance is more for the composite as compared to pure Al. The abrasion is the main mechanism of wear on Al-Al_3Ti composite. The found that the supersaturated Al_3Ti layer formation occurs from the top surface to 100µm depth. It is seen from the graphs that samples sintered at 1100°C shows more wear resistance than 1000°C due to higher hardness. The maximum wear depth of base alloy sintered at 1100°C is around 200µm, whereas wear depth is 340µm for base alloy sintered at 900°C. This is due to higher hardness at 1100°C as compared to 900°C.

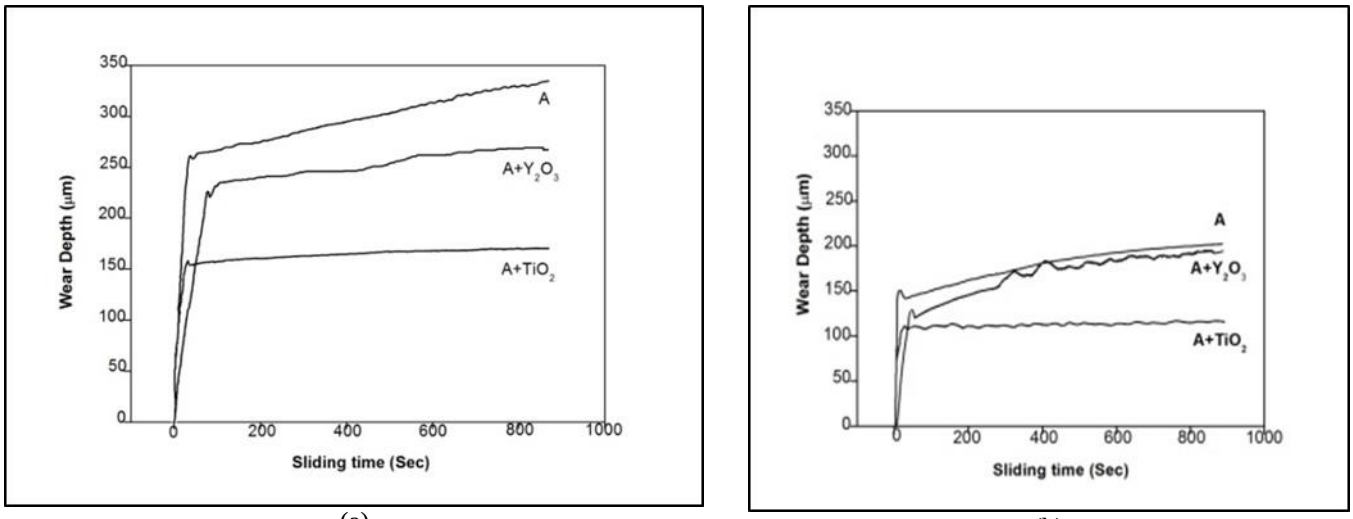

Figure -2 (a) and (b) Variation of wear depth with sliding time of $Al_{70}Cu_{22}Ti_8$ (base alloy), Y_2O_3 and TiO_2 dispersed base alloy sintered at 900 and 1100°C.

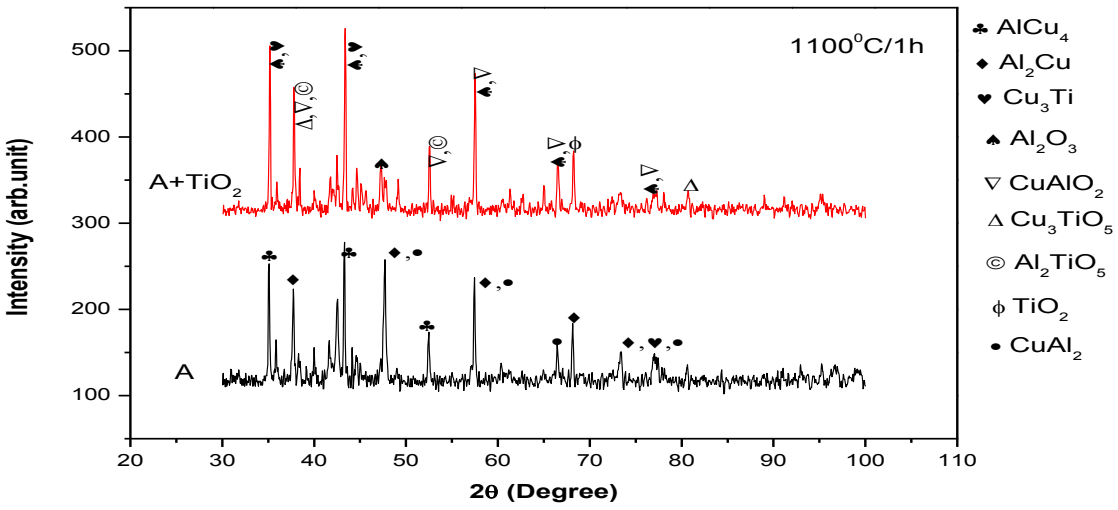

Figure-3 XRD spectrum of base power of composition $Al_{70}Cu_{22}Ti_8$ and Y_2O_3, TiO_2 dispersed intermetallic at 1100^0C for 1 h

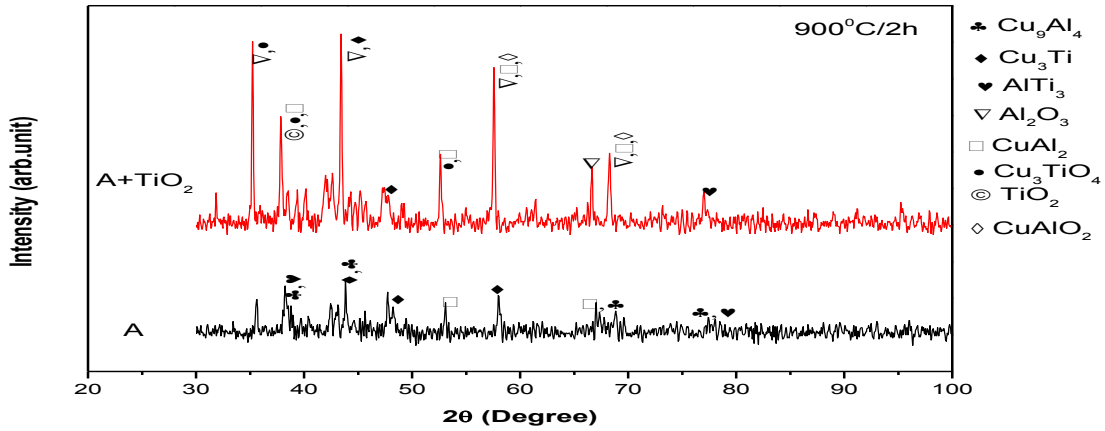

Figure-4 XRD spectrums of base powder of composition $Al_{70}Cu_{22}Ti_8$ and TiO_2 dispersed intermetallic at 900^0C for 2 h.

Figure -3 shows that XRD spectra of 50h milled base power $Al_{70}Cu_{22}Ti_8$, TiO_2 dispersed base powder sintered at 1100 for 1h under argon atmosphere. In base sample the peaks of $AlCu_4$ and $CuAl_2$ peaks are visible. Here, aluminium reacts with Copper to form these above compounds. XRD spectra show the peaks of Al_2O_3, Cu_3TiO_5, $CuAlO_2$ and $CuTi_3$. Formation of these above compounds may be possible due to the reaction of TiO2 with Cu and Al.

Figure -4shows the XRD spectra of 50h milled base powder $Al_{70}Cu_{22}Ti_8$ and TiO2 dispersed base powder sintered at 900^0C for 2h under argon atmosphere. It is found that there is a formation of Cu_9Al_4, Cu_3Ti and $CuAl_2$intermetallics for the base composition after sintering. Formation of Al_2O_3 and Cu_3TiO_4 is evident from XRD spectrum due to reaction of TiO2 with base sample after sintering.

CONCLUSIONS

This study explored the characterization of ball-milled Al-alloy powder and reported the effect of milling and phase formation techniques to study the characteristics of alloy powder. The following important findings derived from the results were presented in this paper.

A maximum Vickers microhardness of 449, 649, 872HV were obtained for base alloy, Y_2O_3 and TiO_2 dispersed alloy sintered at 1100°C for 1h respectively. It was also found that TiO_2 and Y_2O_3 dispersed base alloy have higher wear resistance than base alloy.The XRD study shows the peaks of Cu_2Al_4, AlCu, $AlTi_3$intermetallic phases after 50 h of milling in case of base alloy. After consolidation of the base alloy, formation of new phases like Cu_9Al_4, Cu_3Ti, $CuAl_2$ are visible for the alloy sintered at 900 and 1000^0C but phases like Al_2Cu, $AlCu_4$ also visible for sintering at 1100^0C. After addition of TiO_2 and Y_2O_3 in base alloy there is formation of Al_2O_3.

REFERENCES

[1] Schweitzer P.A.,"MetallicMaterials, Physical, Mechanical and Corrosion Properties", CRC Press (2003)
[2] CallisterW.D.,"Material Science and Engineering" 7th edition ,John Wiley and Sons, University of Utah, (2007) pp. 577-578
[3] SauthoffG.,"Intermetallic" ,Chapman & Hall ,New york
[4] Mikkola D.E., Nic J.P., Zhang S., Milligan W.W.,The Iron and Steel Institute of Japan international,1991;31:1076
[5]Kumar K.S., Darolia R., Lewandowski J.J., Liu C.T., Martin P.L.,Miracle D.B., Nathal M.V., editors," Structural intermetallics",Warrendale, USA: TMS; 1993. p. 87–96
[6]Varin R.A., Winnicka M.B., Virk I.S., In: Darolia R., Lewandowski J.J.,Liu C.T., Martin P.L., Miracle D.B., Nathal M.V., editors. Structural intermetallics.Warrendale, USA: TMS; 1993. p. 117–24
[7] Shull R.D.,Nanostruct Mater 1993;2:213
[8] Moon K.I., Chang K.Y., Lee K.S.J., Alloys Comp 2000;312:273
[9]Anton D.L., Duhn D.N., Giamci A.F.J, Miner Metals Mater Soc 1989;41:12
[10]Nayak S.S., Murty B.S.," Synthesis and stability of L12–Al3Ti by mechanical alloying" , Materials Science and Engineering A 367 (2004) 218–224
[11] Yamaguchi M.,UmakoshiY.,YamaneT., Phil. Mag. 55 (1987) 301.

IOPscience iopscience.iop.org

Home Search Collections Journals About Contact us My IOPscience

Thermoelectric silicides: A review

This content has been downloaded from IOPscience. Please scroll down to see the full text.

2017 Jpn. J. Appl. Phys. 56 05DA04

(http://iopscience.iop.org/1347-4065/56/5S1/05DA04)

View the table of contents for this issue, or go to the journal homepage for more

Download details:

IP Address: 14.139.251.107
This content was downloaded on 14/03/2017 at 05:15

Please note that terms and conditions apply.

You may also be interested in:

Materials for thermoelectric energy conversion
C Wood

Silicides: Materials for thermoelectric energy conversion
Mikhail I. Fedorov and Grigory N. Isachenko

Concepts for medium-high to high temperature thermoelectric heat-to-electricity conversion: a review of selected materials and basic considerations of module design
Gabi Schierning, Ruben Chavez, Roland Schmechel et al.

Current trends in the physics of thermoelectric materials
Aleksei V Dmitriev and Igor P Zvyagin

Tuning phonon properties in thermoelectric materials
G P Srivastava

Layered oxychalcogenide in the Bi--Cu--O--Se system as good thermoelectric materials
C Barreteau, L Pan, E Amzallag et al.

Thermoelectric effects in graphene nanostructures
Philippe Dollfus, Viet Hung Nguyen and Jérôme Saint-Martin

Nanoscale solid-state cooling: a review
Amirkoushyar Ziabari, Mona Zebarjadi, Daryoosh Vashaee et al.

Searching for new thermoelectric materials: some examples among oxides, sulfides and selenides
S Hébert, D Berthebaud, R Daou et al.

Japanese Journal of Applied Physics **56**, 05DA04 (2017)
https://doi.org/10.7567/JJAP.56.05DA04

PROGRESS REVIEW

Thermoelectric silicides: A review

Amin Nozariasbmarz[1,2], Aditi Agarwal[1], Zachary A. Coutant[1], Michael J. Hall[2], Jie Liu[1], Runze Liu[1], Abhishek Malhotra[1], Payam Norouzzadeh[1], Mehmet C. Öztürk[1], Viswanath P. Ramesh[1], Yasaman Sargolzaeiaval[1], Francisco Suarez[1], and Daryoosh Vashaee[1,2*]

[1]*Electrical and Computer Engineering Department, Monteith Research Center, North Carolina State University, Raleigh, NC 27606, U.S.A.*
[2]*Material Science and Engineering Department, Monteith Research Center, North Carolina State University, Raleigh, NC 27606, U.S.A.*

*E-mail: dvashae@ncsu.edu
†The names after the first author are listed alphabetically. All authors contributed equally in this work.

Received October 2, 2016; accepted November 27, 2016; published online March 3, 2017

Traditional research on thermoelectric materials focused on improving the figure-of-merit zT to enhance the energy conversion efficiency. With further growth and commercialization of thermoelectric technology beyond niche applications, other factors such as materials availability, toxicity, cost, recyclability, thermal stability, chemical and mechanical properties, and ease of fabrication become important for making viable technologies. Several silicide alloys were identified that have the potential to fulfill these requirements. These materials are of interest due to their abundancy in earth's crust (e.g., silicon), non-toxicity, and good physical and chemical properties. In this paper, an overview of the silicide thermoelectrics from traditional alloys to advanced material structures is presented. In addition, some of the most effective approaches as well as fundamental physical concepts for designing and developing efficient thermoelectric materials are presented and future perspectives are discussed.
© 2017 The Japan Society of Applied Physics

1. Introduction

Thermoelectric generators with the ability to produce useful electric power from low-grade or waste heat can play a significant role in reducing carbon emissions and mitigating global warming. Over the past two decades, thermoelectric technology has made significant scientific progress and many good thermoelectric materials have been developed for their use in clean and sustainable energy sources. A good thermoelectric material has large electrical conductivity, σ, high Seebeck coefficient, S, and low thermal conductivity, κ, resulting in a large dimensionless-figure-of-merit, zT, where $zT = S^2\sigma T/\kappa$, in which T is the absolute temperature. The efforts to find or develop good thermoelectric materials mainly followed two directions. The first approach is finding new bulk materials and their further engineering to increase their zT.[1,2] Some examples representative of this direction are the filled skutterudites,[3] such as $Sr_{0.16}Yb_{0.03}Co_4Sb_{12}$,[4] clathrates, such as $Ba_8Ga_{16}Ge_{30}$,[5] Zintl phases, such as $Yb_{14}Mn_{1-x}Al_xSb_{11}$,[6] metal silicides, such as $Mg_2Si_{1-x}Sn_x$, and other materials such as $(GeTe)_{75}(AgSbTe_2)_{25}$ (TAGS-75),[7] $AgPb_{18}SbTe_{20}$ (LAST),[8] PbTe(Tl),[9] and SnSe.[10] Another direction is the use of nanostructures (e.g., superlattices) that improve the power factor ($S^2\sigma$) through quantum size effects,[11–13] or interface energy filtering,[14–16] while their thermal conductivity is reduced through scattering of phonons at interfaces.[12,17] Some examples of these groups include ErAs rare earth nanocomposites and ScN/ZrWN multilayers for thermoelectric energy conversion.[18–21] The improved zT in these structures comes mainly from the reduction in phonon thermal conductivity and to a lesser extent, from enhancing the power factor. Nanostructured bulk Bi_2Te_3[22–24] and PbTe[25] based materials have also shown to have high zT, resulting from their incorporation of nano-domains.[26]

A review of the thermoelectric materials developed to date indicate that some of these materials are toxic and many of them are based on the elements with low abundance in Earth's crust such as tellurium (Te), antimony (Sb), germanium (Ge), ytterbium (Yb), bismuth (Bi), selenium (Se), silver (Ag), and gallium (Ga). In comparison, most metal silicide thermoelectric materials are benign and some of them such as Mg_2Si, $MnSi_x$, $CrSi_2$, and β-$FeSi_2$ are made of elements with high crustal abundance. Transition metal silicides (TM) have especially achieved high Seebeck coefficients, which is often associated with the d-band states of the TM element.

Most metal silicides have appropriate melting temperature and bandgap for medium temperature power generation applications. The most favorable silicides include Mg_2Si, $MnSi_x$, $CrSi_2$, β-$FeSi_2$, and $ReSi_{1.75}$. In particular, the compounds of Mg_2X^{IV} (where X^{IV} = Si, Ge, and Sn) and their solid solutions have been of interest in recent studies[27–30] due to their demonstration of high zTs in medium temperature range comparable to some of the good thermoelectric materials such as lead telluride. Their abundance in nature and non-toxic features make them even more attractive, which fuel ongoing efforts to enhance their thermoelectric properties via different techniques such as nanostructuring. Nanostructuring has already shown zT improvement for silicides of germanium (germanium silicide is often referred to as silicon germanium). In the Si CMOS world, silicides are also widely used as low-resistivity contact and interconnect materials and the term germanosilicide is used for compounds of SiGe and metals such as Ti, Co, Ni, and Pt.[31–33] However, as we will discuss, nanostructuring is not very effective for the case of Mg_2Si due to the small difference of the phonon and electron mean free paths in this material. Therefore, other methods, such as band engineering have been pursued to improve the power factor. In particular, Sb doped $Mg_2Si_{0.4}Sn_{0.6}$ has shown $zT \sim 1.1$ at 800 K, which is comparable to the zT of PbTe.

Silicon germanium ($Si_{1-x}Ge_x$) and ruthenium silicide (Ru_2Si_3) are both good candidates for high temperature applications. Silicon germanium ($Si_{1-x}Ge_x$, $0.15 < x < 0.3$) is the only non-metal silicide, which has good thermoelectric properties. At higher temperatures (~1300 K), it has a fairly large Seebeck coefficient (>200 μV/K) and low thermal conductivity (<5 $W\,m^{-1}\,K^{-1}$), both resulting from the material's relatively large bandgap (~0.9 eV). The good thermoelectric properties and high melting temperature has made

© 2017 The Japan Society of Applied Physics

germanium silicides appropriate for high temperature power generation applications such as radioisotope thermoelectric generators (RTG) used in spacecrafts. Nanostructured $Si_{1-x}Ge_x$ has shown enhanced zT both for p- and n-type materials.[34] Ru_2Si_3 also has good thermoelectric properties and can be potentially better than $Si_{1-x}Ge_x$ at high temperatures if it could be doped to the optimum carrier concentration, which has been historically challenging.[35]

Silicide nanocomposite engineering is another interesting direction that has been recently pursued. While the high frequency phonons are strongly scattered by point defects in alloys, the scattering of the low frequency phonons can be significantly enhanced resulting in even smaller thermal conductivity in nanocomposites consisting of nanoinclusions. The electrical conductivity is not significantly affected as the electron scattering by ionized impurities or acoustic phonons is usually more dominant than the scattering due to nanoinclusions. The addition of silicide nanoinclusions to the $Si_{0.88}Ge_{0.12}$ alloy maintained or increased the power factor while further reduced the thermal conductivity compared to the nanostructured single phase alloy. This resulted in zT enhancements in both $Si_{0.88}Ge_{0.12}$–$FeSi_2$[36] and $Si_{0.88}Ge_{0.12}$–Mg_2Si[37] nanocomposites reaching $zT \sim 1.2$ and 1.3, respectively, at 1200 K. These results confirmed the importance of nanostructuring in germanium silicide alloys proposed earlier by Mingo et al.[38] suggesting a new approach for making efficient thermoelectric materials.

2. Overview of silicide thermoelectrics

Since Nikitin[39,40] came up with the idea of using silicides as thermoelectrics in 1958, different silicides have been studied for mid- and high-temperature applications.[41] Among these materials, silicon germanium (SiGe) has been the best material for high temperature applications such as in RTGs used in spacecrafts for deep space science exploration.[42,43] Extensive theoretical and experimental studies have been carried out for the material system.[34,44–48]

SiGe alloys used to synthesize the first silicides used in RTGs were initially made by zone leveling and Czochralski techniques in 1960's. Boron and phosphorus (or arsenic) were used as the p- and n-type dopants, respectively. The solid solubility limit of these dopants are very small at room temperatures.[49] Accordingly, during measurement of the thermoelectric properties from room to high temperature, transport properties of heavily doped p- and n-type alloys alter with time due to the precipitation of dopants in SiGe lattice or grain boundaries.[50] To avoid loss of active dopants in heavily doped n-type alloys, the samples were annealed at ~925 °C, then, quenched to room temperature. Furthermore, they were measured from room temperature to 325 °C (metastable condition), then, they were measured as quickly as possible at higher temperatures. In p-type alloys with hole concentrations exceeding 3×10^{20}, precipitation happened only above 825 °C. The behavior of zT for both p- and n-type materials used in RTGs were similar, except that the maximum zT for n-type SiGe alloys was 30% more than the p-type alloys. The actual efficiency of the RTGs over the temperature range of 27–925 °C was 10% for the best developed samples.[51]

Many silicide compounds are considered as potential thermoelectric materials. The most well-known and applicable silicides are those of $Si_{1-x}Ge_x$ which have already demonstrated excellent thermoelectric properties. $Mg_2(Si,Sn)$ and $MnSi_{1.7}$ are also considered as highly promising silicides. In addition to these silicides, $ReSi_2$, $CrSi_2$, WSi_2, and $MoSi_2$ have large effective masses as well as high mobility along with low thermal conductivity, which make them potentially interesting candidates for RTGs. However, since the bandgaps of these materials are typically too small to prevent thermal excitation of the minority carriers, they suffer from bipolar transport at high temperatures for any doping concentration, which results in a low zT.[52]

In transition metal silicides, electrons in d-orbitals change the transport properties and bonding characteristics of the materials compared to s- and p-bonded compounds.[53] The d-band state results in a high Seebeck coefficient (150–200 μV/K) in silicides such as β-$FeSi_2$ and $MnSi_x$.[54]

Metal silicides are divided into different groups as follows: Group IA and IIA (alkali and alkaline earth) silicides are mostly semiconductors with bandgaps in the range of 0.5–1.3 eV. NaSi, Mg_2Si, Ca_2Si, $BaSi_2$, and Sr_2Si belong to these two groups. All these compounds can easily oxidize due to high chemically reactivity of the alkali and alkaline earth metals and need special handling. Group IIIB and rare earth (Sc, Y, and La–Lu) silicides have mostly metallic properties except α-$LaSi_2$ which has semiconducting properties. Group IVB (Ti, Zr, and Hf) silicides and group VB (V, Na, and Ta) silicides also have metallic properties. Group VIB (Cr, Mo, and W) silicides are all semiconductors and they have the potential to serve as thermoelectric materials. Group VIIB (Mn and Re) silicides are also semiconductors and they are widely used in thermoelectric applications. Group VIIIB (Fe, Ru, and Os) silicides too are semiconductors; of these, β-$FeSi_2$ is one of the most inexpensive silicides available.[53] Ru_2Si_3 can theoretically be a better thermoelectric material than SiGe at high temperatures. However, the lack of appropriate dopants and scarcity of Ru resources are the main obstacles of using this material.[54] Group IXB (Co, Rh, and Ir) silicides are not considered as good thermoelectric materials. Group XB (Ni, Pd, and Pt) silicides are all metallic compounds with no applications in thermoelectrics.[53] Group XIB (Cu, Ag, and Au) silicides are also not considered as potential thermoelectric materials. Cu and Si yield several intermetallic phases.[55] Ag has a eutectic point with Si.[56] Au is used for metallization of Si. Au and Si gives a very low eutectic point and all of the crystalline compounds are metastable.[57] Group XIIB (Zn, Cd, and Hg) silicides are also not considered in thermoelectrics mainly due to negligibly small solubility of Zn, Cd, and Hg in Si.[58–60]

In summary, metal silicides of β-$FeSi_2$, $CrSi_2$, $MnSi_{1.75}$, $Mg_2(Si,Sn)$, Ru_2Si_3, and $ReSi_{1.75}$, along with those of SiGe are the most promising thermoelectric silicides. These materials are appropriate for mid (300–600 °C) and high (over 600 °C) temperatures, which are within the range of waste heat in most industries.[61]

3. Traditional silicide thermoelectrics

Throughout the thermoelectric history, two different approaches were adopted to improve the zT figure-of-merit; reducing the thermal conductivity and/or improving the power factor. Introduction of particles of a second phase

© 2017 The Japan Society of Applied Physics

in the alloy was initiated using gallium phosphide (GaP) incorporation into SiGe by Pisharody in 1978.[62] This resulted in 40–50% reduction of the thermal conductivity in both n- and p-type materials and improved zT in SiGe silicides. Another influential work was performed by Rowe[63] in 1974, which introduced fine grained SiGe in which, grain boundary scattering of phonons resulted in a reduced thermal conductivity.[64–66] This work inspired a series of new studies on SiGe.[36–38,44,46,47,67]

Despite the fact there is no theoretical limit for zT, the maximum zT of the state-of-the-art thermoelectric materials such as SiGe and $(Bi,Sb)_2(Se,Te)_3$ remained near unity for several decades.[68] In order to make thermoelectric systems with efficiencies comparable to the current technologies such as mechanical engines, it is highly desirable to have $ZT > 1.5$ for power generation and $ZT > 2$ for cooling[68–71] (here ZT refers to the device figure-of-merit, which includes parasitic losses due to electrical and thermal resistances). Furthermore, thermoelectric materials should be inexpensive, robust, non-hazardous and environmentally friendly for waste heat recovery applications.

Different strategies have been used to improve the zT figure-of-merit, such as using compounds of heavy element, complex crystal structures, point defect scattering, and resonant doping.[70] Until early 1990s, the maximum reported zT was ~1 and the energy conversion efficiency could not pass 10%, which restricted the application of thermoelectrics for spacecraft and electronic cooling.[52,72–74] In the last two decades, discovery of new thermoelectric materials along with nanostructuring techniques have continuously improved zT for several compounds.[3–10,36,37,75] These improvements inspired new applications with particular emphasis on waste heat recovery at different industries,[76,77] and to some extent for solar thermoelectric generators.[78] In addition, the National Aeronautics and Space Administration (NASA) is interested in high performance thermoelectric materials to improve the conversion efficiencies of their RTGs for the next generation space science missions.[79,80] In an RTG, even a small improvement in the thermoelectric properties of the materials while maintaining lifetime and reliability results in large amounts of energy savings. This is specially desired for multi-year planetary exploration spacecrafts such as Galile and Voyeger.[52]

4. Recent prospective

4.1 Nanostructured thermoelectrics

Since early 1990s, two approaches were followed to realize the next generation thermoelectric materials. The first approach relies on employing new bulk materials with low thermal conductivity and/or high power factor. The other approach focuses on engineering the microstructure to benefit from low-dimensional size effects.[11,81]

There have been quite a few successes in achieving enhanced zT in nanostructured n- and p-type SiGe.[44,46,47] However, nanostructuring did not show significant zT enhancement in other silicide alloys such as $MnSi_{1.7}$,[82] Mg_2Si,[83,84] or $FeSi_2$.[85,86]

Phonon scattering in bulk thermoelectric materials happens in several ways including phonon–phonon scattering, phonon–electron scattering, and phonon–point defect scattering. In $Si_{1-x}Ge_x$ alloys, point defect scattering is dominant for short wavelength phonons, whereas phonon–electron scattering is dominant for long wavelength phonons. It should also be noted that nanostructured thermoelectrics are generally highly doped to achieve the peak zT. Therefore, the phonon–electron scattering can be significant reducing the thermal conductivity especially at low temperatures. Bulk nanostructuring produces a high density of two-dimensional defects such as interfaces and grain boundaries as well as nano-scale particles along with point defects. Consequently, due to the broad distribution of the size of the defects, phonon scattering can happen at both short and long wavelengths.[80] The interfaces can have a secondary effect in improving the zT. Due to the preferential scattering of low energy (long wavelength) charged carriers at interfaces, the Seebeck coefficient in nanostructured thermoelectric materials is usually higher than that of the crystalline material at similar doping concentration. In addition, since the minority carriers will have a smaller energy than majority carriers, they are scattered more strongly at interfaces leading to lower bipolar transport, which explains the higher effectiveness of nanostructuring at high temperatures.[44,87]

4.2 Nanocomposite approach

Nanocomposite refers to a class of materials that are made of more than one phase. It can be made of different phases of the same material, such as amorphous–crystalline nanocomposites, or it can be made of different materials. Nanocomposites, like nanostructured single phase materials, can have a lower thermal conductivity than the "alloy limit".[18] They may also have a larger power factor than the constituent phases. Although a classical composite material cannot have higher zT than each of the constituent phases,[88,89] the nano-scale effects in nanocomposites can result in zT improvement. For example, high zT has been obtained in several thermoelectric nanocomposites such as InGaAs/ErAs,[18,90] PbTe–SrTe,[47] SiGe–$CrSi_2$,[91] and BiSbTe.[23] In another related approach, Mingo et al. predicted enhanced zT in nanocomposites made of silicide nanoparticles in SiGe alloys[38] and several follow-up studies further confirmed this prediction.[36,37]

A review of the properties of the best reported silicide thermoelectric materials is presented in the following sections. However, the reader should note that due to the complexity of the measurements, the measured zT values may include a significant error. Even with today's commercially available equipment for measuring the electrical conductivity, Seebeck coefficient, and thermal conductivity, the deducted zT can be off by as much as 20%.[92] Besides, improper sample geometries can further increase the tolerance. Such a tolerance should be taken into consideration when comparing the zT values reported from different laboratories; hence, small zT improvements may be within the measurement variations. Unfortunately, some commercial equipment of the Seebeck coefficient and electrical conductivity measurement do not eliminate the residual voltage at zero temperature gradient (a.k.a. dark EMF) in the calculation of the Seebeck coefficient and result in erroneously large Seebeck values. Such measurements may also result in large estimation of the zT values. It should be noted that considering only the maximum zT as an indication of the thermoelectric material excellency is not accurate as one must also consider the average zT over the working temperature.[93]

© 2017 The Japan Society of Applied Physics

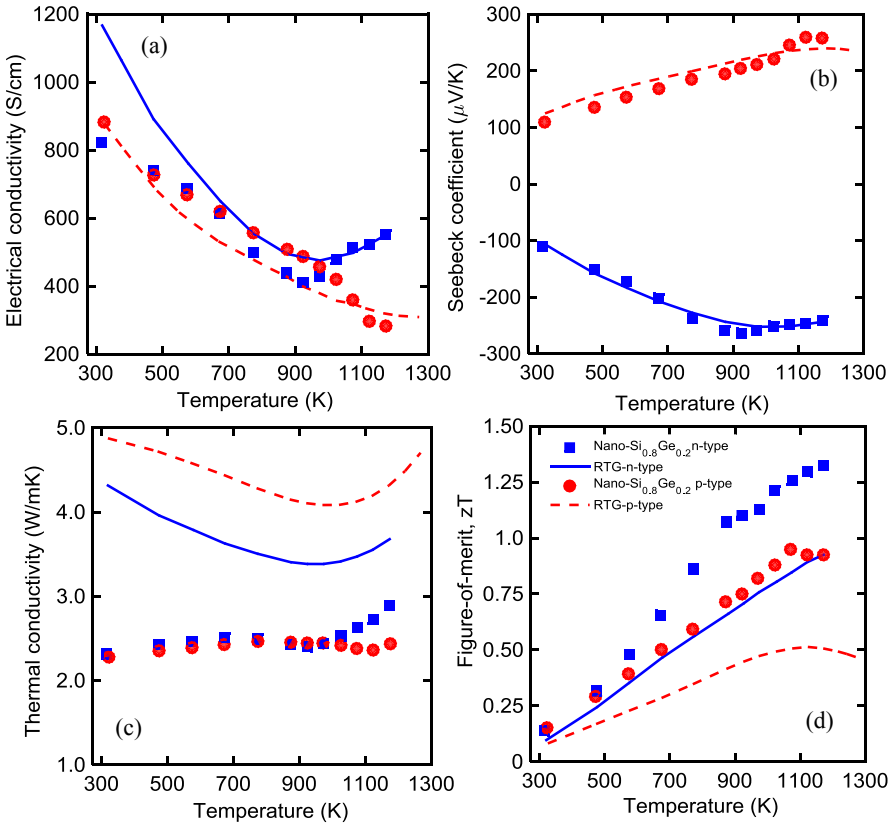

Fig. 1. (Color online) (a) Electrical conductivity, (b) Seebeck coefficient, (c) thermal conductivity, and (d) zT of n- and p-type nanostructured bulk $Si_{0.8}Ge_{0.2}$ samples compared with those of the n- and p-type RTG reference sample. Ref: n-type $Si_{0.8}Ge_{0.2}$[47] and p-type $Si_{0.8}Ge_{0.2}$.[46]

The data reported here is taken from the literature. In some cases, a missing material property, wherever possible, was estimated from the reported material properties, e.g., electrical conductivity from the plotted Seebeck coefficient and the power factor.

5. Silicon germanium (SiGe)

SiGe is a widely used thermoelectric material for high temperature applications such as RTGs.[94] Germanium is added to silicon to decrease the thermal conductivity significantly without sacrificing the electrical conductivity. Consequently, the zT value of the SiGe alloy material can be significantly increased compared to Si. In order to improve the performance of the SiGe material, much research has been done so far which is briefly summarized here.

5.1 Crystalline and polycrystalline SiGe

Back in 1964, the thermal and electrical properties of SiGe alloy were studied by Dismukes.[51] The maximum zT of n- and p-type $Si_{0.7}Ge_{0.3}$ was measured to be about 1 and 0.7, respectively. At the early stage of the SiGe study, the main technique employed to improve the zT was boundary scattering of phonons. Goldsmid and Penn presented this idea in 1968.[95] They pointed out the thermal conductivity of the material can be decreased by boundary scattering even when the sizes of the crystals are much larger than the phonon mean free path. It was believed that the electrical conductivity will not be affected since in highly doped SiGe the electron mean free path is much smaller than the phonon mean free path. In 1981, Rowe et al. reported the first experimental results of fine grained hot pressed compacts of heavily doped n-type SiGe.[65] The results showed that when the grain size is smaller than 5 μm, the thermal conductivity can be decreased by 28% compared with single crystal SiGe. Later, Vining et al. demonstrated pressure-sintered $Si_{0.8}Ge_{0.2}$ with particle sizes ranging from 1 to 100 μm.[96] The results showed that the thermal conductivity can be significantly reduced by 50% with particle sizes around 2 μm. However, the improved zT values were not observed. The maximum zT of pressure-sintered n- and p-type $Si_{0.8}Ge_{0.2}$ was measured to be about 1 and 0.6. The authors claimed that this is due to the reduction of the electrical conductivity.

5.2 Bulk SiGe nanocomposites

There was little progress for SiGe thermoelectric materials research from 1960s to 1990s; the zT values were limited to ~1 and ~0.7 for n- and p-type SiGe, respectively. However, during the past twenty years, significant progresses were achieved by employing nanostructured bulk of SiGe. In 2008, Wang et al. reported a peak zT value of 1.3 at 1173 K for n-type nanostructured bulk SiGe alloy.[47] $Si_{0.8}Ge_{0.2}$ was fabricated by hot pressing from ball milled Si, Ge chunks and P micro-powders. The grain size of the material was measured to be 10–20 nm. At this grain size level, the phonon scattering was significantly increased and the thermal conductivity was greatly decreased. The Seebeck coefficient and high temperature electrical conductivity did not change noticeably compared to that of RTG alloy. As a result, the zT value of the nanostructured bulk SiGe was effectively improved as shown in Fig. 1.

P-type nanostructured bulk SiGe alloy with a peak zT value of 0.95 at 900–950 °C was also reported by Joshi et al.[46] Employing the hot pressing and ball milling technique, the boron doped nanostructured bulk SiGe with

© 2017 The Japan Society of Applied Physics

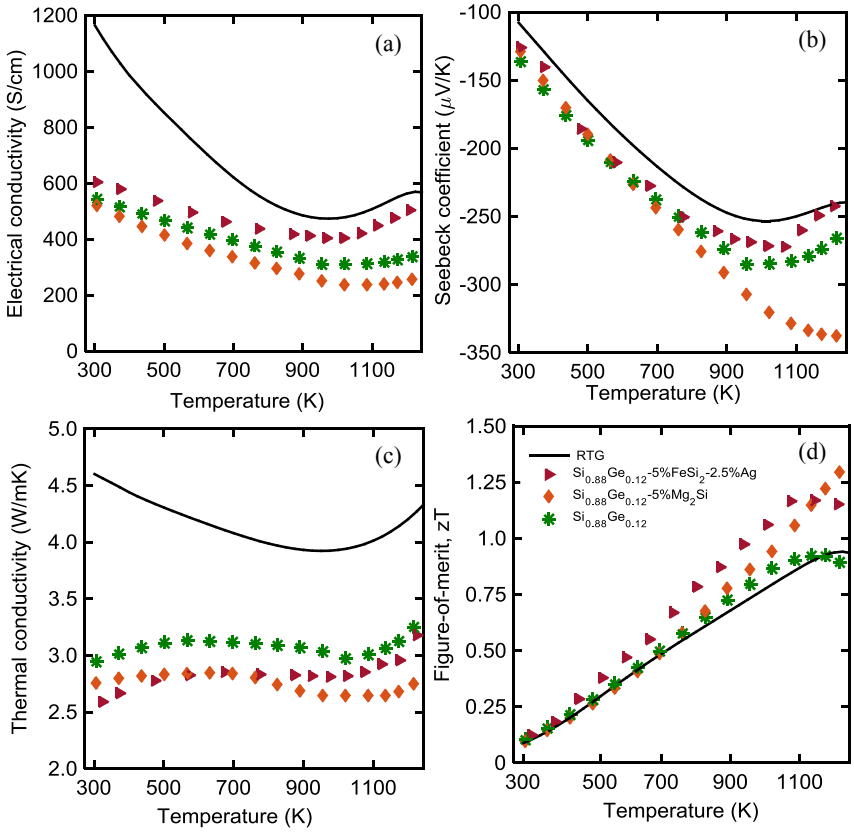

Fig. 2. (Color online) (a) Electrical conductivity, (b) Seebeck coefficient, (c) thermal conductivity, and (d) zT of nanocomposites of SiGe–$FeSi_2$ and SiGe–Mg_2Si in symbols. The solid line shows the data of the RTG sample. Ref: SiGe–$FeSi_2$[36] and SiGe–Mg_2Si.[37]

grain sizes ranging from 5 to 50 nm was obtained. Similar to the n-type counterpart, the improvement of the zT value was mainly due to the significant decrease of the thermal conductivity as shown in Fig. 1.

5.3 Effect of nanoinclusions

In 2009, Mingo et al. introduce the idea of a nanocomposite SiGe material based on silicide nanoparticles embedded in a SiGe alloy matrix.[38] According to the modeling results, at room temperature, a potential 5-fold increase in zT was predicted, which is ~0.5; and at 900 °C, a potential 2.5-fold increase in zT was predicted, which is ~1.7. The main reason for zT enhancement was due to reduction of thermal conductivity via phonon scattering by the nano-inclusions. Furthermore, as discussed, the silicide nanoinclusions may improve the thermoelectric power factor through preferential scattering of the low energy charge carriers. Experimental results showed that Mg_2Si–$Si_{0.88}Ge_{0.12}$ and $FeSi_2$–$Si_{0.88}Ge_{0.12}$ nanocomposites have smaller thermal conductivity compared with nanostructured $Si_{0.8}Ge_{0.2}$. In these materials, the Seebeck coefficient increased and the electrical conductivity decreased resulting in almost similar power factor compared to that of RTG SiGe alloy. Therefore, the reduction of thermal conductivity resulted in higher zT (Fig. 2).[36,37] This also allowed reducing the amount of germanium from 20 to 12% in the alloy, which reduces the materials cost, while still improving the zT.

In another study, cost-effective fabrication of n-type SiGe–$FeSi_2$ nanocomposite was studied.[97] The cost was optimized by using low purity components, especially oxidized germanium powder, and utilizing induction melting over mechanical alloying for obtaining a uniform alloy in much shorter time. Furthermore, the effect of addition of carbon for oxide reduction was studied and a high zT of 0.8 was achieved around 1200 K.

5.4 Low-dimensional SiGe

Besides bulk nanostructuring, low dimensional structures, such as nanowires and superlattices, were employed to improve the zT of SiGe. In one and two-dimensional materials, the phonon scattering is enhanced due to the boundaries of the low-dimensional structure. Martinez et al. studied the thermal and electrical properties of an individual p-type SiGe nanowire for the first time.[98] Thermal conductivity of the nanowire was effectively decreased due to the phonon scattering at the wire boundaries. The zT value of the nanowire was improved by a factor of 2 compared to single crystal counterpart. Later, Lee et al. demonstrated n-type SiGe nanowires with an improved zT of 0.46 at 450 K.[99] In this study, SiGe nanowires with diameters ranging from 26 to 161 nm were grown by vapor–liquid–solid (VLS) method. The authors also predicted zT values higher than 2 at 800 K using theoretical simulations based on Boltzman transport equation.[99] For two-dimensional superlattices, early in 1997, Lee presented a thermal conductivity study on two-dimensional SiGe superlattices.[100] The thermal conductivity of the n-type SiGe superlattice was decreased to 1–2 $W\,m^{-1}\,K^{-1}$ at temperatures up to 500 K. Recently, Samarelli demonstrated Ge/SiGe modulation doped superlattices with enhanced power factor and zT value at room temperature compared to Ge and $Si_{1-y}Ge_y$ materials.[101]

5.5 Thermal conductivity of SiGe: Lowest value

There has been much effort to find techniques for suppressing the thermal conductivity of SiGe and improving the zT. It is

© 2017 The Japan Society of Applied Physics

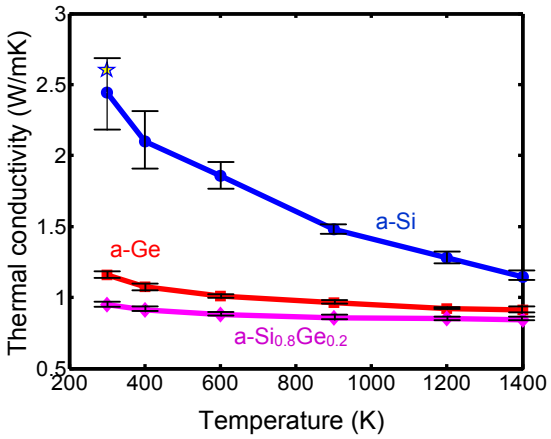

Fig. 3. (Color online) Calculated thermal conductivity of amorphous silicon, germanium and $Si_{0.8}Ge_{0.2}$. Reproduced from Ref. 103.

important to know how far the thermal conductivity can be reduced. Lee et al. investigated the theoretical limit of the thermal conductivity of SiGe alloys.[102] In this work, the authors discovered that the thermal conductivity is strongly related to the size of the random alloy unit cell in their study. The theoretical analysis of the thermal conductivity converged to a minimum around 1–2 $W\,m^{-1}\,K^{-1}$ for the composition of $Si_{0.8}Ge_{0.2}$.

In another computational study, Norouzzadeh et al. analyzed the thermal conductivity of amorphous $Si_{1-x}Ge_x$ compound versus x and temperature, which sets the minimum thermal conductivity achievable by nanostructuring and compositional change of $Si_{1-x}Ge_x$.[103] Although amorphous SiGe suffers from low electrical conductivity, the thermal conductivity can reach the lower limit since the lattice is fully disordered. Figure 3 illustrates the calculated thermal conductivity of amorphous silicon, germanium and $Si_{0.8}Ge_{0.2}$ versus temperature. It is shown that the thermal conductivity of the amorphous $Si_{0.8}Ge_{0.2}$ is less than $1\,W\,m^{-1}\,K^{-1}$ with small reduction as the temperature increases from 300 to 1400 K.

6. Magnesium silicide (Mg_2Si) alloys

Mg_2Si and CaMgSi are promising candidates for thermoelectric materials due to the natural abundance and nontoxicity of the constituent elements, low material density, and tailorable electronic structure.[83] Mg_2Si is a semiconductor with an indirect bandgap of 0.61 eV at 300 K (0.69 eV at 4 K).[104] Due to its high Seebeck coefficient and low thermal conductivity, Mg_2Si was initially thought to be a good candidate for nanostructuring to improve zT. For some materials such as $Si_{1-x}Ge_x$, zT was significantly enhanced by producing a nanostructure with grain sizes smaller than the mean free path of broad range of phonons and larger than the mean free path of charge carriers. This turned out not to be the case for Mg_2Si as the losses in electrical conductivity due to a significant decrease of mobility largely negate the beneficial effects of decreased lattice thermal conductivity and slightly improved Seebeck due to the carrier filtering effect.[84] Due to these difficulties, other strategies for improving the efficiency of these materials are being explored such as alloying, carrier pocket engineering, and incorporation of different dopants.

Sb is the preferred electron donor for n-type doping of this material. A co-doping scheme using Ge and Sb produced a maximum zT value of 0.74 at 756 K for n-type material, while material not containing Ge had a maximum zT value of ~0.5, as shown in Fig. 4.[105] The working principle is that point defects decrease the lattice contribution to thermal conductivity by scattering short wavelength phonons, so while Ge addition caused a moderate decrease in mobility, this was outweighed by a significant decrease in thermal conductivity and improvement in Seebeck coefficient at high Sb doping which contributed to a significant enhancement in zT. The high electrical conductivity due to Sb doping also increased the thermal conductivity due to the enhancement of the electronic thermal conductivity.

Mg_2Si performance can be greatly improved by alloying with Mg_2Sn. An n-type composition of $Mg_{2.15}Si_{0.28}Sn_{0.71}$-$Sb_{0.006}$ achieved a zT value of over 1.3.[106] The power factor enhancement was assumed to be the result of the convergence of the heavy and light conduction bands at this composition. This band convergence increases the power factor by enhancing the density of states effective mass by adding carrier pockets near the band edge, which serves to increase the magnitude of the Seebeck coefficient for a given carrier concentration. Also due to a decrease in bandgap resulted from alloying, or the reduction of the Fermi energy due to larger density of states near the band edge, the onset of the bipolar carrier effects caused the maximum zT to occur at ~700 K, while for doped Mg_2Si such effects were not apparent until ~800 K.

One issue that hinders the use of Mg_2Si materials is the lack of a comparable p-type material that demonstrates similar performance in the same temperature range. Ag-doped materials exhibit $zT \sim 0.11$, which is over an order of magnitude lower than the best n-type materials.[108] Without a well matched p-type material, it is impossible to achieve optimum performance in a traditional thermoelectric device. Several possibilities for improving p-type performance have been used, mainly trying to find dopants that are more easily activated (shallow acceptor states) and can produce the optimum carrier concentration in the valence band for similar high temperature performance to the n-type materials.

Figure 5 shows the reported zT of several Mg_2Si alloys doped with different elements. Improvements in zT due to alloying with Ge are apparent for Ga-doped materials. Ga-doped (0.8 at. %) Mg_2Si has a maximum $zT < 0.13$ at 650 K. With the same level of Ga doping, $Mg_2Si_{0.6}Ge_{0.4}$ has a maximum zT of ~0.36 at 623 K. Ga-doping decreased the lattice thermal conductivity, but the samples with Ge had roughly twice the carrier concentration at similar doping levels. Significantly lower thermal conductivity at all temperatures and an improved Seebeck coefficient at high temperatures lead to significantly improved material performance.

A similar composition to the n-type Mg_2Si–Mg_2Sn alloys, which exhibited enhanced $zT \sim 0.5$, was $Mg_{1.86}Li_{0.14}Si_{0.3}$-$Sn_{0.7}$ in which Li was doped as an acceptor.[109] Li was assumed to substitute for Mg in the alloy crystal structure, but the degree of ionization of Li was estimated to be no more than about 30% (~30% of Li atoms contributed holes to the crystal). The alloy composition was designed using relatively simple modeling to engineer a band structure which has a low

© 2017 The Japan Society of Applied Physics

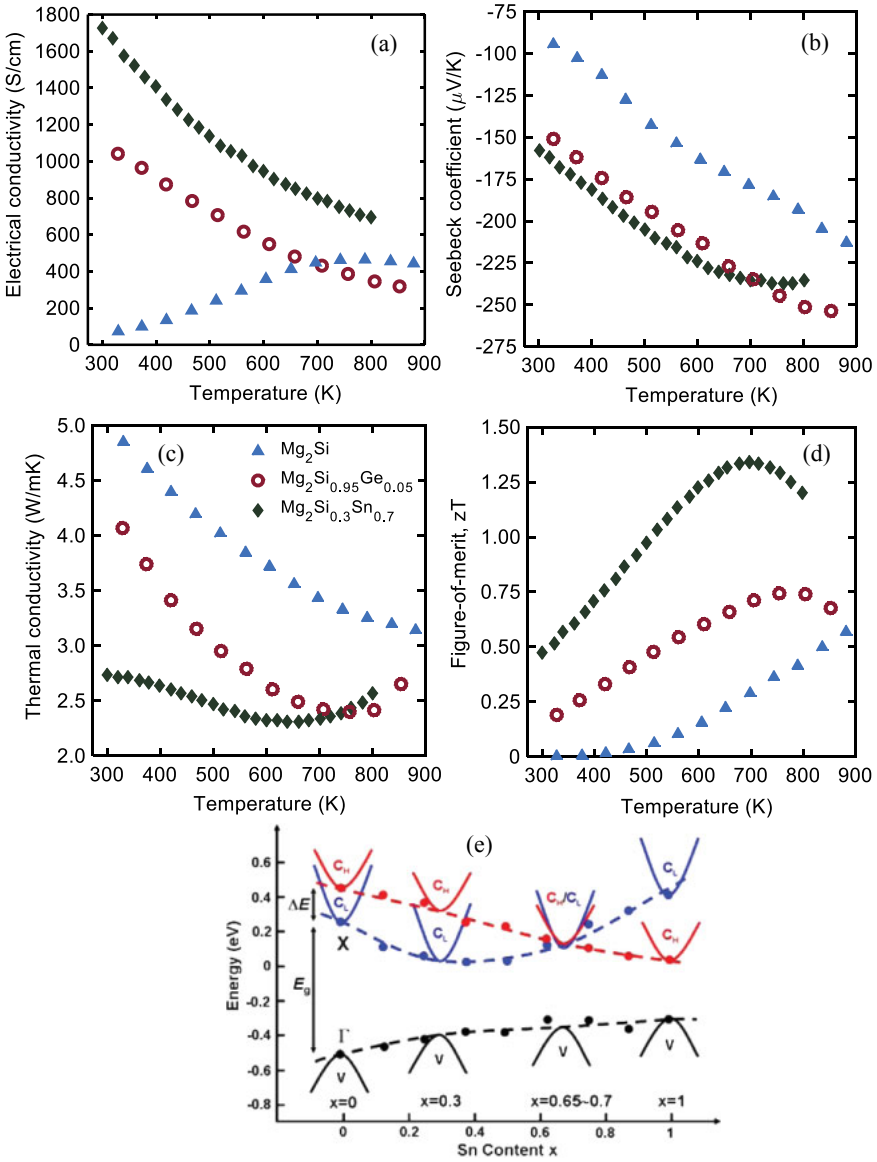

Fig. 4. (Color online) (a) Electrical conductivity, (b) Seebeck coefficient, (c) thermal conductivity, and (d) zT versus temperature for selected compositions of n-type Mg_2Si alloys, all of which are doped with Sb. Ref: Mg_2Si,[107] $Mg_2Si_{0.95}Ge_{0.05}$,[105] and $Mg_2Si_{0.3}Sn_{0.7}$.[106] (e) The highest valence band and the comparative location of the light and heavy conduction bands for $Mg_2Si_{1-x}Sn_x$ as a function of Sn content. The red dashed line shows energy variation of heavy conduction band versus Sn content. The blue and black dashed lines show change of the light conduction band and valance band, respectively. The solid dots describe the calculated data for various Sn content.[106]

density of states near the Fermi level and a large slope of density of states per unit energy. The significantly higher onset temperature for the decrease in zT from bipolar effects also indicated more successful doping than other p-type materials.

As another p-type candidate based on Mg_2Si system, CaMgSi intermetallic phase is thought to be a promising one due to lower electrical resistivity compared to Mg_2Si and high positive Seebeck coefficient estimated at 750–900 μV/K for intrinsic type material.[110] Further studies of thermal and electrical transport properties and doping still need to be assessed to determine the effectiveness of this material as a thermoelectric.

7. Manganese silicides ($MnSi_x$)

Manganese silicides ($MnSi_x$) with x ranging from 1.71 to 1.75,[94] also known as higher manganese silicides (HMS), are made up of complex chimney-ladder structures with tetragonal cells. HMS forms with a variety of compositions such as Mn_7Si_{12},[111] $Mn_{11}Si_{19}$,[112,113] $Mn_{26}Si_{45}$,[111] $Mn_{15}Si_{26}$,[114,115] $Mn_{19}Si_{33}$,[111] $Mn_{27}Si_{47}$,[116] $Mn_{39}Si_{68}$,[111] and Mn_4Si_7.[117] HMS crystals consist of regions of homogenous composition separated by regions of abrupt phase transitions. These transition regions are generally composed of manganese monosilicide (MnSi). The MnSi precipitate layers are formed perpendicular to the C-axis and are independent of growth technique. In undoped HMS the precipitate layers are around 1 μm thick separated by a distance of 10–120 μm.[118] These MnSi precipitates act as energy barriers and can influence the transport properties of the charge carriers. HMS naturally is a p-type semiconductor with a carrier concentration of $10^{21}\,cm^{-3}$ and a carrier mobility of $\sim 10\,cm^2\,V^{-1}\,s^{-1}$ at 300 K. $Mn_{11}Si_{19}$ has an indirect band gap with absorption edge energy of approximately 0.64 eV at 5 K.[119] The monocrystals

© 2017 The Japan Society of Applied Physics

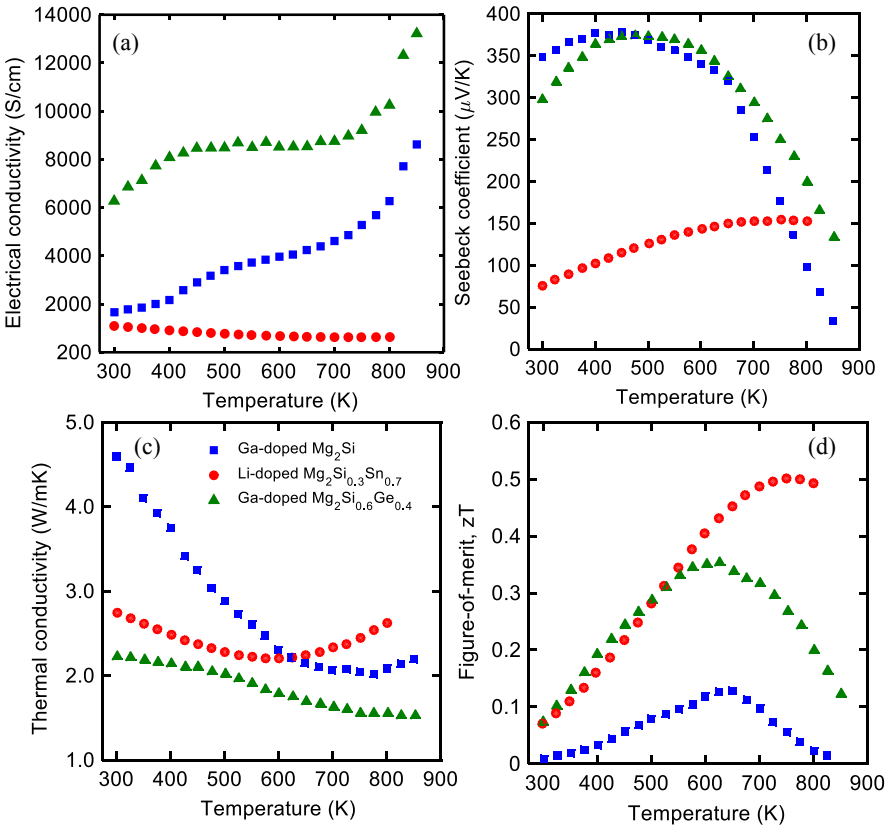

Fig. 5. (Color online) (a) Electrical conductivity, (b) Seebeck coefficient, (c) thermal conductivity, and (d) zT values for different p-type Mg_2Si materials. Refs: Ga-doped Mg_2Si,[108] Ga-doped $Mg_2Si_{0.6}Ge_{0.4}$,[108] and Li-doped $Mg_2Si_{0.3}Sn_{0.7}$.[109]

of HMS exhibit anisotropy in Seebeck coefficient. The ratio of Seebeck coefficient between perpendicular and parallel direction to the C-axis can be ~1.7. Similarly, the ratio of electrical conductivity and thermal conductivity between perpendicular and parallel direction to the C-axis is 5 to 170 and 2, respectively at 300 K.[43] Therefore, polycrystalline HMS is preferred if isotropic properties are desired.

Norouzzadeh et al.[82] have used a two-band semi-emperical model to explain and compare the thermoelectric properties of bulk and nanostructured phase of HMS phase. They were able to show that the nanostructuring does not significantly improve the zT of HMS, which can explain why there has not been much success in improving its zT by bulk nanostructuring. This was due to the significant decrease in electrical conductivity as a result of increased electron scattering at the grain boundaries. Band structure engineering was, therefore, recommended as a more efficient approach than nanostructuring to improve its zT.

Apart from thermoelectric properties, HMS alloys are also mechanically robust, inexpensive, non-toxic and highly resistant to oxidation. HMS samples prepared by different techniques show zT of around 0.3–0.5. Different approaches such as nanostructuring, Mn and Si substitution and nanoparticle inclusion have been used to improve the thermoelectric properties of HMS, which are briefly discussed below.

Synthesis: The most common way to synthesize HMS is to perform induction melting or mechanical alloying of the elemental powders of Mn and Si of the desired stoichiometry followed by spark plasma sintering (SPS) or hot pressing (HP). Zamanipour et al.[120] studied the thermoelectric properties of different nanostructured phases of HMS prepared by mechanical milling (50 h) and hot pressing (950 °C for 5 min). Out of the phases studied $MnSi_{1.75}$ displayed the best thermoelectric properties with a maximum zT of 0.55 at 600 °C. However, the nanostructuring of the material resulted in only a small improvement of its zT.

A comparison has been performed between wet and dry milling for synthesis of HMS by Truong et al.[121] Wet milled material showed better thermoelectric properties with higher Seebeck and lower thermal conductivity. This was attributed to the finer particle size achieved by wet milling compared to dry milling which was limited due to the welding of particles during the dry mill. They also noticed the absence of the undesired MnSi phase after the wet milling process.

Ge substitution of Si in HMS has shown to improve the zT to 0.6.[122] According to this study Ge addition resulted in a decrease in thermal conductivity which can be attributed to the increase in phonon scattering due to the introduction of defects to the lattice structure. Al substitution, which introduced defects and increased the charge carriers, resulted in slightly higher zT of 0.65 at 527 °C[123] although such small changes of zT can be well within the measurement tolerances. In both cases, the optimal zT was at the solubility limits of the additives. In addition, different ratios of co-doped Al and Ge has been studied by Chen et al. which showed no improvement compared to Al doping.[124]

Alumina nanoparticles was also used to reduce the thermal conductivity.[125] This showed more reduction in thermal conductivity due to the increased phonon scattering by nanoparticles. However, the particle addition also resulted in a reduction of electrical conductivity. The best zT was again

© 2017 The Japan Society of Applied Physics

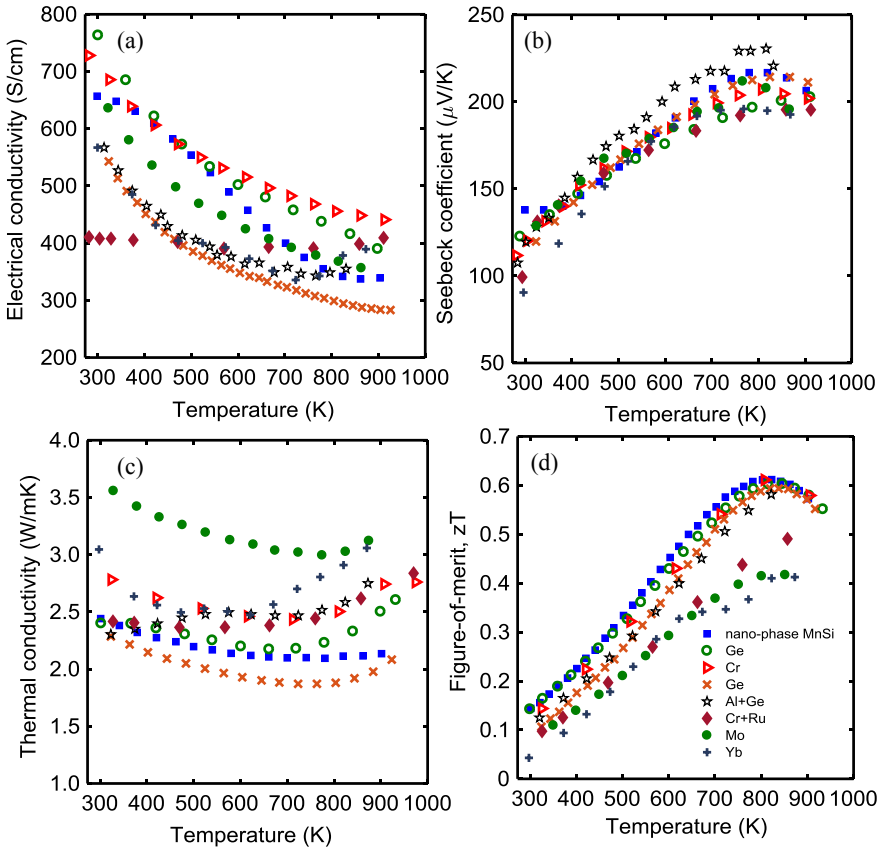

Fig. 6. (Color online) Comparison of (a) electrical conductivity, (b) Seebeck coefficient, (c) thermal conductivity, and (d) zT values of HMS prepared with different dopants. Refs: nano-phase MnSi,[126] Ge-doped,[132] Cr-doped,[133] Cr+Ru-doped,[133] Ge-doped,[122] Al+Ge-doped,[124] Mo-doped,[134] and Yb-doped.[135]

~0.59 at 527 °C, which was obtained for HMS with 1% alumina.

Luo et al. have shown improvements in zT by adding MnSi nano-inclusions resulting from the process of melt spinning followed by SPS.[126] It is generally known that MnSi phase is detrimental to thermoelectric properties due to the small band gap and high conductivity, which results in a low Seebeck coefficient. MnSi nanoinclusion has resulted in decreased thermal conductivity which was attributed to the reduction of ambipolar diffusion due to energy dependent scattering of charge carriers.[127] Their process resulted in 50–100 nm MnSi particles and a peak zT of 0.62 at 527 °C.

Godke et al. showed that heavy atom substitution increases alloy scattering which can result in a reduction of lattice thermal conductivity. Chen et al.[128] explored this approach by using Re substitution of Mn.[129] A solid-state reaction followed by ball milling and SPS resulted in a maximum zT of 0.57 at 527 °C for $Re_{0.04}Mn_{0.96}Si_{1.8}$. The Re substitution resulted in an unchanged power factor but a reduced thermal conductivity. The amount of Re was limited by its solid solubility in HMS.

Yamamoto et al.[130] observed that addition of Re above the solubility limit resulted in production of large amounts of $ReSi_2$ as a secondary phase which decreased the power factor of the material. Recently, the solubility limit of Re was increased using a liquid quenching technique.[131] This resulted in a material with the high $zT \approx 1$ at 647 °C.[130]

Overall, different methods have been explored to improve the thermoelectric properties of HMS with most of these focused on reducing the thermal conductivity of the material. Nevertheless, the maximum zT remained persistently around 0.6. A comparison of zT of selected HMS materials with different dopants is represented in Fig. 6.

8. Chromium disilicide ($CrSi_2$)

Chromium disilicide ($CrSi_2$) has been of interest for thermoelectric applications because of its natural abundance, nontoxicity, good mechanical properties, oxidation resistance in air, and thermal stability at high temperature (up to 1000 K).[136]

$CrSi_2$ is a degenerate p-type semiconductor[137] with a hexagonal crystal structure, i.e., the so-called C40-type structure. It has a narrow indirect band gap of 0.35 eV.[138] $CrSi_2$ has significant anisotropy of Seebeck coefficient in a wide temperature range. However, its high thermal conductivity and a medium Seebeck coefficient result in a small zT with maximum value of 0.25 for the undoped material[139] as shown in Fig. 7. Compared with other silicides, $CrSi_2$ has high thermal conductivity, high electric conductivity, and medium Seebeck coefficient. Around room temperature, its zT value is higher than most other silicides.

Several methods have been employed to enhance the Seebeck coefficient and reduce the thermal conductivity including varying its stoichiometry, structural disordering and nanostructuring. $CrSi_2$ has been prepared by mechanical alloying and subsequent hot pressing like many other nanostructured bulk materials. For example, by decreasing the thermal conductivity and electric conductivity of $CrSi_2$ and $CrSi_{2.1}$, a modest incensement in zT (5% compared with un-milled $CrSi_2$) was observed in $CrSi_{2.1}$ alloy composi-

© 2017 The Japan Society of Applied Physics

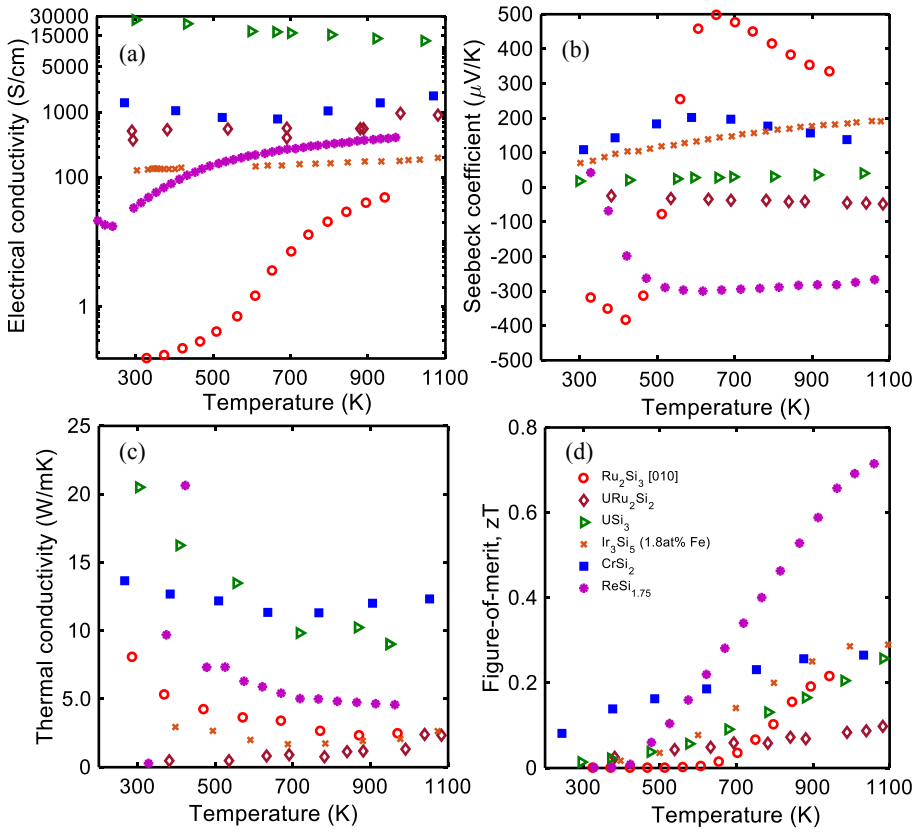

Fig. 7. (Color online) Comparison of (a) electrical conductivity, (b) Seebeck coefficient, (c) thermal conductivity, and (d) zT values of $CrSi_2$,[139] $ReSi_{1.75}$,[144] Ru_2Si_3,[146] URu_2Si_2,[147] USi_3,[148] and Ir_3Si_5.[151]

tion.[136] More recently, substitution of different elements have been studied. It was found that the maximum zT value for $Cr_{1-x}V_xSi_2$ was ~0.2 for $x = 0.08$ at 450 K due to the reduction of the thermal conductivity.[140] Mo substitution was also effective in improving the zT value. The maximum zT value of $Cr_{1-x}Mo_xSi_2$ increased from 0.13 to 0.23 for $x = 0.30$ at 800 K.[141] Nb substitution could reduce the thermal conductivity and increase the maximum zT by a factor of about 1.2 (0.20 in $Cr_{0.95}Nb_{0.05}Si_2$) relative to that of Nb-free $CrSi_2$.[142]

9. Rhenium silicide ($ReSi_{1.75}$)

It has been shown that higher rhenium silicide has the composition of $ReSi_{1.75}$ rather than previously thought $ReSi_2$. The crystal structure of $ReSi_{1.75}$ should be described as a triclinic (space group $P1$, $a = 0.3138$; $b = 0.3120$; $c = 0.7670$ nm; $\alpha = 89°90$).[143] One important feature of the band structure of $ReSi_{1.75}$ is that the highest valence band in the [001] direction is almost flat. This results in a very large hole effective mass, which explains the large anisotropy of the thermoelectric properties of $ReSi_{1.75}$. The value of electrical resistivity is higher along [001] than along [100]. Its electrical conduction is of n-type when measured along [001] while it is of p-type when measured along [100]. When measuring along [001], a large zT of 0.7 is achieved at 1073 K, as shown in Fig. 7. The zT value is further increased to 0.8 with a small amount of Mo addition (2% substitution for Re).[144] Compared with other silicides, $ReSi_{1.75}$ has small electrical conductivity, large Seebeck coefficient and zT along [001] direction. Its zT value at high temperature is significantly larger than many other silicides.

10. Ruthenium silicide (Ru_2Si_3)

Although Ru_2Si_3 has the disadvantage of being expensive, it is still considered to be a potential thermoelectric material for high temperature applications. Ru_2Si_3 is one of the family of related compounds Ru_2X_3 where X can be Si, Ge, or Sn. It has a high-temperature and a low-temperature phase. The phase transition happens at ~1240 K.[145] Low-temperature phase α-Ru_2Si_3 has an orthorhombic structure, whereas high-temperature phase β-Ru_2Si_3 has a tetragonal structure (a Nowotny chimney-ladder).[61] The α/β phase transformation is expected to have a significant effect on the use of Ru_2Si_3 as a thermoelectric material with greater interest in the α-phase.[146] Simkin et al.[146] performed floating-zone crystal growth of stoichiometric Ru_2Si_3 and measured the thermoelectric properties, which is shown in Fig. 7. The measured thermoelectric properties for the intrinsic (p-type) Ru_2Si_3 were clearly superior along the [010] orientation, consistent with the band structure models. Compared with other silicides, Ru_2Si_3 has small thermal and electric conductivity, and a medium zT.

11. Uranium ruthenium silicide (URu_2Si_2)

A large amount of uranium is discharged during a nuclear fuel cycle. The amount of depleted uranium is large and they cannot be reused for nuclear fuel. Therefore, uranium could be used for thermoelectric materials after about 50 years when they become non-radioactive. Since uranium has 5f-electrons, some uranium compounds are heavy fermion compounds, which can have a large effective mass of electron or hole.[147] This could result in a high Seebeck coefficient.

© 2017 The Japan Society of Applied Physics

The thermoelectric properties of URu_2Si_2 were studied, as shown in Fig. 7.[147] A maximum zT of ~0.1 was reached at 1100 K in this study. The thermoelectric properties were poor above room temperature. However, since there has not been much study on this material, further optimization may be possible to improve it zT.

12. Uranium silicide (USi_3)

The high atomic mass difference in USi_3 should be in favor of a low thermal conductivity. Thermoelectric properties of USi_3 were studied as shown in Fig. 7. Compared with other silicides, USi_3 has low Seebeck coefficient, very high electric conductivity and a medium zT. $U(Si,Ge)_3$ solid solutions have been also studied, where they showed to be essentially metallic in nature reflected from their very high electric conductivity.[148]

13. Iridium silicide (Ir_3Si_5)

Ir_3Si_5 is a wide bandgap semiconductor with an optical gap of 1.56 eV,[149] which allows for applications at high temperatures. Its bulk material and single crystals were studied, but the zT value for the iridium silicides hardly exceeded 0.1.[150] Properties of semiconducting iridium silicide films have also been studied. Fe-doped iridium silicide films with high thermoelectric power factors were successfully obtained and the maximum zT reached ~0.3 when the amount of Fe dopant was 1.8 at. %,[151] as shown in Fig. 7, which is in the same order as some other silicides at high temperature.

14. Iron disilicide ($FeSi_2$)

Iron disilicide has three phases of ε-$FeSi_2$ (cubic), α-$FeSi_2$ (tetragonal), and β-$FeSi_2$ (orthorhombic). β-$FeSi_2$ is semiconductor and of interest for thermoelectric applications. It is a good candidate for thermoelectric applications due to low cost, non-toxicity and ease of fabrication. It is also chemically stable and has a sufficiently high figure of merit. Moreover, it has been combined with other high zT materials like SiGe[85] to form more efficient and cost-effective nanocomposites. β-$FeSi_2$ has a direct band gap of 0.80–0.95 eV and an indirect band gap of 0.7–0.78 eV,[152,153] which makes it a suitable option for making optoelectronic devices, light detector and photovoltaic applications.

14.1 $FeSi_2$: Properties and different phases

Iron disilicide has a metallic high temperature phase (α-$FeSi_2$) and a semiconducting low temperature phase (β-$FeSi_2$) with a transition temperature of about 1210 K. Undoped β-$FeSi_2$ single crystals obtained from very high purity starting material showed n-type conduction at room temperature.[154] Room temperature Seebeck coefficient of $-750\,\mu V/K$ and electrical resistivity of $230\,\Omega$cm was reported for pure β-$FeSi_2$ single crystals. It was suggested by Behr et al.[154] that the p-type conductivity for undoped $FeSi_2$ single crystals reported in literature occurs due to unintentional contamination by impure starting materials.

The high temperature metallic phase of the iron disilicide consists of a eutectic structure comprising cubic ε-phase and tetragonal α-phase. The ε-phase is an iron monosilicide FeSi, and the α-phase exists within a wide composition range, being represented by the chemical formula Fe_2Si_5. While the phase transition from semiconducting to metallic phase is fast, the phase transformation from metallic to semiconducting phase is slow and occurs in three stages. In the first stage, a peritectoid reaction occurs between α- and ε-phases to form the β-phase above 1138 K ($\alpha + \varepsilon \rightarrow \beta$). In the second stage eutectoid decomposition of α phases to β and Si occurs below 1133 K ($\alpha \rightarrow \beta + \mathrm{Si}$). In the third stage, remaining ε-phase reacts with Si to form the β-phase ($\varepsilon + \mathrm{Si} \rightarrow \beta$), completing the transformation through heat treatment.[155] This process takes several hours to complete due to slow reaction kinetics.

14.2 $FeSi_2$: Methods of fabrication

Since 1964, when iron disilicide was first suggested as a potential thermoelectric material by Ware and McNeill,[156] much work has been done to improve the properties and cost-effectiveness of this material. Different fabrication techniques have been employed to synthesize bulk or thin films of iron disilicide in the form of single crystalline, polycrystalline, nanostructured materials, or even nanocomposites. Recent advances in preparation of bulk and single crystal iron disilicide, their thermoelectric properties and applications are discussed in Ref. 157.

14.3 $FeSi_2$ single crystals

Preparation of β-$FeSi_2$ single crystals has been carried out by chemical vapor transport (CVT) using I_2 as the transport agent and 5N purity starting materials.[154] In case of high purity materials, stoichiometric composition played an important role in determining transport properties. The thermoelectric properties of doped β-$FeSi_2$ single crystals grown using CVT comparison with polycrystalline β-$FeSi_{2+x}$ thin films prepared by e-beam evaporation and DC magnetron sputtering using source materials with different Si/Fe ratio were further studied in Ref. 158.

14.4 $FeSi_2$ polycrystalline/crystalline thin film

Iron disilicide thin films have been obtained by deposition techniques like electron beam evaporation (e.g., Ref. 159), magnetron sputtering (e.g., Ref. 160), RF sputtering (e.g., Ref. 162), and plasma ion processing (e.g., Ref. 161) followed by an annealing step. The results suggest that the thermoelectric properties vary widely depending upon the fabrication technology, purity of starting materials and the process conditions.

Effects of adding various p-type dopants like V, Cr, Mn and n-type dopants like Co, Ni, Pd, Pt were studied in Ref. 162. The films were deposited on Si discs by RF sputtering and then annealed to form crystalline doped $FeSi_2$. For the p-type dopants, V and Cr were found to yield better thermoelectric power factor than Mn (2.3×10^{-4} and $2.6 \times 10^{-4}\,W\,m^{-1}\,K^{-2}$ respectively at room temperature). For n-type dopants, Pt was the most suitable with power factor of $4.9 \times 10^{-4}\,W\,m^{-1}\,K^{-2}$.

14.5 $FeSi_2$: Powder metallurgical synthesis

The most conventional method of preparing bulk samples of β-$FeSi_2$ has been detailed in various publications (e.g., Ref. 163). The procedure involves smelting of the raw materials by induction or resistance heating. The ingot obtained is made into powder form by spraying or milling. This powder is densified by hot pressing or cold pressing and subsequent sintering. Annealing is then carried out to bring about phase transformation from metallic to semiconducting β-$FeSi_2$.

The most effective dopants for making n- and p-type $FeSi_2$ are Co and Mn/Al, respectively. The most efficient bulk

© 2017 The Japan Society of Applied Physics

Table I. Summary of thermoelectric properties of $FeSi_2$ obtained by different dopants.

Type	Dopant	Type/Method	σ (S/cm)	S (μV/K)	PF ($W m^{-1} K^{-2}$)	κ ($W m^{-1} K^{-1}$)	Z_{max} (/K)	Temp. (K)	Ref.
	Co	Powder metallurgy	140–180	−200 to −220	—	7.5	3.43×10^{-4}	823	164, 171, 172
	Co	RF sputtering	53	−225	2.6×10^{-4}	—	—	300	162
	Co + Al	Powder metallurgy	260	−210	—	4.5	3.74×10^{-4}	823	163
	Co + Ge	Powder metallurgy	225	−160		5	1.26×10^{-4}	843	164
n-type	Co + Ru	Hot pressing	589	−160	1×10^{-3}	—	—	803	165
	Ni	RF sputtering	13	−113	1.7×10^{-5}	—	—	300	162
	Pd	RF sputtering	32	−241	1.9×10^{-4}	—	—	300	162
	Pt	RF sputtering	111	−202	4.9×10^{-4}	—	—	300	162
	Cu	Hot pressing	173	−173	8.53×10^{-4}	3.097	2.28×10^{-4}	933	37
	Cr	Powder metallurgy	40	370	—	7.5	5.2×10^{-5}	663	164
	Cr	RF sputtering	32	288	2.6×10^{-4}	—	—	300	162
	Cr + Ge	Powder metallurgy	90	240	—	6.7	6.6×10^{-5}	653	164
	Cr + Ru	Hot pressing	708	190	1.5×10^{-3}	4.6	3.35×10^{-4}	733	165
p-type	Mn	HP+annealing	50–150	200–380	—	—	—	150–900	171,172
	Mn	RF sputtering	4	81	2.4×10^{-6}	—	—	300	162
	Mn + Al	Mechanical alloying	—	270	—	5	1.3×10^{-4}	720	166
	V	RF sputtering	29	278	2.3×10^{-4}	—	—	300	162
	Zr	Mechanical alloying	3390	36	—	—	3.38×10^{-5}	1070	167

n-type β-$FeSi_2$ was found by partial compensation of Co with Al.[163] Effects of Cu and Ge doping in n- and p-type β-$FeSi_2$ were studied in Ref. 164. It was found that zT increases by the addition of Cr, Co, and Ge, but slightly decreases by addition of Cu. Efficient p-type β-$FeSi_2$ was also found by alloying with Ru and Cr.[165]

It was also shown in Refs. 166 and 167 that mechanical alloying can be used to produce homogeneous, fine-grained β-$FeSi_2$, without the need for heat treatment or any long-time annealing steps and can yield higher figure of merit due to smaller grain sizes.

In Refs. 168 and 169, bulk nanostructured β-$FeSi_2$ was prepared by melt spinning, rapid solidification and spark plasma sintering, which was found to significantly reduce the annealing time for phase transformation. Another fast method of preparation of Co and Mn-doped alloys by induction-field activated combustion/static pseudo isostatic compaction was studied in Ref. 170 and samples produced by this method were found to exhibit better thermoelectric properties than their hot-pressed and spark-plasma-sintered counterparts.

14.6 $FeSi_2$ thermoelectric properties

The literature consists of wide range of results that vary according to the method of fabrication, purity of the starting material, type of dopants and compositions, or annealing temperatures and time.[154] P-type material can be obtained from $FeSi_2$ by doping with transition elements lying on the left side of Fe in the periodic table, like Mn and Cr, while doping with elements on its right side, like Co and Ni yield n-type material. Approximate values of certain thermoelectric properties for different p- and n-type dopants are given in Table I. Also, Fig. 8 compares the thermoelectric properties of p-type iron disilicide with different dopants and compositions. Another noteworthy data was achieved for the nanocomposite of $(FeSi_2)_{0.75}(Si_{0.8}Ge_{0.2})_{0.25}$, which showed nearly 170% enhancement in zT compared to single phase β-$FeSi_2$[85] as shown in Fig. 9.

15. Cobalt monosilicide (CoSi)

Cobalt monosilicide is a semimetal, meaning that its band structure indicates a slight overlap of conduction and valence bands. It has a cubic crystal structure, a mass density of $6.58\,g/cm^3$, and melting temperature of 1450 °C. The room temperature Seebeck coefficient of $-83\,\mu V/K$, electrical conductivity of $1000\,S/cm$, and thermal conductivity of $20\,W m^{-1} K^{-1}$ has been reported by Ref. 173. It has been reported that strictly stoichiometric CoSi is n-type with carrier concentration of about $10^{20}\,cm^{-3}$.[174] Electron and hole effective masses are $2m_e$ and $6m_e$, respectively,[174] which means that the electron mobility is much higher than the hole mobility. The electron concentration can be increased by using Ni as the dopant or deceased by using Fe as a dopant. However, this substitution leads to a reduced Seebeck coefficient and figure-of-merit.[174]

Comparison of the thermoelectric properties of CoSi with various dopants is shown in Fig. 10. A study of thermal conductivities of CoSi shows that the lattice thermal conductivity makes up only a small fraction of the total thermal conductivity. Hence, nanostructuring and reduction of the grain sizes will not lead to an appreciable improvement in its thermoelectric efficiency. Alternative ways for improving the thermoelectric efficiency of CoSi has been suggested in Ref. 175, like reducing valence band and conduction band overlap by introducing crystal deformation or designing structures that strongly scatter only one type of carrier.

Many attempts have been made by different authors to improve the thermoelectric efficiency of CoSi. Doping of CoSi with Al has been studied in Refs. 173, 174, and 176, with Ge and B in Refs. 177, 178, and 179, and with Fe and Ni in Ref. 175. Moreover, effects of Ni, Pd, and Pt substitutions have been studied in Ref. 180. The comparison of the results obtained by these studies is shown in Fig. 10. Thermoelectric properties of $CoSi_{1-x}Al_x$ ($x = 0$ to 0.5) single crystals prepared by floating zone technique were studied in Ref. 174 and zT

© 2017 The Japan Society of Applied Physics

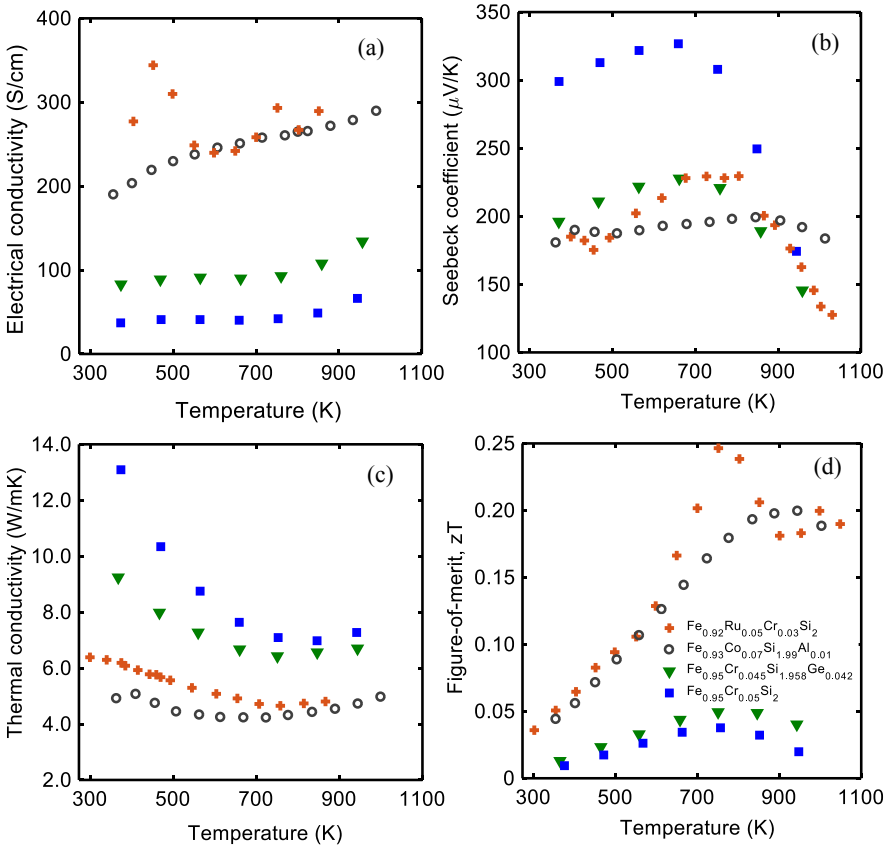

Fig. 8. (Color online) (a) Electrical conductivity, (b) Seebeck coefficient, (c) thermal conductivity, and (d) zT versus temperature for p-type $FeSi_2$ doped with (Cr, Cr+Ge, Ru) dopants. Refs: $Fe_{0.93}Co_{0.07}Si_{1.99}Al_{0.01}$,[163] $Fe_{0.95}Cr_{0.07}Si_{1.958}Ge_{0.042}$,[164] $Fe_{0.95}Cr_{0.05}Si_2$,[164] and $Fe_{0.92}Ru_{0.05}Cr_{0.03}Si_2$.[165] Figures created by author from the data in the mentioned sources.

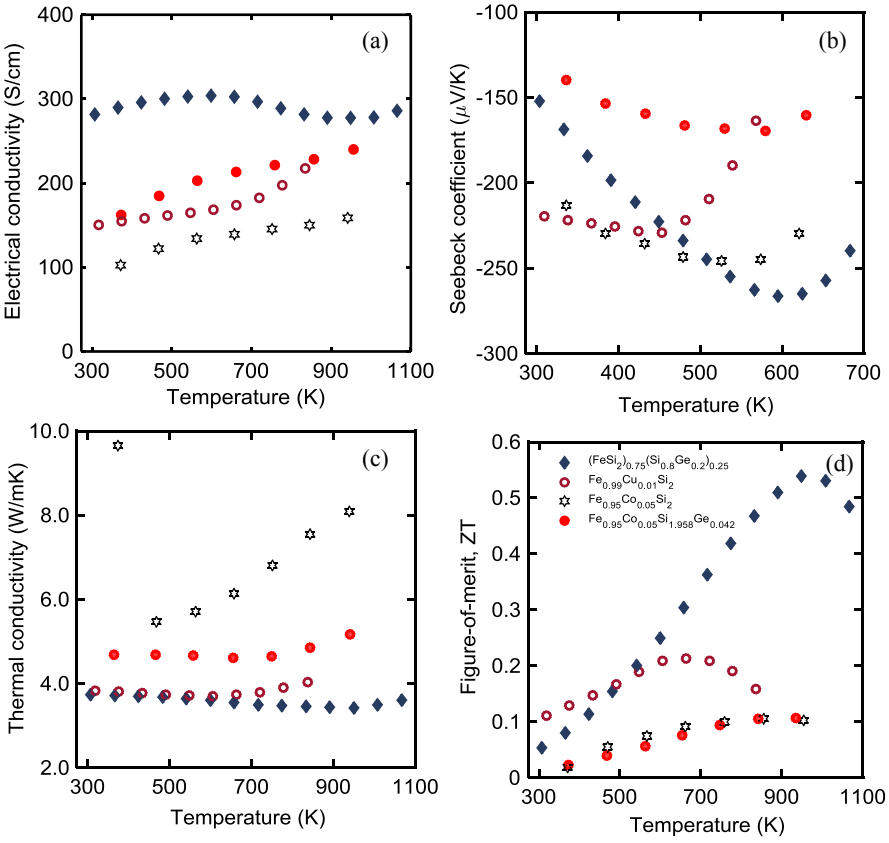

Fig. 9. (Color online) (a) Electrical conductivity, (b) Seebeck coefficient, (c) thermal conductivity, and (d) zT versus temperature for n-type $FeSi_2$ doped with Co,[37] Co+Ge,[164] and Cu[164] dopants, and nanocomposite of $(FeSi_2)_{0.75}(SiGe)_{0.25}$.[85] Figures created by author from the data in the mentioned sources.

© 2017 The Japan Society of Applied Physics

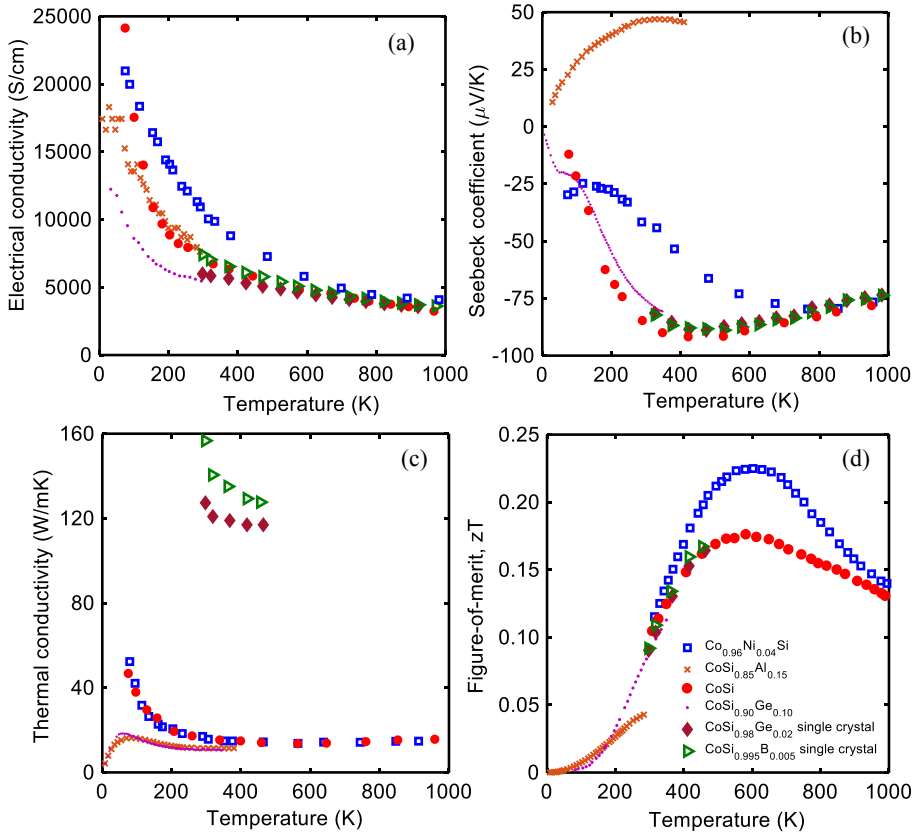

Fig. 10. (Color online) (a) Electrical conductivity, (b) Seebeck coefficient, (c) thermal conductivity, and (d) zT versus temperature for cobalt monosilicide obtained by various dopants. Refs: CoSi,[175] $Co_{0.96}Ni_{0.04}Si$,[175] $CoSi_{0.85}Al_{0.15}$,[173] $CoSi_{0.995}B_{0.005}$ single crystal,[177] $CoSi_{0.98}B_{0.02}$ single crystal,[177] and $CoSi_{0.90}Ge_{0.10}$.[179] Figures created by author from the data in the mentioned sources.

was found to be lower as compared to the undoped CoSi. Other studies have found that Al substitution dramatically decreases electrical resistivity and thermal conductivity. Although zT increased by increasing the amount of Al doping, it was still much lower than zT values of other thermoelectric materials.[173,176] Ge and B substitution, on the other hand, increased the thermoelectric power factor and figure of merit for single crystals[177,178] by reducing the electrical resistivity and thermal conductivity (see Fig. 10).

Thermoelectric performance of devices fabricated from $CrSi_2$–CoSi thermomodules was studied in Ref. 181. A comparison between materials made by high-purity versus low-purity starting material was made and it was found that 99% purity suffices for practical applications.

16. Cerium silicide ($CeSi_2$)

Pure $CeSi_2$ exhibits high electrical conductivity and low absolute value of the Seebeck coefficient ($\sigma \sim 106\,S/m$ and $S \sim -55\,\mu V/K$ at 300 K) in comparison with good thermoelectric materials.[182] $CeSi_2$ compounds are known to exhibit $GdSi_2$-type structure in low temperature, and $ThSi_2$ type structure in high temperature.[183] There are several $CeSi_2$ based compounds used as thermoelectric materials namely, $CeSi_2$, $Y_{0.5}Ce_{0.5}Si_2$, CeSiGa, CeSiGe, and $CeSi_{1.6}Ge_{0.4}$. These compounds can be fabricated by different methods like electric arc melting, milling, and thermal pressing. $CeSi_2$ and CeSiGa alloys exhibit metallic like conductivity with similar values of the electrical conductivity.[182–184] The electrical conductivity of CeSiGe and $Y_{0.5}Ce_{0.5}Si_2$ alloys are like semi-metallic materials, and $CeSi_{1.6}Ge_{0.4}$ shows semiconductors behavior.[183] It was found that the electrical conductivity of CeSiGe is strongly affected by Si(Ge) phase.[183] Seebeck coefficient, electrical conductivity, thermal conductivity and zT versus temperature of all mentioned materials are compared in Fig. 11.

17. Molybdenum silicide (Mo–Si) and tungsten silicide (W–Si)

Mo–Si based materials have multiple intermetallic compounds, namely, Mo_3Si, Mo_5Si_3, and $MoSi_2$. These materials have properties such as a high melting point, low electrical resistance, high-temperature stability and strength, and low density. They have usage as heating elements and protective coating.[185] Similarly, W_3Si, W_5Si_3, and WSi_2 phases exist in the W–Si based-materials. $MoSi_2$ and WSi_2 possess stable tetragonal phases and can be used as gate electrodes, interconnects and diffusion barriers in CMOS technology.[185,186] $MoSi_2$ and WSi_2 can be grown as epitaxial layers on Si substrates to form hexagonal phases. These two hexagonal materials have narrow bandgap.[186] The conventional fabrication method for Mo and W silicide is mechanical alloying.[184] Electrical conductivity and Seebeck coefficient of these two compounds are shown in Fig. 12. Mo- and W-silicide exhibit a narrow gap semiconductor behavior due to their temperature dependence of the conductivities. Also, both these silicides show p-type conductivity.[186]

Two different polymorphs of $MoSi_2$ are the α-$MoSi_2$, stable phase, and the β-$MoSi_2$, metastable phase.[185] α-$MoSi_2$

© 2017 The Japan Society of Applied Physics

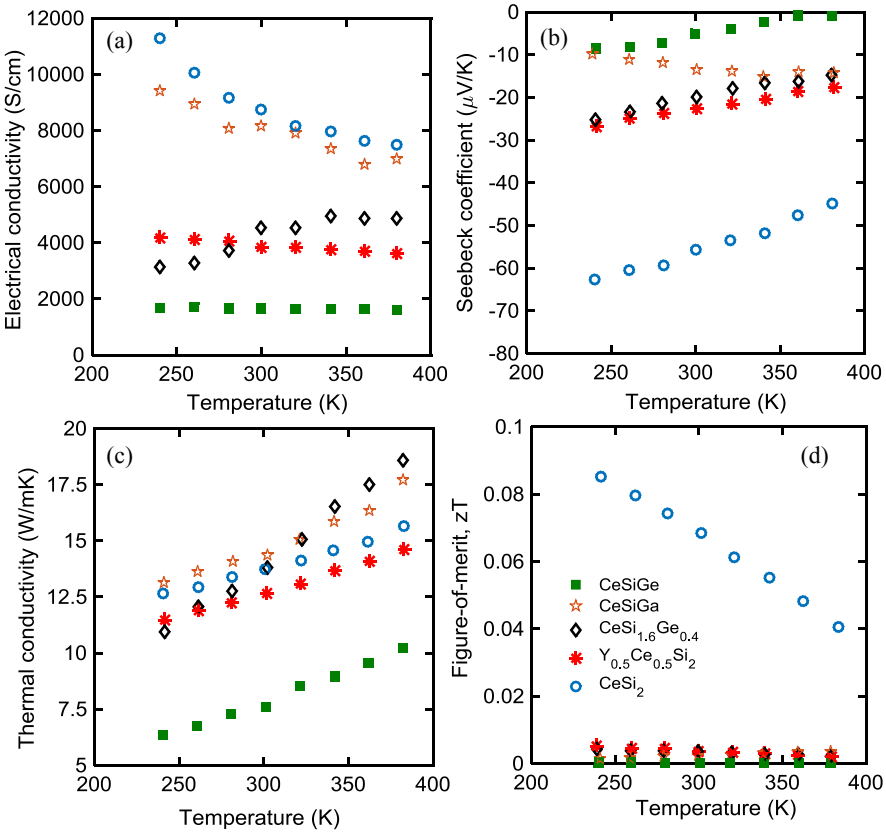

Fig. 11. (Color online) (a) Electrical conductivity, (b) Seebeck coefficient, (c) thermal conductivity, and (d) zT versus temperature for $CeSi_2$, $Y_{0.5}Ce_{0.5}Si_2$, CeSiGa, CeSiGe, and $CeSi_{1.6}Ge_{0.4}$ compiled from Ref. 183.

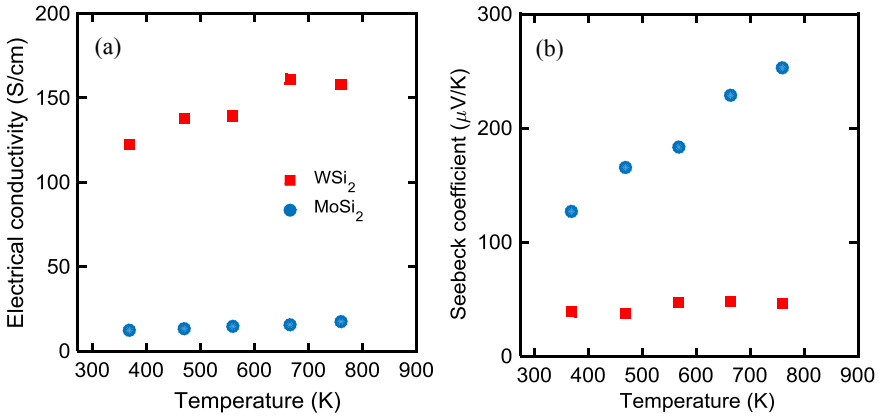

Fig. 12. (Color online) Comparison of (a) electrical conductivity and (b) Seebeck coefficient of $MoSi_2$ and WSi_2.[186)]

can be fabricated in amorphous, polycrystalline, and crystalline phase. β-$MoSi_2$ powders can be synthesized as amorphous phase by mechanical alloying or as a mixture with α-$MoSi_2$.[185)] Annealing β-$MoSi_2$ mixture in temperatures 973–1273 K can irreversibly transform it to α-$MoSi_2$.[185)] The crystal structure of α-$MoSi_2$ is the tetragonal body-centered $C11_b$ with space group $I4/mmm$ and the crystal structure of β-$MoSi_2$ is a hexagonal close-packed C40 with $P6_222$.[187)] Electrical conductivity and Seebeck coefficient versus temperature for α-$MoSi_2$ and β-$MoSi_2$ are shown in Fig. 13. It can be seen that both of these parameters increase with the temperature for both compounds; however, β-$MoSi_2$ has much higher Seebeck coefficient making it more suitable for thermoelectric applications.

It has been also showed that inclusion of $MoSi_2$ or WSi_2 nanoparticles in other silicides such as SiGe can decrease the thermal conductivity considerably resulting in a higher zT.[188,189)]

18. Lanthanum silicide (LaSi)

LaSi crystallizes with the orthorhombic FeB-type structure and the space group is *Pnma*. In comparison to other thermoelectric materials, for LaSi, both the electrical resistivity and Seebeck coefficient are very low (2.38 μΩ m and −1.5 μV/K at 333 K, respectively) and it behaves like metals. The Seebeck coefficient versus temperature for LaSi is shown in Fig. 14.[190)]

© 2017 The Japan Society of Applied Physics

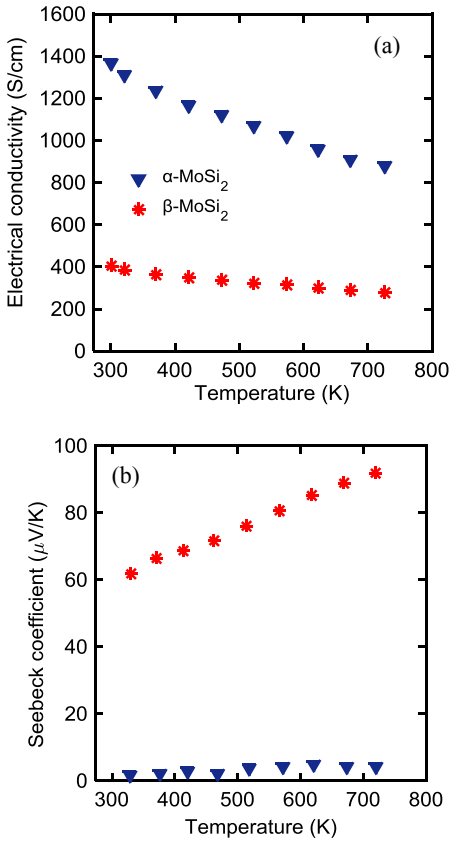

Fig. 13. (Color online) Comparison of (a) electrical conductivity and (b) Seebeck coefficient of α-$MoSi_2$ and β-$MoSi_2$.[185)]

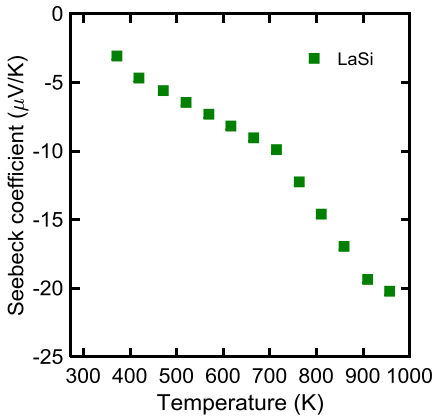

Fig. 14. (Color online) Seebeck coefficient of LaSi versus temperature.[190)]

19. Alkaline earth silicides

19.1 Strontium disilicide ($SrSi_2$)

Alkaline-earth-metal disilicide $SrSi_2$ is composed of non-toxic and naturally abundant elements which makes it an ecofriendly material. $SrSi_2$ is a narrow-gap semiconductor with a 35 meV band gap based on the electrical transport studies,[191)] whereas the band structure calculations predicted the presence of a sharp pseudogap of about 3 meV. However, a recent study estimated the value of band gap to be ~13 meV.[192)] $SrSi_2$ has a moderate Seebeck coefficient of about 130 μV/K at room temperature.[193)] Additionally, it possesses a fairly high electrical conductivity (~1000 S/cm).

Table II. The comparison of thermoelectric properties of $SrSi_2$-based alloys at room temperature.[193)]

Material	σ (S/cm)	S (μV/K)	κ ($W m^{-1} K^{-1}$)	zT
$Sr_{1.06}Si_2$	75	88.8	3.91	0.01
$SrSi_{1.94}Al_{0.06}$	602	63.1	5.23	0.01
$SrSi_2$	540	131.4	5.46	0.05
$Sr_{0.94}Si_2$	303	168.1	4.86	0.05
$Sr_{0.93}Ba_{0.07}Si_2$	704	156.7	4.90	0.11
$SrSi_{1.94}Ge_{0.06}$	775	144.3	5.10	0.13
$Sr_{0.9}Ca_{0.1}Si_2$	546	220.8	5.17	0.17
$Sr_{0.77}Ca_{0.1}Si_2$	719	143.9	1.66	0.27
$Sr_{0.92}Y_{0.08}Si_2$	3571	134.3	4.88	0.41

However, its high thermal conductivity (~5 $W m^{-1} K^{-1}$) hinders its thermoelectric performance.[194)] To improve its thermoelectric properties, a combination of three factors have been employed on the $SrSi_2$-based alloys:[192,195–197)] (a) lower electrical resistivity through the enhancement of the charge carriers, (b) higher Seebeck coefficient via the band structure engineering, and (c) lower thermal conductivity through the introduction of point defects or lattice imperfections. These improvements were made by introducing various dopants into the alloy to alter its properties. The effect of different dopants on the thermal and electrical properties is listed on Table II. In order to reveal the phonon–point-defect scattering effect on thermal conductivity of the $SrSi_2$-based alloys, lattice thermal conductivity of the pure, substituted and Sr-deficient/Sr-rich $SrSi_2$ alloys were evaluated. It was found that the Sr-deficient $Sr_{0.77}Ca_{0.1}Si_2$ alloy has the lowest room-temperature thermal conductivity value of about ~1.66 W $m^{-1} K^{-1}$ among the studied alloys shown in Table II.[193)] The table is ordered with respect to zT for comparison.

The estimated zT as a function of temperature for all optimized $SrSi_2$ alloys using the measured values of ρ, S, and κ is shown in Fig. 15. A reduction in zT value for the Al-substituted $SrSi_2$ was observed as a result of a considerable reduction in S value through hole doping (Kuo et al., 2012). On the other hand, the substitution of Ca, Ba, Y, and Ge elements in the $SrSi_2$ lead to an enhancement of their zT value over the entire temperature range of 10–300 K.[192,195,196)] A maximum room temperature zT value of about 0.41 has been attained for the $Sr_{0.92}Y_{0.08}Si_2$ alloy with a large thermoelectric power factor of 6.4×10^{-3} W $m^{-1} K^{-2}$ owing to the induced changes in the electronic band structure and carrier mobility through Y doping.[195)] The zT plot has a positive slope indicating that it will improve further at above room temperature. Moreover, for the so far most optimum alloy $Sr_{0.92}Y_{0.08}Si_2$, the lattice thermal conductivity is high (~4.88 W $m^{-1} K^{-1}$) indicating that a higher zT may be possible by nanostructuring to decrease the thermal conductivity.

Based on these results, it can be concluded that the $SrSi_2$ system is a potentially good candidate for thermoelectric applications if an optimal alloy is made. These encouraging findings suggest that the tuning of electronic band structure by suitable alloying/substitution along with right Sr-deficiency level could lead to enhancement of their thermoelectric performance.[198)]

© 2017 The Japan Society of Applied Physics

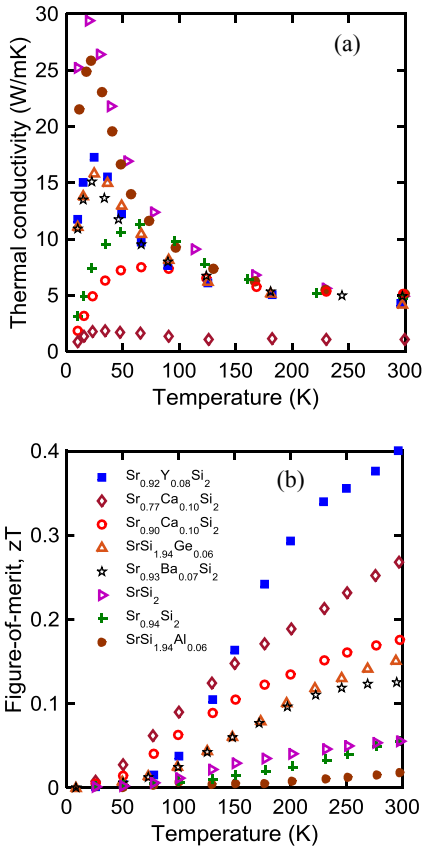

Fig. 15. (Color online) Comparison of (a) thermal conductivity and (b) zT of $SrSi_2$ obtained with various dopants.[193]

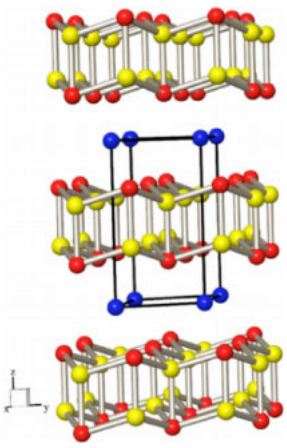

Fig. 16. (Color online) Crystal structure of $SrAl_2Si_2$. Red: Si, yellow: Al, blue: Sr.[199]

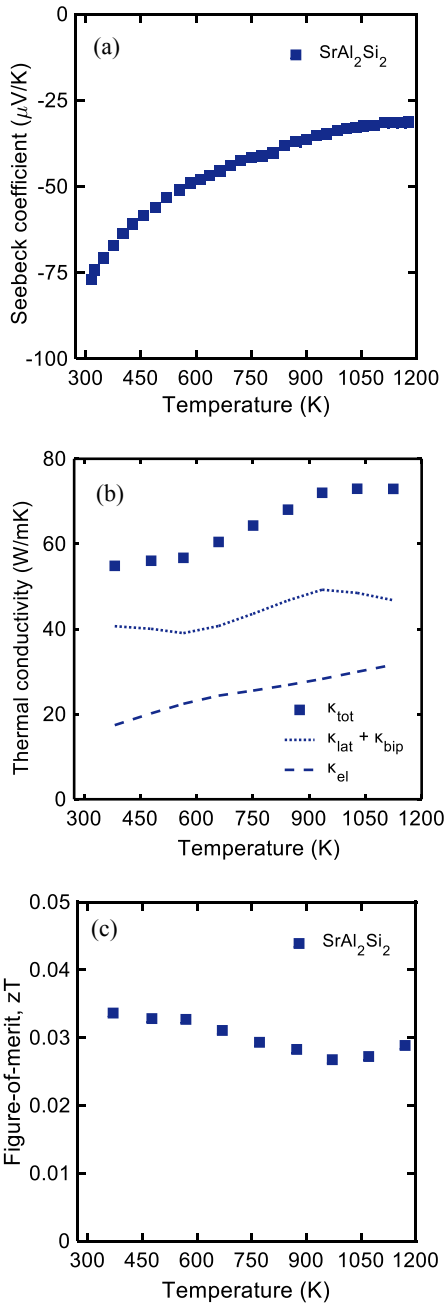

Fig. 17. (Color online) (a) Seebeck coefficient, (b) thermal conductivity, and (c) zT of $SrAl_2Si_2$ versus temperature.[199]

19.2 Strontium aluminum silicide ($SrAl_2Si_2$)

One of the more established alloys of $SrSi_2$ is with the addition of aluminum producing $SrAl_2Si_2$. The crystal structure of $SrAl_2Si_2$ is shown in Fig. 16.[199]

A high temperature metallic solution growth method was employed to prepare the single crystal of $SrAl_2Si_2$ from pure Si, Sr, and Al.[199] Its room temperature resistivity was 7–8 mΩ cm, which may be artificially high due to cracks in the crystals as the structure is fairly brittle. $SrAl_2Si_2$ is classified as a semimetal with the dominant carriers being holes below approximately 150 K and electrons above that temperature.[200] The transport is probably accounted for by both electrons and holes. The electrical resistivity decreases from 0.95 mΩ cm at room temperature to 0.6 mΩ cm at 1173 K with increasing temperature.[199] The isotropic mixture of crystallites could be the reason for its value being lower than that of a single crystal. Figure 17 shows the thermoelectric properties of $SrAl_2Si_2$. The Seebeck coefficient showed negative value from room temperature to 1173 K. The absolute value of the Seebeck coefficient decreased from 78 μV/K at room temperature to 34 μV/K at 1173 K with increasing temperature.[199] The resistivity and Seebeck coefficient values versus temperature are indicative of an intrinsic semiconductor. Minority p-type carriers are excited reducing the absolute Seebeck coefficient and resistivity with the increase of temperature. Thus, both n- and p-type carriers are operative in $SrAl_2Si_2$.

The figure of merit zT was calculated from the experimental electrical conductivity, Seebeck coefficient, and

© 2017 The Japan Society of Applied Physics

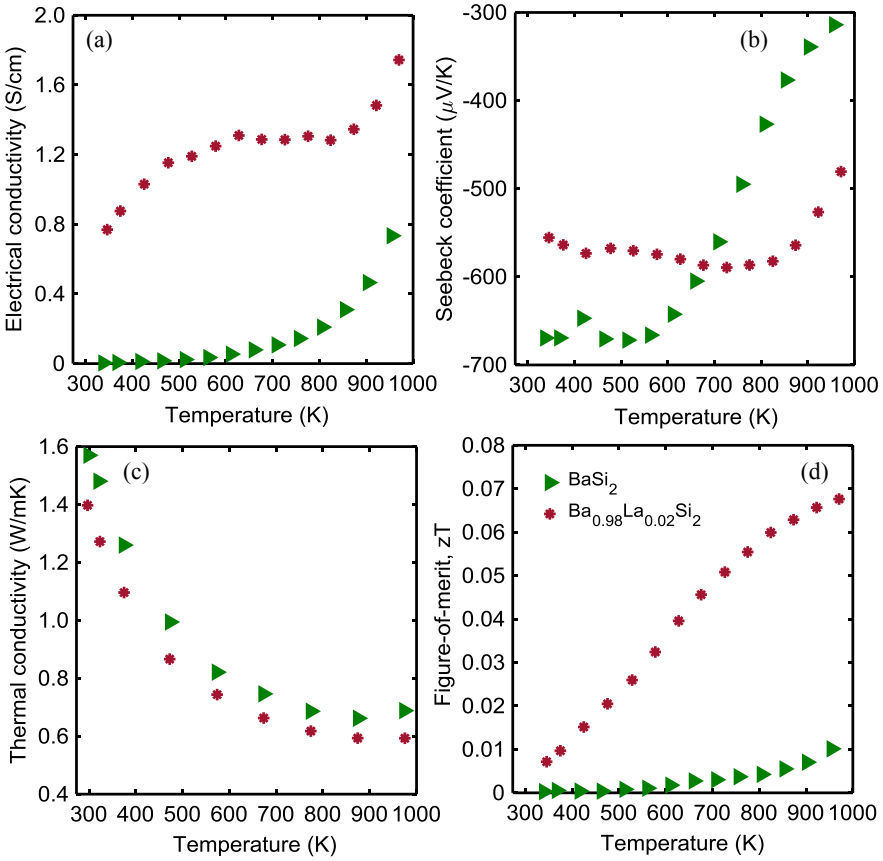

Fig. 18. (Color online) (a) Electrical conductivity, (b) Seebeck coefficient, (c) thermal conductivity, and (d) zT versus temperature of undoped crystalline $BaSi_2$ with La doped $Ba_{0.98}La_{0.02}Si_2$.[204)]

thermal conductivity. At the moment, the zT values being reported are not encouraging for thermoelectric applications, but established methods to lower thermal conductivity such as inducing structural disorder is a possibility. However, the presence of mixed (n- and p-type) carriers is the main reason that is limiting the zT. Therefore, it is necessary to increase the electronic band gap to eliminate the bipolar conduction.

19.3 Barium silicide ($BaSi_2$)

$BaSi_2$ is a semiconductor that crystallizes with the orthorhombic structure (space group: *Pnma*) at atmospheric pressure and room temperature. $BaSi_2$ has a large absorption coefficient and a band gap of 1.13 eV. This has been especially of interest for thin-film solar cell applications.[201)] Ba_2Si has been also considered for use as a thermoelectric material owing to its low thermal conductivity and high Seebeck coefficient. Temperature dependence of the electrical conductivity and Seebeck coefficient of undoped $BaSi_2$ are shown in Fig. 18. The data of these figures are from reference.[202,203)] The electrical conductivity of $BaSi_2$ increases with increasing temperature showing non-degenerate doped semiconductor behavior. The electrical conductivity values are approximately similar near room temperature,[202,203)] but they were slightly higher in Ref. 202 at high temperatures. $BaSi_2$ has a negative Seebeck value which is indicative of the majority charge carriers being electrons. The absolute S decreased with increasing temperature above approximately 550 K, which means that Ba_2Si entered the intrinsic region from this temperature. The thermal conductivity is small compared to most silicide thermoelectric materials indicating a good candidate for thermoelectric applications. The absolute S values were also relatively high, e.g., $-669\,\mu V/K$ at 337 K. However, the measured electrical conductivity was very low under 0.001–0.005 S/cm; hence, the power factor was very low less than $10^{-5}\,W\,m^{-1}\,K^{-2}$ over the whole temperature range. This low electrical conductivity is attributed to the low carrier density[204)] as the sample was undoped.

The thermoelectric properties of La doped $BaSi_2$ is also shown in Fig. 18. It can be seen that the electrical conductivity has improved significantly by 2% La doping. The Seebeck coefficient has reduced only moderately and the thermal conductivity has also reduced slightly. As a result, the zT has improved ~7 times compared to the undoped $BaSi_2$. The electrical conductivity of the doped $BaSi_2$ is still small and shows a low doped semiconductor trend versus temperature. Therefore, it is expected that with proper doping of $BaSi_2$ the power factor; hence the zT, should further improve.

19.4 Calcium silicide (CaSi, Ca_2Si, and Ca_5Si_3)

Calcium silicides has multiple phases that are stable at room temperature. Of those phases Ca_5Si_3 and Ca_2Si have been reported to show semiconducting behavior. It has been estimated by pseudopotential calculations that Ca_2Si has the energy gap of 0.36 eV.[10)] This makes the material attractive for thermoelectric applications. The thermoelectric properties of calcium silicide phases are shown in Fig. 19. The figure shows the thermoelectric properties of Ca_5Si_3 and CaSi. Ca_2Si was not measured because the material was too brittle to allow thermoelectric measurements.[205)] The measured electrical conductivity values for CaSi and Ca_5Si_3 are 4000

© 2017 The Japan Society of Applied Physics

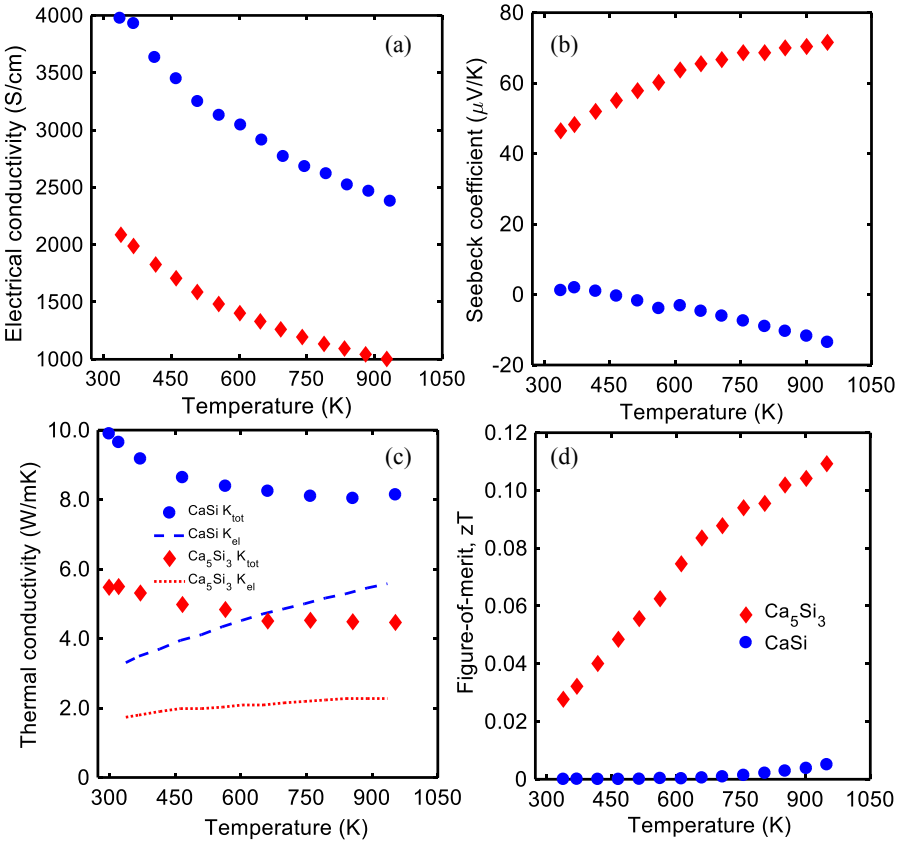

Fig. 19. (Color online) (a) Electrical conductivity, (b) Seebeck coefficient, (c) thermal conductivity, and (d) zT of CaSi and Ca_5Si_3 versus temperature.[205)]

and 2128 S/cm at 320 K, respectively. The electrical conductivity reduces with temperature indicating the metallic nature of the compounds. The magnitude of the Seebeck coefficient increases with increasing temperature for both samples. Both samples retain a positive Seebeck coefficient value until at about 320 K after which, in the case of CaSi, the Seebeck coefficient changes from positive to negative value with increasing temperature. This suggests that the majority carrier changes form hole to electron. Ca_5Si_3 shows positive Seebeck coefficient in all temperature ranges. The highest absolute value is observed for Ca_5Si_3 reaching 71 μV/K at 950 K.

In the thermal conductivity plot, the closed symbols show total thermal conductivity (κ_{total}) and the open symbols show the electronic thermal conductivity (κ_{el}). The ratios of the κ_{el} to the total thermal conductivity of both samples are about 50% at high temperature due to the large electrical conductivity. The lattice thermal conductivities of both samples decrease proportionally to T^{-1} indicating that phonon–phonon scattering is dominant in the temperature range. The lattice thermal conductivity of CaSi and Ca_5Si_3 reaches to 2.5 and 2.1 W/mK at about 970 K, respectively.[205)]

Table III lists some of the main properties of the silicide materials studied for thermoelectric applications so far. The values of thermal conductivity at temperature of highest zT and the peak zT values are also listed whenever available.

20. Thermoelectric module fabrication issues

While an overwhelming majority of thermoelectric research has been focused on developing and advancing material properties, it is equally important to address design challenges that ultimately sets the performance of a completed device. In general, there has been less effort in researching thermoelectric device issues in comparison to materials research, and this stands true for silicides as well. Two of the main challenges that face the integration of these materials into a device is in the metallization of contacts to the thermoelectric material, and the oxidation and sublimation that can become problematic at higher temperatures. A more detailed and in-depth look at these problems can be found in a review by Liu et al.[211)]

20.1 Metallization

A large challenge for interfacing thermoelectric materials with the metal interconnects between each leg is that they exhibit poor wettability to solders. In order to ensure good electrical bonding to the interconnects, thermoelectric materials must undergo a contact metallization which serves to increase its wettability and provide both a mechanically strong and low resistance bond. However, the metallization itself imposes a big challenge. The requirements for a good contact are (a) the metals must match the coefficient of thermal expansion (CTE) of the thermoelectric material to avoid mechanical failure at higher operating temperatures, (b) the metal contact must have low specific contact resistance with the thermoelectric material, and (c) the metal contact must exhibit good mechanical adhesion to the thermoelectric material.

20.2 Metal contacts to SiGe

Studies understanding the CTE and interface stresses of both nanostructured n and p-SiGe as well as mechanically alloyed (MA) SiGe where conducted by Ravi et al. at NASA's Jet Propulsion Laboratory (JPL).[212)] Their findings where that

© 2017 The Japan Society of Applied Physics

Table III. Material properties of silicides.

Material	Type (n or p)	Lattice structure	Density (g/cm^3)	Melting point (°C)	Bandgap (eV)	κ at max. zT ($W\,m^{-1}\,K^{-1}$)	Max. zT	Temp. at max. zT (K)	Ref.[a)]
Mg_2Si	(n)	Cubic	1.99	1102	0.61–0.67	2.9	0.5–0.6	850	108, 107, 104
Mg_2Si	(p)	Cubic	1.96	1102	0.61–0.67	2.2	0.11	650	104, 111
$Mg_2(Si,Sn)$	(n)	Cubic	—	800	—	2.3	1.3	700	106
$Mg_2(Si,Sn)$	(p)	Cubic	—	800	—	2.5	0.5	750	109
Mg_2SiGe	(p)	Cubic	2.42	—	0.68	1.7	0.36	625	111
Mg_2SiGe	(n)	Cubic	1.97	—	—	2.4	0.74	756	108
$MnSi_x$	(p)	Tetragonal	5.186–5.23	1156.85	0.4–0.7	2.8–3.8	0.5–0.6	800	120, 82
$Si_{1-x}Ge_x$[b)]	(p)	Diamond	2.329–5.323	937–1412	0.66–1.12	2.39	0.95	1173	46, 44, 206
$Si_{1-x}Ge_x$[b)]	(n)	Diamond	2.329–5.323	937–1412	0.66–1.12	1.97–2.7	1.2–1.3	1073–1223	36, 37, 47
$ReSi_2$	(p)	Tetragonal	10.78	1977	0.12	—	—	—	—
$ReSi_{1.75}$	(p)	Triclinic		1940	0.16	4.6	0.7	1060	144
Ru_2Si_3	(n)	Orthorhombic	6.96	1697	0.8–1.1	2.2	0.2	900	146
URu_2Si_2	(p)	Tetragonal	—	~1800	0.1	~2.3	0.1	1082	147
USi_3	(p)	Cubic	—	~1600	—	~9	~0.3	1173	148
Os_2Si_3	(p)	Orthorhombic	11.15	—	2.3	—	—	—	—
Ir_3Si_5	(p)	Monoclinic	10.12	1400	1.2	—	~0.3	1100	151
$CrSi_2$	(p)	Hexagonal	4.98	1470	0.32–0.35	12.1	0.25	980	137, 139
α-$FeSi_2$	(p)	Tetragonal	4.99	1217	Metallic	—	—	—	—
β-$FeSi_2$	(p)	Orthorhombic	4.93	Stable <928	0.7–0.95	4.6	0.25	750	165
β-$FeSi_2$	(n)	Orthorhombic	4.93	Stable <928	0.7–0.95	3.4–3.6	0.5	890–1050	85
CoSi	(p)	Cubic	6.58	1450	−0.041	11	0.04	300	173
CoSi	(n)	Cubic	6.58	1450	−0.041	14	0.35	400	175
$CoSi_{1-x}Ge_x$	(n)	Cubic	6.58	1450	—	10.5	0.1	350	179
$SrAl_2Si_2$	(n), (p)	Hexagonal	2.924	1020	~0.02	~55	0.034	381	199
$BaSi_2$	(n)	Orthorhombic	3.54–3.68	1180	1.13–1.30	0.6	0.07	950	204
$SrSi_2$	(n)	Cubic	3.35	1100	0.013–0.035	~5.5	0.4	300	193, 207
CaSi	(n)	Orthorhombic	2.31	1324	—	2.5	5.1×10^{-3}	950	205
Ca_5Si_3	(p)	Tetragonal	—	—	—	2.1	0.11	950	205
$CaSi_2$		Cubic	2.5	1020	0.36	—	—	—	—
$MoSi_2$	(p)	Body-centered tetragonal	6.28	~2030	—	48.5	—	—	—
β-$MoSi_2$	(p)	Hexagonal	6.32	~1900	0.07	—	—	—	—
β-$MoSi_2$	(n)	Hexagonal	6.32	~1900	0.07	—	—	—	—
WSi_2	(p)	Hexagonal	9.88	~2160	0.07	—	—	—	—
$CeSi_2$	(n)	Tetragonal	5.31	1620	—	12.6	0.085	240	183
LaSi	(n)	Orthorhombic	—	1620	0.19	6.71	0.002	957	53, 194

a) The listed references are for the thermal conductivity and zT values. The references for some other material properties are Refs. 208, 209, and 210.
b) Density (g/cm^3): $2.329 + 3.493x - 0.499x^2$, Melting point (°C): $1412 - 738x + 263x^2$ (solidus) and $1412 - 80x - 395x^2$ (liquidus), Bandgap (eV): for $x < 0.85$: $1.12 - 0.41x + 0.008x^2$ for $x > 0.85$: $1.86 - 1.2x$.

under three cyclic temperature tests from 323 to 1273 K the coefficient of variation (CV) for the three materials where 0.05, 12.33, and 4.72% and CTE's of 4.6, 4.4, and 6.0×10^{-6}/K for p-type, n-type nanostructured SiGe, and MA-SiGe, respectively. Simulations concluded that these expansions promote permanent length changes which lead to stresses that could cause cracks and mechanical failure at the thermoelectric-metal contact interface. Proper matching of the CTE of the metal to the thermoelectric material is required in order to ensure reliable application. Many studies have been previously conducted for low resistivity SiGe contacts for source drain formation in CMOS transistors and have found $TiSi_2$ and $CoSi_2$ as suitable candidates.[213–215)] However, these materials do not meet the mechanical requirements of CTE when operated at higher temperatures. Mo and W are more promising candidates as their natural CTEs are around $\sim(4–5) \times 10^{-6}$/K, respectively.[211)] When alloyed with Cu whose CTE sits higher at around 16.5×10^{-6}/K, they can be tuned to have a range of CTE's depending on the alloy composition ratios. To this point, more in depth studies need to be performed on the reliability of these contacts.

20.3 Metal contacts to $MnSi_2$

Petrova et al. explored the diffusion of Cr and Cr/Ni contacts on HMS, $MnSi_{1.75}$ after 3 h of annealing at 1120 K.[216)] Their findings where that Cr diffuses into the HMS forming two distinct Cr–Mn–Si phases, $Cr_{3-q}Mn_pSi$ and $Mn_{1-p}Cr_pSi$. However, the Cr/Ni stack showed a reduction in Cr diffusion into Mn due to the diffusion of Ni itself into the Cr and Mn regions and allowed only one Cr–Mn–Si phase to form, notably the $Cr_{3-q}Mn_pSi$ phase. This reduction in Cr diffusion

© 2017 The Japan Society of Applied Physics

from the Cr/Ni contact not only displayed the same high electrical and thermal conduction of the Cr contact, but showed improved mechanical properties as well since a higher concentration of Cr at the interface prevents interfacial pore formation. Further investigations studied Cu and Ni contacts directly sintered with the $MnSi_2$ material.[217,218] Electrical resistances were suitable for both but the authors noted the lack of mechanical stability under thermal stresses. Shi et al. further explored elemental Co, Ni, Cr, Ti, and Mo as well as MnSi and α-TiS_2 as contacts for HMS.[219] Their findings confirmed that while elemental contacts showed low electrical resistivity's, their CTE mismatch to the HMS was significant and caused poor mechanical bonding to the HMS and therefore is unreliable. On the other hand, silicide contacts, MnSi and α-TiS_2 showed greatly improved mechanical stability as the CTE closer matches that of HMS. Measurements of the contact resistance versus temperature showed comparable values between 10^{-4} to $10^{-5}\,\Omega\,cm^2$ for the contacts sintered directly on HMS. This study also showed the improved contact resistances from 10^{-5} to $10^{-6}\,\Omega\,cm^2$ for finer, nano-grained powders of MnSi and α-TiS_2.

20.4 Metal contacts to Mg_2Si

Nemoto et al. investigated an Al-doped n-type Mg_2Si device with Ni-contact (similar CTE to the thermoelectric material) metalized joined together with an Ag brazing to a Ni interconnect electrode.[220] The resistivity of the individual leg was measured to be $6.52 \times 10^{-6}\,\Omega\,cm^2$ leading to an ideal theoretical leg resistance of 3.86 mΩ. Actual measured resistance after all the contacts were added increased to 6.2 mΩ which lead to a contact resistance of $2 \times 10^{-3}\,\Omega\,cm^2$. Ideally the contact resistance should be at least an order of magnitude smaller than that of the thermoelectric material (typically $<10^{-5}\,\Omega\,cm^2$ for bulk thermoelectrics) as to not contribute additional parasitic resistance losses. The contact resistance, more notably the specific contact resistance between the contact metal and the thermoelectric leg is a problem of energy band alignments at the interface, i.e., choosing work functions of metals that minimize the energy barrier between the two and allow for low resistances. However, it has been known that having a high doping level at this interface can also help with resistances by allowing for not only thermionic emission of charge carriers over the Schottky barrier but tunneling through as well.[211] The authors in this study noted that this could be a useful technique for reducing the resistance between Ni and Mg_2Si. This improvement was investigated again by Nemoto et al. with Sb-doped Mg_2Si legs.[221] Similar to the last experiment, the study employed sintering Ni Contacts directly on the thermoelectric material. It was observed that the calculated specific contact resistance dropped to $7.8 \times 10^{-4}\,\Omega\,cm^2$ with the Sb doped samples and when the Cu electrodes replaced the Ni interconnects, a further reduction down to $5.9 \times 10^{-4}\,\Omega\,cm^2$. While a large improvement, this is still approximately an order of magnitude less than what is needed not to negatively impact the device performance; therefore, further studies on contacts to Mg_2Si material system is needed.

20.5 Sublimation and oxidation

Another consideration when integrating these materials into devices is how they react with the ambient at higher temperatures. Oxidation can lead to degradation in material quality and when operated at higher temperatures, sublimation or vaporization of the material into a gas can cause permanent physical changes to the thermoelectric leg that could lead to both electrical and mechanical issues. Careful investigation into the SiGe based RTG for NASA's Voyager 1 mission was conducted in order to assure the device endured a 50-year lifetime at high operating temperatures.[222] Without the coatings, the precipitation and eventual vaporization of Ge from the SiGe would occur at the outer surfaces of the material, changing both the mechanical and electrical properties. Chemical vapor deposited (CVD) SiO_2 and Si_3N_4 coatings around the legs were used as a means to suppress the sublimation control.[223] SiO_2 was found, however, to react with the silicon in the SiGe and create silicon monoxide, which is highly volatile. Therefore, Si_3N_4 and in combination with an argon gas was used as sufficient coating. Recently, in order to improve and slow down the sublimation rates even further, aerogels have been employed as a filler material in between the legs, instead of a vacuum or gas atmosphere.[223] Tests using skutterudite based materials who have similar sublimation rates to that of SiGe where conducted in order to evaluate the aerogels. The micro porous structure makes it exceedingly difficult for Ge diffusion out of the leg and the low thermal conductivity of the aerogel ensures little heat leakage both vertically and laterally between the hot/cold side contacts and between the legs, respectively. The tests showed a 700 fold improvement in sublimation rates between uncoated and coated samples. This process is believed to likely show the same improvements in other thermoelectric materials such as those in SiGe. There has been severe lack of studies investigating the longevity of other silicide thermoelectric materials at higher temperatures. While sublimation rates may not exhibit a large risk at operating temperature ranges of Mg_2Si and $MnSi_x$, long term oxidation issues could be an issue. Tani et al. studied the oxidation behavior of Mg_2Si and tested the improvement of oxidation resistance with a β-$FeSi_2$ coating at 873 K.[224] They found that oxygen diffuses into the Mg_2Si at temperatures above 723 K to yield volatile MgO and Si. Coatings of β-$FeSi_2$ showed to increase oxidation resistance by preventing the diffusion of oxygen into the silicide.

21. Future perspective of silicide thermoelectrics

Although the primary goal in thermoelectric community is achieving highest possible zT, other factors including the cost and device related issues, such as reliability, ease of fabrication, endurance, oxidation, etc., are equally important to be able to compete with other technologies. Hence, developing inexpensive, nontoxic and easily processed materials and competitive devices is equally important in research endeavors. Some silicide alloys have been identified so far that may meet such requirements, which has been the motivations for studying these materials.

A high peak zT does not necessarily produce an efficient device. At device level, a high zT over the working temperature and also across the hot to cold side temperature is important to achieve a high efficiency. According to Table III, silicide thermoelectrics have the potential to cover thermoelectric applications over a broad temperature range. While some silicides such as SiGe, Mg_2Si, $MnSi_{1.7}$, and $FeSi_2$ have been extensively studied and their thermoelectric properties have been optimized from various angels, some

© 2017 The Japan Society of Applied Physics

other silicides such as $BaSi_2$, $SrSi_2$, CoSi, $ReSi_{1.75}$, and Ru_2Si_3 and have also shown promising band structure and lattice properties, which can make them good candidates for thermoelectric application. However, there have been relatively less efforts in optimizing their properties. As a first step, carrier concentration optimization by doping may produce much higher zT than what has been measured. In addition, other techniques such as nanostructuring and band engineering may be used to further improve the properties of these silicides.

To this end, a computationally guided material research can help to predict the important properties, i.e., electrical conductivity, Seebeck coefficient and thermal conductivity, and to find the optimum doping concentration. It is well known today that the ideal thermoelectric material is described as phonon-glass, electron-crystal and has ideally the low thermal conductivity of a glass but the high electrical conductivity of a crystal. However, even if the lattice thermal conductivity is small like a glass, a high electrical conductivity will result in a high electronic thermal conductivity that will still limit the zT. Therefore, it is highly desired to find ways to reduce the electronic thermal conductivity, or the relevant Lorentz number. In addition, reducing the acoustic phonon deformation potential can enhance the carrier mobility as well as the Seebeck coefficient in materials that phonon scattering is dominant, which applies to many good thermoelectric materials. Such requirements call for theoretical study of the electron and phonon transport and their interaction at fundamental levels. Atomistic modeling provides better insights to understand the transport properties so that the underlying physical mechanisms can be identified and exploited in the design of new generation of thermoelectric materials.

In recent years, researchers have explored bulk materials, with a focus on those with large unit-cells,[225] such as clathrates, which contain angstrom-sized internal cages.[226] The presence of rattle atoms inside these cages or through the small-scale disorder present at the unit cell level can prohibit phonon transport in these materials and decrease the lattice thermal conductivity significantly. The electrical conductivity is related to the material's Fermi energy. In an un-doped semiconductor, where the Fermi energy lies between the valence band and the conduction band, the electrons are bound to the atomic nuclei, and the electrical conductivity is very low while in doped semiconductors the electrical conductivity can approach to that of metals, which is a more appropriate choice for thermoelectric applications. The Seebeck coefficient and thermal conductivity are also related to the material's Fermi energy; therefore, the Fermi energy must be optimized considering all parameters to achieve an optimum zT. For solids at room temperature, the thermal conductivity may vary from about $0.01\,W\,m^{-1}\,K^{-1}$ for aerogels to a few thousand $W\,m^{-1}\,K^{-1}$ for carbon nanotubes and graphene. Amorphous materials have a room-temperature thermal conductivity of $\sim 0.5\,W\,m^{-1}\,K^{-1}$ and silicon, $\sim 150\,W\,m^{-1}\,K^{-1}$. Thermal conductivity has two major sources electrons (mostly in metals) and phonons (mostly in non-metals). Knowledge of a material's electronic band structure and the mobility of the electrons is necessary to predict electrical conductivity, the Seebeck coefficient and the electronic contribution to the thermal conductivity. As the behavior of electrons may be governed by the Schrödinger equation, and quantum based calculations are required at fundamental levels which often necessitates very powerful computational resources and limits the research progress.

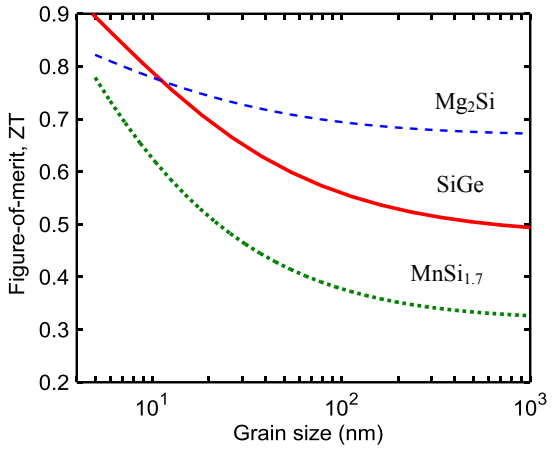

Fig. 20. (Color online) Predicted zT versus grain size for nanostructured p-type $Si_{0.8}Ge_{0.2}$, Mg_2Si, and $MnSi_{1.7}$.

21.1 Nanostructuring

Nanostructuring and band convergence have been adopted to enhance the efficiency of thermoelectric properties. Nanoscale effects have been known since 1990s that can enhance the thermoelectric properties by reducing the thermal conductivity and enhancing the thermoelectric power factor through modifications of the density of states. However, most enhancements so far have been through thermal conductivity reduction with less success on the improvement of the thermoelectric power factor.

The phonon mean free path is typically longer than the electron mean free path; hence, almost any sort of nanostructuring technique can increase phonon scattering (through interfaces or free surfaces) allowing for a decrease of thermal conductivity. A study on the effect of nanostructuring of $MnSi_{1.73}$ revealed that although nanostructuring reduces lattice thermal conductivity, the increased loss of electrical conductivity due to increased scattering at grain boundaries prohibits significant enhancement of the figure-of-merit for Ref. 82. Whenever, crystallite sizes lie between phonon MFPs and carrier MFPs, the reduction in thermal conductivity is coupled to reduction in electrical conductivity and the benefits of nanostructuring are decreased. Another study on the effect of Mg_2Si presented similar results.[83] It was shown that the nanostructuring in Mg_2Si would not be significantly beneficial to enhance figure-of-merit due to the detrimental effect of grain boundary scattering on carrier mobility. However, similar studies have shown that the nanostructuring is effective for $Si_{0.8}Ge_{0.2}$ where the thermal conductivity reduced to nearly 40% for an average crystallite size of 20 nm without noticeable deterioration in electrical conductivity. These trends are compared in Fig. 20.

21.2 Valleytronics of thermoelectric materials

The technique to control over the valley degree of freedom is known as valleytronics, which provides another material design tool for engineering both thermal and electrical transport properties. Valleytronics and engineering the charge carrier transport via multiple valleys has been widely used for designing good thermoelectric materials.[81,227–229] It has been

© 2017 The Japan Society of Applied Physics

generally thought that a multi-valley band structure can improve the thermoelectric power factor. However, more recent studies have shown that the interplay among the valleytronics parameters such as the degeneracy of the band, intervalley transitions, effective mass, scattering exponent, and the Fermi energy may result in improvements or degradation of any or all of the main thermoelectric properties.[230,231] For example, it was demonstrated that tuning the composition in $PbTe_{1-x}Se_x$ alloys can direct the convergence of 12 valleys which in turn results in a remarkable enhancement in power factor and zT.[229] Moreover, it has been shown that the extraordinary thermoelectric performance of n-type $CoSb_3$ skutterudites at high temperatures is resulted from convergence of a secondary conduction band with the degeneracy value of 12 with the primary band.[232] In another study on $Mg_2Si_{1-x}Sn_x$ solid solutions, using both ab-initio calculations and measurements, it was shown that compositional variations can lead to cross over of two conduction bands, which increases the band degeneracy and in turn rises the density-of-states effective mass at $x \sim 0.7$. At this composition, zT reached 1.3 around 700 K due to the enhanced power factor.[109] Such a band convergence with high degeneracy value has been reported for Si clathrates as well.[233] Clathrates have intrinsically low value of thermal conductivity, which, in combination with high degeneracy value of conduction bands, can exceptionally enhance the thermoelectric efficiency.[234] It has been revealed that the group of type VIII Si, Ge, and Sn clathrates has potentially large power factors due to the existence of a large number of carrier pockets near their band edges. The band structure calculations have shown that Si-VIII clathrate has 26 carrier pockets near their valence band edge.[234–236] It was also shown that Si-VIII and its derivatives intercalated by alkali and alkaline-earth atoms have conduction band degeneracy of 19 and 18, respectively.[234,235] Interestingly, the exceptionally high multi-valley band structure of the so far hypothetical Si_{46}-VIII near the Fermi energy can results in a giant power factor. Such a large power factor along with their well-known low thermal conductivity can make this group of clathrates promising thermoelectric materials.

22. Summary

A review of compounds of silicon and transition metal silicides used for thermoelectric applications was presented. Silicides are interesting for thermoelectric application due to several distinct characteristics. In addition to high efficiency, many of them are inexpensive, resistive to oxidation and degradation, mechanically robust, and non-toxic. Many of these materials also have lower density than bismuth and chalcogenide based alloys owing to the small density of silicon. The mainstream research activities to enhance the thermoelectric efficiency of silicides (and many other thermoelectric materials) have been focused on reducing the lattice thermal conductivity through techniques such as alloying, nanostructuring or defect engineering. These efforts have resulted in approaching the lower limit of thermal conductivity where the lattice thermal conductivity becomes comparable to the electronic thermal conductivity. Therefore, the focus is shifting towards the enhancement of the thermoelectric power factor with a focus on increasing the Seebeck coefficient. Engineering of quantum confinement, resonant impurity states to distort the electronic band structure, increasing the number of carrier pockets (or large band multiplicity) near the band edges, or hot carrier filtering through energy barriers are considered as some of the main directions in this context. However, to date, there is no clear roadmap for achieving many of these aims. Theoretical tools and computational advancements can help in the efforts to discover or design new materials. Identification of the underlying parameters that correlate the electron and phonon interaction can also help in designing materials with high thermoelectric power. Some of these techniques have been successfully implemented in several silicides such as $Mg_2(Si,Sn)$ and nanostructured SiGe with many other silicides yet to be engineered. Several metal silicides have shown a large power factor, but have not been very good thermoelectric materials because of their large electronic thermal conductivity. Therefore, material engineering that can reduce the electronic thermal conductivity is also highly desired.

Acknowledgments

This study is partially based upon work supported by Air Force Office of Scientific Research (AFOSR) under contract number FA9550-12-1-0225 and the National Science Foundation (NSF) under grant numbers EEC-1160483, ECCS-1351533, and CMMI-1363485.

1) G. S. Nolas, G. A. Slack, D. T. Modeli, T. M. Tritt, and A. C. Ehrlich, J. Appl. Phys. **79**, 4002 (1996).
2) J. P. Fleurial, T. Caillat, and A. Borshchevsky, Proc. 13th Int. Conf. Thermoelectrics, 1994, p. 40.
3) B. C. Sales, D. Mandrus, and R. K. Williams, Science **272**, 1325 (1996).
4) S. Q. Bai, X. Y. Huang, L. D. Chen, W. Zhang, X. Y. Zhao, and Y. F. Zhou, Appl. Phys. A **100**, 1109 (2010).
5) A. Saramat, G. Svensson, A. E. C. Palmqvist, C. Stiewe, E. Mueller, D. Platzek, S. G. Williams, D. M. Rove, J. D. Bryan, and G. D. Stucky, J. Appl. Phys. **99**, 023708 (2006).
6) S. R. Brown, S. M. Kauzlarich, F. Gascoin, and G. J. Snyder, Chem. Mater. **18**, 1873 (2006).
7) S. H. Yang, T. J. Zhu, T. Sun, J. He, S. N. Zhang, and X. B. Zhao, Nanotechnology **19**, 245707 (2008).
8) K. F. Hsu, S. Loo, F. Guo, W. Chen, J. S. Dyck, C. Uher, T. Hogan, E. K. Polychroniadis, and M. G. Kanatzidis, Science **303**, 818 (2004).
9) J. P. Heremans, V. Jovovic, E. S. Toberer, A. Saramat, K. Kurosaki, A. Charoenphakdee, S. Yamanaka, and G. J. Snyder, Science **321**, 554 (2008).
10) L. Zhao, S. Lo, Y. Zhang, H. Sun, G. Tan, C. Uher, C. Wolverton, V. P. Dravid, and M. G. Kanatzidis, Nature **508**, 373 (2014).
11) L. D. Hicks and M. S. Dresselhaus, Phys. Rev. B **47**, 12727 (1993).
12) G. Chen, Phys. Rev. B **57**, 14958 (1998).
13) R. Venkatasubramanian, E. Siivola, T. Colpitts, and B. O'Quinn, Nature **413**, 597 (2001).
14) D. Vashaee, Y. Zhang, A. Shakouri, G. Zeng, and Y. Chiu, Phys. Rev. B **74**, 195315 (2006).
15) D. Vashaee and A. Shakouri, J. Appl. Phys. **95**, 1233 (2004).
16) G. Zeng, X. Fan, C. LaBounty, E. Croke, Y. Zhang, J. Christofferson, D. Vashaee, A. Shakouri, and J. E. Bowers, MRS Proc. **793**, S2 (2003).
17) T. C. Harman, P. J. Taylor, M. P. Walsh, and B. E. LaForge, Science **297**, 2229 (2002).
18) J. M. O. Zide, D. Vashaee, G. Zeng, J. E. Bowers, A. Shakouri, and A. C. Gossard, Phys. Rev. B **74**, 205335 (2006).
19) J. M. Zide, D. O. Klenov, S. Stemmer, A. C. Gossard, G. Zeng, J. E. Bowers, D. Vashaee, and A. Shakouri, Appl. Phys. Lett. **87**, 112102 (2005).
20) W. Kim, S. L. Singer, A. Majumdar, D. Vashaee, Z. Bian, A. Shakouri, G. Zeng, J. E. Bowers, J. M. O. Zide, and A. C. Gossard, Appl. Phys. Lett. **88**, 242107 (2006).

© 2017 The Japan Society of Applied Physics

21) X. Fan, G. Zeng, E. Croke, C. LaBounty, D. Vashaee, A. Shakouri, and J. E. Bowers, Electron. Lett. **37**, 126 (2001).
22) B. Poudel, Q. Hao, Y. Ma, Y. Lan, A. Minnich, B. Yu, X. Yan, D. Wang, A. Muto, D. Vashaee, X. Chen, J. Liu, M. S. Dresselhaus, G. Chen, and Z. Ren, Science **320**, 634 (2008).
23) A. M. Dehkordi and D. Vashaee, Phys. Status Solidi A **209**, 2131 (2012).
24) N. Satyala, A. Tahmasbi Rad, Z. Zamanipour, P. Norouzzadeh, J. S. Krasinski, L. Tayebi, and D. Vashaee, J. Appl. Phys. **115**, 044304 (2014).
25) K. Biswas, J. He, I. D. Blum, C. Wu, T. P. Hogan, D. N. Seidman, V. P. Dravid, and M. G. Kanatzidis, Nature **489**, 414 (2012).
26) N. Satyala, P. Norouzzadeh, and D. Vashaee, in *Nanoscale Thermoelectrics*, ed. X. Wang and Z. M. Wang (Springer International Publishing, Cham, 2014) Lecture Notes in Nanoscale Science and Technology, Vol. 16, Chap. 4.
27) N. Hirayama, T. Iida, H. Funashima, S. Morioka, M. Sakamoto, K. Nishio, Y. Kogo, Y. Takanashi, and N. Hamada, Jpn. J. Appl. Phys. **54**, 07JC05 (2015).
28) S. Tada, Y. Isoda, H. Udono, H. Fujiu, S. Kumagai, and Y. Shinohara, J. Electron. Mater. **43**, 1580 (2014).
29) Q. Zhang, J. He, T. J. Zhu, S. N. Zhang, X. B. Zhao, and T. M. Tritt, Appl. Phys. Lett. **93**, 102109 (2008).
30) Y. Hayakawa, M. Arivanandhan, Y. Saito, T. Koyama, Y. Momose, H. Ikeda, A. Tanaka, C. Wen, Y. Kubota, T. Nakamura, S. Bhattacharya, D. K. Aswal, S. M. Babu, Y. Inatomi, and H. Tatsuoka, Thin Solid Films **519**, 8532 (2011).
31) H. Mo, J. Liu, and M. C. Öztürk, MRS Proc. **745**, N4 (2002).
32) J. Liu and M. C. Öztürk, IEEE Trans. Electron Devices **52**, 1535 (2005).
33) E. Alptekin, C. J. Kirkpatrick, V. Misra, and M. C. Öztürk, IEEE Trans. Electron Devices **56**, 1220 (2009).
34) A. J. Minnich, H. Lee, X. W. Wang, G. Joshi, M. S. Dresselhaus, Z. F. Ren, G. Chen, and D. Vashaee, Phys. Rev. B **80**, 155327 (2009).
35) C. B. Vining and C. E. Allevato, Proc. 27th Intersociety Energy Conversion Engineering Conf. (IECEC-92), 1992, Vol. 3, p. 489.
36) A. Nozariasbmarz, Z. Zamanipour, P. Norouzzadeh, J. S. Krasinski, and D. Vashaee, RSC Adv. **6**, 49643 (2016).
37) A. Nozariasbmarz, P. Roy, Z. Zamanipour, J. H. Dycus, M. J. Cabral, J. M. LeBeau, J. S. Krasinski, and D. Vashaee, APL Mater. **4**, 104814 (2016).
38) N. Mingo and D. Hauser, Nano Lett. **9**, 711 (2009).
39) E. N. Nikitin, Sov. Phys. Tech. Phys. **3**, 20 (1958).
40) E. N. Nikitin, Sov. Phys. Tech. Phys. **3**, 23 (1958).
41) M. I. Fedorov, J. Thermoelectr. **2**, 51 (2009).
42) C. B. Vining, J. Appl. Phys. **69**, 331 (1991).
43) D. M. Rowe, *Thermoelectrics Handbook: Macro to Nano* (CRC Press, Boca Raton, FL, 2005).
44) Z. Zamanipour, X. Shi, A. M. Dehkordi, J. S. Krasinski, and D. Vashaee, Phys. Status Solidi A **209**, 2049 (2012).
45) A. Nozariasbmarz, A. Tahmasbi Rad, Z. Zamanipour, J. S. Krasinski, L. Tayebi, and D. Vashaee, Scr. Mater. **69**, 549 (2013).
46) G. Joshi, H. Lee, Y. Lan, X. Wang, G. Zhu, D. Wang, R. W. Gould, D. C. Cuff, M. Y. Tang, M. S. Dresselhaus, G. Chen, and Z. F. Ren, Nano Lett. **8**, 4670 (2008).
47) X. W. Wang, H. Lee, Y. C. Lan, G. H. Zhu, G. Joshi, D. Z. Wang, J. Yang, A. J. Muto, M. Y. Tang, J. Klatsky, S. Song, M. S. Dresselhaus, G. Chen, and Z. F. Ren, Appl. Phys. Lett. **93**, 193121 (2008).
48) B. L. Liao, B. Qiu, J. W. Zhou, S. Huberman, K. Esfarjani, and G. Chen, Phys. Rev. Lett. **114**, 115901 (2015).
49) F. A. Trumbore, Bell Labs Tech. J. **39**, 205 (1960).
50) Z. Zamanipour, J. S. Krasinski, and D. Vashaee, J. Appl. Phys. **113**, 143715 (2013).
51) J. P. Dismukes, L. Ekstrom, E. F. Steigmeier, I. Kudman, and D. S. Beers, J. Appl. Phys. **35**, 2899 (1964).
52) C. B. Vining, Proc. 9th Int. Conf. Thermoelectrics, 1990, p. 249.
53) C. B. Vining, *CRC Handbook of Thermoelectrics* (CRC Press, Boca Raton, FL, 1995) p. 277.
54) R. Amatya and R. J. Ram, J. Electron. Mater. **41**, 1011 (2012).
55) R. W. Olesinski and G. J. Abbaschian, Bull. Alloy Phase Diagrams **7**, 170 (1986).
56) *Landolt–Börnstein: Group IV Physical Chemistry* (Springer, Heidelberg, 2002) Vol. 19B1, p. 296.
57) M. Zhang, J. G. Wen, M. Y. Efremov, E. A. Olson, Z. S. Zhang, L. Hu, L. P. de la Rama, R. Kummamuru, K. L. Kavanagh, Z. Ma, and L. H. Allen, J. Appl. Phys. **111**, 093516 (2012).
58) *Landolt–Börnstein: Group IV Physical Chemistry* (Springer, Heidelberg, 1998) Vol. 5J, p. 1.
59) *Landolt–Börnstein: Group IV Physical Chemistry* (Springer, Heidelberg, 1993) Vol. 5C, p. 1.
60) *Landolt–Börnstein: Group IV Physical Chemistry* (Springer, Heidelberg, 1997) Vol. 5G, p. 1.
61) M. I. Fedorov and G. N. Isachenko, Jpn. J. Appl. Phys. **54**, 07JA05 (2015).
62) R. K. Pisharody and L. P. Garvey, Proc. 13th Intersoc. Energy Conversion Engineering Conf., 1978, p. 1963.
63) D. M. Rowe, J. Phys. D **7**, 1843 (1974).
64) C. M. Bhandari and D. M. Rowe, Proc. 2nd Int. Conf. Thermoelectric Energy Conversion, 1978, p. 32.
65) D. M. Rowe, V. S. Shukla, and N. Savvides, Nature **290**, 765 (1981).
66) D. M. Rowe and V. S. Shukla, J. Appl. Phys. **52**, 7421 (1981).
67) C. B. Vining and J.-P. Fleurial, Proc. 10th Symp. Space Nuclear Power and Propulsion, 1993, p. 10.
68) F. J. DiSalvo, Science **285**, 703 (1999).
69) L. E. Bell, Science **321**, 1457 (2008).
70) J. R. Szczech, J. M. Higgins, and S. Jin, J. Mater. Chem. **21**, 4037 (2011).
71) X. Fan, G. Zeng, C. LaBounty, D. Vashaee, J. Christofferson, A. Shakouri, and J. E. Bowers, Proc. 20th Int. Conf. Thermoelectrics, 2001, p. 405.
72) D. M. Rowe, Appl. Energy **40**, 241 (1991).
73) J. W. Vandersande and J.-P. Fleurial, 15th Int. Conf. Thermoelectrics, 1996.
74) A. Majumdar, Science **303**, 777 (2004).
75) L. D. Zhao, G. Tan, S. Hao, J. He, Y. Pei, H. Chi, H. Wang, S. Gong, H. Xu, V. P. Dravid, C. Uher, G. J. Snyder, C. Wolverton, and M. G. Kanatzidis, Science **351**, 141 (2016).
76) J. LaGrandeur, D. Crane, S. Hung, B. Mazar, and A. Eder, 25th Int. Conf. Thermoelectrics, 2006.
77) D. M. Rowe, Int. J. Innovations Energy Syst. Power **1**, 13 (2006).
78) D. Kraemer, B. Poudel, H.-P. Feng, J. C. Caylor, B. Yu, X. Yan, Y. Ma, X. Wang, D. Wang, A. Muto, K. McEnaney, M. Chiesa, Z. Ren, and G. Chen, Nat. Mater. **10**, 532 (2011).
79) G. R. Schmidt, R. L. Wiley, and R. L. Richardson, AIP Conf. Proc. **746**, 429 (2005).
80) J. P. Fleurial, P. Gogna, G. Chen, M. S. Dresselhaus, H. Lee, M. Y. Tang, Z. F. Ren, D. Wang, S. Bux, D. King, R. Kaner, and R. Blair, 6th European Conf. Thermoelectrics, 2008, I-04-1.
81) M. S. Dresselhaus, G. Chen, M. Y. Tang, R. Yang, H. Lee, D. Wang, Z. Ren, J.-P. Fleurial, and P. Gogna, Adv. Mater. **19**, 1043 (2007).
82) P. Norouzzadeh, Z. Zamanipour, J. S. Krasinski, and D. Vashaee, J. Appl. Phys. **112**, 124308 (2012).
83) N. Satyala and D. Vashaee, Appl. Phys. Lett. **100**, 073107 (2012).
84) N. Satyala and D. Vashaee, J. Appl. Phys. **112**, 093716 (2012).
85) M. Mohebali, Y. Liu, L. Tayebi, J. S. Krasinski, and D. Vashaee, Renewable Energy **74**, 940 (2015).
86) M. I. Fedorov and V. K. Zaitsev, in *Modules, Systems, and Applications in Thermoelectrics*, ed. D. M. Rowe (CRC Press, Boca Raton, FL, 2012) Chap. 11.
87) Y. Lan, A. J. Minnich, G. Chen, and Z. Ren, Adv. Funct. Mater. **20**, 357 (2010).
88) D. J. Bergman and O. Levy, J. Appl. Phys. **70**, 6821 (1991).
89) D. J. Bergman and L. G. Fel, J. Appl. Phys. **85**, 8205 (1999).
90) J. H. Bahk, Z. Bian, M. Zebarjadi, P. Santhanam, R. Ram, and A. Shakouri, Appl. Phys. Lett. **99**, 072118 (2011).
91) Z. Zamanipour and D. Vashaee, J. Appl. Phys. **112**, 093714 (2012).
92) K. A. Borup, J. de Boor, H. Wang, F. Drymiotis, F. Gascoin, X. Shi, L. Chen, M. I. Fedorov, E. Muller, B. B. Iversena, and G. J. Snyder, Energy Environ. Sci. **8**, 423 (2015).
93) G. J. Snyder and T. S. Ursell, Phys. Rev. Lett. **91**, 148301 (2003).
94) D. M. Rowe, *CRC Handbook of Thermoelectrics* (CRC Press, Boca Raton, FL, 1995).
95) H. J. Goldsmid and A. W. Penn, Phys. Lett. A **27**, 523 (1968).
96) C. B. Vining, W. Laskow, J. O. Hanson, R. R. Van der Beck, and P. D. Gorsuch, J. Appl. Phys. **69**, 4333 (1991).
97) M. Abudakka, A. Nozariasbmarz, L. Tayebi, J. S. Krasisnki, and D. Vashaee, Energy Harvesting Syst. **2**, 47 (2015).
98) J. A. Martinez, P. P. Provencio, S. T. Picraux, J. P. Sullivan, and B. S. Swartzentruber, J. Appl. Phys. **110**, 074317 (2011).
99) E. K. Lee, L. Yin, Y. Lee, J. W. Lee, S. J. Lee, J. Lee, S. N. Cha, D. Whang, G. S. Hwang, K. Hippalgaonkar, A. Majumdar, C. Yu, B. L. Choi, J. M. Kim, and K. Kim, Nano Lett. **12**, 2918 (2012).
100) S. M. Lee, D. G. Cahill, and R. Venkatasubramanian, Appl. Phys. Lett. **70**, 2957 (1997).
101) A. Samarelli, L. Ferre Llin, S. Cecchi, J. Frigerio, T. Etzelstorfer, E. Müller, Y. Zhang, J. R. Watling, D. Chrastina, G. Isella, J. Stangl, J. P. Hague, J. M. R. Weaver, P. Dobson, and D. J. Paul, J. Appl. Phys. **113**, 233704 (2013).
102) Y. Lee, A. J. Pak, and G. S. Hwang, Phys. Chem. Chem. Phys. **18**, 19544 (2016).
103) P. Norouzzadeh, A. Nozariasbmarz, J. S. Krasinski, and D. Vashaee,

© 2017 The Japan Society of Applied Physics

J. Appl. Phys. **117**, 214303 (2015).
104) H. Udono, H. Tajima, M. Uchikoshi, and M. Itakura, Jpn. J. Appl. Phys. **54**, 07JB06 (2015).
105) K. Arai, A. Sasaki, Y. Kimori, M. Iida, T. Nakamura, Y. Yamaguchi, K. Fujimoto, R. Tamura, T. Iida, and K. Nishio, Mater. Sci. Eng. B **195**, 45 (2015).
106) W. Liu, X. Tan, K. Yin, H. Liu, X. Tang, J. Shi, Q. Zhang, and C. Uher, Phys. Rev. Lett. **108**, 166601 (2012).
107) N. Satyala, J. S. Krasinski, and D. Vashaee, Acta Mater. **74**, 141 (2014).
108) H. Ihou-Mouko, C. Mercier, J. Tobola, G. Pont, and H. Scherrer, J. Alloys Compd. **509**, 6503 (2011).
109) Q. Zhang, L. Cheng, W. Liu, Y. Zheng, X. Su, H. Chi, H. Liu, Y. Yan, X. Tang, and C. Uher, Phys. Chem. Chem. Phys. **16**, 23576 (2014).
110) Y. Niwa, Y. Todaka, T. Masuda, T. Kawai, and M. Umemoto, Mater. Trans. **50**, 1725 (2009).
111) H. Q. Ye and S. Amelinckx, J. Solid State Chem. **61**, 8 (1986).
112) O. Schwomma, H. Nowotny, and A. Wittmann, Monatsh. Chem. **94**, 681 (1963) [in German].
113) O. Schwomma, A. Preisinger, H. Nowotny, and A. Wittmann, Monatsh. Chem. **95**, 1527 (1964) [in German].
114) G. Flieher, H. Vollenkle, and H. Nowotny, Monatsh. Chem. **98**, 2173 (1967) [in German].
115) H. W. Knott, M. H. Mueller, and L. Heaton, Acta Crystallogr. **23**, 549 (1967).
116) G. Zwilling and H. Nowotny, Monatsh. Chem. **104**, 668 (1973) [in German].
117) U. Gottlieb, A. Sulpice, B. Lambert-Andron, and O. Laborde, J. Alloys Compd. **361**, 13 (2003).
118) L. D. Ivanova, N. K. Abrikosov, E. I. Elagina, and V. D. Khvostikova, Izv. Akad. Nauk SSSR, Neorg. Mater. **5**, 1933 (1969) [in Russian].
119) M. Iioka, D. Ishada, S. Kojima, and H. Udono, Phys. Status Solidi C **10**, 1808 (2013).
120) Z. Zamanipour, X. Shi, M. Mozafari, J. S. Krasinski, L. Tayebi, and D. Vashaee, Ceram. Int. **39**, 2353 (2013).
121) D. Y. Nhi Truong, H. Kleinke, and F. Gascoin, Intermetallics **66**, 127 (2015).
122) A. J. Zhou, T. J. Zhu, X. B. Zhao, S. H. Yang, T. Dasgupta, C. Stiewe, R. Hassdorf, and E. Mueller, J. Electron. Mater. **39**, 2002 (2010).
123) W. Luo, H. Li, F. Fu, W. Hao, and X. Tang, J. Electron. Mater. **40**, 1233 (2011).
124) X. Chen, A. Weathers, D. Salta, L. Zhang, J. Zhou, J. B. Goodenough, and L. Shi, J. Appl. Phys. **114**, 173705 (2013).
125) T. Itoh and N. Ono, MRS Proc. **1490**, 127 (2012).
126) W. Luo, H. Li, Y. Yan, Z. Lin, X. Tang, Q. Zhang, and C. Uher, Intermetallics **19**, 404 (2011).
127) S. V. Faleev and F. Léonard, Phys. Rev. B **77**, 214304 (2008).
128) C. Fu, H. Xie, T. J. Zhu, J. Xie, and X. B. Zhao, J. Appl. Phys. **112**, 124915 (2012).
129) X. Chen, S. N. Girard, F. Meng, E. Lara-Curzio, S. Jin, J. B. Goodenough, J. Zhou, and L. Shi, Adv. Energy Mater. **4**, 1400452 (2014).
130) A. Yamamoto, S. Ghodke, H. Miyazaki, M. Inukai, Y. Nishino, M. Matsunami, and T. Takeuchi, Jpn. J. Appl. Phys. **55**, 020301 (2016).
131) S. Ghodke, N. Hiroishi, A. Yamamoto, H. Ikuta, M. Matsunami, and T. Takeuchi, J. Electron. Mater. **45**, 5279 (2016).
132) X. She, X. Su, H. Du, T. Liang, G. Zheng, Y. Yan, R. Akram, C. Uher, and X. Tang, J. Mater. Chem. C **3**, 12116 (2015).
133) V. Ponnambalam, D. T. Morelli, S. Bhattacharya, and T. M. Tritt, J. Alloys Compd. **580**, 598 (2013).
134) D. Y. Nhi Truong, D. Berthebaud, F. Gascoin, and H. Kleinke, J. Electron. Mater. **44**, 3603 (2015).
135) M. Saleemi, A. Famengo, S. Fiameni, S. Boldrini, S. Battiston, M. Johnsson, M. Muhammed, and M. S. Toprak, J. Alloys Compd. **619**, 31 (2015).
136) S. Perumal, S. Gorsse, U. Ail, M. Prakasam, B. Chevalier, and A. M. Umarji, J. Mater. Sci. **48**, 6018 (2013).
137) I. Nishida, J. Mater. Sci. **7**, 1119 (1972).
138) M. C. Bost and J. E. Mahan, J. Appl. Phys. **63**, 839 (1988).
139) B. K. Voronov, L. D. Dudkin, and N. N. Trusova, *Khimicheskaya Svyaz v Poluprovodnikah* (Nauka i Tekhnika, Minsk, 1969) p. 291 [in Russian].
140) Z. J. Pan, L. T. Zhang, and J. S. Wu, Scr. Mater. **56**, 257 (2007).
141) Y. Ohishi, A. Mohamad, Y. Miyazaki, H. Muta, K. Kurosaki, and S. Yamanaka, J. Phys. Chem. Solids **87**, 153 (2015).
142) H. Nagai, T. Takamatsu, Y. Iijima, K. Hayashi, and Y. Miyazaki, J. Alloys Compd. **687**, 37 (2016).
143) U. Gottlieb, B. Lambert-Andron, F. Nava, M. Affronte, O. Laborde, A. Rouault, and R. Madar, J. Appl. Phys. **78**, 3902 (1995).
144) H. Inui, MRS Proc. **886**, 0886-F06-08 (2005).
145) D. J. Poutcharovsky, K. Yvon, and E. Parthe, J. Less-Common Met. **40**, 139 (1975).
146) B. A. Simkin, Y. Hayashi, and H. Inui, Intermetallics **13**, 1225 (2005).
147) Y. Arita, K. Terao, S. Mitsuda, Y. Nishi, T. Matsui, and T. Nagasaki, J. Nucl. Mater. **294**, 206 (2001).
148) L. H. Brixner, J. Inorg. Nucl. Chem. **25**, 783 (1963).
149) J. Schumann, D. Elefant, C. Gladun, A. Heinrich, W. Pitschke, H. Lange, W. Henrion, and R. Grotzschel, Phys. Status Solidi A **145**, 429 (1994).
150) C. E. Allevato and C. B. Vining, Proc. 28th Intersoc. Energy Conversion Engineering Conf. (IECEC-93), 1993, Vol. 1, p. 239.
151) W. Pitschke, R. Kurt, A. Heinrich, J. Schumann, H. Grießmann, H. Vinzelberg, and A. T. Burkov, J. Mater. Res. **15**, 772 (2000).
152) H. Udono, I. Kikuma, T. Okuno, Y. Masumoto, H. Tajima, and S. Komuro, Thin Solid Films **461**, 182 (2004).
153) M. C. Bost and J. E. Mahan, J. Vac. Sci. Technol. B **4**, 1336 (1986).
154) G. Behr, J. Werner, G. Weise, A. Heinrich, A. Burkov, and C. Gladun, Phys. Status Solidi A **160**, 549 (1997).
155) I. Yamauchi, S. Ueyama, and I. Ohnaka, Mater. Sci. Eng. A **208**, 108 (1996).
156) R. M. Ware and D. J. McNeill, Proc. IEE **111**, 178 (1964).
157) Y. Isoda and H. Udono, in *Materials, Preparation, and Characterization in Thermoelectrics*, ed. D. M. Rowe (CRC Press, Boca Raton, FL, 2012) Chap. 18.
158) A. Heinrich, H. Griessmann, G. Behr, K. Ivanenko, J. Schumann, and H. Vinzelberg, Thin Solid Films **381**, 287 (2001).
159) H. P. Geserich, S. K. Sharma, and W. A. Theiner, Philos. Mag. **27**, 1001 (1973).
160) M. Nikolaeva, M. Sendova-Vassileva, D. Dimova-Malinovska, D. Karpuzov, J. C. Pivin, and G. Beshkov, Vacuum **69**, 221 (2002).
161) K. Matsubara, N. Minemura, J. Miyata, K. Kishimoto, K. Kawamura, T. Koyanagi, and T. Miki, Proc. 10th Int. Conf. Therrnoelectrics, 1991, p. 40.
162) M. Komabayashi, K. Hijikata, and S. Ido, Jpn. J. Appl. Phys. **30**, 331 (1991).
163) E. Groβ, M. Riffel, and U. Stöhrer, J. Mater. Res. **10**, 34 (1995).
164) S. W. Kim, M. K. Cho, Y. Mishima, and D. C. Choi, Intermetallics **11**, 399 (2003).
165) H. Takizawa, P. F. Mo, T. Endo, and M. Shimada, J. Mater. Sci. **30**, 4199 (1995).
166) M. Umemoto, Mater. Trans. JIM **36**, 373 (1995).
167) M. Ito, H. Nagai, T. Tahata, S. Katsuyama, and K. Majima, J. Appl. Phys. **92**, 3217 (2002).
168) L. Han, X.-F. Tang, W.-Q. Cao, and Q.-J. Zhang, Chin. Phys. B **18**, 287 (2009).
169) X. Qu, S. Lü, J. Hu, and Q. Meng, J. Alloys Compd. **509**, 10217 (2011).
170) M. Shibuya, M. Kawata, Y. Shinohara, and M. Ohyanagi, Trans. Mater. Res. Soc. Jpn. **40**, 219 (2015).
171) I. Nishida, Phys. Rev. B **7**, 2710 (1973).
172) T. Kojima, Phys. Status Solidi A **111**, 233 (1989).
173) C. S. Lue, Y. K. Kuo, C. L. Huang, and W. J. Lai, Phys. Rev. B **69**, 125111 (2004).
174) C. C. Li, W. L. Ren, L. T. Zhang, K. Ito, and J. S. Wu, J. Appl. Phys. **98**, 063706 (2005).
175) M. I. Fedorov and V. K. Zaitsev, in *CRC Handbook of Thermoelectrics*, ed. D. M. Rowe (CRC Press, Boca Raton, FL, 1995) p. 299.
176) Z. J. Pan, L. T. Zhang, and J. S. Wu, Comput. Mater. Sci. **39**, 752 (2007).
177) W. L. Ren, C. C. Li, L. T. Zhang, K. Ito, and J. S. Wu, J. Alloys Compd. **392**, 50 (2005).
178) E. Skoug, C. Zhou, Y. Pei, and D. T. Morelli, Appl. Phys. Lett. **94**, 022115 (2009).
179) Y. K. Kuo, K. M. Sivakumar, S. J. Huang, and C. S. Lue, J. Appl. Phys. **98**, 123510 (2005).
180) H. Sun, X. Lu, and D. T. Morelli, J. Electron. Mater. **42**, 1352 (2013).
181) T. Tokushima, I. Nishida, K. Sakata, and T. Sakata, J. Mater. Sci. **4**, 978 (1969).
182) A. J. Zhou, T. J. Zhu, H. L. Ni, Q. Zhang, and X. B. Zhao, J. Alloys Compd. **455**, 255 (2008).
183) A. V. Morozkin, V. A. Stupnikov, V. N. Nikiforov, N. Imaoka, and I. Morimoto, J. Alloys Compd. **415**, 12 (2006).
184) V. N. Nikiforov, V. Y. Irkhin, and A. V. Morozkin, in *Low-Dimensional Functional Materials*, ed. R. Egger, D. Matrasulov, and K. Rakhimov (Springer, Dordrecht, 2013) NATO Science for Peace and Security Series B: Physics and Biophysics, Chap. 19.
185) T. Yamada and Y. Hisanori, Intermetallics **19**, 908 (2011).
186) T. Nonomura, C. Wen, A. Kato, K. Isobe, Y. Kubota, T. Nakamura, M. Yamashita, Y. Hayakawa, and H. Tatsuoka, Phys. Procedia **11**, 110 (2011).
187) F. M. d'Heurle, C. S. Petersson, and M. Y. Tsai, J. Appl. Phys. **51**, 5976

© 2017 The Japan Society of Applied Physics

(1980).
188) K. Favier, G. Bernard-Granger, C. Navone, M. Soulier, M. Boidot, J. Leforestier, J. Simon, J.-C. Tedenac, and D. Ravot, Acta Mater. **64**, 429 (2014).
189) J. Mackey, F. Dynsys, and A. Sehirlioglu, Acta Mater. **98**, 263 (2015).
190) K. Hashimoto, K. Kurosaki, Y. Imamura, H. Muta, and S. Yamanaka, 26th Int. Conf. Thermoelectrics (ICT 2007), 2007, p. 245.
191) Y. Imai and A. Watanabe, Intermetallics **14**, 666 (2006).
192) C. S. Lue, C. N. Kuo, J. Y. Huang, H. L. Hsieh, H. Y. Liao, B. Ramachandran, and Y. K. Kuo, J. Phys. D **46**, 315303 (2013).
193) Y. K. Kuo, B. Ramachandran, and C. S. Lue, Front Chem. **2**, 1 (2014).
194) K. Hashimoto, K. Kurosaki, Y. Imamura, H. Muta, and S. Yamanaka, J. Appl. Phys. **102**, 063703 (2007).
195) C. S. Lue, M. D. Chou, N. Kaurav, Y. T. Chung, and Y. K. Kuo, Appl. Phys. Lett. **94**, 192105 (2009).
196) C. S. Lue, S. F. Wong, J. Y. Huang, H. L. Hsieh, H. Y. Liao, B. Ramachandran, and Y. K. Kuo, J. Appl. Phys. **113**, 013710 (2013).
197) Y. K. Kuo, C. S. Lue, G. Hsu, J. Y. Huang, and H. L. Hsieh, Mater. Chem. Phys. **137**, 604 (2012).
198) M. Imai, A. Sato, T. Kimura, and T. Aoyagi, Thin Solid Films **519**, 8496 (2011).
199) S. M. Kauzlarich, C. L. Condron, J. K. Wassei, T. Ikeda, and G. J. Snyder, J. Solid State Chem. **182**, 240 (2009).
200) M. Imai, H. Abe, and K. Yamada, Inorg. Chem. **43**, 5186 (2004).
201) T. Suemasu, T. Saito, K. Toh, A. Okada, and M. A. Khan, Thin Solid Films **519**, 8501 (2011).
202) M. Imai and T. Hirano, J. Alloys Compd. **224**, 111 (1995).
203) T. Nakamura, T. Suemasu, K. Takakura, F. Hasegawa, A. Wakahara, and M. Imai, Appl. Phys. Lett. **81**, 1032 (2002).
204) K. Hashimoto, K. Kurosaki, H. Muta, and S. Yamanaka, Mater. Trans. **49**, 1737 (2008).
205) Y. Imamura, H. Muta, K. Kurosaki, and S. Yamanaka, Int. Conf. Thermoelectrics, 2006.
206) Z. Zamanipour, E. Salahinejad, P. Norouzzadeh, J. S. Krasinski, L. Tayebi, and D. Vashaee, J. Appl. Phys. **114**, 023705 (2013).
207) *CRC Handbook of Chemistry and Physics* (CRC Press, Boca Raton, FL, 2010) 90th ed.
208) R. C. Ropp, *Encyclopedia of the Alkaline Earth Compounds* (Elsevier, Amsterdam, 2013).
209) V. Borisenko, *Semiconducting Silicides: Basics, Formation, Properties* (Springer, Heidelberg, 2000) Springer Series in Materials Science, Vol. 39.
210) Landolt–Börnstein Online Library, Vol. III [http://www.springermaterials.com/].
211) W. Liu, Q. Jie, H. S. Kim, and Z. Ren, Acta Mater. **87**, 357 (2015).
212) V. Ravi, S. Firdosy, T. Caillat, E. Brandon, K. Van Der Walde, L. Maricic, and A. Sayir, J. Electron. Mater. **38**, 1433 (2009).
213) W. J. Qi, B. Z. Li, W. N. Huang, Z. G. Gu, H. Q. Lu, X. J. Zhang, M. Zhang, G. S. Dong, D. C. Miller, and R. G. Aitken, J. Appl. Phys. **77**, 1086 (1995).
214) W. J. Qi, B. Z. Li, G. B. Jiang, W. N. Huang, and Z. G. Gu, IEEE Region 10 Int. Conf. Microelectronics and VLSI (TENCON 95), 1995, p. 278.
215) M. Glück, A. Schüppen, M. Rösler, W. Heinrich, J. Hersener, U. König, O. Yam, C. Cytermann, and M. Eizenberg, Thin Solid Films **270**, 549 (1995).
216) L. I. Petrova, L. D. Dudkin, M. I. Fedorov, F. Y. Solomkin, V. K. Zaitsev, and I. S. Eremin, Inorg. Mater. **40**, 558 (2004).
217) Y. Thimont, Q. Lognoné, C. Goupil, F. Gascoin, and E. Guilmeau, J. Electron. Mater. **43**, 2023 (2014).
218) H. Fateh, C. A. Baker, M. J. Hall, and L. Shi, Appl. Energy **129**, 373 (2014).
219) X. Shi, Z. Zamanipour, J. S. Krasinski, A. Tree, and D. Vashaee, J. Electron. Mater. **41**, 2331 (2012).
220) T. Nemoto, T. Iida, J. Sato, T. Sakamoto, T. Nakajima, and Y. Takanashi, J. Electron. Mater. **41**, 1312 (2012).
221) T. Nemoto, T. Iida, J. Sato, T. Sakamoto, N. Hirayama, T. Nakajima, and Y. Takanashi, J. Electron. Mater. **42**, 2192 (2013).
222) F. de Winter, G. Stapfer, and E. Medina, IEEE Aerosp. Electron. Syst. Mag. **15**, 5 (2000).
223) J. Sakamoto, T. Caillat, J.-P. Fleurial, S. Jones, J.-A. Paik, and W. Dong, in *Electroceramic Materials and Applications*, ed. R. W. Schwartz (Wiley, Hoboken, NJ, 2006) Ceramic Transactions, Vol. 196, Chap. 27.
224) J. Tani, M. Takahashi, and H. Kido, IOP Conf. Ser.: Mater. Sci. Eng. **18**, 142013 (2011).
225) G. J. Snyder and E. S. Toberer, Nat. Mater. **7**, 105 (2008).
226) T. Takabatake, K. Suekuni, T. Nakayama, and E. Kaneshita, Rev. Mod. Phys. **86**, 841 (2014).
227) T. Koga, X. Sun, S. Cronin, and M. Dresselhaus, Appl. Phys. Lett. **73**, 2950 (1998).
228) O. Rabina, Y. Lin, and M. Dresselhaus, Appl. Phys. Lett. **79**, 81 (2001).
229) Y. Pei, X. Shi, A. LaLonde, H. Wang, L. Chen, and G. J. Snyder, Nature **473**, 66 (2011).
230) P. Norouzzadeh and D. Vashaee, Sci. Rep. **6**, 22724 (2016).
231) P. Norouzzadeh and D. Vashaee, J. Electron. Mater. **44**, 636 (2015).
232) Y. Tang, Z. M. Gibbs, L. A. Agapito, G. Li, H. S. Kim, M. B. Nardelli, S. Curtarolo, and G. J. Snyder, Nat. Mater. **14**, 1223 (2015).
233) P. Norouzzadeh, C. W. Myles, and D. Vashaee, J. Alloys Compd. **587**, 474 (2014).
234) P. Norouzzadeh, J. S. Krasinski, C. W. Myles, and D. Vashaee, Phys. Chem. Chem. Phys. **17**, 8850 (2015).
235) P. Norouzzadeh, C. W. Myles, and D. Vashaee, Sci. Rep. **4**, 7028 (2014).
236) P. Norouzzadeh, C. W. Myles, and D. Vashaee, J. Appl. Phys. **114**, 163509 (2013).

Amin Nozariasbmarz is currently a Ph.D. candidate in Electrical Engineering (nanoelectronics) with a minor degree in Materials Science and Engineering at North Carolina State University. His B.Sc. and M.Sc. degrees are in Materials Science and Engineering from Sharif University of Technology and University of Tehran, respectively. His main research is on nanostructured and decrystallized thermoelectric materials, particularly on p- and n-type SiGe alloy and its nanocomposites for high temperature power generation applications, and p- and n-type bismuth telluride for body heat harvesting. He has published over 20 papers in peer-reviewed scientific journals.

Aditi Agarwal is currently pursuing M.S. in Electrical Engineering at North Carolina State University. Her research is focused on study of nanostructured bulk materials for thermoelectric and thermomagnetic applications, and calculation of transport properties using Monte Carlo method. Her research interests include solid state physics, nanoelectronics and quantum phenomena. She got her undergraduate degree from Delhi Technological University in New Delhi, India.

Zachary A. Coutant is currently an undergraduate student in electrical engineering at NC State University. His current research is related to the fabrication of thin film thermoelectric devices. His academic interests include solid state physics and devices as well as nano-fabrication.

Michael J. Hall received a B.Sc. in Materials Science and Engineering and a Masters in Nano-engineering at NC State University. Currently working toward a Ph.D. in Materials Science, his research is focused on the fabrication of bulk nanocrystalline and amorphous materials and the study of the electrical and thermal properties of these materials.

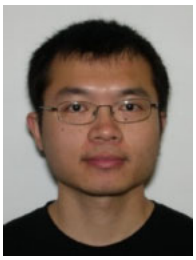

Jie Liu received his Ph.D. degree from Pennsylvania State University in 2013. His Ph.D. work focused on the development of monolithically integrated semiconductor devices by integrating GaN LEDs and Schottky barrier diodes on commercially available LED wafers. He also worked on the investigation of colloidal quantum dot phosphors and LEDs. He obtained his B.S. and M.S. degree in electronics and optical engineering from Tsinghua University, Beijing, China. He joined NCSU as a postdoc in 2015. Currently he is working on development of thin film thermoelectric devices based on SiGe material.

© 2017 The Japan Society of Applied Physics

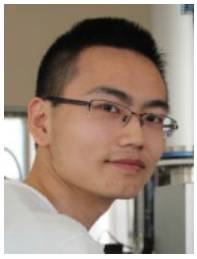

Runze Liu is a Ph.D. student in ECE department, NCSU. Currently he is studying nanostructured n-type bismuth telluride materials.

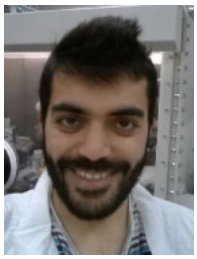

Abhishek Malhotra was born in the town of Jammu in India. He finished his Bachelors of Technology from Manipal Institute of technology, Karnataka in the field of Electronics and Communications. He is presently a Ph.D. student in Electrical Engineering at the North Carolina State University. He is currently working in the field of room temperature bulk thermoelectrics. His research interests include Bulk and Thin film Thermoelectrics, Hydration Sensing and QCMs.

Payam Norouzzadeh received his B.Sc. and M.Sc. degrees in Applied Physics from Sharif University of Technology, and Iran University of Science and Technology, respectively in 1996 and 1999. He received his Ph.D. in Electrical Engineering from Oklahoma State University in 2012 based on his work on application of coherent potential approximation for charge carrier and phonon transport in nanostructured thermoelectrics. He is currently a post-doctoral fellow at Department of Physics and Astronomy, University of Missouri-Columbia working on the application of Density Functional Theory, Molecular Dynamics and Boltzmann Transport Theory for designing novel electronic materials.

Viswanath P. Ramesh completed his Bachelor's degree in Electrical Engineering from Anna University, India in 2013. He is currently working towards a Ph.D. in the Electrical and Computer Engineering specializing in Nanoelectronics and Photonics. His research primarily deals with fabricating flexible Thermoelectric devices for body energy harvesting. His other areas of interest include thin film technology, flexible electronics, MEMS devices, and Aerogel technology.

Yasaman Sargolzaeiaval received her B.Sc. and M.Sc. degrees in Electrical Engineering-Nanoelectronics from Sharif University of Technology in Tehran, Iran, respectively in 2011 and 2013. She worked as a research assistant working on superconductor devices in Superconductor Electronics Research Lab (SERL) in Sharif University for 4 years through her undergraduate and Masters degrees. She is currently a Ph.D. candidate at Department of Electrical and Computer Engineering, North Carolina State University. Her main research activity is fabrication of wearable and flexible thermoelectric generators for body heat harvesting.

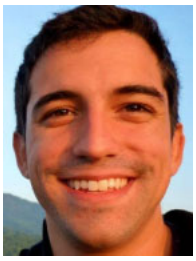

Francisco Suarez completed his Ph.D. in Electrical Engineering from North Carolina State University in 2016. His research was part of the NSF funded Advanced Self-Powered Systems of Integrated Sensors and Technologies (ASSIST) engineering research center, under the direction of Dr. Mehmet C. Oztürk, where he explored the system challenges and design of both rigid and flexible thermoelectric devices for on body wearable power generation. His research interests include renewable energy, energy harvesting, low/self-powered electronics, flexible and stretchable interconnects.

Mehmet C. Ozturk is a graduate of Bogazici University in Istanbul, Turkey in 1980. He received his Ph.D. degree in Electrical Engineering from NC State in 1988. Immediately after graduation, he joined the faculty in his department. He is currently serving as the deputy director of the NSF Sponsored ASSIST Engineering Research Center. Dr. Ozturk's current research interests center around flexible thermoelectric energy harvesting technologies for wearable electronics. He was named an IEEE fellow in 2009 for his contributions in Si and SiGe Epitaxy and their applications in advanced MOS field effect transistors.

Daryoosh Vashaee is an expert in superlattices and nanostructured materials for energy conversion and sensing applications. In the past, he has contributed to the development of several key thermoelectric structures including heterostructure thermionic devices and bulk nanocomposite thermoelectric materials. He is the recipient of the NSF CAREER award and the Goldsmid Award for research excellence in thermoelectrics from the International Thermoelectric Society. He received his Ph.D. from University of California at Santa Cruz in 2004, worked at MIT as postdoctoral scholar, at Oklahoma State University as assistant professor, and joined North Carolina State University ECE department as associate professor in 2014.

© 2017 The Japan Society of Applied Physics